frontiers

RESEARCH TOPICS

NEUROANATOMY AND TRANSGENIC TECHNOLOGIES

Topic Editors
Alexander C. Jackson, Chen Liu, Makoto Fukuda, Michael Lazarus and Laurent Gautron

frontiers in NEUROANATOMY

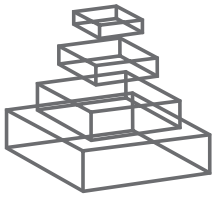

frontiers

ISSN 1664-8714
ISBN 978-2-88919-513-8
DOI 10.3389/978-2-88919-513-8

ABOUT FRONTIERS

Frontiers is more than just an open-access publisher of scholarly articles: it is a pioneering approach to the world of academia, radically improving the way scholarly research is managed. The grand vision of Frontiers is a world where all people have an equal opportunity to seek, share and generate knowledge. Frontiers provides immediate and permanent online open access to all its publications, but this alone is not enough to realize our grand goals.

FRONTIERS JOURNAL SERIES

The Frontiers Journal Series is a multi-tier and interdisciplinary set of open-access, online journals, promising a paradigm shift from the current review, selection and dissemination processes in academic publishing.
All Frontiers journals are driven by researchers for researchers; therefore, they constitute a service to the scholarly community. At the same time, the Frontiers Journal Series operates on a revolutionary invention, the tiered publishing system, initially addressing specific communities of scholars, and gradually climbing up to broader public understanding, thus serving the interests of the lay society, too.

DEDICATION TO QUALITY

Each Frontiers article is a landmark of the highest quality, thanks to genuinely collaborative interactions between authors and review editors, who include some of the world's best academicians. Research must be certified by peers before entering a stream of knowledge that may eventually reach the public - and shape society; therefore, Frontiers only applies the most rigorous and unbiased reviews.
Frontiers revolutionizes research publishing by freely delivering the most outstanding research, evaluated with no bias from both the academic and social point of view.
By applying the most advanced information technologies, Frontiers is catapulting scholarly publishing into a new generation.

WHAT ARE FRONTIERS RESEARCH TOPICS?

Frontiers Research Topics are very popular trademarks of the Frontiers Journals Series: they are collections of at least ten articles, all centered on a particular subject. With their unique mix of varied contributions from Original Research to Review Articles, Frontiers Research Topics unify the most influential researchers, the latest key findings and historical advances in a hot research area!
Find out more on how to host your own Frontiers Research Topic or contribute to one as an author by contacting the Frontiers Editorial Office: researchtopics@frontiersin.org

NEUROANATOMY AND TRANSGENIC TECHNOLOGIES

Topic Editors:
Alexander C. Jackson, University of Connecticut
Chen Liu, University of Texas Southwestern Medical Center at Dallas Dallas, USA
Makoto Fukuda, Baylor College of Medicine, USA
Michael Lazarus, Tsukuba University, Japan
Laurent Gautron, UTSouthwestern Medical Center, USA

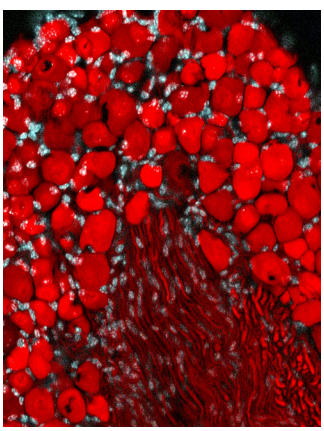

Fluorescently tagged nodose ganglion neurons (red somas) from a Phox2b-cre-tdTomato mouse. Tissue was counterstained with DAPI (white nuclei).

Neuroanatomists increasingly rely on techniques enabling them to manipulate genes in defined brain cell populations. In particular, engineered transgenes, which encode a variety of fluorescent reporter proteins can be inserted into the genome or delivered into desired brain regions using viral vectors, thereby allowing the labeling of molecularly-defined populations of neurons and/or glial cells. Transgenic technology can also be used to selectively delete genes in targeted neuronal populations or bi-directionally modulate their electrical excitability using optogenetic or chemogenetic techniques. One of the primary advantages of using transgenic reagents is to simplify the identification and tracing of targeted population of brain cells, which can be laborious using traditional techniques in neuroanatomy. In this research topic, we assembled up-to-date reviews and original articles that demonstrate the versatility and power of transgenic tools in advancing our knowledge of the nervous system, with a special emphasis on the application of transgenic technology to neuroanatomical questions.

Table of Contents

frontiers in
NEUROANATOMY

EDITORIAL
published: 21 January 2015
doi: 10.3389/fnana.2014.00157

Neuroanatomy and transgenic technologies

Alexander C. Jackson[1], Chen Liu[2], Makoto Fukuda[3], Michael Lazarus[4] and Laurent Gautron[2]*

[1] *Department of Physiology and Neurobiology, University of Connecticut, Storrs, CT, USA*
[2] *Division of Hypothalamic Research, Department of Internal Medicine, University of Texas Southwestern Medical Center, Dallas, TX, USA*
[3] *Baylor College of Medicine, Childrens Nutrition Research Ct, Houston, TX, USA*
[4] *International Institute for Integrative Sleep Medicine (WPI-IIIS), University of Tsukuba, Tsukuba, Japan*
**Correspondence: laurent.gautron@utsouthwestern.edu*

Edited and reviewed by:
Javier DeFelipe, Cajal Institute, Spain

Keywords: mouse models, transgenic, tracing, morphology, neurochemistry

Gerald Edelman once wrote: "If someone held a gun to my head and threatened oblivion if I did not identify the single word most significant for understanding the brain, I would say 'neuroanatomy.' Indeed, perhaps the most important general observation that can be made about the brain is that its anatomy is the most important thing about it" (Edelman and Tononi, 2000).

Neuroscientists increasingly rely on techniques enabling them to manipulate genes in defined cell populations in the brain. In particular, engineered transgenes, which encode a variety of fluorescent reporter proteins, can be inserted into the genome or delivered into desired brain regions using viral vectors, thereby allowing the labeling of molecularly-defined populations of neurons or glial cells (Callaway, 2005). Transgenic technology can also be used to selectively delete genes in genetically-targeted cell populations (Nagy, 2000) or bi-directionally modulate electrical excitability using optogenetic or chemogenetic techniques (Aston-Jones and Deisseroth, 2013). One of the primary advantages of using transgenic reagents is to simplify the identification of targeted populations of neurons and their projections, which can be laborious using traditional techniques in neuroanatomy. In this research topic, we will be focusing on the application of transgenic technology to neuroanatomical questions and have collected up-to-date reviews and original articles that demonstrate the versatility and power of transgenic tools in advancing our knowledge of the nervous system. Kou et al. (2013) used a GAD67-GFP transgenic mouse to examine changes in components of GABAergic neurotransmission among neuronal populations in the dorsal cochlear nucleus, in a mouse model of noise-induced hearing loss. This was complemented by the article of Zhang et al. (2013), characterizing the efferent projections of adenosine A_{2A} receptor-expressing neurons in the nucleus accumbens using a virally-mediated anterograde tracing method in adenosine A_{2A} receptor-cre mice. In addition to its utility in tagging and tracing targeted neuronal populations, transgenic technology can be applied to the study of morphological and neurochemical changes occurring in the brains of animals lacking a specific gene. For instance, Xu et al. (2014) examined changes in CART expression in neurons of the Edinger–Westphal nucleus in leptin receptor deficient mice.

Needless to say, the study of the peripheral nervous system has also greatly benefited from the aforementioned transgenic tools (Braz et al., 2014). Several articles included in this research topic focused on the peripheral nervous system. We highly recommend the reading of the article by Le Pichon and Chesler (2014), as it is a comprehensive and thoughtful review entirely dedicated to mouse models useful for the manipulation and categorization of somatosensory neurons in the dorsal root ganglion. Many investigators and clinicians are also interested in identifying new ways of delivering transgenes, particularly ones with therapeutic value, to the brain by targeting neurons in the peripheral nervous system. In fact, it has been suggested that virally-mediated gene delivery to the human brain may have the potential to treat numerous neurological diseases (Janson et al., 2002). Three articles in this research topic highlighted the versatility of virally-mediated gene delivery to peripheral pathways. The original articles by Schuster et al. (2014a,b) and Salegio et al. (2014) described the central distribution of intrathecally-delivered adeno-associated viruses expressing reporter proteins. Finally, the article by Jara et al. (2014) focused on approaches for the retrograde labeling of spinal motor neurons using reporter proteins.

In spite of the growing number of sophisticated tools available to neuroscientists, currently available tools greatly limit our ability to collect high resolution images encompassing large areas of the mammalian nervous system (Lichtman and Denk, 2011). The opinion article by Pabba (2013) briefly discussed how the anatomical organization of the central nervous system, with a special emphasis on the amygdaloid complex, has increased in complexity during the course of evolution, while conserving a common basic plan, recognizable across animal species. Henceforth, studying the nervous system of lower organisms is immediately relevant to the understanding of the basic principles governing the anatomical organization of the mammalian nervous system (Amat et al., 2014). This research topic included two original articles focusing on the zebrafish nervous system. Using a zebrafish transgenic line expressing eGFP, Djenoune et al. (2014) described a poorly characterized group of specialized neurons that make contact with the cerebrospinal fluid. This was complemented by an article by Lopez-Schier et al. (Pinto-Teixeira et al., 2013) describing a novel method for the visualization of sensory hair-cell regeneration in the lateral line of transgenic zebrafish larvae using selective plane illumination microscopy (SPIM). The technique described in this latter article offers a unique model for the study of neuroplasticity in a living organism.

In summary, the anatomical complexity of the nervous system remains a subject of tremendous fascination among neuroscientists. Unraveling the myriad cells and circuits in the nervous system is as much a pressing question now as it was over 100 years ago in the time of Cajal and Golgi. In order to tackle this extraordinary complexity, powerful transgenic technologies are continually being developed, improved upon and used in the study of such diverse questions as cell lineage mapping, neural tract tracing, protein trafficking, neuronal excitability and morphological plasticity of dendritic spines and axonal arbors. In addition to giving neuroscientists an update on these rapidly evolving techniques used in neuroanatomy, we hope that the articles included in this research topic will spark new ideas among investigators interested in the "most important thing" about the brain—its anatomy.

REFERENCES

Amat, F., Lemon, W., Mossing, D. P., McDole, K., Wan, Y., Branson, K., et al. (2014). Fast, accurate reconstruction of cell lineages from large-scale fluorescence microscopy data. *Nat. Methods* 11, 951–958. doi: 10.1038/nmeth.3036

Aston-Jones, G., and Deisseroth, K. (2013). Recent advances in optogenetics and pharmacogenetics. *Brain Res.* 1511, 1–5. doi: 10.1016/j.brainres.2013.01.026

Braz, J., Solorzano, C., Wang, X., and Basbaum, A. I. (2014). Transmitting pain and itch messages: a contemporary view of the spinal cord circuits that generate gate control. *Neuron* 82, 522–536. doi: 10.1016/j.neuron.2014.01.018

Callaway, E. M. (2005). Neural substrates within primary visual cortex for interactions between parallel visual pathways. *Prog. Brain Res.* 149, 59–64. doi: 10.1016/S0079-6123(05)49005-6

Djenoune, L., Khabou, H., Joubert, F., Quan, F. B., Nunes Figueiredo, S., Bodineau, L., et al. (2014). Investigation of spinal cerebrospinal fluid-contacting neurons expressing PKD2L1: evidence for a conserved system from fish to primates. *Front. Neuroanat.* 8:26. doi: 10.3389/fnana.2014.00026

Edelman, G., and Tononi, G. (2000). *A Universe of Consciousness: How Matters Becomes Imagination*. New York, NY: Basic Books.

Janson, C., McPhee, S., Bilaniuk, L., Haselgrove, J., Testaiuti, M., Freese, A., et al. (2002). Clinical protocol. Gene therapy of Canavan disease: AAV-2 vector for neurosurgical delivery of aspartoacylase gene (ASPA) to the human brain. *Hum. Gene Ther.* 13, 1391–1412. doi: 10.1089/104303402760128612

Jara, J. H., Genc, B., Klessner, J. L., and Ozdinler, P. H. (2014). Retrograde labeling, transduction, and genetic targeting allow cellular analysis of corticospinal motor neurons: implications in health and disease. *Front. Neuroanat.* 8:16. doi: 10.3389/fnana.2014.00016

Kou, Z. Z., Qu, J., Zhang, D. L., Li, H., and Li, Y. Q. (2013). Noise-induced hearing loss is correlated with alterations in the expression of GABAB receptors and PKC gamma in the murine cochlear nucleus complex. *Front. Neuroanat.* 7:25. doi: 10.3389/fnana.2013.00025

Le Pichon, C. E., and Chesler, A. T. (2014). The functional and anatomical dissection of somatosensory subpopulations using mouse genetics. *Front. Neuroanat.* 8:21. doi: 10.3389/fnana.2014.00021

Lichtman, J. W., and Denk, W. (2011). The big and the small: challenges of imaging the brain's circuits. *Science* 334, 618–623. doi: 10.1126/science.1209168

Nagy, A. (2000). Cre recombinase: the universal reagent for genome tailoring. *Genesis* 26, 99–109. doi: 10.1002/(SICI)1526-968X(200002)26:2<99::AID-GENE1>3.0.CO;2-B

Pabba, M. (2013). Evolutionary development of the amygdaloid complex. *Front. Neuroanat.* 7:27. doi: 10.3389/fnana.2013.00027

Pinto-Teixeira, F., Muzzopappa, M., Swoger, J., Mineo, A., Sharpe, J., and Lopez-Schier, H. (2013). Intravital imaging of hair-cell development and regeneration in the zebrafish. *Front. Neuroanat.* 7:33. doi: 10.3389/fnana.2013.00033

Salegio, E. A., Streeter, H., Dube, N., Hadaczek, P., Samaranch, L., Kells, A. P., et al. (2014). Distribution of nanoparticles throughout the cerebral cortex of rodents and non-human primates: implications for gene and drug therapy. *Front. Neuroanat.* 8:9. doi: 10.3389/fnana.2014.00009

Schuster, D. J., Belur, L. R., Riedl, M. S., Schnell, S. A., Podetz-Pedersen, K. M., Kitto, K. F., et al. (2014b). Supraspinal gene transfer by intrathecal adeno-associated virus serotype 5. *Front. Neuroanat.* 8:66. doi: 10.3389/fnana.2014.00066

Schuster, D. J., Dykstra, J. A., Riedl, M. S., Kitto, K. F., Belur, L. R., McIvor, R. S., et al. (2014a). Biodistribution of adeno-associated virus serotype 9 (AAV9) vector after intrathecal and intravenous delivery in mouse. *Front. Neuroanat.* 8:42. doi: 10.3389/fnana.2014.00042

Xu, L., Janssen, D., van der Knaap, N., Roubos, E. W., Leshan, R. L., Myers, M. G. Jr., et al. (2014). Integration of stress and leptin signaling by CART producing neurons in the rodent midbrain centrally projecting Edinger-Westphal nucleus. *Front. Neuroanat.* 8:8. doi: 10.3389/fnana.2014.00008

Zhang, J. P., Xu, Q., Yuan, X. S., Cherasse, Y., Schiffmann, S. N., de Kerchove d'Exaerde, A., et al. (2013). Projections of nucleus accumbens adenosine A2A receptor neurons in the mouse brain and their implications in mediating sleep-wake regulation. *Front. Neuroanat.* 7:43. doi: 10.3389/fnana.2013.00043

Conflict of Interest Statement: The authors declare that the research was conducted in the absence of any commercial or financial relationships that could be construed as a potential conflict of interest.

Received: 25 November 2014; accepted: 02 December 2014; published online: 21 January 2015.

Citation: Jackson AC, Liu C, Fukuda M, Lazarus M and Gautron L (2015) Neuroanatomy and transgenic technologies. Front. Neuroanat. ***8****:157. doi: 10.3389/fnana.2014.00157*

This article was submitted to the journal Frontiers in Neuroanatomy.

frontiers in
NEUROANATOMY

ORIGINAL RESEARCH ARTICLE
published: 30 July 2013
doi: 10.3389/fnana.2013.00025

Noise-induced hearing loss is correlated with alterations in the expression of $GABA_B$ receptors and PKC gamma in the murine cochlear nucleus complex

Zhen-Zhen Kou[1†], Juan Qu[1,2†], Dong-Liang Zhang[1], Hui Li[1]* and Yun-Qing Li[1]*

[1] *Department of Anatomy, Histology and Embryology, K. K. Leung Brain Research Centre, The Fourth Military Medical University, Xi'an, China*
[2] *Department of Otolaryngology, Xijing Hospital, The Fourth Military Medical University, Xi'an, China*

Edited by:
Alexander C. Jackson, University of California, San Francisco, USA

Reviewed by:
Jun Lu, Harvard Medical School, USA
Alan R. Palmer, Medical Research Council Institute of Hearing Research, UK

****Correspondence:***
Hui Li and Yun-Qing Li, Department of Anatomy, Histology and Embryology, K. K. Leung Brain Research Centre, The Fourth Military Medical University, No. 169, West Changle Road, Xi'an 710032, China
e-mail: li_hui@fmmu.edu.cn; deptanat@fmmu.edu.cn
† These authors have contributed equally to this work.

Noise overexposure may induce permanent noise-induced hearing loss (NIHL). The cochlear nucleus complex (CNC) is the entry point for sensory information in the central auditory system. Impairments in gamma-aminobutyric acid (GABA)—mediated synaptic transmission in the CNC have been implicated in the pathogenesis of auditory disorders. However, the role of protein kinase C (PKC) signaling pathway in GABAergic inhibition in the CNC in NIHL remains elusive. Thus, we investigated the alterations of glutamic acid decarboxylase 67 (GAD67, the chemical marker for GABA-containing neurons), PKC γ subunit (PKCγ) and $GABA_B$ receptor ($GABA_BR$) expression in the CNC using transgenic GAD67-green fluorescent protein (GFP) knock-in mice, BALB/c mice and C57 mice. Immunohistochemical results indicate that the GFP-labeled GABAergic neurons were distributed in the molecular layer (ML) and fusiform cell layer (FCL) of the dorsal cochlear nucleus (DCN). We found that 69.91% of the GFP-positive neurons in the DCN were immunopositive for both PKCγ and $GABA_BR1$. The GAD67-positive terminals made contacts with PKCγ/$GABA_BR1$ colocalized neurons. Then we measured the changes of auditory thresholds in mice after noise exposure for 2 weeks, and detected the GAD67, PKCγ, and $GABA_BR$ expression at mRNA and protein levels in the CNC. With noise over-exposure, there was a reduction in $GABA_BR$ accompanied by an increase in PKCγ expression, but no significant change in GAD67 expression. In summary, our results demonstrate that alterations in the expression of PKCγ and $GABA_BRs$ may be involved in impairments in GABAergic inhibition within the CNC and the development of NIHL.

Keywords: CNC, GABA, $GABA_BR$, PKCγ, GAD67-GFP knock-in mice

INTRODUCTION

Human exposure to excessive noise has been linked to noise-induced hearing loss (NIHL) (Chung et al., 2005). Recent studies have suggested that noise overexposure potentially results in auditory threshold shifts in young adult animals via a series of neuroplastic changes in central auditory structures (Fritschy et al., 2008; Wang et al., 2009a).

The cochlear nucleus complex (CNC) occupies a pivotal position in the hierarchy of functional processes leading to convergence of auditory information. The CNC can be divided into the dorsal cochlear nucleus (DCN) and the ventral cochlear nucleus (VCN). The DCN receives peripheral afferents and sets up processing pathways into the inferior colliculus (IC). The DCN forms a layered structure: the molecular layer (ML), the fusiform cell layer (FCL), and the deep layer (DL) (Osen, 1969).

As shown in **Figure 7**, in the ML and FCL of the DCN, the glutamatergic fusiform cells receive inputs from auditory nerve afferents and parallel fibers, and project to the IC (Osen, 1969; Browner and Baruch, 1982). The inhibitory interneurons, GABA-containing cartwheel cells receive parallel fibers and make contacts on fusiform cells and other cartwheel cells (Nelson, 2004). The auditory nerve conducts auditory signals from the inner ear, and the parallel fibers integrate the multimodal sensory inputs, which encode proprioceptive information about the sound source and/or the suppression of body-generated sounds or vocal feedback (Nelson, 2004). It has been confirmed that noise overexposure alters synaptic transmission originating from both auditory nerve and parallel fibers within the DCN (Shore et al., 2008; Shore, 2011). Moreover, in auditory disorders, including hearing loss and tinnitus, dysfunction of the DCN, particularly in the neuronal circuitry of the ML and FCL has been linked to the disruption of GABAergic inhibition (Ling et al., 2005; Middleton et al., 2011).

Elucidating the intracellular mechanisms underlying long-term synaptic changes in the CNC is critical to understanding the development of auditory disorders (Chang et al., 2003). A group of key enzymes involved in intracellular signal transduction cascades are the family of phospholipid-dependent kinases, the protein kinases C (PKC). Although at least 10 isoenzymes have been described, the gamma subtype of PKC (PKCγ) is calcium-dependent and exclusively expressed in neurons in the central nervous system (CNS) (Tanaka and Nishizuka, 1994; Saito and Shirai, 2002; Ding et al., 2005). PKCγ is activated by diacylglycerol (DAG) and Ca^{2+} in the presence of phosphatidylserine. PKCγ has

been demonstrated to play a significant role in the neuroplasticity of the auditory pathway, particularly in the DCN (Tanaka and Nishizuka, 1994; Saito and Shirai, 2002; Kou et al., 2011). However, little is known about the possible relationship between the PKCγ signaling pathway and GABAergic inhibition in the DCN, particularly in NIHL.

It is reported that gamma-aminobutyric acid is synthesized by two glutamic acid decarboxylases (GAD): GAD67 and GAD65 (Pinal and Tobin, 1998), which readily influence the cellular and vesicular GABA content (Murphy et al., 1998; Engel et al., 2001). Between the two isoforms, GAD67 is responsible for over 90% of basal GABA synthesis and is produced at limiting levels in the CNS (Asada et al., 1997; Chattopadhyaya et al., 2007). Because there is a lack of suitable reagents to positively identify GABAergic neurons, GAD67-GFP knock-in mice have been used to reveal many (if not most) GABAergic neurons in brain.

GABA mediates its inhibitory effects by activating GABA receptors, including GABAA receptors ($GABA_ARs$) and $GABA_B$ receptors ($GABA_BRs$) (Jones et al., 1998; Kaupmann et al., 1998). It has been reported that in the CNC, $GABA_AR$ was unchanged after acoustic injury (Song and Messing, 2005; Dong et al., 2010). In contrast, NIHL has been reported to be associated with the reduced $GABA_BR$-mediated GABAergic inhibition in IC and auditory cortex. However, there is little information regarding the expression of $GABA_BRs$ in the DCN following NIHL (Szczepaniak and Moller, 1995; Aizawa and Eggermont, 2006).

To better understand how PKCγ in GABAergic inhibition might function within the CNC, we studied the distribution patterns of GAD67, PKCγ and $GABA_BRs$ in the CNC, particularly in the DCN. Then we investigated whether GAD67, PKCγ and $GABA_BRs$ were correlated with NIHL.

For this purpose, we first specified the exact localizations of GAD67, PKCγ, and $GABA_BRs$ in the CNC. Because BALB/c mice and C57 mice are vulnerable to NIHL (Ohlemiller et al., 2000), then we used the two strains to detect the alterations of GAD67, PKCγ, and $GABA_BR$ expression at both mRNA and protein levels in NIHL.

METHODS

SUBJECTS

Because of the limited ability to identify the GABAergic neurons in brainstem with the use of antibodies against GABA or GAD (Sloviter and Nilaver, 1987; Sloviter et al., 2001) and GAD67 is responsible for over 90% of basal GABA synthesis in brain, we revealed the localization of GABAergic neurons in the CNC by employing the GAD67-GFP knock-in mice, in which the GAD67 mRNA is colocalized with GFP, and GFP is expressed in GABAergic neurons (Tamamaki et al., 2003; Huang et al., 2008; Han et al., 2010). The generation of GAD67-GFP knock-in mice has been reported previously and used widely for detecting GABAergic neurons (Tamamaki et al., 2003; May et al., 2008; Young and Sun, 2009; Chen et al., 2010; Han et al., 2010; Bang and Commons, 2012). In our studies, the mice were housed in standard conditions (12 h light/dark cycles) with water and food available *ad libitum*. Both young C57 and BALB/c mice are especially vulnerable to noise (Ohlemiller et al., 2000). In the present study, 6 young (2-month-old) male GAD67-GFP knock-in mice (C57 genetic background), 30 C57 mice (2-month-old) and 30 BALB/c mice (2-month-old) weighing 25–30 g were utilized. The Animal Care and Use Committees of the Fourth Military Medical University reviewed and approved all protocols.

IMMUNOHISTOCHEMISTRY

The mice were anesthetized and perfused for microscopy examination. Briefly, after deeply anaesthetizing by intraperitoneal injection of pentobarbital sodium (5 mg/100 g for mice), we perfused the mice with 80 ml of 4% (w/v) formaldehyde in 0.1 M PB as a fixative and post-fixed at 4°C for 4 h. The brainstems were obtained from 6 GAD67-GFP knock-in mice, 6 C57 mice and 6 BALB/c mice respectively, and then stored in 30% (w/v) sucrose solution in 0.05 M phosphate-buffered saline (PBS; pH 7.4) overnight at 4°C. The tissues were cut into transverse 20 μm thick serial sections in a cryostat (Leica CM1800, Germany), and used for immunofluoresence and Nissl staining (Hefti, 1986; Zhao et al., 2001).

The immunofluoresence protocol was performed as follows: the sections were blocked within 10% normal goat serum for 1 h. Triple-labeling fluorescent immunohistochemistry for GFP/$GABA_BR1$/PKCγ was performed in GAD67-GFP knock-in mice. In order to identify the localization of GAD67-positive terminals specifically, we also did immunohistochemistry for GAD67/$GABA_BR1$/PKCγ in C57 mice and BALB/c mice. The primary antibodies for triple-labeling fluorescent immunohistochemistry includes mouse antisera against GFP (1:500 dilution; Chemicon, Temecula, CA) or mouse antisera against GAD67 (1:500 dilution; Chemicon, Temecula, CA), guinea pig antisera against $GABA_BR1$ (1:1000; Chemicon, Temecula, CA) and rabbit antisera against PKCγ (1:1000 dilution; Santa Cruz Biotechnology, Santa Cruz, CA). The sections were incubated with the primary antibodies for 48 h at 4°C. Then, after rinsing with 0.01 M PBS, the sections were incubated with species-specific secondary antibodies overnight in solutions containing: Alexa488-conjugated donkey anti-mouse IgG (1:500 dilution; Invitrogen, Carlsbad, CA), Alexa594-conjugated donkey anti-guinea pig IgG (1:500 dilution; Invitrogen, Carlsbad, CA) and Alexa647-conjugated donkey anti-rabbit IgG (1:500 dilution; Invitrogen, Carlsbad, CA). Finally, the sections were rinsed with 0.01 M PBS, mounted onto clean glass slides, air-dried and cover slipped with a mixture of 0.05 M PBS containing 50% (v/v) glycerin and 2.5% (w/v) triethylenediamine. The sections were observed under a confocal laser scanning microscope (FV-1000, Olympus, Japan), using appropriate laser beams and filters.

NOISE EXPOSURE

Noise exposure was performed in a double-walled sound attenuating room as described in previous studies (Ohlemiller et al., 1999; Han et al., 2009; Groschel et al., 2010). 24 BALB/c mice and 24 C57 mice were placed in two ventilated chambers, respectively. The mice had free access to food and water, and were acclimated to the environment for 1 week. Then 12 BALB/c mice and 12 C57 mice were exposed to a noise (4 kHz octave band, 110 dB SPL), 8 h per day for 14 days. The same number of mice was used as controls. Control mice were placed in the noise booth but not exposed to noise. In order to develop a noise-induced lesion, a

RadioShack Supertweeter was attached to the top of the cages and driven by a power amplifier (Yamaha AX-500U, Japan) and a loudspeaker. The noise was amplified with noise levels being measured with a sound level meter (Bruel and Kjaer, type 2606). The noise level variation was less than 2 dB within the space available to the animals.

AUDITORY BRAINSTEM RESPONSE

Auditory brainstem response (ABR) was measured in the form of two blind tests at 1 day before noise exposure to determine the baseline and 14 days afterwards to determine auditory thresholds in each group as previously (Han et al., 2009; Kou et al., 2011; Lin et al., 2011; Qu et al., 2012). A previous study confirmed that after noise exposure for 14 days, the mice suffered from NIHL (Ohlemiller et al., 1999). Briefly, mice were anaesthetized with an injection of pentobarbital sodium (5 mg/100 g, i.p.) and the body temperatures were maintained at 37°C with a warm pad. The needle electrodes were inserted subcutaneously behind the pinna of the measured ear (active), at the vertex (reference) and in the back (ground). The stimulus signal was generated through Intelligent Hearing Systems (Bio-logic Systems, USA) which was controlled by computer and delivered by a Telephonics earphone (TDH 39, USA). Evoked responses to the ABR click stimuli were recorded and the thresholds were obtained for two ears. The stimulus signal was generated through an Intelligent Hearing Systems device (Bio-logic Systems, USA) controlled by a computer and delivered by an earphone. Stimuli (1-ms duration) were presented at a repetition rate of 10/s. The raw ABR waveforms were filtered from 100–3000 Hz bandwidth (Han et al., 2011, 2012; Li et al., 2011). Potentials were sent to a computer where the average waveform in response to 1024 sweeps was displayed. ABRs were obtained using descending intensity steps beginning at 80 dB sound pressure level (SPL) with steps of 5 dB and ending when visually discernible ABR waveforms could no longer be detected (Turner and Willott, 1998; Willott and Turner, 1999). Thresholds were then defined as the lowest intensity level at which a clear waveform was visible in the evoked trace.

REAL-TIME PCR

After deeply anesthetizing the mice, the fresh CNCs of mice in each group ($n = 6$) were harvested. Total RNA was extracted with Trizol reagent (Gibco BRL, USA) according to the manufacturer's instructions to synthesize single-stranded complementary DNA (cDNA). 2 μg of total RNA were subjected to reverse transcription reaction. The cDNA synthesis was performed using a synthesis kit (RR037A, TakaRa, Japan). The sequences of the primers for Real-Time PCR are listed in **Figure 5A**, in which glyceraldehyde 3-phosphate dehydrogenase (GAPDH) was selected as the housekeeping gene. For the amplification, 2 μg cDNA was prepared with the SYBR@Premix Ex Taq™ (RR041A, TakaRa, Japan) and performed in a Real-Time PCR detection system (Applied Biosystems™, USA). The amplification protocols included 3 min at 95°C, denaturating at 95°C for 5 s by 40 cycles and annealing and extension at 60°C for 30 s. Calibrated and non-template controls were included in each assay. In each experiment, PCR reactions were done in triplicate and repeated three times in order to measure statistically valid results. Melting curve analysis was always performed at the end of each PCR assay. For the comparison of each gene, each relative mRNA expression was calculated with the following formula: $2^{-\text{deltadeltaCt}}$ (Livak and Schmittgen, 2001). The $2^{-\text{deltadeltaCt}}$ method is a valid way to analyze the relative changes in gene expression from real-time quantitative PCR (Lehrke et al., 2004; Pinto et al., 2011; Su et al., 2011). The threshold cycle (C_t) indicates the fractional cycle number at which the amount of amplified target reaches a fixed threshold. The deltadeltaCt defined as the difference in Ct values between experimental and control samples. For calibration, the control sample in each group was used and set to 100%.

WESTERN BLOTTING

Because it is difficult to isolate the DCN from the CNC, and the results from immunohistochemistry indicated that the GFP/$GABA_BR1$/PKCγ only distributed in the superficial layer of the DCN, not in the VCN, we harvested the whole fresh CNCs from anesthetized mice ($n = 6$ in each group). All procedures were performed on ice. Briefly, the materials were lysed in Eppendorf tube with 10 volumes of 50 mM Tris-HCl (pH 7.4), containing 300 mM NaCl, 1% Nonidet P-40, 10% Glycerol, 1 mM EDTA, 1 mM Na_3VO_4 and protease inhibitor cocktail (Roche, Switzerland). Then, the homogenized samples were centrifuged at 12,000 × g for 10 min at 4°C. Next, the lysate protein concentrations were determined with a BCA protein assay kit (Pierce, USA), and mixed with 5 × sodium dodecyl sulfate (SDS) sample buffer; boiled for 10 min. Equal samples of protein were electrophoresed by SDS-PAGE in 10% polyacrylamide gel. After electrophoretic transfer to nitrocellulose membrane, the blots were blocked with a blocking buffer (5% nonfat dry milk in TBS-T) for 2 h at room temperature and then incubated with primary antibodies diluted in 5% nonfat dry milk in TBS-T overnight at 4°C. The following primary antibodies were used: mouse antisera against GAD67, guinea pig antisera against $GABA_BR1$, guinea pig antisera against $GABA_BR2$ (1:500; Chemicon, Temecula, CA) and rabbit antisera against PKCγ. After incubation of the membrane with peroxidase-conjugated anti-rabbit secondary antibodies (Santa Cruz Biotechnology, Santa Cruz, CA) for 2 h at room temperature, the reaction products were visualized with enhanced chemiluminescence (Amersham Life Science, Amersham, UK).

STATISTICAL ANALYSIS

All data were subjected to statistical analysis using one-way ANOVA. Results are expressed as mean ± SEM by SPSS 13.0 (SPSS Inc.). The differences between groups were considered as statistically significant at a value of $p < 0.05$.

RESULTS

IMMUNOHISTOCHEMICAL DETECTION OF GFP, GAD67, $GABA_BR1$s, AND PKCγ IN THE CNC

Our studies indicate the localization of GABAergic neurons in the CNC by employing the GAD67-GFP knock-in mouse, in which GFP is specifically expressed in GABAergic neurons (Tamamaki et al., 2003; Li et al., 2005; Huang et al., 2008; Huo et al., 2009; Han et al., 2010).

Confocal microscopy revealed an intense band of immunolabeling for the GFP-labeled neurons in the ML and FCL of the

DCN (**Figures 1A–C**). The diameter of the GFP-labeled neurons is between 10 and 15 μm (**Figures 1B,D**). Occasionally, labeled neurons could be seen in the DL of the DCN (**Figures 1A,C**). In the VCN, the GFP-positive neurons were virtually absent (**Figure 2**).

It is believed that heterodimeric assemblies of GABA$_B$R1 and GABA$_B$R2 subunits are required to form full functional receptors (Jones et al., 1998; Kaupmann et al., 1998; White et al., 1998). It has been confirmed that GABA$_B$R1 is colocalized with GABA$_B$R2 in brain, including the CNC (Lujan et al., 2004). Thus, the antibody used in the present study was a useful tool for detecting heteromeric assembly for the functional GABA$_B$Rs. In the present study, the immunoreactivities for GABA$_B$R1 were scattered throughout the CNC, including both DCN and VCN (**Figures 1**, **2**). However, the immunolabeling for GABA$_B$R1 was most obvious in the ML and FCL of the DCN and gradually decreased to the DL (**Figures 1A,C**). In the VCN, the staining for GABA$_B$R1-positive neurons was much weaker than in the DCN (**Figure 2**). We found that 53.81% of GABA$_B$R1-positive neurons were GFP/GABA$_B$R1/PKCγ triple-labeled neurons (**Table 1**). In addition, the GABA$_B$R1-positive terminals were observed as punctate labeling in the DCN (**Figures 1C,D**).

Our previous work revealed the specific distribution pattern of PKCγ in the mouse DCN (Kou et al., 2011). The PKCγ-positive cells were abundant in the DCN with moderate to strong staining in the ML and FCL, demonstrating an overlapping pattern with the GFP-labeled neurons (**Figures 1A,C**). The immunoreactivities for PKCγ were detected in the cell bodies and the processes of neurons (**Figures 1B,D,E**). We found that 85.95% of PKCγ-positive neurons were GFP/GABA$_B$R1/PKCγ triple-labeled neurons (**Table 1**).

In GAD67-GFP knock-in mice, strong coexpression of GABA$_B$R1 and PKCγ in the GFP-labeled neurons was observed in the ML and FCL of the DCN (**Figure 1**). We found that 90.43 and

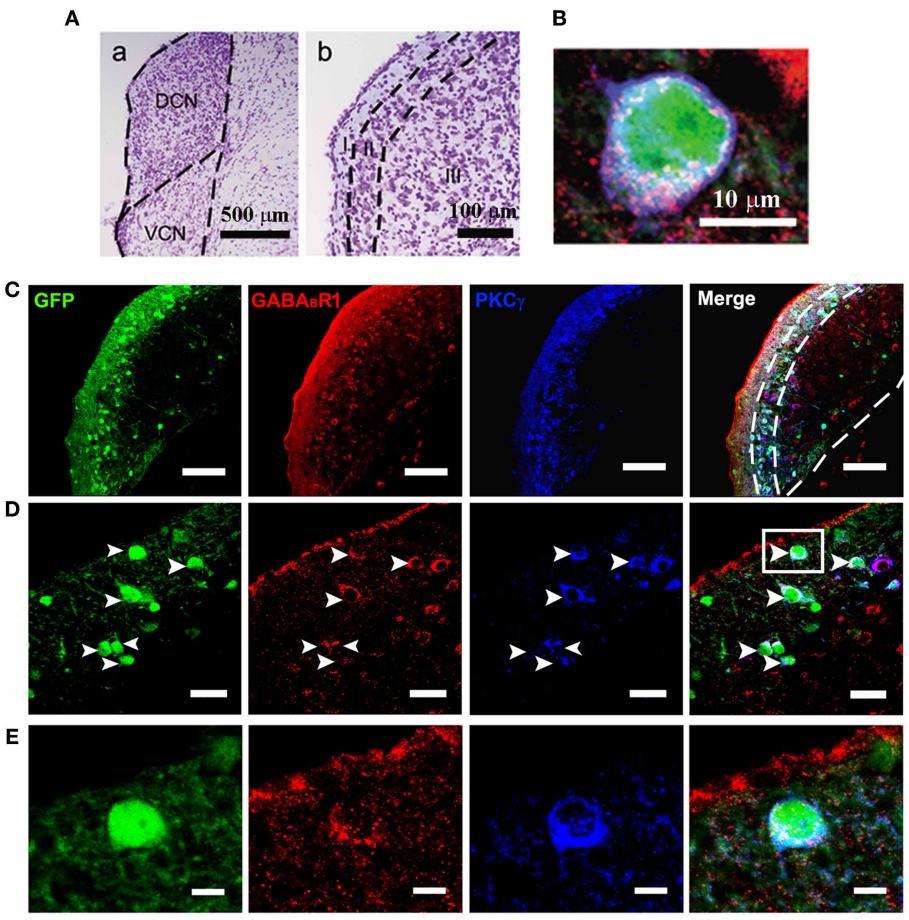

FIGURE 1 | Photomicrographs representing sections of the brainstem of GAD67-GFP knock-in mice in the DCN. Nissl staining in the CNC **(A)** showing the dorsal part (DCN) and the ventral part (VCN) (a in **A**). The DCN organized into a layered structure (b in **A**): the molecular layer (I), the fusiform cell layers (II) and the deep layer (III). Triple-labeled neurons for GFP/GABA$_B$R1/PKCγ were shown **(B)**. Fluorescent photomicrographs showing the distribution of the GFP-labeled (green), GABA$_B$R1-positive (red) and PKCγ-positive (blue) cells in the molecular layer and fusiform cell layer of the DCN of the GAD67-GFP knock-in mice **(C)**. The arrowheads indicate the triple-labeled neurons for GFP/GABA$_B$R1/PKCγ shown in **(D)**. The GABA$_B$R1-immunoreactivities are located at the GFP-labeled GABAergic neurons which contain PKCγ (**E**, higher magnification areas, inserted panels in **D**). Scale bar: 500 μm in **(A**a**)**; 100 μm in **(A**b**)**; 10 μm in **(B)**; 100 μm in **(C)**; 30 μm in **(D)**; 10 μm in **(E)**.

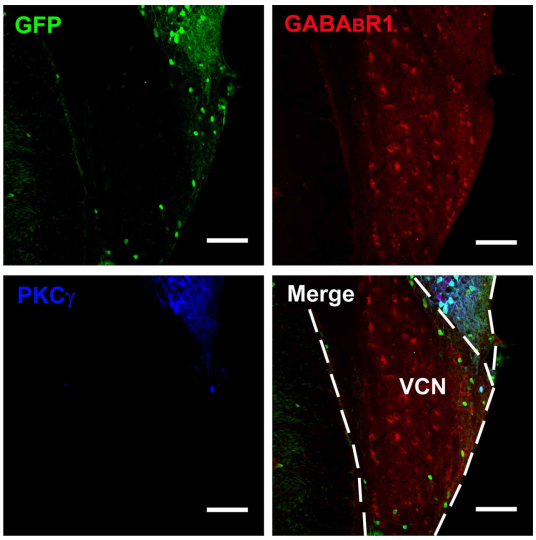

FIGURE 2 | Photomicrographs representing sections of the brainstem of GAD67-GFP knock-in mice in the VCN. Fluorescent photomicrographs showing the distribution of GFP (green), $GABA_BR1$-positive (red), and PKCγ-positive (blue) cells in the VCN of the GAD67-GFP knock-in mice. Triple-labeled neurons for GFP/$GABA_BR1$/PKCγ were rare in the VCN. The bottom of the DCN can also be observed. Scale bar: 100 μm.

Table 1 | The numbers of neurons immunopositive for GFP, $GABA_BR1$, PKCγ, and triple-labeled neurons in CNC of the GAD67-GFP transgenic mice.

	CNC
(1) GFP^+ neuron (mean ± S.E.M.)	1243 ± 57.15
(2) $GABA_BR1^+$ neuron (mean ± S.E.M.)	1615 ± 27.28
(3) $PKC\gamma^+$ neuron (mean ± S.E.M.)	1011 ± 23.34
(4) GFP/PKCγ (mean ± S.E.M.)	902 ± 16.15
(5) GFP/$GABA_BR1$ (mean ± S.E.M.)	1124 ± 15.26
(6) GFP/PKCγ/$GABA_BR1$ (mean ± S.E.M.)	869 ± 25.69
(7) (4)/(1) × 100%	72.57%
(8) (5)/(1) × 100%	90.43%
(7) (6)/(1) × 100	69.91%
(8) (6)/(2) × 100	53.81%
(9) (6)/(3) × 100	85.95%

Counts in mouse were made by using ten sections from a series of every fourth serial section of 20 μm thickness.

72.57% of the GFP-labeled neurons were also immunopositive for $GABA_BR1$ and PKCγ, respectively. GFP/$GABA_BR1$/PKCγ triple-labeled neurons accounted for 69.91% of GFP-labeled neurons (**Table 1**). The triple-labeled neurons for GFP/$GABA_BR1$/PKCγ were observed in small- to medium-sized neurons, with diameters were between 10 and 15 μm (**Figures 1B,E**).

By using GAD67-GFP transgenic mice, we could observe the cell bodies of the GFP-labeled neurons, but it is difficult to define whether the GAD67-positive terminals are associated with the cell bodies. So we used the GAD67 antibody to recognize the GAD67-positive terminals in wild-type C57 and BALB/c mice, in order to determine the distribution of GABAergic terminals in the DCN. We found that GAD67-positive terminals were densely distributed in the ML and FCL of the DCN in both C57 (**Figure 3A**) and BALB/c mice (data not shown). The GAD67/$GABA_BR1$/PKCγ triple-labeling experiments showed that a subpopulation of GAD67-positive puncta were associated with the cell bodies and the processes of the neurons colocalized with $GABA_BR1$s and PKCγ (**Figures 3B,C**).

AUDITORY THRESHOLD SHIFTS AFTER NOISE EXPOSURES

There was no significant difference between the thresholds of ABR before noise exposure in groups, and hearing levels were essentially equivalent (18.04 ± 0.68 dB SPL in C57 mice, 19.35 ± 0.85 dB SPL in BALB/c mice, $p > 0.05$). NIHL was assessed on day 14 following noise exposure. As shown in **Figure 4**, there were elevations of ABR thresholds in noise-treated C57 mice ($p < 0.05$) and BALB/c mice ($p < 0.05$). In BALB/c mice exposed to noise, the hearing threshold increased significantly to 45.5 ± 1.4 dB SPL ($p < 0.05$). Compared with controls, the hearing threshold in C57 mice increased as well, being 35.4 ± 2.3 dB SPL after noise exposure ($p < 0.05$).

NOISE-INDUCED ALTERATIONS OF GAD67, $GABA_BR$s, AND PKCγ EXPRESSION AT mRNA LEVEL

To examine whether GAD67, $GABA_BR$ and PKCγ mRNA levels are changed after noise stimulation, the mRNA expression were measured by Real-Time PCR. The transcript levels of them were normalized to GAPDH. The $2^{-\text{deltadeltaCt}}$ analysis was adopted to quantify the relative changes of target gene expression (Livak and Schmittgen, 2001).

As demonstrated in **Figures 5B,C**, after noise exposure, there were slight decreases in GAD67 mRNA expression in both BALB/c and C57 strains, but no significant difference ($p > 0.05$). However, we found a decrease in $GABA_BR$ mRNA expression, showing significant differences between the control group and the noise exposure group in both BALB/c mice ($p < 0.05$) and C57 mice ($p < 0.05$). A prominent increase in PKCγ mRNA expression was found in the noise exposure group. The data showed that the PKCγ mRNA expression increased by 2.3-fold compared with controls in BALB/c mice (**Figure 5B**, $p < 0.05$). In C57 mice, the PKCγ mRNA expression also showed an increase of 1.7-fold compared to the controls (**Figure 5C**, $p < 0.05$). Taken together, these results indicate that noise exposure induced a decrease in $GABA_BR$ mRNA and increases in PKCγ mRNA in the CNC, but GAD67 mRNA was unaffected.

NOISE-INDUCED ALTERATIONS OF GAD67, $GABA_BR$, AND PKCγ EXPRESSION AT PROTEIN LEVEL

We next examined whether GAD67, $GABA_BR$, and PKCγ protein levels were also changed after noise exposure. To this end, we performed Western Blotting and quantified GAD67, $GABA_BR$, and PKCγ protein levels at the same time points as mRNA detection. The results were normalized to the densitometry values of β-actin, the relative protein levels were presented in **Figure 6A**. As for the mRNA analysis, a one-way ANOVA indicate that there was no significant effect of noise on GAD67 protein levels in BALB/c mice ($p > 0.05$) and C57 mice ($p > 0.05$). However, in $GABA_BR$

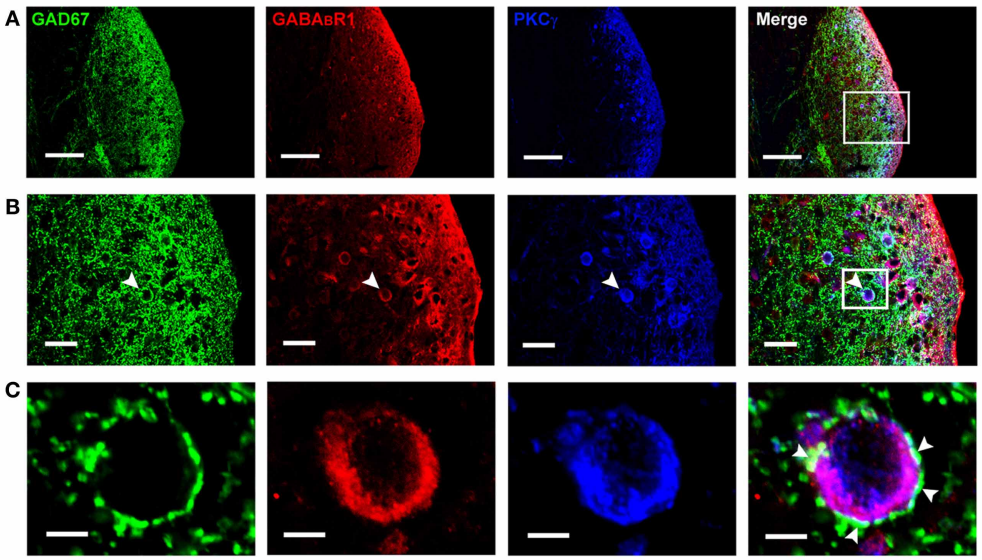

FIGURE 3 | Photomicrographs representing sections of the brainstem of C57 mice in the DCN. Fluorescent images showing the GAD67-positive puncta are distributed densely in the molecular layer and fusiform cell layer of the DCN **(A)**. In **(B)**, the arrowheads indicate the triple-labeled neuron for GAD67/GABA$_B$R1/PKCγ (higher magnification areas, inserted panels in **A**). In **(C)**, The arrowheads indicate that the GAD67-positive terminals made connections on the double-labeled neurons (higher magnification areas, inserted panels in **B**). Scale bar: 100 μm in **(A)**; 30 μm in **(B)**; 10 μm in **(C)**.

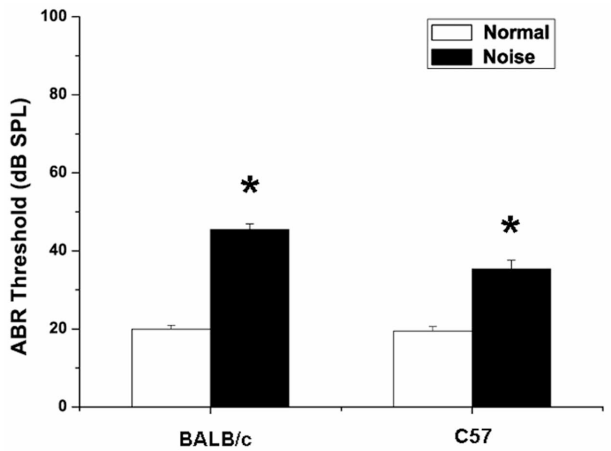

FIGURE 4 | Changes in auditory brainstem response of BALB/c mice and C57 mice after noise exposure. Normal group: mice received no treatment and placed in the noise booth but not exposed to noise. Noise group: mice were exposed to 4-kHz octave-band noise at 110 dB SPL for 8 h per day for 14 consecutive day. *$P < 0.05$.

protein expression, data obtained here indicate that there was a significant decrease in the noise exposure group (**Figure 6**, $p < 0.05$). In BALB/c mice, the PKCγ protein level increased significantly after noise exposure (**Figures 6A,B**, $p < 0.05$). In C57 strain, the expression of PKCγ was significantly elevated in the noise exposure group (**Figures 6A,C**, $p < 0.05$). These results suggest that after noise treatment, the alterations of GABA$_B$R and PKCγ at protein levels were statistically significant in the CNC of BALB/c mice and C57 mice.

DISCUSSION

Our results suggest that a large subpopulation of GABAergic neurons in the ML and FCL of the DCN coexpress GABA$_B$R1s and PKCγ. The GAD67-positive terminals were attached to the GABA$_B$R1/PKCγ double-labeled neurons. Moreover, after noise exposure, both C57 mice and BALB/c mice exhibited obvious hearing deficits and these functional effects were accompanied with changes in GABA$_B$R and PKCγ expression in the CNC. Thus, the alterations of GABA$_B$Rs and PKCγ in GABAergic inhibition in the DCN might be associated with NIHL.

GABAergic INHIBITION IN NIHL

It is noteworthy that disruption in GABAergic inhibition within the DCN has been implicated in the development of hearing impairment in rodents (Ling et al., 2005; Wang et al., 2009a). In addition, another important inhibitory neurotransmitter, glycine and its receptor (GlyR) have been reported in the DCN (Rubio and Juiz, 2004). In age-related hearing loss or unilateral cochlear ablation, decreased glycine levels and the reduction of the total number of GlyR binding sites were found in the DCN, suggesting the down-regulation of glycinergic inhibition is also associated with hearing loss in the DCN (Willott et al., 1997; Potashner et al., 2000; Wang et al., 2009b).

The suppression of GABAergic inhibition in hearing loss could be attributed to two reasons: decreased GABA synthesis and release or down-regulation of its receptors. In our study, results from Real-Time PCR and Western Blotting analysis showed that after noise stimulation, the GABA$_B$R expression decreased at both mRNA and protein levels. In contrast, the endogenous promoter of GAD67, a specific marker for GABAergic neurons remained unchanged in hearing impaired mice. Thus, our data suggest that rather than decreased GABA synthesis and release in the CNC,

A Primer sequence and amplicons generated by Real-Time RT-PCR

Taget Gene	Sequence of primers (5'-3')	Amplicon size (bp)	GenBank accession number
GAD67	Forward:GGGTTCCAGATAGCCCTGAGCGA Reverse:TGGCCTTGTCCCCTTGAGGCT	120	NM_008077.4
PKCγ	Forward:ACCCTCGTAGAGAAGCGTGT Reverse:TGAAAGGTGGAGTGAAGCTG	89	X67129.1
GABA$_B$R1	Forward:GGTTGTGCTCTTTGTGCCTA Reverse:CTGTGCTTCAGACTGCCATT	67	NM_019439.3
GABA$_B$R2	Forward:AGCAAGCGTTCGGGTGTA Reverse:TGGCGTTGAGGATGATTCT	148	NM_001081141.1
GAPDH	Forward:CACAAACTCAGCGGCATAGAAA Reverse:GGAAGAGGTAGCCTGCACACAT	110	NC_000072.5

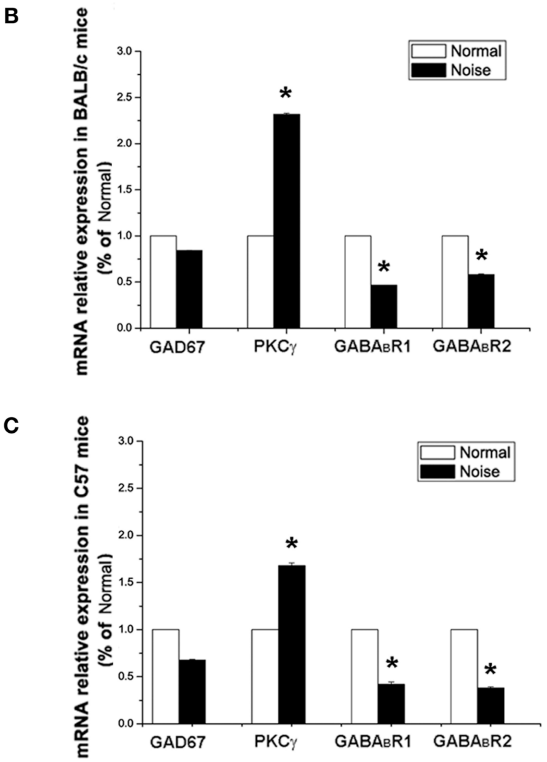

FIGURE 5 | The alterations of GAD67, GABA$_B$R1, GABA$_B$R2 and PKCγat mRNA levels after noise exposure in BALB/c mice and C57 mice. (A) Sequences of specific primers and associated amplicon lengths for Real-Time PCR. **(B)** The noise-induced changes of GAD67, GABA$_B$R1, GABA$_B$R2, and PKCγ mRNA levels in BALB/c mice of each group. The sample of control group was set as 100%. **(C)** The noise-induced changes of GAD67, GABA$_B$R1, GABA$_B$R2, and PKCγ mRNA levels in C57 mice. The sample of control group was set as 100%. $*P < 0.05$.

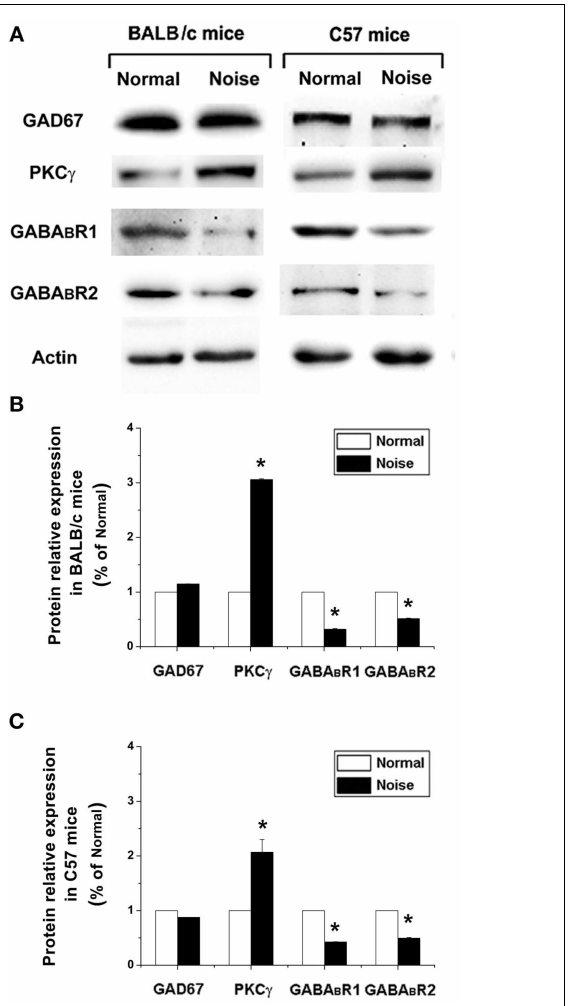

FIGURE 6 | The alterations of GAD67, GABA$_B$R1, GABA$_B$R2, and PKCγ at protein levels after noise exposure in BALB/c mice and C57 mice. (A) GAD67, GABA$_B$R1, GABA$_B$R2, and PKCγ protein levels detected by Western blotting. **(B)** The noise-induced changes of GAD67, GABA$_B$R1, GABA$_B$R2, and PKCγ expressions in BALB/c mice. **(C)** The noise-induced changes of GAD67, GABA$_B$R1, GABA$_B$R2, and PKCγ expressions in C57 mice. $*P < 0.05$.

the preferential decrease in GABA$_B$R expression may reflect a selective loss of GABAergic inhibition in NIHL.

DECREASED GABA$_B$RS AFTER NOISE INJURY IN NIHL

Previous results indicate that GABA$_B$Rs are expressed in both GABAergic cartwheel cells and glutamatergic fusiform cells in the DCN, suggesting that GABA$_B$Rs may participate in both inhibitory and excitatory effects in the DCN (Lujan et al., 2004; Irie and Ohmori, 2008). Moreover, the excitability of both cartwheel and fusiform cells was shown to be enhanced in the DCN following noise trauma (Brozoski et al., 2002; Chang et al., 2002).

The morphological features of cartwheel cells have been identified in the DCN (Osen, 1969; Wouterlood and Mugnaini, 1984). Firstly, cartwheel cells distribute at the ML and FCL. Secondly, cartwheel cells (10–20 μm in mean cell body diameter) are small- to medium size, and have large primary dendrites (Wouterlood and Mugnaini, 1984). Thirdly, the axons of cartwheel cells terminate over a relatively restricted area and make contact with other cartwheel neurons as well as fusiform neurons (Berrebi and Mugnaini, 1991). Fourthly, the cartwheel cells are thought to be inhibitory because they are strongly labeled by antisera against GAD, GABA, and glycine (Mugnaini, 1985). Finally, unlike other types of cells in the DCN, it has been demonstrated that cartwheel cells express PKCγ specifically. (Garcia and Harlan, 1997).

According to these features, the cartwheel cell could be identified (Idrizbegovic et al., 2004; Kou et al., 2011). In the present study, the triple-labeled neurons for GFP/GABA$_B$R1/PKCγ (10–15 μm in mean cell body diameter), in addition to the morphology and the distribution in the DCN, suggest that they might correspond to cartwheel cells in the ML and FCL of the DCN (**Figure 7**).

Cartwheel cells send GABAergic axons and contact other cartwheel neurons and fusiform cells. Our results also suggest that the GAD67-positive terminals were attached to the GABA$_B$R1/PKCγ double-labeled neurons. Therefore, we presumed that after noise stimulation, the increased activity of cartwheel cells could be partially explained by disinhibition, through our observed decrease in GABA$_B$R expression.

Because GABA$_B$Rs were also located at both presynaptic and postsynaptic sites of glutamatergic fusiform cells in the DCN (Lujan et al., 2004). At the presynaptic site, electrophysiological investigations have shown that GABA$_B$R mediates presynaptic inhibition of excitatory neurotransmission through G protein-mediated modulation of presynaptic Ca^{2+} channels, or lowering cyclic AMP and then blocking the stimulatory effect of increased Ca^{2+} on vesicle recruitment (Isaacson, 1998; Sakaba and Neher, 2003). Importantly, noise exposure has also been implicated in stimulating glutamate activation (Isaacson, 1998; Groschel et al., 2011; Shore, 2011; Dehmel et al., 2012). Thus, the downregulation of presynaptic GABA$_B$Rs at fusiform glutamatergic terminals may result in the disinhibition of glutamate release in the DCN, possibly contributing to NIHL.

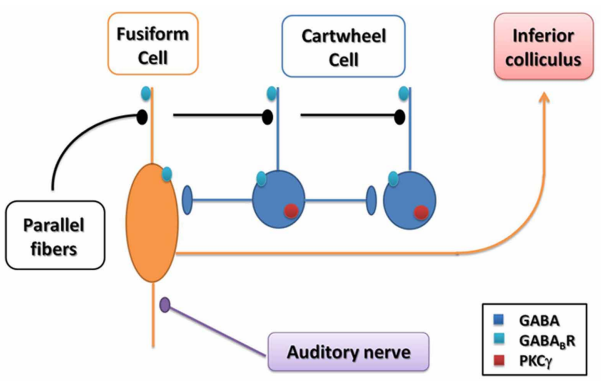

FIGURE 7 | Summary diagram of the circuitry in the DCN. The GABA/GABA$_B$R/PKCγ triple-labeled neurons are distributed in the molecular layer and fusiform cell layer. Most of these neurons are presumed to be cartwheel cells, which receive input from parallel fibers. As inhibitory interneurons, their GABAergic terminals were attached to the other cartwheel cells and fusiform cells. The glutamatergic fusiform cells, which might also express GABA$_B$Rs, receiving inputs from parallel fibers and auditory nerve afferents, finally project to the inferior colliculus (IC). The noise stimulation could activate both cartwheel cells and fusiform cells. The activation of cartwheel cells could be attributed to the decreased GABA$_B$Rs, leading to the disinhibition among the GABA-containing cartwheel cells. The noise injury also increases PKCγ in these activated cartwheel cells. In the glutamatergic fusiform cells expressing GABA$_B$Rs, because of the reduction of GABA$_B$Rs, the loss of presynaptic and postsynaptic inhibition of glutamate activation might promote glutamate neurotransmission in NIHL.

Previous results suggest that GABA "spillover" from neighboring sites may represent a possible source of GABA in the activation of GABA$_B$Rs in the DCN (Lujan et al., 2004). GABA$_B$Rs located at a distance from GABA releasing sites could be activated by GABA "spillover" has also been confirmed in the hippocampus and the cerebellum (Lopez-Bendito et al., 2002, 2004). At postsynaptic sites, GABA$_B$R could activate inwardly rectifying K^+ channels (GIRK/Kir3) via G protein β/γ subunits (Otmakhova and Lisman, 2004). The GIRK channels mediate slow hyperpolarizing currents which are important for shunting excitatory synaptic currents and can control glutamate receptor activation (Otmakhova and Lisman, 2004). Therefore, GABA$_B$Rs located at the postsynaptic sites of glutamatergic fusiform cells (**Figure 7**), might fulfill a control function on glutamate excitatory transmission by GABA "spilling over" from nearby GABAergic circuitry. Moreover, in the present study, the reduced GABA$_B$Rs might suggest a role in the decreased GABAergic inhibition from the GABAergic terminals on the fusiform cells in NIHL (**Figure 7**).

It has been reported that GABA$_A$Rs are distributed in the CNC. However, after acoustic trauma, there was no significant difference in GABA$_A$R mRNA expression in the CNC between the control mice and the hearing impaired mice (Song and Messing, 2005; Dong et al., 2010). Therefore, alterations in the expression of GABA$_B$Rs may play a more important role than changes in GABA$_A$R expression in the development of hearing loss.

INCREASED PKCγ AFTER NOISE INJURY IN NIHL

As an important second-messenger-activated protein kinase, it is accepted that PKCγ plays an important role in brain, including the DCN (Colombo and Gallagher, 2002; Rossi et al., 2005; Kou et al., 2011) In this study, 85.95% PKCγ-positive cells were found to coexpress GAD67 and GABA$_B$R1s, suggesting a possible role in GABAergic inhibition.

PKCγ has been suggested to be an injury-activated intracellular modulator that promotes neuronal activity in various neuroprotective signal pathways (Colombo and Gallagher, 2002; Hayashi et al., 2005; Rossi et al., 2005). Noise stimulation could increase the activity of GABA-containing cartwheel cells in the DCN (Brozoski et al., 2002; Chang et al., 2002). In addition, PKCγ is specifically expressed in cartwheel cells (Garcia and Harlan, 1997). In our study, we found that 85.95% of PKCγ-positive neurons coexpressed GAD67 and GABA$_B$R1s, indicating that the selective increase in PKCγ expression may serve as a noise injury-induced intracellular modulator in the subpopulation of GABA/GABA$_B$R1/PKCγ cartwheel cells in the DCN (**Figure 7**).

In addition, we noted that there was no statistically significant difference in GAD67 expression at both mRNA and protein levels. Although the neuroprotective role of PKCγ has been reported, after noise stimulation, whether the unchanged GAD67 expression was due to the activated PKCγ or the feedback effects of the reduced GABA$_B$Rs needs further investigation in NIHL.

Although the triple-labeled neurons contained GAD67, GABA$_B$R1s, and PKCγ distributed densely in the DCN, there were also several neurons which expressed PKCγ, GABA$_B$R1s, or GAD67 but were not triple-labeled. This might be explained by the following reasons. First, a group of fusiform cells might express GABA$_B$Rs. Second, as well as the cartwheel cells (the

diameter of cell bodies is between 10 and 20 μm), the stellate cells (the diameter of cell bodies is usually less than 10 μm) could contain GABA (Mugnaini, 1985). Third, the tissue treatment or the process of triple-labeling immunohistochemistry might also affect the detection levels of the antibodies.

CONCLUSION

In summary, our results focused on the CNC of mice subjected to the influence of noise exposure, particularly in the GABAergic neurons in the ML and FCL of the DCN. Because disruption of GABAergic inhibition in the DCN has been confirmed in auditory disorders, particularly in hearing loss (Ling et al., 2005; Middleton et al., 2011), the decreased expression of $GABA_BRs$ may, at least in part, play a role in altered inhibitory processing in NIHL. Although we assume that the unchanged GAD67 may be associated with the neuroprotective role of PKCγ, investigating the interactions of GABA, PKCγ, and $GABA_BR$ in the CNC in greater detail should be informative in developing a better understanding of the pathogenesis of NIHL.

ACKNOWLEDGMENTS

We thank Prof. Harry W. M. Steinbusch (School for Mental Health and Neuroscience, Maastricht University) and Dr. Michael L. Wilson for editing and reviewing this article. This work was supported by grants from the National Natural Science Foundation of China (Nos. 30771133, 30971123) and the National Program of Basic Research of China (G2006CB500808).

REFERENCES

Aizawa, N., and Eggermont, J. J. (2006). Effects of noise-induced hearing loss at young age on voice onset time and gap-in-noise representations in adult cat primary auditory cortex. *J. Assoc. Res. Otolaryngol.* 7, 71–81. doi: 10.1007/s10162-005-0026-3

Asada, H., Kawamura, Y., Maruyama, K., Kume, H., Ding, R. G., Kanbara, N., et al. (1997). Cleft palate and decreased brain gamma-aminobutyric acid in mice lacking the 67-kDa isoform of glutamic acid decarboxylase. *Proc. Natl. Acad. Sci. U.S.A.* 94, 6496–6499. doi: 10.1073/pnas.94.12.6496

Bang, S. J., and Commons, K. G. (2012). Forebrain GABAergic projections from the dorsal raphe nucleus identified by using GAD67-GFP knock-in mice. *J. Comp. Neurol.* 520, 4157–4167. doi: 10.1002/cne.23146

Berrebi, A. S., and Mugnaini, E. (1991). Distribution and targets of the cartwheel cell axon in the dorsal cochlear nucleus of the guinea pig. *Anat. Embryol.* 183, 427–454. doi: 10.1007/BF00186433

Browner, R. H., and Baruch, A. (1982). The cytoarchitecture of the dorsal cochlear nucleus in the 3-month- and 26-month-old C57BL/6 mouse: a Golgi impregnation study. *J. Comp. Neurol.* 211, 115–138. doi: 10.1002/cne.902110203

Brozoski, T. J., Bauer, C. A., and Caspary, D. M. (2002). Elevated fusiform cell activity in the dorsal cochlear nucleus of chinchillas with psychophysical evidence of tinnitus. *J. Neurosci.* 22, 2383–2390.

Chang, E. H., Kotak, V. C., and Sanes, D. H. (2003). Long-term depression of synaptic inhibition is expressed postsynaptically in the developing auditory system. *J. Neurophysiol.* 90, 1479–1488. doi: 10.1152/jn.00386.2003

Chang, H., Chen, K., Kaltenbach, J. A., Zhang, J., and Godfrey, D. A. (2002). Effects of acoustic trauma on dorsal cochlear nucleus neuron activity in slices. *Hear. Res.* 164, 59–68. doi: 10.1016/S0378-5955(01)00410-5

Chattopadhyaya, B., Di Cristo, G., Wu, C. Z., Knott, G., Kuhlman, S., Fu, Y., et al. (2007). GAD67-mediated GABA synthesis and signaling regulate inhibitory synaptic innervation in the visual cortex. *Neuron* 54, 889–903. doi: 10.1016/j.neuron.2007.05.015

Chen, L., McKenna, J. T., Leonard, M. Z., Yanagawa, Y., McCarley, R. W., and Brown, R. E. (2010). GAD67-GFP knock-in mice have normal sleep-wake patterns and sleep homeostasis. *Neuroreport* 21, 216–220. doi: 10.1097/WNR.0b013e32833655c4

Chung, J. H., Des Roches, C. M., Meunier, J., and Eavey, R. D. (2005). Evaluation of noise-induced hearing loss in young people using a web-based survey technique. *Pediatrics* 115, 861–867. doi: 10.1542/peds.2004-0173

Colombo, P. J., and Gallagher, M. (2002). Individual differences in spatial memory among aged rats are related to hippocampal PKCgamma immunoreactivity. *Hippocampus* 12, 285–289. doi: 10.1002/hipo.10016

Dehmel, S., Pradhan, S., Koehler, S., Bledsoe, S., and Shore, S. (2012). Noise overexposure alters long-term somatosensory-auditory processing in the dorsal cochlear nucleus–possible basis for tinnitus-related hyperactivity? *J. Neurosci.* 32, 1660–1671.

Ding, Y. Q., Xiang, C. X., and Chen, Z. F. (2005). Generation and characterization of the PKC gamma-Cre mouse line. *Genesis* 43, 28–33. doi: 10.1002/gene.20151

Dong, S., Mulders, W. H., Rodger, J., Woo, S., and Robertson, D. (2010). Acoustic trauma evokes hyperactivity and changes in gene expression in guinea-pig auditory brainstem. *Eur. J. Neurosci.* 31, 1616–1628.

Engel, D., Pahner, I., Schulze, K., Frahm, C., Jarry, H., Ahnert-Hilger, G., et al. (2001). Plasticity of rat central inhibitory synapses through GABA metabolism. *J. Physiol.* 535, 473–482. doi: 10.1111/j.1469-7793.2001.00473.x

Fritschy, J. M., Harvey, R. J., and Schwarz, G. (2008). Gephyrin: where do we stand, where do we go? *Trends Neurosci.* 31, 257–264.

Garcia, M. M., and Harlan, R. E. (1997). Protein kinase C in central auditory pathways of the rat. *J. Comp. Neurol.* 385, 1–25.

Groschel, M., Gotze, R., Ernst, A., and Basta, D. (2010). Differential impact of temporary and permanent noise-induced hearing loss on neuronal cell density in the mouse central auditory pathway. *J. Neurotrauma* 27, 1499–1507. doi: 10.1089/neu.2009.1246

Groschel, M., Muller, S., Gotze, R., Ernst, A., and Basta, D. (2011). The possible impact of noise-induced Ca2+-dependent activity in the central auditory pathway: a manganese-enhanced MRI study. *Neuroimage* 57, 190–197. doi: 10.1016/j.neuroimage.2011.04.022

Han, L. C., Zhang, H., Wang, W., Wei, Y. Y., Sun, X. X., Yanagawa, Y., et al. (2010). The effect of sevoflurane inhalation on gabaergic neurons activation: observation on the GAD67-GFP knock-in mouse. *Anat. Rec. (Hoboken)* 293, 2114–2122. doi: 10.1002/ar.21113

Han, Y., Hong, L., Chen, Y., Zhong, C., Wang, Y., Zhao, D., et al. (2011). Up-regulation of Nob1 in the rat auditory system with noise-induced hearing loss. *Neurosci. Lett.* 491, 79–82. doi: 10.1016/j.neulet.2011.01.010

Han, Y., Hong, L., Zhong, C., Chen, Y., Wang, Y., Mao, X., et al. (2012). Identification of new altered genes in rat cochleae with noise-induced hearing loss. *Gene* 499, 318–322. doi: 10.1016/j.gene.2012.02.042

Han, Y., Zhong, C., Hong, L., Wang, Y., Qiao, L., and Qiu, J. (2009). Effect of c-myc on the ultrastructural structure of cochleae in guinea pigs with noise induced hearing loss. *Biochem. Biophys. Res. Commun.* 390, 458–462. doi: 10.1016/j.bbrc.2009.09.091

Hayashi, S., Ueyama, T., Kajimoto, T., Yagi, K., Kohmura, E., and Saito, N. (2005). Involvement of gamma protein kinase C in estrogen-induced neuroprotection against focal brain ischemia through G protein-coupled estrogen receptor. *J. Neurochem.* 93, 883–891. doi: 10.1111/j.1471-4159.2005.03080.x

Hefti, F. (1986). Nerve growth factor promotes survival of septal cholinergic neurons after fimbrial transections. *J. Neurosci.* 6, 2155–2162.

Huang, J., Wang, Y., Wang, W., Wei, Y., Li, Y., and Wu, S. (2008). Preproenkephalin mRNA is expressed in a subpopulation of GABAergic neurons in the spinal dorsal horn of the GAD67-GFP knock-in mouse. *Anat. Rec. (Hoboken)* 291, 1334–1341. doi: 10.1002/ar.20755

Huo, F. Q., Chen, T., Lv, B. C., Wang, J., Zhang, T., Qu, C. L., et al. (2009). Synaptic connections between GABAergic elements and serotonergic terminals or projecting neurons in the ventrolateral orbital cortex. *Cereb. Cortex* 19, 1263–1272. doi: 10.1093/cercor/bhn169

Idrizbegovic, E., Bogdanovic, N., Willott, J. F., and Canlon, B. (2004). Age-related increases in calcium-binding protein immunoreactivity in the cochlear nucleus of hearing impaired C57BL/6J mice. *Neurobiol.*

Aging 25, 1085–1093. doi: 10.1016/j.neurobiolaging.2003.11.004

Irie, T., and Ohmori, H. (2008). Presynaptic GABA(B) receptors modulate synaptic facilitation and depression at distinct synapses in fusiform cells of mouse dorsal cochlear nucleus. *Biochem. Biophys. Res. Commun.* 367, 503–508. doi: 10.1016/j.bbrc.2008.01.001

Isaacson, J. S. (1998). GABAB receptor-mediated modulation of presynaptic currents and excitatory transmission at a fast central synapse. *J. Neurophysiol.* 80, 1571–1576.

Jones, K. A., Borowsky, B., Tamm, J. A., Craig, D. A., Durkin, M. M., Dai, M., et al. (1998). GABA(B) receptors function as a heteromeric assembly of the subunits GABA(B)R1 and GABA(B)R2. *Nature* 396, 674–679. doi: 10.1038/25348

Kaupmann, K., Malitschek, B., Schuler, V., Heid, J., Froestl, W., Beck, P., et al. (1998). GABA(B)-receptor subtypes assemble into functional heteromeric complexes. *Nature* 396, 683–687. doi: 10.1038/25360

Kou, Z. Z., Zhang, Y., Zhang, T., Li, H., and Li, Y. Q. (2011). Age-related increase in PKC gamma expression in the cochlear nucleus of hearing impaired C57BL/6J and BALB/c mice. *J. Chem. Neuroanat.* 41, 20–24. doi: 10.1016/j.jchemneu.2010.10.003

Lehrke, M., Reilly, M. P., Millington, S. C., Iqbal, N., Rader, D. J., and Lazar, M. A. (2004). An inflammatory cascade leading to hyperresistinemia in humans. *PLoS Med.* 1:e45. doi: 10.1371/journal.pmed.0010045

Li, J. L., Wu, S. X., Tomioka, R., Okamoto, K., Nakamura, K., Kaneko, T., et al. (2005). Efferent and afferent connections of GABAergic neurons in the supratrigeminal and the intertrigeminal regions. An immunohistochemical tract-tracing study in the GAD67-GFP knock-in mouse. *Neurosci. Res.* 51, 81–91. doi: 10.1016/j.neures.2004.10.005

Li, Y., Ding, D., Jiang, H., Fu, Y., and Salvi, R. (2011). Co-administration of cisplatin and furosemide causes rapid and massive loss of cochlear hair cells in mice. *Neurotox. Res.* 20, 307–319. doi: 10.1007/s12640-011-9244-0

Lin, Y., Kashio, A., Sakamoto, T., Suzukawa, K., Kakigi, A., and Yamasoba, T. (2011). Hydrogen in drinking water attenuates noise-induced hearing loss in guinea pigs. *Neurosci. Lett.* 487, 12–16. doi: 10.1016/j.neulet.2010.09.064

Ling, L. L., Hughes, L. F., and Caspary, D. M. (2005). Age-related loss of the GABA synthetic enzyme glutamic acid decarboxylase in rat primary auditory cortex. *Neuroscience* 132, 1103–1113. doi: 10.1016/j.neuroscience.2004.12.043

Livak, K. J., and Schmittgen, T. D. (2001). Analysis of relative gene expression data using real-time quantitative PCR and the 2(-Delta Delta C(T)) Method. *Methods* 25, 402–408. doi: 10.1006/meth.2001.1262

Lopez-Bendito, G., Shigemoto, R., Kulik, A., Paulsen, O., Fairen, A., and Lujan, R. (2002). Expression and distribution of metabotropic GABA receptor subtypes GABABR1 and GABABR2 during rat neocortical development. *Eur. J. Neurosci.* 15, 1766–1778. doi: 10.1046/j.1460-9568.2002.02032.x

Lopez-Bendito, G., Shigemoto, R., Kulik, A., Vida, I., Fairen, A., and Lujan, R. (2004). Distribution of metabotropic GABA receptor subunits GABAB1a/b and GABAB2 in the rat hippocampus during prenatal and postnatal development. *Hippocampus* 14, 836–848. doi: 10.1002/hipo.10221

Lujan, R., Shigemoto, R., Kulik, A., and Juiz, J. M. (2004). Localization of the GABAB receptor 1a/b subunit relative to glutamatergic synapses in the dorsal cochlear nucleus of the rat. *J. Comp. Neurol.* 475, 36–46. doi: 10.1002/cne.20160

May, C. A., Nakamura, K., Fujiyama, F., and Yanagawa, Y. (2008). Quantification and characterization of GABA-ergic amacrine cells in the retina of GAD67-GFP knock-in mice. *Acta Ophthalmol.* 86, 395–400. doi: 10.1111/j.1600-0420.2007.01054.x

Middleton, J. W., Kiritani, T., Pedersen, C., Turner, J. G., Shepherd, G. M., and Tzounopoulos, T. (2011). Mice with behavioral evidence of tinnitus exhibit dorsal cochlear nucleus hyperactivity because of decreased GABAergic inhibition. *Proc. Natl. Acad. Sci. U.S.A.* 108, 7601–7606. doi: 10.1073/pnas.1100223108

Mugnaini, E. (1985). GABA neurons in the superficial layers of the rat dorsal cochlear nucleus: light and electron microscopic immunocytochemistry. *J. Comp. Neurol.* 235, 61–81. doi: 10.1002/cne.902350106

Murphy, S. M., Pilowsky, P. M., and Llewellyn-Smith, I. J. (1998). Pre-embedding staining for GAD67 versus postembedding staining for GABA as markers for central GABAergic terminals. *J. Histochem. Cytochem.* 46, 1261–1268. doi: 10.1177/002215549804601106

Nelson, S. B. (2004). Hebb and anti-Hebb meet in the brainstem. *Nat. Neurosci.* 7, 687–688. doi: 10.1038/nn0704-687

Ohlemiller, K. K., McFadden, S. L., Ding, D. L., Flood, D. G., Reaume, A. G., Hoffman, E. K., et al. (1999). Targeted deletion of the cytosolic Cu/Zn-superoxide dismutase gene (Sod1) increases susceptibility to noise-induced hearing loss. *Audiol. Neurootol.* 4, 237–246. doi: 10.1159/000013847

Ohlemiller, K. K., Wright, J. S., and Heidbreder, A. F. (2000). Vulnerability to noise-induced hearing loss in 'middle-aged' and young adult mice: a dose-response approach in CBA, C57BL, and BALB inbred strains. *Hear. Res.* 149, 239–247. doi: 10.1016/S0378-5955(00)00191-X

Osen, K. K. (1969). Cytoarchitecture of the cochlear nuclei in the cat. *J. Comp. Neurol.* 136, 453–484. doi: 10.1002/cne.901360407

Otmakhova, N. A., and Lisman, J. E. (2004). Contribution of Ih and GABAB to synaptically induced afterhyperpolarizations in CA1: a brake on the NMDA response. *J. Neurophysiol.* 92, 2027–2039. doi: 10.1152/jn.00427.2004

Pinal, C. S., and Tobin, A. J. (1998). Uniqueness and redundancy in GABA production. *Perspect. Dev. Neurobiol.* 5, 109–118.

Pinto, C., Souza, R. P., Lioult, D., Semeralul, M., Kennedy, J. L., Warsh, J. J., et al. (2011). Parent of origin effect and allelic expression imbalance of the serotonin transporter in bipolar disorder and suicidal behaviour. *Eur. Arch. Psychiatry Clin. Neurosci.* 261, 533–538. doi: 10.1007/s00406-011-0192-8

Potashner, S. J., Suneja, S. K., and Benson, C. G. (2000). Altered glycinergic synaptic activities in guinea pig brain stem auditory nuclei after unilateral cochlear ablation. *Hear. Res.* 147, 125–136. doi: 10.1016/S0378-5955(00)00126-X

Qu, J., Li, X., Wang, J., Mi, W., Xie, K., and Qiu, J. (2012). Inhalation of hydrogen gas attenuates cisplatin-induced ototoxicity via reducing oxidative stress. *Int. J. Pediatr. Otorhinolaryngol.* 76, 111–115. doi: 10.1016/j.ijporl.2011.10.014

Rossi, M. A., Mash, D. C., and Detoledo-Morrell, L. (2005). Spatial memory in aged rats is related to PKCgamma-dependent G-protein coupling of the M1 receptor. *Neurobiol. Aging* 26, 53–68. doi: 10.1016/j.neurobiolaging.2004.02.029

Rubio, M. E., and Juiz, J. M. (2004). Differential distribution of synaptic endings containing glutamate, glycine, and GABA in the rat dorsal cochlear nucleus. *J. Comp. Neurol.* 477, 253–272. doi: 10.1002/cne.20248

Saito, N., and Shirai, Y. (2002). Protein kinase C gamma (PKC gamma): function of neuron specific isotype. *J. Biochem.* 132, 683–687. doi: 10.1093/oxfordjournals.jbchem.a003274

Sakaba, T., and Neher, E. (2003). Direct modulation of synaptic vesicle priming by GABA(B) receptor activation at a glutamatergic synapse. *Nature* 424, 775–778. doi: 10.1038/nature01859

Shore, S. E. (2011). Plasticity of somatosensory inputs to the cochlear nucleus–implications for tinnitus. *Hear. Res.* 281, 38–46. doi: 10.1016/j.heares.2011.05.001

Shore, S. E., Koehler, S., Oldakowski, M., Hughes, L. F., and Syed, S. (2008). Dorsal cochlear nucleus responses to somatosensory stimulation are enhanced after noise-induced hearing loss. *Eur. J. Neurosci.* 27, 155–168. doi: 10.1111/j.1460-9568.2007.05983.x

Sloviter, R. S., Ali-Akbarian, L., Horvath, K. D., and Menkens, K. A. (2001). Substance P receptor expression by inhibitory interneurons of the rat hippocampus: enhanced detection using improved immunocytochemical methods for the preservation and colocalization of GABA and other neuronal markers. *J. Comp. Neurol.* 430, 283–305.

Sloviter, R. S., and Nilaver, G. (1987). Immunocytochemical localization of GABA-, cholecystokinin-, vasoactive intestinal polypeptide-, and somatostatin-like immunoreactivity in the area dentata and hippocampus of the rat. *J. Comp. Neurol.* 256, 42–60. doi: 10.1002/cne.902560105

Song, M., and Messing, R. O. (2005). Protein kinase C regulation of GABAA receptors. *Cell. Mol. Life Sci.* 62, 119–127. doi: 10.1007/s00018-004-4339-x

Su, C., Underwood, W., Rybalchenko, N., and Singh, M. (2011). ERK1/2 and ERK5 have distinct roles in the regulation of brain-derived neurotrophic factor expression. *J. Neurosci. Res.* 89, 1542–1550. doi: 10.1002/jnr.22683

Szczepaniak, W. S., and Moller, A. R. (1995). Evidence of decreased GABAergic influence on temporal

integration in the inferior colliculus following acute noise exposure: a study of evoked potentials in the rat. *Neurosci. Lett.* 196, 77–80. doi: 10.1016/0304-3940(95)11851-M

Tamamaki, N., Yanagawa, Y., Tomioka, R., Miyazaki, J., Obata, K., and Kaneko, T. (2003). Green fluorescent protein expression and colocalization with calretinin, parvalbumin, and somatostatin in the GAD67-GFP knock-in mouse. *J. Comp. Neurol.* 467, 60–79. doi: 10.1002/cne.10905

Tanaka, C., and Nishizuka, Y. (1994). The protein kinase C family for neuronal signaling. *Annu. Rev. Neurosci.* 17, 551–567. doi: 10.1146/annurev.ne.17.030194.003003

Turner, J. G., and Willott, J. F. (1998). Exposure to an augmented acoustic environment alters auditory function in hearing-impaired DBA/2J mice. *Hear. Res.* 118, 101–113. doi: 10.1016/S0378-5955(98)00024-0

Wang, H., Brozoski, T. J., Turner, J. G., Ling, L., Parrish, J. L., Hughes, L. F., et al. (2009a). Plasticity at glycinergic synapses in dorsal cochlear nucleus of rats with behavioral evidence of tinnitus. *Neuroscience* 164, 747–759.

Wang, H., Turner, J. G., Ling, L., Parrish, J. L., Hughes, L. F., and Caspary, D. M. (2009b). Age-related changes in glycine receptor subunit composition and binding in dorsal cochlear nucleus. *Neuroscience* 160, 227–239.

White, J. H., Wise, A., Main, M. J., Green, A., Fraser, N. J., Disney, G. H., et al. (1998). Heterodimerization is required for the formation of a functional GABA(B) receptor. *Nature* 396, 679–682. doi: 10.1038/25354

Willott, J. F., Milbrandt, J. C., Bross, L. S., and Caspary, D. M. (1997). Glycine immunoreactivity and receptor binding in the cochlear nucleus of C57BL/6J and CBA/CaJ mice: effects of cochlear impairment and aging. *J. Comp. Neurol.* 385, 405–414.

Willott, J. F., and Turner, J. G. (1999). Prolonged exposure to an augmented acoustic environment ameliorates age-related auditory changes in C57BL/6J and DBA/2J mice. *Hear. Res.* 135, 78–88. doi: 10.1016/S0378-5955(99)00094-5

Wouterlood, F. G., and Mugnaini, E. (1984). Cartwheel neurons of the dorsal cochlear nucleus: a Golgi-electron microscopic study in rat. *J. Comp. Neurol.* 227, 136–157. doi: 10.1002/cne.902270114

Young, A., and Sun, Q. Q. (2009). GABAergic inhibitory interneurons in the posterior piriform cortex of the GAD67-GFP mouse. *Cereb. Cortex* 19, 3011–3029. doi: 10.1093/cercor/bhp072

Zhao, X., Lein, E. S., He, A., Smith, S. C., Aston, C., and Gage, F. H. (2001). Transcriptional profiling reveals strict boundaries between hippocampal subregions. *J. Comp. Neurol.* 441, 187–196. doi: 10.1002/cne.1406

Conflict of Interest Statement: The authors declare that the research was conducted in the absence of any commercial or financial relationships that could be construed as a potential conflict of interest.

Received: 20 April 2013; accepted: 11 July 2013; published online: 30 July 2013.
Citation: Kou Z-Z, Qu J, Zhang D-L, Li H and Li Y-Q (2013) Noise-induced hearing loss is correlated with alterations in the expression of $GABA_B$ receptors and PKC gamma in the murine cochlear nucleus complex. Front. Neuroanat. 7:25. doi: 10.3389/fnana.2013.00025

frontiers in
NEUROANATOMY

ORIGINAL RESEARCH ARTICLE
published: 10 December 2013
doi: 10.3389/fnana.2013.00043

Projections of nucleus accumbens adenosine A_{2A} receptor neurons in the mouse brain and their implications in mediating sleep-wake regulation

Jian-Ping Zhang[1], Qi Xu[2,3], Xiang-Shan Yuan[1], Yoan Cherasse[3,4], Serge N. Schiffmann[5], Alban de Kerchove d'Exaerde[5], Wei-Min Qu[2], Yoshihiro Urade[3,4], Michael Lazarus[3,4]*, Zhi-Li Huang[2]* and Rui-Xi Li[1]*

[1] *Department of Anatomy, Histology and Embryology, Shanghai Medical College, Fudan University, Shanghai, China*
[2] *Department of Pharmacology, State Key Laboratory of Medical Neurobiology, Institute of Brain Sciences, Shanghai Medical College, Fudan University, Shanghai, China*
[3] *Department of Molecular Behavioral Biology, Osaka Bioscience Institute, Suita, Osaka, Japan*
[4] *International Institute for Integrative Sleep Medicine, University of Tsukuba, Tsukuba, Ibaraki, Japan*
[5] *Laboratory of Neurophysiology, Université Libre de Bruxelles, ULB Neuroscience Institute, Brussels, Belgium*

Edited by:
Chen Liu, University of Texas Southwestern Medical Center at Dallas, USA

Reviewed by:
Huxing Cui, University of Iowa Carver College of Medicine, USA
Yongli Shan, University of Texas Southwestern Medical Center, USA

***Correspondence:**
Rui-Xi Li, Department of Anatomy, Histology and Embryology, Shanghai Medical College, Fudan University, Yixueyuan Road 138, Shanghai 200032, China
e-mail: ruixilee@163.com;
Zhi-Li Huang, Department of Pharmacology, State Key Laboratory of Medical Neurobiology, Institute of Brain Science, Shanghai Medical College, Fudan University, Yixueyuan Road 138, Shanghai 200032, China
e-mail: huangzl@fudan.edu.cn;
Michael Lazarus, International Institute for Integrative Sleep Medicine, University of Tsukuba, 1-1-1 Tennodai, Tsukuba, Ibaraki 305-8575, Japan
e-mail: lazarus.michael.ka@u.tsukuba.ac.jp

Adenosine A_{2A} receptors (A_{2A}Rs) in the nucleus accumbens (Acb) have been demonstrated to play an important role in the arousal effect of adenosine receptor antagonist caffeine, and may be involved in physiological sleep. To better understand the functions of these receptors in sleep, projections of A_{2A}R neurons were mapped utilizing adeno-associated virus (AAV) encoding humanized Renilla green fluorescent protein (hrGFP) as a tracer for long axonal pathways. The Cre-dependent AAV was injected into the core (AcbC) and shell (AcbSh) of the Acb in A_{2A}R-Cre mice. Immunohistochemistry was then used to visualize hrGFP, highlighting the perikarya of the A_{2A}R neurons in the injection sites, and their axons in projection regions. The data revealed that A_{2A}R neurons exhibit medium-sized and either round or elliptic perikarya with their processes within the Acb. Moreover, the projections from the Acb distributed to nuclei in the forebrain, diencephalon, and brainstem. In the forebrain, A_{2A}R neurons from all Acb sub-regions jointly projected to the ventral pallidum, the nucleus of the diagonal band, and the substantia innominata. Heavy projections from the AcbC and the ventral AcbSh, and weaker projections from the medial AcbSh, were observed in the lateral hypothalamus and lateral preoptic area. In the brainstem, the Acb projections were found in the ventral tegmental area, while AcbC and ventral AcbSh also projected to the median raphe nucleus, the dorsal raphe nucleus, and the ventrolateral periaqueductal gray. The results supply a solid base for understanding the roles of the A_{2A}R and A_{2A}R neurons in the Acb, especially in the regulation of sleep.

Keywords: nucleus accumbens, adeno-associated virus, Cre-Lox, green fluorescent protein, mouse, sleep

INTRODUCTION

The adenosine A_{2A}receptors (A_{2A}Rs) in the nucleus accumbens (Acb), that consists of the core and shell sub-regions, play a critical role in many important physiological and pathological processes, including sleep, feeding, locomotion, motivation, and addiction (Barraco et al., 1993, 1994; Nagel et al., 2003; Kelley, 2004; Huang et al., 2007, 2011; Mingote et al., 2008; Lazarus et al., 2011, 2012, 2013; O'Neill et al., 2012). However, the cellular morphology and projection patterns of Acb have been characterized based

Abbreviations: 3V, 3rd ventricle; 4V, 4th ventricle; Ac, anterior commissural nucleus; Aca, anterior commissure, anterior part; Acb, accumbens nucleus; AcbC, accumbens nucleus, core; AcbSh, accumbens nucleus, shell; acp, anterior commissure, posterior; AHA, anterior hypothalamic area, anterior part; AHP, anterior hypothalamic area, posterior part; Aq, aqueduct; Arc, arcuate hypothalamic nucleus; BLA, basolateral amygdaloid nucleus, anterior part; BMA, basomedial amygdaloid nucleus, anterior part; BST, bed nucleus of the stria terminalis; BSTLP, bed nucleus of the stria terminalis, lateral division, posterior part; cp, cerebral peduncle, basal part; CPu, caudate putamen; D3V, dorsal 3rd ventricle; DM, dorsomedial hypothalamic nucleus; DR, dorsal raphe nucleus; DRI, dorsal raphe nucleus, ventral part; DTM, dorsal tuberomammillary nucleus; EP, entopeduncular nucleus; f, fornix; HDB, nucleus of the horizontal limb of the diagonal band; iC, internal capsule; LC, locus coeruleus; LGP, lateral globus pallidus; LH, lateral hypothalamus; LHa, anterior part of lateral hypothalamus; LHM, mammillary part of lateral hypothalamus; LHt, tuberal part of lateral hypothalamus; LPO, lateral preoptic area; LV, lateral ventricle; ME, median eminence; MnR, median raphe nucleus; MnR, nucleus of the vertical limb of the diagonal band; MPB, medial parabrachial nucleus; ns, nigrostriatal bundle; opt, optic tract; ox, optic chiasm; Pe, periventricular hypothalamic nucleus; PH, posterior hypothalamic area; SI, substantia innominata; STh, subthalamic nucleus; SuM, supramammillary nucleus; VDB, ventrolateral periaqueductal gray; VLPAG, ventromedial hypothalamic nucleus, dorsomedial part; VMHDM, ventral pallidum; VP, ventral tegmental area; VTA, ventral tuberomammillary nucleus.

mainly on traditional tracing techniques with nonspecific tracers (Heimer et al., 1991; Meredith et al., 1992; Zahm and Heimer, 1993; Jongen-Rêlo et al., 1994; Goto and Grace, 2008), which is insufficient to explain the role of the adenosine $A_{2A}R$ in the Acb. The $A_{2A}R$-expressing neurons and their related neural pathways execute the specific actions triggered by the type of receptor, and so specifically analyzing the neural pathway is critical to fully understand the function of the receptor. Because of this, identifying the projections of $A_{2A}R$ neurons has become an important issue (Lazarus et al., 2012).

Because of limitations in tracing techniques, little data are available describing the efferent projections of $A_{2A}R$ neurons in the Acb. Those data that are available have been obtained using conventional tracers, such as autoradiographic fiber-tracing (Nauta et al., 1978), wheat germ agglutinin conjugated to horseradish peroxidase (WGA-HRP; Heimer et al., 1991), phaseolus vulgaris-leucoagglutinin (PHA-L; Zahm and Heimer, 1993), and biotinylated dextran amine (BDA; Usuda et al., 1998). These studies report that Acb targets the ventral pallidum, lateral hypothalamus, ventral tegmental area, substantia nigra pars compacta, and the pedunculopontine tegmental nucleus (Heimer et al., 1991; Zahm and Heimer, 1993; Usuda et al., 1998). Neurons in the Acb are divided into the GABAergic projection neurons and interneurons (Ferré et al., 2007; Schiffmann et al., 2007), and GABAergic projection neurons, which can be further sub-characterized into enkephalinergic and dynorphinergic neurons. Adenosine $A_{2A}Rs$ are predominantly localized in the GABAergic enkephalinergic neurons and the glutamatergic terminals in the Acb (Ferré et al., 2007; Schiffmann et al., 2007). The efferent regions of Acb neurons therefore do not stand for projection sites of $A_{2A}R$ neurons in Acb.

The approaches based on Cre-LoxP technology have been used for the neural tracing of selected neurons, whereby an adeno-associated virus (AAV) is carrying a humanized Renilla green fluorescent protein (hrGFP) that is transcriptionally silenced by a neo cassette flanked by LoxH/LoxP sites (Gautron et al., 2010), but can be activated as a tracer in the presence of Cre recombinase. The AAV is stereotaxically injected into a brain that expresses Cre under the control of the adenosine $A_{2A}R$ promoter, resulting in robust hrGFP expressions specifically in $A_{2A}R$ neurons (Durieux et al., 2009, 2012). Moreover, in these studies hrGFP was efficiently transported to brain regions that were innervated by $A_{2A}R$ neurons.

Using the techniques mentioned above, we stereotaxically injected the AAV into the core (AcbC) and shell (AcbSh) of the nucleus accumbens. We then used immunohistochemical and/or immunofluorescence techniques to detect the expression of the $A_{2A}R$ neurons in the injection sites and their axon distributions in various brain regions after 4 weeks of injections (Chamberlin et al., 1998). Special emphasis was placed on well-established projection sites related with the function of sleep-wake controlled by $A_{2A}R$ neurons.

MATERIALS AND METHODS

ANIMALS

The adenosine $A_{2A}R$-Cre mice have been well characterized in a previous study (Durieux et al., 2009, 2012). Adenosine $A_{2A}R$-Cre and wild type (WT) mice were maintained in the Department of Molecular Behavioral Biology, Osaka Bioscience Institute, Osaka, Japan. Animals were given free access to food and water, and were housed in a room with an automatically controlled light-dark cycle (lights on at 07:00 and off at 19:00), an ambient temperature of $22 \pm 0.5°C$, and a relative humidity of $60 \pm 2\%$. Animal Administrative Committee of Osaka Bioscience Institute approved all experimental procedures. All effort was made to minimize the numbers of animals used, and the suffering of the animals.

BRAIN SURGERY

Adenosine $A_{2A}R$-Cre and WT mice aged 18–20 weeks, weighing an average of 25 g, were stereotaxically injected with AAV-lox-stop-hrGFP following the procedure optimized by Chamberlin et al. (1998) and Baldwin et al. (2013). Under pentobarbital anesthesia (50 mg/kg, i.p.), the adenosine $A_{2A}R$-Cre and WT mice were positioned in a stereotaxic apparatus, before a burr hole was made under aseptic conditions. A glass micropipette (10–20 μm outer tip diameter) containing the AAV-lox-Stop-hrGFP was connected to an air compression system. The glass micropipette was lowered into the brain at stereotaxic coordinates based on the mouse brain atlas (Paxinos and Franklin, 1997), viz, the AcbC (AP: +1.1 mm; ML: 1.0 mm; DV: 3.8 mm), the medial AcbSh (AP: +0.98 mm; ML: 0.5 mm; DV: 4.0 mm), and the ventral AcbSh (AP: +1.10 mm; ML: 1.0 mm; DV: 5.0 mm). The AAV-lox-Stop-hrGFP was delivered by slow pressure injection lasting 15 min to allow the tracer to diffuse into the brain. After leaving the pipette in the brain for an additional 10 min, the pipette was slowly retracted. Finally, a layer of gel-film was placed over the region of the craniotomy, and surgical staples were used to close the incision. Mice were then placed on a constant temperature plate and monitored during recovery. Mice were then returned to their home cage when fully awake.

TISSUE PREPARATION

Four weeks after surgery, mice were deeply anesthetized with chloral hydrate (500 mg/kg, i. p.), and transcardially perfused with 0.9% saline followed by 4% paraformaldehyde (Sigma) in 0.1 M phosphate buffer (PB, pH 7.4). Brains were removed from the skull immediately after perfusion, post fixed in 4% paraformaldehyde at 4°C for 2 h, and transferred to 20% sucrose in 0.1 M PB. Serial sections of 30 μm were cut on a Leica freezing microtome in the coronal plane, collected in 0.1 M PB (pH 7.4), protected in a cryoprotectant solution, and stored at −20°C until further processing for immunohistochemistry.

IMMUNOHISTOCHEMICAL STAINING

To identify $A_{2A}R$ neurons and their projections in various brain regions, hrGFP-expressing AAV was injected into the Acb. We had intended to use fluorescence microscopy to directly monitor the fluorescence of hrGFP in the brain sections. However, the hrGFP fluorescence in anterogradely labeled perikarya and axons of the neurons was too weak to be visualized. Brain sections of the transgenic mice were therefore stained with anti-hrGFP antibody to detect hrGFP at a higher sensitivity using both avidin–biotin complex (ABC) and 3, 3′-diaminobenzidine tetrahydrochloride (DAB; Vector Laboratories; cat. no. SK-4100).

For the ABC method, stored free-floating sections were washed in PBS for 15 min with three changes of buffer, and treated for 30 min in 3% H_2O_2 to quench endogenous peroxidase activity. After washing, the sections were blocked for non-specific binding of the secondary antibody in 5% normal goat serum (NGS; Vector Laboratories; cat. no. S-1000, lot no. X0815) and 0.3% Triton X-100 in PBS for 1 h at room temperature (RT). The sections were then incubated overnight at 4°C with hrGFP polyclonal rabbit antiserum (Stratagene; cat. no. 240142; lot no. 0830269; 1:30,000) followed by a biotinylated goat anti-rabbit IgG antibody (Vector Laboratories; cat. no. BA-1000; lot no. W2206), and ABC solution (Vectastain Elite ABC Kit; Vector Laboratories; cat. no. PK-4000; 1:1,000). After washing in PBS, the sections were visualized using DAB, washed in PBS, mounted on gelatin-coated slides, and air dried overnight. Some sections were also counter-stained with 0.1% cresyl violet. Finally, the sections were dehydrated in ascending alcohol concentrations, cleared in xylene, and cover slipped.

For immunofluorescence, the sections were blocked for non-specific binding of the secondary antibody in 5% NGS and 0.3% Triton X-100 in PBS for 1 h at RT. Sections were then incubated overnight at 4°C in rabbit anti-hrGFP antiserum (Stratagene; cat. no. 240142, lot no.0830269; 1:5,000) in 5% NGS (Vector, laboratories, cat. no. S-1000; lot no. X0815) with 0.3% Triton X-100 in PBS. Following incubation in primary antiserum, the sections were incubated with Alexa 488-conjugated anti-rabbit IgG (H + L) secondary antibody (Invitrogen, La Jolla, CA, USA; cat. no. A11034; lot no. 1073084; 1:500) for 1 h at RT. After washing in PBS, the sections were mounted on glass slides and coverslipped with Fluoromount-G^{TM} mounting medium (Southern Biotech; Catalog No, 0100-01). Negative controls omitting the primary antibody were carried out in all experiments, and did not show any immunoreactivity.

MICROSCOPY AND CHARTING

The sections were observed and photographed on an Olympus IX71 microscope with fluorescent and bright-field optics. Adobe Photoshop CS2 was used for post-processing of digital photomicrographs and the schematic illustrations. The sharpness, color balance, and contrast were adjusted to obtain an optimal match of labeled cells or fibers against the background. Anatomical landmarks and abbreviations used in the present study were based on the Paxinos and Franklin mouse brain atlas (Paxinos and Franklin, 1997). High resolution fluorescent images of hrGFP were generated using a Leica SP2 confocal laser scanning microscope (Leica, Mannheim, Germany).

We evaluated the outlines of sections and major structures at low magnification (4×), and then mapped the profiles of the hrGFP immunoreactive (hrGFP-IR) perikarya and projection fibers under high magnification. Plotting of labeled cell bodies and fibers was done by Adobe Photoshop CS2. Using a method for semi-quantitative evaluation optimized by Gautron et al. (2010) and Bálint et al. (2011), the density of hrGFP-IR terminal networks was subjectively determined in six grades of fiber weight as follows: ++++, abundant; +++, numerous; ++, moderate; +, few; ±, sparse; and −, absent (**Table 1**). Processing and measurement of the varicosities/boutons were performed using image analysis Image J (National Institutes of Health, USA) as shown in **Table 1**.

RESULTS

INJECTION LOCATION AND MORPHOLOGY OF A_{2A}R NEURONS

Visualized by either fluorescent or ABC techniques, injections of AAV-lox-Stop-hrGFP revealed small deposit sites in the Acb in 15 animals of the present study. Three typical injections affected the AcbC (M-7; **Figures 1A–E**), the medial AcbSh (M-11; **Figures 1F–H**), and ventral AcbSh (M-21; **Figures 1I,J**), and were chosen for the present analyses. The injection locations of three cases were schematically described in **Figure 1**. Three cases showed that hrGFP was almost exclusively confined to the AcbC, mAcbSh, and vAcbSh, respectively, except for the case (M-7) showed few expressiones outside the AcbC in neurons located in the caudate putamen (**Figure 1A**) and the dorsal part of AcbSh (**Figures 1A–D**).

On the sections, the presence of hrGFP-IRc, indicating A_{2A}R neurons, was observed as strong fluorescent or DAB reactive elements in clustered perikarya, dendrites, and proximal axons within both the AcbC and the AcbSh in adenosine A_{2A}R-Cre mice (**Figures 2A–F**), but not in the WT mice (**Figures 2G,H**). Additionally, we analyzed the A_{2A}R neuron cell bodies within the Acb and the distribution of the hrGFP-IR axonal fibers using the hrGFP-IRc antibody in samples from the three animals on typical serial sections of the brain from bregma +0.98 to −5.40 mm (**Figures 4–7**).

At high magnification (**Figures 3A–D**), hrGFP-IR neurons were observed as multipolar or bipolar neurons, and a higher density of the perikarya was observed in the lateral part of the core compared with the medial region. The perikarya of the neurons were mainly round or oval in shape, and measured approximately 10–15 μm in diameter. Dendrites extended from their perikarya and bifurcated in different directions. Most dendrites possessed puncta, indicating dendritic spines and the features of less-spiny neurons. hrGFP-IR axons were thin thread-like fibers that coursed straight off the Acb **Figure 3A**. These observations are consistent with the previous reports in rat models (Meredith et al., 1992).

PROJECTIONS OF THE ACB A_{2A}R NEURONS

hrGFP-IR axons from Acb A_{2A}R neurons were distributed in the ipsilateral hemisphere to the injection site. The distribution patterns of hrGFP-IR axons after injection into the AcbC, medial AcbSh, and ventral AcbSh are demonstrated schematically in **Figure 4**, respectively. Finally, we depict the brain areas related to sleep-arousal in detail in **Figures 5–7**. The relative density of hrGFP-IR axons and terminals in each targeted area is summarized in **Table 1**.

FORBRAIN PROJECTIONS

Following injection into the AcbC (M-7), hrGFP-IR axons extended laterally from the injection site into the adjacent ventral portion of the caudate putamen (CPu; 38 boutons/varicosities), ventrally into the ventral pallidum (VP; 998 boutons/varicosities), and medially into the caudal portion of the nucleus of the vertical limb of the diagonal band (VDB; 189 boutons/varicosities;

Table 1 | Distribution of hrGFP-positive varicosities and terminal networks following AAV-lox-Stop-hrGFP injections into the AcbC, mAcbSh, and vAcbSh.[1]

Regions	Acbc		mAcbSh		vAcbSh	
	Varicosities	Terminal networks	Varicosities	Terminal networks	Varicosities	Terminal networks
Forebrain						
BST	–	–	81	+	–	–
BSTLP	267	++	–	–	–	–
VP	998	++++	80	++	197	+++
VDB	189	+	38	++	93	++
HDB	126	++	157	+	–	–
BMA	433	++	–	–	–	–
BLA	423	++	–	–	–	–
CPU	38	+	–	–	–	–
SI	272	+++	165	++	794	+++
LGP	187	+++	–	–	–	–
Diencephalon						
LPO	212	+++	475	++	204	++
LHa	936	++++	244	++	215	+++
LHt	2023	++++	324	+++	571	+++
LHm	334	+++	155	++	772	+++
AHP	423	+++	–	–	–	–
Pe	138	±	–	–	–	–
DM	1228	+++	–	–	99	++
EP	33	+	–	–	–	–
VMHDM	822	++	–	–	–	–
PH	244	++	442	+++	203	++
VTM	47	+	–	–	–	–
DTM	64	±	–	–	–	–
STh	96	++	–	–	–	–
Brainstem						
VTA	295	+++	39	+	119	+++
MnR	244	++	–	–	82	+++
DR	278	++	–	–	214	++
VLPAG	127	+	–	–	234	++
DRI	–	–	–	–	39	++
MPB	–	–	–	–	23	++
LC	–	–		–	12	+

[1] *++++, Abundant; +++, numerous; ++, moderate; +, few; ±, sparse; –, absent. All abbreviations are defined in the abbreviation section.*

Figure 4A1). At a more posterior level, some axons with varicosities proceeded longitudinally in the ventromedial portion of the anterior commissure, throughout the caudal AcbSh into the medial VP, the caudal VDB, and the rostral nucleus of the horizontal limb of the diagonal band (HDB; 126 boutons/varicosities; **Figure 4A2**). Axons were coursing in a wavy form and varicosities were appearing big round and small ellipse (**Figure 5A**). The mean diameter of varicosities in the HDB (2.103 μm) was bigger than in the VDB (1.939 μm). At the caudal level of the optic chiasm, a dense plexus of axons with numerous varicosities were observed in the dorsal portion of the VP, which turned dorsally into the ventral part of the lateral globus pallidus (LGP; 187 boutons/varicosities), ventromedially to enter the substantia innominata (SI; 272 boutons/varicosities), and medially into the sub-regions of the bed nucleus of the stria terminalis (BST; **Figure 4A3**). More caudally, a number of axons were still found in the ventral LGP and the SI (**Figure 4A4**), and hrGFP-IR-positive axons formed small ellipse varicosities

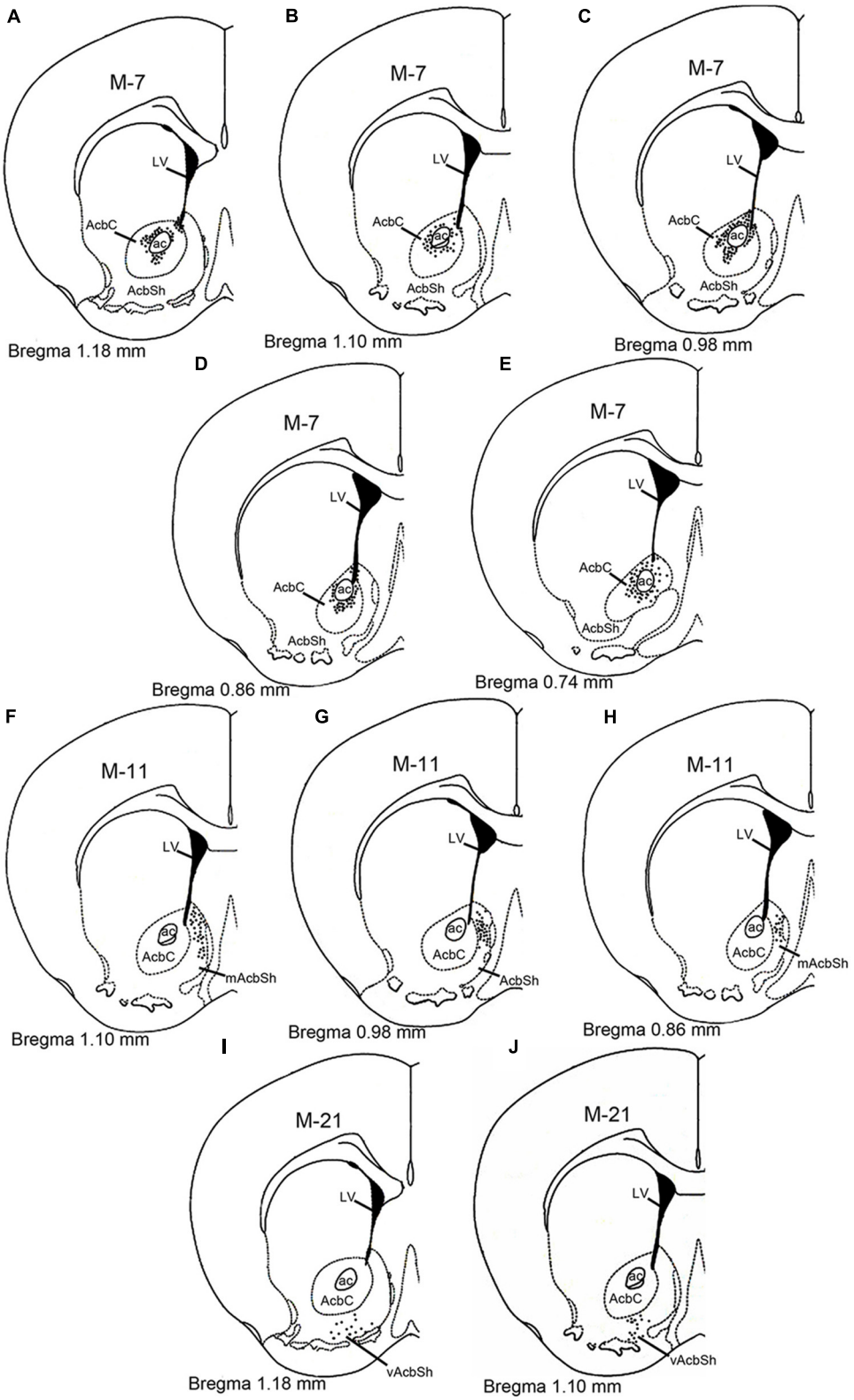

FIGURE 1 | Schematic diagram showing the AAV-lox-Stop-hrGFP injection sites in the nucleus accumbens. The dotted areas indicate the injection locations in the core **(A–E)**, medial shell **(F–H)**, and ventral shell **(I–J)**. Each dark dot represents one labeled cell body. Abbreviations are as follows: ac, anterior commissural nucleus; AcbC: nucleus accumbens, core; AcbSh, nucleus accumbens, shell; mAcSh, medial AcbSh; vAcSh, ventral AcbSh; LV, lateral ventricle.

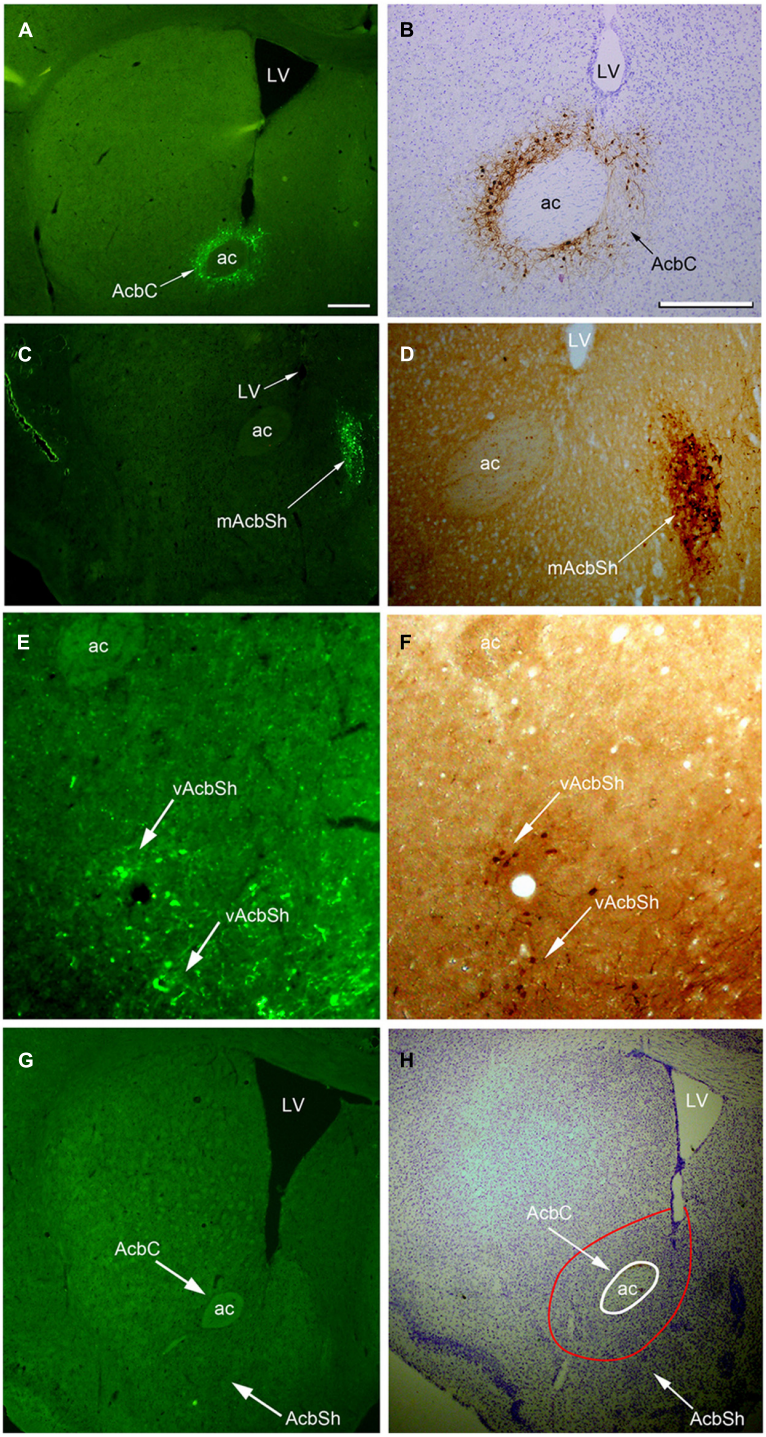

FIGURE 2 | Images of hrGFP immunoreactivity (hrGFP-IRc) showing examples of the AAV-lox-Stop-hrGFP injection sites. (A,B) hrGFP-IRc in the Acb visualized by fluorescent and ABC techniques with Nissl-counterstaining. hrGFP-IRc staining, confirming the presence of the $A_{2A}R$ neurons, was deposited around the Acb and covered most of the core area (arrows) in two labeled adjacent sections of this example (M-7). **(C,D)** hrGFP-IRc staining, indicating $A_{2A}R$ neurons in the AcbSh, visualized by fluorescence and ABC techniques. Positive staining with hrGFP-IRc occupied the mAcbSh in **(C,D)** in two labeled adjacent sections of this case (M-11). **(E,F)** hrGFP-IRc staining, indicating $A_{2A}R$ neurons in the vAcbSh, visualized by fluorescence and ABC techniques. Positive staining with hrGFP-IRc occupied vAcbSh in **(E,F)** in two labeled adjacent sections in this case (M-21). **(G,H)** A brain section from the wild type mouse with fluorescent staining **(G)** and ABC techniques with Nissl-counterstaining **(H)** showing no hrGFP-IRc in Acb. Abbreviations are as follows: AC, anterior commissural nucleus; LV, lateral ventricle; AcbC, nucleus accumbens core; AcbSh, nucleus accumbens shell; mAcbSH, medial AcbSh; vAcbSh, ventral AcbSh. Scale bar = 500 μm in **(A)**; 100 μm in **(B)**; 500 μm in **(C)**; 100 μm in **(D)**; 100 μm in **(E)**; 100 μm in **(F)**; 500 μm in **(G);** 500 μm in **(H)**.

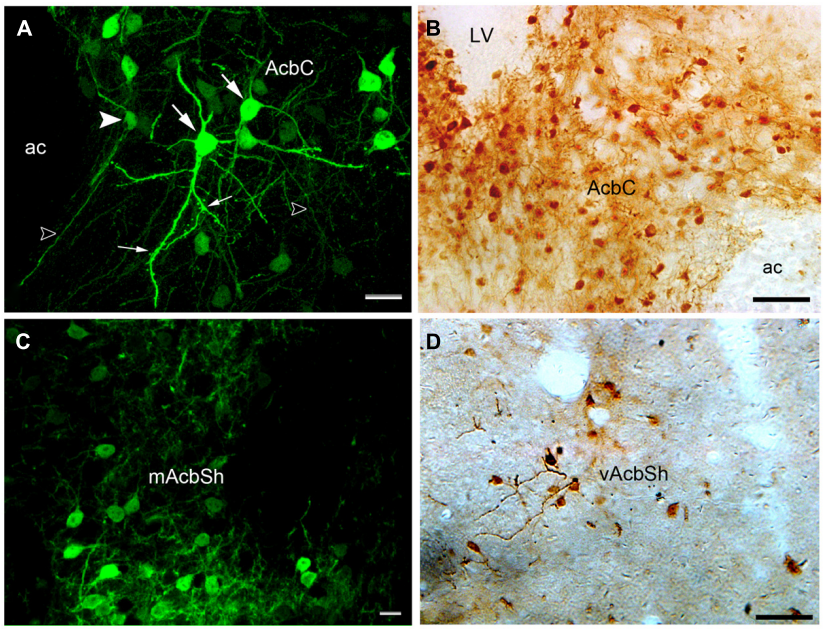

FIGURE 3 | Images showing hrGFP-IR-positive neurons in the Acb of the adenosine A_{2A}R Cre mouse. (A,B) The hrGFP-IR neurons in the core visualized by fluorescent and ABC techniques. Most of the perikarya in the core were observed as multipolar (large arrows) and bipolar (arrowhead) neurons. The dendrites extending from the perikarya were thick, and some of them had punctuate spines (small arrows). The axons were thin, straight fibers (opened arrows). **(C)** hrGFP-IR neurons in the mAcbSh visualized by fluorescent and ABC techniques. The neurons in this region were similar in shape to those in the core. **(D)** The neurons in the vAcbSh visualized by ABC techniques. AC, anterior commissural nucleus; LV, lateral ventricle; mAcbSh, medial AcbSh; vAcbSh, ventral AcbSh. Scale bar = 20 μm in **(A)**; 50 μm in **(B)**; 10 μm in **(C)**; 50 μm in **(D)**.

(1.841 μm mean diameter) within the SI and shifted medially into the rostral portion of the anterior lateral hypothalamus (LHa; **Figures 4A4** and **5B**). Injection in to the AcbC therefore resulted in more anterograde labeling in the VP than injections into the medial or ventral AcbSh (**Table 1**). In addition, moderate projections were observed in the anterior part of basomedial amygdaloid nucleus (BMA) and the anterior part of basolateral amygdaloid nucleus (BLA; **Figure 4A7**), visualized as diencephalic projections.

After the medial AcbSh injection (M-11), hrGFP-IR axons spread ventromedially from the injection site into the adjacent caudal VDB (38 boutons/varicosities; **Figures 4B1** and **5C**). Approximately 0.12 mm caudally from the injection site, axons were observed in the dorsomedial portion of the VP and the lateral margin of the caudal VDB (**Figure 4B2**). More distally, labeled ventrally oriented axons passed below the anterior commissure into the dorsolateral portion of the rostral lateral pre-optic area (LPO), the ventro-lateral portion of the rostral SI, and the HDB (**Figure 4B3**). Labeled fibers also formed small round and ellipse varicosities within the SI and HDB (**Figure 5D**). Injection in to the medial AcbSh therefore generated increased labeling in the VDB compared with injection into the AcbC (**Table 1**).

After ventral AcbSh injection (M-21), hrGFP-IR axons projected ventrally to the VP, and medially to the lateral border of the VDB (93 boutons/varicosities; **Figure 4C1**). Within the VDB, fibers, and terminals bearing few small ellipse varicosities were observed (**Figure 5E**). At the level of the caudal VDB, numerous stained fibers, and terminals were seen in the ventromedial VP (**Figure 4C2**). At the level of the caudal optic chiasm, hrGFP-IR axons formed a number of fascicles in the ventral portion of the VP, which spread ventrally into the dorsal portion of the SI (**Figure 4C3**). Within the SI, wavy hrGFP-IR axons appeared with small round varicosities (794 boutons/varicosities), sent some terminals to the SI (**Figure 5F**), and further extended medially into the dorsal portion of the adjacent LPO (**Figure 4C3**). More caudally, moderate hrGFP-IR axons with varicosities were still observed in the dorsomedial portion of the SI (**Figure 4C4**). Injection into the ventral AchSh therefore generated more hrGFP-IR axons and terminals in the SI than medial AcbSh injection (**Table 1**).

DIENCEPHALIC PROJECTIONS

hrGFP-IR-stained axons from the AcbC (M-7), medial AcbSh (M-11), and ventral AcbSh (M-21) were observed in the LPO (**Figures 4A3,B3,4,C3**), and in the lateral hypothalamus (LH; **Figures 4A4–8,B5–7,C4–6**). The densest projections and the biggest varicosity were found in the tuberal part of the lateral hypothalamus (LHt; 2023 boutons/varicosities and 4.837 μm), originating in the core region (**Figures 4A5,6** and **6B**). In the rostral LHa and caudal LHt, numerous varicosity-bearing fibers and terminals were observed (**Figures 6A,B**). In mice that had been injected in the ventral AcbSh, numerous axons with moderate varicosities were also found in the LH (**Figures 4C4–6** and **6G–I**). However, these projection axons bearing less varicosities were fewer in number in mice injected into the medial AcbSh (**Figures 4B5–7** and **6D–F**; **Table 1**).

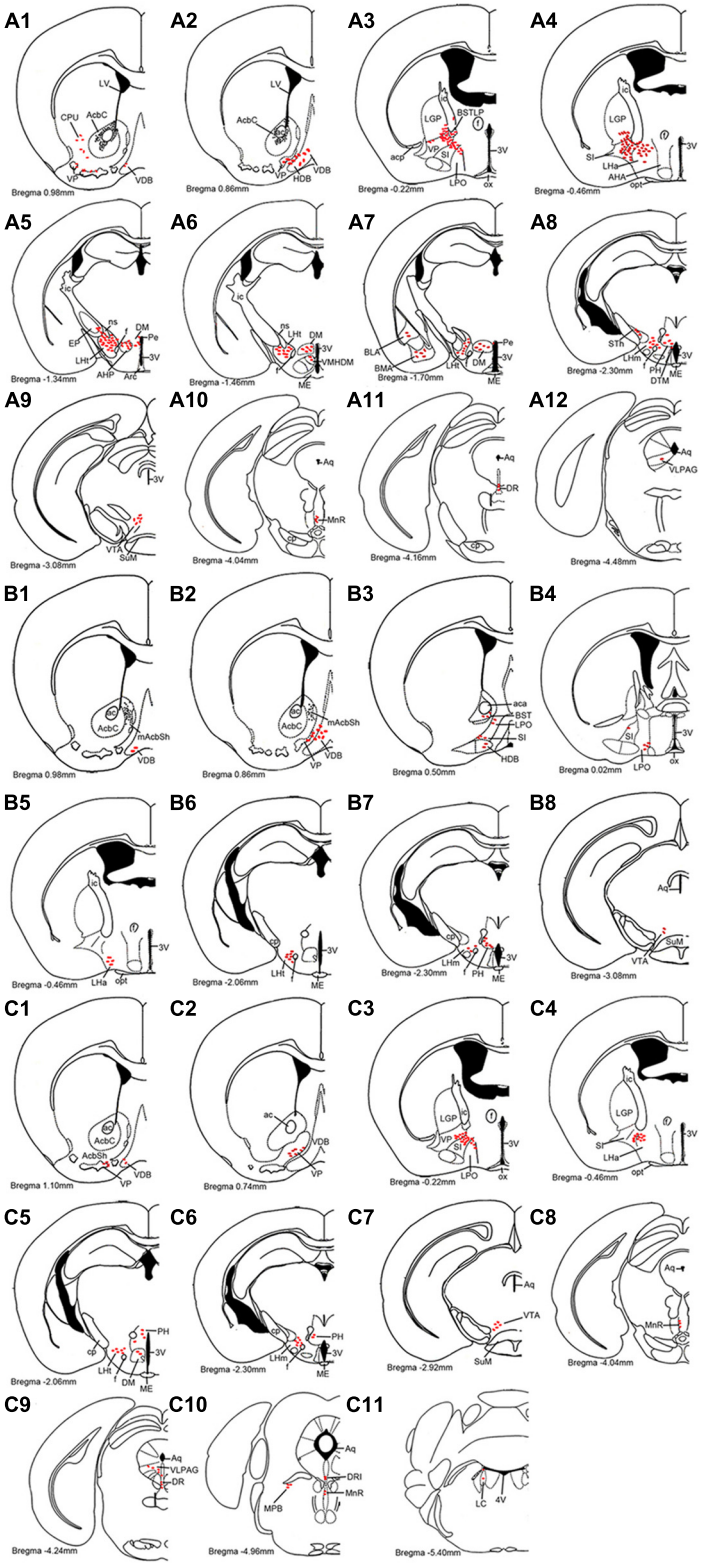

FIGURE 4 | Schematic drawings showing the distribution profiles of hrGFP-IR fibers and termini from the AcbC (A1–A12; M-7), medial AcbSh (B1–B8; M-11), and ventral AcbSh (C1–C11; M-21) injections. The hrGFP-IR axons and terminals are indicated by red ellipse dots. The projections from the AcbC and ventral AcbSh extend more caudally than those from medial AcbSh. All abbreviations are defined in the abbreviation section.

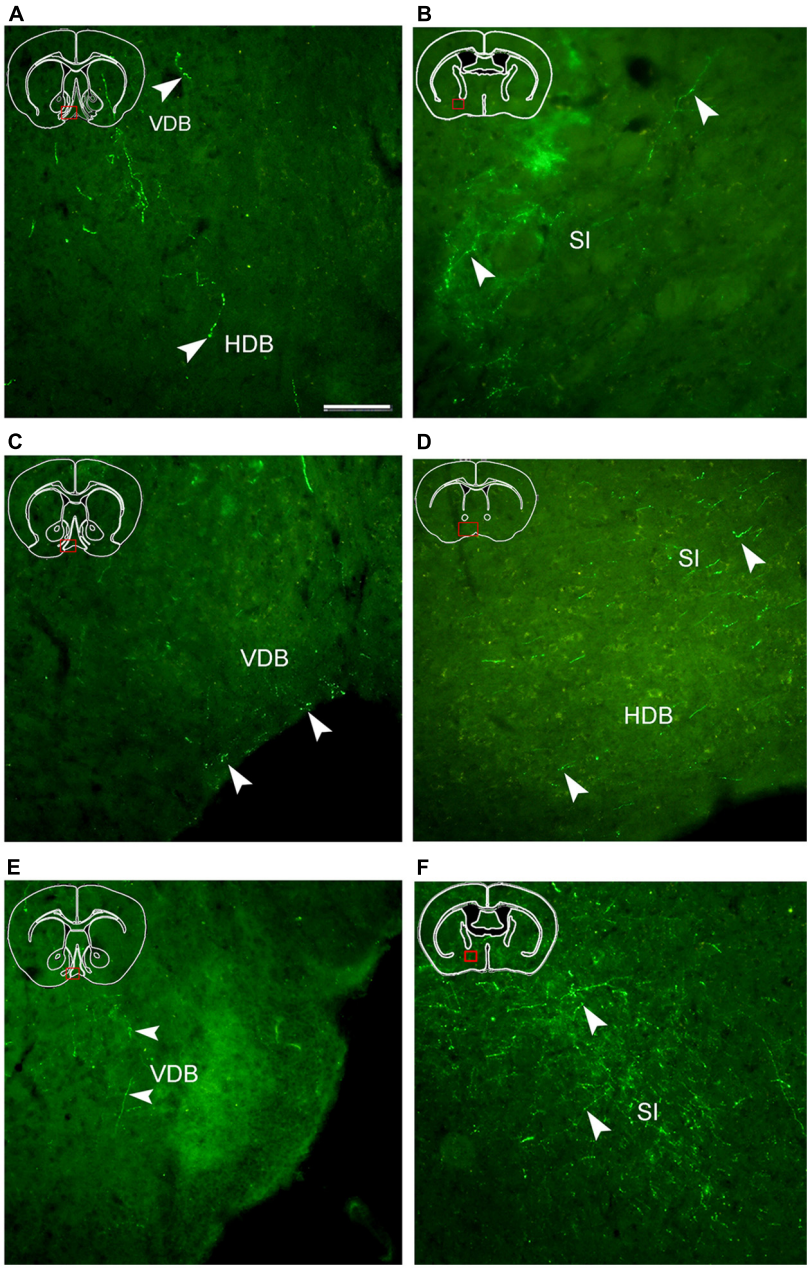

FIGURE 5 | Fluorescent images showing hrGFP-IR fibers and termini from the AcbC (A,B; M-7), medial AcbSh (C,D; M-11), and ventral AcbSh (E,F; M-21) injections. Axons with varicosities invade the nucleus of the vertical limb of the diagonal band (VDB; **A,C,E)**, the nucleus of the horizontal limb of the diagonal band (HDB; **A,D)**, and the substantia innominate (SI; **B,D,F)**. **(A,B)** hrGFP-IR axons and termini in the VDB, the HDB, and the SI following the injection of AAV-lox-Stop-hrGFP into the AcbC. **(C,D)** hrGFP-IR axons and termini in the VDB, the HDB, and the SI following the injection of AAV-lox-Stop-hrGFP into the medial AcbSh. **(E,F)** hrGFP-IR axons and termini in the VDB and the SI following the injection of AAV-lox-Stop-hrGFP into the ventral AcbSh. Arrowheads indicate varicosities. Scale bar = 100 μm.

Following AcbC injection (M-7), hrGFP-IR axons were located in the dorsal portion of the LPO (212 boutons/varicosities) at the level of optic chiasm (**Figure 4A3**), and the dorsal LHa (936 boutons/varivosities) at the level of optic tract (**Figure 4A4**). Within the LHa, varicosities formed groups and mainly showed small round (**Figure 6A**). Axons from the medial AcbSh projected in to the dorsolateral LPO beneath the anterior commissural nucleus (ac; **Figure 4B3**), the ventromedial LPO at the level of optic chiasm (**Figure 4B4**), and the ventral LHa. Within the LHa, varicosities were sparsely distributed and showed small round and ellipse (**Figure 6D**). However, after ventral AcbSh injection, hrGFP-IR axons were found in the dorsal part of LPO at the level of optic chiasm (**Figure 4C3**), and the dorsolateral portion of LHa (**Figure 4C4**). The mean diameter (1.575 μm) of the varicosities

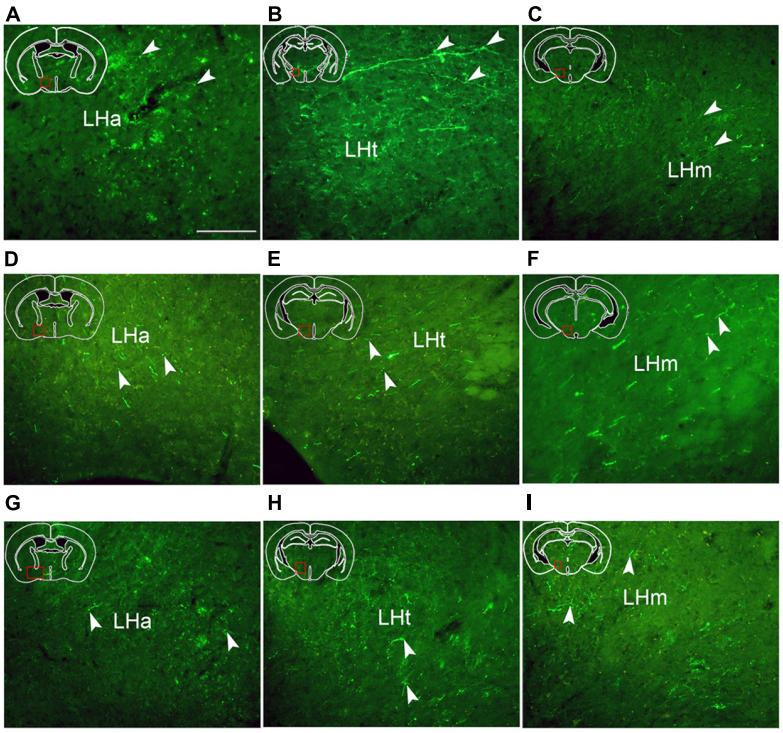

FIGURE 6 | Fluorescent images demonstrating hrGFP-IR axons and termini from the AcbC (A,B,C; M-7), the medial AcbSh (D,E,F; M-11), and the ventral AcbSh (G,H,I; M-21). Axons invade the anterior part of lateral hypothalamus (LHa), the tuberal part of lateral hypothalamus (LHt), and the mammillary part of lateral hypothalamus (LHm) after AcbC, medial AchSh, and ventral AcbSh injection, respectively. Arrowheads indicate varicosities. Scale bar = 100 μm.

in the LHa following injection into ventral AcbSh was smaller than the mean diameter of both varicosities of the AcbC (2.085 μm) and mAcbSh (1.838 μm).

Throughout the length of the hypothalamus, hrGFP-IR axons extended around the LH after AcbC injection (M-7). At the level of the rostral LHt, the fibers traversed along the dorsal portion of the fornix, extended medially into the AHP (423 boutons/varicosities), and the periventricular hypothalamic zone, and spread dorsolaterally to reach the ventromedial part of the entopeduncular nucleus (EP; 33 boutons/varicosities; **Figures 4A5** and **6B**). The nerve plexus then spread out medially into the dorsomedial hypothalamic nucleus (DM; 1228 boutons/varicosities), and the dorsomedial portion of the ventromedial hypothalamic nucleus (VMHDM; 822 boutons/varicosities; **Figure 4A6**). Caudally to this, some axons extended laterally through the sublenticular region to the BMA and BLA (**Figure 4A7**). At the rostral mammillary part of lateral hypothalamus (LHm), axons spread dorsomedially into the posterior hypothalamic area (PH), and the dorsal tuberomammillary nucleus (DTM; **Figure 4A8**). In addition, some hrGFP-IR axons were found to run along the medial margin of the subthalamic nucleus (STh), projecting terminals into the STh (96 boutons/varicosities; **Figure 4A8**). Adjacent to this, there were also some projections to the ventral tuberomammillary nucleus (VTM; **Figure 7A**).

After medial AcbSh injection (M-11), hrGFP-IR axons only extended dorsomedially into the PH (442boutons/varicosities) at the level of the rostral LHm (**Figure 4B7**). In contrast, hrGFP-IR axons spread out medially or dorsomedially into the DM (99 boutons/varicosities) or the PH (203 boutons/varicosities) at the level of the caudal LHt after ventral AcbSh injection (**Figure 4C5**).

BRAINSTEM PROJECTIONS

$A_{2A}R$ neurons of the AcbC (M-7), medial AcbSh (M-11), and ventral AcbSh (M-21) were found to project to similar areas of the ventral tegmental area (VTA; **Figures 4A9,B8,C7**). In case of AcbC, hrGFP-IR fibers were mainly located in the dorsal part of the VTA, formed numerous varicosities (295 boutons/varicosities), and had short, straight processes (**Figure 7B**). For ventral AcbSh injection, hrGFP-IR fibers bearing moderate varicosities were observed mainly in the ventral portion of the VTA (119 boutons/varicosities), and also processed shortly and straightly (**Figure 7F**). In case of medial AcbSh injection, however, few projections were found in the medial part of the VTA (39 boutons/varicosities; **Figure 4B8**), and so their processes could not be followed. The varicosities mean diameter in the VTA following injection of AcbC, mAcbSh, and vAcbSh was 1.801, 1.67, and 1.635 μm, respectively.

After AcbC injection (M-7), the axons shifted dorsomedially through the lateral margin of the rostral median raphe nucleus (MnR; **Figures 4A10** and **7C**), while some axons continued to the ventral portion of the dorsal raphe nucleus (DR; **Figures 4A11** and **7D**), and into the ventrolateral periaqueductal gray (VLPAG;

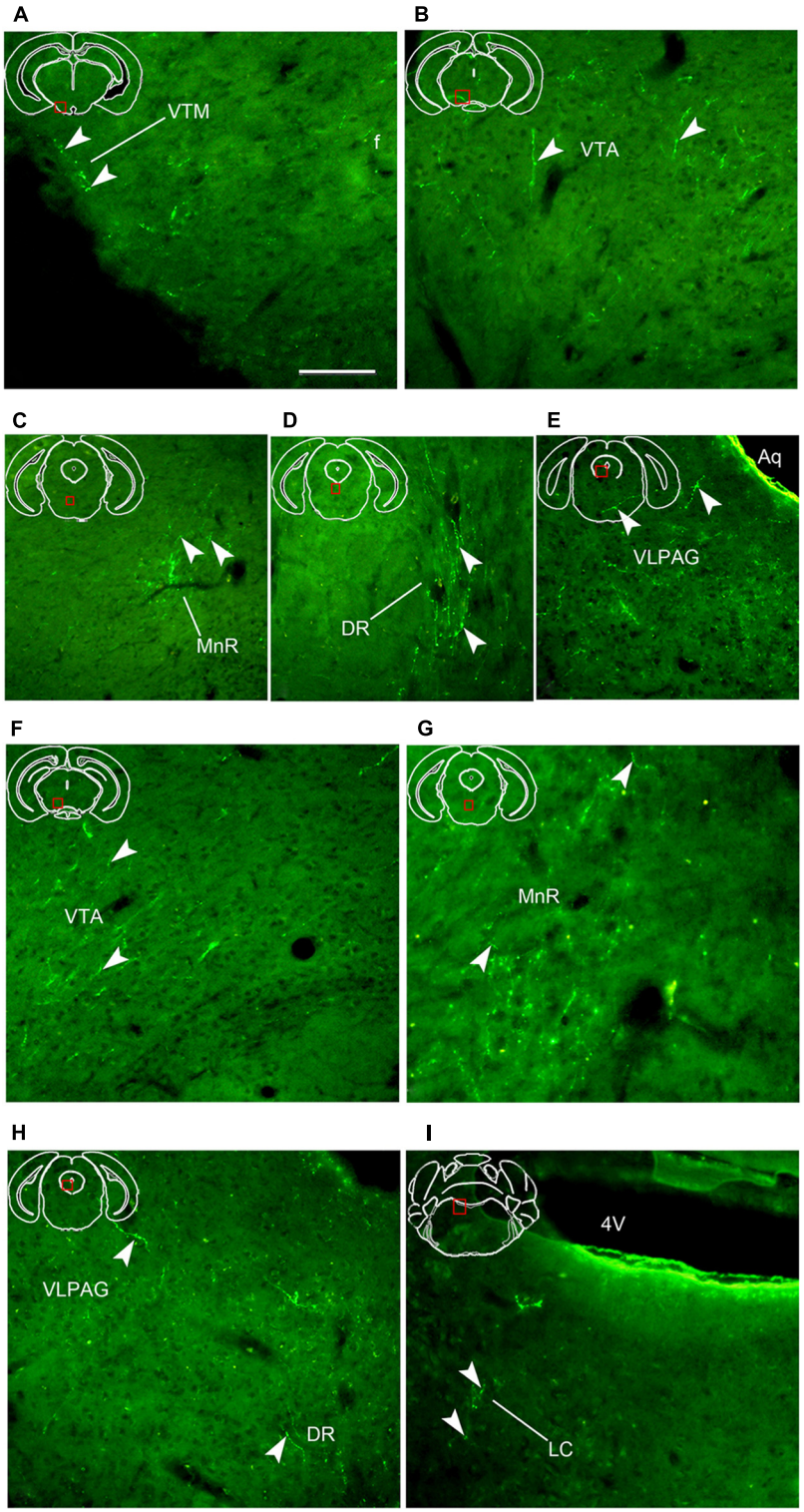

FIGURE 7 | Fluorescent images showing hrGFP-IR axons and termini from the AcbC (A–E; M-7) and ventral AcbSh (F–I; M-21) injections. **(A–E)** Axons with varicosities invade the ventral tuberomammillary nucleus [**(A)**, VTM], the ventral tegmental area [**(B)**, VTA], the medial raphe nucleus [**(C)**, MnR], the dorsal raphe nucleus [**(D)**, DR], and the ventrolateral periaqueductal gray [**(E)**, VLPAG] after injection with AAV-lox-hrGFP into the AcbC (M-7). **(F–I)** Axons with varicosities invade the ventral tegmental area [**(F)**, VTA], the medial raphe nucleus [**(G)**, MnR], the dorsal raphe nucleus [**(H)**, DR], the ventrolateral periaqueductal gray [**(H)**, VLPAG], and the locus coeruleus [**(I)**, LC] following the injection of AAV-lox-hrGFP into the mAcbSh (M-22). Arrowheads indicate varicosities. Abbreviations: 4V, forth ventricle; Aq, aqueduct; f, fornix. Scale bar = 100 μm.

Figures 4A12 and **7E**). Within the DR, varicosities showed medium round and vertical distribution. The varicosities in the VLPAG were small round or ellipse and transverse distribution.

In case of the ventral AcbSh injection (M-21), the axons traveled dorsally along the lateral border of the MnR (**Figures 4C8** and **7G**), continuing to the caudal DR (**Figures 4C9** and **7H**). The remaining axons then entered the VLPAG (**Figure 4C9**), and ran wavy (**Figure 7H**). More caudally, hrGFP-IR axons bearing few varicosities were found in the caudal MnR (82 boutons/varicosities), and turned into the ventral part of dorsal raphe nucleus (DRI; **Figure 4C10**). Additionally, moderate fibers with few varicosities and termini were found in the medial parabrachial nucleus (MPB; **Figure 4C10**). Finally, few axons were traced into the locus coeruleus (LC) and formed sparse swellings (12 boutons/varicosities) in the rostral forth ventricle (**Figures 4C11** and **7I**), but nothing further was observed. The boutons in the MnR mainly presented medium round (**Figure 7G**), whereas in the VLPAG and DR they were small round or ellipse (**Figure 7H**).

DISCUSSION

Because of the important physiological, pathological, and pharmacological functions of the $A_{2A}R$ in Acb, the present study mapped the projections of $A_{2A}R$ neurons in various brain regions in $A_{2A}R$-Cre mice using a tracer of AAV-lox-Stop-hrGFP. Our data revealed significant differences in the areas innervated by the AcbC, medial AcbSh, and ventral AcbSh. The projection sites of Acb $A_{2A}R$ neurons were summarized, allowing the formation of a neuromorphological basis to better understand the functions of the Acb $A_{2A}R$, and especially its role in regulating sleep-wake behavior.

TECHNICAL CONSIDERATIONS

Efferent projections of Acb have previously been studied in great detail using conventional neuroanatomical methods (Heimer et al., 1991; Zahm and Heimer, 1993; Usuda et al., 1998). Systematic tracing of axonal projections from specific neurons remains challenging using conventional tracking methods. However, novel technologies allowing individual neurons to be selectively traced have been developed. First, DeFalco et al. (2001) used virus-assisted mapping to identify leptin receptor-expressing neuronal afferent projections. Additional work developed transgenic mouse models expressing a fusion protein of the C-terminal fragment of tetanus toxin and GFP specifically in orexin neurons, allowing visualization of orexin neurons (Sakurai et al., 2005). Recently, Hnasko et al. (2012) used approach similar to that used here to trace the projection of glutamate neurons in the ventral tegmental area using a conditional channel rhodpsin-expressing AAV (AAV-EF1a-DIO-ChR2-mCherry). Although these approaches differ from the approach taken here, these methods provide a useful reference for tracing other axonal projections of selected neurons.

The approach used in the present study was previously described and optimized by Gautron et al. (2010). Additionally, the transgenic mouse model used here has been well characterized in a previous report (Durieux et al., 2009, 2012). Because of the inherent difficulty of conventional approaches for the tracing of specific neurons, we used a novel approach based on the conditional expression of hrGFP. Briefly, AAV was stereotaxically injected into the AcbC and AcbSh of mice expressing Cre recombinase under the control of the adenosine $A_{2A}R$ promoter (Durieux et al., 2009, 2012). Consequently, mice exhibited robust hrGFP expression specifically in Acb $A_{2A}R$ neurons after injection. Importantly, hrGFP was efficiently transported in axonal projections to brain regions innervated by the Acb $A_{2A}R$ neurons.

ACB $A_{2A}R$ NEURONS PROJECTIONS AND COMPARISONS WITH PREVIOUS STUDIES

For the AcbC, the main forebrain projections occur to the BST sub-regions, the VP, the CPu, the diagonal band nucleus, the SI, the LGP, the BLA, and the BMA, while the primary diencephalon targets are the LPO, the LH, the AHP, the DM, the VMHDM, the PH, the TMN, and the STh. Finally, the major brain stem projections are to the VTA, the MnR, the DR, and the VLPAG. In case of medial AcbSh, the major forebrain projection sites are the BST, the VP, the diagonal band nucleus, and the SI. In contrast, the projected areas from the diencephalon are the LPO, the LH, and the PH, while in the brainstem, the medial AcbSh only projects to the VTA. When projections from ventral AcbSh are considered, the forebrain targets are the diagonal band nucleus, the VP, and the SI, while the main diencephalon sites are the LPO, the LH, the DM, and the PH. Finally the primary brainstem targets are the VTA, the MnR, the DR, the VLPG, the DRI, the MPB, and LC.

As described above, $A_{2A}R$ neurons from Acb sub-regions jointly project to the VP. Although the projections of Acb $A_{2A}R$ neurons to the VP have been well described in rats (Mingote et al., 2008), little research has been carried out to characterize the overall projection patterns of Acb $A_{2A}R$ neurons. The most thorough analysis of Acb efferent projections was carried out in an early study using an autoradiographic fiber-tracing method (Nauta et al., 1978) and BDA tracer (Usuda et al., 1998). Additional studies, using PHA-L and BDA, described Acb projections in the cat (Troiano and Siegel, 1978; Groenewegen and Russchen, 1984), rhesus monkey (Haber et al., 1990), rat (Heimer et al., 1991; Zahm and Heimer, 1993), and chicken (Bálint et al., 2011).

In general, our findings are consistent with the previous studies, with the exception that some reports (Heimer et al., 1991; Usuda et al., 1998) revealed fairly widespread projections from the middle to caudal Acb to other sites, including the substantia nigra pars compacta (SNC), retrorubral area (RR), pedunculopontine tegmental nucleus (PPTg), substantia nigra pars reticulate (SNr), substantia nigra pars lateralis (SNI), paramedian raphe nucleus (PMR). We did not observe axons in any of these structures, which may be explained by the absence of projections from Acb neurons expressing $A_{2A}Rs$. In the ventral striatum, GABAergic efferent neurons can be characterized into two major classes: GABAergic enkephalinergic, and GABAergic dynorphinergic neurons (Ferré et al., 2007). In addition to these two groups, large cholinergic interneurons and GABAergic striatal interneurons also exist (Rosin et al., 2003). Adenosine $A_{2A}Rs$ are found in the dendritic spines of GABAergic enkephalinergic neurons or in the glutamatergic terminals (Ferré et al., 2007; Schiffmann et al., 2007). It is plausible that efferent enkephalinergic and dynorphinergic Acb neurons project differentially to other brain sites. Moreover,

absence of projection in these regions could be due to insufficient coverage of employed AAVs to whole caudal Acb or less sensitivity of the technique in the present study than conventional tracers.

The present mapping showed that AcbC projects to the lateral nucleus of amygdala, consistent with previous findings (Nauta et al., 1978). AcbC injection results in the projection of axons into the periventricular hypothalamic zones, the dorsal hypothalamus area, the PH, the mammillary body, and the EP. However, unlike this study, we demonstrated that AcbC also projects some axons to the BLA. In addition, we also observed that caudal AcbC injection results in projections to the BMA and the DR, none of which had been previously described. A previous study revealed that the medial AcbSh projects to the VP, the BST, the LPO, the LH, and VTA (Usuda et al., 1998). We also observed numerous projections to the VDB and the PH, and few to the HDB. Consistent with the present data, Usuda et al. (1998) depicted ventral AcbSh projections to the VP, the SI, the LPO, the LH, the VTA, the PAG, the PB, and the LC. Furthering these observations, we also detected numerous axons projecting to the HDB and the MnR, and to a lesser extent to the DR, and DRI. Although the reason for this discrepancy could be explained by the different techniques used, or by differences in species of the animals used in each study, we also suggest other important considerations in the following aspects: (1) specific injection site results in the different projections, which is not an exception for this method. For example, AcbC injection in the present study covers the greatest extent core area, although not whole, while the tracer is separately located in a restricted position in the previous studies; (2) few off-site infected neurons, if any, may send projections to those new findings. (3) The possibility of tracer uptake by fibers of passage also lead to those projections; (4) few employed AAVs possibly may be from transport to second-order neurons, which send fibers to those regions. However, the above-mentioned problems are inherent in most tracing approaches but are not specific to our study. In spite of these differences, it is reassuring to see that these techniques identify many of the same efferent projections, but additional studies should be carried out to further explain the discrepancies.

FUNCTIONAL IMPLICATIONS

The major functional implication for the present results is that the Acb adenosine A_{2A}R may have functions in the brain sites receiving axon projections from A_{2A}R neurons. A comparison of the axon distributions with the prior studies (Nauta et al., 1978; Heimer et al., 1991; Usuda et al., 1998) may support the current paradigms of the related functions of Acb adenosine A_{2A}Rs. However, the problem emerges as to whether there is a unified understanding of how anatomical considerations and fiber projections regulate behavioral or physiological processes. The established functional roles of the region most heavily innervated by the A_{2A}R neurons suggests that Acb adenosine A_{2A}Rs are involved in the regulation of sleep (Huang et al., 2007, 2011; Lazarus et al., 2011, 2012, 2013).

A compelling framework that Acb and A_{2A}R modulate wakefulness and sleep comes from the studies of Acb lesions and blocking adenosine A_{2A}R. Acb lesions lead to a significant increase in the amount of wakefulness (Qiu et al., 2010), while ablating both AcbC and AcbSh increases wakefulness but the core lesion plays a more important role in sleep-wake regulation (Qiu et al., 2012). Adenosine A_{2A}Rs are abundantly expressed in the Acb (Rosin et al., 1998). Recent studies have revealed that A_{2A}Rs play a crucial role in the regulation of sleep (Huang et al., 2005; Lazarus et al., 2012, 2013), and that AcbSh A_{2A}R mediates the arousal effect of caffeine, a non-specific adenosine A1R and A_{2A}R antagonist (Lazarus et al., 2011). However, the neural pathways exerting these effects have not yet been identified. The sites identified in the current work provide some insight, since Acb A_{2A}R neurons give off the densest projection to the LH (containing orexin/hypocretin) which can activate the noradrenergic cells of the LC, the dopaminergic cells of the VTA, the serotonergic cells of the DR, and the histaminergic cells of the tuberomammillary nucleus (TMN), all of which cause arousal from sleep (Sakurai, 2007). In addition, Acb A_{2A}R neurons project to the TMN, the VTA, the DR, the VLPAG, and the LC. As a group, these structures form the ascending arousal system, and fire fastest during wakefulness (Saper et al., 2005). Other innervated sites are located in the basal forebrain, including the VDB, the HDB, and the SI, and these neurons augment the ascending arousal system (Saper et al., 2005), or project to the wake-regulating lateral hypothalamus (Henny and Jones, 2006). A consistent observation is that adenosine A_{2A}R in the Acb is almost entirely expressed in striatopallidal projection neurons in rodents as well as in primates (Schiffmann et al., 1991a,b; Fink et al., 1992). This suggests that A_{2A}R neurons are inhibitory GABAergic projection neurons. Taken together, our data reveal relationships between Acb A_{2A}R and the areas related with wakefulness, and suggest the possible neural pathways mediating the regulation of Acb A_{2A}Rs in promoting sleep. Furthermore, injection to the AcbC, medial AcbSh, and ventral AcbSh projects to the above-mentioned sites as well as different sites related to wakefulness and sleep. We therefore suggest various candidate sub-regions in the Acb regulating sleep. Based on our data, the best candidates for the effect of AcbC adenosine A_{2A}R on sleep would be basal forebrain (including VDB, HDB, and SI), orexin field, VTM, VTA, dorsal raphe, and VLPAG, for the medial AcbSh would be basal forebrain (including VDB, HDB, and SI), orexin field, VTA, and for the ventral AcbSh the basal forebrain (including VDB and SI), orexin field, VTA, DR, VLPAG, and LC. Indeed, the recent study reveals that GABAergic medium-sized spiny neurons in the AcbSh have marked differences in the receptor expression pattern, which activate the different signaling pathways and play the corresponding functions (Gangarossa et al., 2013). Future studies should therefore be directed to better understand whether characteristic synapses exist between Acb axons of A_{2A}R neurons and these innervated sites.

CONCLUSION

In summary, the present study specifically demonstrated the projections of Acb A_{2A}R neurons by means of an injection of hrGFP-expressing AAV as a tracer in A_{2A}R-Cre transgenic mouse. The results reveal that Acb A_{2A}R neurons distribute their axons to several brain fields. As a consequence of these findings, the present results provide an anatomical basis for the physiologic, pathologic, and pharmacologic implications of Acb A_{2A}R neurons. In particular, the present studies provide important data from which further

studies can be designed to better understand the potential role of Acb A_{2A}Rs in the regulation of sleep.

ACKNOWLEDGMENTS

We are grateful to Dr. Jun Lu (Harvard Medical School) for helpful comments on the experiment, to Dr. Yi-Qun Wang and Ms. Yan-Jia Luo for technical assistance. This research was supported by the National Natural Science Foundation of China (81171299, 31070957, 31171010, 31121061, 31271164, and 81271466), National Basic Research Program of China (2011CB711000), Shanghai Leading Academic Discipline Project (B119), Ph.D. Programs Foundation of Ministry of Education of China (20110071110033), Japan Society for the Promotion of Science (24300129), World Premier International Research Center Initiative (WPI) from the Ministry of Education, Culture, Sports, Science, and Technology of Japan, Fondation Médicale Reine Elisabeth (Belgium), FRS-FNRS (Belgium), FER from ULB, the Interuniversity Attraction Poles Program (IUAP – P7/10) from Belgian State-Federal Office for Scientific Affairs, Action de Recherche Concertée from the Fédération Wallonie-Bruxelles, and the State Key Laboratory of Medical Neurobiology, Fudan University, Shanghai, China. Alban de Kerchove d'Exaerde is a Senior Research Associate of the FRS-FNRS (Belgium).

AUTHOR CONTRIBUTIONS

Jian-Ping Zhang and Qi Xu have contributed equally to this work. All authors had full access to all the results in the study and take responsibility for the integrity of the results. Jian-Ping Zhang and Qi Xu were involved in studying concept and design, acquisition and analysis of data, and writing the article. Rui-Xi Li, Zhi-Li Huang, Michael Lazarus, and Yoshihiro Urade took part in the experimental design, helped in the analysis of the results and wrote the article. Serge N. Schiffmann and Alban de Kerchove d'Exaerde provided A_{2A}R Cre mice. Wei-Min Qu was involved in designing the experiments and analysis of data.

REFERENCES

Baldwin, M. K., Balaram, P., and Kaas, J. H. (2013). Projections of the superior colliculus to the pulvinar in prosimian galagos (*Otolemur garnettii*) and VGLUT2 staining of the visual pulvinar. *J. Comp. Neurol.* 521, 1664–1682. doi: 10.1002/cne.23252

Bálint, E., Mezey, S., and Csillag, A. (2011). Efferent connections of nucleus accumbens subdivisions of the domestic chicken (*Gallus domesticus*): an anterograde pathway tracing study. *J. Comp. Neurol.* 15, 2922–2953. doi: 10.1002/cne.22672

Barraco, R. A., Martens, K. A., Parizon, M., and Normile, H. J. (1993). Adenosine A2a receptors in the nucleus accumbens mediate locomotor depression. *Brain Res. Bull.* 31, 397–404. doi: 10.1016/0361-9230(93)90233-2

Barraco, R. A., Martens, K. A., Parizon, M., and Normile, H. J. (1994). Role of adenosine A2a receptors in the nucleus accumbens. *Prog. Neuropsychopharmacol. Biol. Psychiatry* 18, 545–553. doi: 10.1016/0278-5846(94)90011-6

Chamberlin, N. L., Du, B., de Lacalle, S., and Saper, C. B. (1998). Recombinant adeno-associated virus vector: use for transgene expression and anterograde tract tracing in the CNS. *Brain Res.* 793, 169–175. doi: 10.1016/S0006-8993(98)00169-3

DeFalco, J., Tomishima, M., Liu, H., Zhao, C., Cai, X., Marth, J. D., et al. (2001). Virus-assisted mapping of neural inputs to a feeding center in the hypothalamus. *Science* 291, 2608–2613. doi: 10.1126/science.1056602

Durieux, P. F., Bearzatto, B., Guiducci, S., Buch, T., Waisman, A., Zoli, M., et al. (2009). D2R striatopallidal neurons inhibit both locomotor and drug reward processes. *Nat. Neurosci.* 12, 393–395. doi: 10.1038/nn.2286

Durieux, P. F., Schiffmann, S. N., and de Kerchove d'Exaerde, A. (2012). Differential regulation of motor control and response to dopaminergic drugs by D1R and D2R neurons in distinct dorsal striatum subregions. *EMBO J.* 31, 640–653. doi: 10.1038/emboj.2011.400

Ferré, S., Diamond, I., Goldberg, S. R., Yao, L., Hourani, S. M., Huang, Z. L., et al. (2007). Adenosine A2A receptors in ventral striatum, hypothalamus and nociceptive circuitry implications for drug addiction, sleep and pain. *Prog. Neurobiol.* 83, 332–347. doi: 10.1016/j.pneurobio.2007.04.002

Fink, J. S., Weaver, D. R., Rivkees, S. A., Peterfreund, R. A., Pollack, A. E., Adler, E. M., et al. (1992). Molecular cloning of the rat A2 adenosine receptor: selective co-expression with D2 dopamine receptors in rat stratum. *Brain Res. Mol. Brain Res.* 14, 186–195. doi: 10.1016/0169-328X(92)90173-9

Gautron, L., Lazarus, M., Scott, M. M., Saper, C. B., and Elmquist, J. K. (2010). Identifying the efferent projections of leptin-responsive neurons in the dorsomedial hypothalamus using a novel conditional tracing approach. *J. Comp. Neurol.* 518, 2090–2108. doi: 10.1002/cne.22323

Gangarossa, G., Espalergues, J., de Kerchove d'Exaerde, A., EI Mestikawy, S., Gerfen, C. R., Hervé, D., et al. (2013). Distribution and compartmental organization of GABAergic medium-sized spiny neurons in the mouse nucleus accumbens. *Front. Neural. Circuits.* 7:22. doi: 10.3389/fncir.2013.00022

Goto, Y., and Grace, A. A. (2008). Limbic and cortical information processing in the nucleus accumbens. *Trends. Neurosci.* 31, 552–558. doi: 10.1016/j.tins.2008.08.002

Groenewegen, H. J., and Russchen, F. T. (1984). Organization of the efferent projections of the nucleus accumbens to pallidal, hypothalamic, and mesencephalic structures: a tracing and immunohistochemical study in the cat. *J. Comp. Neurol.* 223, 347–367. doi: 10.1002/cne.902230303

Haber, S. N., Lynd, E., Klein, C., and Groenewegen, H. J. (1990). Topographic organization of the ventral striatal efferent projections in the rhesus monkey: an anterograde tracing study. *J. Comp. Neurol.* 293, 282–298. doi: 10.1002/cne.902930210

Henny, P., and Jones, B. E. (2006). Vesicular glutamate (VGluT), GABA (VGAT), and acetylcholine (VACht) transporters in basal forebrain axon terminals innervating the lateral hypothalamus. *J. Comp. Neurol.* 496, 453–467. doi: 10.1002/cne.20928

Heimer, L., Zahm, D. S., Churchill, L., Kalivas, P. W., and Wohltmann, C. (1991). Specificity in the projection patterns of accumbal core and shell in the rat. *Neuroscience* 41, 89–125. doi: 10.1016/0306-4522(91)90202-Y

Hnasko, T. S., Hjemstad, G. O., Fields, H. L., and Edwards, R. H. (2012). Ventral tegmental area glutamate neurons: electrophysiological properties and projections. *J. Neurosci.* 32, 15076–15085. doi: 10.1523/JNEUROSCI.3128-12.2012

Huang, Z. L., Qu, W. M., Eguchi, N., Chen, J. F., Schwarzachild, M. A., Fredholm, B. B., et al. (2005). Adenosine A2A, but not A1, receptors mediate the arousal effect of caffeine. *Nat. Neurosci.* 7, 858–859. doi: 10.1038/nn1491

Huang, Z. L., Urade, Y., and Hayaishi, O. (2007). Prostaglandins and adenosine in the regulation of sleep and wakefulness. *Curr. Opin. Pharmacol.* 7, 33–38. doi: 10.1016/j.coph.2006.09.004

Huang, Z. L., Urade, Y., and Hayaishi, O. (2011). The role of adenosine in the regulation of sleep. Curr. *Top. Med. Chem.* 11, 1047-1057. doi: 10.2174/156802611795347654

Jongen-Rêlo, A. L., Voorn, P., and Groenewegen, H. J. (1994). Immunohistochemical characterization of the shell and core territories of the nucleus accumbens in the rat. *Eur. J. Neurosci.* 6, 1255–1264. doi: 10.1111/j.1460-9568.1994.tb00315.x

Kelley, A. E. (2004). Ventral striatal control of appetitive motivation: role in ingestive behavior and reward-related learning. *Neurosci. Biohehav. Rev.* 27, 765–776. doi: 10.1016/j.neubiorev.2003.11.015

Lazarus, M., Chen, J. F., Urade, Y., and Huang, Z. L. (2013). Role of the basal ganglia in the control of sleep and wakefulness. *Curr. Opin. Neurobiol.* 23, 780–785. doi: 10.1016/j.conb.2013.02.001

Lazarus, M., Shen, H. Y., Cherasse, Y., Qu, W. M., Huang, Z. L., Bass, C. E., et al. (2011). Arousal effect of caffeine depends on adenosine A2A receptors in the shell of the nucleus accumbens. *J. Neurosci.* 31, 10067–10075. doi: 10.1523/JNEUROSCI.6730-10.2011

Lazarus, M., Huang, Z. L., Lu, J., Urade, Y., and Chen, J. F. (2012). How do the basal ganglia regulate sleep-wake behavior? *Trends. Neurosci.* 35, 723–732. doi: 10.1016/j.tins.2012.07.001

Meredith, G. E., Agolia, R., Arts, M. P., Groenewegen, H. J., and Zahm, D. S. (1992). Morphological differences between projection neurons of the core and shell in

the nucleus accumbens of the rat. *Neuroscience* 50, 149–162. doi: 10.1016/0306-4522(92)90389-J

Mingote, S., Font, L., Farrar, A. M., Vontell, R., Worden, L. T., Stopper, C. M., et al. (2008). Nucleus accumbens adenosine A2A receptors regulate exertion of effort by acting on the ventral striatopallidal pathway. *J. Neurosci.* 28, 9037–9046. doi: 10.1523/JNEUROSCI.1525-08.2008

Nagel, J., Schladebach, H., Koch, M., Schwienbacher, I., Müller, C. E., and Hauber, W. (2003). Effects of an adenosine A2A receptor blockade in the nucleus accumbens on locomotion, feeding, and prepulse inhibition in rats. *Synapse* 49, 279–286. doi: 10.1002/syn.10240

Nauta, W. J., Smith, G. P., Faull, R. L., and Domesick, V. B. (1978). Efferent connections and nigral afferents of the nucleus accumbens septi in the rat. *Neuroscience* 3, 385–401. doi: 10.1016/0306-4522(78)90041-6

O'Neill, C. E., LeTendre, M. L., and Bachtell, R. K. (2012). Asenosine A2A receptors in the nucleus accumbens bi-directionally alter cocaine seeking in rats. *Neuropsychopharmacology* 37, 1245–1256. doi: 10.1038/npp.2011.312

Paxinos, G., and Franklin, K. B. J. (1997). *The Mouse Brain in Stereotaxic Coordinates.* San Diego: Academic Press.

Qiu, M. H., Liu, W., Qu, W. M., Urade, Y., Lu, J., and Huang, Z. L. (2012). The role of nucleus accumbens core/shell in sleep-wake regulation and their involvement in Modafinil-induced arousal. *PLoS ONE* 7:e45471. doi: 10.1371/journal.pone.0045471

Qiu, M. H., Vetrivelan, R., Fuller, P. M., and Lu, J. (2010). Basal ganglia control of sleep-wake behavior and cortical activation. *Eur. J. Neurosci.* 31, 499–507. doi: 10.1111/j.1460-9568.2009.07062.x

Rosin, D. L., Hettinger, B. D., Lee, A., and Linden, J. (2003). Anatomy of adenosine A2A receptors in brain: morphological substrates for integration of striatal function. *Neurology* 61, S12–S18. doi: 10.1212/01.WNL.0000095205.33940.99

Rosin, D. L., Robeva, A., Woodard, R. L., Guyenet, P. G., and Linden, L. (1998). Immunohistochemical localization of adenosine A2A receptors in the rat central nervous system. *J. Comp. Neurol.* 401, 163–186. doi: 10.1002/(SICI)1096-9861(19981116)401:2<163::AID-CNE2>3.0.CO;2-D

Sakurai, T. (2007). The neural circuit of orexin (hypocretin): maintaining sleep and wakefulness. *Nat. Rev. Neurosci.* 8, 171–181. doi: 10.1038/nrn2092

Sakurai, T., Nagata, R., Yamanaka, A., Kawamura, H., Tsujino, N., Muraki, Y., et al. (2005). Input of orexin/hypocretin neurons revealed by a genetically encoded tracer in mice. *Neuron* 46, 297–308. doi: 10.1016/j.neuron.2005.03.010

Saper, C. B., Scammell, T. E., and Lu, J. (2005). Hypothalamic regulation of sleep and circadian rhythms. *Nature* 437, 1257–1263. doi: 10.1038/nature04284

Schiffmann, S. N., Fisone, G., Moresco, R., Cunha, R. A., and Ferré, S. (2007). Adenosine A2A receptors and basal ganglia physiology. *Prog. Neurobiol.* 83, 277–292. doi: 10.1016/j.pneurobio.2007.05.001

Schiffmann, S. N., Jacobs, O., and Vanderhaeghen, J. J. (1991a). Striatal restricted adenosine A2 receptor (RDC8) is expressed by encephalin but no by substance P neurons: an in situ hybridization histochemistry study. *J. Neurochem.* 57, 1062–1067. doi: 10.1111/j.1471-4159.1991.tb08257.x

Schiffmann, S. N., Libert, F., Vassart, G., and Vanderhaeghen, J. J. (1991b). Distribution of adenosine A2 receptor mRNA in the human brain. *Neurosci. Lett.* 130, 177–181. doi: 10.1016/0304-3940(91)90391-6

Troiano, R., and Siegel, A. (1978). Efferent connections of the basal forebrain in the cat: the nucleus accumbens. *Exp. Neurol.* 61, 185–197. doi: 10.1016/0014-4886(78)90190-5

Usuda, I., Tanaka, K., and Chiba, T. (1998). Efferent projections of the nucleus accumbens in the rat with special reference to subdivision of the nucleus: biotinylated dextran amine study. *Brain Res.* 797, 73–93. doi: 10.1016/S0006-8993(98)00359-X

Zahm, D. S., and Heimer, L. (1993). Specificity in the efferent projections of the nucleus accumbens in the rat: comparison of the rostral pole projection patterns with those of the core and shell. *J. Comp. Neurol.* 327, 220–232. doi: 10.1002/cne.903270205

Conflict of Interest Statement: The authors declare that the research was conducted in the absence of any commercial or financial relationships that could be construed as a potential conflict of interest.

Received: 07 October 2013; accepted: 21 November 2013; published online: 10 December 2013.

*Citation: Zhang J-P, Xu Q, Yuan X-S, Cherasse Y, Schiffmann SN, de Kerchove d'Exaerde A, Qu W-M, Urade Y, Lazarus M, Huang Z-L and Li R-X (2013) Projections of nucleus accumbens adenosine A2A receptor neurons in the mouse brain and their implications in mediating sleep-wake regulation. Front. Neuroanat. **7**:43. doi: 10.3389/fnana.2013.00043*

This article was submitted to the journal Frontiers in Neuroanatomy.

frontiers in
NEUROANATOMY

ORIGINAL RESEARCH ARTICLE
published: 03 March 2014
doi: 10.3389/fnana.2014.00008

Integration of stress and leptin signaling by CART producing neurons in the rodent midbrain centrally projecting Edinger–Westphal nucleus

Lu Xu[1†], Donny Janssen[1†], Noortje van der Knaap[2], Eric W. Roubos[1], Rebecca L. Leshan[3], Martin G. Myers Jr[3], Balázs Gaszner[4] and Tamás Kozicz[1]*

[1] *Department of Anatomy, Donders Institute for Brain, Cognition and Behaviour, Radboud University Nijmegen Medical Centre, Nijmegen, Netherlands*
[2] *Department of Cognitive Neuroscience, Donders Institute for Brain, Cognition and Behaviour, Radboud University Nijmegen Medical Centre, Nijmegen, Netherlands*
[3] *Division of Metabolism, Endocrinology and Diabetes – Department of Internal Medicine, University of Michigan, Ann Arbor, MI, USA*
[4] *Department of Anatomy, University of Pécs, Pécs, Hungary*

Edited by:
Laurent Gautron, The University of Texas Southwestern Medical Center, USA

Reviewed by:
Huxing Cui, University of Iowa Carver College of Medicine, USA
Maria Panayotacopoulou, University of Athens, Greece
Adam Weitemier, RIKEN Brain Science Institute, Japan

***Correspondence:**
Tamás Kozicz, Department of Anatomy, Donders Institute for Brain, Cognition and Behaviour, Radboud University Nijmegen Medical Centre, P.O. Box 9101, 6500 HB Nijmegen, Netherlands
e-mail: tkozicz2000@yahoo.com

† *Lu Xu and Donny Janssen have contributed equally to this work.*

Leptin targets the brain to regulate feeding, neuroendocrine function and metabolism. The leptin receptor is present in hypothalamic centers controlling energy metabolism as well as in the centrally projecting Edinger–Westphal nucleus (EWcp), a region implicated in the stress response and in various aspects of stress-related behaviors. We hypothesized that the stress response by cocaine- and amphetamine-regulated transcript (CART)-producing EWcp-neurons would depend on the animal's energy state. To test this hypothesis, we investigated the effects of changes in energy state (mimicked by low, normal and high leptin levels, which were achieved by 24 h fasting, normal chow and leptin injection, respectively) on the response of CART neurons in the EWcp of rats subjected or not to acute restraint stress. Our data show that leptin treatment alone significantly increases CART mRNA expression in the rat EWcp and that in leptin receptor deficient (*db/db*) mice, the number of CART producing neurons in this nucleus is reduced. This suggests that leptin has a stimulatory effect on the production of CART in the EWcp under non-stressed condition. Under stressed condition, however, leptin blunts stress-induced activation of EWcp neurons and decreases their CART mRNA expression. Interestingly, fasting, does not influence the stress-induced activation of EWcp-neurons, and specifically EWcp-CART neurons are not activated. These results suggest that the stress response by the EWcp depends to some degree on the animal's energy state, a mechanism that may contribute to a better understanding of the complex interplay between obesity and stress.

Keywords: *db/db* mice, depression, centrally projecting Edinger–Westphal nucleus, fasting, obesity, restraint

INTRODUCTION

In order to maintain homeostasis, vertebrates have to adapt to intrinsic or extrinsic stressors by a highly complicated process in which both neural and endocrine messengers from diverse sources are involved. Depending on the type of stressor, specific stress-sensitive hypothalamic and extrahypothalamic brain centers interact with each other to eventually control the secretion of corticosteroids by the hypothalamic–pituitary–adrenal (HPA)-axis (for references, see e.g., Chrousos and Gold, 1992). These hormones enable the organism to cope with the stress challenge (Sapolsky et al., 2000) but at the same time, urge it to spend a high amount of energy to this adaptation (Kozicz et al., 2011; Morava and Kozicz, 2013). Consequently, the brain needs to be informed about the amount of energy available, so that it can adjust its feeding and metabolic activities and accurately distribute the available energy over essential life processes including adaptation. For this purpose the organism employs various neurochemical brain messengers, such as neuropeptide Y (NPY), insulin, cholecystokinin (CCK), urocortin1 (Ucn1), and nesfatin-1 (e.g., Kalra et al., 1999; Dietrich and Horvath, 2009; Kozicz et al., 2011; Williams and Elmquist, 2012) and ghrelin/leptin-based signaling systems that inform the brain about the amount of peripheral energy information (Zhang et al., 1994; Meier and Gressner, 2004; Roubos et al., 2012). Evidently, prevention and therapy of disorders such as obesity and depression would enormously benefit from a better insight into the ways stress and feeding stimuli are integrated by this complex neuroendocrine signaling system. The present study is concerned with two main players in this system, the anorexigenic peptide, cocaine- and amphetamine-regulated transcript (CART) and the peripheral metabolic hormone, leptin. We focus in particular on the roles of leptin and CART in the stress- and feeding-sensitive extrahypothalamic, centrally projecting Edinger–Westphal nucleus (EWcp).

The EWcp is situated in the rostroventral part of the midbrain, and its activity is strongly influenced by both stressors and the nutritional state that change the neuronal contents of the neuropeptide Ucn1 and Ucn1 mRNA (Gaszner et al., 2004; Kozicz, 2007). The EWcp targets various other stress- and/or feeding-sensitive brain nuclei such as the ventromedial hypothalamus, the lateral septum and the dorsal raphe nucleus, and, moreover,

brown adipose tissue (Bittencourt et al., 1999; Ohata et al., 2000; Weitemier et al., 2005; Zhang et al., 2011). Furthermore, lesioning EWcp inhibits food intake (Weitemier and Ryabinin, 2005). Recently, the EWcp has also been demonstrated to receive afferents from different brain regions involved in stress responses and feeding behavior, such as the paraventricular and posterior hypothalamic nuclei and the lateral hypothalamic area (Da Silva et al., 2013). Therefore, the EWcp is supposed to integrate both stress and feeding-related signals in order to contribute to energy-dependent stress adaptation (Kozicz et al., 2011; Xu et al., 2012). In addition to Ucn1, the rodent EWcp produces CART (Kozicz, 2003; Xu et al., 2009), which fully colocalizes with Ucn1 and which mRNA expression is up-regulated by stressors and long-term fasting (Kozicz, 2003; Xu et al., 2009). These data suggest that CART in the EWcp plays a role in integrating stress and feeding signals (Xu et al., 2009).

Involvement of the EWcp in such an integration also appears from the presence of the functional leptin receptor, LepRb (Ahima and Osei, 2004) on 50–60% of the Ucn1 neurons in the rat EWcp (Xu et al., 2011). The 16 kDa adipose derived and blood transported leptin is a product of the *Obese* (*Ob)* gene and an important regulator of energy metabolism; i.e., it reduces food intake and increases energy expenditure (Zhang et al., 1994). The protein acts on LepRb (Ahima and Osei, 2004), which can initiate intracellular signaling cascades (Xu et al., 2011). Leptin can also mediate the stress response, as LepRbs have been identified in stress-sensitive areas (Håkansson and Meister, 1998; Malendowicz et al., 2007). Furthermore, systemic leptin injections improve behavioral impairments in stressed rats (Heiman et al., 1997; Lu et al., 2006). Peripheral leptin administration increases the Ucn1 content of the EWcp, while stimulating STAT3 phosphorylation and inhibiting the electrical activity of these neurons (Xu et al., 2011). The findings above show the complex interplay between leptin and the stress response.

These data together indicate a relationship between stress, leptin signaling and CART expression in the EWcp. The mechanism(s) by which these signals are integrated by the EWcp remain unclear, and with the present study, we aimed to elucidate the link between the EWcp and leptin, fasting and stress. Special attention was placed on the transcriptional and translational dynamics of CART in low (24 h fasting), normal (fed with chow), and high (systemic leptin injection) energy states, and to what extent various energy states would modulate these dynamics under stress conditions. Studies were performed using male rats, wildtype mice and mice lacking the LepRb receptor (*db/db* mice), using semi-quantitative immunocytochemistry and *in situ* hybridization.

MATERIALS AND METHODS

ANIMAL HANDLING

Male Wistar-R Amsterdam rats (225–250*g*; bred in the Animal Facility of the Department of Anatomy, Pécs, Hungary) were used for the leptin and stress experiment, and five male C57BL/6J (WT) and five B6.Cg-m+/+Lepr^{db}/J (*db/db*) mice (10–12 wk old; obtained from The Jackson Laboratory, Bar Harbor, ME, USA), housed in the Unit for Laboratory Animal Medicine at the University of Michigan, were used for studying the effect of LepRb deficiency. All animals were housed in standard plastic cages, in a temperature- and humidity-controlled environment, on a 12 h light/dark cycle (lights on at 6:00 a.m.) with free access to food and water *ad libitum*. They were allowed 1 week of acclimatization before the start of the experiment. All animal procedures had the approval of the respective University care and use committees.

PEPTIDE AND ANTISERA

Recombinant mouse leptin was obtained from the National Hormone and Peptide Program (Dr. A. F. Parlow, Los Angeles, CA, USA), mouse anti-CART was a generous gift from Dr. J. T. Claussen (no. Ca6-1 F4D4; Novo Nordisk A/S, Bagsvaerd, Denmark), rabbit anti-c-Fos was from Santa Cruz Biotechnology (no. sc-52, Santa Cruz, CA, USA). Normal donkey serum (NDS), biotinylated donkey-anti-rabbit immunoglobulin (Ig)G and the cyanine^2 (Cy^2)-conjugated donkey-anti-mouse, Cy^3-conjugated donkey-anti-rabbit sera were from Jackson ImmunoResearch (West Grove, PA, USA). ABC Elite solution were purchased from Vector Laboratories (Burlingame, CA, USA). All other immunoreagents were from Sigma Chemical (St. Louis, MO, USA).

EXPERIMENTAL PROTOCOLS

Experiment 1: kinetics of leptin-induced c-Fos activation, twenty-eight animals were randomly divided into seven equal groups of four animals. Four saline injected rats were sacrificed immediately after intraperitoneal (i.p.) injection (0 h). Other rats were injected i.p. with either leptin (3 mg/kg) or an equal volume saline, and sacrificed 1, 2, 4 h later.

Experiment 2: effects of leptin on the stress response of EWcp-CART neurons, thirty rats were divided into six groups based on different treatments (**Figure 1**): PBS injection, leptin injection or fasting, and exposure or no exposure to restraint stress. Rats exposed to a 24 h fasting paradigm (groups E and F) were deprived of rat chow at 9:00 a.m. on day 1 and groups A, B, C, D were fed normally. At 9:00 a.m. on day 2, 3 mg/kg leptin based on previous studies by Münzberg et al. (2003), Huo et al. (2004), Xu et al. (2011) in sterile sodium phosphate-buffered saline (PBS; pH 7.4) was injected i.p. into rats of groups C and D; an equal volume of PBS was injected into controls (groups A and B). To test the effect of the state of energy on the EWcp stress response, rats of groups B, D, and F were subjected to acute restraint stress by placing the animal in a plastic tube (length 200 mm, diameter 45 mm, with several ventilation holes at its side and top) at noon on day 2. Rats not subjected to restraint stress were kept in their home cages.

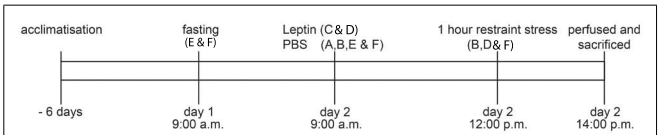

FIGURE 1 | Timeline showing the animal handling and exposure to the various experimental treatments. The experiment started on day 1. Letters between brackets indicate the experimental groups (A: PBS + no stress; B: PBS + stress; C: Leptin + no stress; D: Leptin + stress; E: Fasting + no stress; F: Fasting + stress).

All the rats were deeply anesthetized with Nembutal (Sanofi, Budapest, Hungary, 100 mg/kg). For experiment 2, after exposing their chest cavity, first a 1 ml blood sample was collected through the left ventricle in an ice-chilled EDTA-containing tube. Next, rats were transcardially perfused with 50 ml 0.1 PBS followed by 250 ml 4% ice-cold paraformaldehyde (PFA) in 0.2 Millonig sodium phosphate buffer (pH 7.4). After decapitation, brains were dissected and stored in PFA fixative, for 2 days. Of each brain, six series of 20 μm thick coronal slices were cut with a Lancer microtome (Ted Pella, Redding, CA, USA) through the entire length of the EWcp (5.0–7.0 mm caudal to Bregma: see Paxinos and Franklin, 2001). Sections were stored in sterile antifreeze solution (0.1 M PBS, 30% ethylene glycol and 20% glycerol) at −20°C. Blood samples were centrifuged at 3000 rpm., for 10 min. A plasma aliquot of 50 μl was stored at −20°C until performing duplicate leptin radioimmunoassay (Linco Research, St. Charles, MI, USA).

Experiment 3: effect of disrupted leptin signaling on CART neurons in the EWcp; five non-stressed WT and five *db/db* mice were deeply anesthetized with i.p. sodium pentobarbital (150 mg/kg), transcardially perfused with ice-cold PBS followed by 4% PFA, for 30 min, decapitated, and brains removed and post-fixed in 4% PFA (Münzberg et al., 2003), for 16 h. Four representative series of coronal sections (30 μm) were cut with a sliding microtome, into a cryoprotective solution (30% ethylene glycol, 30% glycerol; in PBS), and stored at −20°C until use for immunohistochemistry.

IN SITU HYBRIDIZATION

For CART mRNA determination, antisense and sense (control) RNA probes were generated using a full length 520 bp CART cDNA, subcloned in pBluescript (Stratagene, Agilent Technologies, Santa Clara, CA, USA) and labeled with DIG (digoxygenin)-11-UTP using a labeling kit from Roche Molecular Biochemicals (Basel, Switzerland). Sections were fixed in 4% PFA (pH = 7.3) at 4°C for 72 h and rinsed 3 min × 10 min in 0.1 M PBS. Subsequently, the sections were pre-incubated for 10 min at 37°C in proteinase K medium (0.1 M Tris/HCl, 0.05 M EDTA, 0.01 mg/ml proteinase K: Invitrogen, Carlsbad, CA, USA). After rinsing 1 min in autoclaved diethyl pyrocarbonate (DEPC; 100 μl DEPC in 100 ml MQ water) and 1 min in 0.1 M tri-ethanolamine buffer (TEA; pH = 8), acetylation was performed with 0.25% acetic acid anhydride in 0.1 M TEA buffer for 10 min, followed by a 5 min rinse in 2x concentrated standard saline citrate buffer (SSC; pH = 7.0). Hybridization mixture (50% deionized formamide, 0.3 M NaCl, 0.001 M EDTA, Denhardt's solution, 10% dextran sulfate; pH = 7.0), together with 0.5 mg/ml tRNA and the mRNA-DIG probe (CART: 0.2 ng/ml) were placed in a water bath, at 80°C for 5 min and then on ice for another 5 min. Sections were incubated in hybridization solution, for 16 h at 58°C, rinsed 3 min × 10 min with 4x SSC, incubated with pre-heated RNAse medium (0.5 M NaCl, 0.01 M Tris/HCl, 0.001 M EDTA, 0.01 mg/ml RNAse A: Roche; pH = 8.0) that had been added just before the start of incubation, and rinsed in steps with decreasing SSC concentrations (2x, 1x, 0.5x, 0.1x), for 30 min at 58°C. DIG label was detected with the alkaline phosphatase (AP) procedure with nitroblue tetrazolium chloride/5-bromo-4-chloro-3-indolyl phosphatase-toluidine salt (NBT/BCIP) as substrate. After rinsing 2 min × 10 min in buffer A (0.1 M Tris/HCl, 0.15 M NaCl; pH = 7.5), sections were pre-incubated in Buffer A containing 0.5% blocking agent (Roche) for 1 h, followed by 3 h incubation with sheep anti-DIG-AP (Roche, 1:5.000) in buffer A containing 0.5% blocking agent. Subsequently, sections were rinsed for 2 min × 10 min in buffer A, followed by 2min × 5 min rinsing in buffer B (0.1 M Tris/HCl, 0.15 M NaCl, 0.05 M $MgCl_2$; pH = 9.5). After 6 h incubation in NBT/BCIP medium (buffer B, 0.24 mg/ml levamisole: Sigma Chemical, 175 μl NBT/BCIP mixture: Roche) in a light-tight box, the reaction was stopped by washing the sections 2min × 5 min in buffer C (0.1 M Tris/HCl, 0.01 M EDTA; pH = 8.0). Finally, sections were mounted on gelatin-coated glass slides and coverslipped with Kaiser's glycerol gelatin (Merck, Darmstadt, Germany).

IMMUNOHISTOCHEMISTRY

We determine relative changes in the amount of substances using semi-quantitative measurements. We used a controlled randomization protocol to make sure that each six-well plate contains sections from one animal per experimental group. In this way, animals belonging to the same group were always assigned in different plates. This procedure minimizes the bias and prevents introducing false positive statistical results. All antibody incubations were performed at the same time using comparable conditions (antibody concentration, incubation time, temperature). Samples from all groups were coded to ensure unbiased data collection. All sections were viewed and confocal settings were determined for the brightest section. All images were collected on the same day using the same settings (for more details, see Image analysis). Diaminobenzidine (DAB) immunohistochemistry was performed in Experiment 1 and fluorescent immunohistochemistry was performed in Experiment 2 and 3.

For c-Fos immunuhistochemistry with DAB, sections were washed 4 min × 15 min in 0.1 M PBS followed by 0.5% Triton X-100 in PBS for 30 min to enhance antigen penetration. After an additional 15 min wash in PBS, sections were incubated in 1% H_2O_2 for 10 min. After 3 min × 5 min washes in PBS, the sections were placed for 1 h into a solution of 2% NDS to block non-specific binding sites. After a brief wash in PBS, the sections were transferred into vials containing the primary polyclonal (rabbit) anti c-Fos antibody at a dilution of 1:2000 overnight. The next day, after 4 min × 15 min washes in PBS, sections were incubated into biotinylated donkey-anti-rabbit immunoglobulin (Ig)G (1:200) for 1 h and subsequently into ABC Vector (1:200) for 1 h. The c-Fos signal was visualized with adding 10 mg DAB and 35 mg ammonium-nickel-sulfate in 50 ml Tris buffer (pH 7.6). The reaction was stopped after 9 min in Tris buffer. The sections were washed and mounted on gelatin coated slides and air dried. After drying they were dehydrated by gradual steps of alcohol, iso-propanol and xylene and mounted with Entallan.

For single immunolabeling of CART, sections were treated with 0.5% Triton X-100 in PBS, for 30 min, blocked in 2% NDS for 1 h, and incubated in primary monoclonal mouse anti-CART (1:1500) overnight. This was followed by 2 h incubation with secondary

Cy^2-conjugated anti-mouse IgG (1:100). Finally, sections were rinsed 3 min × 10 min in PBS, mounted on gelatin-coated glass slides, air-dried and coverslipped with FluorSave reagent (EMD Biosciences, San Diego, CA, USA).

For double-immunolabeling of CART and c-Fos, sections were processed as described for single immunofluorescent labeling but with incubation in a mixture of primary monoclonal mouse anti-CART (1:1500) and polyclonal rabbit anti-c-Fos serum (1:800) overnight and then in a mixture of Cy^3-conjugated donkey anti-rabbit IgG antiserum (1:100) and Cy^2-conjugated donkey anti-mouse IgG antiserum (1:100) in 2% NDS for 2 h.

The high specificities of the mouse anti-CART (Koylu et al., 1997) and rabbit anti-c-Fos (Gaszner et al., 2004; Korosi et al., 2005) sera have been previously reported.

IMAGE ANALYSIS

Immunostainings were studied with a DM IRE2 inverted epifluorescence microscope (Leica Microsystems, Mannheim, Germany) attached to a TCS SP2-AOBS confocal laser scanning unit (Leica Microsystems, Wetzlar, Germany) using a 488 nm Argon laser, a 561 nm orange laser and a x20 dry objective. The fluorescent signal from each image was thresholded at the same level to eliminate saturation. For double immunofluorescence measurements, Images were taken using sequential scanning for each channel, with the same settings in laser intensity, detector gain and amplifier offset. Images were saved in tagged image file format (TIFF) to prevent loss of information. For semi-quantitative determination of the amounts of CART and c-Fos protein contents in the EWcp, two parameters were determined using Image J software version 1.41 (NIH, Bethesda, MD, USA): (1) the representative number of immunoreactive neurons per section generated by averaging three sections of the midlevel of the EWcp (bregma −5.5 to −6.4 mm; Paxinos and Franklin, 2001), and (2) per neuron, the specific immunoreactivity signal density (SSD) averaged over all neurons present in the sections. The SSD was corrected for background density outside the EWcp, and expressed in arbitrary units (AUs) per neuron.

STATISTICAL ANALYSIS

Data are presented as the mean ± standard error of the mean (SEM). To compare different conditions, two-way analysis of variance (ANOVA with independent variables "leptin" and "stress") with Bonferroni post-test was performed using Graphpad Prism version 5.04 for Windows (GraphPad Software, La Jolla, CA, USA), after appropriate transformation of some data on the basis of Levene's test for homogeneity of variance (Levene, 1960). For comparison of WT with *db/db* mice, student's *t*-test was performed. In all cases, $p < 5\%$ was considered to be significant.

RESULTS

EXPERIMENT 1: KINETICS OF LEPTIN-INDUCED c-Fos ACTIVATION IN EWcp

Figure 2 shows the time effect of injected leptin on the activity of EWcp, as measured by c-Fos immunoreactivity (i.r.). Two-way ANOVA revealed significant effects of time ($F_{3,24} = 70.7$; $P < 0.0001$) and time × leptin interaction ($F_{3,24} = 4.2$; $P < 0.05$). *Post hoc* test revealed that at 1 h after injection, the EWcp exhibited increased number of c-Fos-ir neurons. This increase was significantly higher in the PBS injected animals compared with leptin injected ones (PBS: 7.2 times; leptin: 5.4 times). We observed fewer c-Fos-ir neurons 2 h after injection (either PBS or leptin) vs. 1 h post-injection, however, more c-Fos-ir neurons when compared with baseline (PBS: 3.1 times; leptin: 3.8 times). Four hours after injection of either PBS or leptin, the number of c-Fos-ir neurons was not different between 0 h and 4 h post-injection.

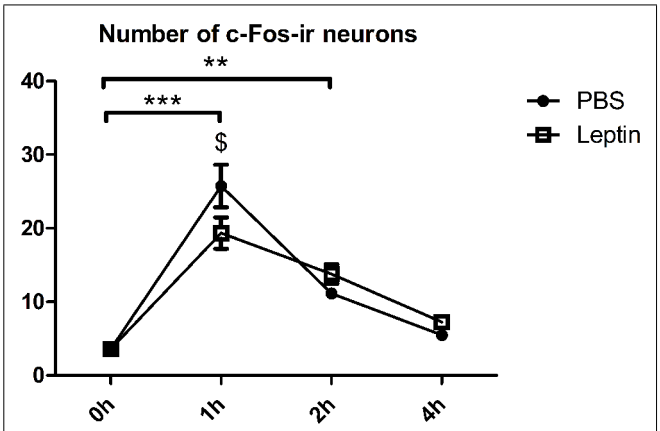

FIGURE 2 | The number of c-Fos-ir neurons in the EWcp after administration of PBS or leptin for 0, 1, 2, and 4 h. Vertical bars represent the means ± SEM; $N = 4$. Significant difference between groups treated for different periods with PBS and leptin is marked by "*"; significant difference between leptin and PBS group is marked by "$". $\$P < 0.05$; $**P < 0.01$; $***P < 0.005$.

EXPERIMENT 2: LEPTIN'S EFFECT ON STRESS-INDUCED ACTIVATION OF EWcp-CART NEURONS

Leptin plasma measurement

The leptin plasma concentrations 5 h after injecting either PBS or leptin are presented in **Figure 3**. ANOVA showed a main effect of leptin injection ($F_{2,24} = 79.13$; $P < 0.0001$). *Post hoc* analysis

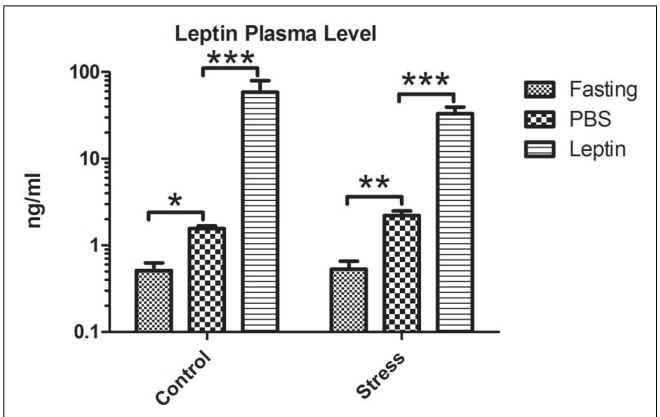

FIGURE 3 | Leptin plasma level in the various experimental groups. Vertical bars represent the means + SEM; $N = 5$. Asterisks indicate significant differences between fasting, PBS and leptin treated groups. $*P < 0.05$; $**P < 0.01$; $***P < 0.005$.

revealed that in both non-stressed and stressed rats, plasma leptin was significantly lower after fasting ($P < 0.05$) and higher after leptin-injection ($P < 0.001$) compared with PBS-injected controls.

c-Fos immunofluorescence and activation of CART expressing neurons

The general activation of the EWcp in response to a changed peripheral energy level and/or stress was determined by counting the number of c-Fos-ir neurons (**Figures 4A–F**). ANOVA showed main effects of leptin ($F_{2,24} = 5.3$, $P < 0.05$), stress ($F_{1,24} = 35.83$, $P < 0.0001$) and leptin × stress interaction ($F_{2,24} = 3.89$, $P < 0.05$; **Figure 4J**). Although the number of c-Fos-ir neurons was not different between fasted, PBS- or leptin-treated animals under non-stressed condition, it was noticeably higher in stressed rats in either fasted ($P < 0.01$) or PBS-treated ($P < 0.001$) animals. It is noteworthy that leptin injection significantly blunted stress-induced neuronal activation. More specifically, c-Fos-ir number was 2.5 times higher in fasted, 3.75 higher in PBS injected and only 1.55 higher in leptin injected rats compared with control (no stress) condition.

In order to test for activation of CART-neurons, we determined the percentage of CART-containing neurons that also exhibited c-Fos-ir (**Figures 4G–I**). We found significant effects of stress ($F_{1,24} = 19.19$, $P < 0.005$) and leptin × stress interaction ($F_{2,24} = 3.2$, $P < 0.05$; **Figure 4K**). *Post hoc* analysis revealed that stressed PBS-treated rats had approximately 3.5 times more c-Fos-ir in EWcp CART-ir neurons vs. non-stressed PBS-treated rats ($P < 0.001$); whereas leptin treatment and fasting significantly blunted stress-induced activation of EWcp CART-ir neurons (**Figure 4K**).

Quantification of CART mRNA and peptide amounts

To test if leptin, fasting or stress have an effect on the transcriptional activity of CART in the EWcp, we performed *in situ* hybridization(**Figures 5A–H**). After counting the number of mRNA-expressing neurons and measuring the hybridization signal density (SSD), ANOVA (**Figures 5G,H**) revealed a main effect of leptin × stress interaction ($F_{2,21} = 5.81$; $P < 0.01$; $F_{2,21} = 5.63$; $P < 0.05$ respectively). *Post hoc* analysis showed that in the non-stressed condition, leptin treatment increased the SSD of CART mRNA ($P < 0.05$), but in the stressed condition, the same treatment decreased the number of CART mRNA-expressing neurons ($P < 0.05$). When comparing stressed with non-stressed rats, injection of leptin significantly lowered the number and SSD of CART mRNA-positive neurons ($P < 0.01$ and $P < 0.05$, respectively).

Next, we assessed the amount of CART-ir neurons in the EWcp using semi-quantitative immunohistochemistry (**Figures 6A–F**). We counted the number of immunopositive perikarya as well as measured SSD per perikaryon (**Figures 6G,H**) to estimate CART peptide content. We found no difference for any of these parameters.

EXPERIMENT 3: EFFECTS OF DISRUPTED LEPTIN SIGNALING ON EWcp-CART NEURONS

Finally, to assess the effect of leptin signaling deficiency, we compared CART-ir immunoreactivity in the EWcp of *db/db* mice with that of wild type littermates (WT; **Figures 7A,B**). We observed a lower number of EWcp-CART-ir neurons in *db/db* mice ($P < 0.05$; **Figure 7C**) and a strong tendency toward lower SSD of CART-ir in *db/db* mice ($P = 0.05$; **Figure 7D**).

DISCUSSION

Based on the expression of LepRb in the EWcp and the involvement of EWcp in stress response and energy balance, we hypothesized that EWcp neurons would respond to stress differentially under various energy states mimicked by low, normal and high plasma leptin levels. The present study demonstrates that leptin not only attenuates the overall activation of EWcp neurons, but it also inhibits the activation of EWcp-CART neurons in response to acute (restraint) stress. Interestingly, although fasted rats and normal fed animals exhibited comparable activation pattern of EWcp neurons, in fasted animals this activation did not include EWcp-CART neurons.

As we aimed to investigate the interaction of leptin and stress in the EWcp, we needed to minimize the effect of the initial injection stress and maximize the effect of leptin. For this reason, we have assessed the kinetics of c-Fos expression in the EWcp after leptin injection. The activation of c-Fos by PBS or leptin injection within 1 h most probably represents an acute stress response. Interestingly, this initial c-Fos response was dampened by leptin, an effect that was transient and disappeared within 2 h. Whether the dampening effect of leptin on stress-associated activation of c-Fos in the first hour is due to a direct inhibitory action, remains to be investigated. At 4 h, in both PBS and leptin injected animals, c-Fos was not activated anymore in the EWcp. Therefore, we conclude that leptin alone does not result in c-Fos activation in the EWcp. Our previous study showed that pSTAT3 activation reaches its peak in the EWcp 2 h after leptin injection (Xu et al., 2011). Based on these data, we decided to subject the rats to restraint stress 3 h after leptin injection in Experiment 2.

In Experiment 2, we have assessed the interaction of leptin and stress in the EWcp. Under non-stressed, basal conditions, systemic leptin injection does not change the general activity of the EWcp. However, leptin injection did up-regulate CART mRNA production in the EWcp. These results suggest that leptin has a specific stimulatory effect on the production of CART in the EWcp. This notion is corroborated by the present data obtained with *db/db* mice, which lack the LepRb and show a lower CART content in the EWcp than WT mice. It is well established that leptin, by acting on receptors in various parts of the brain, reduces food intake, thereby causing body weight loss (e.g., Campfield et al., 1995; Gorska et al., 2010). In the EWcp, leptin acts on LepRb in CART/Ucn1 neurons and activates the JAK2-STAT3 pathway (Xu et al., 2011). In addition, the presence of a STAT-binding motif in the CART gene promoter suggests that this gene could be regulated directly via cytokine signaling (Dominguez et al., 2002). These, taken together with the fact that CART exerts an anorexigenic effect (Rogge et al., 2008), the stimulatory action of leptin on CART mRNA expression would account for leptin's inhibitory effect on food intake.

Restraint stress appears to activate about 50% of the EWcp CART neurons. However, this activation is not accompanied by the

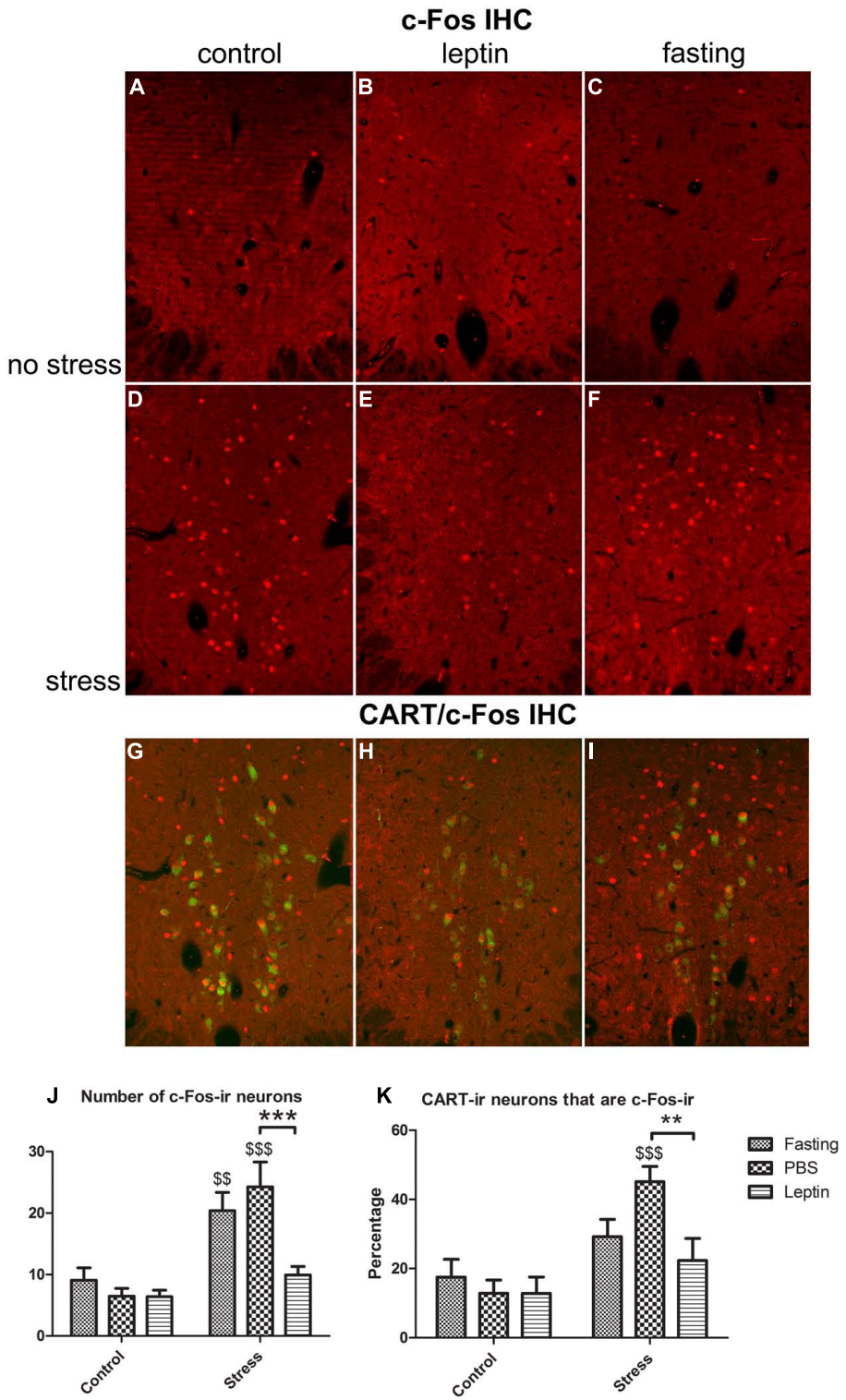

FIGURE 4 | Activation of EWcp CART expressing neurons by restraint stress. (A–C) c-Fos-ir in fasting, PBS-injected and leptin-injected rats, **(D–F)** the same three treatments, respectively, but stressed. **(G–I)** Merged images of fluorescent double labeling showing CART- and c-Fos-ir in EWcp neurons. **(J)** Quantitative analysis of stress-induced activation of EWcp neurons and **(K)** percentage of CART neurons exhibiting c-Fos-ir in the various experimental groups. Vertical bars represent the means + SEM; $N = 5$. Asterisks with lines indicate significant differences between fasting, PBS and leptin treated groups. $^{**}P < 0.01$; $^{***}P < 0.005$; dollar signs alone indicate significant differences of stressed group with respective control group. $\$\$P < 0.01$; $\$\$\$P < 0.005$. Scale bars: 50 μm.

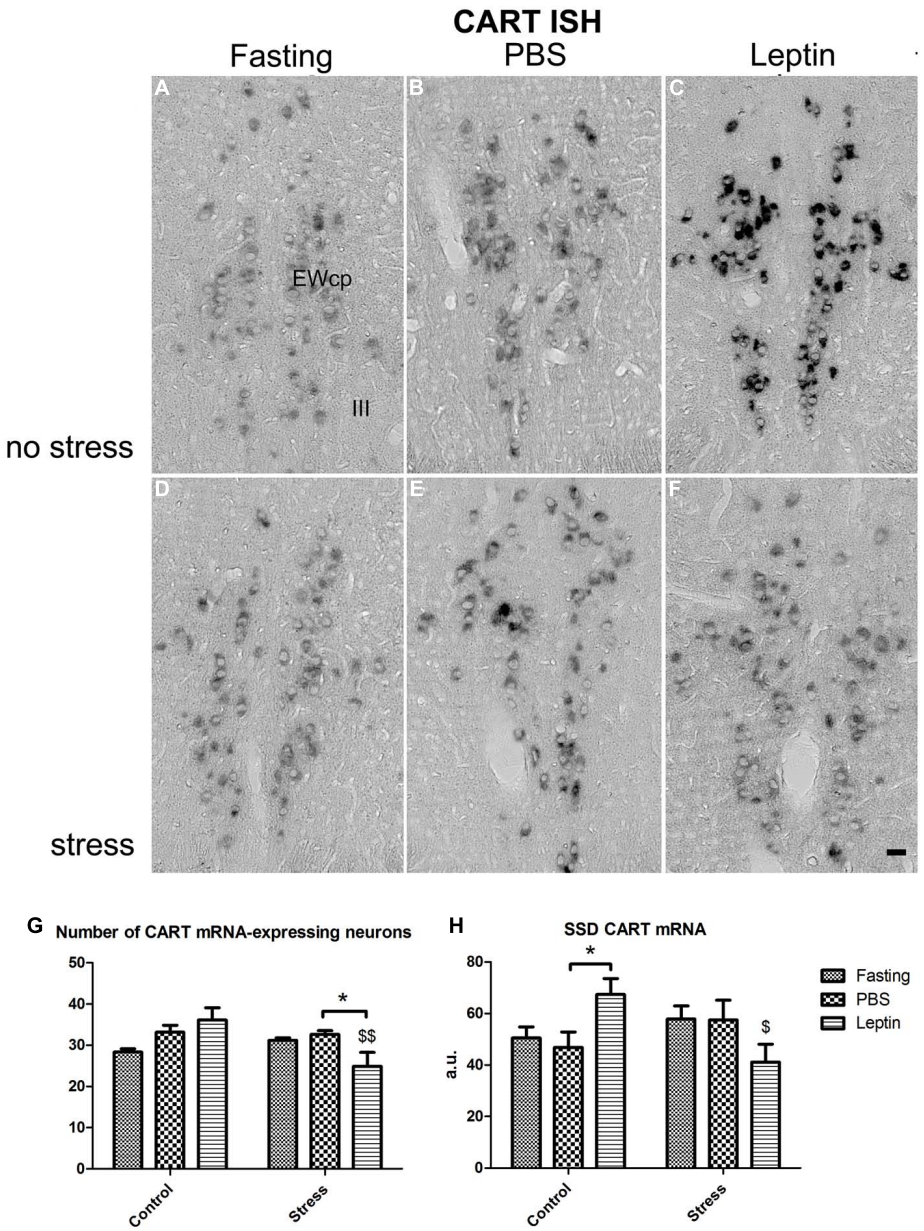

FIGURE 5 | *In situ* hybridization of CART mRNA in EWcp neurons. **(A–C)** Fasting, PBS-injected and leptin-injected rats, **(D–F)** the same three treatments, respectively, but stressed. **(G)** Number of CART mRNA expressing neurons and **(H)** SSD per perikaryon, expressed in arbitrary units (a.u.). Vertical bars represent the means + SEM; $N = 5$. Asterisks with lines indicate significant differences between fasting, PBS and leptin treated groups. $^*P < 0.05$; dollar signs alone indicate significant differences of stressed group with respective control group. $\$P < 0.05$; $\$\$P < 0.001$. Scale bars: 50 μm.

induction of CART gene. One might suggest that the induction of CART mRNA by stress needs longer time to occur. This is possible, however, not very likely, because previous studies have shown that 2 h after initiation of various acute stressors (e.g., pain, restraint or foot shock), Ucn1 mRNA in the EWcp can be significantly up-regulated, accompanied by increased expression of c-Fos (Kozicz et al., 2001; Cespedes et al., 2010; Rouwette et al., 2011). Therefore, we suggest that CART mRNA, in contrast to that of Ucn1, is not induced by acute restraint stress, a hypothesis that needs further investigation.

In the present study, we found that leptin injection strongly attenuates restraint stress-induced activation of EWcp neurons, which occurs concomitantly with attenuated CART mRNA expression. This could represent an important mechanism by which leptin participates in the regulation of stress response. Leptin has been reported to produce antidepressant- (Lu et al., 2006; Lu, 2007) and anxiolytic-like (Liu et al., 2010) effects in rats and mice. However, these behavioral studies were performed in either non-stressed or chronically stressed animals. So far, only one study has addressed the effect of leptin on acute stress-induced

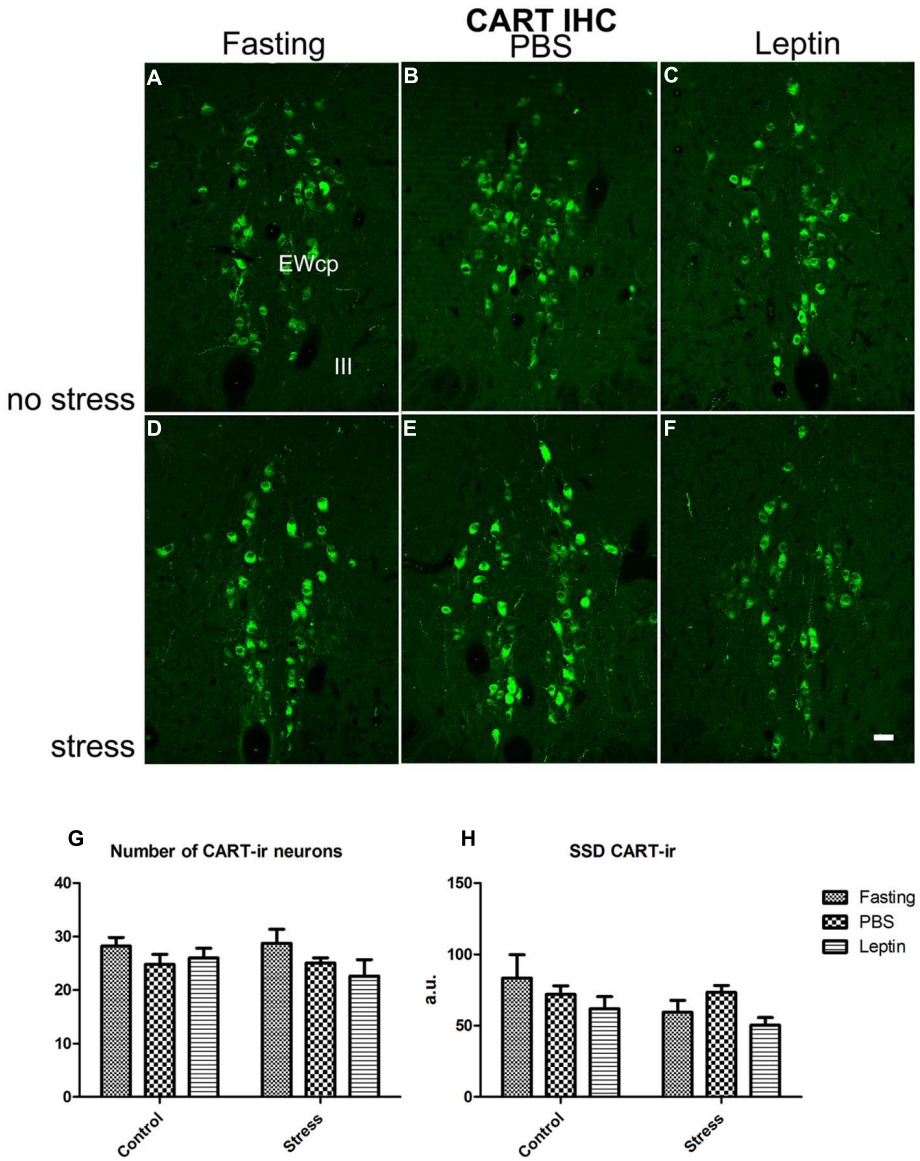

FIGURE 6 | Immunofluorescence labeling of EWcp neurons expressing CART. (A–C) CART-ir in fasting, PBS-injected and leptin-injected rats, **(D–F)** the same three treatments, respectively, but stressed. **(G)** Number of CART-ir and **(H)** SSD per perikaryon, expressed in arbitrary units (a.u.). Vertical bars represent the means + SEM; $N = 5$. No significant differences were present. Scale bars: 50 μm.

behavioral deficits (Haque et al., 2013). This study has shown that immobilization stress-induced anorexia and decrease in body weight can be reversed by leptin injection (Haque et al., 2013). These results might be striking at the first sight and are not explainable in terms of the conventional function of leptin (i.e., reducing food intake). However, this inhibitory action of leptin on stress-induced anorexia could well represent an anxiolytic/antidepressant-like effect. Here, we demonstrate that leptin blunts the activation of EWcp neurons and decreases CART mRNA expression in stressed rats. This may indicate that CART is a downstream component of a leptin-regulated mechanism that reduces anxiety-related behavior under stress conditions.

The role of midbrain CART in stress is further corroborated by the fact that CART in the rat EWcp was significantly elevated after applying a two-week mild stress paradigm (Xu et al., 2010). In two different rat models for depression, it was noted that depressive-like behavior correlated with a drastic reduction in CART-immunoreactivity not only in the hypothalamic paraventricular and arcuate nuclei but also in the EWcp. Moreover, CART treatment could reverse depression-like phenotypes (Dandekar et al., 2009; Wiehager et al., 2009). The association between CART and mood disorders has also been suggested. Specifically, CART mRNA expression was markedly higher in the EWcp in depressed suicide victims vs. controls (Bloem et al., 2012). Although these results do not permit to conclude whether CART

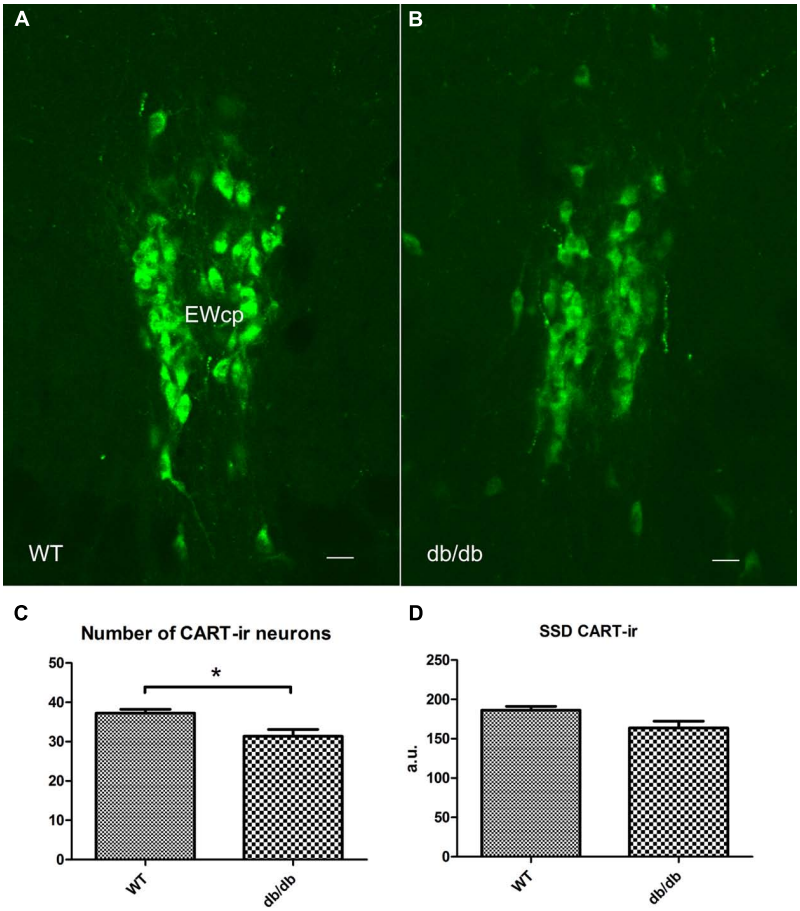

FIGURE 7 | CART content in the EWcp by disrupted leptin signaling. (A,B), fluorescent immunohistochemistry shows CART-ir in the EWcp in WT and *db/db* mice. **(C,D)**, the number and SSD of CART-ir neurons are decreased in *db/db* mice compared with WT. Scale bars: 20 μm. $*P < 0.05$.

in the EWcp is anxiogenic or anxiolytic, they collectively position midbrain CART as a possible modulator of stress-related behavior.

Another notable observation is that leptin down-regulates CART mRNA in stressed condition, but not CART peptide contents. We found similar CART peptide and mRNA dynamics in mouse exposed to acute restraint stress (Okere et al., 2010). The dissociation between CART mRNA and CART peptide content may be explained by assuming that leptin not only inhibits CART mRNA expression, but it attenuates too the axonal transport of CART peptide out of the cell body. This would leave the amount of CART peptide stored in the cell body unchanged.

In contrast to the strong attenuating effect of leptin on stress-induced activation of EWcp, the activation of EWcp by stress was comparable between fasted and normal fed rats. Interestingly, when we assessed the phenotype of neurons recruited by stress, CART neurons were strongly activated by stress in normal fed rats, but remained inactive in fasted rats. This suggests that another population of EWcp neurons is activated upon stress under fasted conditions. In the absence of food, another fuel signal, ghrelin, is released from the stomach to strongly stimulate food intake (Date et al., 2000; Tschöp et al., 2000). Ghrelin receptor protein as well as its mRNA are abundantly present in the rat EWcp (Zigman et al., 2006; Spencer et al., 2012). Taken together, it is plausible that ghrelin, induced by 24 h fasting, would specifically induce stress-associated activation of non-CART neurons in the EWcp, and/or inhibit the activation of CART neurons in EWcp.

In conclusion, here we show that the EWcp CART neurons respond differently to acute stress under fasted, normally sated (normal chow diet) and highly sated (artificially mimicked by i.p. leptin injection) conditions. We suggest that this mechanism may play a physiological role in the central integration of stressful and peripheral fuel signals. Such a mechanism would allow an animal to prepare the appropriate stress response under various energy states. Consequently, failure of this mechanism could contribute to the pathogenesis of feeding-related and stress-induced disorders.

ACKNOWLEDGMENT

Balázs Gaszner was supported by the Bolyai Scholarship of the Hangarian Academy of Sciences and by the research grant OTKA PD 100706. Balázs Gaszner is the co-author of this manuscript.

REFERENCES

Ahima, R. S., and Osei, S. Y. (2004). Leptin signaling. *Physiol. Behav.* 81, 223–241. doi: 10.1016/j.physbeh.2004.02.014

Bittencourt, J. C., Vaughan, J., Arias, C., Rissman, R. A., Vale, W. W., and Sawchenko, P. E. (1999). Urocortin expression in rat brain: evidence against a pervasive relationship of urocortin-containing projections with targets bearing type 2 CRF receptors. *J. Comp. Neurol.* 415, 285–312. doi: 10.1002/(SICI)1096-9861(19991220)415:3<285::AID-CNE1>3.0.CO;2-0

Bloem, B., Xu, L., Morava, E., Faludi, G., Palkovits, M., Roubos, E. W., et al. (2012). Sex-specific differences in the dynamics of cocaine- and amphetamine-regulated transcript and nesfatin-1 expressions in the midbrain of depressed suicide victims vs. controls. *Neuropharmacology* 62, 297–303. doi: 10.1016/j.neuropharm.2011.07.023

Campfield, L. A., Smith, F. J., Guisez, Y., Devos, R., and Burn, P. (1995). Recombinant mouse OB protein: evidence for a peripheral signal linking adiposity and central neural networks. *Science* 269, 546–549. doi: 10.1126/science.7624778

Cespedes, I. C., de Oliveira, A. R., da Silva, J. M., da Silva, A. V., Sita, L. V., and Bittencourt, J. C. (2010). mRNA expression of corticotropin-releasing factor and urocortin 1 after restraint and foot shock together with alprazolam administration. *Peptides* 31, 2200–2208. doi: 10.1016/j.peptides.2010.08.022

Chrousos, G. P., and Gold, P. W. (1992). The concepts of stress and stress system disorders. Overview of physical and behavioral homeostasis. *JAMA* 267, 1244–1252. doi: 10.1001/jama.1992.03480090092034

Dandekar, M. P., Singru, P. S., Kokare, D. M., and Subhedar, N. K. (2009). Cocaine- and amphetamine-regulated transcript peptide plays a role in the manifestation of depression: social isolation and olfactory bulbectomy models reveal unifying principles. *Neuropsychopharmacology* 34, 1288–1300. doi: 10.1038/npp.2008.201

Da Silva, A. V., Torres, K. R., Haemmerle, C. A., Céspedes, I. C., and Bittencourt, J. C. (2013). The Edinger–Westphal nucleus II: hypothalamic afferents in the rat. *J. Chem. Neuroanat.* 54, 5–19. doi: 10.1016/j.jchemneu.2013.04.001

Date, Y., Kojima, M., Hosoda, H., Sawaguchi, A., Mondal, M. S., Suganuma, T., et al. (2000). Ghrelin, a novel growth hormone-releasing acylated peptide, is synthesized in a distinct endocrine cell type in the gastrointestinal tracts of rats and humans. *Endocrinology* 141, 4255–4261. doi: 10.1210/endo.141.11.7757

Dietrich, M. O., and Horvath, T. L. (2009). Feeding signals and brain circuitry. *Eur. J. Neurosci.* 30, 1688–1696. doi: 10.1111/j.1460-9568.2009.06963.x

Dominguez, G., Lakatos, A., and Kuhar, M. J. (2002). Characterization of the cocaine- and amphetamine-regulated transcript (CART) peptide gene promoter and its activation by a cyclic AMP-dependent signaling pathway in GH3 cells. *J. Neurochem.* 80, 885–893. doi: 10.1046/j.0022-3042.2002.00775.x

Gaszner, B., Csernus, V., and Kozicz, T. (2004). Urocortinergic neurons respond in a differentiated manner to various acute stressors in the Edinger–Westphal nucleus in the rat. *J. Comp. Neurol.* 480, 170–179. doi: 10.1002/cne.20343

Gorska, E., Popko, K., Stelmaszczyk-Emmel, A., Ciepiela, O., Kucharska, A., and Wasik, M. (2010). Leptin receptors. *Eur. J. Med. Res.* 15(Suppl. 2), 50–54.

Håkansson, M. L., and Meister, B. (1998). Transcription factor STAT3 in leptin target neurons of the rat hypothalamus. *Neuroendocrinology* 68, 420–427. doi: 10.1159/000054392

Haque, Z., Akbar, N., Yasmin, F., Haleem, M. A., and Haleem, D. J. (2013). Inhibition of immobilization stress-induced anorexia, behavioral deficits, and plasma corticosterone secretion by injected leptin in rats. *Stress* 16, 353–362. doi: 10.3109/10253890.2012.736047

Heiman, M. L., Ahima, R. S., Craft, L. S., Schoner, B., Stephens, T. W., and Flier, J. S. (1997). Leptin inhibition of the hypothalamic-pituitary-adrenal axis in response to stress. *Endocrinology* 138, 3859–3863. doi: 10.1210/endo.138.9.5366

Huo, L., Münzberg, H., Nillni, E. A., and Bjørbaek, C. (2004). Role of signal transducer and activator of transcription 3 in regulation of hypothalamic trh gene expression by leptin. *Endocrinology* 145, 2516–2523. doi: 10.1210/en.2003-1242

Kalra, S. P., Dube, M. G., Pu, S., Xu, B., Horvath, T. L., and Kalra, P. S. (1999). Interacting appetite-regulating pathways in the hypothalamic regulation of body weight. *Endocr. Rev.* 20, 68–100. doi: 10.1210/edrv.20.1.0357

Korosi, A., Schotanus, S., Olivier, B., Roubos, E. W., and Kozicz, T. (2005). Chronic ether stress-induced response of urocortin 1 neurons in the Edinger–Westphal nucleus in the mouse. *Brain Res.* 1046, 172–179. doi: 10.1016/j.brainres.2005.04.012

Koylu, E. O., Couceyro, P. R., Lambert, P. D., Ling, N. C., DeSouza, E. B., and Kuhar, M. J. (1997). Immunohistochemical localization of novel CART peptides in rat hypothalamus, pituitary and adrenal gland. *J. Neuroendocrinol.* 9, 823–833. doi: 10.1046/j.1365-2826.1997.00651.x

Kozicz, T. (2003). Neurons colocalizing urocortin and cocaine and amphetamine-regulated transcript immunoreactivities are induced by acute lipopolysaccharide stress in the Edinger–Westphal nucleus in the rat. *Neuroscience* 116, 315–320. doi: 10.1016/S0306-4522(02)00772-8

Kozicz, T. (2007). On the role of urocortin 1 in the non-preganglionic Edinger–Westphal nucleus in stress adaptation. *Gen. Comp. Endocrinol.* 153, 235–240. doi: 10.1016/j.ygcen.2007.04.005

Kozicz, T., Li, M., and Arimura, A. (2001). The activation of urocortin immunoreactive neurons in the Einger-Westphal nucleus following stress in rats. *Stress* 4, 85–90. doi: 10.3109/10253890109115724

Kozicz, T., Sterrenburg, L., and Xu, L. (2011). Does midbrain urocortin 1 matter? A 15-year journey from stress (mal)adaptation to energy metabolism. *Stress* 14, 376–383. doi: 10.3109/10253890.2011.563806

Levene, H. (1960). "Robust tests for equality of variances," in *Contributions to Probability and Statistics: Essays in Honor of Harold Hotelling,* eds I. Olkin, S. G. Ghurye, W. Hoeffding, W. G. Madow, and H. B. Mann (Menlo Park, CA: Stanford University Press), 278–292.

Liu, J., Garza, J. C., Bronner, J., Kim, C. S., Zhang, W., and Lu, X. Y. (2010). Acute administration of leptin produces anxiolytic-like effects: a comparison with fluoxetine. *Psychopharmacology* (*Berl.*) 207, 535–545. doi: 10.1007/s00213-009-1684-3

Lu, X. Y. (2007). The leptin hypothesis of depression: a potential link between mood disorders and obesity? *Curr. Opin. Pharmacol.* 7, 648–652. doi: 10.1016/j.coph.2007.10.010

Lu, X. Y., Kim, C. S., Frazer, A., and Zhang, W. (2006). Leptin: a potential novel antidepressant. *Proc. Natl. Acad. Sci. U.S.A.* 103, 1593–1598. doi: 10.1073/pnas.0508901103

Malendowicz, L. K., Rucinski, M., Belloni, A. S., Ziolkowska, A., and Nussdorfer, G. G. (2007). Leptin and the regulation of the hypothalamic-pituitary-adrenal axis. *Int. Rev. Cytol.* 263, 63–102. doi: 10.1016/S0074-7696(07)63002-2

Meier, U., and Gressner, A. M. (2004). Endocrine regulation of energy metabolism: review of pathobiochemical and clinical chemical aspects of leptin, ghrelin, adiponectin, and resistin. *Clin. Chem.* 50, 1511–1525. doi: 10.1373/clinchem.2004.032482

Morava, E., and Kozicz, T. (2013). Mitochondria and the economy of stress (mal)adaptation. *Neurosci. Biobehav. Rev.* 37, 668–680. doi: 10.1016/j.neubiorev.2013.02.005

Münzberg, H., Huo, L., Nillni, E. A., Hollenberg, A. N., and Bjørbaek, C. (2003). Role of signal transducer and activator of transcription 3 in regulation of hypothalamic proopiomelanocortin gene expression by leptin. *Endocrinology* 144 2121–2131. doi: 10.1210/en.2002-221037

Ohata, H., Suzuki, K., Oki, Y., and Shibasaki, T. (2000). Urocortin in the ventromedial hypothalamic nucleus acts as an inhibitor of feeding behavior in rats. *Brain Res.* 861, 1–7. doi: 10.1016/S0006-8993(99)02378-1

Okere, B., Xu, L., Roubos, E. W., Sonetti, D., and Kozicz, T. (2010). Restraint stress alters the secretory activity of neurons co-expressing urocortin-1, cocaine- and amphetamine-regulated transcript peptide and nesfatin-1 in the mouse Edinger–Westphal nucleus. *Brain Res.* 1317, 92–99. doi: 10.1016/j.brainres.2009.12.053

Paxinos, G., and Franklin, K. B. J. (2001). *The Mouse Brain in Stereotaxic Coordinates,* 3rd Edn. New York: Academic Press.

Rogge, G., Jones, D., Hubert, G. W., Lin, Y., and Kuhar, M. J. (2008). CART peptides: regulators of body weight, reward and other functions. *Nat. Rev. Neurosci.* 9, 747–758. doi: 10.1038/nrn2493

Roubos, E. W., Dahmen, M., Kozicz, T., and Xu, L. (2012). Leptin and the hypothalamo-pituitary-adrenal stress axis. *Gen. Comp. Endocrinol.* 177, 28–36. doi: 10.1016/j.ygcen.2012.01.009

Rouwette, T., Klemann, K., Gaszner, B., Scheffer, G. J., Roubos, E. W., Scheenen, W. J., et al. (2011). Differential responses of corticotropin-releasing factor and urocortin 1 to acute pain stress in the rat brain. *Neuroscience* 183, 15–24. doi: 10.1016/j.neuroscience.2011.03.054

Sapolsky, R. M., Romero, L. M., and Munck, A. U. (2000). How do glucocorticoids influence stress responses? Integrating permissive, suppressive, stimulatory, and preparative actions. *Endocr. Rev.* 21, 55–89. doi: 10.1210/edrv.21.1.0389

Spencer, S. J., Xu, L., Clarke, M. A., Lemus, M., Reichenbach, A., Geenen, B., et al. (2012). Ghrelin regulates the hypothalamic-pituitary-adrenal axis and restricts anxiety after acute stress. *Biol. Psychiatry* 72, 457–465. doi: 10.1016/j.biopsych.2012.03.010

Tschöp, M., Smiley, D. L., and Heiman, M. L. (2000). Ghrelin induces adiposity in rodents. *Nature* 407, 908–913. doi: 10.1038/35038090

Weitemier, A. Z., and Ryabinin, A. E. (2005). Lesions of the Edinger–Westphal nucleus alter food and water consumption. *Behav. Neurosci.* 119, 1235–1243. doi: 10.1037/0735-7044.119.5.1235

Weitemier, A. Z., Tsivkovskaia, N. O., and Ryabinin, A. E. (2005). Urocortin 1 distribution in mouse brain is strain-dependent. *Neuroscience* 132, 729–740. doi: 10.1016/j.neuroscience.2004.12.047

Wiehager, S., Beiderbeck, D. I., Gruber, S. H., El-Khoury, A., Wamsteeker, J., Neumann, I. D., et al. (2009). Increased levels of cocaine and amphetamine regulated transcript in two animal models of depression and anxiety. *Neurobiol. Dis.* 34, 375–380. doi: 10.1016/j.nbd.2009.02.010

Williams, K. W., and Elmquist, J. K. (2012). From neuroanatomy to behavior: central integration of peripheral signals regulating feeding behavior. *Nat. Neurosci.* 15, 1350–1355. doi: 10.1038/nn.3217

Xu, L., Bloem, B., Gaszner, B., Roubos, E. W., and Kozicz, T. (2009). Sex-specific effects of fasting on urocortin 1, cocaine- and amphetamine-regulated transcript peptide and nesfatin-1 expression in the rat Edinger–Westphal nucleus. *Neuroscience* 162, 1141–1149. doi: 10.1016/j.neuroscience.2009.05.003

Xu, L., Bloem, B., Gaszner, B., Roubos, E. W., and Kozicz, T. (2010). Stress-related changes in the activity of cocaine- and amphetamine-regulated transcript and nesfatin neurons in the midbrain non-preganglionic Edinger–Westphal nucleus in the rat. *Neuroscience* 170, 478–488. doi: 10.1016/j.neuroscience.2010.07.001

Xu, L., Scheenen, W. J., Leshan, R. L., Patterson, C. M., Elias, C. F., Bouwhuis, S., et al. (2011). Leptin signaling modulates the activity of urocortin 1 neurons in the mouse nonpreganglionic Edinger–Westphal nucleus. *Endocrinology* 152, 979–988. doi: 10.1210/en.2010-1143

Xu, L., Scheenen, W. J., Roubos, E. W., and Kozicz, T. (2012). Peptidergic Edinger–Westphal neurons and the energy-dependent stress response. *Gen. Comp. Endocrinol.* 177, 296–304. doi: 10.1016/j.ygcen.2011.11.039

Zhang, Y., Kerman, I. A., Laque, A., Nguyen, P., Faouzi, M., Louis, G. W., et al. (2011). Leptin-receptor-expressing neurons in the dorsomedial hypothalamus and median preoptic area regulate sympathetic brown adipose tissue circuits. *J. Neurosci.* 31, 1873–1884. doi: 10.1523/JNEUROSCI.3223-10.2011

Zhang, Y., Proenca, R., Maffei, M., Barone, M., Leopold, L., and Friedman, J. M. (1994). Positional cloning of the mouse obese gene and its human homologue. *Nature* 372, 425–432. doi: 10.1038/372425a0

Zigman, J. M., Jones, J. E., Lee, C. E., Saper, C. B., and Elmquist, J. K. (2006). Expression of ghrelin receptor mRNA in the rat and the mouse brain. *J. Comp. Neurol.* 494, 528–548. doi: 10.1002/cne.20823

Conflict of Interest Statement: The authors declare that the research was conducted in the absence of any commercial or financial relationships that could be construed as a potential conflict of interest.

Received: 25 November 2013; accepted: 14 February 2014; published online: 03 March 2014.

Citation: Xu L, Janssen D, van der Knaap N, Roubos EW, Leshan RL, Myers MG Jr, Gaszner B and Kozicz T (2014) Integration of stress and leptin signaling by CART producing neurons in the rodent midbrain centrally projecting Edinger–Westphal nucleus. Front. Neuroanat. ***8****:8. doi: 10.3389/fnana.2014.00008*

This article was submitted to the journal Frontiers in Neuroanatomy.

frontiers in
NEUROANATOMY

REVIEW ARTICLE
published: 22 April 2014
doi: 10.3389/fnana.2014.00021

The functional and anatomical dissection of somatosensory subpopulations using mouse genetics

Claire E. Le Pichon*[1] *and Alexander T. Chesler*[2]*

[1] *National Institute of Neurological Disorders and Stroke, National Institutes of Health, Bethesda, MD, USA*
[2] *Intramural Pain Program, Section on Sensory Cells and Circuits, National Center for Complementary and Alternative Medicine, National Institutes of Health, Bethesda, MD, USA*

Edited by:
Laurent Gautron, UT Southwestern Medical Center, USA

Reviewed by:
Fan Wang, Duke University, USA
Qiufu Ma, Harvard Medical School, USA

****Correspondence:***
Alexander T. Chesler, Intramural Pain Program, Section on Sensory Cells and Circuits, National Center for Complementary and Alternative Medicine, National Institutes of Health, Building 35A, 1E450, 35 Convent Drive, Bethesda, MD 20892-3711, USA
e-mail: alexander.chesler@nih.gov

The word somatosensation comes from joining the Greek word for body (soma) with a word for perception (sensation). Somatosensory neurons comprise the largest sensory system in mammals and have nerve endings coursing throughout the skin, viscera, muscle, and bone. Their cell bodies reside in a chain of ganglia adjacent to the dorsal spinal cord (the dorsal root ganglia) and at the base of the skull (the trigeminal ganglia). While the neuronal cell bodies are intermingled within the ganglia, the somatosensory system is in reality composed of numerous sub-systems, each specialized to detect distinct stimuli, such as temperature and touch. Historically, somatosensory neurons have been classified using a diverse host of anatomical and physiological parameters, such as the size of the cell body, degree of myelination, histological labeling with markers, specialization of the nerve endings, projection patterns in the spinal cord and brainstem, receptive tuning, and conduction velocity of their action potentials. While useful, the picture that emerged was one of heterogeneity, with many markers at least partially overlapping. More recently, by capitalizing on advances in molecular techniques, researchers have identified specific ion channels and sensory receptors expressed in subsets of sensory neurons. These studies have proved invaluable as they allow genetic access to small subsets of neurons for further molecular dissection. Data being generated from transgenic mice favor a model whereby an array of dedicated neurons is responsible for selectively encoding different modalities. Here we review the current knowledge of the different sensory neuron subtypes in the mouse, the markers used to study them, and the neurogenetic strategies used to define their anatomical projections and functional roles.

Keywords: somatosensation, pain, nociception, TRP channel, touch, thermodetection, itch, sensory neuron

INTRODUCTION

We can all appreciate the richness of sensation that originates from within even a small patch of skin thanks to the neurons of the somatosensory system. The peripheral targets of somatosensory neuron afferents span from the tips of your toes to the inner organs of your body where they report on the presence of a striking diversity of stimuli. The pleasant feeling of a breeze on a summer's day might involve the activation of fibers sensitive to cooling but also perhaps the silencing of warm-activated fibers. The gentle mechanical forces generated by the wind might stimulate fibers that sense the bending of single hairs or subtle pressure changes across the surface of your skin. Now imagine the breeze stops and the baking sun heats up that same piece of skin. Suddenly a different class of fibers is recruited—thermosensitive nociceptors. These fibers, whose activation can also result in the stinging sensation from a paper cut, initiate signals that we interpret as pain.

Such diversity of sensations underlies the somatosensory system's myriad of functions. For example, we easily discriminate between gradations of mechanical stimuli ranging from a gentle caress to sharp stabbing or pinching. The same is true for thermal detection where cooling or warming can be pleasurable while searing heat or extreme cold are unbearable. In addition to differentiating between innocuous and noxious stimuli, the activity of somatosensory neurons also reports on the state of the body. Alterations in nociceptor thresholds during injury and inflammation from tissue damage result in hypersensitivity. Thus, if our same patch of skin (to which we forgot to apply sunblock) is overexposed to sunlight and incurs UV damage, gentle touch suddenly becomes painful, a process referred to as mechanical *allodynia*, and it also becomes much more sensitive to heat, a process also known as thermal *hyperalgesia*.

Such acuity begs the question—how are diverse stimuli detected and encoded by the somatosensory system? Or stated slightly differently—how many sensory neuron subtypes exist and what are their relative functions? In this review we examine recent approaches that have been taken to address these questions. First, we will briefly summarize the general anatomy and physiological properties of sensory neurons as they have been traditionally classified. Then, we will highlight several recent genetic strategies that have begun to elucidate the different classes of sensory neurons and their functional roles.

GENERAL FEATURES OF THE PERIPHERAL SOMATOSENSORY SYSTEM

The cell bodies of the somatosensory neurons reside in ganglia that are found just outside the spinal cord (dorsal root ganglia or DRGs; **Figure 1A**) and at the base of the skull (trigeminal

ganglia or TGs; **Figure 1B**). The sensory endings of the TGs cover the head and face, and those from the DRGs the rest of the body. These neurons are "pseudo-unipolar" with no dendrite but, instead, a single axon that bifurcates, creating one branch projecting to the periphery and another branch projecting into the central nervous system (CNS) at the level of the spinal cord and brainstem (Kandel et al., 2012; Purves et al., 2012).

Traditionally, somatosensory neurons were distinguished from one another through quantification of cell body size, degree of myelination, types of afferent endings, and the laminar targets of their efferent terminals in the spinal cord (**Figure 1C**; Kandel et al., 2012). Differences in anatomical features were correlated with physiological signatures that include receptive tuning, electrical properties, and neurochemistry. Using such criteria, somatosensory neurons were classified in four general fiber types: C, Aδ, Aβ, and proprioceptors (summarized in **Table 1**), each sub-serving broadly different roles in sensation. While this classification scheme has proved useful for many decades, it fails to account for the extraordinary molecular and functional diversity of somatosensory neuron subtypes that has emerged in recent years, and which is the focus of this review. Nevertheless, these categories are worth introducing, as their use remains common.

C fibers are the most abundant type, making up more than half of all somatosensory neurons (Kandel et al., 2012; Purves et al., 2012). They have small cell bodies, ranging in diameter from 10 to 30 μm. They are unmyelinated and thus conduct slowly (~2 m/s). C fibers are capable of responding to differing combinations of temperatures, pruritogens, tissue damage, chemical irritants, and mechanical stimuli (**Figure 1C**). C fibers are often defined as falling within two broad categories, peptidergic and non-peptidergic. These classes can be distinguished by the expression of neuropeptides such as substance P or calcitonin gene related-peptide (CGRP; the peptidergic class of C fibers) or, conversely, binding by a histological marker called the isolectin IB4 (the non-peptidergic class of C fibers; Averill et al., 1995). However, some overlap between these markers exists (see below) and it is important to note that neuropeptides are found in other fiber types (McCoy et al., 2013). Additionally, there are other non-pepdidergic C fibers not labeled by IB4 (Abraira and Ginty, 2013). Thus, such markers are only partially selective. Activation of C fibers often, but not always, results in the sensation of pain (i.e., nociceptors). However, there are other classes of C fibers that respond rather specifically to cold, itch, or pleasurable touch (Zotterman, 1939). In the periphery, C fibers terminate as free nerve endings in the skin, organs, and bone. Centrally, they project to the superficial layers of the spinal cord (dorsal horn), a region known to be critical for the first stage processing of noxious and thermal stimuli (laminae I–III; Kandel et al., 2012; Purves et al., 2012).

Aδ fibers have medium diameter cell bodies and are lightly myelinated, and thus faster conducting than C fibers (up to

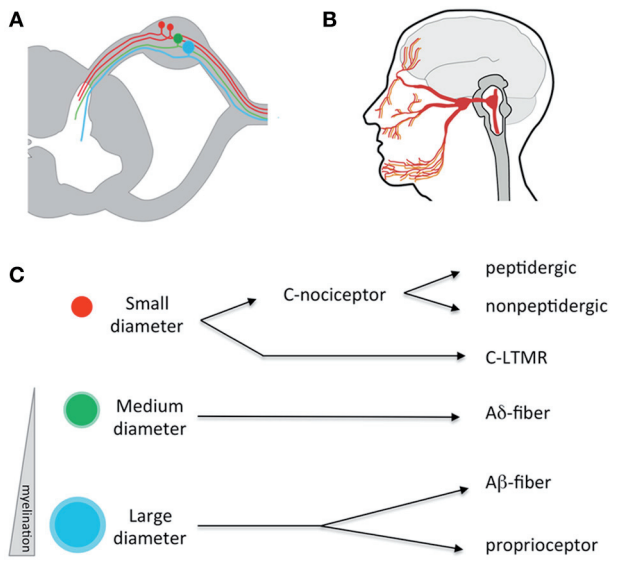

FIGURE 1 | Anatomy of the somatosensory system. (A) Somatosensory neuron cell bodies reside outside the spinal cord in the dorsal root ganglia (DRG). They have a single process that splits, sending an afferent projection to the periphery and an efferent projection to the spinal cord. **(B)** Somatosensory neurons residing in the trigeminal send processes that innervate peripheral targets through the face, mouth, and dura and central targets in the brainstem. **(C)** Somatosensory neurons can be divided into three broad categories based on the size of their cell bodies and degree of myelination. Within these broad categories, numerous sub-specializations exist-for example small diameter C fibers are mostly nociceptors while large diameter A neurons respond to low threshold mechanical stimuli. LTMR, low-threshold mechano-receptor.

Table 1 | Somatosensory cell type markers.

Marker	Sensory cell type
Parvalbumin	Proprioceptors and Aβ fibers
CGRP	Peptidergic C fibers, sub-population of Aδ fibers
Substance P	Peptidergic C fibers
NF200	Myelinated Aδ fibers, Aβ fibers, and proprioceptors
IB4	Non-peptidergic C fibers
Trpv1	Small diameter C fibers (heat and pain)
Trpm8	Small diameter C fibers (cold and pain)
MrgprD	Small diameter C fibers (noxious mechanical, pain)
MrgprA3	Small diameter C fibers (itch)
MrgprB4	Small diameter C fibers (innocuous mechanical)
VGlut3	Non-peptidergic C fibers (innocuous mechanical, cooling)
TH	Non-peptidergic C fibers (innocuous mechanical, cooling)
TrkB	Aδ fibers (innocuous mechanical, cooling)
Npy2r	Aβ fibers (innocuous mechanical)
Chondrolectin	Aβ fibers (innocuous mechanical)
DOR	Sub-populations of non-peptidergic C fibers and myelinated NF200-positive fibers

Abbreviations: CGRP, calcitonin gene-related peptide; NF200, neurofilament heavy chain 200; IB4, isolectin B4; Trpv1, transient receptor potential cation channel subfamily V member 1; Trpm8, transient receptor potential cation channel subfamily M member 8; MrgprD, Mas-related G-protein-coupled receptor D; MrgprA3, Mas-related G-protein-coupled receptor A3; MrgprB4, Mas-related G-protein-coupled receptor B4; VGluT3, vesicular glutamate transporter type 3; TH, tyrosine hydroxylase; TrkB, tyrosine receptor kinase B; Npy2r, neuropeptide Y receptor type 2; DOR, delta opioid receptor.

30 m/s). Like C fibers, they are responsive to combinations of temperature, force, and irritants (Kandel et al., 2012; Purves et al., 2012). A subset of Aδ fibers has been shown to be sensitive to innocuous temperatures (i.e., Hensel and Iggo, 1971; Darian-Smith et al., 1973; Duclaux and Kenshalo, 1980). Given their faster conduction velocity, it is believed additional classes are specialized for detecting highly localized "fast pain" rather than the more spatially diffuse "slow" pain associated with C fiber nociceptors (Basbaum et al., 2009). Aδ fibers also sensitize to repeated stimulation and/or tissue injury, thus playing a key role in inflammatory pain (Basbaum et al., 2009). Like C fibers, Aδ fibers project to the dorsal horn. These target similar superficial laminae as well as deeper layers of the spinal cord (lamina V) where they initiate nocifensive reflexes, such as innate withdrawal from noxious stimuli (for example, a hot stove).

In terms of size, the largest somatosensory neurons are the Aβ fibers dedicated to the detection of low-threshold mechanical stimuli and the Aα fibers that respond to muscle twitch (also called proprioceptors). Both types of somatosensory neurons have cell bodies averaging >50 μm. They are heavily myelinated and have fast conduction velocities (in the range of 30–70 m/s). Aβ fibers are low-threshold mechanoreceptors (LTMRs) and different subclasses are tuned to specific types of mechanical stimuli such as touch, vibration, and hair deflection. The nerve endings associated with Aβ fibers, including Meissner's corpuscles, Pacinian corpuscles, Merkel cell endings, and the lanceolate nerve endings that enwrap hair follicles, each display a unique morphology that is likely to sub-serve the tuning specializations of their associated nerve fibers (Kandel et al., 2012; Purves et al., 2012). Proprioceptor endings are also quite specialized. These innervate muscle spindles or Golgi tendon organs and are uniquely adapted to the detection of muscle tension and contraction. Centrally, Aβ fibers project to the dorsal column nuclei in the brainstem with branches in laminae III–V of spinal cord while proprioceptors also project to these deeper laminae, notably to local motor-stretch reflex circuits.

Despite decades of physiological and anatomical studies, many questions remained unanswered. In particular, an understanding of the signal transduction events lagged behind that for other sensory systems, notably olfaction, taste, and vision. Breakthroughs began to happen in the 1990's as genes critical to the sensing of somatosensory stimuli began to be discovered. Molecules required for pain signaling, such as sodium channels, as well as the receptors for key noxious agents, allowed researchers to address the specificity question from a new angle (Akopian et al., 1996; Caterina et al., 1997). These studies have helped elucidate the specificity of sensory neuron subtypes (i.e., Abrahamsen et al., 2008). Together with classical physiological studies, genetic studies are helping to create a clearer picture of how specific modalities are encoded by the somatosensory system.

TRANSIENT RECEPTOR POTENTIAL (TRP) CHANNEL EXPRESSION DIFFERENTIATES SOMATOSENSORY NEURON SUBTYPES DEDICATED TO NOCICEPTION AND TEMPERATURE DETECTION

Work over the past two decades has uncovered a family of ionotropic receptors that respond to specific somatosensory stimuli (**Figure 2A**; Jordt et al., 2003; Bandell et al., 2007). Perhaps the most studied of these molecules is the non-selective cation channel, TRPV1 (transient receptor potential cation channel subfamily V member 1). Initially identified as the capsaicin receptor, TRPV1 is a principle detector of noxious heat (>42°C; **Figure 2A**; Caterina et al., 1997). TRPV1-knockout mice exhibit deficits in heat detection as measured by behavioral assays (Caterina et al., 2000). It is notable that the behavioral responses to heat are only diminished, suggesting that other sensory pathways for noxious temperature detection must exist (more on this below). TRPV1 is also activated by tissue acidification and lipid metabolites (Tominaga et al., 1998). The receptor becomes sensitized by many of the intracellular signaling pathways that are engaged during injury and inflammation (Chuang et al., 2001). Corroborating such findings, TRPV1-knockout mice have been shown to develop less thermal hyperalgesia in the context of inflammation, lending credence to the notion that TRPV1 is critical for noxious heat detection (Caterina et al., 2000). These studies have led to the emergence of TRPV1 as a therapeutic target of numerous pharmaceutical companies for pain management (Patapoutian et al., 2009).

In a similar manner, other TRP channels are expressed in unique subpopulations of sensory neurons. They too are tuned to unique forms of somatosensory stimuli (**Figure 2B**). For example, TRPA1 (transient receptor potential subfamily A member 1) is expressed in a subset of $TRPV1^+$ neurons where it can be directly activated by pain-inducing chemical irritants, such as mustard oil, or indirectly activated through cellular signaling, such as calcium or GPCR activation (Jordt et al., 2004; Bautista et al., 2006; Kwan et al., 2006). In contrast, TRPM8 (transient receptor potential cation channel subfamily M member 8) is expressed in a largely non-overlapping subset of small-diameter neurons mostly lacking both TRPV1 and TRPA1. TRPM8 is activated by cooling (<27°C) as well as natural products that induce the sensation of cooling such as menthol (McKemy et al., 2002; Peier et al., 2002). Remarkably, mice in which TRPM8 is genetically deleted have profound defects in detecting cold temperatures (Bautista et al., 2007; Colburn et al., 2007; Dhaka et al., 2007).

Given the properties of these channels and the consequences of perturbing their function, it is believed that TRPV1 is a marker for nociceptors tuned to heat. A subset of TRPV1 neurons co-expressing TRPA1 is thought to detect chemical irritants and pruritogens. The $TRPM8^+$ neurons, in contrast, are a relatively rare population of neurons that are thought to be cold sensors. Recently, several lines of mice have been generated to label and manipulate these neurons *in vivo* to directly test the properties of these neurons.

TRPV1 REPORTER MICE REVEAL THE ANATOMY OF A CLASS OF NOCICEPTORS

Upon the discovery of TRPV1, several anatomical methods were used to examine the expression pattern of this important receptor (Caterina et al., 1997). *In situ* hybridization offered excellent sensitivity but lacked the ability to determine neuronal morphology. Antibodies to TRPV1 were developed, but these had limited sensitivity and specificity. Thus, a more elegant solution was to capitalize on the power of mouse genetics and engineer

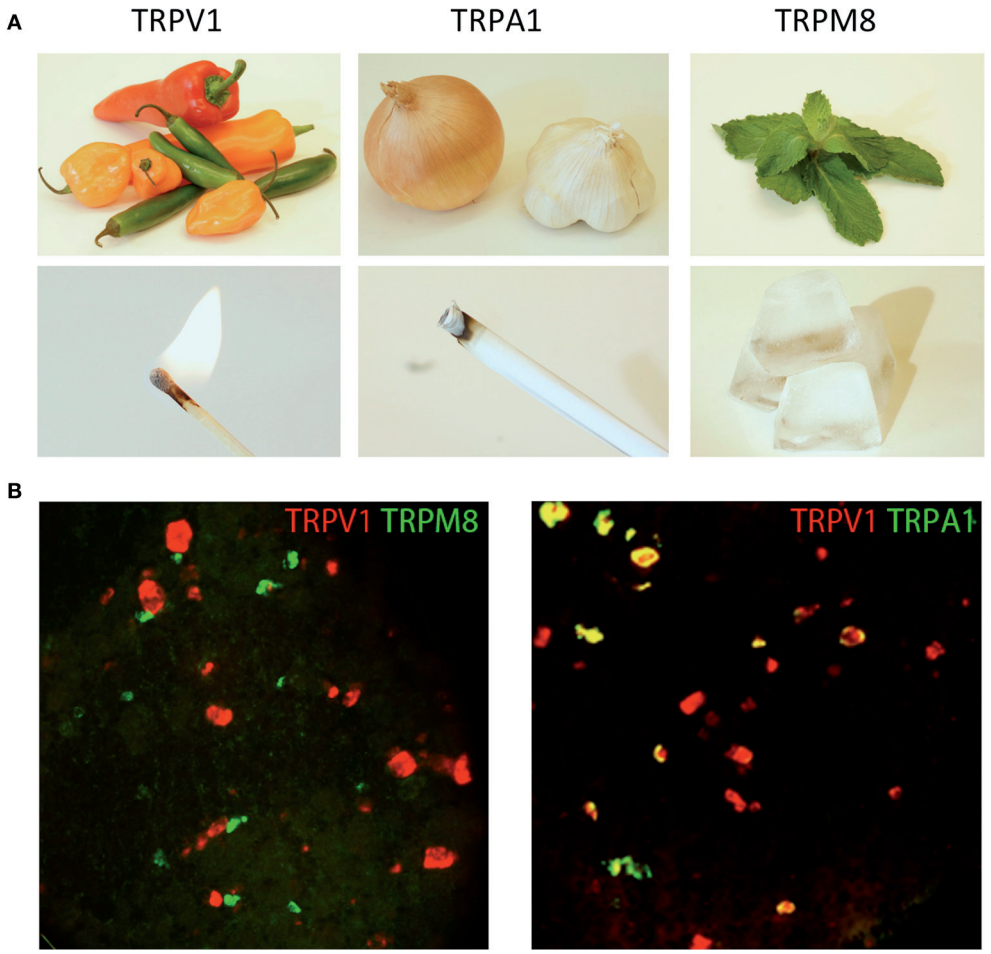

FIGURE 2 | TRP channels respond to unique types of stimuli. (A) Natural products from chili peppers, onions/garlic, and mint leaves selectively activate TRP channels (TRPV1, TRPA1, and TRPM8, respectively). The psychophysical effects of these compounds directly correlate with the environmental stimuli to which these TRP channels are responsive. Activation of TRPV1 by either capsaicin from chili peppers or heat evokes a burning sensation, activation of TRPA1 by mustard oil and environmental irritants evokes a stinging pain, and activation of TRPM8 by menthol from mint leaves or cold evokes the sensation of cooling. **(B)** TRP channels are differentially expressed in somatosensory neurons. Two-color fluorescent *in situ* hybridization demonstrates little overlap between TRPM8 and TRPV1 (left hand image). Meanwhile, TRPA1 is expressed in a subset of TRPV1 neurons (right hand image). Image courtesy of Mark Hoon, NIH/NIDCD.

a strain that selectively expressed a highly sensitive marker in all TRPV1$^+$ neurons (Cavanaugh et al., 2011b). To examine the expression of TRPV1 *in vivo*, a mouse was created in which the placental alkaline phosphatase (PLAP) and a nuclear-localized β-galactosidase gene (nLacZ) were knocked in just after the stop codon of TRPV1 (**Figure 3**; **Table 2**; Shah et al., 2004). Internal ribosomal entry sites (IRES) were used such that TRPV1, PLAP, and nLacZ were translated as three independent proteins. Thus, the function of TRPV1 protein was preserved while allowing for the co-expression of two independent histological markers from the same mRNA transcript. Critically, this strategy preserved all the genomic regulatory elements upstream of the TRPV1 start site, ensuring the most faithful expression of the markers as possible.

As observed by more traditional neuroanatomical techniques, nLacZ and PLAP staining in the adult reporter mice indicated that TRPV1 expression is enriched in peptidergic C fibers (Cavanaugh et al., 2011a). The TRPV1$^+$ neurons accounted for nearly all of the unmyelinated, peptidergic DRG neurons while being largely absent from the non-peptidergic C fibers as defined by IB4 (**Figure 4**). Highlighting the utilities of the reporter expression technique, the greater sensitivity of nLacZ staining revealed neurons with weak TRPV1 expression that were previously missed by standard approaches relying on TRPV1-specific probes and antibodies. The increased sensitivity resulted in the unexpected observation that a significant number (>20%) of TRPV1$^+$ neurons are negative for both peptidergic and non-peptidergic markers. Thus, the traditional classes of peptidergic and IB4-binding non-peptidergic C fibers do not account for the entirety of small diameter neurons (more on this below).

The improved sensitivity of PLAP staining also afforded a much more detailed picture of the peripheral and central projections of TRPV1$^+$ sensory neurons with single fiber resolution (Cavanaugh et al., 2011a,b). Staining revealed extensive

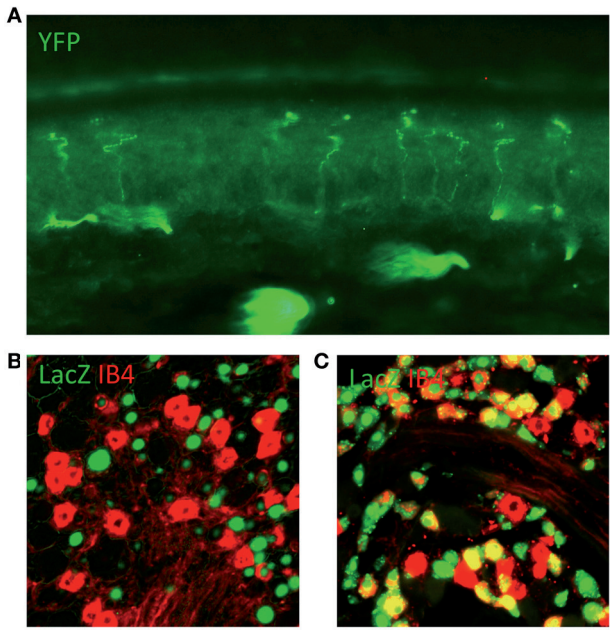

FIGURE 3 | TRPV1 Reporter mice reveal the anatomy of neurons that expressed TRPV1 throughout their lineage. (A) Skin section from TRPV1-Cre × YFP reporter strain showing primary afferent arborizations in the various epidermal layers. **(B)** DRG section from adult TRPV1-PLAP-nlacZ mouse, showing minimal overlap between β-Gal reaction product (green) and IB4 (red). **(C)** DRG section from adult TRPV1-Cre × LacZ reporter strain. Anti-LacZ (green) shows significantly more overlap with IB4 (red) since the entire TRPV1 lineage is marked. Image courtesy of Danial Cavanaugh and Allan Basbaum, Department of Anatomy UCSF.

axonal labeling of peripheral tissues in numerous areas, including the bladder, cornea, and glabrous and hairy skin of the hind paw, as well as previously unobserved single axonal endings that terminated in the outermost epidermal layers. The analysis of these mice has also led to a greater appreciation of the extent of primary afferent innervation in central tissues. PLAP staining revealed numerous projections from trigeminal and nodose ganglia to regions in the brainstem and medulla such as the superficial layers of the medullary dorsal horn (also referred to as the nucleus caudalis), the nucleus of the solitary tract, and the area postrema. PLAP$^+$ fibers found in the region of the rostral ventrolateral reticular nucleus raised the intriguing possibility of a monosynaptic input from TRPV1$^+$ afferents to motor neurons of the nucleus ambiguus. Additionally, axons were observed coursing throughout the parabrachial nucleus suggesting significant monosynaptic input from nociceptors (Cavanaugh et al., 2011b). This is of particular interest since parabrachial neurons in turn project to the amygdala, which has been implicated in emotional aspects of the pain experience (Feil and Herbert, 1995; Jasmin et al., 1997).

In addition to its well-established role in somatosensation, a flurry of recent papers suggests TRPV1 might be functioning in other tissues (Kauer and Gibson, 2009). Particular focus has been in the CNS, where TRPV1 has been proposed to participate in a myriad of functions that include osmodetection in the hypothalamus and/or the modulation of synaptic strength in several brain regions (Sharif Naeini et al., 2006; Chávez et al., 2010; Grueter et al., 2010). Given the exquisite sensitivity of the reporter strain, one would expect to find significant PLAP and/or nLacZ staining within the brains of the reporter mice (Cavanaugh et al., 2011a). Given nLacZ's nuclear localization coupled with the enzymatic amplification of the X-gal reaction used for detection, this is likely the most sensitive means of detecting TRPV1 expression to date. Quite surprisingly, such analyses failed to detect TRPV1 expression in the populations of neurons involved in the previously described forms of TRPV1-dependent synaptic plasticity. That said, a scattering of cells positive for nLacZ was observed within the CNS. This analysis, coupled with RT-PCR and radioactive *in situ* hybridization showed that TRPV1 is expressed in neurons that are present in a limited number of brain regions, the most prominent of which are in a contiguous band, centered along the midline of the posterior hypothalamus and rostral midbrain (Cavanaugh et al., 2011b).

In light of the sensitivity of the detection method, the absence of CNS staining almost certainly reflects a level of TRPV1 expression far below anything functionally meaningful. It seems very unlikely that the physiological and/or pharmacological effects reported could be mediated by TRPV1 as it would require these processes to be working on only a handful of molecules that the cell might be expressing. That said, there does seem to be appreciable expression of TRPV1 in a discrete population of neurons in the posterior hypothalamus, although its functional consequence remains to be determined.

EXAMINING THE LINEAGE OF TRPV1-EXPRESSING NEURONS WITH Cre-REPORTER MICE

Two groups constructed mice where Cre recombinase is expressed under control of the TRPV1 promoter either via direct knock-in to the TRPV1 locus (Cavanaugh et al., 2011a,b) or by using transgenics based on Bacterial Artificial Chromosomes (BACs; Mishra et al., 2011). Both groups crossed the resultant mice strains to ROSA-reporter strains. Since Cre-mediated genetic recombination is irreversible, crossing the TRPV1-Cre mice to floxed reporter strains allows one to mark all the cells that expressed TRPV1 throughout development, even transiently. Indeed, when these crosses were generated, >50% more labeled neurons were observed as compared to the TRPV1-PLAP-nLacZ mice. This expansion of labeled cells reflects the much broader expression of TRPV1 during development and its eventual down-regulation after birth. Also of note, neither group observed appreciable numbers of labeled neurons in the CNS with this highly sensitive approach, further supporting the conclusion that TRPV1 is unlikely to be expressed widely in the brain, even during embryonic development. Sensory neurons that transiently expressed TRPV1 included neurons dedicated to cold temperatures, as evidenced by the co-expression of the marker with TRPM8.

VISUALIZING COLD-SENSING NEURONS WITH TRPM8 REPORTER MICE

Two distinct populations of cold-sensing neurons have been identified in human and primates—slowly conducting neurons that are believed to signal cold pain (>18°C) and faster conducting

Table 2 | Summary of the mouse lines discussed, with nerve ending descriptions for the neuron types labeled.

Mouse line #	Mouse line	Sensory cell type labeled or ablated	Peripheral nerve ending (skin)	Central projection (spinal cord)	Original reference(s)
1	TRPV1-i-PLAP-i-nLacZ	Small diameter C fibers and subset of medium diameter Aδ fibers (heat, pain)	Free nerve endings	Laminae I–II and V	Cavanaugh et al., 2011a
2	TRPV1-Cre	Small diameter C fibers and subset of medium diameter Aδ fibers (heat, pain)	Free nerve endings	Laminae I–II and V	Cavanaugh et al., 2011b; Mishra et al., 2011
3	TRPV1-DTR	Small diameter C fibers and subset of medium diameter Aδ fibers (heat, pain)	Free nerve endings	Laminae I–II and V	Pogorzala et al., 2013
4	TRPM8-GFP	Small diameter C fibers and subset of medium diameter Aδ fibers (cold, pain)	Free nerve endings	Primarily lamina I	Takashima et al., 2007
5	TRPM8-fGFP	Small diameter C fibers and subset of medium diameter Aδ fibers (cold, pain)	Free nerve endings	Primarily lamina I	Dhaka et al., 2008
6	TRPM8-DTR	Small diameter C fibers and subset of medium diameter Aδ fibers (cold, pain)	Free nerve endings	Primarily lamina I	Pogorzala et al., 2013
7	CGRP-GFP-DTR	Peptidergic small diameter C fibers and subset of medium diameter Aδ fibers (heat, pain)	Free nerve endings	Laminae I–II and V	McCoy et al., 2013
8	MrgprD-EGFP	Small diameter C fibers (high threshold mechanical, pain)	Free nerve endings	Lamina II	Zylka et al., 2005
9	MrgprD-PLAP	Small diameter C fibers (high threshold mechanical, pain)	Free nerve endings	Lamina II	Zylka et al., 2005
10	MrgprD-DTR	Small diameter C fibers (high threshold mechanical, pain)	Free nerve endings	Lamina II	Cavanaugh et al., 2009
11	MrgprD-ChR2	Small diameter C fibers (high threshold mechanical, pain)	Free nerve endings	Lamina II	Wang and Zylka, 2009
12	Nav1.8:ChR2	Small diameter C fibers (all types)	Free nerve endings	Laminae I–II and V	Madisen et al., 2012; Daou et al., 2013
13	MrgprA3-EGFP:Cre	Non-peptidergic, small diameter C fibers (itch)	Free nerve endings	Lamina II	Han et al., 2012
14	MrgprB4-PLAP	Non-peptidergic, small diameter C fibers (stroking)	Free nerve endings	Lamina II	Liu et al., 2007
15	MrgprB4-tdTomato-2A-Cre	Non-peptidergic, small diameter C fibers (stroking)	Free nerve endings	Lamina II	Vrontou et al., 2013
16	VGLUT3-EGFP	Non-peptidergic, small diameter C fibers (low threshold mechanical)	Longitudinal lanceolate endings	Lamina II	Seal et al., 2009
17	VGLUT3-KO	Non-peptidergic, small diameter C fibers (low threshold mechanical)	Longitudinal lanceolate endings	Lamina II	Seal et al., 2009
18	TH-CreER	Non-peptidergic, small diameter C fibers (low threshold mechanical)	Longitudinal lanceolate endings	Lamina II	Li et al., 2011
19	TrkB-tauEGFP	Medium diameter Aδ fibers (low threshold mechanical)	Longitudinal lanceolate endings	Laminae II–III	Li et al., 2011
20	Npy2r-GFP	large diameter Aβ fibers (low threshold mechanical)	Longitudinal lanceolate endings	Laminae III–V	Li et al., 2011
21	Chondrolectin-PLAP	Large diameter Aβ fibers (low threshold mechanical)	Longitudinal lanceolate endings (in mystacial pad)	No data	Sakurai et al., 2013
22	Parvalbumin:Cre	Large diameter Aα and Aβ fibers (low threshold mechanical; and muscle tension and contraction)	Muscle spindle, Golgi tendon; Merkel and lanceolate endings (in mystacial pad)	Laminae III–V	Sakurai et al., 2013
23	DOR-EGFP	Sub-populations of both non-peptidergic C fibers and myelinated NF200-positive fibers (mechanical pain)	Meissner corpuscles, Merkel, and circumferential endings	Laminae I–V	Scherrer et al., 2009; Bardoni et al., 2014

*The numbers in the first column are referred to in **Figure 4** to show the origin of the data classifying the neuron types. Abbreviations: TRPV1, transient receptor potential cation channel subfamily V member 1; i, IRES; PLAP, placental alkaline phosphatase; nLacZ, nuclear-localized β-galactosidase; Cre, cre recombinase; DTR, diphtheria toxin receptor; TRPM8, transient receptor potential cation channel subfamily M member 8; GFP, green fluorescent protein; fGFP, farnesylated green fluorescent protein; CGRP, calcitonin gene-related peptide; MrgprD, Mas-related G-protein-coupled receptor D; ChR2, channelrhodopsin 2; Nav1.8, voltage-gated sodium channel 1.8; MrgprA3, Mas-related G-protein-coupled receptor A3; MrgprB4, Mas-related G-protein-coupled receptor B4; VGluT3, vesicular glutamate transporter type 3; TH, tyrosine hydroxylase; TrkB, tyrosine receptor kinase B; Npy2r, neuropeptide Y receptor type 2; DOR, delta opioid receptor.*

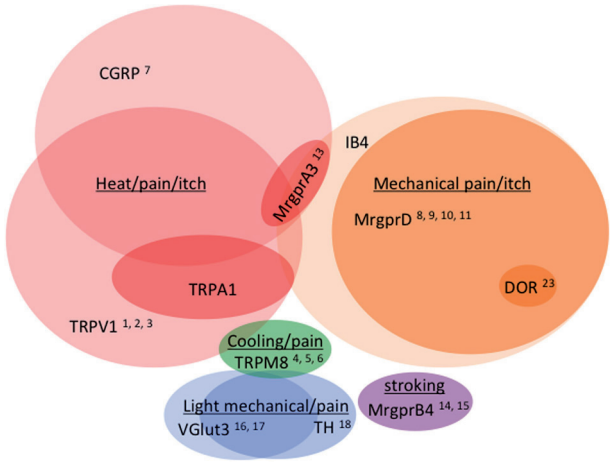

FIGURE 4 | Venn diagram illustrating the distribution of markers across different classes of C fibers (not to scale). Numbers reference the mouse lines listed in **Table 2**.

neurons believed to be Aδ fibers that respond to innocuous cooling (Darian-Smith et al., 1973; Dubner et al., 1975; Georgopoulos, 1976). Just as TRPV1 expression has been successfully exploited to label heat-sensitive somatosensory neurons, the expression of the menthol/cold receptor TRPM8 has been used to delineate those neurons believed to be dedicated to the detection of cold. Given that the population of TRPM8-expressing neurons is relatively small (∼10% of DRG neurons), transgenic labeling provides an excellent means of locating these neurons in tissue sections, *in vitro*, and *in vivo*. Two lines of mice have been generated that express variants of GFP under the control of the TRPM8 promoter. Interestingly, while these mice have many similarities, their construction methods and analyses have some notable differences.

Takashima et al. used a BAC-transgenic approach to express GFP in TRPM8$^+$ neurons while leaving the endogenous promoter region untouched (Takashima et al., 2007). The BAC approach has the added benefit that TRPM8 protein is also expressed normally and the mice retain normal behavior responses to cooling. The large genomic regions included in BACs are preferable to smaller transgenes in that they often retain the long-range regulatory elements required for faithful gene expression and, as such, these types of transgenic mice suffer less from positional effects and/or multiple random targeting events (Heintz, 2001). However, as with small transgenes, careful analyses are still required to ensure the expression observed truly reflects endogenous patterns.

In order to validate the TRPM8 reporter strain, several key predictions from the Takashima study needed to be examined. For example, it is well established that TRPM8 is robustly activated by menthol, a cooling compound found in mint leaves, and the receptor is the sole detector of this molecule in sensory neurons (Bautista et al., 2007; Dhaka et al., 2007). Therefore, one would expect that the preponderance of GFP$^+$ neurons in the BAC-transgenic TRPM8-GFP mouse line should be sensitive to this compound. Analyses of these mice found that 81.5 ± 4.8% of the GFP$^+$ DRG neurons were menthol-sensitive. While this is an impressive degree of overlap, it is important to consider the 18.5% of neurons that failed to respond. It is difficult to determine from this study if these neurons were not expressing TRPM8 at sufficient levels, were physiologically compromised, or, more importantly, whether GFP expression was the result of some "leaky" transcription from the BAC promoter.

A separate group used an alternate strategy to create a TRPM8 reporter mouse. Rather than using BAC transgenesis, Dhaka et al. (2008) generated mice via gene targeting in which the TRPM8 coding sequence was replaced with a farnesylated GFP (fGFP), resulting in functional disruption of the receptor (Dhaka et al., 2008). However, since TRPM8 is haplosufficient, heterozygous mice retained normal responses to cooling and thus could be used for functional analyses. An interesting side note was that when these mice were first described in 2007, the authors originally failed to observe any fGFP expression (Dhaka et al., 2007). The marker expression was only recovered after the removal of loxP-flanked EM7-PGK-NEO cassette. Again, such nuances call attention to the delicate nature of genome engineering.

When Dhaka et al. subjected their strain to the same control testing as Takashima et al., their knock-in mice appeared to faithfully mark neurons expressing TRPM8. Dhaka et al. reported that 19/20 fGFP$^+$ neurons responded to both cooling and menthol. The histochemical analyses from the two groups seemed to follow the same trend, with the BAC line expressing GFP in a greater percentage of DRG neurons than the knock-in line. One explanation for the discrepancy is that the BAC line captures even extremely low levels of TRPM8 expression, below what would be required for functional detection. Therefore, the knock-in mouse seems to more conservatively estimate the true TRPM8 population while perhaps missing some cells with low-level expression while the BAC line may be overestimating the extent of TRPM8 expression.

Regardless of the differences, just as with the TRPV1 reporter mice, both TRPM8 strains provided far more sensitive detection than previously available. While TRPM8 *in situ* probes work beautifully, the generation of effective antibodies has proven more challenging. Therefore, these new strains offer the opportunity to better resolve the neurochemistry of TRPM8$^+$ neurons through co-labeling with antibodies as well as the chance to observe the projection patterns of TRPM8$^+$ afferents at single fiber resolution. Both studies conclude that TRPM8 is expressed predominantly in both C and Aδ fibers that completely lack binding of the isolectin IB4 (**Figure 4**; **Table 2**). As reported previously, TRPM8$^+$ neurons are found in greater percentages in the TG vs. the DRG (McKemy et al., 2002).

The analyses of these two strains reveal, as with TRPV1, that TRPM8$^+$ neurons are not homogenous but in fact are likely comprised of distinct subtypes dedicated to unique aspects of cold sensation. For example, while the numbers in the two studies differ, it is clear that a significant proportion of TRPM8 neurons co-express TRPV1 (18% of TG neurons in the knock-in vs. 38.8% in the BAC). It is tempting to speculate that these neurons are nociceptors that report on painful temperatures regardless of whether they are cold or hot. Moreover, given that both TRP channels are modulated by intracellular signaling pathways that are engaged during injury and inflammation, these neurons are

strong candidates for being critical actuators of hyperalgesia at both ranges of temperatures. A distinct population of TRPM8$^+$ neurons lacked all known markers for nociceptors entirely, suggesting these are a unique group of cells. One possibility is that these neurons encode the sensation of cooling (rather than cold pain). Finally, Takashima et al. present evidence that a subpopulation of Aδ fibers are TRPM8$^+$, thereby identifying another unique set of neurons that possibly report on either innocuous cooling or perhaps the fast component of cold pain. Indeed, physiological studies point to such neurons existing in humans (Hensel and Iggo, 1971).

A great benefit of reporter mouse strains is the ability to visualize projections with up to single fiber resolution and these studies, for the first time, provide a map of the nerve endings of cold sensors throughout the body. Analyses from these strains revealed that TRPM8$^+$ free nerve endings could be found in multiple layers of the epidermis of glabrous skin (stratum granulosum and stratum spinosum) while they were mostly absent from the dermis. These fibers also target the epidermis of the intervibrissal fur of the mystacial pad, fungiform papillae of the tongue, and both the dentin and pulp of teeth. The latter is one of particular interest given the well-documented sensitivity of teeth to cold stimuli.

The central projections of TRPM8$^+$ neurons target the dorsal spinal cord. As demonstrated with antibody staining, TRPM8$^+$ fibers largely terminate in the most superficial layer (lamina I; Bautista et al., 2007). This layer receives most of the input from peptidergic nociceptors with no projections to lamina II (as evidenced by the lack of overlap with IB4$^+$ projections or PKCγ$^+$ spinal interneurons) or lamina III. Therefore, it appears that cooling information is specifically routed to the most superficial layers of the spinal cord.

Finally, Dhaka et al. observed a small cohort of GFP$^+$ neurons (22%) from homozygous mice (hence completely deficient in TRPM8 expression) that retained responses to cold, albeit at temperatures far below the threshold reported for TRPM8, thus suggesting an alternative cold detection pathway may exist in these neurons. Physiological responses to temperatures below 0°C in nerve recordings in rats have been demonstrated to be more widespread than those reported for cloned TRPM8 channels (<18°C; Simone and Kajander, 1997). This is unlikely to be attributable to TRPA1. TRPA1 and TRPM8 are not co-expressed and despite early reports, it seems unlikely that TRPA1 contributes to cold sensation in mice (Bautista et al., 2006). Indeed, such a finding is consistent with studies showing that TRPM8-knockout mice retain behavioral responses to extreme cold that persist even in TRPM8/TRPA1 double knockouts (Knowlton et al., 2010).

CELL TYPE-SPECIFIC ABLATION OF TRP CHANNEL EXPRESSING NEURONS DEFINE THE ROLES OF SPECIFIC SENSORY NEURON CLASSES IN TEMPERATURE SENSATION AND PAIN

In addition to marking sub-populations for anatomical studies, TRP channel loci have also been exploited to manipulate the function of heat/cold sensing neurons. Mishra et al. crossed ROSA-stop-DTA mice, which conditionally express the diptheria toxin (DTA), to TRPV1-Cre strains, to generate offspring in which any neuron in the TRPV1 lineage would selectively undergo cell death (Mishra et al., 2011). Since TRPV1 is more widely expressed in somatosensory neurons during development, these mice lack neurons expressing TRPV1, TRPA1, and TRPM8 (Cavanaugh et al., 2011a; Mishra et al., 2011). Thus, offspring were found to have profound deficits in the detection of a wide range of temperatures (−5 to 55°C), chemical irritants, and pruritogens. More importantly, the mice retained the ability to respond to light touch and mechanical pain, underscoring the selectivity of the ablation strategy. Also worth noting, in other behavioral tests (such as for cognition and locomotion) these mice were completely normal, again arguing against widespread TRPV1 expression in the CNS.

Since several classes of sensory neurons were ablated in TRPV1-Cre X ROSA-stop-DTA mice, alternate strategies were needed to selectively ablate the neurons that express TRPV1 in adult mice. While several groups have used strong TRPV1 agonists to induce excitotoxicity, a more refined genetic approach is preferable, since it does not rely on strong overstimulation of neural circuits or incomplete ablation (Mishra and Hoon, 2010). Using BAC transgenics, Pogorzala et al. (2013) addressed this need by creating a new strain of mice that express the diptheria toxin receptor (DTR) directly from the TRPV1 promoter via an expression cassette that also included a separately translatable GFP-coding region, to allow for direct observation of the neurons (Pogorzala et al., 2013). Expression of DTR renders neurons susceptible to ablation through systemic injection of diphtheria toxin.

Diptheria toxin administration to adult TRPV1-DTR mice resulted in complete ablation of all TRPV1-expressing neurons. After ablation, these mice retained normal responses to cold but completely lacked aversion to noxious heat (40–50°C). Therefore, TRPV1 expression in the adult defines the sensory neurons needed for encoding heat stimuli. The phenotype created by ablating these neurons was much more profound compared to genetic deletion of TRPV1. Thus, there must be additional pathways through which heat stimuli activate these cells. As an alternative to the existence of specific receptors for extreme heat, it is possible that factors released after cellular damage (such as ATP and protons) might stimulate non-heat sensitive receptors, such as P2X purinergic receptors and acid-sensing ion channels (ASIC; Birdsong et al., 2010). That said, other ion channels expressed in somatosensory neurons have been demonstrated to be responsive to thermal stimuli (Vriens et al., 2011).

It is also remarkable that, despite their lack of responses to noxious heat, mice with all their TRPV1-expressing neurons ablated retained normal responses to cold. Therefore, the detection of different temperatures is encoded by separately dedicated thermosensitive neurons. As discussed above, TRPM8 expression seems to completely describe the cold-sensing neurons. To formally test this hypothesis, transgenic mice were generated to selectively ablate this sub-population of sensory neurons (Pogorzala et al., 2013). Analysis of the TRPM8-DTR mouse revealed that these neurons are required for sensing cold. Much like the TRPV1-DTR mice, the phenotype was more severe than the genetic deletion of the receptor alone, with deficits in the detection range down to 0°C.

TRPM8-DTR mice had normal responses to heat, thus reinforcing the notion of distinct channels for hot and cold sensation. Indeed, when the TRPM8-DTR mice were crossed to TRPV1-DTR mice, the resultant depletion of both populations could roughly be approximated by the addition of the two phenotypes. Even given the removal of the hot- and cold-dedicated neurons, there remained some responses to extreme temperatures. Such responses may be due to molecules (such as lipids and/or ATP) released during tissue damage and sensed by other classes of nociceptors (see below).

Finally, by removing the hot and cold channels, these mice no longer were attracted to warm. Thus, one possible conclusion is that all the information needed to detect the complete range of physiologically relevant temperatures is accounted for by TRPV1- and TRPM8-expressing somatosensory neurons. In the simplest model, attraction to warmth would be viewed as the balance between two aversive stimuli, in this case hot and cold. However, it is important to point out that an alternative hypothesis is equally supported by the current data. One cannot rule out the possibility that there exist subsets of neurons whose specific activation by warm temperatures produce attraction. Physiological studies in human and primates from the 1970s support this latter model (i.e., Hensel and Iggo, 1971).

DEFINING A ROLE FOR THE PEPTIDERGIC CLASS OF SENSORY NEURONS

Since CGRP (calcitonin gene-related peptide) has been traditionally used as a marker of peptidergic C fibers, what would be the phenotype of a mouse lacking CGRP$^+$ peptidergic fibers? Based on the coexpression of TRPV1 in some but not all of these neurons, one might have predicted they would lack some type of heat sensation. To study this subset of peptidergic C fibers, McCoy et al. (2013) generated a mouse in which the peptidergic CGRPα-expressing cells could be visualized by means of expression of a fGFP knocked into the CGRPα locus (CGRPα-GFP). The construct also included a loxP-STOP-DTR sequence, enabling the recombination of diphtheria toxin receptor (DTR) into the CGRPα locus in Cre-expressing cells (CGRPα-GFP-loxP-STOP-hDTR mice; **Table 2**) and thus the ability to selectively ablate these neurons. When crossed with an advillin-Cre line that expresses Cre in sensory neurons only (Minett et al., 2012), the CGRPα-positive DRG neurons are sensitive to ablation by administration of diphtheria toxin (DTX). The advillin promoter provided sensory neuron specificity, leaving other central CGRP-expressing cells intact.

Using quantification of immunostained sections, McCoy et al. (2013) show that in DTX-treated mice, >90% CGRP$^+$ DRGs are ablated, and this includes 50% of TRPV1$^+$ cells as well as 36% of IB4-binding cells. TRPM8$^+$ cells, on the other hand, were spared. In concordance with these findings, through electrophysiological recordings in an *ex vivo* skin-nerve preparation in which an intact nerve still attached to skin is stimulated in the periphery while isolated fibers are recorded from, the ablated mice were shown to lack sensitivity to noxious heat but not to cold or mechanical stimulation. In behavior tests, the ablated mice showed a loss of heat sensitivity (shown in 3 tests: tail immersion at 46.5 and 49°C, hot plate at 52°C, and intraplantar capsaicin injection) and no change to mechanosensitivity (von Frey, tail clip test for noxious mechanical, and cotton swab test for innocuous mechanical sensitivity). But surprisingly, they also showed an increase in cold sensitivity in various tests (acetone application to paw skin, tail immersion at −10°C, intraplantar injection of icilin, and cold plantar assay), and an enhanced avoidance of cooler temperatures in a two-choice test, in which the mouse can choose which of two plates (each set at a different temperature) to spend time on. The disparity between the electrophysiological and behavioral results suggested that the increase in cold sensitivity might be a central mechanism since the cold afferents appear to be normal in the ablated mice.

In a deeper examination of the intriguing finding that DTX-treated mice display behavioral changes to cold responses but no alteration in the electrophysiological response of their primary afferents to cold, the authors performed patch recordings from lamina II in spinal cord slices from these mice. Compared to saline-treated mice, the DTX-treated mice were less responsive to capsaicin, but more responsive to icilin both for number and frequency of events, and corresponding to a five-fold increase in tonic and evoked activity. The authors therefore hypothesized that the CGRPα$^+$ DRGs normally provide tonic inhibition of TRPM8 neurons and thus when ablated, the TRPM8 input to the spinal cord is greater, causing hypersensitivity to cold. However, ablation of TRPV1 neurons does not result in cold hypersensitivity, thus suggesting this circuit may involve TRPV1$^-$/CGRP$^+$ neurons or that these ablations result in unexpected perturbations yet to be understood.

Mas-RELATED G-PROTEIN-COUPLED RECEPTORS MARK DISTINCT SUBTYPES OF C FIBERS DEDICATED TO IRRITANTS AND MECHANOSENSATION

While the TRPV1 and TRPM8 loci are invaluable tools for genetically manipulating the sensory neurons dedicated to temperature sensation, to define additional subtypes of C fibers, let alone all the different classes of somatosensory neurons, other markers are required. For example, TRPV1 and TRPM8 are both largely absent from non-peptidergic C fibers (Pogorzala et al., 2013). Moreover, as summarized above, the neurons that express either TRP channel can themselves be subdivided even further. Some TRPV1$^+$ neurons might be dedicated to heat while others are responsive to irritants (Bautista et al., 2006). Some TRPM8$^+$ neurons might be dedicated to innocuous cooling while others to cold pain (McKemy, 2013).

To gain further genetic access to additional C fiber classes, the loci from the Mas-related G-protein-coupled receptors (Mrgprs) have proven particularly effective. The Mrgprs are a large family of receptors expressed in sensory neurons, with >50 members in mice (Dong et al., 2001). In DRGs, differential expression of members of the four Mrgpr subfamilies (designated MrgprA-D) can be used to define distinct somatosensory neuron subtypes. While the majority of Mrgprs remain "orphan receptors" (i.e., their endogenous ligands are still unknown), anatomical studies utilizing reporter mice and functional studies relying on knock-in and knock-out mice have been instrumental in demonstrating that the expression of these genes delineates classes of neurons

that respond to both noxious (mechanical pain, itch, and tissue damage) and innocuous (stroking) stimuli.

MrgprD MARKS NON-PEPTIDERGIC POLYMODAL C FIBERS

Two knock-in reporter strains have been generated that express either EGFP or PLAP under control of a single Mrgpr gene by utilizing the endogenous MrgprD promoter (Zylka et al., 2005). Analysis revealed that MrgprD is expressed in the majority of non-peptidergic C fibers that bind the isolectin IB4 (>75%). Remarkably, MrgprD$^+$ neurons exclusively innervate hairy and glabrous skin, where they overwhelmingly form free nerve endings throughout the epidermis. The fibers preferentially terminate in the *stratum granulosum* and make up ∼60% of all free nerve endings present there. Histochemical analysis of these mice revealed that peptidergic and non-peptidergic fibers are uniquely distributed in skin, further supporting the model that somatosensory neurons form highly specialized subpopulations.

Similar to the exquisite specificity observed in peripheral innervation, MrgprD$^+$ projections form a narrow band within lamina II (also called the *substantia gelatinosa*, or SG) of the dorsal horn of the spinal cord. Quite unexpectedly, the MrgprD$^+$ projections sit nicely between markers for lamina I and II$_{outer}$ (as defined by CGRP staining) and lamina II$_{inner}$(as defined by PKCγ expression), thus refining our understanding of the anatomical specialization that exists within a single lamina in the dorsal horn, in this case lamina II. Such specificity suggests the information coding in the dorsal spinal cord should exhibit a high degree of regional specialization. For example, based on MrgprD projection patterns, the middle of lamina II may be biased toward encoding nociceptive information generated from the outer layers of the epidermis of hairy and glabrous skin.

In much the same way as the roles of TRPV1$^+$ and TRPM8$^+$ neurons were assessed, the contributions of MrgprD$^+$ neurons to behavior were tested using a genetic ablation strategy. MrgprD knock-in mice were generated where the coding region of MrgprD was replaced with a DTR-ires-EGFPf cassette (Cavanaugh et al., 2009). When MrgprD$^+$ neurons were ablated in adult mice, there was a significant reduction in the responses to noxious mechanical stimuli. Mice lacking MrgprD$^+$ neurons required larger forces from a von Frey filament than wild-type littermates to elicit a paw withdrawal. MrgprD-DTR mice also exhibited a reduction in mechanical hypersensitivity after inflammation induced by Complete Freund's adjuvant (CFA) following toxin administration. The deficits were modality-specific in that the responses of the MrgprD-DTR mice to thermal stimuli remained indistinguishable from wild-type mice. However, unlike the deletion of hot or cold neurons, which produced complete insensitivity to thermal stimuli, mice depleted of MrgprD$^+$ neurons retained some ability to sense noxious mechanical stimuli, albeit with less sensitivity. This is not unexpected given the majority of somatosensory neurons have some ability to respond to mechanical stimulation (Delmas et al., 2011). That said, the remaining sensitivity to noxious mechanical stimuli cannot be attributed to TRPV1$^+$ neurons. Silencing of heat-sensitive neurons in the MrgprD-ablated mice revealed no additional mechanosensory deficits. Therefore, other classes of neurons must contribute to sensing noxious mechanical stimuli.

While co-deleting both the MrgprD$^+$ and TRPV1$^+$ neurons in a single mouse does not enhance deficits in mechanosensation, it does impact the ability to detect painful temperatures. As mentioned above, while deletion of TRPV1$^+$ sensory neurons clearly results in profound deficits, behavioral responses to temperatures >50°C remain. Such nocifensive responses are significantly blunted by removing both sub-populations of neurons such that co-deletion results in mice that will stand on a hot plate at 55°C as if it were at room temperature (Pogorzala et al., 2013). Notably, MrgprD$^+$ neurons also appear to contribute to extreme cold sensation. In much the same manner, co-deleting MrgprD$^+$ and TRPM8$^+$ neurons results in mice with significantly less cold sensitivity than mice lacking TRPM8$^+$ neurons alone. While one cannot rule out that at least some MrgprD$^+$ neurons selectively respond to noxious hot and cold, it seems unlikely. The simplest explanation is extreme temperatures result in factors being released from damaged tissue and it is these molecules that stimulate MrgprD$^+$ neurons. Indeed, MrgprD neurons have been shown to be robustly activated by extracellular ATP (Dussor et al., 2008).

Finally, pharmacological activation of MrgprD$^+$ neurons causes a mild itch response. Injection of β-alanine, a MrgprD ligand, into mouse cheeks provokes a scratching behavior that require MrgprD$^+$ neurons (Han et al., 2012; Liu et al., 2012). A high dose of β-alanine, which is used as a nutritional supplement for body builders, evokes paresthesia in humans that include tingling, pins and needles, and numbness. Whether MrgprD$^+$ neurons are homogenous or comprise multiple sub-populations remains to be seen.

MrgprA3 DEFINES A CLASS OF SENSORY NEURONS DEDICATED TO ITCH

In addition to temperature and noxious mechanical stimuli, nociceptors are also required for the detection of pruritogens. Numerous compounds exist that can evoke scratching behavior, the most widely studied being histamine, which signals through TRPV1$^+$ neurons (Shim et al., 2007; Imamachi et al., 2009). However, several itch conditions, such as atopic dermatitis, operate through non-histaminergic pathways (Wilson et al., 2013). One such pathway is the itch that is induced as a side effect of taking the anti-malarial drug chloroquine. Functional studies have found that MrgprA3 is the predominant chloroquine receptor expressed in sensory neurons in mice (Liu et al., 2009). MrgprA3 is both necessary and sufficient for the detection of chloroquine and activation of MrgprA3$^+$ neurons results in robust scratching behavior.

To selectively label and identify sensory neurons dedicated to itch, a BAC transgenic mouse line was engineered that expresses a GFP-Cre fusion protein under control of the MrgprA3 promoter (Han et al., 2012). Thus, this approach enables transgene expression in itch-sensitive neurons as well as manipulation of gene expression within these neurons by means of Cre-mediated recombination. These mice were crossed to a Cre reporter line, yielding mice with a subset of sensory neurons that robustly expressed tdTomato, an exceptionally bright fluorescent protein that efficiently labeled both the cell bodies and fine processes of these neurons. The expression of tdTomato faithfully represented

the distribution of the endogenous MrgprA3 gene product, as measured by overlaying the tdTomato fluorescence and *in situ* hybridization (>95% overlap). Critically, >90% of GFP$^+$ neurons from these mice could be activated by chloroquine.

MrgprA3$^+$ neurons represent a small percentage of DRG neurons (6.8%) and constitute a subpopulation of TRPV1$^+$ neurons (19%). Co-labeling with a battery of markers revealed that the majority of MrgprA3$^+$ neurons not only express TRPV1 (88.3%) but also the neuropeptide CGRP (84.2%). Interestingly, many also bind IB4 and thus make up a rare cohort of CGRP$^+$ neurons that are also marked by the isolectin. Electrophysiological characterization of MrgprA3$^+$ neurons revealed these are indeed polymodal nociceptors that respond not only to pruritogens but also noxious heat and mechanical stimuli.

Remarkably, the peripheral and central targets of MrgprA3$^+$ neurons were identical to those of MrgprD$^+$ neurons, even though these two receptors are not co-expressed in the same neurons. Both populations exclusively innervate the superficial epidermis of skin (*stratum granulosum*) and no other tissues in the body. They also both project to the middle of lamina II where their nerve endings are co-mingled. Given that activation of these two subpopulations of neurons evokes distinct sensations (mechanical pain vs. itch), mapping the circuitry of this region of the dorsal horn should prove to be fascinating. One dorsal horn cell type that is of particular interest are the gastrin-releasing peptide receptor (GRPR)$^+$ neurons, known to be critical for the detection of pruritogens (Sun and Chen, 2007; Sun et al., 2009). Indeed, Han et al. provide evidence that links activation of MrgprA3$^+$ cells to activity-dependent expression of the immediate early gene FOS in GRPR-neurons.

In the same vein as TRPV1, TRPM8, and MrgprD, conditional cell ablation was used to demonstrate the function of MrgprA3$^+$ neurons *in vivo*. Crossing the MrgprA3-EGFP:Cre line with a ROSA-DTA strain allowed for selective ablation of virtually all MrgprA3$^+$ neurons. While ablation had no effect on responses to noxious thermal and mechanical stimuli (cheek injection with capsaicin or allyl isothiocyanate, tail immersion test at 50°C, hot plate, and von Frey tests), these mice were compromised in their ability to respond to pruritogens. That said, scratching behavior persisted for almost all compounds tested and thus other neuronal populations must also contribute to the detection of pruritogens. These likely include additional TRPV1$^+$ subpopulations, particularly those that co-express TRPA1 (Wilson et al., 2011).

While ablation strategies can be used to evaluate the contribution of a particular sub-population of sensory neurons to behavior, they do not speak to whether activation is sufficient. To address sufficiency, Han et al. generated a mouse strain that expresses the TRPV1 receptor solely in MrgprA3$^+$ neurons. To accomplish this, MrgprA3-EGFP:Cre mice were crossed to a ROSA-TRPV1 strain, thus enabling robust expression of TRPV1 from the ROSA locus in all MrgprA3$^+$ neurons (Arenkiel et al., 2008). When these mice were placed in a TRPV1-knockout background, the endogenous receptor was no longer expressed, leaving only MrgprA3$^+$ neurons responsive to capsaicin. Normally, application of capsaicin elicits nocifensive behaviors. However, in the TRPV1 gain of function transgenic mice, capsaicin evoked scratching behavior instead. These experiments elegantly argue that activation of MrgA3$^+$ neurons is sufficient to cause itch.

In addition to MrgprA3, another marker for sensory neurons dedicated to itch is TLR7 (Toll-like receptor 7). While reporter lines for TLR7 are still lacking there is some evidence that its expression is at least partially overlapping with MrgprA3 (Liu et al., 2010). The lack of sensitivity of TLR7 knockout mice to non-histaminergeic pruritogens demonstrates that TLR7 is a direct mediator of pruritis. TLR7 may also mediate itch through non-neuronal cells in the skin. Thus, transgenic strategies to label and manipulate these specific cell types should prove informative.

MrgprB4 MARKS A UNIQUE CLASS OF C FIBERS THAT RESPOND TO GENTLE STROKING

In situ hybridization studies have demonstrated that members of the Mrgpr family have non-overlapping expression patterns in small-diameter somatosensory neurons (Dong et al., 2001). Given the distinct functions of MrgprD$^+$ and MprgprA3$^+$ neurons, it stands to reason that other members of this receptor family can be used to distinguish additional subpopulations of C fibers. MrgprB4 is one member that marks a unique subset of small-diameter neurons that express neither MrgprD nor MrgprA3. To understand the anatomy of these neurons further, Liu et al. (2007) created a knock-in line that replaces the MrgprB4 coding region with PLAP. Analyses of these mice revealed that MrgprB4 marks an exceptionally small population of non-peptidergic, IB4$^+$ small diameter somatosensory neurons ($\leq$2%). Like MrgprD- and MrgprA3$^+$ neurons, neurons expressing MrgprB4 specifically target the epidermis, but in this case show selectivity for hairy skin. MrgprB4$^+$ free nerve endings show exceptionally large arborizations that are associated with hair follicles and the adjacent epidermis. Such arborization patterns resemble the C-tactile endings previously described in humans (Olausson et al., 2002). Centrally, MrgprB4$^+$ fibers terminate in the same region of lamina II as MrgprD$^-$ and MrgprA3$^+$ neurons. Whether spinal horn neurons receive inputs from unique or multiple Mrgpr fiber types remains to be seen.

To investigate the functional specialization of the MrgprB4$^+$ population, Vrontou et al. (2013) created a MrgprB4-tdTomato-2A-Cre mouse line. They first used this line to selectively express the genetically encoded calcium sensor GCamp3.0 in neurons expressing MrgprB4 (Tian et al., 2009). Expression was accomplished by infecting transgenic mice with a Cre-dependent adeno-associated virus (AAV). The authors developed an *in vivo* spinal cord preparation in which transduced MrgprB4$^+$ fibers expressing GCaMP3 could be imaged by two-photon microscopy while being stimulated in the periphery. The MrgprB4$^+$ cells responded to innocuous mechanical stimuli designed to mimic stroking and allogrooming, but not to rapid noxious mechanical stimuli. Thus, MrgprB4 likely marks a class of C fibers that are tuned to gentle mechanical stimuli first described in humans in the 1930s (Zotterman, 1939).

In contrast, the same imaging approach was employed to demonstrate that MrgprD$^+$ neurons respond only to pinching but not stroking stimuli. Thus, the expression of these two Mrgpr genes nicely differentiates C fiber subtypes tuned to different mechanical stimuli. Moreover, activation of these different C fiber

types likely conveys different valences (pleasurable/calming vs. noxious/alarming). Interestingly, the MgrprB4$^+$ neurons could only be activated via mechanical stimulation at the periphery in an intact preparation, but not in an *ex vivo* skin-nerve preparation, whereas MrgprD$^+$ cells could be activated in either type of preparation. The reason for this discrepancy is unknown, although the authors hypothesize that intact hair as well as underlying connective tissue might be important to the detection of the stroking stimulus, which is more spatially distributed, whereas the MrgprD cells respond to a much more narrowly applied stimulus (e.g., von Frey stimulation).

To understand the behavioral consequence of activating MrgprB4$^+$ neurons, the authors sought to selectively excite these neurons. To achieve pharmacological control, they used the same MrgprB4-tdTomato-2A-Cre line and viral approach to selectively express DREADD, a GPCR engineered to be activated by the synthetic ligand CNO that is not naturally produced in the mice (Lee et al., 2013). The authors examined the consequences of inducing DREADD activity in either MrgprB4$^+$ or MrgprD$^+$ neurons in behaving mice. In a conditioned place preference (CPP) paradigm, the initial preference of mice for one chamber was reversed in favor of another that was associated with CNO (i.e., activation of the MrgprB4$^+$ neurons) during conditioning. This suggested that sensation mediated by MrgprB4$^+$ cells has a positive affective valence. However, since this was the only behavior test used to examine the valence question in these mice, further testing would be an informative and valuable area of investigation. Furthermore, activation of MrgprD$^+$ cells in the same CPP assay promoted neither preference nor aversion. The latter result is somewhat surprising, as one might have expected that activation of these nociceptors would have a strong negative valence.

MOLECULAR DISSECTION OF OTHER C FIBERS TUNED TO LOW THRESHOLD MECHANICAL STIMULI (C-LTMRs)

There exist other classes of C fibers that respond to low-threshold stimuli (C-LTMRs), distinct from those described above that express MrgprB4 and those that respond to high threshold stimulation and express MrgprD. Two markers have recently been described as selectively labeling unique classes of C-LTMRs in mice, the vesicular glutamate transporter type 3 (VGluT3; Seal et al., 2009) and tyrosine hydroxylase (TH; Li et al., 2011).

Glutamatergic neurons rely on transporters to load the glutamate into synaptic vesicles. Three such transporters exist in mice (VGLUT1-3) and are differentially expressed (Fremeau et al., 2004). To examine the distribution of VGLUT3, a BAC transgenic strain was created to express EGFP under the VGluT3 promoter (Seal et al., 2009). Examination of these mice revealed that, in the periphery, VGLUT3 is expressed in a subpopulation of small-diameter somatosensory neurons. VGLUT3$^+$ neurons are unmyelinated, non-peptidergic neurons. These neurons project to spinal cord laminae I and II and account for roughly 10% of L4/L5 DRG and trigeminal neurons. They do not coexpress TRPV1 and only a small percentage (7%) bind IB4. VGlut3 is also found in the cochlea and regions of the CNS (Fremeau et al., 2002; Gras et al., 2002; Seal et al., 2008).

In a separate study, genetic examination of the TH$^+$ sensory neuron population revealed this gene is also expressed in unmyelinated C fibers that are non-peptidergic, do not express any of the TRP channels or Mrgprs characterized to date, and do not bind IB4 (Li et al., 2011). However, there is significant overlap in expression between VGLUT3 and TH, suggesting that the expression of these two genes mark a similar population of C-LTMRs (Li et al., 2011). To visualize the axonal endings of C-LTMRs in the skin, Li et al. (2011) crossed the TH-CreER mouse line to two reporter strains. C-LTMRs exclusively innervated hairy but not glabrous skin. In addition, an individual C-LTMR axon branch was found to arborize extensively into longitudinal lanceolate endings, associating with about 18 hair follicles in the back skin of the mouse. These results correlate well with studies in humans that also found that physiologically defined C-tactiles exclusively innervate hairy skin (Olausson et al., 2002).

Ex vivo recordings from an intact preparation of thoracic spinal cord, DRG, nerves, and skin from the VGLUT3-EGFP mice showed that VGLUT3$^+$ sensory neurons are exquisitely sensitive to mechanostimulation (i.e., 0.07 mN von Frey stimulus; Seal et al., 2009). They respond better to slowly moving stimuli than to rapidly moving ones and adapt to stationary stimuli. Finally, the authors found that these neurons respond to cooling but not heating stimuli. These physiological attributes are nearly identical to those found in TH$^+$ C-LTMRs, again supporting the notion that these are largely the same class of neurons (Li et al., 2011).

Since VGLUT1 and 2 are not co-expressed with VGLUT3 in somatosensory neurons, VGLUT3-knockout neurons fail to release glutamate and excite their downstream synaptic partners. VGLUT3-knockout mice were found to be essentially normal in their sensitivity to cold, heat, formalin, and von Frey stimuli (Seal et al., 2009). However, when challenged in chronic pain paradigms (intraplantar carrageenan injection; spared nerve injury; hindpaw incision; capsaicin injection into the ankle), compared with wild-type littermates, these mice were protected from mechanical but not from temperature hypersensitivity. In addition, given their sensitivity to low threshold stimuli as demonstrated by the skin-nerve recordings, it seems likely that VGluT3$^+$ sensory neurons have functions other than sensing noxious mechanical stimuli. Moreover, the widespread expression of VGluT3 throughout the CNS confounds interpretation of these behavioral experiments (Fremeau et al., 2002; Gras et al., 2002). And in contradiction with this result, the work of Lou et al. (2013) has shown that Runx1 (runt domain transcription factor 1) knockout mice, which lack proper development of VGluT3 neurons, have unimpaired acute and chronic mechanical pain. Ultimately, conditional knockout of VGLUT3 solely in sensory neurons will be required to resolve this discrepancy.

MARKERS FOR ADDITIONAL CLASSES OF TOUCH NEURONS

In addition to the TH$^+$ C-LTMRs described above, mouse lines have also been described that selectively label Aδ-LTMRs and Aβ-RA-LTMRs (rapidly-adapting LTMRs; Li et al., 2011). The authors characterized both the peripheral and central innervation patterns of each of these LTMR subtypes. In a search for additional markers, the authors generated tyrosine receptor kinase B (TrkB-tauEGFP) knock-in mice to test the hypothesis that

the Aδ-LTMRs are TrkB$^+$. Interestingly, TrkB expression is especially dense in thoracic-level DRGs but very low at limb levels (whether cervical or lumbar). TrkB$^+$ neurons lacked markers of mechanosensitive C fibers such as TH and IB4. Critically, these TrkB$^+$ neurons exhibited all the characteristic properties of Aδ-LTMRs in an *ex vivo* skin-nerve preparation, including extreme mechanical sensitivity (i.e., von Frey threshold <0.07 mN), rapidly adapting responses to suprathreshold stimuli, intermediate conduction velocities, and sensitivity to cooling but not warming of the skin. Similar to the TH$^+$ C-LTMRs, the TrkB$^+$ Aδ-LTMRs form lanceolate endings associated with hair follicles of the trunk.

Li et al. (2011) identified the neuropeptide Y receptor type 2 (Npy2r-GFP) mouse line by screening through the available BAC-GFP GENSAT lines for the expected projection pattern of Aβ-LTMR neurons to laminae III through V of spinal cord dorsal horn (Gong et al., 2003). The Npy2r-GFP cells account for 6% of thoracic DRG neurons. They are heavily myelinated large-diameter cells that co-express a marker for myelinated sensory neurons (neurofilament heavy chain 200 or NF200) and lack expression of C- and Aδ-LTMRs markers TH or TrkB, respectively. They also have the electrophysiological hallmarks of the rapidly adapting subtype of Aβ-LTMRs, Aβ-RA-LTMRs, characterized by low mechanical threshold (0.07 mN), rapid conduction velocities, and rapidly adapting responses. All of the peripheral endings of Npy2r-GFP$^+$ cells form longitudinal lanceolate endings.

In an informative and complex series of matings, the authors managed to cross various combinations of three lines of labeled LTMRs (TH$^+$, TrkB$^+$, and Npy2r$^+$) thus allowing them to visualize the organization of cutaneous endings of the different neuron types relative to each other. This painstaking investigation affords us a glimpse into the complexity of the touch-sensitive detection organs innervated by LTMRs in the skin as well as a nascent appreciation of the organization of sensory neuron projections in the spinal cord.

These crosses revealed that each of the three types of hair follicles in mouse (guard, awl/auchene, and zigzag) is a neurophysiologically distinct mechanosensory organ, innervated by different combinations of mechanosensory fiber types. Zigzag hair follicles are innervated by both C- and Aδ-LTMRs; guard hairs are innervated only by Aβ-LTMRs; and awl/auchene hairs are triply innervated by all three fiber types. Furthermore, crossing the TH-reporter mice with the TrKB-reporter mice demonstrated that the lanceolate endings of C- and Aδ-LTMRs were interdigitated with one another around the same hair follicles. This comingled spatial organization correlates with their functional similarities, since both neuron types respond to very light touch (0.07 mN) as well as to rapid cooling.

When the authors examined the central projections of the different neuron classes in the spinal cord, they observed that each class projected to a distinct but overlapping termination zone in the dorsal horn. C-LTMRs terminated within lamina II; Aδ-LTMRs within lamina II and III, and Aβ-RA-LTMRs within layers III-V. Retrograde labeling of cutaneous sensory neurons revealed a columnar organization within the spinal cord, such that LTMR neurons innervating the same patch of skin project to a spatially restricted column in the spinal cord that is perpendicular to the laminae, extending from laminae II through V in concordance with the termination zone of each neuron class.

When two different labels were retrogradely injected in patches of skin in close proximity, the projections of the labeled neurons were found to be near each other in spinal cord, revealing a somatotopic organization. Thus, using genetic-labeling strategies (combined, for some experiments, with viral expression), the authors were able to derive insights into spinal cord processing of light touch in much the same manner as had been employed using TRP channels and Mrgprs for temperature, nociception, and itch. In addition, the divisions between the subclasses of LTMRs appear to be preserved in the spinal cord, with maintenance of the segregation between neuron subtypes within the central projections. It will be extremely interesting to examine these three types of LTMRs functionally and behaviorally in a paradigm similar to that published on for MrgprB4 and MrgprD (Vrontou et al., 2013).

Another group has searched for markers of specific subtypes of trigeminal ganglion touch neurons innervating the whiskers. Sakurai et al. (2013) characterized chondrolectin-PLAP mice as well as parvalbumin-Cre mice crossed to Cre-dependent reporter lines. They found that chondrolectin labels RA touch neurons innervating the mystacial pad with lanceolate endings. In contrast, parvalbumin labeled two types of touch neurons: SA (slowly adapting) neurons with Merkel endings, and a small number of RA neurons with longitudinal lanceolate endings. By crossing the two lines together, the authors found that 25% of parvalbumin$^+$ cells in the TG coexpress chondrolectin, and that 22% of the chondrolectin$^+$ neurons also express parvalbumin (Sakurai et al., 2013).

BEYOND CELL TYPES: USING TRANSGENIC MICE TO STUDY IMPORTANT DRUG TARGETS

While the focus of this review has been on markers that narrowly define specific subpopulations, several key molecules involved in somatosensory function span multiple sensory neuronal classes. Opioids have long been known to exert analgesic effects and alleviate pain, however, it was unclear how and where this was taking place since opioid receptors are present both centrally and peripherally. Furthermore, in the periphery, mu and delta opioid receptors (MOR and DOR, respectively) had previously been thought to be co-expressed within the same C fibers, confounding the ability to parse out their relative contributions (Gomes et al., 2004).

To better understand the expression of opioid receptors in the peripheral nervous system, Scherrer et al. (2009) created a mouse where the DOR coding region was fused to EGFP. With these mice, the authors were able to clarify the actual distribution of these important receptors within sensory neurons. Quite surprisingly, they found that DORs are only expressed in about 17% of DRGs and that MORs and DORs are almost never co-expressed in the same neurons but rather segregate into different classes of C fibers. DOR mostly does not overlap with TRPV1 (**Figure 5**) but rather is found in roughly half of the myelinated fibers and about a third of the non-peptidergic C fibers. Such a distribution contrasts with that of MOR, which is expressed mainly in TRPV1$^+$ neurons. More recently, Bardoni et al. (2014) have confirmed the expression pattern observed in the DOR-EGFP mouse,

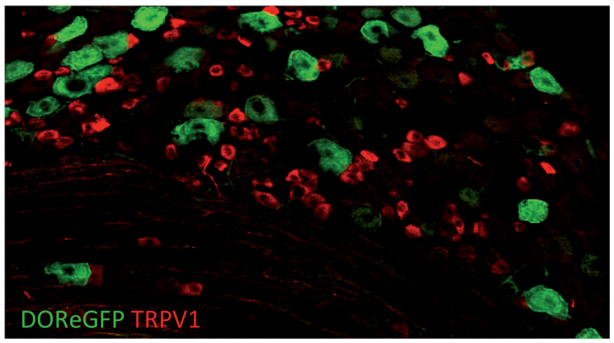

FIGURE 5 | Delta opioid receptor (DOR-eGFP mice, green) rarely overlaps with TRPV1 (red). Image courtesy of Grégory Scherrer, Stanford University.

using an ultrasensitive *in situ* hybridization method as well as radioligand binding studies. They also further investigated MOR and DOR coexpression and found that fewer than 5% of DRG neurons coexpress both opioid receptors, with most of these cells being NF200$^+$ CGRP$^+$ nociceptors (∼88%), and the rest being NF200$^-$ IB4-binding MrgprD$^+$ mechanoreceptors or peptidergic TRPV1$^+$ thermonociceptors.

Based on this expression pattern, one might thus expect a role for DORs in mechanical sensitivity vs. one for MORs in heat sensitivity. Using pharmacological inhibition of each type of opioid receptor in combination with ablation of TRPV1$^+$ neurons in models of inflammatory and neuropathic pain, Scherrer et al. (2009) indeed found that MORs selectively contribute to heat pain while DORs contribute to mechanical pain. In this way, the authors were able to show that the two receptors selectively regulate mechanical vs. heat hypersensitivity. This mouse thus provides insight into the potential for modality-specific opioid drug targets, and the development of novel pain therapeutics. Beyond the periphery, the central mechanisms of opioid function remains an area that still requires further elucidation.

It should be mentioned that the expression pattern of DOR in the DRGs is a matter of some controversy, since another group has obtained quite different results using double *in situ* hybridization, immunohistochemistry with multiple antibodies, single-cell PCR, and electrophysiology (Wang et al., 2010; He et al., 2011). This group found that a much larger population of sensory neurons expresses DORs (∼70–80%), and that these comprise both large and small diameter peptidergic neurons. Furthermore, they observed that DORs and MORs are coexpressed in small peptidergic neurons (73% of MOR$^+$ neurons are also DOR$^+$). Reconciling these findings will perhaps require the generation of another labeled mouse line, to test whether the findings in the DOR-EGFP line can be reproduced by another group. Overall, one would have expected the genetic method to be more reliable than other expression analyses.

BEYOND THE PERIPHERY: REVEALING CENTRAL MECHANISMS OF INTEGRATION OF SOMATOSENSORY INFORMATION WITH TRANSGENIC MICE

Although the references cited throughout our review initially focused on defining markers of various sensory neuron types, these studies also derived new insights into the central integration of somatosensory information, sometimes based on the anatomy of spinal cord projections alone. These studies have set the stage for a deeper appreciation of the neural circuits that encode information from the periphery.

For example, a major finding of the work of Li et al. (2011) on C-LTMRs is that touch neurons of different types that innervate the same small patch of hairy skin all project to a spatially circumscribed column in the spinal cord, with different LTMR types projecting to distinct but overlapping bands of the column. An additional finding from this study is the existence of a somatotopic map in the spinal cord, such that neurons of the same type innervating neighboring patches of skin project to neighboring columns in the spinal cord. Thus, despite comingling of cell bodies belonging to different LTMR neuron classes in the DRG, the columnar and somatotopic organization of their central projections suggest the spinal cord is a likely integration site for mechanosensory information. Another region that would be interesting to examine in these mice in future studies would be the organization of projections to the dorsal column nuclei, a region of the brainstem known to be important for the sensation of touch.

Similarly, the CGRP$^+$ neuron ablation study revealed aspects of central processing, some of which are still not fully understood (McCoy et al., 2013). First, the phenotype of mice lacking CGRPα$^+$ neurons was greater than anticipated, showing that CGRPα$^+$ neurons likely contribute not only to heat sensitivity, but also indirectly to the perception of cold, by providing tonic inhibition to TRPM8 inputs. Thus, in addition to providing valuable information on the modalities detected by peptidergic C fiber afferents, this mouse line also points to crosstalk between modalities in the spinal cord, as somatosensory information from one population of neurons (e.g., TRPM8$^+$) appears to be modulated by another (CGRP$^+$). How widespread this phenomenon is remains to be addressed. Second, and likely relating to more central mechanisms, the authors also reported further intriguing phenotypes of these mice, possibly related to the cold hypersensitivity phenotype. The coats of DTX-treated mice were piloerect and their core temperature dropped lower than wild type mice in response to immersion in warm water. The DTX-treated mice also weighed less than saline-treated counterparts, suggesting a role for CGRPα$^+$ neurons in metabolism. Indeed, perturbation of core temperature regulation has also been demonstrated following pharmacological activation and inhibition of TRPV1 and TRPM8 (Patapoutian et al., 2009). How thermosensitive sensory neurons modulate metabolism remains a central mystery yet to be elucidated.

SUMMARY AND FUTURE DIRECTIONS

The somatosensation field has benefitted immensely from the identification of a number of key genes required for the signaling of distinct sensory modalities (for example heat, cooling, pain, and itch). These discoveries have led to remarkable mechanistic insights into how sensory stimuli are detected, and have also provided neuroanatomists and geneticists with key molecules and loci that can be used to identify and probe the function of cohorts of specialized sensory neurons (**Figure 4**). Indeed, the discovery of a panel of ion channels and somatosensory receptor genes has

presented researchers with genetic loci with which to selectively investigate and manipulate somatosensory neurons (**Table 2**). Gene-targeting strategies have been used to introduce histological markers (such as GFP, LacZ, and/or PLAP) that have allowed for the tracking of neuronal projections with single process resolution (i.e., **Figure 3**). Beyond anatomy, these loci have been used to express toxin receptors for cell ablation or Cre recombinases that enable ectopic expression of gene silencers/activators with a high degree of cell-type specificity. These studies have allowed researchers to probe the function of specific subtypes of somatosensory neurons with unprecedented resolution.

HOW MANY SUBTYPES EXIST?

While great progress has been made, we still do not know how many distinct subtypes exist. Indeed, further molecular dissection of the sensory neurons classes seems likely to continue to advance our understanding. In the case of thermosensation, we are still ignorant of the processes by which attraction to warm stimuli vs. aversion to noxious thermal stimuli are encoded. The TRPV1 population seems to have a particularly diverse set of functions that remain to be parsed out. TRPV1$^+$ neurons are required for the detection of heat, irritants, and pruritogens, but exactly how these distinct sensations arise remains unknown. One population that clearly would benefit from genetic labeling is the group of TRPA1-expressing neurons. TRPA1 is expressed in a subset of TRPV1$^+$ neurons (Jordt et al., 2004). Activation of TRPA1 is required for the response to environmental irritants such as mustard oil (Bautista et al., 2006). However, TRPA1 is also required for the detection of classes of pruritogens such as chloroquine (Wilson et al., 2011). These two chemicals clearly elicit unique sensations (stinging vs. itch) and thus hint at further, yet to be discovered, neuronal specializations. Unfortunately, no TRPA1 reporter mice or Cre strains are available as of yet.

Another unique class of TRPV1$^+$ neurons seems to be those that co-express CGRP. The profound thermal deficits in the CGRP$^+$ neuron ablation studies are quite surprising, given that half of the TRPV1$^+$ neurons are preserved (McCoy et al., 2013). What is the function of the remaining TRPV1$^+$ neurons? Along similar lines, what is the role of the TRPV1$^+$ neurons that also express TRPM8 (Takashima et al., 2007; Dhaka et al., 2008)? There would seem to be little logic for co-expression if the goal was temperature discrimination. Perhaps the TRPV1/TRPM8 neurons are general noxious temperature sensors?

Beyond thermosensation, our understanding of touch transduction is still in its infancy. As the molecules involved in mechanotransduction are discovered, they will surely offer exciting prospects for genetic manipulation of these classes of neurons. For example, the identification of the putative mechanosensitivity channel-like protein Piezo 1 and 2 offers yet another ripe genetic target to study touch neurons (Coste et al., 2010). More broadly, advances in molecular profiling of both RNA and protein make it safe to predict new markers are on the horizon.

WHAT IS HAPPENING DOWNSTREAM OF THE SENSORY NEURONS?

As exciting as they are, the studies described above are in some ways just the preamble to the much larger task of understanding how the brain encodes somatosensory information. Knowing there exist classes of neurons that specifically encode cold, heat, and gentle touch presents a groundbreaking opportunity to begin unraveling the downstream pathways. The manipulation of sensory neuron populations has already begun to yield insights into the potential organization of neural circuits that receive sensory neuron input. For example, the ablation of CGRP$^+$ neurons showed that they normally provide tonic inhibition to TRPM8$^+$ neurons, revealing crosstalk between different modalities (McCoy et al., 2013). Similarly, the investigation of Bhlhb5-knockout mice revealed that this transcription factor is required for the survival of a population of spinal interneurons that regulate itch via inhibition (Ross et al., 2010). Furthermore, deletion of the testicular orphan nuclear receptor 4 (TR4) leads to the loss of a population of excitatory interneurons and a dramatic insensitivity to itch and pain (Wang et al., 2013). Finally, another transcription factor knockout study (Tlx3) finds that lack of excitatory interneurons in the dorsal spinal cord dramatically alters nocifensive behaviors to a wide variety of stimuli (Xu et al., 2013).

The transgenic strains coupled with those developed for studying the CNS will allow further access to technologies for circuit mapping. Optogenetic techniques have been catalyzing advances throughout neuroscience, and there is no reason to believe the same will not hold true for somatosensory research (Madisen et al., 2012). For example, targeting channelrhodopsin (ChR) to specific sensory neuron classes will allow selective activation of neurons that currently lack defined pharmacology. Indeed, ChR2 has already been targeted to nociceptors where it was found to be sufficient to drive nocifensive behaviors (Daou et al., 2013). Similarly, the use of chemical genetics, such as DREADDS, have also proved valuable in dissecting the behavioral contributions of defined sensory neuron populations (Lee et al., 2013; Vrontou et al., 2013). Finally, such reagents will hopefully result in a better understanding of the neural circuits that receive input from sensory neurons. For example, by expressing ChR2 in MrgprD$^+$ neurons, Wang and Zylka (2009) have characterized the synaptic partners of this class of sensory neurons in lamina II, and detected distinct functional modules in the spinal cord. The stage is now set for subsequent studies to capitalize on the current knowledge of the different classes of somatosensory neurons coupled with opto- and chemical genetic techniques. The circuits and functions of the somatosensory system have thus become a ripe area for future investigation.

ACKNOWLEDGMENTS

We would like to thank Catherine Bushnell (NIH/NCCAM), Mark Pitcher (NIH/NCCAM), Mark Hoon (NIH/NIDCR), Alexander Jackson (University of Connecticut), and Anna-Lisa Lucido (The Jackson Laboratory) for their helpful comments on our manuscript. We are particular grateful to Mark Hoon (NIH/NIDCR), Danial Cavanaugh (University of Pennsylvania), Allan Basbaum (UCSF), and Grégory Scherrer (Stanford University) for generously sharing their data and providing images. This work was funded by the NIH Intramural program for Pain in NCCAM as well as NIH/NINDS.

REFERENCES

Abrahamsen, B., Zhao, J., Asante, C. O., Cendan, C. M., Marsh, S., Martinez-Barbera, J. P., et al. (2008). The cell and molecular basis of mechanical,

cold, and inflammatory pain. *Science* 321, 702–705. doi: 10.1126/science.1156916

Abraira, V. E., and Ginty, D. D. (2013). The sensory neurons of touch. *Neuron* 79, 618–639. doi: 10.1016/j.neuron.2013.07.051

Akopian, A. N., Sivilotti, L., and Wood, J. N. (1996). A tetrodotoxin-resistant voltage-gated sodium channel expressed by sensory neurons. *Nature* 379, 257–262. doi: 10.1038/379257a0

Arenkiel, B. R., Klein, M. E., Davison, I. G., Katz, L. C., and Ehlers, M. D. (2008). Genetic control of neuronal activity in mice conditionally expressing TRPV1. *Nat. Methods* 5, 299–302. doi: 10.1038/nmeth.1190

Averill, S., McMahon, S. B., Clary, D. O., Reichardt, L. F., and Priestley, J. V. (1995). Immunocytochemical localization of trkA receptors in chemically identified subgroups of adult rat sensory neurons. *Eur. J. Neurosci.* 7, 1484–1494. doi: 10.1111/j.1460-9568.1995.tb01143.x

Bandell, M., Macpherson, L. J., and Patapoutian, A. (2007). From chills to chilis: mechanisms for thermosensation and chemesthesis via thermoTRPs. *Curr. Opin. Neurobiol.* 17, 490–497. doi: 10.1016/j.conb.2007.07.014

Bardoni, R., Tawfik, V. L., Wang, D., François, A., Solorzano, C., Shuster, S. A., et al. (2014). Delta opioid receptors presynaptically regulate cutaneous mechanosensory neuron input to the spinal cord dorsal horn. *Neuron* 81, 1–16. doi: 10.1016/j.neuron.2014.03.006

Basbaum, A. I., Bautista, D. M., Scherrer, G., and Julius, D. (2009). Cellular and molecular mechanisms of pain. *Cell* 139, 267–284. doi: 10.1016/j.cell.2009.09.028

Bautista, D. M., Jordt, S.-E., Nikai, T., Tsuruda, P. R., Read, A. J., Poblete, J., et al. (2006). TRPA1 mediates the inflammatory actions of environmental irritants and proalgesic agents. *Cell* 124, 1269–1282. doi: 10.1016/j.cell.2006.02.023

Bautista, D. M., Siemens, J., Glazer, J. M., Tsuruda, P. R., Basbaum, A. I., Stucky, C. L., et al. (2007). The menthol receptor TRPM8 is the principal detector of environmental cold. *Nature* 448, 204–208. doi: 10.1038/nature05910

Birdsong, W. T., Fierro, L., Williams, F. G., Spelta, V., Naves, L. A., Knowles, M., et al. (2010). Sensing muscle ischemia: coincident detection of acid and ATP via interplay of two ion channels. *Neuron* 68, 739–749. doi: 10.1016/j.neuron.2010.09.029

Caterina, M. J., Leffler, A., Malmberg, A. B., Martin, W. J., Trafton, J., Petersen-Zeitz, K. R., et al. (2000). Impaired nociception and pain sensation in mice lacking the capsaicin receptor. *Science* 288, 306–313. doi: 10.1126/science.288.5464.306

Caterina, M. J., Schumacher, M. A., Tominaga, M., Rosen, T. A., Levine, J. D., and Julius, D. (1997). The capsaicin receptor: a heat-activated ion channel in the pain pathway. *Nature* 389, 816. doi: 10.1038/39807

Cavanaugh, D. J., Chesler, A. T., Bráz, J. M., Shah, N. M., Julius, D., and Basbaum, A. I. (2011a). Restriction of transient receptor potential vanilloid-1 to the peptidergic subset of primary afferent neurons follows its developmental downregulation in nonpeptidergic neurons. *J. Neurosci.* 31, 10119–10127. doi: 10.1523/JNEUROSCI.1299-11.2011

Cavanaugh, D. J., Chesler, A. T., Jackson, A. C., Sigal, Y. M., Yamanaka, H., Grant, R., et al. (2011b). Trpv1 reporter mice reveal highly restricted brain distribution and functional expression in arteriolar smooth muscle cells. *J. Neurosci.* 31, 5067–5077. doi: 10.1523/JNEUROSCI.6451-10.2011

Cavanaugh, D. J., Lee, H., Lo, L., Shields, S. D., Zylka, M. J., Basbaum, A. I., et al. (2009). Distinct subsets of unmyelinated primary sensory fibers mediate behavioral responses to noxious thermal and mechanical stimuli. *Proc. Natl. Acad. Sci. U.S.A.* 106, 9075–9080. doi: 10.1073/pnas.0901507106

Chávez, A. E., Chiu, C. Q., and Castillo, P. E. (2010). TRPV1 activation by endogenous anandamide triggers postsynaptic long-term depression in dentate gyrus. *Nat. Neurosci.* 13, 1511–1518. doi: 10.1038/nn.2684

Chuang, H. H., Prescott, E. D., Kong, H., Shields, S., Jordt, S. E., Basbaum, A. I., et al. (2001). Bradykinin and nerve growth factor release the capsaicin receptor from PtdIns(4,5)P2-mediated inhibition. *Nature* 411, 957. doi: 10.1038/35082088

Colburn, R. W., Lubin, M. L., Stone, D. J. Jr., Wang, Y., Lawrence, D., D'Andrea, M. R., et al. (2007). Attenuated cold sensitivity in TRPM8 null mice. *Neuron* 54, 379–386. doi: 10.1016/j.neuron.2007.04.017

Coste, B., Mathur, J., Schmidt, M., Earley, T. J., Ranade, S., Petrus, M. J., et al. (2010). Piezo1 and Piezo2 are essential components of distinct mechanically activated cation channels. *Science* 330, 55–60. doi: 10.1126/science.1193270

Daou, I., Tuttle, A. H., Longo, G., Wieskopf, J. S., Bonin, R. P., Ase, A. R., et al. (2013). Remote optogenetic activation and sensitization of pain pathways in freely moving mice. *J. Neurosci.* 33, 18631–18640. doi: 10.1523/JNEUROSCI.2424-13.2013

Darian-Smith, I., Johnson, K. O., and Dykes, R. (1973). "Cold" fiber population innervating palmar and digital skin of the monkey: responses to cooling pulses. *J. Neurophysiol.* 36, 325–346.

Delmas, P., Hao, J., and Rodat-Despoix, L. (2011). Molecular mechanisms of mechanotransduction in mammalian sensory neurons. *Nat. Rev. Neurosci.* 12, 139–153. doi: 10.1038/nrn2993

Dhaka, A., Earley, T. J., Watson, J., and Patapoutian, A. (2008). Visualizing cold spots: TRPM8-expressing sensory neurons and their projections. *J. Neurosci.* 28, 566–575. doi: 10.1523/JNEUROSCI.3976-07.2008

Dhaka, A., Murray, A. N., Mathur, J., Earley, T. J., Petrus, M. J., and Patapoutian, A. (2007). TRPM8 is required for cold sensation in mice. *Neuron* 54, 371–378. doi: 10.1016/j.neuron.2007.02.024

Dong, X., Han, S., Zylka, M. J., Simon, M. I., and Anderson, D. J. (2001). A diverse family of GPCRs expressed in specific subsets of nociceptive sensory neurons. *Cell* 106, 619–632. doi: 10.1016/S0092-8674(01)00483-4

Dubner, R., Sumino, R., and Wood, W. I. (1975). A peripheral "cold" fiber population responsive to innocuous and noxious thermal stimuli applied to monkey's face. *J. Neurophysiol.* 38, 1373–1389.

Duclaux, R., and Kenshalo, D. R. (1980). Response characteristics of cutaneous warm receptors in the monkey. *J. Neurophysiol.* 43, 1–15.

Dussor, G., Zylka, M. J., Anderson, D. J., and McCleskey, E. W. (2008). Cutaneous sensory neurons expressing the Mrgprd receptor sense extracellular ATP and are putative nociceptors. *J. Neurophysiol.* 99, 1581–1589. doi: 10.1152/jn.01396.2007

Feil, K., and Herbert, H. (1995). Topographic organization of spinal and trigeminal somatosensory pathways to the rat parabrachial and Kölliker-Fuse nuclei. *J. Comp. Neurol.* 353, 506–528. doi: 10.1002/cne.903530404

Fremeau, R. T., Burman, J., Qureshi, T., Tran, C. H., Proctor, J., Johnson, J., et al. (2002). The identification of vesicular glutamate transporter 3 suggests novel modes of signaling by glutamate. *Proc. Natl. Acad. Sci. U.S.A.* 99, 14488–14493. doi: 10.1073/pnas.222546799

Fremeau, R. T., Voglmaier, S., Seal, R. P., and Edwards, R. H. (2004). VGLUTs define subsets of excitatory neurons and suggest novel roles for glutamate. *Trends Neurosci.* 27, 98–103. doi: 10.1016/j.tins.2003.11.005

Georgopoulos, A. P. (1976). Functional properties of primary afferent units probably related to pain mechanisms in primate glabrous skin. *J. Neurophysiol.* 39, 71–83.

Gomes, I., Gupta, A., Filipovska, J., Szeto, H. H., Pintar, J. E., and Devi, L. A. (2004). A role for heterodimerization of μ and δ opiate receptors in enhancing morphine analgesia. *Proc. Natl. Acad. Sci. U.S.A.* 101, 5145–5139. doi: 10.1073/pnas.0307601101

Gong, S., Zheng, C., Doughty, M. L., Losos, K., Didkovsky, N., Schambra, U. B., et al. (2003). A gene expression atlas of the central nervous system based on bacterial artificial chromosomes. *Nature* 425, 917–925. doi: 10.1038/nature02033

Gras, C., Herzog, E., Bellenchi, G. C., Bernard, V., Ravassard, P., Pohl, M., et al. (2002). A third vesicular glutamate transporter expressed by cholinergic and serotoninergic neurons. *J. Neurosci.* 22, 5442–5451.

Grueter, B. A., Brasnjo, G., and Malenka, R. C. (2010). Postsynaptic TRPV1 triggers cell type-specific long-term depression in the nucleus accumbens. *Nat. Neurosci.* 13, 1519–1525. doi: 10.1038/nn.2685

Han, L., Ma, C., Liu, Q., Weng, H.-J., Cui, Y., Tang, Z., et al. (2012). A subpopulation of nociceptors specifically linked to itch. *Nat. Neurosci.* 16, 174–182. doi: 10.1038/nn.3289

He, S. Q., Zhang, Z. N., Guan, J. S., Liu, H. R., Zhao, B., Wang, H. B., et al. (2011). Facilitation of μ-opioid receptor activity by preventing δ-opioid receptor-mediated codegradation. *Neuron* 69, 123–131. doi: 10.1016/j.neuron.2010.12.001

Heintz, N. (2001). Bac to the future: the use of bac transgenic mice for neuroscience research. *Nat. Rev. Neurosci.* 2, 861–870. doi: 10.1038/35104049

Hensel, H., and Iggo, A. (1971). Analysis of cutaneous warm and cold fibres in primates. *Pflugers Arch.* 329, 1–8. doi: 10.1007/BF00586896

Imamachi, N., Park, G. H., Lee, H., Anderson, D. J., Simon, M. I., Basbaum, A. I., et al. (2009). TRPV1-expressing primary afferents generate behavioral responses to pruritogens via multiple mechanisms. *Proc. Natl. Acad. Sci. U.S.A.* 106, 11330–11335. doi: 10.1073/pnas.0905605106

Jasmin, L., Burkey, A. R., Card, J. P., and Basbaum, A. I. (1997). Transneuronal labeling of a nociceptive pathway, the spino-(trigemino-)parabrachio-amygdaloid, in the rat. *J. Neurosci.* 17, 3751–3765.

Jordt, S.-E., Bautista, D. M., Chuang, H.-H., McKemy, D. D., Zygmunt, P. M., Högestätt, E. D., et al. (2004). Mustard oils and cannabinoids excite sensory nerve fibres through the TRP channel ANKTM1. *Nature* 427, 260–265. doi: 10.1038/nature02282

Jordt, S. E., McKemy, D. D., and Julius, D. (2003). Lessons from peppers and peppermint: the molecular logic of thermosensation. *Curr. Opin. Neurobiol.* 13, 487–492. doi: 10.1016/S0959-4388(03)00101-6

Kandel, E., Schwartz, J., Jessell, T., Siegelbaum, S., and Hudspeth, A. J. (2012). *Principles of Neural Science, 5th Edn*. McGraw Hill Professional.

Kauer, J. A., and Gibson, H. E. (2009). Hot flash: TRPV channels in the brain. *Trends Neurosci.* 32, 215–224. doi: 10.1016/j.tins.2008.12.006

Knowlton, W. M., Bifolck-Fisher, A., Bautista, D. M., and McKemy, D. D. (2010). TRPM8, but not TRPA1, is required for neural and behavioral responses to acute noxious cold temperatures and cold-mimetics *in vivo*. *Pain* 150, 340–350. doi: 10.1016/j.pain.2010.05.021

Kwan, K. Y., Allchorne, A. J., Vollrath, M. A., Christensen, A. P., Zhang, D.-S., Woolf, C. J., et al. (2006). TRPA1 contributes to cold, mechanical, and chemical nociception but is not essential for hair-cell transduction. *Neuron* 50, 277–289. doi: 10.1016/j.neuron.2006.03.042

Lee, H.-M., Giguere, P. M., and Roth, B. L. (2013). DREADDs: novel tools for drug discovery and development. *Drug Discov. Today*. doi: 10.1016/j.drudis.2013.10.018. [Epub ahead of print].

Li, L., Rutlin, M., Abraira, V. E., Cassidy, C., Kus, L., Gong, S., et al. (2011). The functional organization of cutaneous low-threshold mechanosensory neurons. *Cell* 147, 1615–1627. doi: 10.1016/j.cell.2011.11.027

Liu, Q., Sikand, P., Ma, C., Tang, Z., Han, L., Li, Z., et al. (2012). Mechanisms of itch evoked by β-alanine. *J. Neurosci.* 32, 14532–14537. doi: 10.1523/JNEUROSCI.3509-12.2012

Liu, Q., Tang, Z., Surdenikova, L., Kim, S., Patel, K. N., Kim, A., et al. (2009). Sensory neuron-specific GPCR Mrgprs are itch receptors mediating chloroquine-induced pruritus. *Cell* 139, 1353–1365. doi: 10.1016/j.cell.2009.11.034

Liu, Q., Vrontou, S., Rice, F. L., Zylka, M. J., Dong, X., and Anderson, D. J. (2007). Molecular genetic visualization of a rare subset of unmyelinated sensory neurons that may detect gentle touch. *Nat. Neurosci.* 10, 946–948. doi: 10.1038/nn1937

Liu, T., Xu, Z.-Z., Park, C.-K., Berta, T., and Ji, R.-R. (2010). Toll-like receptor 7 mediates pruritis. *Nat. Neurosci.* 13, 1460–1462. doi: 10.1038/nn.2683

Lou, S., Duan, B., Vong, L., Lowell, B. B., and Ma, Q. (2013). Runx1 controls terminal morphology and mechanosensitivity of VGLUT3-expressing C-mechanoreceptors. *J. Neurosci.* 33, 870–882. doi: 10.1523/JNEUROSCI.3942-12.2013

Madisen, L., Mao, T., Koch, H., Zhuo, J.-M., Berenyi, A., Fujisawa, S., et al. (2012). A toolbox of Cre-dependent optogenetic transgenic mice for light-induced activation and silencing. *Nat. Neurosci.* 15, 793–802. doi: 10.1038/nn.3078

McCoy, E. S., Taylor-Blake, B., Street, S. E., Pribisko, A. L., Zheng, J., and Zylka, M. J. (2013). Peptidergic CGRPα primary sensory neurons encode heat and itch and tonically suppress sensitivity to cold. *Neuron* 78, 138–151. doi: 10.1016/j.neuron.2013.01.030

McKemy, D. D. (2013). The molecular and cellular basis of cold sensation. *ACS Chem. Neurosci.* 4, 238–247. doi: 10.1021/cn300193h

McKemy, D. D., Neuhausser, W. M., and Julius, D. (2002). Identification of a cold receptor reveals a general role for TRP channels in thermosensation. *Nature* 416, 52. doi: 10.1038/nature719

Minett, M. S., Nassar, M. A., Clark, A. K., Passmore, G., Dickenson, A. H., Wang, F., et al. (2012). Distinct Nav1.7-dependent pain sensations require different sets of sensory and sympathetic neurons. *Nat. Commun.* 3, 791. doi: 10.1038/ncomms1795

Mishra, S. K., and Hoon, M. A. (2010). Ablation of TrpV1 neurons reveals their selective role in thermal pain sensation. *Mol. Cell. Neurosci.* 43, 157–163. doi: 10.1016/j.mcn.2009.10.006

Mishra, S. K., Tisel, S. M., Orestes, P., Bhangoo, S. K., and Hoon, M. A. (2011). TRPV1-lineage neurons are required for thermal sensation. *EMBO J.* 30, 582–593. doi: 10.1038/emboj.2010.325

Olausson, H., Lamarre, Y., Backlund, H., Morin, C., Wallin, B. G., Starck, G., et al. (2002). Unmyelinated tactile afferents signal touch and project to insular cortex. *Nat. Neurosci.* 5, 900–904. doi: 10.1038/nn896

Patapoutian, A., Tate, S., and Woolf, C. J. (2009). Transient receptor potential channels: targeting pain at the source. *Nat. Rev. Drug Discov*. 8, 55–68. doi: 10.1038/nrd2757

Peier, A. M., Moqrich, A., Hergarden, A. C., Reeve, A. J., Andersson, D. A., Story, G. M., et al. (2002). A TRP channel that senses cold stimuli and menthol. *Cell* 108, 705–715. doi: 10.1016/S0092-8674(02)00652-9

Pogorzala, L. A., Mishra, S. K., and Hoon, M. A. (2013). The cellular code for mammalian thermosensation. *J. Neurosci.* 33, 5533–5541. doi: 10.1523/JNEUROSCI.5788-12.2013

Purves, D., Augustine, G. J., Fitzpatrick, D., Hall, W. C., LaMantia, A. S., and White, L. E. (2012). *Neuroscience, 5th Edn.* Sinauer Associates, Inc.

Ross, S. E., Mardinly, A. R., McCord, A. E., Zurawski, J., Cohen, S., Jung, C., et al. (2010). Loss of inhibitory interneurons in the dorsal spinal cord and elevated itch in Bhlhb5 mutant mice. *Neuron* 65, 886–898. doi: 10.1016/j.neuron.2010.02.025

Sakurai, K., Akiyama, M., Cai, B., Scott, A., Han, B.-X., Takatoh, J., et al. (2013). The organization of submodality-specific touch afferent inputs in the vibrissa column. *Cell Rep.* 5, 87–98. doi: 10.1016/j.celrep.2013.08.051

Scherrer, G., Imamachi, N., Cao, Y.-Q., Contet, C., Mennicken, F., O'Donnell, D., et al. (2009). Dissociation of the opioid receptor mechanisms that control mechanical and heat pain. *Cell* 137, 1148–1159. doi: 10.1016/j.cell.2009.04.019

Seal, R. P., Akil, O., Yi, E., Weber, C. M., Grant, L., Yoo, J., et al. (2008). Sensorineural deafness and seizures in mice lacking vesicular glutamate transporter 3. *Neuron* 57, 263–275. doi: 10.1016/j.neuron.2007.11.032

Seal, R. P., Wang, X., Guan, Y., Raja, S. N., Woodbury, C. J., Basbaum, A. I., et al. (2009). Injury-induced mechanical hypersensitivity requires C-low threshold mechanoreceptors. *Nature* 462, 651–655. doi: 10.1038/nature08505

Shah, N. M., Pisapia, D. J., Maniatis, S., and Mendelsohn, M. M. (2004). Visualizing sexual dimorphism in the brain. *Neuron* 43, 313–319. doi: 10.1016/j.neuron.2004.07.008

Sharif Naeini, R., Witty, M.-F., Séguéla, P., and Bourque, C. W. (2006). An N-terminal variant of Trpv1 channel is required for osmosensory transduction. *Nat. Neurosci.* 9, 93–98. doi: 10.1038/nn1614

Shim, W.-S., Tak, M.-H., Lee, M.-H., Kim, M., Kim, M., Koo, J.-Y., et al. (2007). TRPV1 mediates histamine-induced itching via the activation of phospholipase A2 and 12-lipoxygenase. *J. Neurosci.* 27, 2331–2337. doi: 10.1523/JNEUROSCI.4643-06.2007

Simone, D. A., and Kajander, K. C. (1997). Responses of cutaneous A-fiber nociceptors to noxious cold. *J. Neurophysiol.* 77, 2049–2060.

Sun, Y.-G., and Chen, Z.-F. (2007). A gastrin-releasing peptide receptor mediates the itch sensation in the spinal cord. *Nature* 448, 700–703. doi: 10.1038/nature06029

Sun, Y.-G., Zhao, Z.-Q., Meng, X.-L., Yin, J., Liu, X.-Y., and Chen, Z.-F. (2009). Cellular basis of itch sensation. *Science* 325, 1531–1534. doi: 10.1126/science.1174868

Takashima, Y., Daniels, R. L., Knowlton, W., Teng, J., Liman, E. R., and McKemy, D. D. (2007). Diversity in the neural circuitry of cold sensing revealed by genetic axonal labeling of transient receptor potential melastatin 8 neurons. *J. Neurosci.* 27, 14147–14157. doi: 10.1523/JNEUROSCI.4578-07.2007

Tian, L., Hires, S. A., Mao, T., Huber, D., Chiappe, M. E., Chalasani, S. H., et al. (2009). Imaging neural activity in worms, flies and mice with improved GCaMP calcium indicators. *Nat. Methods* 6, 875–881. doi: 10.1038/nmeth.1398

Tominaga, M., Caterina, M. J., Malmberg, A. B., Rosen, T. A., Gilbert, H., Skinner, K., et al. (1998). The cloned capsaicin receptor integrates multiple pain-producing stimuli. *Neuron* 21, 531–543. doi: 10.1016/S0896-6273(00)80564-4

Vriens, J., Owsianik, G., Hofmann, T., Philipp, S. E., Stab, J., Chen, X., et al. (2011). TRPM3 is a nociceptor channel involved in the detection of noxious heat. *Neuron* 70, 482–494. doi: 10.1016/j.neuron.2011.02.051

Vrontou, S., Wong, A. M., Rau, K. K., Koerber, H. R., and Anderson, D. J. (2013). Genetic identification of C fibres that detect massage-like stroking of hairy skin *in vivo*. *Nature* 493, 669–673. doi: 10.1038/nature11810

Wang, H., and Zylka, M. J. (2009). Mrgprd-expressing polymodal nociceptive neurons innervate most known classes of substantia gelatinosa neurons. *J. Neurosci.* 29, 13202–13209. doi: 10.1523/JNEUROSCI.3248-09.2009

Wang, H.-B., Zhao, B., Zhong, Y.-Q., Li, K.-C., Li, Z.-Y., Wang, Q., et al. (2010). Coexpression of δ- and μ-opioid receptors in nociceptive sensory neurons. *Proc. Natl. Acad. Sci. U.S.A.* 107, 13117–13122. doi: 10.1073/pnas.1008382107

Wang, X., Zhang, J., Eberhart, D., Urban, R., Meda, K., Solorzano, C., et al. (2013). Excitatory superficial dorsal horn interneurons are functionally heterogeneous and required for the full behavioral expression of pain and itch. *Neuron* 78, 312–324. doi: 10.1016/j.neuron.2013.03.001

Wilson, S. R., Gerhold, K. A., Bifolck-Fisher, A., Liu, Q., Patel, K. N., Dong, X., et al. (2011). TRPA1 is required for histamine-independent, Mas-related G protein-coupled receptor-mediated itch. *Nat. Neurosci.* 14, 595–602. doi: 10.1038/nn.2789

Wilson, S. R., Thé, L., Batia, L. M., Beattie, K., Katibah, G. E., McClain, S. P., et al. (2013). The epithelial cell-derived atopic dermatitis cytokine TSLP activates neurons to induce itch. *Cell* 155, 285–295. doi: 10.1016/j.cell.2013.08.057

Xu, Y., Lpoes, C., Wende, H., Guo, Z., Cheng, L., Birchmeier, C., et al. (2013). Ontogeny of excitatory spinal neurons processing distinct somatic sensory modalities. *J. Neurosci.* 33, 14738–14747. doi: 10.1523/JNEUROSCI.5512-12.2013

Zotterman, Y. (1939). Touch, pain and tickling: an electro-physiological investigation on cutaneous sensory nerves. *J. Physiol.* 95, 1–28.

Zylka, M. J., Rice, F. L., and Anderson, D. J. (2005). Topographically distinct epidermal nociceptive circuits revealed by axonal tracers targeted to Mrgprd. *Neuron* 45, 17–25. doi: 10.1016/j.neuron.2004.12.015

Conflict of Interest Statement: The authors declare that the research was conducted in the absence of any commercial or financial relationships that could be construed as a potential conflict of interest.

Received: 31 January 2014; accepted: 24 March 2014; published online: 22 April 2014.
Citation: Le Pichon CE and Chesler AT (2014) The functional and anatomical dissection of somatosensory subpopulations using mouse genetics. Front. Neuroanat. ***8****:21. doi: 10.3389/fnana.2014.00021*
This article was submitted to the journal Frontiers in Neuroanatomy.

frontiers in
NEUROANATOMY

ORIGINAL RESEARCH ARTICLE
published: 05 August 2014
doi: 10.3389/fnana.2014.00066

Supraspinal gene transfer by intrathecal adeno-associated virus serotype 5

Daniel J. Schuster[1], Lalitha R. Belur[2], Maureen S. Riedl[1], Stephen A. Schnell[1], Kelly M. Podetz-Pedersen[2], Kelley F. Kitto[1], R. Scott McIvor[2], Lucy Vulchanova[3] and Carolyn A. Fairbanks[1,3,4]*

[1] *Department of Neuroscience, University of Minnesota, Minneapolis, MN, USA*
[2] *Department of Genetics, Cell Biology and Development, University of Minnesota, Minneapolis, MN, USA*
[3] *Department of Pharmacology, University of Minnesota, Minneapolis, MN, USA*
[4] *Department of Pharmaceutics, University of Minnesota, Minneapolis, MN, USA*

Edited by:
Laurent Gautron, University of Texas Southwestern Medical Center, USA

Reviewed by:
Isabelle Decosterd, University Hospital Center and University of Lausanne, Switzerland
Michael Lazarus, University of Tsukuba, Japan

****Correspondence:***
Carolyn A. Fairbanks, Department of Pharmaceutics, University of Minnesota, 9-143A Weaver-Densford Hall, 308 Harvard St. SE, Minneapolis, MN 55455-0217, USA
e-mail: carfair@umn.edu

We report the pattern of transgene expression across brain regions after intrathecal delivery of adeno-associated virus serotype 5 (AAV5). Labeling in hindbrain appeared to be primarily neuronal, and was detected in sensory nuclei of medulla, pontine nuclei, and all layers of cerebellar cortex. Expression in midbrain was minimal, and generally limited to isolated neurons and astrocytes in the cerebral peduncles. GFP immunoreactivity (-ir) in thalamus was most prominent in medial geniculate nucleus, and otherwise limited to posterior nuclei of the dorsal and lateral margins. Labeling was also observed in neurons and astrocytes of the hippocampal formation and amygdaloid complex. In the hippocampal formation, GFP-ir was found in neuronal cell bodies of the rostral ventral portion, but was largely restricted to fiber-like staining in the molecular layer of dentate gyrus and stratum lacunosum-moleculare of the rostral dorsal region. GFP-ir was seen in neurons and astroglia throughout caudal cortex, whereas in rostral regions of neocortex it was limited to isolated neurons and non-neuronal cells. Labeling was also present in olfactory bulb. These results demonstrate that intrathecal delivery of AAV5 vector leads to transgene expression in discrete CNS regions throughout the rostro-caudal extent of the neuraxis. A caudal-to-rostral gradient of decreasing GFP-ir was present in choroid plexus and Purkinje cells, suggesting that spread of virus through cerebrospinal fluid plays a role in the resulting transduction pattern. Other factors contributing to the observed expression pattern likely include variations in cell-surface receptors and inter-parenchymal space.

Keywords: adeno-associated, AAV5, intrathecal, CNS, mannitol

INTRODUCTION

In recent years a growing body of evidence has indicated that adeno-associated virus (AAV) is a useful vector for delivery of therapeutic genes to the central nervous system (CNS). Direct injection of AAV vectors into a specific CNS nucleus can result in a high level of gene expression in that nucleus, as well as physically adjacent and functionally connected areas (Fu et al., 2002; Ciesielska et al., 2011; White et al., 2011). However, this method carries the drawback of tissue damage that is potentially both detrimental and irreparable. Therefore, alternative approaches for CNS delivery of AAV vectors, such as delivery to the cerebrospinal fluid (CSF), are necessary for translational development of AAV-mediated gene therapy.

Delivery to the CSF can be achieved in a variety of ways including injection into the cerebral ventricles, the posterior cistern, and the spinal intrathecal space. Acute injection of AAV vectors into the posterior cistern, without the use of any method to enhance distribution, has resulted in a relatively limited pattern of gene expression that appears analogous to that seen with ventricular injection (Fu et al., 2003). On the other hand, methods to improve vector distribution upon cisternal administration, such as pretreatment with mannitol delivered intravenously or removal of some CSF followed by a large injection volume, have shown the potential for an enhanced pattern of gene expression spanning several CNS regions (Fu et al., 2003; Iwamoto et al., 2009).

Surgical access to the posterior cistern has also been used for intrathecal catheter placement with the goal of delivery of AAV6 or AAV8 directed at the lumbar spinal level (Storek et al., 2008; Towne et al., 2009). Substantial transduction of lumbar dorsal root ganglion (DRG) neurons was achieved in both of these studies. Additionally, Towne et al. (2009) observed transduction in cervical DRG and several areas of the brain. An alternative method for delivery to the lumbar intrathecal space is direct lumbar puncture, which is minimally invasive, does not require anesthesia, presents negligible risk for tissue damage, and has long been used both experimentally and clinically.

We recently demonstrated transduction of DRG neurons following delivery of AAV5 or AAV8 by direct lumbar puncture with an intravenous mannitol pretreatment (Vulchanova et al., 2010). The goal of the current study was to determine the

extent of expression in the CNS after lumbar puncture delivery of AAV5.

MATERIALS AND METHODS

AAV VECTOR AND PACKAGING

AAV vector TRUF11, containing a CBA- (cytomegalovirus enhancer with a chicken β-actin promoter) regulated GFP sequence, has been previously described (Kaemmerer et al., 2000). Packaging using AAV5 serotype capsid was carried out at the University of Florida Vector Core Lab of the Gene Therapy Center (Gainesville, Florida) as previously described (Zolotukhin et al., 2002).

ANIMALS

Experimental subjects were 20–25 g adult male C57BL/6 mice (Harlan, Madison, WI). All experiments were reviewed and approved by the Institutional Animal Care and Use Committee (IACUC) of the University of Minnesota.

Table 1 | Relative abundance of GFP-ir in brain after intrathecal AAV5-GFP delivery with an intravenous mannitol pretreatment (evaluated in 8 animals from two separate experiments; each structure was observed in at least 3 different sections).

Brain area	Neuronal somata	Neuronal fibers	Non-neuronal cells
Gracile/Cuneate n.	−	+++	−
Spinal Trigeminal n. and tract	+	++	−
NTS, Solitary tract, and AP	++	++	−
Vestibular/Cochlear n.	+	+	−
Facial n.	+	+	−
Cerebellum	++	++	−
4th Ventricle Choroid Plexus	−	−	++++
Pons	++	++	−
Inferior Colliculus	+	+	−
Superior Colliculus	+	+	−
Cerebral Peduncles	−	−	++
Medial Geniculate n.	++	++	−
LGN and Posterior Thalamic n.	+	++	−
Hypothalamus	+	+	−
3rd Ventricle Choroid Plexus	−	−	+++
Subiculum	+++	++	++
Entorhinal Ctx.	+++	++	++
Caudal visual & Retrosplenial Ctx.	++	++	++
Rostral visual & Retrosplenial Ctx.	+	+	+
Rostral–Ventral Hippocampal Form.	+++	++	+
Rostral–Dorsal Hippocampal Form.	−	+++	−
Amygdala	++	+	−
Lateral Ventricles Choroid Plexus	−	−	+++
Cingulate, Motor & Sensory Ctx.	+	+	+
Olfactory bulb	++	++	++

Definitions of relative abundance: −, no GFP labeling observed; +, isolated cells; ++, multiple labeled cells observed in close proximity to one another; +++, GFP-ir at least as prevalent as ++ throughout the structure, with some areas showing markedly increased GFP-ir; ++++ = a substantial fraction of cells throughout the entire structure showed GFP-ir. Abbreviations: n, nucleus; NTS, nucleus of the solitary tract; AP, area postrema; LGN, lateral geniculate nucleus; Ctx, cortex.

INJECTIONS

Subjects were injected via the tail vein with 25% mannitol solution (200 μL) 20 min prior to intrathecal or intravenous injection of the viral construct. For intrathecal delivery, the AAV construct was delivered by direct lumbar puncture in awake mice by an experimenter (KFK) with extensive experience in this method of drug delivery (Hylden and Wilcox, 1980). In a minor modification to the protocol, the needle (30-gauge, 0.5-inch) was connected to a length of PE10 tubing, which was then connected to a second needle that was attached to a 50 μl Luer-hub Hamilton syringe. Ten microliters containing $\sim 10^{11}$ vector genomes was injected intrathecally. The injection was administered by gently gripping the iliac crest of the rodent and inserting the needle (bevel side up) at about a 45° angle centered between the hipbones. A reflexive flick of the tail indicated puncture of the dura. For intravenous AAV5 injections, the same total dose of vector ($\sim 10^{11}$ vector genomes) was diluted 10-fold in sterile saline to a final volume of 100 μL. Following injection of AAV, the animals were returned to the vivarium where they remained for 6 weeks, until the time of transcardial perfusion, fixation, and extraction of fixed brain tissue for immunohistochemical analysis.

IMMUNOHISTOCHEMISTRY

All animals were sacrificed by perfusion fixation as previously described (Vulchanova et al., 1998). Briefly, animals were isoflurane anesthetized via nosecone inhalation and perfused with a solution of calcium-free tyrodes solution (in mM:NaCl 116, KCl 5.4, $MgCl_2 \cdot 6H_20$ 1.6, $MgSO_4 \cdot 7H_2O$ 0.4, NaH_2PO_4 1.4, glucose 5.6, and $NaHCO_3$ 26) followed by fixative (4% paraformaldehyde and 0.2% picric acid in 0.1 M phosphate buffer, pH 6.9) followed by 10% sucrose in PBS. Brain was removed and incubated in 10% sucrose overnight at 4°C. Sections were cut at 14 μm thickness and thaw mounted onto gel-coated slides. Tissue sections were incubated for 1 h at room temperature in diluent (PBS containing 0.3% Triton, 1% BSA, 1% normal donkey serum) and then incubated overnight at 4°C in primary antisera diluted in the same solution. Primary antibodies used

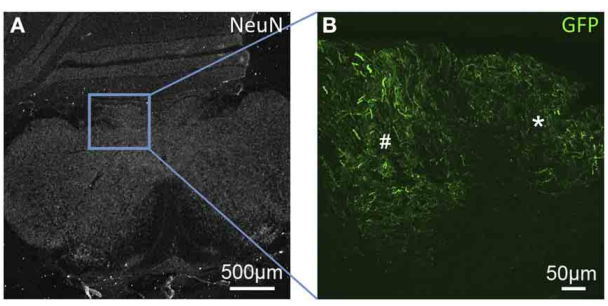

FIGURE 1 | GFP-ir fibers in somatosensory nuclei of the medulla. (A) Low-magnification image showing the pattern of NeuN-ir in this tissue section (approximately −7.3 mm Bregma). **(B)** GFP-ir in the gracile (*) and cuneate (#) nuclei.

were: rabbit anti-GFP, 1:500 (Invitrogen; Eugene, OR), mouse anti-NeuN, 1:500 (Chemicon; Temecula, CA), mouse anti-GFAP, 1:400 (Sigma; St. Louis, MO), and mouse anti-calbindin, 1:1000 (Sigma; St. Louis, MO), rat anti-CD68, 1:100 (AbD Serotec, Oxford, UK). After rinsing with PBS, sections were incubated 1 h at room temperature with appropriate combinations of Cy2-, Cy3-, and Cy5- (1:300) conjugated secondary antisera (Jackson ImmunoResearch, West Grove, CA). Sections were rinsed again, and in some cases, were also incubated with DAPI nucleic acid stain for 3–5 min, 300 nM (Invitrogen; Eugene, OR). Following the final rinses, sections were cover-slipped using glycerol and PBS containing 0.1% p-phenylenediamine (Sigma).

MICROSCOPY

Anatomical analysis was based on the "The Mouse Brain In Stereotaxic Coordinates," Second Edition (Paxinos and Franklin, 2001). Images for **Figures 3** and **10** were collected at a resolution of 1600 by 1200 pixels on an Olympus BX60 fluorescence microscope with a Spot Insight camera and Spot image acquisition software. Images in **Figures 4E,F**, **7** and **8B** were collected with an Olympus BX50FA fluorescence microscope equipped with a CCD camera. All other images were collected on an Olympus Fluoview 1000 confocal microscope with associated software at a resolution of 512 by 512 pixels. Images were processed for contrast, brightness, and color in Adobe Photoshop.

QUANTIFICATION

For quantification of number of fourth ventricle choroid plexus cells transduced, 3 sections per ventricle, spaced at least 100 μm apart were counted for each of 4 animals. The total number of choroid plexus cells in each section was determined by counting

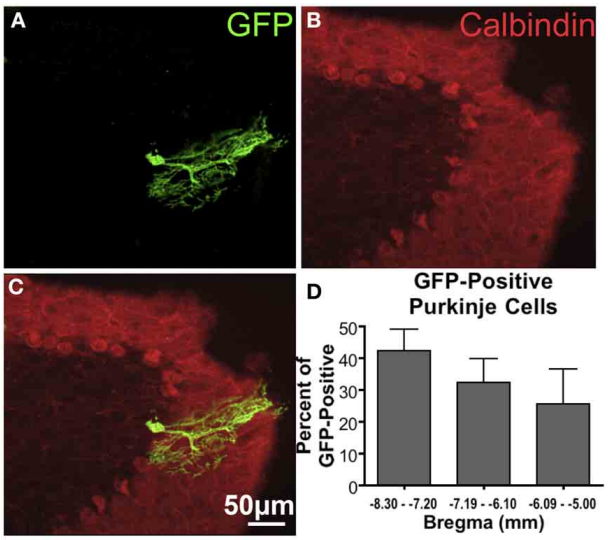

FIGURE 3 | GFP-ir in Purkinje cells of the cerebellum. (A) GFP-ir, showing one labeled cell. **(B)** Calbindin-ir illustrating the difference in morphology between the molecular, Purkinje, and granule cell layers of the cerebellum. **(C)** Overlay of images in **(A)** and **(B)** illustrating that this GFP-positive neuron is a Purkinje cell. **(D)** A graph showing the fraction of GFP-positive Purkinje cells found at different distances from Bregma indicates a trend toward decreasing transduction of Purkinje cells in more rostral portions of cerebellum. Only GFP-positive Purkinje cells were counted. The graph represents counted cells for each range of distances from Bregma as percent of all GFP-positive Purkinje cells (78 total cells counted). There was no significant difference in the number of GFP-positive Purkinje cells found in each range of distances from Bregma (One-Way ANOVA, $P > 0.05$, $n = 4$).

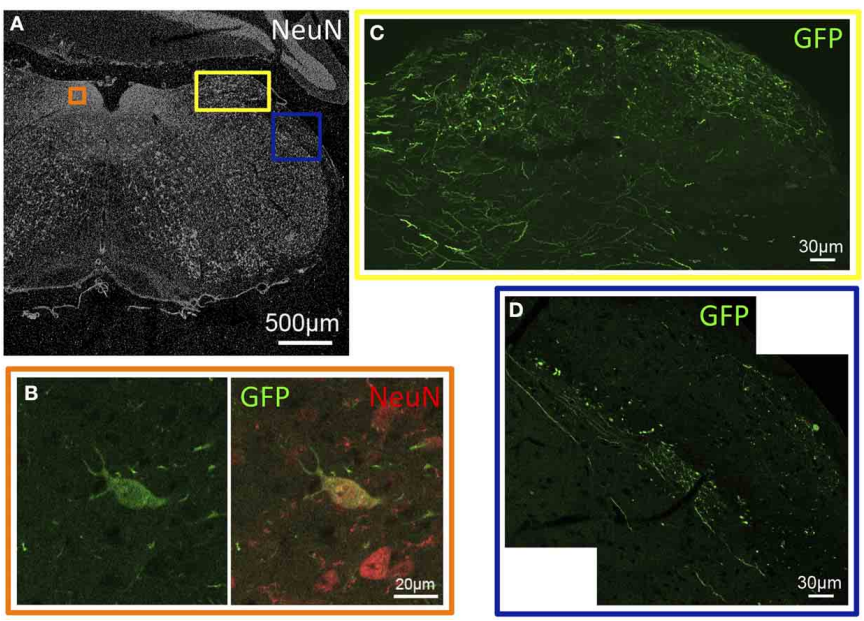

FIGURE 2 | GFP-ir in sensory nuclei of the medulla. (A) Low-magnification image showing the pattern of NeuN-ir in this tissue section (approximately −6.8 mm Bregma). Colored inset boxes show the locations of the images in **(B–D)**. **(B)** A GFP-positive neuron in the nucleus of the solitary tract. **(C)** GFP-ir in the external cuneate nucleus. **(D)** GFP-ir in the spinal trigeminal tract (center diagonal) and lateral to that in the inferior cerebellar peduncle (right).

nuclei within each ventricle identified by DAPI stain. Choroid plexus cells immuno-positive for GFP were identified by overlaying images of DAPI fluorescence and GFP-ir, and counting nuclei that were surrounded by GFP-ir. Two independent observers performed counts yielding results that consistently varied by less than six percent per section. Results are graphed as percent of counted choroid plexus cells for a given ventricle that displayed GFP immunoreactivity (-ir).

For quantification of transduced Purkinje cells, at least 6 sections spaced at least 70 μm apart were counted for each of the 4 animals. Only Purkinje cell bodies that showed GFP-ir were counted, and were identified by co-labeling with calbindin-ir. Results are graphed as the percent of counted cells that were located in a given range of distances from Bregma.

STATISTICS

For quantification of choroid plexus cells and Purkinje cells, data are represented as mean ± standard error of the mean. Data were analyzed using one-way analysis of variance (ANOVA) followed by a Bonferroni *post-hoc* test. Data analysis, and production of graphs, was done with GraphPad Prism 4.0 software.

RESULTS

Six weeks after intrathecal administration of AAV5, GFP expression was observed in discrete areas of the central nervous system (CNS), while intravenous delivery of an equivalent total dose of vector resulted in no detectable expression in the CNS. The figures illustrating localization of GFP-ir are presented in a caudal-to-rostral sequence and are referenced as necessary for the descriptions of anatomical regions, which may be represented on more than one figure. The relative abundance of GFP-positive cells in different structures is shown in **Table 1**. Throughout the CNS we observed GFP-positive neurons and astrocytes, as evidenced by colocalization with NeuN and GFAP, respectively. To address the immune status of the brains of AAV treated animals we performed labeling for the microglial marker CD68, and found no qualitative difference in CD68 labeling between naïve and AAV5 treated animals (data not shown).

In the medulla, (as seen in **Figures 1A**, **2A**) GFP-immunoreactivity (-ir) was found primarily in dorsal sensory, and cranial nerve nuclei. In the gracile, cuneate and external cuneate nuclei (**Figures 1**, **2C**), as well as in the spinal trigeminal tract (**Figure 2D**), labeling was observed in neuronal fibers, but was absent from cell bodies. Fiber labeling in the gracile, cuneate, and external cuneate nuclei is likely to have originated from primary sensory neurons in dorsal root ganglia (DRG), as supported by our previously published observations of GFP-ir in nerve fibers within the dorsal columns of spinal cord (Vulchanova et al., 2010). In line with this observation, fibers in the spinal trigeminal tract are likely to have originated from neurons in the trigeminal ganglion. In vestibular nuclei and the solitary nuclear complex (**Figure 2B**), GFP-ir was found in neuronal cell bodies as well as fibers. GFP expression was also observed in cochlear and facial nuclei, and the area postrema (not shown).

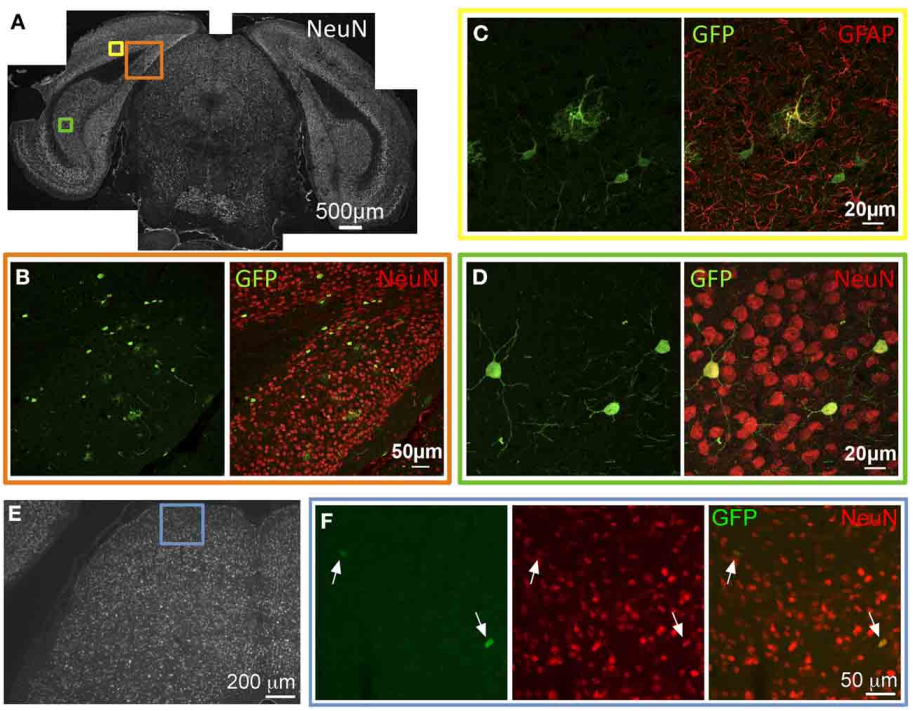

FIGURE 4 | GFP-ir in caudal cortex and midbrain. (A–D) Co-localization of GFP with neuronal and astroglial markers in caudal cortex. **(A)** Low magnification image of NeuN-ir and colored inset boxes illustrate the locations of images in **(B–D)** (approximately −4.2 mm Bregma). **(B)** GFP-ir in cells across areas of primary visual cortex (v), retrosplenial cortex (rs), and presubiculum (prs). **(C)** Co-localization of GFP-ir with GFAP-ir illustrates that astrocytes are transduced, and can be distinguished by their morphology. **(D)** GFP-ir in neurons of the subiculum as evidenced by colocalization with NeuN-ir. **(E,F)** GFP-ir in isolated neurons in the superior colliculus. Arrows indicate GFP-positive neurons.

In cerebellum, GFP-ir was observed in Purkinje cells (**Figure 3**), as well as cell bodies and fibers of the granular cell layer (not shown). Quantification of GFP-ir Purkinje cells co-labeled for calbindin showed a trend toward decreasing transduction of Purkinje cells in caudal-to-rostral fashion (**Figure 3D**). Although this trend did not reach significance, it supports the hypothesis that vector is distributed partially via rostral movement through CSF.

GFP expression was observed in several areas of the caudal cortices including primary and secondary visual cortex, retrosplenial cortex, presubiculum, parasubiculum, subiculum, and entorhinal cortex. In these locations, GFP-ir was seen in both neurons and astrocytes as evidenced by co-localization of GFP-ir with NeuN-ir or GFAP-ir respectively (**Figures 4A–D**). GFP-ir in midbrain, thalamus, and hypothalamus was predominantly limited to neurons, with the exception of astrocytes in the cerebral peduncles. In midbrain, GFP expression was minimal and observed primarily in isolated neurons within the intermediate gray matter of superior colliculus (**Figures 4E,F**).

In the most caudal portions of the hippocampus, (as seen in **Figure 5A**) GFP expression was found in granule cells of the dentate gyrus (**Figure 5B**), as well as pyramidal cells of the CA3 region (**Figure 5C**). The same tissue section shows GFP- ir in neurons of the medial geniculate nucleus (**Figures 5D,E**) of the thalamus, as well as in pontine nuclei (**Figures 5F,G**). The most rostral sections of hippocampus (as seen in **Figure 6A**) revealed many GFP-positive neuronal cell bodies only in the ventral portions (**Figure 6B**), whereas the dorsal portions contained primarily fiber-like staining in the molecular layer of the dentate gyrus and the stratum lacunosum-moleculare of the hippocampus proper (**Figure 6E**). Some GFP-expressing neurons were also observed in the amygdaloid nuclear complex (**Figure 6C**). A few neurons and some neuronal fibers were also observed in the pretectal, lateral geniculate, and posterior nuclei of thalamus (**Figure 6E**, dorsolateral surface of thalamus indicated by arrows). Labeling of non-neuronal cells, possibly astrocytes based on cell morphology similar to that shown in **Figure 4C**, in the cerebral peduncles is shown in **Figures 6B,C** (cp). In hypothalamus, GFP-ir was limited to isolated neurons (**Figure 7**).

Evaluation of tissue sections in more rostral regions of neocortex revealed that GFP expression became less prevalent with labeling present only in isolated neurons and non-neuronal cells, which appeared to be astrocytes based on morphology. (**Figure 8**). GFP-ir was generally absent from striatum and minimal in surrounding neocortex. Sparse GFP-ir was seen in the islands of Calleja, the olfactory tubercles, and more rostrally in orbital cortex (not shown). In the olfactory bulbs expression of GFP was considerable, and was found in neurons and

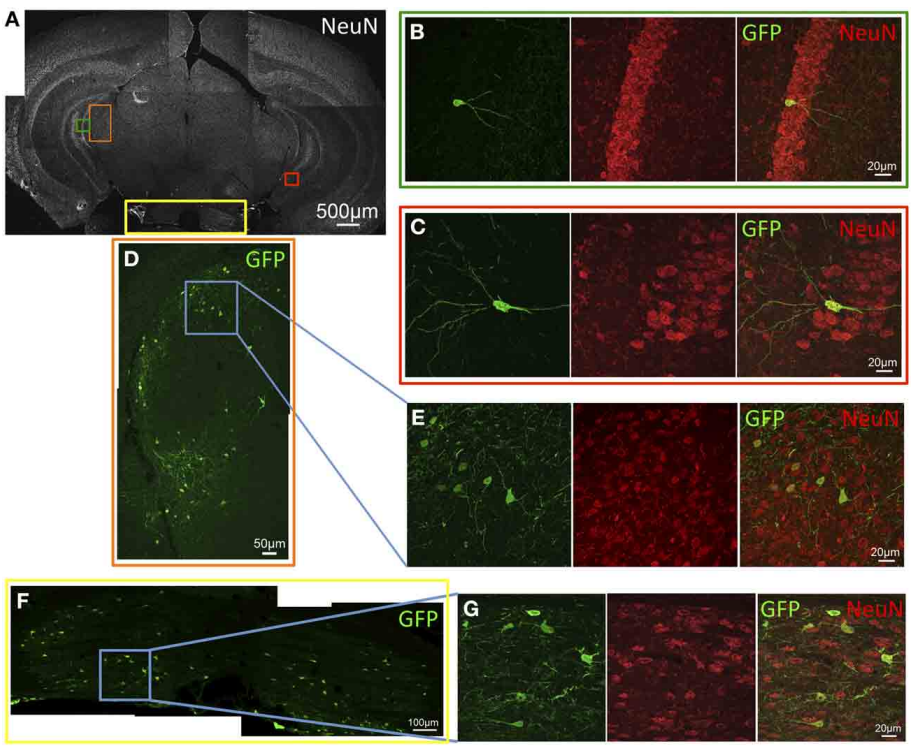

FIGURE 5 | GFP-ir in the caudal thalamus, hippocampal formation, and pons. (A) Low magnification image of NeuN-ir and colored inset boxes illustrate the locations of images in B-G (approximately −3.0 mm Bregma). **(B–G)** Green shows GFP-ir, red shows NeuN-ir, and merged images illustrate co-localization in yellow. **(B)** A GFP-positive neuron in the granular layer of the dentate gyrus. **(C)** A GFP-positive neuron in the pyramidal layer of hippocampus area CA3. **(D)** GFP-ir in the medial geniculate nucleus (MGN) of the thalamus. **(E)** High magnification image of the area outlined by the blue box in D, illustrating that expression in the MGN is neuronal. **(F)** GFP expression in pontine nuclei. **(G)** High magnification image of the area outlined by the blue box in F, illustrating co-localization with NeuN-ir.

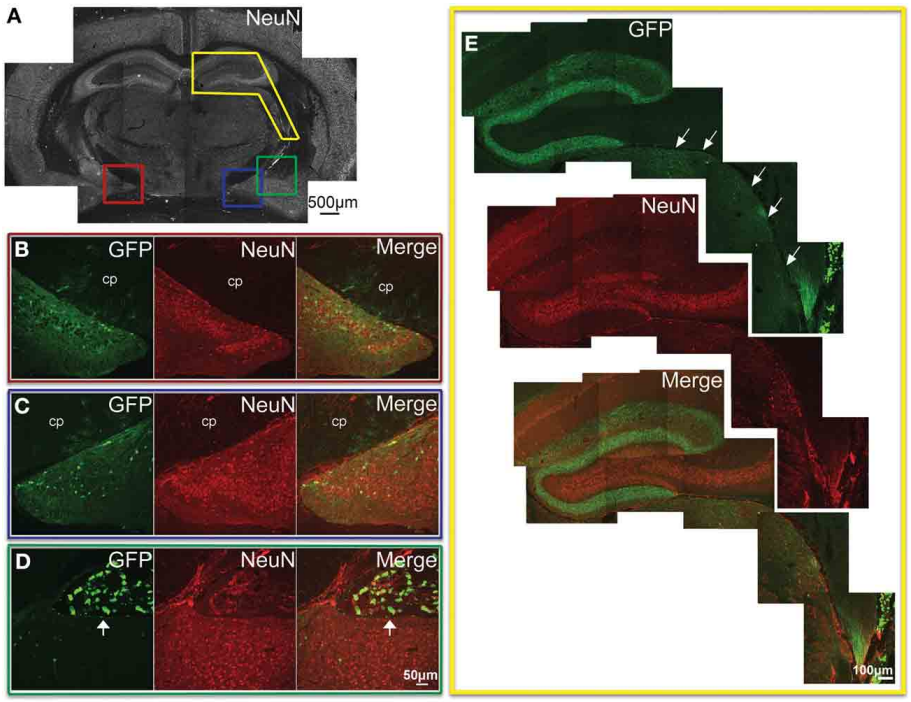

FIGURE 6 | GFP-ir in the hippocampal formation, amygdala, and thalamus. **(A)** Low magnification image of NeuN-ir and colored inset boxes illustrate the locations of images in **(B–D)** (approximately −1.9 mm Bregma). **(B)** Substantial GFP-ir in neurons of the ventral dentate gyrus, ventral hippocampus, and superior to those, astrocytes in the cerebral peduncle (cp). **(C)** GFP expression in the amygdalohippocampal area, and superior to that, astrocytes in the cerebral peduncle (cp). **(D)** GFP-ir in the amygdaloid nuclear complex, and superior to that, in choroid plexus of the lateral ventricle (arrow). **(E)** GFP-ir in the dorsal hippocampal formation, and inferior and lateral to that (arrows), in thalamus including portions of the lateral geniculate, and posterior nuclei. Note that GFP-ir in the dorsal hippocampal formation appears restricted to fibers in the molecular layer of the dentate gyrus and the stratum lacunosum-moleculare of the hippocampus.

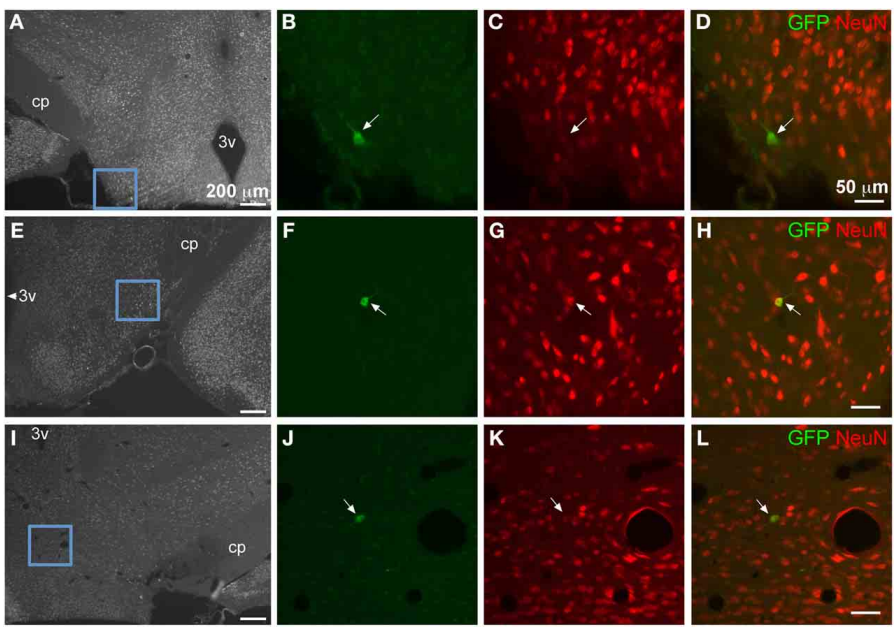

FIGURE 7 | GFP-ir in isolated neurons in hypothalamus. Blue insets in **(A,E,I)** show the location of the corresponding higher magnification images relative to the third ventricle (3v) and the cerebral peduncle (cp). Green shows GFP-ir, red shows NeuN-ir, and merged images illustrate co-localization in yellow. Neurons within lateral hypothalamus are shown in **(B–D)** and **(F–H)**. **(J–L)** show a neuron in the supramammillary complex. All arrows indicate GFP-positive neurons.

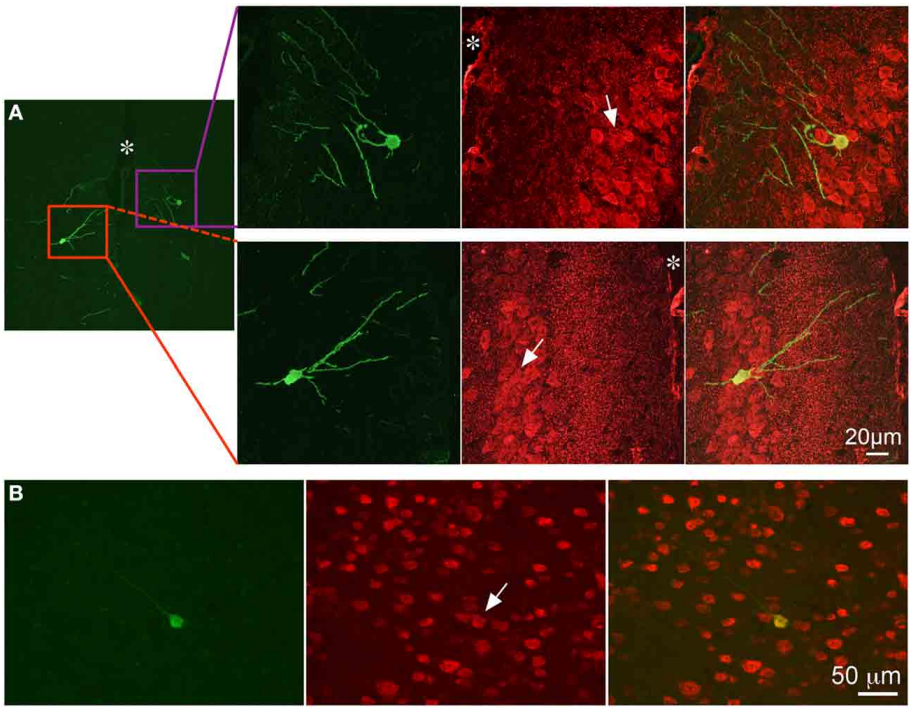

FIGURE 8 | GFP-ir in neocortex. Colocalization of GFP-ir (green) and NeuN-ir (red) in cingulate cortex (**A**, * indicates the location of the median fissure) and somatosensory cortex **(B)**. All arrows indicate GFP-positive neurons.

non-neuronal cells with astrocytic morphology in the medial portions of the glomerular, external plexiform, and mitral cell layers (**Figure 9**).

GFP-ir was evident in the choroid plexus (**Figure 10** – 4th ventricle; **Figure 6D**, arrow – lateral ventricle), the structure that produces and secretes cerebrospinal fluid (CSF). Quantification of transduced choroid plexus cells throughout the ventricular system revealed that expression in the fourth ventricle was significantly higher than in the third or lateral ventricles (**Figure 10D**). This finding indicates that rostral movement through CSF from the injection site is an important factor in vector distribution.

DISCUSSION

In this report we have demonstrated AAV5-mediated gene transfer to the CNS using direct lumbar puncture intrathecal injection. Although GFP labeling was present throughout the rostro-caudal extent of the neuraxis, transgene expression was non-uniform and restricted to discrete brain regions. We have considered several factors that may influence the distribution of viral particles and the observed pattern of AAV5 transduction in the CNS.

We observed a caudal-to-rostral gradient of GFP expression within certain brain structures. For example, we found that a significantly larger portion of fourth ventricle choroid plexus cells express GFP relative to the third and lateral ventricles after AAV5. Considering the closer proximity of the fourth ventricle to the injection site, these results suggest that virus particles become less concentrated as they move through CSF rostral to the spinal column. Consistent with this observation, in cerebellum there appears to be a caudal to rostral trend from higher to lower number of GFP-expressing Purkinje cells.

The expression of vector genes or protein products in peripheral tissues suggests that intrathecally delivered viral vectors may also be distributed through the vascular system. We have consistently observed GFP expression in liver in our experiments (not shown), which is in line with previous reports of lumbar intrathecal AAV administration (Towne et al., 2009; Gray et al., 2013). These observations raise the possibility that some of the CNS expression observed may be the result of virus that has been distributed through the circulatory system. To address this hypothesis, we injected the same total dose of AAV5 that was given intrathecally, but delivered it intravenously after mannitol pretreatment. With this method we saw no detectable expression in the CNS (not shown). These results suggest that the vector does not regain access to the CNS after entering the peripheral circulation following intrathecal delivery at the doses we have used.

A remarkable finding that is not consistent with a simple caudal-to-rostral distribution of virus particles through the CSF is the relatively high (compared to other rostral forebrain regions) level of GFP expression in the medial portion of the olfactory bulb. Although the mechanism by which this level of expression is achieved is unknown, other groups have reported similar findings after injection of other AAV serotypes (AAV1 and AAV2) into either the posterior cistern or the lumbar intrathecal space (Fu et al., 2003; Watson et al., 2006; Iwamoto et al., 2009). Considering the position of the olfactory bulb in a small recess

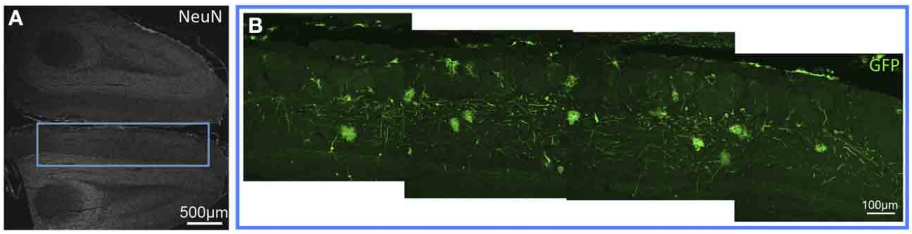

FIGURE 9 | GFP-ir in the olfactory bulb. (A) Low magnification image showing NeuN-ir. **(B)** GFP-ir in neurons and astrocytes of the glomerular, external plexiform, and mitral cell layers of the medial olfactory bulb.

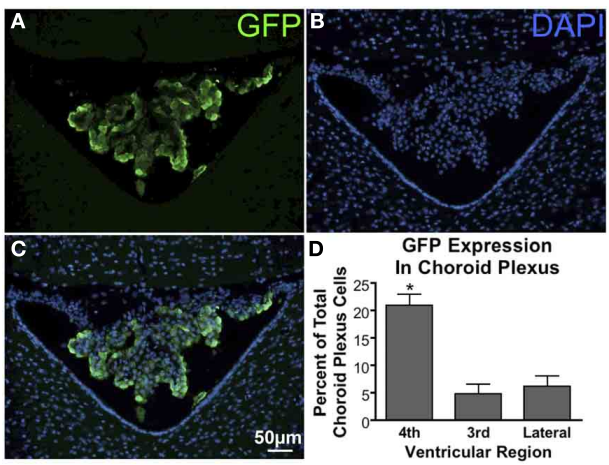

FIGURE 10 | GFP expression in the choroid plexus. (A) GFP-ir in choroid plexus of the 4th ventricle. **(B)** DAPI staining in the same section showing cellular nuclei in the choroid plexus (center), cerebellum (top), and medulla (bottom left and right). **(C)** Overlay of images in **(A)** and **(B)** showing a substantial portion of the choroid plexus cells to be transduced. **(D)** Graph illustrating that transduction of choroid plexus cells is significantly higher in the 4th ventricle compared to the third and lateral ventricles. *Indicates significance as determined by one-way ANOVA followed by Bonferroni *post-hoc* analysis, ($p < 0.001$, $n = 4$). Across all animals and ventricles 35,071 nuclei were counted, 3708 of which were identified as GFP-positive.

at the rostral end of the skull, it is possible that in this pocketed structure CSF flow may be restricted in a way that increases the retention of virus particles. In fact, it is known that CSF is able to drain along the olfactory nerve through the cribriform plate, and that this drainage constitutes a major pathway for CSF absorption in multiple species (Erlich et al., 1986; Williams and Blakemore, 1990; Kiwic et al., 1998; Mollanji et al., 2001). Significant CSF flow toward the olfactory nerve may cause virus particles following this current to get congested in the space near the olfactory bulb. An alternative explanation for the observed expression in olfactory bulb is that the cells may have migrated from the subventricular zone through the rostral migratory stream. We observed little to no GFP-ir in the subventricular zone (not shown); however, as tissue was examined 6 weeks after vector injection, we cannot rule out the possibility that GFP-positive cells in olfactory bulb may have been transduced in the subventricular zone prior to migration through the rostral migratory stream.

Another brain region with a noteworthy expression pattern that was non-uniform within the structure was the hippocampal formation. GFP-positive cell bodies (primarily neuronal) were found in the hippocampal formation, and were most prevalent in the rostral-ventral region. Although GFP-ir was also present in the rostral-dorsal hippocampal formation, labeling was primarily neuropil-like, and rarely found in neuronal cell bodies. This suggests that the fiber staining originates from neuronal cell bodies in another location, most likely the entorhinal cortex, where GFP-positive neurons were observed. It is unclear why neurons in ventral hippocampus were transduced much more efficiently that in dorsal hippocampus. One possible explanation is variation in the level of expression of cell surface receptors for virus particles. For AAV5, there are two known receptors: α2,3 N-linked sialic acid and platelet-derived growth factor receptor (PDGFR) types alpha and beta (Walters et al., 2001; Di Pasquale et al., 2003). There is currently no literature directly describing the pattern of expression of α2,3 N-linked sialic acid in the mouse brain. We have previously used lectin-histochemistry to investigate α2,3 N-linked sialic acid in DRG and observed diffuse staining with no apparent relationship between labeling intensity and expression of vector-delivered GFP (unpublished observations). For both PDGFR alpha and beta, high expression levels have been reported in CNS regions where AAV5 transduction was limited or absent in our experiments, suggesting that PDGFR is not the limiting factor for transduction by AAV5 in the CNS (Fruttiger et al., 1999; Ishii et al., 2006). Though we cannot make a direct link between AAV5 receptor expression and our observed transduction pattern, the dorsal and ventral hippocampus have been shown to differ both in function and molecular expression (Fanselow and Dong, 2010). Additionally, we have previously shown in dorsal root ganglia that AAV5 differentially targets subpopulations of DRG neurons that are defined by differences in molecular expression and function (Vulchanova et al., 2010). Our observations in the hippocampal formation may also reflect AAV vector tropism for specific cellular subpopulations.

One anatomical feature of the CNS that could explain differences in expression across brain regions is parenchymal permeability due to differences in the structure of the pia mater. Although it has been reported that the organization of the pia mater varies substantially (Morse and Low, 1972), this variability has not been examined systematically. Moreover, there is evidence for the presence of fenestrations within the pia mater, which, at least at the level of spinal cord, appear to be differentially

distributed (Reina et al., 2004). Interestingly, the lack of fenestrations at thoracic levels correlates with the reduced transduction frequency at thoracic levels compared to lumbar and cervical levels (Towne et al., 2009; Vulchanova et al., 2010), supporting the idea that differential membrane permeability may influence the distribution of viral vector delivered intrathecally.

In summary, the pattern of transduction in the CNS following intrathecal administration of an AAV vector with an intravenous mannitol pretreatment appears to be the result of several factors discussed above, including: rostral movement through CSF, overall CSF flow, membrane permeability, and expression of cell surface receptors for virus particles. The current study has revealed that under these specific spinal drug delivery conditions, discrete brain areas appear to be transduced by AAV5.

AUTHOR CONTRIBUTIONS

Daniel J. Schuster participated in perfusions and dissections, performed immunohistochemistry, imaging, cell quantification, and some of the intravenous injections. He analyzed the data, prepared the figures, participated in interpretation of the results, and drafted and edited the manuscript. Lalitha R. Belur initiated the studies and contributed to the experimental design and edited the manuscript. Maureen S. Riedl performed all perfusions and dissections and participated in histochemical analyses and interpretation of results. Stephen A. Schnell contributed to data analysis and figure preparation. Kelly M. Podetz-Pedersen performed some of the IV injections. Kelley F. Kitto conducted all intrathecal injections of vector and is responsible for the quality assurance of this key technique. R. Scott McIvor initiated the study with CF as collaborators and edited the manuscript. Lucy Vulchanova participated in all perfusions and dissections, as well as contributed to the experimental design, histochemical analyses, interpretation of results, generation of figures, and editing of the manuscript. Carolyn A. Fairbanks organized the team, contributed to the experimental design, edited the manuscript, and supported the studies.

ACKNOWLEDGMENTS

The authors would like to thank Galina Kalyuzhnaya for her technical assistance, and Caroline Churchill for valuable discussion. The National Institute on Drug Abuse (DA025164 to Carolyn A. Fairbanks; K01DA017236 to Lucy Vulchanova), the National Institute of Child Health and Development (HD032652 to R. Scott McIvor), the National Institute of Neurological Disorders and Stroke (T32 NS048944 to Timothy J. Ebner) the University of Minnesota Academic Health Center, and the University of Minnesota College of Pharmacy Engebretson Grant Award (Carolyn A. Fairbanks) supported this work. An individual NRSA from the National Institute of Neurological Disorders and Stroke (F31NS063634) and a 3M Fellowship supported Daniel J. Schuster.

REFERENCES

Ciesielska, A., Mittermeyer, G., Hadaczek, P., Kells, A. P., Forsayeth, J., and Bankiewicz, K. S. (2011). Anterograde axonal transport of AAV2-GDNF in rat basal ganglia. *Mol. Ther.* 19, 922–927. doi: 10.1038/mt.2010.248

Di Pasquale, G., Davidson, B. L., Stein, C. S., Martins, I., Scudiero, D., Monks, A., et al. (2003). Identification of PDGFR as a receptor for AAV-5 transduction. *Nat. Med.* 9, 1306–1312. doi: 10.1038/nm929

Erlich, S. S., McComb, J. G., Hyman, S., and Weiss, M. H. (1986). Ultrastructural morphology of the olfactory pathway for cerebrospinal fluid drainage in the rabbit. *J. Neurosurg.* 64, 466–473. doi: 10.3171/jns.1986.64.3.0466

Fanselow, M. S., and Dong, H. W. (2010). Are the dorsal and ventral hippocampus functionally distinct structures? *Neuron* 65, 7–19. doi: 10.1016/j.neuron.2009.11.031

Fruttiger, M., Karlsson, L., Hall, A. C., Abramsson, A., Calver, A. R., Bostrom, H., et al. (1999). Defective oligodendrocyte development and severe hypomyelination in PDGF-A knockout mice. *Development* 126, 457–467.

Fu, H., Muenzer, J., Samulski, R. J., Breese, G., Sifford, J., Zeng, X., et al. (2003). Self-complementary adeno-associated virus serotype 2 vector: global distribution and broad dispersion of AAV-mediated transgene expression in mouse brain. *Mol. Ther.* 8, 911–917. doi: 10.1016/j.ymthe.2003.08.021

Fu, H., Samulski, R. J., McCown, T. J., Picornell, Y. J., Fletcher, D., and Muenzer, J. (2002). Neurological correction of lysosomal storage in a mucopolysaccharidosis IIIB mouse model by adeno-associated virus-mediated gene delivery. *Mol. Ther.* 5, 42–49. doi: 10.1006/mthe.2001.0514

Gray, S. J., Nagabhushan Kalburgi, S., McCown, T. J., and Jude Samulski, R. (2013). Global CNS gene delivery and evasion of anti-AAV-neutralizing antibodies by intrathecal AAV administration in non-human primates. *Gene Ther.* 20, 450–459. doi: 10.1038/gt.2012.101

Hylden, J. L., and Wilcox, G. L. (1980). Intrathecal morphine in mice: a new technique. *Eur. J. Pharmacol.* 67, 313–316. doi: 10.1016/0014-2999(80)90515-4

Ishii, Y., Oya, T., Zheng, L., Gao, Z., Kawaguchi, M., Sabit, H., et al. (2006). Mouse brains deficient in neuronal PDGF receptor-beta develop normally but are vulnerable to injury. *J. Neurochem.* 98, 588–600. doi: 10.1111/j.1471-4159.2006.03922.x

Iwamoto, N., Watanabe, A., Yamamoto, M., Miyake, N., Kurai, T., Teramoto, A., et al. (2009). Global diffuse distribution in the brain and efficient gene delivery to the dorsal root ganglia by intrathecal injection of adeno-associated viral vector serotype 1. *J. Gene Med.* 11, 498–505. doi: 10.1002/jgm.1325

Kaemmerer, W. F., Reddy, R. G., Warlick, C. A., Hartung, S. D., McIvor, R. S., and Low, W. C. (2000). *In vivo* transduction of cerebellar Purkinje cells using adeno-associated virus vectors. *Mol. Ther.* 2, 446–457. doi: 10.1006/mthe.2000.0134

Kiwic, G., Slusarczyk, K., and Slusarczyk, R. (1998). The central nervous system and the lymphatic system. Lymphatic drainage of the cerebrospinal fluid. *Neurol. Neurochir. Pol.* 32, 633–641.

Mollanji, R., Bozanovic-Sosic, R., Silver, I., Li, B., Kim, C., Midha, R., et al. (2001). Intracranial pressure accommodation is impaired by blocking pathways leading to extracranial lymphatics. *Am. J. Physiol. Regul. Integr. Comp. Physiol.* 280, R1573–R1581.

Morse, D. E., and Low, F. N. (1972). The fine Structure of the pia mater of the rat. *Am. J. Anat.* 133, 349–367.

Paxinos, G., and Franklin, K. B. J. (2001). *The Mouse Brain in Stereotaxic Coordinates*. San Diego, CA: Academic Press.

Reina, M. A., De Leon Casasola Ode, L., Villanueva, M. C., Lopez, A., Maches, F., and De Andres, J. A. (2004). Ultrastructural findings in human spinal pia mater in relation to subarachnoid anesthesia. *Anesth. Analg.* 98, 1479–1485. doi: 10.1213/01.ANE.0000113240.09354.E9

Storek, B., Reinhardt, M., Wang, C., Janssen, W. G., Harder, N. M., Banck, M. S., et al. (2008). Sensory neuron targeting by self-complementary AAV8 via lumbar puncture for chronic pain. *Proc. Natl. Acad. Sci. U.S.A.* 105, 1055–1060. doi: 10.1073/pnas.0708003105

Towne, C., Pertin, M., Beggah, A. T., Aebischer, P., and Decosterd, I. (2009). Recombinant adeno-associated virus serotype 6 (rAAV2/6)-mediated gene transfer to nociceptive neurons through different routes of delivery. *Mol. Pain* 5:52. doi: 10.1186/1744-8069-5-52

Vulchanova, L., Riedl, M. S., Shuster, S. J., Stone, L. S., Hargreaves, K. M., Buell, G., et al. (1998). P2X3 is expressed by DRG neurons that terminate in inner lamina II. *Eur. J. Neurosci.* 10, 3470–3478. doi: 10.1046/j.1460-9568.1998.00355.x

Vulchanova, L., Schuster, D. J., Belur, L. R., Riedl, M. S., Podetz-Pedersen, K. M., Kitto, K. F., et al. (2010). Differential adeno-associated virus mediated gene

transfer to sensory neurons following intrathecal delivery by direct lumbar puncture. *Mol. Pain* 6:31. doi: 10.1186/1744-8069-6-31

Walters, R. W., Yi, S. M., Keshavjee, S., Brown, K. E., Welsh, M. J., Chiorini, J. A., et al. (2001). Binding of adeno-associated virus type 5 to 2,3-linked sialic acid is required for gene transfer. *J. Biol. Chem.* 276, 20610–20616. doi: 10.1074/jbc.M101559200

Watson, G., Bastacky, J., Belichenko, P., Buddhikot, M., Jungles, S., Vellard, M., et al. (2006). Intrathecal administration of AAV vectors for the treatment of lysosomal storage in the brains of MPS I mice. *Gene Ther.* 13, 917–925.

White, E. A., Bienemann, A. S., Sena-Esteves, M., Taylor, H., Bunnun, C., Castrique, E. S., et al. (2011). Evaluation and optimisation of the administration of recombinant adeno-associated viral vectors (Serotypes 2/1, 2/2, 2/rh8, 2/9 and 2/rh10) by convection-enhanced delivery to the striatum. *Hum. Gene Ther.* 22, 237–251. doi: 10.1089/hum.2010.129

Williams, A. E., and Blakemore, W. F. (1990). Pathology of Streptococcal meningitis following intravenous intracisternal and natural routes of infection. *Neuropathol. Appl. Neurobiol.* 16, 345–356. doi: 10.1111/j.1365-2990.1990.tb01268.x

Zolotukhin, S., Potter, M., Zolotukhin, I., Sakai, Y., Loiler, S., Fraites, T. J. Jr., et al. (2002). Production and purification of serotype 1, 2, and 5 recombinant adeno-associated viral vectors. *Methods* 28, 158–167. doi: 10.1016/S1046-2023(02)00220-7

Conflict of Interest Statement: The authors declare that the research was conducted in the absence of any commercial or financial relationships that could be construed as a potential conflict of interest.

Received: 25 January 2014; accepted: 23 June 2014; published online: 05 August 2014. Citation: Schuster DJ, Belur LR, Riedl MS, Schnell SA, Podetz-Pedersen KM, Kitto KF, McIvor RS, Vulchanova L and Fairbanks CA (2014) Supraspinal gene transfer by intrathecal adeno-associated virus serotype 5. Front. Neuroanat. ***8****:66. doi: 10.3389/fnana.2014.00066*

This article was submitted to the journal Frontiers in Neuroanatomy.

frontiers in
NEUROANATOMY

ORIGINAL RESEARCH ARTICLE
published: 10 June 2014
doi: 10.3389/fnana.2014.00042

Biodistribution of adeno-associated virus serotype 9 (AAV9) vector after intrathecal and intravenous delivery in mouse

Daniel J. Schuster[1], Jaclyn A. Dykstra[2], Maureen S. Riedl[1], Kelley F. Kitto[1], Lalitha R. Belur[3], R. Scott McIvor[3], Robert P. Elde[1], Carolyn A. Fairbanks[1,4] and Lucy Vulchanova[1]*

[1] *Departments of Neuroscience, University of Minnesota, Minneapolis, MN, USA*
[2] *Department of Veterinary and Biomedical Sciences, University of Minnesota, Saint Paul, MN, USA*
[3] *Departments of Genetics Cell Biology and Development, University of Minnesota, Minneapolis, MN, USA*
[4] *Departments of Pharmaceutics, University of Minnesota, Minneapolis, MN, USA*

Edited by:
Laurent Gautron, University of Texas Southwestern Medical Center, USA

Reviewed by:
Yoland Smith, Emory University, USA
Chen Liu, University of Texas Southwestern Medical Center at Dallas, USA

****Correspondence:***
Lucy Vulchanova, Departments of Neuroscience, University of Minnesota, 6-145 Jackson Hall, 321 Church St. Se, Minneapolis, MN 55455, USA
e-mail: vulch001@umn.edu

Adeno-associated virus serotype 9 (AAV9)-mediated gene transfer has been reported in central nervous system (CNS) and peripheral tissues. The current study compared the pattern of expression of Green Fluorescent Protein (GFP) across the mouse CNS and selected peripheral tissues after intrathecal (i.t.) or intravenous (i.v.) delivery of equivalent doses of single-stranded AAV9 vector. After i.t. delivery, GFP immunoreactivity (-ir) was observed in spinal neurons, primary afferent fibers and corresponding primary sensory neurons at all spinal levels. Robust transduction was seen in small and large dorsal root ganglion (DRG) neurons as well as trigeminal and vagal primary afferent neurons. Transduction efficiency in sensory ganglia was substantially lower in i.v. treated mice. In brain, i.v. delivery yielded GFP-immunoreactivity (-ir) primarily in spinal trigeminal tract, pituitary, and scattered isolated neurons and astrocytes. In contrast, after i.t. delivery, GFP-ir was widespread throughout CNS, with greater intensity and more abundant neuropil-like staining at 6 weeks compared to 3 weeks. Brain regions with prominent GFP-ir included cranial nerve nuclei, ventral pons, cerebellar cortex, hippocampus, pituitary, choroid plexus, and selected nuclei of midbrain, thalamus and hypothalamus. In cortex, GFP-ir was associated with blood vessels, and was seen in both neurons and astrocytes. In the periphery, GFP-ir in colon and ileum was present in the enteric nervous system in both i.v. and i.t. treated mice. Liver and adrenal cortex, but not adrenal medulla, also showed abundant GFP-ir after both routes of delivery. In summary, i.t. delivery yielded higher transduction efficiency in sensory neurons and the CNS. The observation of comparable gene transfer to peripheral tissues using the two routes indicates that a component of i.t. delivered vector is redistributed from the subarachnoid space to the systemic circulation.

Keywords: adeno-associated, AAV9, intrathecal, intravenous, CNS, DRG, trigeminal

INTRODUCTION

Adeno-associated virus serotype 9 (AAV9) vector has engendered considerable interest in its therapeutic development for treating neurological disorders (Dayton et al., 2012), in part because it has been heralded as capable of traversing the blood brain barrier to target the central nervous system (CNS), where it has been shown to transduce astrocytes and neurons (Foust et al., 2009; Gray et al., 2011; Samaranch et al., 2013). Enthusiasm for using AAV9-mediated gene therapy for global CNS transduction or targeting of specific neuronal populations has lead to investigations on the optimal route of administration to the CNS, scalability from rodent models to larger animal species, and appropriate promoters for broad distribution, cell-specific targeting, or improved duration of expression (Gray et al., 2011; Snyder et al., 2011; Federici et al., 2012; Samaranch et al., 2012, 2013; Dirren et al., 2014). Whereas the intravenous route of delivery of AAV9 has been examined extensively and successfully utilized in models of neurological disorders (Foust et al., 2009; Fu et al., 2011; Ruzo et al., 2012; Garg et al., 2013; Shen et al., 2013; Yamashita et al., 2013; Elmallah et al., 2014), AAV9 administration into the CSF has been employed less frequently in rodents (Snyder et al., 2011; Haurigot et al., 2013; Hirai et al., 2014), and the biodistribution of the vector following intrathecal delivery has not been fully characterized. This direct CNS route of administration offers advantages such as reduction in the vector dose required for CNS transduction, and potentially restricted distribution, minimizing off-target effects (Gray et al., 2011, 2013; Snyder et al., 2011; Samaranch et al., 2013).

We and others have shown that delivery of AAV vectors within the lumbar intrathecal space leads to expression of green fluorescent protein (GFP) in dorsal root ganglion (DRG) neurons as well as brain and peripheral tissues (Storek et al., 2008; Towne et al., 2009; Mason et al., 2010; Vulchanova et al., 2010; Schuster et al., 2013). Although AAV9-mediated transduction of primary sensory neurons has been previously reported in rodents and

non-human primates (Hirai et al., 2012, 2014; Gray et al., 2013), the pattern of AAV9-driven transgene expression in sensory ganglia has not been thoroughly examined. In the present study, we evaluated the ability of AAV9 to transduce primary sensory neurons as well as its distribution to brain regions due to rostral flow of CSF when delivered intrathecally by direct lumbar puncture. In addition, we examined the extent of GFP expression in selected peripheral organs and tissues to assess potential systemic redistribution of the vector or transport of the transgene in peripheral nerves. We hypothesized that, in comparison to titer-matched intravenous delivery, intrathecal administration of AAV9-GFP will result in enhanced transduction of primary sensory neurons, spinal cord and brain and reduced transduction in peripheral tissues and organs.

MATERIALS AND METHODS

VECTOR

AAV9-GFP was purchased from the vector core at the University of Pennsylvania (AAV9.CB7.Cl.eGFP.WPRE.rBG; cat # AV-9-PV1963).

ANIMALS

Experimental subjects were 20–25 g adult male C57BL/6 mice (6–8 weeks old at the time of treatment; Harlan, Madison, WI). All experiments were reviewed and approved by the Institutional Animal Care and Use Committee (IACUC) of the University of Minnesota.

INJECTIONS

For the comparison of intrathecal (i.t.) and intravenous (i.v.) delivery in the presence or absence of mannitol, 16 mice were divided into four groups: mannitol +i.v. injection, mannitol + i.t. injection, i.t. injection only, and i.v. injection only. *Mannitol pretreatment*: Mannitol is a hyperosmotic agent that enhances intraparenchymal diffusion following intracerebroventricular (i.c.v.) injection of AAV particles (Mastakov et al., 2002; Fu et al., 2003). Previously, we observed that mannitol pretreatment enhanced AAV5-mediated transduction of primary sensory neurons (Vulchanova et al., 2010) and in the present study sought to determine whether it also impacts AAV9 particle distribution. Subjects were injected via the tail vein with 25% mannitol solution (200 μL) 20 min prior to i.t. or i.v. injection of AAV9-GFP. *Intravenous delivery:* AAV9-GFP ($\sim 3.3 \times 10^{11}$ vector genomes) was diluted 10-fold in sterile saline for a final injectate volume of 100 μL, injected via the tail vein. *Intrathecal delivery:* AAV9-GFP (10 μL containing $\sim 3.3 \times 10^{11}$ vector genomes) was delivered by direct lumbar puncture in awake mice as previously described (Hylden and Wilcox, 1981; Fairbanks, 2003; Vulchanova et al., 2010). In addition, 4 mice were injected i.t. with a reduced AAV9-GFP dose ($\sim 6.6 \times 10^{9}$ vector genomes) following mannitol pretreatment. Three weeks after injection, mice were subjected to transcardial perfusion fixation. Prior to the 3-week endpoint one mouse from the mannitol + i.t. injection group was euthanized due to seizures. Finally, four mice received mannitol + i.t. injection (1.73×10^{11} vector genomes) and were evaluated 6 weeks after vector delivery.

IMMUNOHISTOCHEMISTRY

All animals were sacrificed by perfusion fixation as previously described (Vulchanova et al., 1997). Briefly, animals were deeply anaesthetized and perfused with a solution of calcium-free tyrodes solution (in mM:NaCl 116, KCl 5.4, $MgCl_2 \cdot 6H_20$ 1.6, $MgSO_4 \cdot 7H_2O$ 0.4, NaH_2PO_4 1.4, glucose 5.6, and $NaHCO_3$ 26) followed by fixative (4% paraformaldehyde and 0.2% picric acid in 0.1 M phosphate buffer, pH 6.9). Tissues were removed and stored in PBS containing 10% sucrose and 0.05% sodium azide at 4°C until further use. Sections were cut at 14 μm thickness and thaw mounted onto gel-coated slides. Tissue sections were incubated for 1 h at room temperature in diluent (PBS containing 0.3% Triton, 1% BSA, 1% normal donkey serum) and then incubated overnight at 4°C in primary antisera diluted in the same solution. Primary antibodies used were: chicken anti-GFP, 1:1000 (Abcam, cat# 13970; specificity confirmed by lack of labeling in the absence of AAV9-GFP treatment); rabbit anti-GFP, 1:500 (Invitrogen; Eugene, OR; specificity confirmed by lack of labeling in the absence of AAV9-GFP treatment); rabbit anti-GFAP, 1:1000 (ICN, Costa Mesa, CA; pattern of labeling equivalent to that obtained with a mouse anti-GFAP antibody and consistent with exclusive staining of astrocytes); rabbit anti-Iba1 [Wako Chemicals USA, Inc.; cat# 019-1974; specificity established based on Western blot (Imai et al., 1996) and colocalization with other microglial markers (Ito et al., 1998)]; rabbit anti-calcitonin gene related peptide (CGRP), 1:1000 (ImmunoStar, Hudson WI, cat# 24112; specificity established by preabsorption with CGRP and unrelated peptides—manufacturer's information); guinea pig anti-P2X3, 1:1000 [the generation and specificity of this antiserum is described in (Vulchanova et al., 1997)]; rat anti-substance P (SP), 1:100, [Abd Serotec, Oxford, UK; the specificity of this antibody is described in (Riedl et al., 2009)]; rat anti-CD31, 1:300 (BD Pharmingen, cat# 557355; pattern of labeling consistent with staining of blood vessels). After rinsing with PBS, sections were incubated for 1 h at room temperature with appropriate combinations of Cy2-, Cy3-, and Cy5- (1:300) conjugated secondary antisera (Jackson ImmunoResearch, West Grove, CA). Sections were rinsed again, and in some cases, were also incubated with DAPI nucleic acid stain for 3–5 min, 300 nM (Invitrogen; Eugene, OR) or NeuroTrace (Invitrogen) according to manufacturer's instructions. Following the final rinses, sections were cover-slipped using glycerol and PBS containing 0.1% p-phenylenediamine (Sigma). Tissues from a naïve mouse processed in parallel with the AAV9-GFP treated tissues were included in all immunohistochemical experiments to control for non-specific staining of the GFP antibody.

MICROSCOPY

Anatomical analysis was based on the "The Mouse Brain In Stereotaxic Coordinates," Second Edition (Paxinos and Franklin, 2001) and the Mouse Brain Library C57BL/6 mouse brain atlas (Rosen et al., 2000). Images were collected on an Olympus Fluoview 1000 confocal microscope with associated software. For comparisons of tissues from i.t. and i.v. treated mice, images were collected using the same microscope setting with a few exception where adjustments were necessary to allow detection of labeling in i.v. treated tissues or avoid saturation in i.t. treated tissues.

Similarly image adjustments for contrast, brightness and color in Adobe Photoshop were performed in parallel for i.t. and i.v. treated tissues.

QUANTIFICATION OF GFP EXPRESSION IN SENSORY GANGLIA

For each ganglion, 7–8 non-overlapping images taken across 4–5 tissue sections, which were spaced by at least 56 μm, were used for analysis. Neurons were outlined based on NeuroTrace Nissl-like labeling, and only cells with a visible nucleus were counted. Measurements of GFP-ir fluorescence intensity and cell area were obtained using Image J software. The intensity measurements of unlabeled cells were used to determine the labeling threshold for unbiased identification of GFP-positive neurons. For each ganglion the number of GFP-positive neurons was determined as percentage of all neurons in the sampled sections. The data are expressed as Mean ± Standard Error. Statistical analysis was performed using GraphPad Prism 5 software. Comparisons were made using One-Way ANOVA followed by Bonferroni *post-hoc* test or by *t*-test.

ANALYSIS OF HISTOPATHOLOGY

Routine hematoxylin and eosin staining was performed on cryosections mounted on gel-coated slides. For each animal in the 3-week treatment groups, 4–6 section per ganglion were evaluated by a trained, blinded observer and scored based on lesion number and severity. Lesion scoring: 0, No gross lesions; 1, Increased mononuclear cells without neuron loss; 2, Distinct nodular aggregate of mononuclear cells replacing one neuron; 3, Discrete nodular aggregates of mononuclear cells replacing more than one neuron; 4, Mononuclear infiltrates and nodular aggregates replacing at least three neurons. For each ganglion, average lesion score was calculated based on the lesion score of each of the examined sections. The data is reported as mean ± SE of the average lesion score for each experimental group. Tissues included dorsal root ganglia, spinal cord, liver, skeletal muscle, ileum, and colon.

RESULTS

AAV9-MEDIATED TRANSDUCTION OF PRIMARY SENSORY NEURONS AND THEIR CNS PROJECTION TARGETS

Three weeks after i.t. AAV9-GFP delivery, intense GFP-ir was observed at all levels of spinal cord (**Figures 1A–D**). GFP-ir fibers were abundant in dorsal horn and dorsal columns, and labeling was seen in neuronal cell bodies in both dorsal and ventral horn (**Figures 1E,F**). In contrast, i.v. delivery of the viral vector resulted in limited labeling of fibers in dorsal horn and isolated cell bodies in ventral horn (**Figures 1G,H**). Consistent with the observations in spinal cord, GFP-positive neurons were present in DRG (**Figure 2**). Quantitative image analysis indicated that 73 ± 12% of L4 DRG neurons were GFP-positive after i.t. delivery (range 47–95%, $n = 4$), compared to 9 ± 1% after i.v. delivery (range 7–10%, $n = 4$) (**Figure 4A**). Mannitol pretreatment did not significantly enhance the transduction of DRG neurons by AAV9-GFP after i.t. or i.v. delivery (**Figure 4A**). Reduction in the number of viral particles delivered i.t. (50× dilution) correspondingly lead to reduction of the number of labeled neurons to 8 ± 4% (range 2–15%, $n = 4$). Analysis of the size distribution of GFP-positive DRG neurons suggested preferential transduction of large-diameter neurons, particularly after i.t. delivery of the 1/50 dose and after i.v. delivery (**Figure 4B**). However, i.t. delivery of full-strength AAV9-GFP resulted in substantial transduction of small-diameter DRG neurons (64 ± 17% of all small-diameter neurons, range 27–94%; **Figure 4B**), which was also illustrated by the frequent colocalization of GFP-ir with the markers of peptidergic and non-peptidergic small-diameter neurons, CGRP and P2X3 (**Figures 2A–C**).

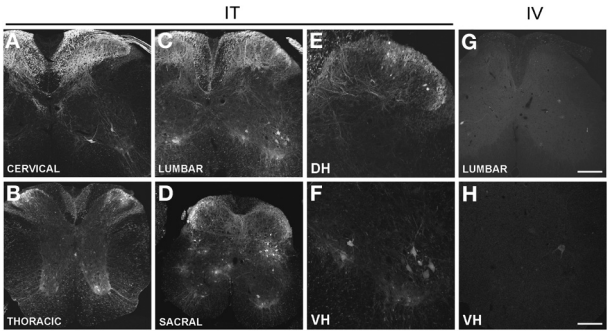

FIGURE 1 | (A–H) Localization of GFP-ir in the spinal cord 3 weeks after i.t. (IT) or i.v. (IV) delivery of AAV9-GFP without mannitol. **(A–D)**, GFP-ir in cervical **(A)**, thoracic **(B)**, lumbar **(C)**, and sacral **(D)** spinal cord after i.t. delivery. **(E,F)** GFP-ir in dorsal (DH, **E**) and ventral (VH, **F**) horn of lumbar spinal cord after i.t. delivery. **(G,H)** GFP-ir in lumbar spinal cord **(G)** and ventral horn (VH, **H**) after i.v. delivery. Scale bars: 200 μm in **(A–D)**, and **(G)**; 100 μm in (**E,F,H**).

AAV9-GFP transduction was also observed in the trigeminal sensory system (**Figures 3A–D**). Similar to spinal cord, GFP labeling in the spinal trigeminal tract and nucleus was substantially more abundant after i.t. delivery compared to i.v. delivery (**Figures 3A,C**). In trigeminal ganglia, GFP-ir was present in 52 ± 7% (range 37–69%, $n = 4$) and 21 ± 3% (range 15–27%, $n = 4$) of neurons in the i.t. and i.v. treatment groups, respectively (**Figure 4A**). Notably, the number of GFP-positive neurons after i.v. delivery was significantly higher in trigeminal ganglia compared to DRG (**Figure 4A**). As in DRG, mannitol pretreatment did not enhance the transduction of trigeminal sensory neurons. Finally, in addition to DRG and trigeminal ganglia, in i.t. treated mice GFP-ir was also seen in the vagal sensory system (**Figures 3E–G**). Labeling in the solitary tract and its associated nucleus was seen throughout their rostral-caudal extent (caudal medulla shown in **Figure 3E**). GFP-ir was also present in neurons of the nodose ganglion in i.t. treated mice. In i.v. treated mice detection of faint GFP-ir in the region of the solitary tract and nucleus was only seen using higher magnification and laser power (**Figure 3G**).

In the course of quantitative image analysis, we noted abnormal Nissl labeling, visualized by NeuroTrace, in some sections. This included intensely GFP-labeled neurons that were devoid of NeuroTrace staining (**Figures 5A,B**, arrows) as well as morphology consistent with satellite cell proliferation (**Figures 5A,B**, arrowhead). Subsequent histopathological evaluation revealed the presence of mononuclear aggregates and infiltrates in DRG, and to a lesser extent in trigeminal ganglia, of mice receiving i.t.

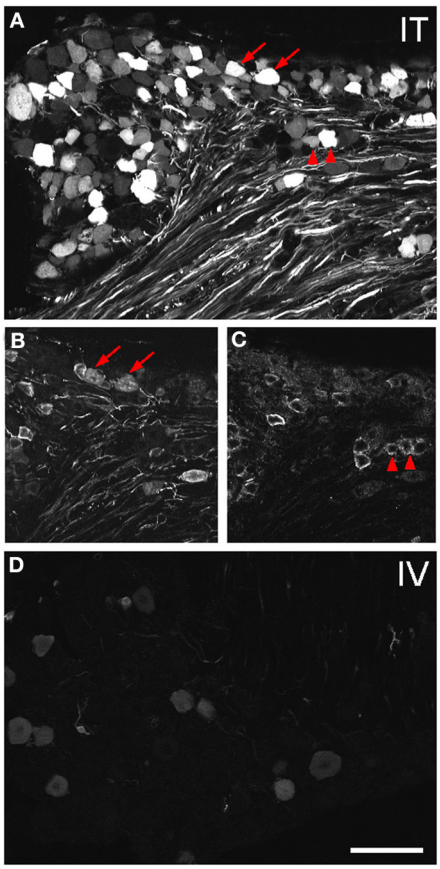

FIGURE 2 | Localization of GFP-ir in lumbar DRG 3 weeks after i.t. or i.v. delivery of AAV9-GFP without mannitol. (A–C) GFP-ir in L4 DRG after i.t. delivery and its relationship to CGRP- **(B)** and P2X3-ir **(C)** Arrows and arrowheads indicate colocalization of GFP- and CGRP-ir and GFP- and P2X3-ir, respectively. **(D)** GFP-ir in L4 DRG after i.v. delivery. Scale bar: 100 μm.

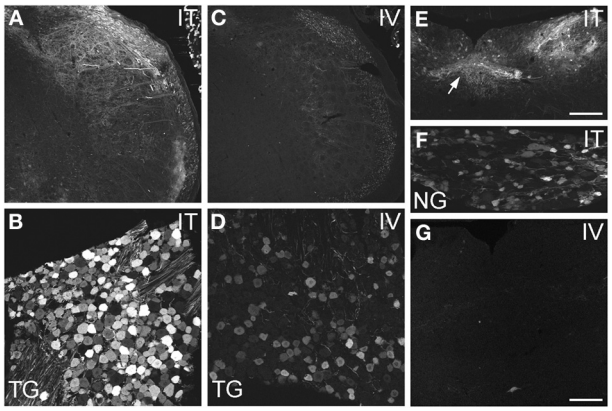

FIGURE 3 | Localization of GFP-ir in spinal trigeminal nucleus and nucleus of the solitary tract (NTS) and their corresponding sensory ganglia. (A–D) GFP-ir in the spinal trigeminal nucleus **(A,C)** and trigeminal ganglion neurons **(B,D)** after i.t. **(A,B)** or i.v. **(C,D)** delivery. **(E–G)** Localization of GFP-ir in NTS (arrows, **E**) and the nodose ganglion **(F)** after i.t. delivery, and in NTS after i.v. delivery **(G)**. Detection of labeling in G required higher magnification and laser power than in E. Scale bars: 200 μm in **(A,C,E)**; 100 μ min **(B,D,F,G)**.

AAV9. Lesions ranged in severity from infrequent, discrete nodules of residual satellite glial cells replacing solitary neurons to exuberant satellite glial cell proliferation with multifocal neuronal necrosis and loss. The mean lesion score for i.t. treated mice was 1 ± 0.8 for DRG, and 0.03 ± 0.2 for TG, and for i.t.+mannitol treated mice was 2.5 ± 1.2 for DRG and 0.8 ± 0 for TG (for the i.v. treatment groups the mean score was <0.05). A cursory examination of other tissues, including spinal cord, liver, skeletal muscle, and gut, did not reveal additional lesions.

AAV9-MEDIATED GFP EXPRESSION IN THE CNS

Expression of GFP in the CNS was examined using immunohistochemistry across several brain regions 3 weeks after intravenous (i.v.) or intrathecal (i.t.) delivery of AAV9-GFP (**Figures 6–10**). Overall, i.v. delivery of vector resulted in substantially lower GFP-ir in brain compared to i.t. delivery. In i.v. treated mice, low-intensity GFP-ir was seen in isolated neurons throughout the brain without an apparent association with specific CNS regions (**Figures 3G**, **7A2-IV**, **9B**). GFP labeling was also present in astrocytes and outlined CNS blood vessels following i.v. treatment (**Figure 9B**).

The localization of GFP-ir in brains of i.t. treated mice is described below. All brain regions where GFP-ir was observed in neuronal cell bodies are listed in **Table 1**. Unlike the scattered pattern of neuronal labeling seen after i.v. delivery, in brains from i.t. treated mice the majority of GFP-positive neurons were seen within discrete nuclei and in some cases within subdivisions of certain nuclei. However, there were also numerous instances, particularly in cortex, where clusters of intensely labeled cells were sporadically associated with blood vessels rather than with a particular anatomical region. Astrocytes were always seen in association with blood vessels. It is unclear at present what factors govern the vasculature-related access of viral particles to CNS parenchyma.

Medulla, pons, and cerebellum

Within cranial nerve (Cn) nuclei, GFP-ir was abundant in gracile, cuneate (**Figures 6B,C**), external cuneate, spinal (**Figures 3A,B**, **6B,C**), and chief sensory trigeminal nuclei as well as in the nucleus of the solitary tract (**Figures 3E,G**). Labeling was also present in vestibular and cochlear nuclei and in some motor nuclei of cranial nerves. GFP-ir in neurons and fibers appeared to be more abundant in cochlear nuclei compared to vestibular and, within the vestibular nuclear complex, more abundant in caudal than in rostral regions. In motor nuclei, GFP-ir was most prominent in neurons of the facial nucleus, followed by hypoglossal, whereas neurons of the trigeminal motor nucleus were faintly labeled. We could not establish conclusively whether GFP-ir was present in the mesensephalic trigeminal nucleus, dorsal motor nucleus of cranial nerve X (CnX), and the nuclei of CnXI, CnVI, CnIV, and CnIII. In the medulla and pons, GFP-ir cell bodies were also found in the area postrema, inferior olivary nuclei, the superior olivary complex, nuclei of the lateral lemniscus, and pontine muclei, which are shown in **Figure 7B1**. Labeling in the raphe nuclear complex was not conclusively detected. GFP-ir was

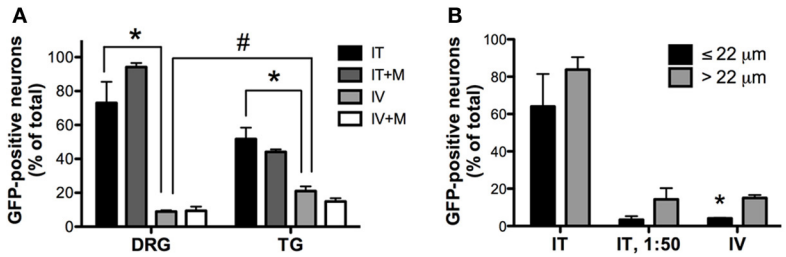

FIGURE 4 | Quantitative image analysis of the transduction of sensory neurons. (A) Analysis of the proportions of GFP-positive DRG and trigeminal ganglion (TG) neurons [$n = 4$ for i.t. (IT) and i.v. (IV) groups; $n = 2$ for i.t. and i.v. groups with mannitol pretreatment (IT+M and IV+M, respectively)]. *, indicates significant difference between i.t. and i.v. treatment groups in DRG and TG ($p < 0.005$; One-Way ANOVA for each type of ganglia followed by Bonferroni *post-hoc* test). #, indicates significant difference between DRG and TG in the i.v. treatment group ($p < 0.01$; *t*-test). **(B)** Analysis of the proportions of small-diameter (≤22 um) and large-diameter (>22 um) GFP-positive DRG neurons. *, indicates significant difference between small- and large-diameter DRG neurons in the i.v. treatment group ($p < 0.005$; paired *t*-test).

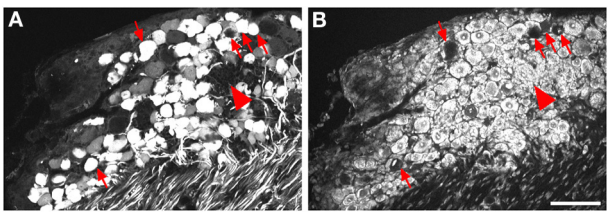

FIGURE 5 | Labeling for GFP (A) and NeuroTrace (B) shows GFP-positive neurons devoid of NeuroTrace staining (arrows) and clusters of satellite cell nuclei (arrowhead) indicative of gliosis. Scale bar: 100 µm.

observed in all layers of cerebellar cortex (Cb; **Figure 6B**). Fiber-like labeling, presumably originating from Purkinje cells, was present in the deep cerebellar nuclei (not shown), but we saw no evidence of labeling of neurons within the nuclei.

Midbrain

In midbrain, GFP-ir was most prominent in clusters of neurons in layer 2 of the inferior colliculus, and neurons in the internal gray layer of the superior colliculus (**Figure 7A1**). In the substantia nigra GFP-ir neurons were noted in the ventral region of pars reticulata at caudal levels and at more rostral levels neurons were also present in the ventromedial portion of pars compacta. Labeling was also observed in the interpeduncular nucleus and parabrachial nucleus and to a lesser extent the ventral tegmental area. All other regions of midbrain, including the periaqueductal gray and the red nucleus, were devoid of GFP-ir neurons.

Thalamus, hypothalamus, and pituitary

With the exception of the medial geniculate nucleus (MGN), which contained many GFP-positive neurons in all subdivisions (**Figure 7B2**), relatively little GFP labeling was observed in the caudal nuclei of the thalamus. Faintly labeled neurons were noted in lateral geniculate and lateral posterior thalamic nuclei as well as in the region of ventroposterior lateral and medial nuclei. In the anterior thalamic nuclei, there were many GFP-ir fibers and a few neuronal cell bodies (**Figure 7D1**). Axons of the mammillothalamic tract (mt) could be observed crossing into the anterior

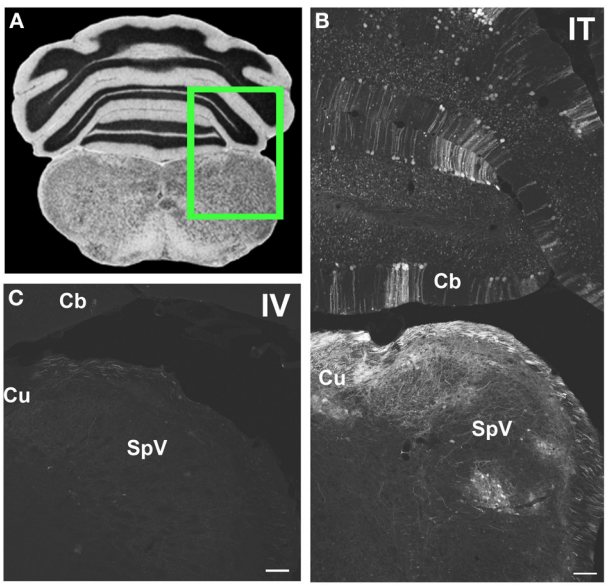

FIGURE 6 | Representative images of GFP-ir in medulla and cerebellum 3 weeks after i.t. (IT) or intravenous i.v. (IV) AAV9-GFP delivery. (A) Coronal section labeled with cresyl violet was selected from the Mouse Brain Library (Rosen et al., 2000) C57BL/6 mouse brain atlas. Inset indicates approximate relative location of images shown in **(B,C)**. **(B)** GFP-ir associated with cuneate nucleus (Cu), spinal nucleus of V (SpV), and cerebellar cortex (Cb) after i.t. delivery. **(C)** Limited GFP-ir in cuneate and spinal trigeminal nucleus after i.v. delivery. Scale bar: 100 µm.

nuclear complex of the thalamus (**Figure 7D1**). In the hypothalamus, GFP-ir neurons and nerve fibers were observed in a number of nuclei including portions of the mammillary nuclear complex, lateral hypothalamus (**Figure 7C1**), and arcuate, suprachiasmatic, paraventricular (PeV), and supraoptic (SON) nuclei (PeV and SON shown in **Figure 7D1**). Substantial GFP expression was also found in the pituitary gland (**Figure 8D**). Labeling in the anterior pituitary (^ in **Figures 8D,E**) was comparable between i.t. and i.v. delivery, however, labeling in the posterior pituitary (+ in **Figures 8D,E**) was consistently more intense in animals that received i.t. vector. The increase in posterior pituitary

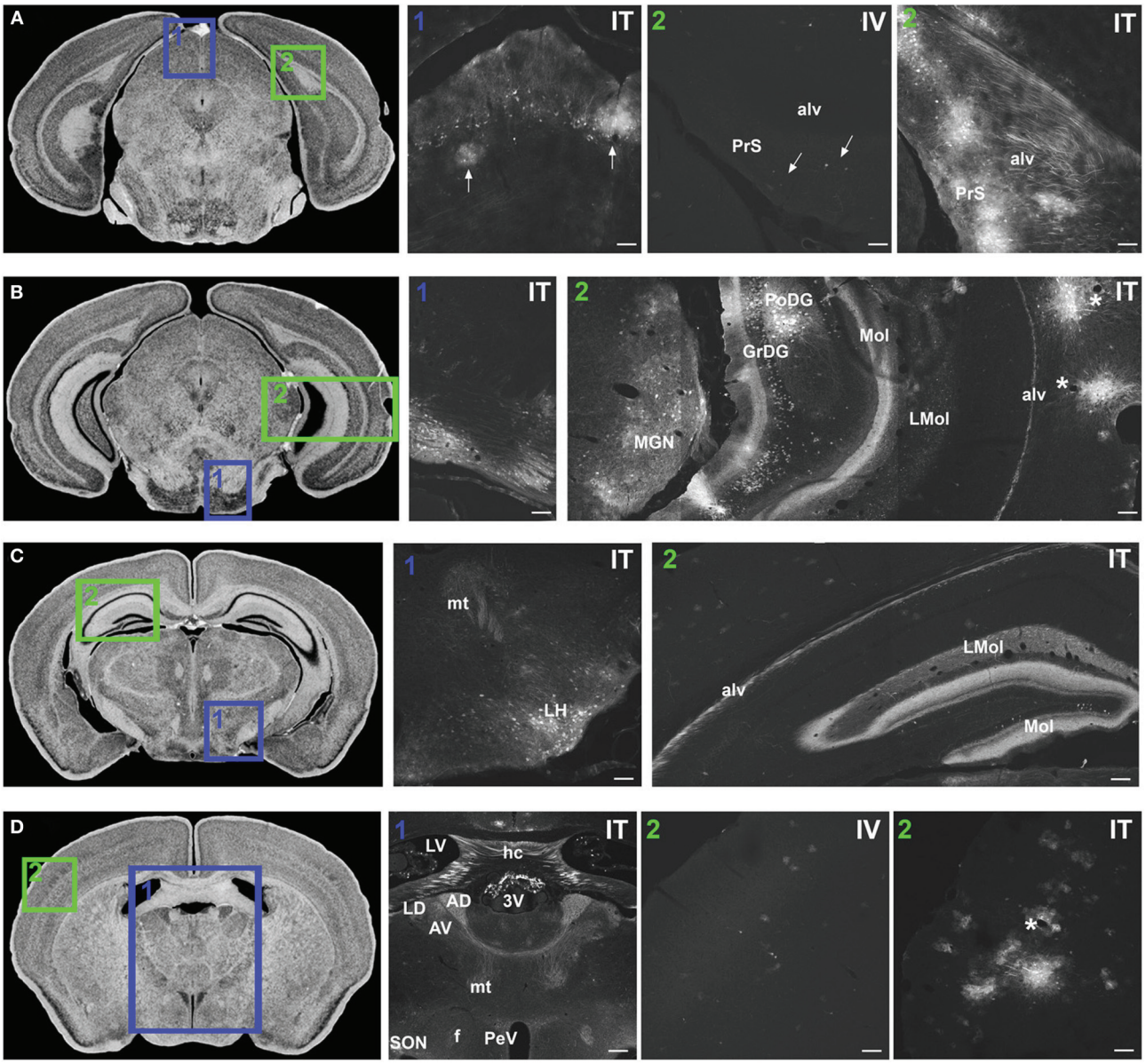

FIGURE 7 | Representative images of GFP-ir in midbrain and diencephalon. Coronal sections labeled with cresyl violet were selected from the Mouse Brain Library (Rosen et al., 2000) C57BL/6 mouse brain atlas. Insets indicate approximate relative location of images shown in the associated panels. **(A) Panel A1:** GFP-ir in superior colliculus. Neuronal cell bodies appear as a band of puncta in the internal gray layer of the superior colliculus. Arrows indicate clusters of astrocytes associated with blood vessels. **Panel A2:** Intense GFP-ir is present in presubiculum (PrS) and alveus (alv) of the hippocampal formation after i.t. delivery, whereas after i.v. delivery labeling is limited to isolated cells (arrows). **(B) Panel B1:** GFP-ir in pontine nuclei and transverse pontine fibers. **Panel B2:** GFP-ir in the medial geniculate nucleus (MGN) of the thalamus, hippocampal formation, and temporal cortex. GFP-ir is present in many neurons of the polymorph (PoDG) and granular layers (GrDG) of the dentate gyrus as well as in nerve fibers of the molecular layer of dentate gyrus (Mol), stratum lacunosum-moleculare (LMol), and alveus (alv). Asterisks indicate blood vessels in proximity to clusters of labeled cells in cortex. **(C) Panel C1:** GFP-ir in lateral hypothalamus (LH) and mammilothalamic tract (mt). **Panel C2:** GFP-ir in the rostral-dorsal hippocampal formation. The molecular layer of the dentate gyrus (Mol), stratum lacunosum-moleculare (LMol), and alveus (alv) are highlighted by GFP-ir. **(D) Panel D1:** GFP-ir in the lateral dorsal nucleus (LD) of thalamus and in axons from the mammillo-thalamic tract (mt) entering portions of the anterior nuclear complex (AD and AV). Labeling is also present in the fornix (f), paraventricular (PeV), and supraoptic (SON) nuclei of hypothalamus, the hippocampal commissure (hc), and choroid plexus of the third (3V) and lateral ventricles (LV). **Panels D2 IV** and ITillustrate the difference in cortical expression between delivery routes. Asterisk indicates a blood vessel surrounded by GFP-ir cells. Scale bars: 100 μm in all panels except **Panel D1**, for which the scale bar is 250 μm.

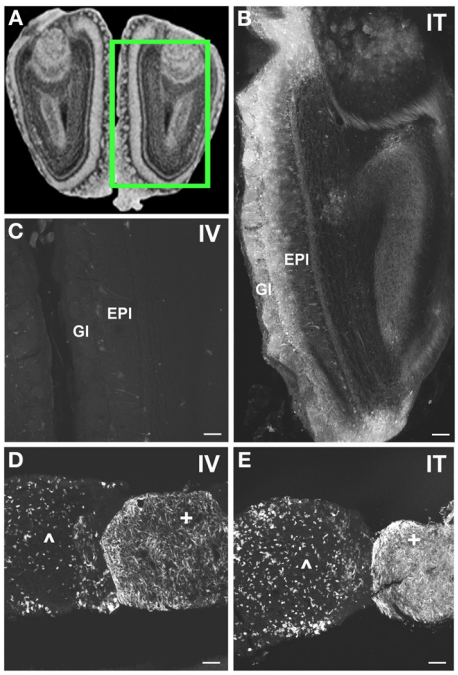

FIGURE 8 | Localization of GFP-ir in olfactory bulb and pituitary gland. **(A)** Coronal section labeled with cresyl violet was selected from the Mouse Brain Library (Rosen et al., 2000) C57BL/6 mouse brain atlas. Inset indicates approximate relative location of images shown in **(B,C)**. **(B)** After i.t. delivery, GFP-ir was found throughout the olfactory bulb, but was most intense in the glomerular (Gl) and external plexiform (EPl) layers. **(C)** Limited GFP-ir in olfactory bulb after i.v. delivery. **(D,E)** Localization of GFP-ir in pituitary. Labeling in anterior pituitary (^) was comparable between delivery routes; however, labeling in posterior pituitary (+) appeared more intense after i.t. **(D)** delivery compared to i.v. **(E)**. Scale bars: 100 μm.

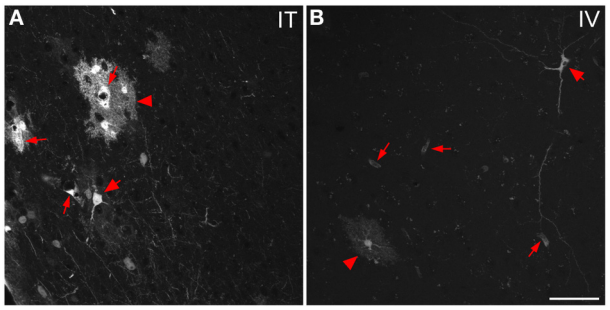

FIGURE 9 | Representative images of GFP-ir cells in cortex. (A) After i.t. administration, intensely labeled clusters of cells were observed in close proximity to blood vessels, which are indicated by small arrows. The morphology of labeled cells was consistent with astrocytes (arrowheads) and neurons (large arrows). **(B)** After i.v. delivery, GFP-labeling was associated with blood vessels (small arrows) as well as isolated neurons (large arrow) and astrocytes (arrowhead). Scale bar: 50 μm.

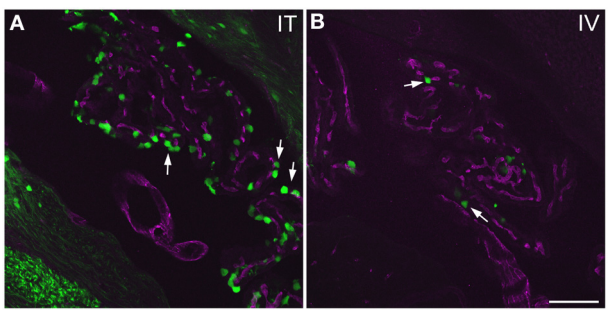

FIGURE 10 | GFP-ir in choroid plexus of the fourth ventricle. GFP-ir (green) is present in many epithelial cells (examples indicated by arrows) after i.t. delivery **(A)** whereas labeling after i.v. delivery is limited **(B)**. Blood vessels within the choroid plexus are visualized using CD31 (purple). Scale bar: 100 μm.

expression associated with i.t. delivery corresponded well with labeling observed in the paraventricular (PeV) and supraoptic nuclei (SON) of the hypothalami of i.t. treated animals.

Hippocampal formation and amygdaloid complex

There was intense GFP-ir in the presubiculum (PrS; **Figure 7A2-IT**), parasubiculum, and subiculum. In the caudal portions of the dentate gyrus (DG), many neuronal cell bodies were observed in the polymorph (PoDG) and granular cell (GrDG) layers. The molecular layer (Mol) of the dentate gyrus and the stratum lacunosum-moleculare (LMol) of the hippocampus were clearly defined by GFP-ir both in the caudal-ventral (**Figure 7B2**) and rostral-dorsal (**Figure 7C2**) portions of the hippocampal formation. However, the rostral-dorsal hippocampus contained very few GFP-positive neurons compared to more caudal and ventral regions. GFP-ir was also noted in fibers entering the alveus of the hippocampus (alv; **Figure 7B2**) and well as fibers within the fornix (f) and the hippocampal commissure (hc) (**Figure 7D1**). In addition to hippocampus, GFP-ir was observed in portions of the amygdaloid complex (not shown).

Cortex, forebrain, and olfactory bulb

In the forebrain GFP-ir was prominent in the islands of Calleja, nuclei of the diagonal band, ventral pallidum, preoptic area, and septal nuclei (not shown). Labeling of neuronal cell bodies was not seen in the nucleus accumbens and was limited in the striatum. Intense GFP labeling was observed in the olfactory tubercle (not shown) and olfactory bulbs (**Figure 8B**). GFP-ir was found throughout the olfactory bulb in nerve fibers, neuronal cell bodies and astrocytes, but was most concentrated in the medial portions of the glomerular (Gl) and external plexiform (EPl) layers. In cortex, GFP-ir neurons and astroglia were found in clusters that were often very near to larger blood vessels (see * in **Figures 7B2,D2-IT**; small arrows in **Figure 10A**). This association was particularly striking near the surface of the cortex. The clusters appeared to be most prominent in entorhinal, retrosplenial, and cingulate cortex. With i.v. delivery, isolated GFP-positive astrocytes and neurons were also in proximity to labeled blood vessels (**Figure 10B**), however, association with large blood vessels near the cortical surface was not observed.

Choroid plexus

Labeling of choroid plexus was seen throughout the ventricular system (third (3V) and lateral (LV) ventricles shown in

Table 1 | Relative abundance of GFP-ir neurons in CNS regions that were transduced by AAV9: +, sporadic; ++, consistent intermediate; +++, consistent abundant; ++++, very abundant (e.g., cerebellum, Figure 6B, and olfactory bulb Figure 8B).

CNS subdivision	Structure	
Medulla and pons	gracile n.	+++
	cuneate n.	+++
	external cuneate n.	+++
	spinal n. of CnV	+++
	hypoglossal n.	+++
	nucleus of the solitary tract	+++
	area postrema	+++
	reticular formation	++
	inferior olivary complex	++
	vestibular nuclear complex	++
	cochlear nuclear complex	+++
	principal sensory n. of CnV	+
	motor n. of CnV	+
	facial nucleus	+++
	superior olivary complex	++
	pontine nuclei	+++
	nuclei of the lateral lemniscus	+++
Cerebellum	Purkinje cell layer	++++
	granule cell layer	++++
Midbrain	inferior colliculus (external cortex and dorsal n.)	++
	superior colliculus (internal gray layer, medial zone of deep gray layer)	++
	ventral tegmental area	+
	substantia nigra, reticulata (ventral portion only)	++
	substantia nigra, compacta (rostral vntromedial portion)	++
	interpeduncular nucleus (caudal and lateral divisions)	++
	parabrachial nuclear complex	+
Thalamus	medial geniculate n.	+++
	lateral geniculate n.	+
	lateral posterior n.	+
	ventrolateral n.	+
	ventromedial n.	+
	anterior thalamic nuclei	+
Hypothalamus	mammillary nuclear complex	++
	arcuate n.	+++
	lateral hypothalamus	+++
	tuber cinereum	++
	paraventricular n.	+
	ventromedial n.	+
	suprachiasmatic n.	++
	supraoptic n.	++
Forebrain	hippocampal formation	++++
	amygdaloid complex	+++
	striatum	+
	nuclei of the diagonal band	+++
	septal nuclei	+++
	medial preoptic area	++
	ventral pallidum	++
	islands of Calleja	+++
	cortex (sporadic clusters of neurons)	++
	olfactory bulb	++++

Neuronal GFP labeling was absent or inconclusive in regions not included in the table. The abundance of labeled neurons varied between animals at 3 weeks, but for each animal the relative abundance in different regions was consistent. ***Figures 6–8*** *illustrate examples from animals with higher level of labeling.*

Figure 7D1). GFP-ir was most frequently seen in cells whose morphology and localization relative to blood vessels was consistent with that of epithelial cells (**Figure 11**). These cells were more abundant in i.t. treated compared to i.v. treated mice. Other GFP-positive cell types were also noted, but their identification was not pursued in this study.

Time-dependent increase in GFP-ir

GFP-ir was more abundant at 6 weeks after i.t. vector administration compared to 3 weeks. The intensity of labeling and the density of labeled neurons within the regions described above appeared to be increased. We did not note presence of GFP-ir neurons in areas that were not labeled at 3 weeks. However, labeling within nerve fibers was increased throughout the brain. For example, prominent increase in neuropil-like labeling at 6 weeks relative to 3 weeks was seen in the striatum (CPu; **Figure 11**).

AAV9-MEDIATED GFP EXPRESSION IN PERIPHERAL ORGANS AND TISSUES

GFP-ir was examined in liver, ileum, colon, adrenal gland, skeletal muscle, and skin 3 weeks after i.t. or i.v. AAV9-GFP delivery. Abundant labeling was seen in the liver of both i.t. and i.v. treated mice (**Figure 12**). In the ileum, GFP-ir was present predominantly within the enteric nervous system. Labeling of nerve fibers was prominent in the mucosa, submucosa, and enteric ganglia. GFP-ir was also seen within the cell bodies of some enteric neurons. The abundance and pattern of GFP labeling was comparable in ileum of i.t. and i.v. treated mice (**Figures 13A,B**). GFP-ir was also noted in adipocytes associated with ileal mesentery of both treatment groups (**Figure 13C**). In the colon, the density of GFP-positive nerve fibers was substantially higher in i.t. treated compared to i.v. treated mice (**Figures 13D,E**). GFP-positive myenteric neurons were observed in both groups (**Figure 13F**), but were fewer than in ileum. There was no apparent GFP labeling of immunocytes in lamina propria of either ileum or colon. In the adrenal gland both routes of delivery of AAV9-GFP yielded intense GFP-ir restricted to the zona fasciculata (**Figure 13G**). Muscle fibers

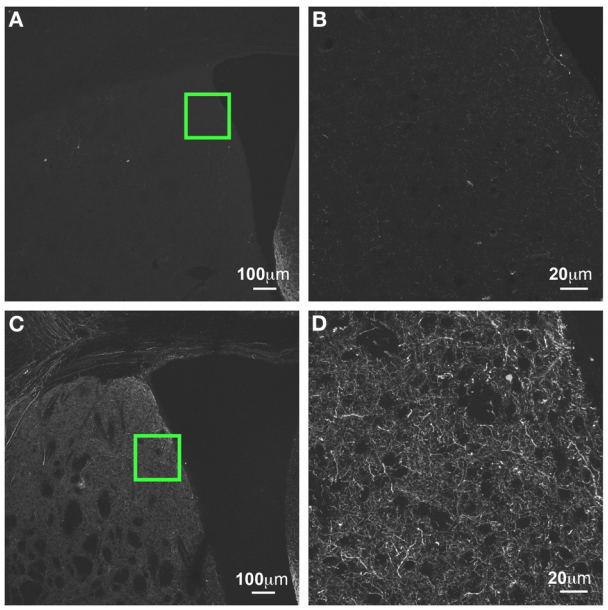

FIGURE 11 | GFP-ir in striatum at 3 weeks compared to 6 weeks after i.t. delivery. (A,B) GFP-ir in striatum (CPu), 3 weeks after intrathecal delivery of AAV9-GFP. **(C,D)** GFP expression in striatum 3 weeks after intrathecal delivery of AAV9-GFP. Green insets in **(A,C)** are shown at higher magnification in **(B,D)** respectively.

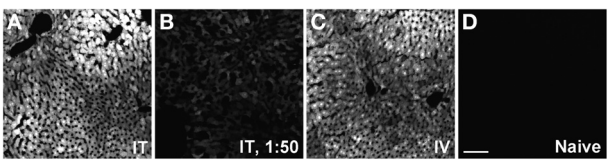

FIGURE 12 | Representative images of GFP-ir in liver 3 weeks after AAV9-GFP administration. (A) i.t. treatment; **(B)** low-dose i.t. treatment; **(C)** i.v. treatment; **(D)** naïve. Scale bar: 100 μm.

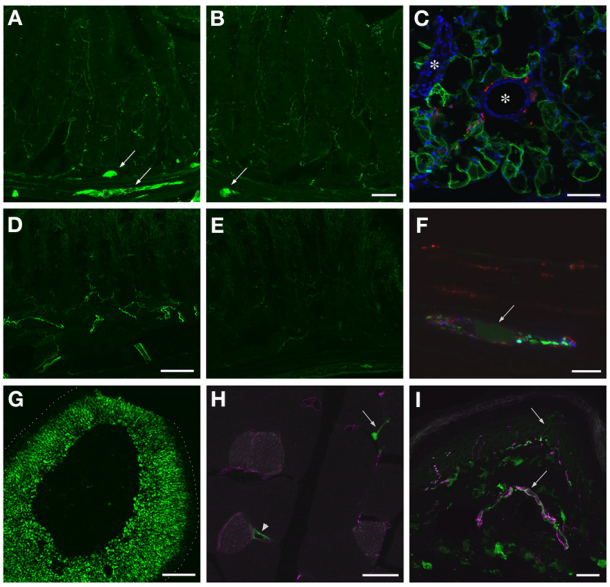

FIGURE 13 | Localization of GFP-ir in peripheral tissues after i.t. or i.v. delivery of AAV9-GFP without mannitol pretreatment. (A,B) GFP-ir in ileum after i.t. **(A)** or i.v. **(B)** delivery. Arrows indicate enteric ganglia. Scale bar: 50 μm. **(C)** GFP-ir (green) in adipocytes associated with ileac mesentery. DAPI (blue) labeling of nuclei outlines blood vessels (*). CGRP-ir nerve fibers in the mesentery are shown in red. Scale bar: 100 μm. **(D,E)** GFP-ir in colon after i.t. **(D)** or i.v. **(E)** delivery. Scale bar: 50 μm. **(F)** GFP-ir (green, arrow) neuron within a myenteric ganglion in colon. GFP-, SP- (red), and CGRP-ir (blue) nerve fibers are seen within the ganglion. Scale bar: 10 μm. **(G)** GFP-ir in adrenal cortex. Dotted line indicates the edge of the tissue. Scale bar: 200 μm. **(H)** GFP-ir in nerve endings (arrow) and blood vessel (arrowhead) in thigh skeletal muscle. CD31 labeling of endothelial cells is shown in purple. Scale bar: 25 μm. **(I)** GFP- and CGRP-ir (purple) in skin. Arrows indicate a nerve bundle in dermis and an epidermal nerve fiber. Scale bar: 25 μm. **(C,F–I)** Show labeling in tissues from i.t. treated mice. The pattern of labeling in the same tissues of i.v. treated mice was similar.

within skeletal muscle were devoid of GFP-ir in both i.t. and i.v. treated mice; however, labeling was observed within nerve fibers with morphology consistent with axon endings of motor neurons (**Figure 13H**, arrow) as well as endings within muscle spindles (not shown). GFP-ir also appeared to be associated with some blood vessels within the muscle (**Figure 13H**, arrowhead). In dermis and epidermis of skin, GFP-ir was observed in nerve fibers (**Figure 13I**), which were more abundant in i.t treated compared to i.v. treated mice, consistent with the transduction levels of sensory neurons in the two groups. Both routes of delivery also resulted in GFP labeling of unidentified cells in the dermis (**Figure 13I**).

DISCUSSION

In the present study, we examined the biodistribution in mouse of intrathecally-delivered AAV9-GFP and compared it to the distribution achieved by an equivalent dose of viral vector administered intravenously. Intrathecal delivery yielded higher transduction efficiency in sensory neurons and the CNS. Mannitol pretreatment did not appear to enhance transduction of sensory neurons via either route of administration, as previously reported for CNS after i.v. delivery (Gray et al., 2011). Remarkably, the majority of peripheral tissues examined in this study were similarly transduced following i.v. and i.t. vector delivery, suggesting that a substantial amount of intrathecally injected viral particles are redistributed from the subarachnoid space to the systemic circulation.

AAV9-MEDIATED TRANSDUCTION OF PRIMARY SENSORY NEURONS

AAV9-mediated transduction of primary sensory neurons has been previously reported in rodents and non-human primates (Hirai et al., 2012, 2014; Gray et al., 2013). However, the pattern of AAV9-driven transgene expression in sensory ganglia has not been thoroughly evaluated. Following i.v. delivery of AAV9-GFP, we observed GFP labeling only in approximately 10% of DRG neurons with or without mannitol pretreatment. In contrast, AAV9-GFP administered i.t. at the same dose demonstrated remarkable transduction efficiency in lumbar DRG. Over 90% of neurons in the L4 DRG were GFP-positive in four of the mice treated i.t. (two with and two without mannitol). The

transduction level in DRG was dose-dependent as only 10% of neurons were GFP-positive following a 50-fold reduction in the dose. Based on the range of AAV9-GFP doses used in these experiments and the doses used in our previous study on AAV5 and AAV8 [approximately 3-fold lower relative to the high dose in this study; (Vulchanova et al., 2010)], we conclude that the transduction efficiency of AAV9 in sensory neurons is superior to that of AAV5 and AAV8 without a requirement for mannitol pretreatment. Moreover, although at the low dose and after i.v. delivery AAV9-GFP transduced predominantly large-diameter neurons, at the high treatment dose large-diameter as well as small-diameter peptidergic and non-peptidergic neurons were targeted. These results suggest that AAV9 viral vectors are suitable for global transduction of sensory neurons, unlike AAV5 and AAV8, which target predominantly large-diameter neurons (Vulchanova et al., 2010; Jacques et al., 2012), and AAV6, which has a preference for small-diameter cells (Towne et al., 2009). Another notable distinction between AAV9 and AAV5 and 8 is that AAV9 yielded more efficient transduction in thoracic spinal cord and ganglia.

AAV-mediated transduction of trigeminal ganglion sensory neurons has not been previously described to our knowledge. We found GFP labeling within trigeminal ganglion neurons and nerve fibers in the spinal trigeminal nucleus after both i.t. and i.v. vector delivery. As would be expected based on their rostral location relative to the site of i.t. delivery, the number of GFP-positive neurons was lower in trigeminal ganglia compared to lumbar DRG. Interestingly, although as in DRG significantly more trigeminal sensory neurons were transduced in i.t. treated compared to i.v. treated mice, the i.v. route of administration yielded significantly more transduced neurons in trigeminal ganglia compared to DRG. Further exploration of AAV9 targeting to trigeminal ganglia by systemic vector delivery in combination with the use of sensory neuron-specific promoters may identify strategies for selective gene transfer to trigeminal sensory neurons. Finally, we also noted robust transduction of sensory neurons in the nodose ganglia after i.t. vector delivery. Administration of lower doses of AAV9 vectors in the cisterna magna rather that the lumbar intrathecal space may achieve preferential gene transfer to nodose compared to spinal ganglia, providing an alternative approach for the study of the vagal sensory innervation of peripheral organs (Kollarik et al., 2010; Gautron et al., 2011). The low level of GFP-ir in the solitary tract after i.v. delivery indicates that transduction in nodose ganglia via this route was limited.

AAV9-MEDIATED TRANSDUCTION IN THE CNS

The distribution of GFP labeling after intrathecal AAV9-GFP delivery observed in the present study is consistent with that reported by Haurigot et al. (2013) after administration of the vector in the cisterna magna, who also found expression in cerebellar Purkinje cells, cortical neurons, hypothalamus and olfactory bulb (Haurigot et al., 2013). The rostral distribution of viral particles in our experiments was clearly dose-related, as we observed very limited GFP labeling in the brain following a 50-fold dilution of the vector. Similarly, Snyder et al. (2011) reported absence of GFP expression in the brain after intrathecal administration of a similar dose of AAV9-GFP (Snyder et al., 2011). The fact that in the present study intrathecal delivery was achieved by direct lumbar puncture in conscious subjects represents an important distinction from delivery of the vector in CSF under conditions of surgical anesthesia in rodents (Snyder et al., 2011; Haurigot et al., 2013). CSF turnover in a mouse takes place within 2 h (Rudick et al., 1982; Johanson et al., 2008), and CSF flow, and likely viral particle distribution, is impacted by heart rate, subject position, and level of motor activity. Therefore, the pattern of transgene expression may be affected by the specific conditions of intrathecal delivery.

It is notable that although GFP-ir neuropil was abundant in brains of i.t. treated mice, labeled neurons were largely restricted to selected nuclei and cortical regions. Moreover, 6 weeks after vector administration, there was a substantial increase in the density of GFP-ir nerve fibers throughout the brain compared to 3 weeks and most strikingly in midbrain, striatum, cerebellum, and hippocampus. This increase was most likely due to accumulation of anterogradely transported GFP in fine neuronal processes. Although there also appeared to be more GFP-ir neurons at the 6-week time point, neuronal cell body labeling remained localized within the same anatomical structures seen at 3 weeks. These observations suggest that neuronal transduction by AAV9 is not uniform throughout the CNS but restricted to discrete regions; however, the projection pattern of the transduced neurons appears to be widespread, resulting in global axonal localization of the transgene product. Thus, intrathecally delivered AAV9 viral vectors may be utilized for gene therapy that targets specific CNS regions by employing appropriate promoters as well as for global CNS distribution of transgenes whose function involves axonal release (e.g., enzymes, growth factors). The latter scenario is relevant for conditions such as lysosomal storage diseases, where neuropathology may be reduced through global enzyme release (Wolf et al., 2011; Haurigot et al., 2013).

The preferential transduction of specific CNS regions is likely influenced by viral tropism. Glycans containing terminal galactose have been identified as cell-surface binding moieties for AAV9 (Bell et al., 2011; Shen et al., 2011), but their availability in specific CNS regions has not been characterized. Interestingly, manipulation of cell-surface glycans altered viral AAV9 tropism (Bell et al., 2011; Shen et al., 2012), suggesting that the pattern of AAV9-mediated gene transfer is likely affected by changes in glycosylation patterns under normal and disease conditions. This possibility should be addressed in the pre-clinical development of gene therapies. In addition, our observations indicate that the vasculature may contribute substantially to CNS transduction after i.t. delivery of AAV9. Association of GFP-ir cells with blood vessels was observed throughout the CNS, but was most striking near the cortical surface of i.t. treated but not i.v. treated mice. A relationship between AAV9-mediated transgene expression and blood vessels was also noted by Samaranch et al. (2012). We speculate that access of viral particles in the CSF to the perivascular space contributes to AAV9-mediated transduction in CNS parenchyma. The pattern of AAV9-driven GFP expression in the CNS may also be influenced by anterograde and/or retrograde transport of viral particles. Samaranch et al. (2014) reported that injection of AAV9-GFP in the striatum resulted in GFP labeling of neurons in substantial nigra and cortex (Samaranch et al., 2014).

In our study we noted GFP expression in neurons of specific CNS pathways. For example, GFP labeling was observed at all levels of the auditory pathway as well as in regions projecting to hippocampus (e.g., entorhinal cortex) and receiving projections from it (e.g., subiculum, mammillary nuclear complex). These observations are consistent with a contribution of axonal transport of viral particles to AAV9-mediated transgene expression. The complexity of factors influencing AAV9-mediated transgene distribution in the CNS is highlighted by the fact that regions in which GFP-positive neuronal cells bodies were limited or absent in our study, such as striatum and a large portion of the thalamus, were robustly transduced following intraparenchymal vector administration. It is possible that neurons in these areas express cell-surface receptors for AAV9 and transduction is enabled after intraparenchymal injection because of overcoming of accessibility barriers. Alternatively, the high local concentrations of vector achieved after intraparenchymal injection may enable entry of AAV9 via binding to low-affinity cell-surface binding sites.

The limited CNS distribution of GFP-ir after i.v. delivery observed in our experiments is consistent with previously reported transduction mediated by single-stranded AAV9 vector (Gray et al., 2011). However, the widespread correction of CNS abnormalities in several mouse disease models (Fu et al., 2011; Ruzo et al., 2012; Garg et al., 2013; Yamashita et al., 2013) contradicts our observations. This apparent discrepancy may be explained by several experimental variables including the type of vector (i.e., single-stranded vs. self-complementary), dose, and duration of transgene expression. It has been demonstrated that self-complementary AAV vectors result in more robust transgene expression compared to single-stranded (Gray et al., 2011) albeit at the expense of packaging capacity. Our comparison of different doses and duration of transgene expression supports the contribution of these variables in achieving widespread CNS expression. Finally, we cannot rule out the possibility that GFP expression is more widespread than the levels detectable by fluorescence. It is possible that functionally relevant transgenes are effective at lower expression levels than those required for detection of reporter gene expression.

EVALUATION OF POTENTIAL AAV9-GFP INDUCED NEUROTOXICITY

Recently, AAV9-mediated CNS expression of "non-self" proteins, and GFP in particular, has been reported to induce neuroinflammation and neurotoxicity (Ciesielska et al., 2013; Samaranch et al., 2014). Based on labeling with Iba1, we did not observe reactive microglia in association with GFP-expressing CNS regions following i.v. or i.t. vector delivery, suggesting that CNS neuroinflammation was absent under our experimental conditions. This observation is consistent with the proposal that the extent of AAV9-mediated immune activation in the CNS may be dependent on a number of factors, including levels of transgene expression (Samaranch et al., 2014). Although we did not observe signs of CNS inflammation or neurotoxicity, in DRG, and to a lower extent trigeminal ganglia, of mice given intrathecally the high treatment dose we noted mononuclear aggregates and infiltrates that appeared to be associated with neuronal damage. As GFP labeling in neurons was very robust in those DRG, it is possible that GFP overexpression resulted in immune activation in the ganglia or in disruption of protein synthesis necessary for normal cell functioning in individual neurons. A relationship between high levels of GFP expression and neurotoxicity is consistent with the observation of intensely GFP-positive cells in which Nissl staining (i.e., ribosomes) was absent. Stereological analysis appropriate for evaluation of cell loss was beyond the scope of this study. However, we noted that sample sizes and proportions of large- and small-diameter neurons were similar in ganglia from i.t. and i.v. treated mice, suggesting that the observed histopathology did not affect our quantitative analysis of proportions of GFP-positive sensory neurons and that the extent of neuronal damage may be limited. Finally, the histopathology was more limited in DRG from mice in the 6-week treatment group, which received viral vector from a different lot, raising the possibility that viral vector preparation may also be a factor. In the context of other reports of GFP-related toxicity (Ciesielska et al., 2013; Samaranch et al., 2014) and the multifactorial determinants of AAV-mediated gene transfer, the present observations call for increased vigilance in evaluating outcomes of AAV9-driven transgene expression in sensory neurons.

DISTRIBUTION OF AAV9-MEDIATED GFP EXPRESSION IN PERIPHERAL TISSUES AND ORGANS

The present study extends previous observations on the peripheral distribution of AAV9-mediated gene transfer (Zincarelli et al., 2008; Fu et al., 2011; Benkhelifa-Ziyyat et al., 2013) and is consistent with the correction of peripheral pathology after AAV9-mediated gene transfer in a mouse model of a lysosomal storage disease (Haurigot et al., 2013). Transduction in the liver was robust and equivalent for i.v. and i.t. delivery. In mice treated i.t. with a 50-fold lower vector dose, GFP-expression in liver was reduced but still appeared uniform. In contrast to these observations, Samaranch et al. (2012) reported very low GFP expression in liver of non-human primates, in which AAV9-GFP was administered in the cisterna magna (Samaranch et al., 2012). It is unclear whether this difference in peripheral transduction is due to dosing differences, type of AAV9 vector (single-stranded vs. self-complementary), or species differences in the extent to which AAV9 vectors are redistributed to the systemic circulation following delivery in the CSF. The potential for such substantial species differences in viral vector distribution between rodent and primate pre-clinical models should be given serious consideration in the translational development of gene therapies.

Our findings of extensive labeling in the enteric nervous system are in agreement with a previous description of transduction in enteric ganglia (Fu et al., 2011). Interestingly, while the pattern of GFP-ir was similar in the ileum of i.t. and i.v. treated mice, in the colon GFP-ir was substantially more abundant following i.t. vector delivery. Furthermore, transduction of intrinsic enteric neurons was less frequent in colon compared to ileum following both routes of delivery. These observations suggest that the ileum is more accessible than colon to systemically available AAV9 viral particles for reasons that are presently unclear. Additionally, the extensive GFP labeling in the colon of i.t. treated mice is likely to be associated with nerve fibers of extrinsic sensory neurons whose cell bodies are located within DRG as we have previously described for AAV8-mediated GFP expression in colon (Schuster

et al., 2013). It is also likely that a proportion of the GFP-ir nerve fibers in colon as well as ileum are vagal primary afferents since in the present study we noted transduction of sensory neurons in nodose ganglia. In addition to GFP labeling within the enteric nervous system, non-neuronal GFP-positive cells were occasionally encountered in both ileum and colon. The identity of these cells remains to be determined. While evaluating GFP labeling in the ileum, we noted transduction of adipocytes with the associated mesentery. Although GFP labeling of more prominent depots of white adipose tissue was not examined in the present study, this observation raises the possibility that AAV9 vectors may be useful for gene transfer to adipocytes.

Our analysis of AAV9-mediated transduction in the periphery included the adrenal gland, which to our knowledge has not been previously evaluated. A similar pattern of GFP expression was observed after i.t. and i.v. delivery of the vector. Interestingly, GFP-ir appeared to be restricted to the zona fasciculata of the adrenal cortex with minimal labeling in the other layers of the cortex or in the adrenal medulla. A similar pattern of labeling with reduced intensity was observed at the lower treatment dose used in this study. These observations suggest potential utility of AAV9 for genetic manipulation of glucocorticoid-producing endocrine cells.

Under the present experimental conditions, transduction of skeletal muscle was not observed, in contrast with previous reports (Zincarelli et al., 2008; Foust et al., 2009; Fu et al., 2011; Elmallah et al., 2014). This discrepancy could be due to differences in type of AAV9 vector (i.e., single-stranded vs. self-complementary), dose, or time point of tissue evaluation. The observation of GFP-positive nerve endings in skeletal muscle is consistent with GFP expression in spinal motor and sensory neurons. Similarly, the presence of GFP-positive nerve fibers in dermis and epidermis is in agreement with the observed transduction of sensory neurons. The identity of other GFP-positive structures in the dermis is presently unknown. We speculate that they may correspond to blood vessels as instances of GFP labeling of blood vessels were also observed in skeletal muscle and intestine. These findings may reflect AAV9-mediated transduction of endothelial cells and require further investigation.

CONCLUSIONS

The present analysis of the biodistribution of single-stranded AAV9-GFP following intrathecal or intravenous delivery yielded several important observations related to AAV9-mediated gene transfer in the central and peripheral nervous system. Intrathecal administration of AAV9-GFP resulted in global transduction of lumbar DRG neurons as well as efficient transduction of trigeminal and nodose ganglion neurons. The adverse effects of transgene expression noted in DRG neurons suggest that the possibility for tissue-dependent, titer-and time-related toxicity associated with gene transfer should be considered and assessed on a case-by-case basis for each serotype and gene employed. Intrathecally delivered AAV9-GFP yielded broad CNS expression of GFP that was substantially elevated relative to intravenous delivery. The pattern of CNS transduction is not uniform and is likely to be influenced by factors such as axonal transport and interactions of viral particles with elements of the blood-brain barrier. Finally, in several peripheral tissues transduction was comparable following i.t. or i.v. delivery, suggesting substantial systemic redistribution of i.t. injected AAV9-GFP. In summary, the present study demonstrates that the intrathecal route of administration results in AAV9-mediated gene transfer to a broad spectrum of discrete central and peripheral nervous system regions as well as peripheral organs in a dose-dependent and time-dependent manner.

AUTHOR CONTRIBUTIONS

Daniel J. Schuster participated in perfusions and dissections, immunohistochemistry, imaging, cell quantification, and performed the intravenous injections. He contributed to data analysis, preparation of figures, interpretation of the results, and edited the manuscript. Jaclyn A. Dykstra participated in perfusions and dissections, performed the histopathological analysis, and contributed to data analysis and interpretation. Maureen S. Riedl participated in perfusions and dissections, histochemical analyses, interpretation of results, and edited the manuscript. Kelley F. Kitto conducted all intrathecal injections of vector and is responsible for the quality assurance of this key technique. Lalitha R. Belur initiated the studies, contributed to the experimental design, and edited the manuscript. R. Scott McIvor contributed to the experimental design, edited the manuscript, and supported the studies. Robert P. Elde contributed to experimental design and data interpretation. Carolyn A. Fairbanks contributed to the experimental design, edited the manuscript, and supported the studies. Lucy Vulchanova participated in perfusions and dissections, immunohistochemistry, imaging, and cell quantification. She contributed to experimental design, data analysis, cell quantification, preparation of figures, interpretation of the results, manuscript preparation, and support of the study.

ACKNOWLEDGMENTS

The authors would like to thank Galina Kalyuzhnaya for her technical assistance. Grant support: R01DE021996 (to Lucy Vulchanova), R21DA025164 (to Carolyn A. Fairbanks), R01HD032652 (to R. Scott McIvor), and the University of Minnesota Academic Health Center. An individual NRSA from the National Institute of Neurological Disorders and Stroke (F31NS063634) and a 3M Fellowship supported Daniel J. Schuster.

REFERENCES

Bell, C. L., Vandenberghe, L. H., Bell, P., Limberis, M. P., Gao, G. P., Van Vliet, K., et al. (2011). The AAV9 receptor and its modification to improve *in vivo* lung gene transfer in mice. *J. Clin. Invest.* 121, 2427–2435. doi: 10.1172/JCI57367

Benkhelifa-Ziyyat, S., Besse, A., Roda, M., Duque, S., Astord, S., Carcenac, R., et al. (2013). Intramuscular scAAV9-SMN injection mediates widespread gene delivery to the spinal cord and decreases disease severity in SMA mice. *Mol. Ther.* 21, 282–290. doi: 10.1038/mt.2012.261

Ciesielska, A., Hadaczek, P., Mittermeyer, G., Zhou, S., Wright, J. F., Bankiewicz, K. S., et al. (2013). Cerebral infusion of AAV9 vector-encoding non-self proteins can elicit cell-mediated immune responses. *Mol. Ther.* 21, 158–166. doi: 10.1038/mt.2012.167

Dayton, R. D., Wang, D. B., and Klein, R. L. (2012). The advent of AAV9 expands applications for brain and spinal cord gene delivery. *Expert Opin. Biol. Ther.* 12, 757–766. doi: 10.1517/14712598.2012.681463

Dirren, E., Towne, C. L., Setola, V., Redmond, D. E. Jr., Schneider, B. L., and Aebischer, P. (2014). Intracerebroventricular Injection of adeno-associated virus 6 and 9 vectors for cell type-specific transgene expression in the spinal cord. *Hum. Gene. Ther.* 25, 109–120. doi: 10.1089/hum.2013.021

Elmallah, M. K., Falk, D. J., Nayak, S., Federico, R. A., Sandhu, M. S., Poirier, A., et al. (2014). Sustained correction of motoneuron histopathology following intramuscular delivery of AAV in pompe mice. *Mol. Ther*. 22, 702–712. doi: 10.1038/mt.2013.282

Fairbanks, C. A. (2003). Spinal delivery of analgesics in experimental models of pain and analgesia. *Adv. Drug Deliv. Rev.* 55, 1007–1041. doi: 10.1016/S0169-409X(03)00101-7

Federici, T., Taub, J. S., Baum, G. R., Gray, S. J., Grieger, J. C., Matthews, K. A., et al. (2012). Robust spinal motor neuron transduction following intrathecal delivery of AAV9 in pigs. *Gene Ther.* 19, 852–859. doi: 10.1038/gt.2011.130

Foust, K. D., Nurre, E., Montgomery, C. L., Hernandez, A., Chan, C. M., and Kaspar, B. K. (2009). Intravascular AAV9 preferentially targets neonatal neurons and adult astrocytes. *Nat. Biotechnol.* 27, 59–65. doi: 10.1038/nbt.1515

Fu, H., Dirosario, J., Killedar, S., Zaraspe, K., and McCarty, D. M. (2011). Correction of neurological disease of mucopolysaccharidosis IIIB in adult mice by rAAV9 trans-blood-brain barrier gene delivery. *Mol. Ther.* 19, 1025–1033. doi: 10.1038/mt.2011.34

Fu, H., Muenzer, J., Samulski, R. J., Breese, G., Sifford, J., Zeng, X., et al. (2003). Self-complementary adeno-associated virus serotype 2 vector: global distribution and broad dispersion of AAV-mediated transgene expression in mouse brain. *Mol. Ther.* 8, 911–917. doi: 10.1016/j.ymthe.2003.08.021

Garg, S. K., Lioy, D. T., Cheval, H., McGann, J. C., Bissonnette, J. M., Murtha, M. J., et al. (2013). Systemic delivery of MeCP2 rescues behavioral and cellular deficits in female mouse models of Rett syndrome. *J. Neurosci.* 33, 13612–13620. doi: 10.1523/JNEUROSCI.1854-13.2013

Gautron, L., Sakata, I., Udit, S., Zigman, J. M., Wood, J. N., and Elmquist, J. K. (2011). Genetic tracing of Nav1.8-expressing vagal afferents in the mouse. *J. Comp. Neurol.* 519, 3085–3101. doi: 10.1002/cne.22667

Gray, S. J., Matagne, V., Bachaboina, L., Yadav, S., Ojeda, S. R., and Samulski, R. J. (2011). Preclinical differences of intravascular AAV9 delivery to neurons and glia: a comparative study of adult mice and nonhuman primates. *Mol. Ther.* 19, 1058–1069. doi: 10.1038/mt.2011.72

Gray, S. J., Nagabhushan Kalburgi, S., McCown, T. J., and Samulski, R. J. (2013). Global CNS gene delivery and evasion of anti-AAV-neutralizing antibodies by intrathecal AAV administration in non-human primate. *Gene Ther.* 20, 450–459. doi: 10.1038/gt.2012.101

Haurigot, V., Marco, S., Ribera, A., Garcia, M., Ruzo, A., Villacampa, P., et al. (2013). Whole body correction of mucopolysaccharidosis IIIA by intracerebrospinal fluid gene therapy. *J. Clin. Invest.* doi: 10.1172/JCI66778. [Epub ahead of print].

Hirai, T., Enomoto, M., Kaburagi, H., Sotome, S., Yoshida-Tanaka, K., Ukegawa, M., et al. (2014). Intrathecal AAV serotype 9-mediated delivery of shRNA against TRPV1 attenuates thermal hyperalgesia in a mouse model of peripheral nerve injury. *Mol. Ther.* 22, 409–419. doi: 10.1038/mt.2013.247

Hirai, T., Enomoto, M., Machida, A., Yamamoto, M., Kuwahara, H., Tajiri, M., et al. (2012). Intrathecal shRNA-AAV9 inhibits target protein expression in the spinal cord and dorsal root ganglia of adult mice. *Hum. Gene. Ther. Methods* 23, 119–127. doi: 10.1089/hgtb.2012.035

Hylden, J. L., and Wilcox, G. L. (1981). Intrathecal substance P elicits a caudally-directed biting and scratching behavior in mice. *Brain Res.* 217, 212–215. doi: 10.1016/0006-8993(81)90203-1

Imai, Y., Ibata, I., Ito, D., Ohsawa, K., and Kohsaka, S. (1996). A novel gene iba1 in the major histocompatibility complex class III region encoding an EF hand protein expressed in a monocytic lineage. *Biochem. Biophys. Res. Commun.* 224, 855–862. doi: 10.1006/bbrc.1996.1112

Ito, D., Imai, Y., Ohsawa, K., Nakajima, K., Fukuuchi, Y., and Kohsaka, S. (1998). Microglia-specific localisation of a novel calcium binding protein, Iba1. *Brain Res. Mol. Brain Res.* 57, 1–9. doi: 10.1016/S0169-328X(98)00040-0

Jacques, S. J., Ahmed, Z., Forbes, A., Douglas, M. R., Vigenswara, V., Berry, M., et al. (2012). AAV8(gfp) preferentially targets large diameter dorsal root ganglion neurones after both intra-dorsal root ganglion and intrathecal injection. *Mol. Cell. Neurosci.* 49, 464–474. doi: 10.1016/j.mcn.2012.03.002

Johanson, C. E., Duncan, J. A. 3rd., Klinge, P. M., Brinker, T., Stopa, E. G., and Silverberg, G. D. (2008). Multiplicity of cerebrospinal fluid functions: New challenges in health and disease. *Cerebrospinal Fluid Res.* 5, 10. doi: 10.1186/1743-8454-5-10

Kollarik, M., Carr, M. J., Ru, F., Ring, C. J., Hart, V. J., Murdock, P., et al. (2010). Transgene expression and effective gene silencing in vagal afferent neurons *in vivo* using recombinant adeno-associated virus vectors. *J. Physiol.* 588, 4303–4315. doi: 10.1113/jphysiol.2010.192971

Mason, M. R., Ehlert, E. M., Eggers, R., Pool, C. W., Hermening, S., Huseinovic, A., et al. (2010). Comparison of AAV serotypes for gene delivery to dorsal root ganglion neurons. *Mol. Ther.* 18, 715–724. doi: 10.1038/mt.2010.19

Mastakov, M. Y., Baer, K., Symes, C. W., Leichtlein, C. B., Kotin, R. M., and During, M. J. (2002). Immunological aspects of recombinant adeno-associated virus delivery to the mammalian brain. *J. Virol.* 76, 8446–8454. doi: 10.1128/JVI.76.16.8446-8454.2002

Paxinos, G., and Franklin, K. B. J. (2001). *The Mouse Brain in Stereotaxic Coordinates*. London; New York, NY; Tokio; San Diego, CA: Academic Press.

Riedl, M. S., Schnell, S. A., Overland, A. C., Chabot-Dore, A. J., Taylor, A. M., Ribeiro-da-Silva, A., et al. (2009). Coexpression of alpha 2A-adrenergic and delta-opioid receptors in substance P-containing terminals in rat dorsal horn. *J. Comp. Neurol.* 513, 385–398. doi: 10.1002/cne.21982

Rosen, G. D., Williams, A. G., Capra, J. A., Connolly, M. T., Cruz, B., Lu, L., et al. (2000). "The Mouse Brain Library," in *Int Mouse Genome Conference,* 166. Available online at: http://www.mbl.org

Rudick, R. A., Zirretta, D. K., and Herndon, R. M. (1982). Clearance of albumin from mouse subarachnoid space: a measure of CSF bulk flow. *J. Neurosci. Methods* 6, 253–259. doi: 10.1016/0165-0270(82)90088-7

Ruzo, A., Marco, S., Garcia, M., Villacampa, P., Ribera, A., Ayuso, E., et al. (2012). Correction of pathological accumulation of glycosaminoglycans in central nervous system and peripheral tissues of MPSIIIA mice through systemic AAV9 gene transfer. *Hum. Gene Ther.* 23, 1237–1246. doi: 10.1089/hum.2012.029

Samaranch, L., Salegio, E. A., San Sebastian, W., Kells, A. P., Bringas, J. R., Forsayeth, J., et al. (2013). Strong cortical and spinal cord transduction after AAV7 and AAV9 delivery into the cerebrospinal fluid of nonhuman primates. *Hum. Gene Ther.* 24, 526–532. doi: 10.1089/hum.2013.005

Samaranch, L., Salegio, E. A., San Sebastian, W., Kells, A. P., Foust, K. D., Bringas, J. R., et al. (2012). Adeno-associated virus serotype 9 transduction in the central nervous system of nonhuman primates. *Hum. Gene Ther.* 23, 382–389. doi: 10.1089/hum.2011.200

Samaranch, L., Sebastian, W. S., Kells, A. P., Salegio, E. A., Heller, G., Bringas, J. R., et al. (2014). AAV9-mediated expression of a non-self protein in nonhuman primate central nervous system triggers widespread neuroinflammation driven by antigen-presenting cell transduction. *Mol. Ther.* 22, 329–337. doi: 10.1038/mt.2013.266

Schuster, D. J., Dykstra, J. A., Riedl, M. S., Kitto, K. F., Honda, C. N., McIvor, R. S., et al. (2013). Visualization of spinal afferent innervation in the mouse colon by AAV8-mediated GFP expression. *Neurogastroenterol. Motil.* 25, e89–e100. doi: 10.1111/nmo.12057

Shen, F., Kuo, R., Milon-Camus, M., Han, Z., Jiang, L., Young, W. L., et al. (2013). Intravenous delivery of adeno-associated viral vector serotype 9 mediates effective gene expression in ischemic stroke lesion and brain angiogenic foci. *Stroke* 44, 252–254. doi: 10.1161/STROKEAHA.112.662965

Shen, S., Bryant, K. D., Brown, S. M., Randell, S. H., and Asokan, A. (2011). Terminal N-linked galactose is the primary receptor for adeno-associated virus 9. *J. Biol. Chem.* 286, 13532–13540. doi: 10.1074/jbc.M110.210922

Shen, S., Bryant, K. D., Sun, J., Brown, S. M., Troupes, A., Pulicherla, N., et al. (2012). Glycan binding avidity determines the systemic fate of adeno-associated virus type 9. *J. Virol.* 86, 10408–10417. doi: 10.1128/JVI.01155-12

Snyder, B. R., Gray, S. J., Quach, E. T., Huang, J. W., Leung, C. H., Samulski, R. J., et al. (2011). Comparison of adeno-associated viral vector serotypes for spinal cord and motor neuron gene delivery. *Hum. Gene Ther.* 22, 1129–1135. doi: 10.1089/hum.2011.008

Storek, B., Reinhardt, M., Wang, C., Janssen, W. G., Harder, N. M., Banck, M. S., et al. (2008). Sensory neuron targeting by self-complementary AAV8 via lumbar puncture for chronic pain. *Proc. Natl. Acad. Sci. U.S.A.* 105, 1055–1060. doi: 10.1073/pnas.0708003105

Towne, C., Pertin, M., Beggah, A. T., Aebischer, P., and Decosterd, I. (2009). Recombinant adeno-associated virus serotype 6 (rAAV2/6)-mediated gene transfer to nociceptive neurons through different routes of delivery. *Mol. Pain* 5:52. doi: 10.1186/1744-8069-5-52

Vulchanova, L., Riedl, M. S., Shuster, S. J., Buell, G., Surprenant, A., North, R. A., et al. (1997). Immunohistochemical study of the P2X2 and P2X3 receptor subunits in rat and monkey sensory neurons and their central terminals. *Neuropharmacology* 36, 1229–1242. doi: 10.1016/S0028-3908(97)00126-3

Vulchanova, L., Schuster, D. J., Belur, L. R., Riedl, M. S., Podetz-Pedersen, K. M., Kitto, K. F., et al. (2010). Differential adeno-associated virus mediated gene transfer to sensory neurons following intrathecal delivery by direct lumbar puncture. *Mol. Pain* 6:31. doi: 10.1186/1744-8069-6-31

Wolf, D. A., Lenander, A. W., Nan, Z., Belur, L. R., Whitley, C. B., Gupta, P., et al. (2011). Direct gene transfer to the CNS prevents emergence of neurologic disease in a murine model of mucopolysaccharidosis type I. *Neurobiol. Dis.* 43, 123–133. doi: 10.1016/j.nbd.2011.02.015

Yamashita, T., Chai, H. L., Teramoto, S., Tsuji, S., Shimazaki, K., Muramatsu, S., et al. (2013). Rescue of amyotrophic lateral sclerosis phenotype in a mouse model by intravenous AAV9-ADAR2 delivery to motor neurons. *EMBO Mol. Med.* 5, 1710–1719. doi: 10.1002/emmm.201302935

Zincarelli, C., Soltys, S., Rengo, G., and Rabinowitz, J. E. (2008). Analysis of AAV serotypes 1-9 mediated gene expression and tropism in mice after systemic injection. *Mol. Ther.* 16, 1073–1080. doi: 10.1038/mt.2008.76

Conflict of Interest Statement: The authors declare that the research was conducted in the absence of any commercial or financial relationships that could be construed as a potential conflict of interest.

Received: 10 March 2014; accepted: 16 May 2014; published online: 10 June 2014.
Citation: Schuster DJ, Dykstra JA, Riedl MS, Kitto KF, Belur LR, McIvor RS, Elde RP, Fairbanks CA and Vulchanova L (2014) Biodistribution of adeno-associated virus serotype 9 (AAV9) vector after intrathecal and intravenous delivery in mouse. Front. Neuroanat. ***8****:42. doi: 10.3389/fnana.2014.00042*
This article was submitted to the journal Frontiers in Neuroanatomy.

frontiers in
NEUROANATOMY

ORIGINAL RESEARCH ARTICLE
published: 17 March 2014
doi: 10.3389/fnana.2014.00009

Distribution of nanoparticles throughout the cerebral cortex of rodents and non-human primates: implications for gene and drug therapy

Ernesto A. Salegio[1†], Hillary Streeter[1], Nikhil Dube[2], Piotr Hadaczek[1], Lluis Samaranch[1], Adrian P. Kells[1], Waldy San Sebastian[1], Yuying Zhai[1], John Bringas[1], Ting Xu[2], John Forsayeth[1] and Krystof S. Bankiewicz[1]*

[1] Department of Neurological Surgery, University of California at San Francisco, San Francisco, CA, USA
[2] Department of Materials Science & Engineering, University of California at Berkeley, Berkeley, CA, USA

Edited by:
Laurent Gautron, UT Southwestern Medical Center, USA

Reviewed by:
Alino Martinez-Marcos, Universidad de Castilla, Spain
Jan Pieter Konsman, Université Victor Ségalen Bordeaux 2, France

***Correspondence:**
Krystof S. Bankiewicz, Department of Neurological Surgery, University of California at San Francisco, San Francisco, CA 94103-0555, USA
e-mail: krystof.bankiewicz@ucsf.edu

[†]***Present address:***
Ernesto A. Salegio, Laboratory for CNS Repair, Department of Neurological Surgery, Brain and Spinal Cord Injury Center, University of California at San Francisco, San Francisco, CA 94110, USA

When nanoparticles/proteins are infused into the brain, they are often transported to distal sites in a manner that is dependent both on the characteristics of the infusate and the region targeted. We have previously shown that adeno-associated virus (AAV) is disseminated within the brain by perivascular flow and also by axonal transport. Perivascular distribution usually does not depend strongly on the nature of the infusate. Many proteins, neutral liposomes and AAV particles distribute equally well by this route when infused under pressure into various parenchymal locations. In contrast, axonal transport requires receptor-mediated uptake of AAV by neurons and engagement with specific transport mechanisms previously demonstrated for other neurotropic viruses. Cerebrospinal fluid (CSF) represents yet another way in which brain anatomy may be exploited to distribute nanoparticles broadly in the central nervous system. In this study, we assessed the distribution and perivascular transport of nanoparticles of different sizes delivered into the parenchyma of rodents and CSF in non-human primates.

Keywords: gene delivery, AAV, liposomes, thalamo-cortico, perivascular, CSF

INTRODUCTION

The movement of macromolecules and nanoparticles within the brain is not a simple process and no single mechanism is entirely responsible for the dissemination of such substances. Three main routes of distribution have been described: rapid perivascular flow, rapid paravascular flow of cerebrospinal fluid (CSF), and slow axonal transport of viral particles both anterograde and retrograde. With tools at hand today, we can isolate and interrogate each pathway substantially independently of the others.

Our initial forays into this area arose from investigations into the therapeutic utility of adeno-associated viral (AAV) vector for the treatment of Parkinson's disease (Bankiewicz et al., 2000). It was soon apparent that pressurized convection-enhanced delivery (CED) infusions of AAV2-hAADC into the primate striatum resulted in pronounced transgene expression in the globus pallidus. At the time, we assumed that this was due to a perivascular mechanism, and subsequent studies have confirmed that this is indeed the case. We showed in rat experiments that perivascular distribution is greatly influenced by heart rate and is extremely rapid (Hadaczek et al., 2006). Infusion of AAV particles or liposomes into rat striatum revealed rapid movement along perivascular tracts leading from the site of infusion into the globus pallidus. This kind of acute distribution is vectorial. Other parts of the basal ganglia, such as substantia nigra, were not the recipient of this type of rapid transport, suggesting that specific vascular tracts are required to enable this process. More recent studies of parenchymal infusion of liposomes visible by real-time magnetic resonance imaging (MRI) have revealed that rapid convective flow is the primary means by which parenchymal infusions can cover volumes of tissue several fold greater than the volume of infusate (Krauze et al., 2005a, 2006, 2009).

In contrast to this rapid distribution of a variety of infusates, the axonal transport of AAV particles occurs over a more extended timeframe. Although AAV particles can indeed be distributed perivascularly in anatomically restricted domains, it is the ability of AAV to be taken up by neurons and transported over long distances that has excited intense interest. We showed some years ago that AAV2 is transported intact from primate thalamus to cortex where release of AAV2 particles results in widespread transduction of neurons in a number of cortical layers to which thalamic neurons project (Kells et al., 2009). Similarly, we described anterograde axonal transport of AAV2 in basal ganglia in primates (Kells et al., 2012) and in rodents (Ciesielska et al., 2011). Anterograde transport is not ubiquitous among AAV serotypes. For example, AAV6 is transported in a retrograde direction and we are actively exploring the repertoire of available serotypes in this regard.

More recently, we have explored CSF infusions as a way to distribute nanoparticles throughout the primate brain (Samaranch

et al., 2013). Both AAV7 and AAV9, infused via intrathecal injection (lumbar puncture) or into cisterna magna (CM) injection, direct robust transgene expression throughout spinal cord, brainstem, cerebellum, and cortex. As we discuss below, the pattern of transgene expression is consistent with the paravascular flow of CSF through these regions. We found also that this phenomenon is not restricted to AAV7 and AAV9. Fluorescent micelles are also extensively distributed through the paravascular pathways deep into the brain.

Due to the presence of the blood–brain barrier (BBB), distribution of therapeutic agents within the central nervous system (CNS) is a major problem in drug delivery. In this study, given our current focus, we provide a more detailed view on the distribution of nanoparticles within the parenchyma of rodents and CSF of non-human primates (NHPs), as alternative routes for delivering therapeutic agents *in vivo*. In particularly, we demonstrate how nanoparticles of different properties and sizes can be rapidly distributed to remote regions within the brain, either propelled by an exogenous pressurized delivery and/or by the endogenous flow of the CSF. Each mechanism displays unique anatomical targeting properties that may be exploited to therapeutic effect. This emerging repertoire of routes for infusate distribution also carries implications for delivery of other types of therapeutic nanoparticles. It should be noted that, given the size and "simpler" axonal connectivity of the rodent's brain relative to that of primates, we generally perform parenchymal injections in rodents and then validate CSF delivery the primate.

MATERIALS AND METHODS

ANIMALS

To investigate the transport of AAV particles, 12 Sprague–Dawley (SD) rats (∼250–350 *g*) received a unilateral infusion into the thalamus of AAV2-green fluorescent protein (GFP) or AAV6-GFP. To examine the perivascular transport of larger particles five SD animals received a single thalamic infusion of fluorescently labeled DiIC^{18}-liposomes (1 μM). To determine whether any ultra-structural changes had occurred after intra-parenchymal pressurized delivery, two animals were processed for electron microscopy (EM) and infused with phosphate buffered saline (PBS) alone with one additional animal serving as a non-infused naïve control. Perivascular transport of AAV particles infused into the CSF (cisterna magna) was examined in four NHPs (*Macaca mulatta*) that received a single injection of either AAV7 or AAV9-GFP ($n = 2$/serotype; Samaranch et al., 2013). To evaluate the transport of larger particles in NHP, one NHP received a single injection of Oregon Green (OG) labeled micelles into the CM. No differences in body weight and/or adverse symptoms were observed throughout the study. All procedures were carried out in accordance with the UCSF Institutional Animal Care and Use Committee (IACUC) and the Animal Care and Use Committee (ACUC) at Valley Biosystems Inc.

INFUSATES

AAV2-GFP (1.3 vg/mL × 10^{13} vg/mL), AAV6-GFP (1.2 vg/mL × 10^{13} vg/mL), AAV7-GFP (2.0 vg/mL × 10^{13} vg/mL), AAV9-GFP (1.8 vg/mL × 10^{13} vg/mL) were manufactured by the Research Vector Core facility at Children's Hospital of Philadelphia (∼20–25 nm in size; Matsushita et al., 1998). Liposomes were fluorescently labeled with membrane-bound DiIC^{18} 1,1′-dioctadecyl-3,3,3′,3′-tetramethylindocarbocyanine perchlorate as described (∼65 nm in size; Krauze et al., 2006). 3-helix micelles are self-assembling amphiphilic peptide-polymer conjugates (∼15 nm in size; Dong et al., 2012). The micelle-forming amphiphile is denoted as dC18-1CW(P2K)-P750. This amphiphile was labeled with the fluorescent agent, OG, and the product denoted as dC18-1CW(P2K)-OG (Dong et al., 2012). 10 mg dC18-1coi(P2K)-P750 and 1 mg of dC18-1CW(P2K)-OG were dissolved in 0.5 mL of methanol in a glass vial and the solvent was evaporated in vacuum oven for 3 h. The dried film was rehydrated with 2 mL of 25 mM phosphate buffer, pH 7.4, and the solution was stirred for 16 h to allow assembly of OG-conjugated fluorescent 3-helix micelles. The micelle solution was washed to remove any unincorporated OG and concentrated by spin filtration. The concentrate was washed with water and lyophilized to obtain OG labeled 3-helix micelles. Fluorescent micelle solution was prepared by directly dissolving the lyophilized fraction in phosphate buffer. Micelles at 6 mg/mL were used for *in vivo* injections. Fluorescence was visualized at 488 nm on a Zeiss Axiomat microscope.

INFUSIONS

Rats were anesthetized with isoflurane (Baxter, Deerfield, IL, USA) and placed in a stereotactic frame (David Kopf Instruments, Tujunga, CA, USA). A 1-cm longitudinal incision was made on the skin overlaying the skull and a burr-hole was drilled at the following coordinates for targeting the thalamus (AP: −2.8, ML: +1.6, DV: −5.5 mm). A fused silica (Polymicro Technologies, USA) with a 1 mm stepped cannula (0.1 mm internal diameter) was used to deliver a total volume of 12 μL in experiments investigating AAV2, AAV6 and EM, whereas, animals infused with liposomes received a total volume of 5 μL at a rate of 0.5 μL/min (for all infusates). Total length of infusion procedure lasted either 24 or 10 min, respectively, plus a final 2 min period prior to cannulae retraction to reduce reflux of infusate.

Non-human primate were sedated with ketamine/xylazine and placed in a prone position in a stereotactic frame with the head flexed. A 3 mL syringe was manually guided into the CM until CSF was aspirated into the syringe. Once the correct position of the needle was verified, 2 mL of infusate was infused into the CM at a rate of 0.5 μL/min. The duration of the infusion procedure was approximately 4 min with a 2 min waiting period prior to withdrawal of the needle.

TISSUE PROCESSING

Animals were subjected to necropsy either at 3 weeks (rats) or 6 weeks (NHP) after vector infusion or 4 h after micelle delivery (NHP) and transcardially perfused with PBS followed by 4% paraformaldehyde (PFA)/PBS. Brains were harvested, post-fixed in 4% PFA/PBS for 24–48 h and cryoprotected in 30% sucrose. All post-fixed brains were cut into 40 μm serial sections that were then processed for immunohistochemistry. Liposome-treated animals were sacrificed 30 min after infusion with an overdose of sodium pentobarbital solution and their brains were immediately frozen in dry-ice cooled

isopentane. Every second 40 μm section was collected and viewed with a Zeiss microscope with a filter appropriate for Cy-3 fluorescence.

ELECTRON MICROSCOPY

Animals used for EM were transcardially perfused with 0.1 M Sodium Cacodylate (pH 7.4) buffer solution and then fixed with a mixture of 2% Glutaraldehyde, 1% PFA and 0.1 M Sodium Cacodylate. PBS-infused animals were used as controls and the thalamus was carefully dissected and embedded in epoxy resin. Tissue was cut into 1 μm thick sections with a diamond knife (1.5 mm wide blade at a 45° angle; Diatome, USA).

IMMUNOPEROXIDASE STAINING

A polyclonal antibody against GFP (rabbit anti-GFP, www.millipore.com, Cat. #06-896) was used for immunodetection of the transgene in animals that received AAV infusions. Briefly, sections were washed with PBS (3 min × 5 min), quenched for endogenous peroxidase activity in 1% H_2O_2/30% ethanol for 30 min, and then washed briefly in PBS/1% Tween [phosphate buffered saline including Tween (PBST)]. Sections were blocked in Background Sniper® (Biocare Medical, BS966G) for 30 min and incubated overnight at 4°C with anti-GFP antibody (1:400) or anti-CD31 (Abcam mouse anti-CD31, clone JC/70A; 1:200) in Da Vinci® green diluent (Biocare Medical, PD900). After washing in PBST, sections were incubated for 1 h in Mach-3-rabbit-probe (Biocare Medical, RP531L) at room temperature (RT), washed again and incubated in Mach-3-rabbit-HRP polymer (Biocare Medical, RH531L) 1 h at RT. After incubation, sections were washed in PBST and developed with 3,3′-diaminobenzidine (DAB) for 1 min (DAB Peroxidase Substrate Kit, Vector Laboratories). DAB-processed sections were washed in PBS and mounted on frosted slides.

RESULTS

AAV SEROTYPES INFLUENCE AXONAL TRANSPORT

The use of AAV vectors encoding fluorescent reporter proteins, such as GFP, permits us to explore anatomical connections *in vivo* by measuring transgene expression at the site of injection and tracking the expression pattern in distal regions. Although axonal transport of viruses is a well-known phenomenon, we were the first to demonstrate that AAV2 not only undergoes anterograde transport but viral particles can apparently be released intact from nerve terminals to transduce other neurons far from the original site of vector infusion in a pattern reflective of known axonal projection pathways. We have demonstrated this in the rodent brain (Ciesielska et al., 2011) and in NHP (Kells et al., 2009). Not all AAV serotypes undergo anterograde transport like AAV2. AAV6, for example, is transported exclusively in a retrograde direction in rodents (Salegio et al., 2013). We initially observed this in a comparison of thalamic infusion of AAV2 with AAV6. In this study, we observed gene transfer throughout all layers of the neocortex (I–VI), including those in pre-frontal regions distal from the site of injection (**Figure 1**). However, the diverse reciprocal connectivity of the thalamus with cortex made definitive analysis difficult. By targeting regions with "simpler" anatomical connections such as the striatum, we could more confidently determine directionality of axonal transport. In rodent striatum, both AAV2 and AAV6 transduce only neurons. AAV2 transduces parts of the basal ganglia to which striatal neurons project, such as substantia nigra pars reticulata (SNr) but does not transduce neurons that project to the striatum such as neurons from the substantia nigra pars compacta (SNc). In contrast, AAV6 transduces SNc, but not SNr, neurons after striatal infusion of AAV6. Moreover, striatal AAV6 transduces cortico-striatal neurons whereas AAV2 does not. This inverse directionality of axonal transport is also seen in NHP with a minor, but potentially significant difference (San Sebastian et al., 2013). AAV6 is not exclusively neurotropic as it is in rodents, although it is a retrogradely transported vector. Although the degree of glial transduction was modest, AAV6-GFP nevertheless triggered a brisk cell-mediated immune response to the non-self transgene, GFP, just as we have seen more intensely with AAV9 (Ciesielska et al., 2013).

Similarly, retrograde transport of adenovirus has been described in rat brain (Kuo et al., 1995). One hypothesis is that differential engagement with molecular machinery that specifies anterograde or retrograde transport may underlie this phenomenon. Herpes simplex virus 1 (HSV-1) interacts with both kinesin and dynein to catalyze anterograde and retrograde axonal transport respectively (Diefenbach et al., 2008). We speculate that these two capacities may be separately defined in structural differences in AAV2 and AAV6 capsids (Gao et al., 2004) and possibly by receptor-cell interactions (Nonnenmacher and Weber, 2012).

AXONAL VERSUS PERIVASCULAR TRANSPORT

Anterograde axonal transport of AAV2 is a relatively slow process taking at least 6 weeks after delivery to reach an easily detectable level of transgene expression distal from the site of injection (Salegio et al., 2013). However, we have established that AAV particles (∼20–25 nm in size), as well as proteins and liposomes (∼65 nm in size), can also be distributed very rapidly by non-axonal means. Perivascular transport of various nanoparticles and proteins takes place during convective (pressurized) infusions, the most clear-cut example being distribution of infusates from putamen to globus pallidus. We found that the driving mechanism appears to be arterial pressure (Hadaczek et al., 2006). Increasing blood pressure in rats undergoing striatal infusions significantly increased distribution of infusates and stopping the heart effectively blocked distribution of infusates beyond the local infusion site.

We delivered fluorescently labeled liposomes into the thalamus of adult rats and evaluated liposomal distribution in the brain 30 min after delivery. Interestingly, we observed liposomes approximately 2.4 mm rostral and 1.6 mm caudal from the site of injection (**Figure 2**). Given that the adult rat brain is approximately 20 mm in length along the anterior–posterior (AP) axis (excluding the olfactory bulb; Paxinos and Watson, 1998), we estimate that these liposomes efficiently traveled up to 4 mm on the AP axis, covering 20% of the rat brain. Consistent with our previous observations, we found fluorescently labeled particles surrounding blood vessels (**Figure 3**), indicative of perivascular transport. Furthermore, examination of the macro-environment by EM, revealed the expansion of the

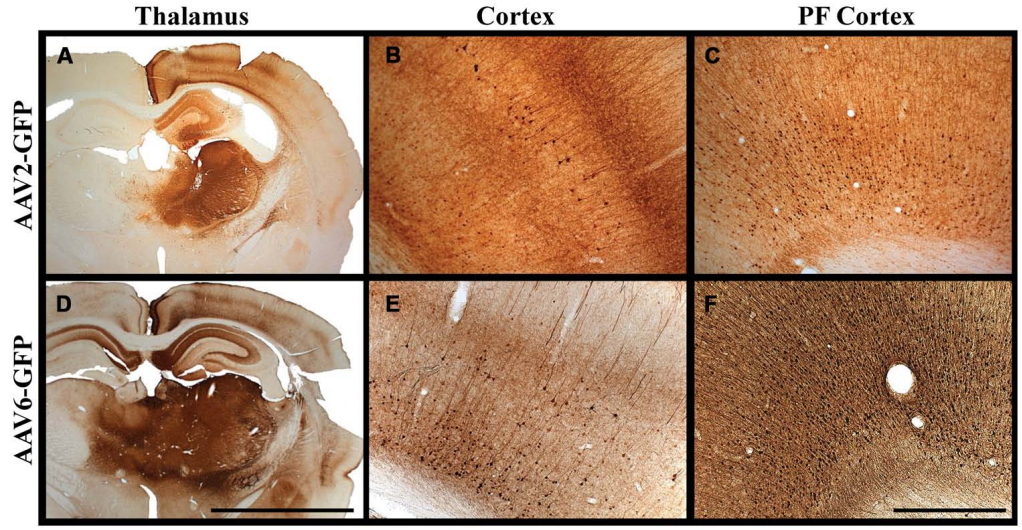

FIGURE 1 | Transgene distribution after AAV2 and AAV6 delivery. (A–F) Unilateral injection into the thalamus of adult rats of either AAV2 or AAV6 resulted in widespread expression of GFP transgene in the neocortex and in pre-frontal regions distal to the site of injection. Scale bars: **A,D** = 5 mm; **B,C,E,F** = 1 mm.

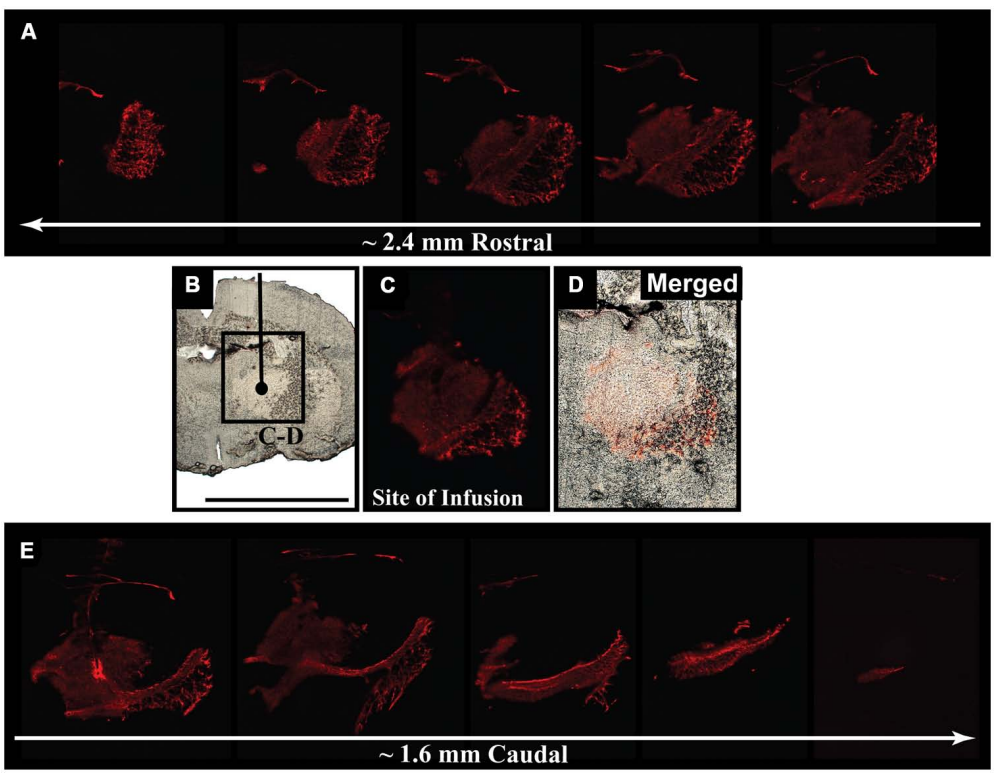

FIGURE 2 | Early parenchymal distribution of fluorescently labeled liposomes. (A–E) Acute survival time-point for liposome-infused animals revealed the rapid spread of fluorescently labeled liposomes 30 min after delivery into the thalamus. Spread of fluorescence reached approximately 2.4 mm rostral and 1.6 mm caudal from the site of infusion, suggesting efficient movement of these particles throughout the brain after CED. Scale bar: **B–D** = 5 mm.

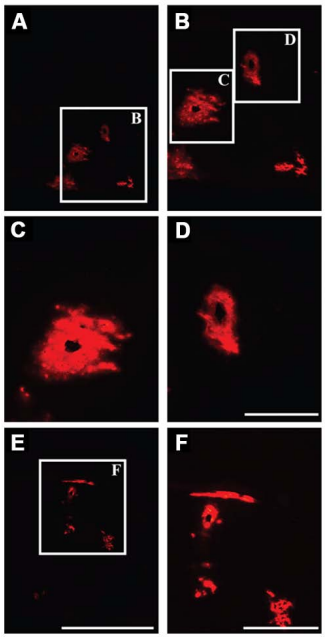

FIGURE 3 | Perivascular transport of liposomes. (A–F) Examination of parenchymal tissue 2 mm rostral from the site of infusion showing the presence of fluorescently labeled liposomes surrounding the lumen of blood vessels, indicating effective transport of these particles along perivascular spaces. Scale bars: **A,E** = 5 mm; **C,D** = 500 μm; **B,F** = 1 mm.

extracellular-perivascular space compared to normal non-infused control tissue (**Figure 4**). Margin measurements of these pockets revealed that the hydrostatic pressure of CED expanded the interstitial (Virchow–Robin) space sufficient to accommodate the distribution of large nanoparticles.

CEREBROSPINAL FLUID (CSF) IS AN EFFICIENT DISTRIBUTOR OF BOTH AAV AND MICELLES

A third means by which nanoparticles and viruses may be distributed efficiently throughout the brain is via CSF. In previous studies, we found that intrathecal (cisterna magna) administration of AAV7 or AAV9 in NHP resulted in extensive transduction of neuronal and non-neuronal cells throughout the spinal cord, brainstem and neocortex (Samaranch et al., 2013). The pattern of distribution throughout white matter was non-uniform and took the form of rosettes that appeared to surround blood vessels indicated by co-staining against the endothelial marker, CD31, and GFP transgene (**Figure 5**). In many cases, the lumen of the vessel is patent and surrounded by endothelium stained blue and brown GFP^+ cells (mostly astrocytes). This pattern is consistent with the concept of para-arterial flow of CSF through the brain (Nedergaard, 2013) and indicates that brisk flow of CSF from choroid plexus offers efficient vectorial flow through the cortex and cerebellum, as well as into the dorsoventral axis of the spine. Little transduction of subcortical gray matter is evident in these experiments, suggesting that binding of AAV7 and AAV9 to perivascular cells is relatively rapid, and the lack of transduction in deeper subcortical structures is a consequence of substantial sequestration of vector particles from superficial cortical surfaces first bathed by the CSF.

Distribution of relatively inert nanoparticles, demonstrated that CSF can easily distribute infusates into the cortical gray matter. Recently developed ultra-small (∼15 nm in size) spherical micelles (Dong et al., 2012), called "3-helix micelles," based on amphiphilic peptide-PEG conjugates where the head-group self-associates into a 3-helix bundle, were covalently labeled with OG and infused into the CM of a *Rhesus* monkey. As shown in **Figure 6**, fluorescent nanoparticles shown in green, filled the perivascular space surrounding blood vessels 4 h after cisternal injection of 18 mg micelles in a 3 mL injection. In contrast to what we observed with AAV, where transduction was confined to white matter tracts, brainstem, cerebellum and spinal cord, infusion of micelles generated prominent perivascular fluorescence not only in brainstem and cerebellum, but also in the ventral tegmental area (VTA) and amygdala.

DISCUSSION

Effective therapies for neurological diseases must take account of the profound anatomical and functional complexity of the brain. This is doubly so for directly delivered therapies. In this study, we demonstrated the distribution of nanoparticles of different sizes, including micelles (∼15 nm in size), AAV (∼20–25 nm) and liposomes (∼65 nm), within the CNS of rodents and NHPs. Early work in understanding the distribution of AAV infused under pressure into the brain parenchyma revealed that the primary means of distributing vector was via perivascular (Virchow–Robin) spaces through which CSF flows. It is important to note that simple injections cannot hope to engage the perivascular system. Specialized infusion cannulae are required that enable constant pressures to be exerted at the tip of the cannula such that the interstitial hydrostatic pressure is exceeded and infusate can flow out into the tissue. Simple needles generate significant reflux and we introduced a reflux-resistant cannula to counter this tendency (Krauze et al., 2005c; Varenika et al., 2009). The advent of MRI-guided infusions further refined our understanding of the mechanics of perivascular flow and we showed in a number of studies that perivascular distribution of liposomes was linear with respect to time (Krauze et al., 2005a, 2006, 2009); the slope of the curve was increased in myelinated regions (Krauze et al., 2005b) and cessation of infusion prevented further expansion in the volume of distribution. Moreover, cannula placement is an important variable due to leakage of infusate into adjacent ventricles and/or white matter tracts (Yin et al., 2009, 2010a,b). No further increase in volume of distribution is seen once significant leakage occurs, presumably because of a sharp reduction in infusion pressure. In addition to a loss in infusion pressure, leakage of infusate into the ventricular system will lead to unrestricted exposure of the delivered agent within the CNS. Similarly, white matter tracts will act as a conduit and greatly distribute infusates throughout, ideal when attempting global exposure but undesirable when delivering therapeutics to localized regions.

This requirement for a pressure gradient in parenchymal delivery is not essential in the delivery of nanoparticles into CSF. The rate of flow of CSF is so high and the compartment so compliant that injections into CSF of quite large relative volumes

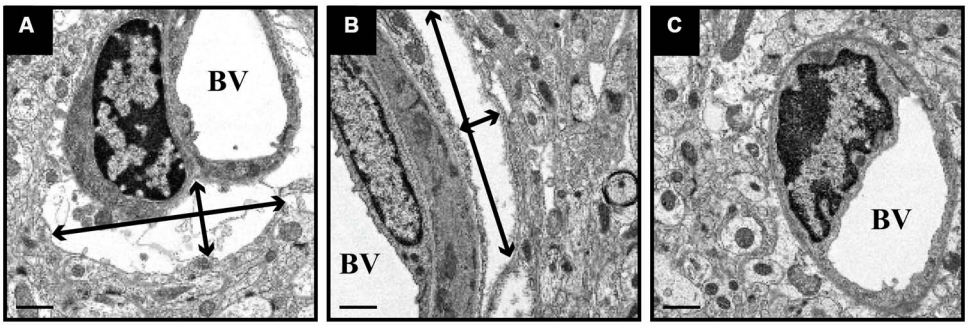

FIGURE 4 | Expansion of perivascular spaces after CED. PBS-infused tissue was processed for EM and revealed the expansion of perivascular spaces after CED. These spaces ranged in size from 11 μm (width) × 3 μm (height; black arrows; **A**) and 2.0 μm (w) × 11.5 μm (h; **B**), as compared to non-infused, naïve control tissue **(C)**. BV = blood vessel lumen. Scale bar: 1 μm.

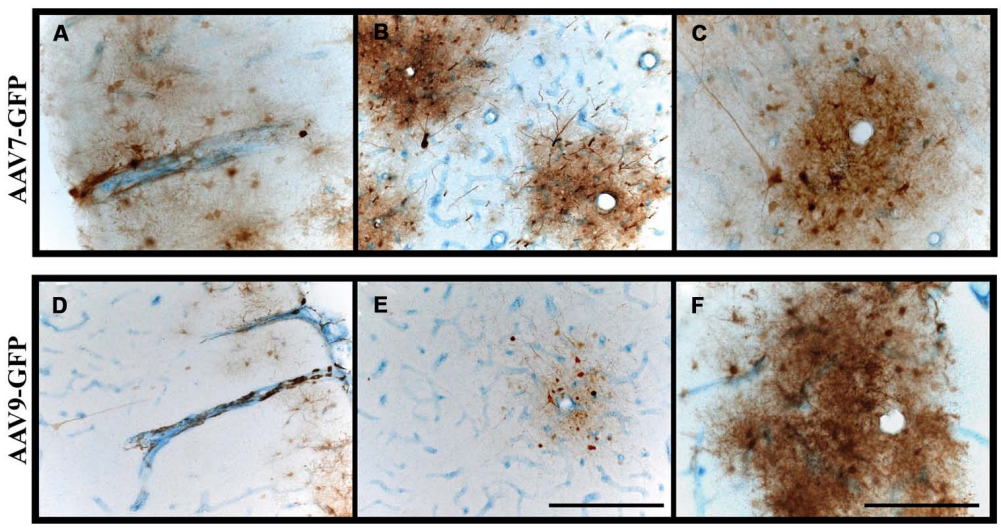

FIGURE 5 | Perivascular transport and pattern of transgene expression. (A–F) Immunostaining against GFP and blood vessels (CD31; endothelial marker) revealed the presence of GFP-positive cells surrounding blood vessels. Transgene expression was frequently observed to form rosette-like patterns in white matter, as demonstrated in cross-sectional views of blood vessels **(B,C,E,F)**, indicative of perivascular transport of AAV particles irrespective of the serotype. Scale bars: **A,B,D,E** = 500 μm; **C,F** = 250 μm.

do not cause significant increases in intracranial pressure in primates. We routinely inject up to 6 mL into either CM or lumbar intrathecal space without complications. The pace of CSF flow acts as a remarkably effective carrier for nanoparticles such as AAV or micelles. However, because this approach has remained relatively unexplored until recently for gene therapy (Snyder et al., 2011; Federici et al., 2012; Samaranch et al., 2013), the transduction properties of different AAV serotypes in primates is still unclear. The rosettes of transduction around blood vessels that we see with AAV7 and AAV9 result primarily from transduction of perivascular astrocytes. On that basis, one would predict that a highly neurotropic virus such as AAV2 would be poorly effective at transducing cells via the CSF route. Conversely, vectors that transduce astrocytes would be expected to be more efficient at CSF-mediated transduction of the brain. This, however, remains to be elucidated. It is clear, also, from infusion of non-viral nanoparticles that rapid distribution of CSF infusates is an inherently efficient process. In addition to distribution of fluorescent micelles throughout cerebellum, brainstem and cortex, we saw quantitative distribution into the amygdala and VTA, which provides encouragement to the idea that chronic drug delivery to the brain could be mediated by CSF infusion of drug-loaded micelles.

Axonal transport of AAV has turned out to be an important discovery. It reminds us forcefully that transduction patterns in the primate brain are strongly influenced by neuroanatomy and that neuronal projections act as efficient conduits through which intact virions may be transported. Indeed, this same propensity for neurons to transport other viruses, such as HSV (Diefenbach et al., 2008), is well-established. In fact, this phenomenon has been proposed as a means by which neurological diseases such as Alzheimer's (Balin et al., 1998, 2008) and Parkinson's disease (Braak et al., 2003) display their characteristic anatomical progression. Thus, it has been proposed that pathogens

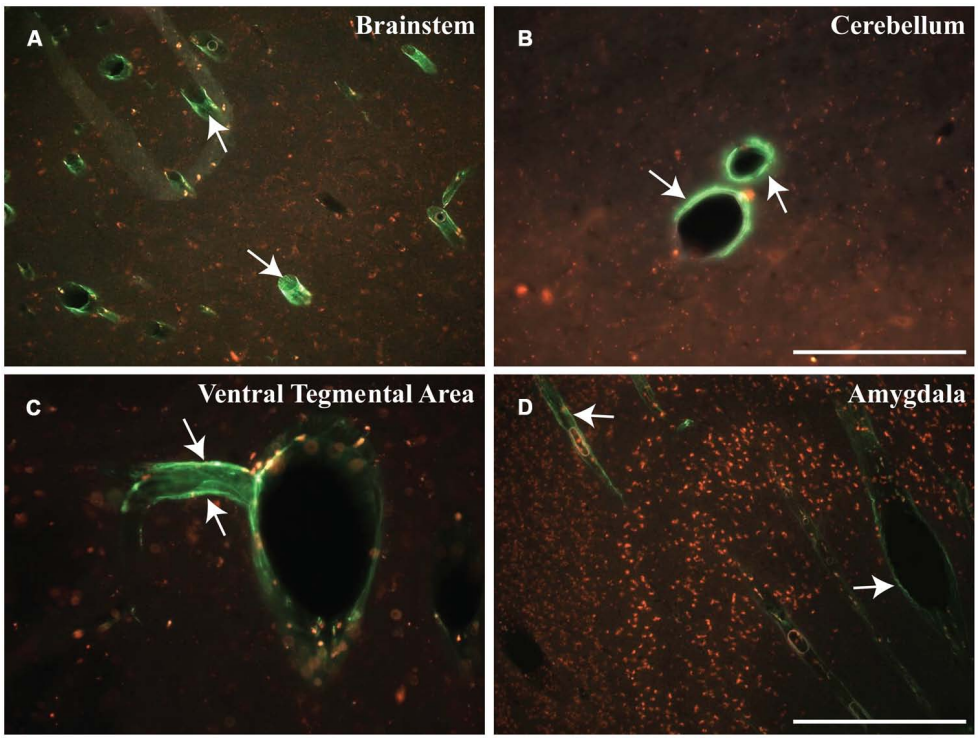

FIGURE 6 | Early distribution of micelles. (A–D) Cisternal injection of fluorescently labeled micelles (shown in green) indicate the rapid transport of these particles within different regions of the NHP brain. These micelles filled the perivascular space of blood vessels throughout the brain, particularly in the brainstem (BS), cerebellum (CB), ventral tegmental area (VTA), and amygdala (AM). Note that these micelles are shown in green (white arrows) and presence of autofluorescent lipofuscin is shown in red. Scale bars: **A,D** = 500 μm; **B,C** = 250 μm.

gain access to the brain via peripheral neurons and then steadily progress through interconnected regions. The Braak hypothesis of Parkinson's disease, for example, is that the vagal nerve serves as a primary conduit through which a pathogen could work its way up through the brainstem to the midbrain and then to cortical regions (Braak and Braak, 2000). This anatomical progression is perfectly consistent with staging and progression of the disease where lesions in specific nuclei give rise to stage-specific symptoms, such as orthostatic hypotension as sympathetic innervation to the heart atrophies as parkinsonian degeneration attacks the brainstem. Relevant to the data shown here, we speculate that, even if disease-compromised neurons were not able to transport therapeutic agents to the region-of-interest, an alternative approach would be to design agents that could be easily transported via the perivascular space, particularly when trying to reach regions of motor control such as the brainstem.

The *in vivo* distribution of nanoparticles within the cerebral cortex, as shown here, invokes certain considerations for gene and drug therapy. For instance, liposomes, almost three times larger in size than an AAV particle, efficiently covered 20% of the rat's brain within 30 min after delivery, indicating the synergistic potential of delivering agents through a pressurized system to engage with the pulsating parenchyma to enhance the amount of brain volume covered by the agent. AAV, liposomes and micelles are essentially nanocarriers designed to deliver therapeutic payloads and in a clinical setting elevation or reduction of a patient's heart rate during anesthesia, could play a significant role in the distribution of therapeutic agents (i.e., at least in those delivered within the parenchyma). Obviously, this requires further investigation.

In conclusion, advances in biomaterials and development of nanoparticles are enabling a better understanding of the complex functionality of the central nervous system. Here we describe the movement of nanoparticles of different composition and size within the brain of rodents and NHPs. Tools such as fluorescent reporter proteins in AAV and fluorophore-conjugated nanoparticles have allowed us to better understand some key aspects associated with perivascular transport, CSF flow and axonal transport. However, even though it is unclear how these routes of transport would be affected in a diseased-brain, the diverse tools we have in hand should continue to advance our knowledge in this area.

AUTHOR CONTRIBUTIONS

Ernesto A. Salegio, Hillary Streeter, Nikhil Dube, Lluis Samaranch, Adrian P. Kells, Waldy San Sebastian, John Forsayeth, Krystof S. Bankiewicz helped design and conduct the rodent experiments. Ernesto A. Salegio, Hillary Streeter, Lluis Samaranch, Adrian P. Kells, Waldy San Sebastian, Krystof S. Bankiewicz helped with NHP surgeries, daily care of animals and tissue processing. Nikhil Dube, Ting Xu made the micelles and helped

with data analysis. All authors contributed to the writing of the manuscript.

ACKNOWLEDGMENT

This study was supported in part by a grant to Krystof S. Bankiewicz from NIH-NINDS (R01NS073940-01).

REFERENCES

Balin, B. J., Gerard, H. C., Arking, E. J., Appelt, D. M., Branigan, P. J., Abrams, J. T., et al. (1998). Identification and localization of chlamydia pneumoniae in the Alzheimer's brain. *Med. Microbiol. Immunol.* 187, 23–42. doi: 10.1007/s004300050071

Balin, B. J., Little, C. S., Hammond, C. J., Appelt, D. M., Whittum-Hudson, J. A., Gerard, H. C., et al. (2008). Chlamydophila pneumoniae and the etiology of late-onset Alzheimer's disease. *J. Alzheimers Dis.* 13, 371–380.

Bankiewicz, K. S., Eberling, J. L., Kohutnicka, M., Jagust, W., Pivirotto, P., Bringas, J., et al. (2000). Convection-enhanced delivery of AAV vector in parkinsonian monkeys; in vivo detection of gene expression and restoration of dopaminergic function using pro-drug approach. *Exp. Neurol.* 164, 2–14. doi: 10.1006/exnr.2000.7408

Braak, H., and Braak, E. (2000). Pathoanatomy of Parkinson's disease. *J. Neurol.* 247(Suppl. 2), II3–II10. doi: 10.1007/PL00007758

Braak, H., Rub, U., Gai, W. P., and Del Tredici, K. (2003). Idiopathic Parkinson's disease: possible routes by which vulnerable neuronal types may be subject to neuroinvasion by an unknown pathogen. *J. Neural Transm.* 110, 517–536. doi: 10.1007/s00702-002-0808-2

Ciesielska, A., Hadaczek, P., Mittermeyer, G., Zhou, S., Wright, J. F., Bankiewicz, K. S., et al. (2013). Cerebral infusion of AAV9 vector-encoding non-self proteins can elicit cell-mediated immune responses. *Mol. Ther.* 21, 158–166. doi: 10.1038/mt.2012.167

Ciesielska, A., Mittermeyer, G., Hadaczek, P., Kells, A. P., Forsayeth, J., Bankiewicz, K. S., et al. (2011). Anterograde axonal transport of AAV2-GDNF in rat basal ganglia. *Mol. Ther.* 19, 922–927. doi: 10.1038/mt.2010.248

Diefenbach, R. J., Miranda-Saksena, M., Douglas, M. W., and Cunningham, A. L. (2008). Transport and egress of herpes simplex virus in neurons. *Rev. Med. Virol.* 18, 35–51. doi: 10.1002/rmv.560

Dong, H., Shu, J. Y., Dube, N., Ma, Y., Tirrell, M. V., Downing, K. H., et al. (2012). 3-Helix micelles stabilized by polymer springs. *J. Am. Chem. Soc.* 134, 11807–11814. doi: 10.1021/ja3048128

Federici, T., Taub, J. S., Baum, G. R., Gray, S. J., Grieger, J. C., Matthews, K. A., et al. (2012). Robust spinal motor neuron transduction following intrathecal delivery of AAV9 in pigs. *Gene Ther.* 19, 852–859. doi: 10.1038/gt.2011.130

Gao, G., Vandenberghe, L. H., Alvira, M. R., Lu, Y., Calcedo, R., Zhou, X., et al. (2004). Clades of Adeno-associated viruses are widely disseminated in human tissues. *J. Virol.* 78, 6381–6388. doi: 10.1128/JVI.78.12.6381-6388.2004

Hadaczek, P., Yamashita, Y., Mirek, H., Tamas, L., Bohn, M. C., Noble, C., et al. (2006). The "perivascular pump" driven by arterial pulsation is a powerful mechanism for the distribution of therapeutic molecules within the brain. *Mol. Ther.* 14, 69–78. doi: 10.1016/j.ymthe.2006.02.018

Kells, A. P., Forsayeth, J., and Bankiewicz, K. S. (2012). Glial-derived neurotrophic factor gene transfer for Parkinson's disease: anterograde distribution of AAV2 vectors in the primate brain. *Neurobiol. Dis.* 48, 228–235. doi: 10.1016/j.nbd.2011.10.004

Kells, A. P., Hadaczek, P., Yin, D., Bringas, J., Varenika, V., Forsayeth, J., et al. (2009). Efficient gene therapy-based method for the delivery of therapeutics to primate cortex. *Proc. Natl. Acad. Sci. U.S.A.* 106, 2407–2411. doi: 10.1073/pnas.0810682106

Krauze, M. T., Forsayeth, J., Park, J. W., and Bankiewicz, K. S. (2006). Real-time imaging and quantification of brain delivery of liposomes. *Pharm. Res.* 23, 2493–2504. doi: 10.1007/s11095-006-9103-5

Krauze, M. T., Forsayeth, J., Yin, D., and Bankiewicz, K. S. (2009). Convection-enhanced delivery of liposomes to primate brain. *Methods Enzymol.* 465, 349–3262. doi: 10.1016/S0076-6879(09)65018-7

Krauze, M. T., McKnight, T. R., Yamashita, Y., Bringas, J., Noble, C. O., Saito, R., et al. (2005a). Real-time visualization and characterization of liposomal delivery into the monkey brain by magnetic resonance imaging. *Brain Res. Brain Res. Protoc.* 16, 20–26. doi: 10.1016/j.brainresprot.2005.08.003

Krauze, M. T., Saito, R., Noble, C., Bringas, J., Forsayeth, J., McKnight, T. R., et al. (2005b). Effects of the perivascular space on convection-enhanced delivery of liposomes in primate putamen. *Exp. Neurol.* 196, 104–111. doi: 10.1016/j.expneurol.2005.07.009

Krauze, M. T., Saito, R., Noble, C., Tamas, M., Bringas, J., Park, J. W., et al. (2005c). Reflux-free cannula for convection-enhanced high-speed delivery of therapeutic agents. *J. Neurosurg.* 103, 923–929. doi: 10.3171/jns.2005.103.5.0923

Kuo, H., Ingram, D. K., Crystal, R. G., and Mastrangeli, A. (1995). Retrograde transfer of replication deficient recombinant adenovirus vector in the central nervous system for tracing studies. *Brain Res.* 705, 31–38. doi: 10.1016/0006-8993(95)01065-3

Matsushita, T., Elliger, S., Elliger, C., Podsakoff, G., Villarreal, L., Kurtzman, G. J., et al. (1998). Adeno-associated virus vectors can be efficiently produced without helper virus. *Gene Ther.* 5, 938–945. doi: 10.1038/sj.gt.3300680

Nedergaard, M. (2013). Neuroscience. Garbage truck of the brain. *Science* 340, 1529–1530. doi: 10.1126/science.1240514

Nonnenmacher, M., and Weber, T. (2012). Intracellular transport of recombinant adeno-associated virus vectors. *Gene Ther.* 19, 649–658. doi: 10.1038/gt.2012.6

Paxinos, G., and Watson, C. (1998). *The Rat Brain,* 4th Edn. San Diego, CA: Academic Press. 1–474p.

Salegio, E. A., Samaranch, L., Kells, A. P., Mittermeyer, G., San Sebastian, W., Zhou, S., et al. (2013). Axonal transport of adeno-associated viral vectors is serotype-dependent. *Gene Ther.* 20, 348–352. doi: 10.1038/gt.2012.27

Samaranch, L., Salegio, E. A., San Sebastian, W., Kells, A. P., Bringas, J. R., Forsayeth, J., et al. (2013). Strong cortical and spinal cord transduction after AAV7 and AAV9 delivery into the cerebrospinal fluid of nonhuman primates. *Hum. Gene Ther.* 24, 526–532. doi: 10.1089/hum.2013.005

San Sebastian, W., Samaranch, L., Heller, G., Kells, A. P., Bringas, J., Pivirotto, P., et al. (2013). Adeno-associated virus type 6 is retrogradely transported in the non-human primate brain. *Gene Ther.* 20, 1178–1183. doi: 10.1038/gt.2013.48

Snyder, B. R., Gray, S. J., Quach, E. T., Huang, J. W., Leung, C. H., Samulski, R. J., et al. (2011). Comparison of adeno-associated viral vector serotypes for spinal cord and motor neuron gene delivery. *Hum. Gene Ther.* 22, 1129–1135. doi: 10.1089/hum.2011.008

Varenika, V., Kells, A. P., Valles, F., Hadaczek, P., Forsayeth, J., Bankiewicz, K. S., et al. (2009). Controlled dissemination of AAV vectors in the primate brain. *Prog. Brain Res.* 175, 163–172. doi: 10.1016/S0079-6123(09)17511-8

Yin, D., Forsayeth, J., and Bankiewicz, K. S. (2010a). Optimized cannula design and placement for convection-enhanced delivery in rat striatum. *J. Neurosci. Methods* 187, 46–51. doi: 10.1016/j.jneumeth.2009.12.008

Yin, D., Richardson, R. M., Fiandaca, M. S., Bringas, J., Forsayeth, J., Berger, M. S., et al. (2010b). Cannula placement for effective convection-enhanced delivery in the non-human primate thalamus and brainstem: implications for clinical delivery of therapeutics. *J. Neurosurg.* 113, 240–248. doi: 10.3171/2010.2.JNS091744

Yin, D., Valles, F. E., Fiandaca, M. S., Bringas, J., Gimenez, F., Berger, M. S., et al. (2009). Optimal region of the putamen for image-guided convection-enhanced delivery of therapeutics in human and non-human primates. *Neuroimage* 187, 46–51. doi: 10.1016/j.neuroimage.2009.08.069

Conflict of Interest Statement: The authors declare that the research was conducted in the absence of any commercial or financial relationships that could be construed as a potential conflict of interest.

Received: 09 December 2013; accepted: 17 February 2014; published online: 17 March 2014.

Citation: Salegio EA, Streeter H, Dube N, Hadaczek P, Samaranch L, Kells AP, San Sebastian W, Zhai Y, Bringas J, Xu T, Forsayeth J and Bankiewicz KS (2014) Distribution of nanoparticles throughout the cerebral cortex of rodents and non-human primates: implications for gene and drug therapy. Front. Neuroanat. ***8****:9. doi: 10.3389/fnana.2014.00009*

This article was submitted to the journal Frontiers in Neuroanatomy.

frontiers in
NEUROANATOMY

REVIEW ARTICLE
published: 26 March 2014
doi: 10.3389/fnana.2014.00016

Retrograde labeling, transduction, and genetic targeting allow cellular analysis of corticospinal motor neurons: implications in health and disease

Javier H. Jara[1†], Barış Genç[1†], Jodi L. Klessner[1] and P. Hande Özdinler[1,2,3]*

[1] *Davee Department of Neurology and Clinical Neurological Sciences, Feinberg School of Medicine, Northwestern University, Chicago, IL, USA*
[2] *Robert H. Lurie Cancer Center, Feinberg School of Medicine, Northwestern University, Chicago, IL, USA*
[3] *Cognitive Neurology and Alzheimer's Disease Center, Feinberg School of Medicine, Northwestern University, Chicago IL, USA*

Edited by:
Laurent Gautron, University of Texas Southwestern Medical Center, USA

Reviewed by:
Arshad M. Khan, University of Texas at El Paso, USA
Veronica Tom, Drexel University College of Medicine, USA

***Correspondence:**
P. Hande Özdinler, Cognitive Neurology and Alzheimer's Disease Center, Feinberg School of Medicine, Northwestern University, Chicago, IL, USA
e-mail: ozdinler@northwestern.edu
† These authors have contributed equally to this work.

Corticospinal motor neurons (CSMN) have a unique ability to receive, integrate, translate, and transmit the cerebral cortex's input toward spinal cord targets and therefore act as a "spokesperson" for the initiation and modulation of voluntary movements that require cortical input. CSMN degeneration has an immense impact on motor neuron circuitry and is one of the underlying causes of numerous neurodegenerative diseases, such as primary lateral sclerosis (PLS), hereditary spastic paraplegia (HSP), and amyotrophic lateral sclerosis (ALS). In addition, CSMN death results in long-term paralysis in spinal cord injury patients. Detailed cellular analyses are crucial to gain a better understanding of the pathologies underlying CSMN degeneration. However, visualizing and identifying these vulnerable neuron populations in the complex and heterogeneous environment of the cerebral cortex have proved challenging. Here, we will review recent developments and current applications of novel strategies that reveal the cellular and molecular basis of CSMN health and vulnerability. Such studies hold promise for building long-term effective treatment solutions in the near future.

Keywords: corticospinal motor neuron, genetic labeling, retrograde labeling, motor neuron disease, upper motor neurons

INTRODUCTION

Our expertise in the precise control of fine movement sets us apart from other mammals. Voluntary movement is initiated, modulated, and controlled via a very complicated neural network, called the motor neuron circuitry, which includes neurons and cells that are located both in the cerebral cortex and the spinal cord. The output of neuron function is manifested by muscle contraction leading to precise movement of the legs, arms, and hands. It is this circuitry that helps define us as human beings by giving us a unique advantage to build and create tools and to express ourselves.

Since cognitive abilities are reflected in our actions, it is unreasonable to think that only one neuron type in the brain would be responsible for movement. Among all other neuron types in the cerebral motor cortex, however, one neuron population stands out with its unique abilities and function. These neurons are characterized by: (1) a large pyramidal cell body, (2) a single apical dendrite that extends toward layer I displaying major branching and arborization, especially within layer II/III, (3) numerous basal dendrites arising from the basolateral surface, and most impressively (4) a very long axon that projects toward spinal cord targets (Molnar and Cheung, 2006; Ozdinler and Macklis, 2006; Molyneaux et al., 2007). These neurons, known as Betz cells in humans, are located in layer V of the motor cortex. They are also referred to as the upper motor neurons, corticospinal neurons, and corticospinal projection neurons. We prefer using the name corticospinal motor neurons (CSMN) due to their unique ability and function and to emphasize their role within the motor neuron circuitry.

CSMN are special neuron populations in our cerebral cortex that can collect, integrate, translate, and transmit both the excitatory and the inhibitory cortical inputs as one single message to long distance spinal cord targets. This distinct ability allows them to act as the "spokesperson" of the cerebral cortex for the motor function. Without CSMN, especially in humans, the connection between the cerebral cortex and the spinal cord would be greatly impaired. Therefore, to emphasize the importance of cortical input to the motor neuron circuitry, we think the word "motor" is necessary when naming these long distance projection neurons of the cerebral cortex.

CSMN are heavily modulated by local neuron circuitry and long distance projection neurons, including, but not restricted to, thalamocortical neurons and callosal projection neurons (CPN) (**Figure 1A**). While details are still emerging about the timing and extent of CSMN regulation, anatomical studies suggest that the major excitatory input to CSMN is mediated by neurons located in layer II/III and layer V of the motor cortex (Thomson and Lamy, 2007; Shepherd, 2011). Thalamacortical neurons are important in carrying cognitive and sensory information to CSMN via neuronal networks that include cerebellum and basal ganglia (Clasca et al., 2012). The heterogeneity of these neurons in terms of somatodendritic morphology, axonal

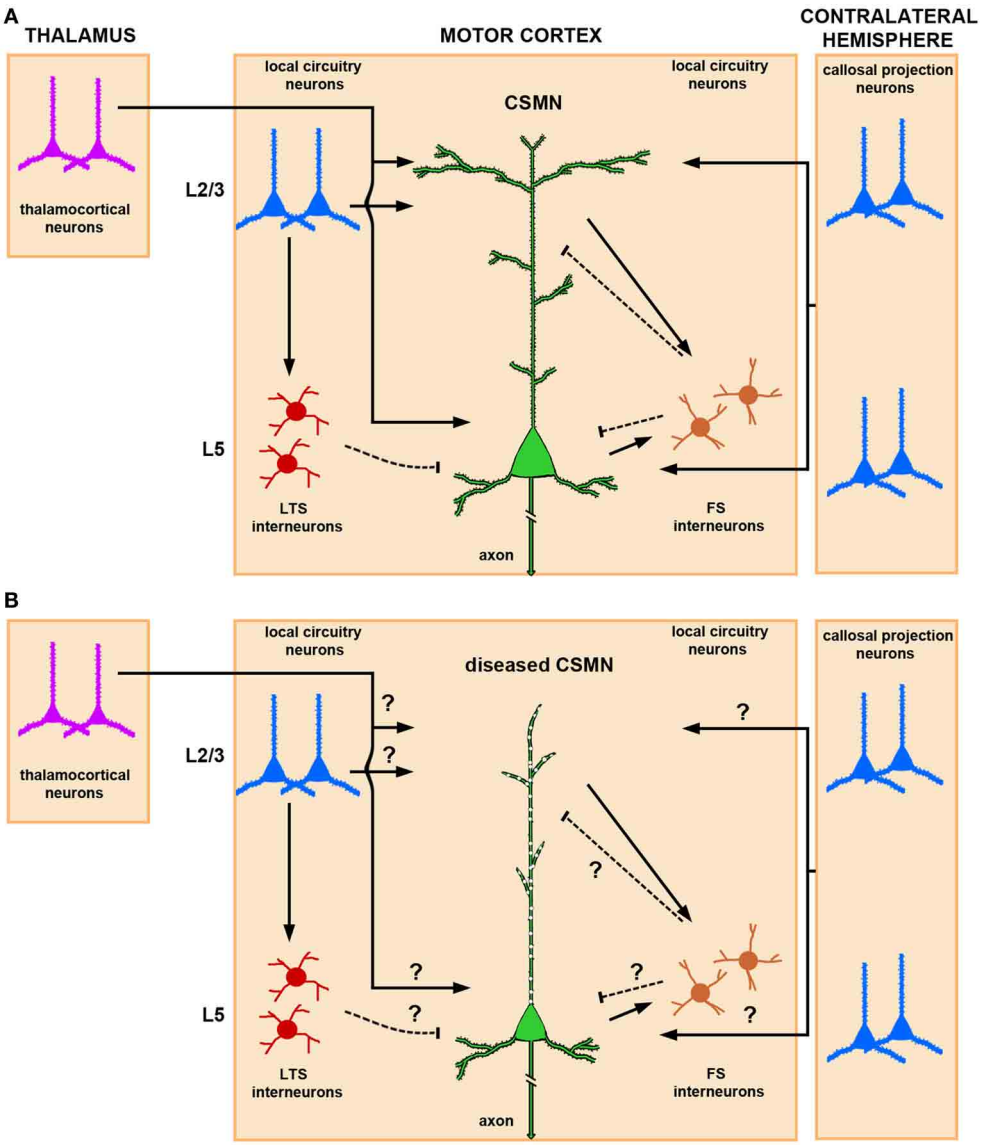

FIGURE 1 | Schematic and simplified representation of CSMN modulation by local neuronal circuitries and long-range projection neurons in normal physiological conditions and in disease. (A) Thalamocortical projections provide excitatory input to CSMN. The site of neuronal modulation is suggested to be mainly within layer II/III and layer V. CSMN are also heavily modulated by both ipsi and contralateral callosal projection neurons that are mainly located within layer II/III and layer V of the cerebral cortex. Local circuitry neurons also modulate CSMN activity either directly or via an interneuron. In particular, LTS (low-threshold-spiking) and FS (fast-spiking) interneurons are differentially involved in the inhibitory microcircuit. While LTS interneurons receive interlaminar input from layer II/III projection neurons, FS receive intralaminar input from CSMN illustrating a possible distinct mechanism for disynaptic CSMN inhibition. Excitatory inputs impinge mainly upon the spines that are located on the dendrites located in layer II/III and layer V, and inhibitory input is conveyed mainly on the spines that are directly located on the apical dendrite and on a subset of spines that are present on basal dendrites. **(B)** In ALS, CSMN show vulnerability and undergo progressive degeneration. At pre-symptomatic stage (i.e., P60) CSMN display major spine loss within apical, but not basal, dendrites and apical dendrites undergo massive vacuolation and lose cytoarchitectural integrity. Such cellular defects would have profound impact on CSMN modulation. How circuitries are affected in disease require further investigation. Excitatory and inhibitory input is denoted by lines and dashed lines, respectively.

branching, and laminar specificity is of great importance. Subtle differences within the same neuron population could account for the variations of thalamocortical input to CSMN.

Another excitatory input is provided by CPN, which include ipsi- and contralateral projections (Anderson et al., 2010). CPN are highly heterogeneous, ranging from small to medium size, and are primarily located in all layers of the cortex, but most prominently in layer V and II/III. They carry integrative circuitry information (Arlotta et al., 2005; Molyneaux et al., 2007). This neuron population is closely related to CSMN; CPN are born from the same progenitor pool, migrate together in the developing cerebral cortex, and a subset of CPN reside together with

CSMN in layer V. However, CPN project to the contralateral side of the cerebral hemisphere and display a different function in cognition, perception, and higher-order thinking.

In addition to long distance projection neurons, local circuitry neurons also have direct input to CSMN. Such neuronal interactions are rather interesting, as they can be mediated both directly and through a secondary neuron population. There is also CSMN-CSMN interaction, as nearby CSMN communicate with each other (Kiritani et al., 2012). Such interactions, which mostly occur within layer V of the motor cortex, could serve both as feedback and feed forward loops (**Figure 1A**).

Modulation of CSMN function involves a delicate and continuous balance between excitatory and inhibitory inputs. Interneurons account for about 20% of the cortical neuron population (Ikrar et al., 2011), and they are subdivided according to their anatomical location, cell morphology, specific-marker expression, dendritic arborization, and targeting of different sites and compartments of the cortical neurons including CSMN (Markram et al., 2004). Fast-spiking (FS) and low-threshold-spiking (LTS) are two types of interneurons that are implicated in CSMN inhibitory pathways (Tanaka et al., 2011). FS neurons have a high number of local connections to CSMN when compared to LTS. Recent studies designed to dissect out inhibitory inputs converging to CSMN have shown that these FS and LTS differentially inhibit CSMN (Apicella et al., 2012). While interlaminar input of pyramidal neurons in the layer II/III via LTS neurons provides disynaptic inhibition to CSMN (layer II/III→layer V), intralaminar input to FS from CSMN (layer V→layer V) delivers inhibition to CSMN in a feed forward manner (**Figure 1A**).

The progressive degeneration of CSMN is accepted as one of the major characteristics of neurodegenerative diseases affecting voluntary movement that require CSMN input to the motor neuron circuitry. For example, hereditary spastic paraplegia (HSP) is best characterized by the progressive degeneration of CSMN (Fink, 2001). The disease manifests itself with stiffness in the legs, paralysis and motor function defects. Primary lateral sclerosis (PLS) is also characterized by CSMN death and corticospinal tract (CST) degeneration. However, in amyotrophic lateral sclerosis (ALS) both the spinal and cortical motor neurons progressively degenerate (Udaka et al., 1986; Brown and Robberecht, 2001), adding complexity to the disease (Eisen and Weber, 2001; Ravits et al., 2007). Although spinal muscular atrophy (SMA) has been characterized by prominent spinal motor neurons (SMN) degeneration, recent evidence also suggests the involvement of CSMN (D'Errico et al., 2013). Lastly, exome sequencing analysis of patients with HSP revealed numerous shared common pathways and molecular networks that are also involved in ALS as well as Alzheimer's disease and Parkinson's disease (Novarino et al., 2014). This is a remarkable finding as it links numerous disorders at a molecular level. CSMN are clinically important and relevant neuron population that deserve immediate attention to improve future therapeutic applications both in injury and disease. If we can understand the molecular mechanisms responsible for their cellular vulnerability and degeneration, then we may begin to unravel the basis of numerous disease pathologies.

Even though mechanisms of CSMN modulation by cortical neurons is beginning to emerge, it is still not clear how that cortical connectivity and communication is hampered during disease. Since CSMN receive most of their input from the apical dendrite, cellular degeneration, disintegration of apical dendrite and spine loss would have significant consequences on the transfer of cortical signals to the spinal cord targets (**Figure 1B**). This indeed could be one of the reasons for a dysfunctional motor neuron circuitry and voluntary movement defects.

While CSMN are a crucial component of the motor neuron circuitry, they are not equally central in all species (Lemon, 2008). In rodents, the CST projects through the striatum, internal capsule, pons and pyramidal decussation, and subsequently descends in the ventral part of the dorsal column (Jones et al., 1982; Stanfield, 1992; Terashima, 1995). In humans, these projections descend laterally, and more than 80% of the axon fibers that originate from the CSMN in the motor cortex connect directly with SMN in the spinal cord (Lemon, 2008). This difference in projection paths affects neuronal circuits and connections defining the speed, specificity, and mode of action. Humans are very dexterous with their hands, but are mostly vulnerable to any injury that damages the CST. CSMN numbers are very limited in the cerebral cortex and their cellular degeneration results in severe consequences and is central to numerous neurodegenerative diseases and injury. For example, CSMN health and connectivity are hampered during spinal cord injury. Lesions of the CST result in deterioration in speed, force, and movement coordination (Lemon, 2008). One of the reasons for long-term paralysis in patients is the cellular degeneration of CSMN and the impaired connection between the cerebral cortex and the spinal cord.

We enter a new era of very exciting times in CSMN biology. Historically, there were serious limitations that hindered detailed studies of CSMN. Their importance as a neuron population was not well appreciated, and applications that allowed their cellular analysis were not available. Recently, numerous novel techniques and approaches to help identify and visualize CSMN within the complex structure of the cerebral cortex have been developed. AAV-mediated gene delivery and novel reporter lines now have the potential to change the future of CSMN investigations. In this review, we will introduce and describe these innovative approaches and comparatively discuss their limitations and advantages for future cellular analysis and therapeutic applications.

RETROGRADE LABELING APPROACHES

With their axons projecting to distant targets, projection neurons are one of the most polarized cells in the body and highly depend on axonal transport to maintain cellular homeostasis. Retrograde transport depends on neurons' ability to carry proteins and molecules from the tip of the axon all the way back to the soma. Early studies revealed the basics of this cellular process in the central nervous system (Lavail and Lavail, 1972). Soon after, the ability of axons to uptake and retrogradely transport tracers and molecular dyes was uncovered making it possible to label, identify, and visualize neurons of interest based on their projection path and the pattern of their target innervation (Lavail et al., 1973). Retrograde transport studies demonstrated the importance of growth factors for the development and maturation of

neurons. For example, when retrograde transport of nerve growth factor (NGF) to the cell body was revealed, the field opened up to a new idea that this phenomenon was actually critically important for the maintenance of neuronal health and function (Paravicini et al., 1975; Stoeckel and Thoenen, 1975), and it was possible for the axon to retrogradely transport large target-derived macromolecules important for their survival and differentiation (Hendry and Hill, 1980). The potential consequence of axonal transport defects became an area of interest (McLeod, 1975) and continues to be so with the identification of its association with a vast majority of neurodegenerative diseases (Morfini et al., 2009). In addition, identification of intrinsic differences between axonal transport of proteins in sensory and motor axons was remarkable as it pointed out the specificities of this phenomenon in different neuron populations (Bisby, 1977).

The anatomical knowledge of the timing and extent of axonal elongation, as well as the neuron's ability to perform retrograde transport, formed the basis of the initial studies that discern a distinct neuron population among many other neuron types. Horseradish peroxidase (HSP) was one of the first reagents used to study retrograde axonal transport and to visualize the cell bodies of projection neurons (Bunt et al., 1974; Kristensson and Olsson, 1974; Lavail and Lavail, 1974). Tetanus toxin and 3H-proline were introduced as agents that can be retrogradely transported in the axon (Kunzle, 1977; Price and Griffin, 1977) and were widely used in retrograde labeling studies, especially those showing transsynaptic transfer of tetanus toxin. These studies generated interest in its use to determine neuronal connections (Schwab et al., 1979).

The first fluorescent retrograde labeling was performed using red fluorescent Evans blue and blue fluorescent DAPI-primuline injections dramatically improving visualization of cells and the extent of their branching (van der Kooy and Kuypers, 1979). Since then, numerous reagents with different fluorescent properties have been used to retrogradely label neurons. For example, the Bisbenzimide and "nuclear yellow" produced green and golden-yellow labeling, respectively. True Blue, Fast Blue, and Fluoro-Gold (FG) produced blue retrograde labeling (Kuypers et al., 1980). Availability of different dyes with different colors allowed double and triple labeling experiments to study the details of axonal projection paths and to reveal the identity of neurons (De Olmos and Heimer, 1980). The disadvantages of these early dyes were their diffusion and lack of sustained stability within the cell, which limited their use in connectivity mapping studies.

The use of modern fluorescent tracers, such as latex-based microspheres (Lanciego and Wouterlood, 2011) and FG (Catapano et al., 2002), have been the most common approach for projection neuron labeling. FG and microspheres are taken up by axons and retrogradely transported to the cell body by fast axonal transport. These dyes are mostly engulfed in lysosomes that fill the somata with stable fluorescence. For example, injection of fluorescent microspheres into the contralateral hemisphere of the motor cortex or spinal cord provided labeling of two distinct projecting neuron populations: CPN and CSMN, respectively (Catapano et al., 2001; Arlotta et al., 2005; Ozdinler and Macklis, 2006). More recently, a novel immunopanning method to culture CSMN combined injection of cholera toxin β (CTB) conjugated to fluorescent microspheres to target the axonal tract of CSMN (Dugas et al., 2008), and CSMN containing CTB were then immunopanned with anti-CTB antibody to yield pure populations of CSMN.

A new era of systems biology began to emerge in the 1970s as the connections among neurons that are located far apart were illuminated. Retrograde labeling and tracing studies began to reveal the unaccounted extent of connectivity in the central nervous system (Cull, 1975; Yorke and Caviness, 1975; Somogyi et al., 1979). Very systematic and well-defined investigations initiated the early stages of cortical connection mapping studies (Broadwell, 1975; Bunt et al., 1975; Liedgren et al., 1976; Walberg et al., 1976; Wise and Jones, 1976), laying the foundation for our current understanding and also identifying defects that occur in the presence of mutations in key genes (Caviness and Yorke, 1976). In addition, dual labeling approaches began to demonstrate the relationship between two different neuron populations located in the same nucleus suggesting that they can have different functions and mode of actions (Steiger and Buttner-Ennever, 1978).

Retrograde labeling approaches also helped investigations of different neuron populations that are located in various regions of the nervous system and project to different targets, including the muscle. Injection of HSP into the developing limb of the chick embryo enabled the first cellular labeling of developing spinal motor neurons (Oppenheim and Heaton, 1975) and the detailed analysis showed the timing and extent of their development and projection (Landmesser, 1978). Similarly, trochlear motor neurons were first visualized by retrograde labeling using HSP (Sohal and Holt, 1978). The early postnatal development of motor neurons located in the facial nucleus of the brainstem were also studied with similar retrograde labeling approaches (Olsson and Kristensson, 1979).

Most relevant to this review, the origins of the pyramidal tract were first determined by HRP retrograde labeling (Biedenbach and Devito, 1980), and early studies employing double labeling approaches demonstrated that in the cat, corticospinal neurons were also present in the sensorimotor cortex, especially in area 3a (Rustioni and Hayes, 1981). Similar experiments in rat demonstrated the somatotopy of corticospinal projection neurons and revealed that CSMN were located in layer Vb of the motor cortex extending within the somatosensory cortex. Most impressively, the neurons projecting to the cervical levels of the spinal cord were located further away from the midline whereas the neurons that projected to distal parts of the spinal cord were found closer to the midline (Ullan and Artieda, 1981). Projection patterns of neuron populations located in different areas of the brain, such as the red nucleus, were also studied using double labeling. These approaches revealed the complexity of the descending spinal pathways (Huisman et al., 1981) and originated many other studies to understand the development and establishment of connections in the motor neuron circuitry that control voluntary movement.

Early and seminal studies, in which the CSMN of the monkey were intracellularly filled with HRP and their anterograde axonal projections were studied in the spinal cord, showed very clearly that CSMN axons mainly terminate in lamina IX and make direct contacts with spinal motor neurons in the spinal cord (Shinoda

et al., 1981). Species-specific differences in axonal path formations, target innervations, and circuitry building also began to emerge with the help of this approach (Jones and Leavitt, 1974). The development of the pyramidal tract and neuronal connectivity was studied in many different species, including the hamster, which can regenerate its pyramidal tract axons upon injury if it occurs early in development (Reh and Kalil, 1981). Retrograde labeling studies also enabled the comparative analysis of species differences. Numerous studies using cats, mice, monkeys, and hamsters demonstrated how these species-specific differences affect neural connections and overall networks (Tolbert et al., 1978; Beckstead et al., 1981).

The CST arises from CSMN located in layer V of the motor cortex. CSMN are born at embryonic day (E) 13.5 in the mouse and start migrating toward layer V of the motor cortex without a major axonal projection (O'Leary and Koester, 1993). By E17, CSMN axons reach the pons and CST axons enter the spinal cord by postnatal day P0 and continue to elongate until P14. By P14, even the most caudal targets in the spinal cord are innervated. This information proves to be very useful when labeling CSMN at different stages of their development. The other important information is related to cellular identity. Even though CSMN can be considered a "pure" neuron population, they are divided into subgroups that innervate different targets within the spinal cord: the cervical, lumbar, and thoracic regions. There are several differences in the CST among species; the anatomical location of CST fibers is in the dorsal columns of the spinal cord in mice, whereas in primates and humans CST fibers are mostly located in the lateral columns and about 10% descends ipsilaterally (Courtine et al., 2007). The CSMN projection field has been extensively studied in rodents. For instance, anterograde studies utilizing HRP have demonstrated the projection field of CSMN in the dorsal funiculus of the spinal cord in rats (Casale et al., 1988), These studies were further confirmed using biotin dextran-amine. CST fibers were found in on all levels of the spinal cord in rats (Brosamle and Schwab, 1997) and mice (Liang et al., 2011). The timing of CSMN axonal growth through the brain to the spinal cord has also been demonstrated with anterograde techniques (Canty and Murphy, 2008). Hence, the anatomical knowledge of axonal projections and their timing is valuable for labeling distinct projection neuron populations and for distinguishing different types of neurons that reside together in the cerebral cortex but project to different areas in the central nervous system.

Understanding the details of CSMN connectivity also depends on retrograde labeling approaches to reveal the location of CSMN within the complex structure of the motor cortex. Retrograde labeling of CSMN in adult mice also facilitated studies during adulthood and when CSMN are affected in disease (**Figures 2C–E**). Studies using FG retrograde labeling demonstrated the presence of CSMN in layer V of the motor cortex under UV light (**Figures 2F,G**). In addition, FG visualization was enhanced by immunocytochemistry with DAB (**Figure 2H**). This allowed for visualization of CSMN somata and a portion of the proximal apical dendrite, depending on the concentration and elapsed time following FG injection. Using this approach, analysis of the hSOD1^{G93A} ALS mouse model has demonstrated that CSMN degeneration is pre-symtomatic and related to apoptotic mechanisms (Ozdinler et al., 2011). During ALS pathology, CSMN degenerate and there are patterns of cortical hyperexcitability that suggest dysfunction of CSMN in the cerebral cortex (Shepherd, 2013).

A wealth of information on CSMN biology has been generated using retrograde labeling approaches coupled with numerous applications. Since microspheres and FG fluorescently label cells, projection neurons can be purified using fluorescent activated cell sorting (FACS). In the case of CTB labeling, immunopanning is used providing a higher yield than FACS. Tissue culture approaches with CSMN purified using immunopanning approach revealed details of their survival requirements (**Figures 2A,B**) (Dugas et al., 2008), and FACS-purified CSMN displayed axon elongation in the presence of insulin-like growth factor 1 (IGF-1) and branching and arborization in the presence of brain-derived neurotrophic factor (BDNF) (Ozdinler and Macklis, 2006). Lastly, microarray analysis coupled with FACS-mediated purification of CSMN and CPN revealed the molecular signatures of CSMN and the genes that are important for their identification and early maturation (Arlotta et al., 2005).

Retrograde labeling coupled with electrophysiology are beginning to elucidate details of CSMN biology. For example, laser-scanning photostimulation in CSMN retrogradely labeled with fluorescent microspheres revealed unique intrinsic properties of CSMN when compared to CPN, such as differences in fast action potentials, firing rates, and hyperpolarization activated current modulation (Sheets et al., 2011; Suter et al., 2012).

Retrograde labeling techniques offer great advantages to study CSMN both *in vivo* and *in vitro*, but it falls short on providing the essential resolution to investigate the details of their cytoarchitecture. While the location of the cell body can be identified by the presence of fluorescent microspheres and the apex of the proximal apical dendrite can be visualized with FG labeling, they do not reveal cellular details. Virus-mediated gene delivery is one potential solution to this limitation.

AAV-MEDIATED RETROGRADE TRANSDUCTION

Adeno-associated viruses (AAV) have been considered for their potential use in future therapeutic applications due to their low toxicity and ability to transduce a wide variety of cells (During and Leone, 1995; McCown, 2005; Han et al., 2010). They have been widely used to deliver genes of interest into the cerebral cortex of mice and rats for a variety of neurodegenerative diseases, such as Parkinson's disease (Mandel et al., 1997; Wang et al., 2002a) and ALS (Wang et al., 2002b; Boillee and Cleveland, 2004; Yamashita et al., 2013; Keifer et al., 2014). Because of their application, mechanistic insights into the pathologies that cause these diseases have been uncovered (Tatom et al., 2009; Langou et al., 2010; Decressac et al., 2012; Davies et al., 2013).

AAV have the potential to transduce a wide variety of cells and neurons. One way to achieve specificity is by retrograde transduction via injection into an axon tract selectively targeting only the cell bodies of neurons projecting through that tract. AAV-mediated retrograde transduction requires binding of the AAV to specific receptors on the axon surface and internalization through a receptor-mediated mechanism. Another way to

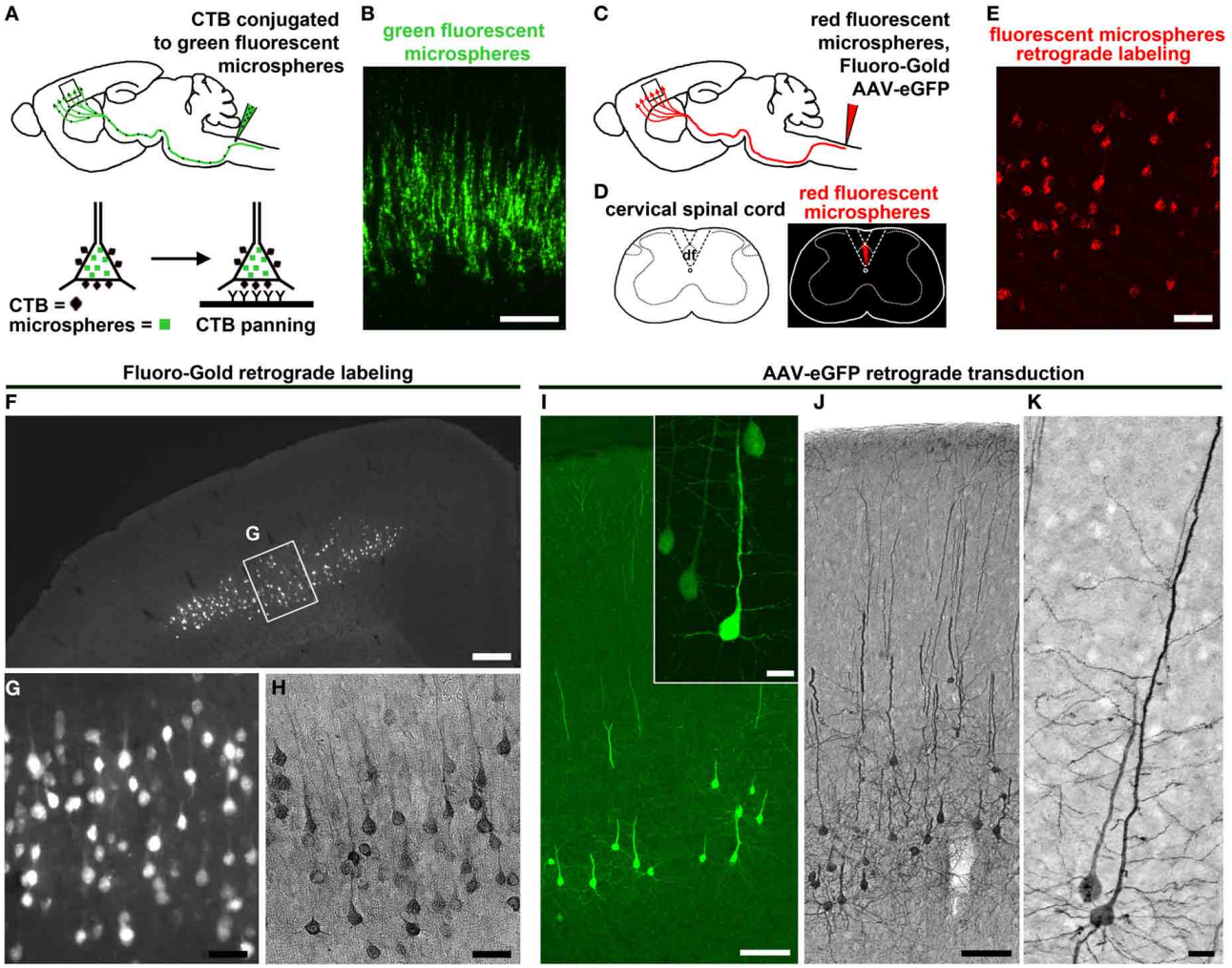

FIGURE 2 | CSMN retrograde labeling and transduction approaches. **(A)** Schematic drawing of CTB injection conjugated to green fluorescent microspheres into the pyramidal decussation of the spinal cord. Retrograde labeled CSMN containing CTB on their surface can be isolated by immunopanning. **(B)** Enlarge inset of the motor cortex enlarged to the right. Modified from Dugas et al. (2008). **(C)** Schematic drawing of retrograde labeling of CSMN by injection into the CST of the cervical spinal cord (C2). **(D)** Injection is restricted to the CST that lies within the dorsal funiculus (df). **(E)** Enlarged inset of the motor cortex showing CSMN retrogadely labeled with red fluorescent microspheres. **(F)** FG retrograde labeling. CSMN are visualized throughout the motor cortex by direct analysis on fluorescent microscope. **(G)** Enlarged inset of CSMN in the motor cortex. **(H)** CSMN cell body and proximal apical dendrite structures are enhanced by FG immunocytochemistry using DAB. **(I)** AAV-mediated retrograde transduction. CSMN are visualized throughout the motor cortex by eGFP immunocytochemistry using fluorescence microscopy. Large inset of a representative CSMN in the right corner. **(J)** CSMN cytoarchitectural structure is enhanced by eGFP immunocytochemistry using DAB. **(K)** large inset of a CSMN shows details of CSMN cell body, basal dendrites, apical dendrite and spines. Scale bars: **(B)** = 100 μm, **(E)** = 50 μm, **(F)** = 500 μm, **(G,H)** = 50 μm, **(I)** = 100 μm (inset = 20 μm), **(J)** = 100 μm, **(K)** = 20 μm.

achieve specificity is by viral vector capsid engineering. Recent advancements involving the discovery and generation of new AAV serotypes offer potential applications for gene delivery in distinct neuron populations (Weinberg et al., 2013). This is especially important considering that in neurodegenerative diseases distinct neuron populations show primary vulnerability and undergoes neurodegeneration. The ability to target the neurons that are vulnerable, without affecting other neurons, cells, and different circuitries, would be critically important for building long-term and effective therapeutic approaches. Here we will focus on the use and application of AAV on the genetic modulation of motor neurons and the components of the motor neuron circuitry.

One of the pioneering works came from studies demonstrating the ability to genetically label a distinct set of SMN by introducing AAV into the muscle fibers they innervate (Martinov et al., 2002). These studies were important as they show that AAV injected to the muscle can retrogradely transduce SMN, and most importantly distinct set of motor neurons are transduced based on their projection field. AAV that encode a gene of interest, such as glial-derived neurotrophic factor (GDNF), were then delivered to the muscle fibers to enhance growth factor expression in a distinct

set of SMN (Lu et al., 2003), showing that it is indeed possible to use AAV to retrogradely transduce SMN and induce selective gene expression.

Neurotrophic growth factors that play key roles in the survival of motor neurons, including IGF-1, vascular endothelial growth factor (VEGF), GDNF, and granulocyte-colony stimulating factor (G-CSF), have been considered for ALS therapies (Hester et al., 2009). AAV2-IGF-1 injected into the muscle of the hSOD1^{G93A} mouse retrogradely transduced SMN, increased life span, and decreased disease progression were very encouraging (Kaspar et al., 2003). Introduction of IGF-1 into the deep cerebellar nuclei, a region of the cerebellum with extensive brainstem and spinal cord connection, via AAV suggested that the reduction of ALS pathology was due in part to its activity on non-neuronal cells in the CNS (Dodge et al., 2008) as it attenuated the release of tumor necrosis factor-alpha (TNF-α) and nitric oxide.

AAV-mediated gene delivery approaches have been increasingly used to modulate gene expression in SMN of ALS mouse models. Most recently, intramuscular delivery of the AAV6 encoding silencer shSOD1 RNA transduced SMN but failed to alter disease course in the hSOD1^{G93A} mice (Towne et al., 2011). However, these approaches have significant limitations as they only target the SMN that innervate specific muscle groups. Intrathecal injections releasing AAV6 or AAV9 serotypes at the level of the lumbar spinal cord transduced SMN throughout the spinal cord (Snyder et al., 2011), and intraspinal delivery of AAV-G-CSF showed a high transduction efficiency in SMN with modest improvement in the motor function as well as delayed disease progression and survival (Henriques et al., 2011).

Gene transduction in the cerebral cortex has also been considered via intracortical injections using different AAV serotypes. Different regions of the cerebral cortex have been transduced with a wide variety of AAV serotypes only to reconfirm the heterogeneity and the cellular complexity of the cerebral cortex and to realize that it is not be possible to transduce distinct neuron populations with one serotype (Burger et al., 2005; Hutson et al., 2011). Understanding the identity of neurons that are transduced in the cerebral cortex has not been easy, but investigating their axonal projection tracts might suggest their identity. For example, detection of transduced axons in the corpus callosum suggests that transduction of at least a subset of CPN as they cross the corpus callosum when projecting to the contralateral side of the cerebral cortex. Similarly, detection of transduced axons within the CST suggests transduction of subcerebral projection neurons in the cerebral cortex. Injection of AAV1-eGFP into the motor cortex resulted in visualization of GFP^{+} axon fibers within CST, suggesting that a subset of CSMN were transduced, and the identity of transduced neurons were further demonstrated with paired retrograde labeling (Hutson et al., 2011). Taking advantage of the retrograde transport capabilities and based on the hypothetical presence of specific receptors for different AAV serotypes, we have recently reported that AAV2 shows high levels of retrograde transduction efficiency in CSMN (Jara et al., 2012).

When compared to retrograde labeling techniques, AAV-mediated gene delivery is far more powerful in clarifying cytoarchitectural details. In addition, this novel technique has brought several improvements to previously reported methods by combining retrograde labeling and transduction applications to the study of CSMN. Retrograde labeling of CSMN, using dyes and microspheres, enables visualization of their cell bodies but fails to reveal the shape and length of dendritic spines. Even though subtle, these details could be particularly important for neuron function and connectivity. Since spines are the sites of active neuronal communication, their modulation, degeneration, and progressive loss could have implications on disease pathology. Indeed, there is now building evidence to suggest a link between spine morphology and a wide variety of neurological diseases (Penzes et al., 2011). Expressing eGFP gene selectively in CSMN using AAV-mediated retrograde transduction of the CST allowed exclusive, homogenous expression of eGFP within CSMN and analysis of neuronal structures (**Figures 2I–K**). AAV-mediated gene delivery demonstrated early and selective apical dendrite degeneration in the hSOD1^{G93A} ALS mouse model (**Figure 1B**). This finding was important because for the first time it deciphered the cellular events that occur in CSMN. Specifically, apical dendrited were filled with vacuoles and spines were lost or vastly degenerated. These defects occurred at P60, a time when SMN begin to show signs of cellular degeneration, suggesting that both upper and lower motor neurons degenerate together in synchrony. Neuronal degeneration was previously thought to develop in a sequence of events that started in the neuromuscular junction spreading to the SMN and CST until finally reaching the CSMN cell body. However, the use of AAV-mediated gene delivery provided a very detailed observation of CSMN and uncovered details about cellular degeneration within the motor neuron circuitry that occurs in ALS. Absence of spines and disintegrating apical dendrites early in the disease may suggest that CSMN do not receive proper input from other cortical neurons that modulate their activity and this could be one of the factors contributing to the observed defects in the motor neuron circuitry. The importance of early apical dendrite degeneration deserves much attention as this is the area CSMN activity is heavily modulated (Shepherd, 2013), and could be one of the underlying causes for circuitry defects and motor dysfunction (**Figure 1B**).

Using AAV-mediated gene delivery as a potential therapeutic application to facilitate the repair and survival of CSMN in neurodegenerative diseases and after spinal cord injury is a provocative idea. Retrograde transduction also provides the means to study different subsets of CSMN by injecting into different regions of the spinal cord. For instance, cervical and lumbar injections can be utilized to study neurons that project to different spinal cord targets. However, in order to be successful, this approach would necessitate improvements in transduction specificity. There are two main approaches to increase specificity: one is the use of engineered capsid proteins and different serotypes, and the other is the choice of the promoter used to derive gene expression. Therefore, a better understanding of the serotype(s) that transduce CSMN and the use of engineered capsid proteins or different promoters to drive gene expression would improve selective transduction.

Even though selective targeting using retrograde labeling in mice is important, novel approaches need to be developed for selective CSMN transduction in the motor cortex of patients. In mice, the CST lies within the dorsal funiculus of the spinal

cord, but in humans the majority of the CST lies within the lateral columns, limiting direct access. This anatomical difference of axon projection path is particularly important. The modulation of genes only in SMN may not be sufficient to implement a long-term and effective treatment strategy in ALS and other related motor neuron diseases. Therefore, approaches to transduce CSMN, in addition to SMN, need to be developed.

AAV approaches are not without their limitations. One disadvantage is related to the variations introduced by the surgical techniques. AAV transduction has very low levels of toxicity, but studies have revealed that intracranial injections might elicit an immune response (Weinberg et al., 2013). AAV have small packaging capacity (<5 kb) that might limit genes of interest. In addition, the timing of intervention and concentration to achieve a therapeutic effect might be challenging. We anticipate that in the future AAV engineering will offer new serotypes with novel properties that might facilitate the transduction of CSMN upon direct injection into the motor cortex. Interestingly, several clinical trials for other neurodegenerative diseases have explored the possibility of intracranial injections (Hester et al., 2009) suggesting that in the future similar approaches could be adapted for transduction of Betz cells in patients. However, prior to any meaningful cellular repair study, the underlying molecular causes of cellular vulnerability and degeneration need to be understood.

GENETIC LABELING OF DISTINCT NEURON POPULATIONS

Genetic labeling allows visualization of cells with spatiotemporal resolution *in vivo*. Compared to surgical approaches, genetic labeling has several advantages such as reducing variability from subject to subject, experiment to experiment and lab-to-lab, ensuring reproducibility of findings. Potential limitations of genetic labeling are the limited availability of unique genes/markers for specific cell types and the alterations in gene expression. Certain genes undergo spatiotemporal alterations throughout development and even environmental factors may affect control of gene expression by epigenetic mechanisms. However, advantages of genetic labeling outweigh any disadvantages and are widely used (Huang and Zeng, 2013).

There are three main different ways to achieve genetic targeting: (1) conventional/bacterial artificial chromosome (BAC) transgene (Schmidt et al., 2013), (2) gene knock-in (Taniguchi et al., 2011), and (3) gene/enhancer trapping (Leighton et al., 2001; Kelsch et al., 2012). Conventional or BAC transgene approaches use a transgene cassette, or BAC, to introduce the promoter/enhancer regions of the gene of interest to drive expression of a reporter which mimics endogenous expression patterns. They are randomly inserted in the genome, which may cause variations in expression patterns among founder lines. Gene knock-in relies on inserting the reporter gene in the endogenous location of the gene of interest to fully recapitulate endogenous expression patterns, however it is technically more challenging and expression of the target gene itself may be altered even using an internal ribosome entry site (IRES) sequence. In enhancer trapping, a reporter driven by a minimal promoter is randomly inserted in the genome, and local enhancers near the insertion site then determine expression of the reporter.

Discovery of green fluorescent protein (GFP) (Tsien, 1998) in 1962 was a significant milestone for cell and molecular biology, and it was granted the Nobel Prize in Chemistry in 2008 (Weiss, 2008). It was not long before GFP was used as a marker for gene expression in eukaryotes (Chalfie et al., 1994). Since then, there has been an explosion of its spectral variants with a wide variety of brightness and colors (Shaner et al., 2005). Transgenic mice expressing GFP under control of the cytomegalovirus (CMV) promoter allowed study of the central nervous system at a level of single individual neuron resolution (van den Pol and Ghosh, 1998). Spectral variants of GFP (yellow, YFP; cyan, CFP; and red, RFP; collectively called XFP) expressed in transgenic mice under the control of Thy-1 promoter allowed imaging and identification of numerous subsets of neurons (Feng et al., 2000). More recently, using a cre/lox recombination system to express multiple distinct colors in diverse genetically labeled neurons gave rise to the "Brainbow" mice (Livet et al., 2007; Cai et al., 2013).

Numerous reporter mouse lines have been generated using genetic targeting methods and extensively used to study various cell types in the mouse CNS, such as layer V pyramidal neurons (Feng et al., 2000; Yu et al., 2008), cortical interneurons (Chattopadhyaya et al., 2004; Lopez-Bendito et al., 2004; Taniguchi et al., 2011), basal ganglia (Gerfen et al., 2013), spinal cord motor neurons and interneurons (Wichterle et al., 2002; Miles et al., 2004; Chang and Martin, 2011). Of these, Thy-1 XFP mice are of particular interest as they allow analysis of labeled cells at a very fine detail, such as dendritic spine dynamics *in vivo* (Grutzendler et al., 2002; Oray et al., 2004; Dombeck et al., 2007). Moreover, they have been used to study mouse models of neurodegenerative diseases at a cellular level, such as dendritic spine loss in triple transgenic Alzheimer's disease mice (Bittner et al., 2010) and motor neuron pathology in the experimental autoimmune encephalomyelitis, and mouse model of multiple sclerosis (Bannerman et al., 2005). Thy1-YFP mice have extensively been used to study motor systems, not only SMN in mouse models of ALS (Schaefer et al., 2005; Wong et al., 2009), but also CSMN (Richter and Roskams, 2009) and their axons in spinal cord injury (Bareyre et al., 2005) and an ALS mouse model (Ozdinler et al., 2011).

Another reporter line extensively used to study motor systems is HB9-GFP, which labels about 90% of SMN in the developing embryo (Wichterle et al., 2002) but only about half of large Choline acetyl transferase $(ChAT)^+$ SMN in the ventral horn of the adult (Chang and Martin, 2011). γ-SMN innervating muscle spindles are GFP^- (Shneider et al., 2009). HB9-GFP mice have been used to follow differentiation of mouse embryonic stem cells into motor neurons (Wichterle et al., 2002; Wu et al., 2012). HP9-GFP^+ embryonic stem cell-derived SMN co-cultured with astrocytes expressing $hSOD1^{G93A}$ displayed increased cell death and shorter axon length (Dodge et al., 2008). HB9-GFP BACs have also been used to characterize human embryonic stem cell-derived motor neuron lineages (Placantonakis et al., 2009) or facilitate FACS purification of human spinal motor neurons from embryonic stem cells (Singh Roy et al., 2005). Human embryonic stem cell-derived motor neurons identified by HB9-GFP expression showed that SMN with hSOD1 mutations displayed reduced survival and shorter axons (Karumbayaram et al., 2009). Primary

and embryonic stem cell-derived motor neurons from HB9-GFP mice have been used to study neurodegenerative properties of human SOD1 mutations, showing glia and astrocytes with SOD1 mutations induce neurodegeneration of co-cultured SMN even when they do not carry the mutation themselves (Di Giorgio et al., 2007; Nagai et al., 2007). HB9-GFP mice have been used to study (1) motor axon guidance *in vivo* by Semaphorin signaling (Huber et al., 2005), (2) *in vitro* by GDNF chemoattraction and ephrinA signaling (Dudanova et al., 2010) during normal development, (3) targeting of regenerating motor axons *in vivo* by polysialylated NCAM in the adult (Franz et al., 2005), and (4) motor axon development *in vivo* in mouse models of disease such as SMA (McGovern et al., 2008).

Gene Expression Nervous System Atlas (GENSAT) database has been invaluable in providing a detailed library of hundreds of distinct, genetically defined cell populations from engineered mice utilizing BAC (Gong et al., 2003, 2007; Doyle et al., 2008; Schmidt et al., 2013). To date, there are almost 400 publications that use GENSAT mice or BACs (www.GENSAT.org). Using this approach, we generated the UCHL1-eGFP mice in which the UCHL1 gene promoter was used to drive eGFP expression (**Figure 3**) (Yasvoina et al., 2013). CSMN identity of $eGFP^+$ neurons was confirmed by retrograde labeling, molecular marker expression profile, electrophysiology, cortical circuit mapping, and mouse genetics studies. CSMN in the motor cortex and their projections were genetically and stably labeled by GFP expression from P0 to P800. In the spinal cord, almost all $ChAT^+$ SMN were $eGFP^+$ at birth but by P30 eGFP expression became restricted to a mixture of small α- and γ-SMN that were resistant to degeneration in motor neuron diseases, such as ALS. Crossing this reporter mouse with $hSOD1^{G93A}$ ALS mouse model (Gurney et al., 1994) generated $hSOD1^{G93A}$-UeGFP mice, which allowed detailed study of CSMN health. We observed a progressive degeneration of $eGFP^+$ CSMN, as previously reported (Ozdinler et al., 2011), with apical dendrite vacuolation and presence of autophagosomes, suggesting an ongoing intrinsic cellular degeneration. This novel reporter mouse model for ALS, now allows the detailed cellular analysis of CSMN without the requirement of retrograde labeling surgeries, which was not possible before.

The main challenge of genetic labeling approaches remains identification of genes/promoters that distinctly and specifically labels a neuronal subpopulation of interest. Once such reporters have been identified and characterized, there are numerous advanced applications. Recent advances in microscopy allow imaging cells in live animals (intravital imaging) (Pittet and Weissleder, 2011; Weigert et al., 2013). *In vivo* imaging has recently been applied to study spinal cord regeneration (Laskowski and Bradke, 2013). Optogenetics approaches take advantage of channelrhodopsin-2, which can be genetically targeted to neurons of interest and used to manipulate neural activity with millisecond precision using light (Packer et al., 2013). This allows imaging and long-range circuit mapping of multiple cell types (Atasoy et al., 2008). Optophysiology also grants success in such studies (Smedemark-Margulies and Trapani, 2013). Recently, optogenetic reactivation of hippocampal neurons activated during fear conditioning was shown to activate fear memory recall induced by light (Liu et al., 2012). Mosaic analysis with double markers (MADM) uses a site-specific recombinase to catalyze inter-chromosomal recombination that creates sparsely labeled neurons only after recombination (Luo, 2007). Type, density, and timing of labeling can be controlled by tissue-specific expression of the recombinase. Genetically encoded fluorescent protein-based biosensors can be used to study a broad assortment of signaling molecules and networks (Depry et al., 2013). For example, fluorescent proteins can be used to monitor protein-protein interactions in living cells using fluorescent resonance energy transfer (FRET) microscopy (Stepanenko et al., 2011; Day and Davidson, 2012). A recent nanobody-based technology utilizes fluorescent proteins commonly used to label cells and neurons as scaffolds for cell-specific gene manipulation allowing selective modulation of diverse GFP-labeled cells across transgenic lines such as optogenetic probing of neural circuits (Tang et al., 2013).

Numerous techniques and applications are being developed simultaneously to target neurons of interest. Advances in genetic labeling of select sets of neuron populations coupled with numerous applications that allow their cellular and molecular analysis at different experimental conditions and disease settings will reveal the underlying mechanisms for proper cellular function as well as the molecular networks that are responsible for their selective vulnerability. This information will be the foundation for future effective treatments strategies in diseases that primarily affect distinct neuron populations at initial stages.

CONCLUSION

Techniques allow detailed analysis, but it is our critical thinking that shapes the field and the future. Many important discoveries are made when approaches and critical thinking develop simultaneously. The definition of "disease," the description of pathologies, and our understanding of symptom development have vastly changed in the last decade. In addition, numerous new techniques and applications, which allow studies that were not previously possible, have become available. These two critical components of innovation have the potential to shape the future of neurodegenerative diseases once understood and applied properly. We now have reasons to believe that numerous discoveries will emerge in the near future.

Recently, the word "spectrum" was introduced when describing numerous neurodegenerative disorders to highlight the blurred boundaries among diseases and place them under an umbrella of systems degeneration with many common features. This is an important shift from disease-based thinking toward a more mechanism-oriented understanding that emphasizes the common underlying pathologies that give rise to different forms of neurodegeneration. This paradigm shift in our understanding has an impact on defining pathologies, disease mechanisms, and symptoms. The neurons that show vulnerability and undergo progressive degeneration have moved center stage. We now realize the importance of understanding the cellular, molecular, and genetic basis of pathology at a cellular level. This change in critical thinking proved to be correct by the failures of clinical trials. The expectation for improved lifespan in mice to translate into success in ALS patient survival is now considered mostly unrealistic.

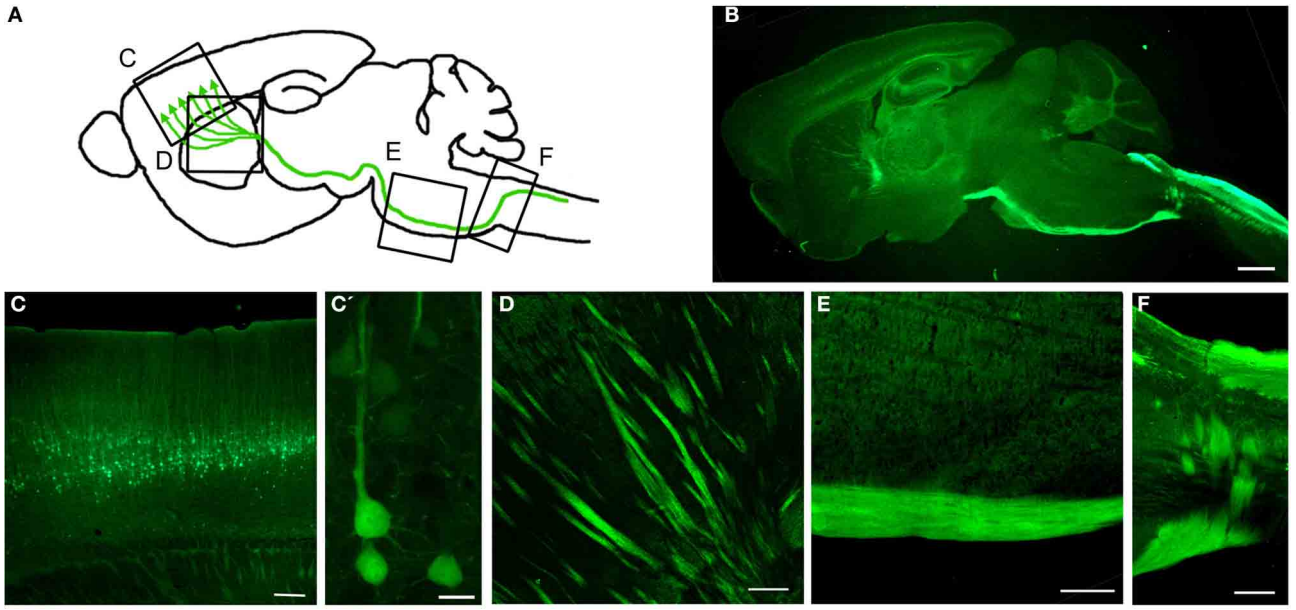

FIGURE 3 | Genetic Labeling of CSMN. (A) Schematic drawing of genetic labeling of CSMN by eGFP expression under control of UCHL1 promoter. **(B)** A representative sagittal section of a P120 mouse brain showing eGFP$^+$ CSMN and their axons. **(C)** In motor cortex, eGFP$^+$ CSMN can be seen in layer 5a and 5b. **(C′)** Higher magnification of individual representative eGFP$^+$ CSMN in the motor cortex. **(D–F)** eGFP$^+$ axons of CSMN projecting through the striatum **(D)**, pons **(E)**, and pyramidal decussation **(F)**. Scale bars: **(B)** = 1 mm, **(C,D** and **E)** = 200μm, **(C′)** = 20μm, **(F)** = 500μm.

Today, clinical companies are more cautious when making a decision to move forward, and seek more cell-based evidence that supports motor neuron survival (Genç and Ozdinler, 2013).

In recent years, there have been significant changes in the meaning of the word "symptom." Previously, symptoms were described as signs of pathology that can be detected by visual examination or various tests. However, it became obvious that our ability to detect signs of pathology at a molecular, cellular, and systems level was different. Even when no obvious signs were present, the pathology was taking its course at a cellular level. If the cellular basis of disease causing pathologies was understood, then these findings would set the stage, not only for early detection of the disease, but also for the development and implementation of effective long-term treatment strategies. Therefore, it is important to detect symptoms at a cellular level before pathologies become evident. We need to develop new approaches to focus our attention on the neuron, on the cell that is affected and has become vulnerable. Because if we understand the molecular and genetic basis of neuronal vulnerability at a cellular level, then we will have the chance to understand the basis of neuronal pathology and systems degeneration.

Studying CSMN biology is especially challenging, not only because they are limited in numbers and not easy to identify, but also because the techniques, technologies, approaches, and model systems to study them are not easy to develop. Due to species differences, modeling CSMN degeneration in mice has intrinsic limitations. Even though a minor defect would lead to a motor dysfunction in patients, mice would not display an obvious defect. This could indeed be one of the reasons why the mouse models of motor neuron diseases do not show a prominent phenotype. Working in models without an obvious functional readout can be challenging. However, if the models are built at a cellular level, or if the focus is shifted from mice to the motor neurons in mice, then the picture and the scope of perception changes dramatically. At a cellular level, the CSMN in humans and in mice are almost identical. It is thus important to develop technologies that reveal the underlying factors that contribute to the cellular vulnerability and degeneration. As long as our focus is the neuron and not the mice, the information gathered from healthy and diseased neurons would be translational.

Understanding the controls over CSMN health is becoming very central to numerous neurodegenerative diseases. Here we reviewed the exciting progress in the study of upper motor neurons. Retrograde labeling is a prominent approach to identify the location of the neuron and to visualize its cell body. AAV-mediated retrograde transduction, on the other hand, is not only a powerful tool to deliver genes of interest, but also important to reveal details of cellular cytoarchitecture. However, both of these applications require surgery and the success of each experiment mostly depends on surgical expertise and mouse survival. Genetic labeling that intrinsically targets a distinct neuron population offers a solution for the potential limitations of retrograde labeling surgeries. Generation and characterization of the UCHL1-eGFP mouse, in which the CSMN are genetically labeled, has been pivotal for overcoming numerous important limitations by allowing *in vivo* visualization and cellular analysis of neurons that are vulnerable in neurodegenerative diseases.

With the advancements made in the study of CSMN biology, the future awaits numerous important discoveries. FACS purification coupled with *in vitro* culturing will allow novel drug

screening and verification platforms using motor neuron health as a readout for success. This application has the potential to discover new molecules and compounds for future clinical trials. In addition, development of AAV-mediated gene delivery, together with the identification of new genes and pathways that are important for disease pathology will enable direct cellular therapies into the motor cortex of patients improving the survival of upper motor neurons and enhancing their connectivity. Identification of the cellular and molecular basis of CSMN vulnerability will be revealed, paving the way for understanding the cellular pathways, networks, and dynamics that are important to improve motor neuron health.

We live in very exciting times due to the numerous improvements in our critical thinking of neurodegenerative diseases, and the technologies that support discoveries are developing faster than ever. The new knowledge gathered from neurons of interest will enable development of novel effective long-term treatment strategies and has the potential to expedite new discoveries that will enable improved health in patients.

REFERENCES

Anderson, C. T., Sheets, P. L., Kiritani, T., and Shepherd, G. M. (2010). Sublayer-specific microcircuits of corticospinal and corticostriatal neurons in motor cortex. *Nat. Neurosci.* 13, 739–744. doi: 10.1038/nn.2538

Apicella, A. J., Wickersham, I. R., Seung, H. S., and Shepherd, G. M. (2012). Laminarly orthogonal excitation of fast-spiking and low-threshold-spiking interneurons in mouse motor cortex. *J. Neurosci.* 32, 7021–7033. doi: 10.1523/JNEUROSCI.0011-12.2012

Arlotta, P., Molyneaux, B. J., Chen, J., Inoue, J., Kominami, R., and Macklis, J. D. (2005). Neuronal subtype-specific genes that control corticospinal motor neuron development *in vivo*. *Neuron* 45, 207–221. doi: 10.1016/j.neuron.2004.12.036

Atasoy, D., Aponte, Y., Su, H. H., and Sternson, S. M. (2008). A FLEX switch targets Channelrhodopsin-2 to multiple cell types for imaging and long-range circuit mapping. *J. Neurosci.* 28, 7025–7030. doi: 10.1523/JNEUROSCI.1954-08.2008

Bannerman, P. G., Hahn, A., Ramirez, S., Morley, M., Bonnemann, C., Yu, S., et al. (2005). Motor neuron pathology in experimental autoimmune encephalomyelitis: studies in THY1-YFP transgenic mice. *Brain* 128, 1877–1886. doi: 10.1093/brain/awh550

Bareyre, F. M., Kerschensteiner, M., Misgeld, T., and Sanes, J. R. (2005). Transgenic labeling of the corticospinal tract for monitoring axonal responses to spinal cord injury. *Nat. Med.* 11, 1355–1360. doi: 10.1038/nm1331

Beckstead, R. M., Edwards, S. B., and Frankfurter, A. (1981). A comparison of the intranigral distribution of nigrotectal neurons labeled with horseradish peroxidase in the monkey, cat, and rat. *J. Neurosci.* 1, 121–125.

Biedenbach, M. A., and Devito, J. L. (1980). Origin of the pyramidal tract determined with horseradish peroxidase. *Brain Res.* 193, 1–17. doi: 10.1016/0006-8993(80)90941-5

Bisby, M. A. (1977). Retrograde axonal transport of endogenous protein: differences between motor and sensory axons. *J. Neurochem.* 28, 249–251. doi: 10.1111/j.1471-4159.1977.tb07737.x

Bittner, T., Fuhrmann, M., Burgold, S., Ochs, S. M., Hoffmann, N., Mitteregger, G., et al. (2010). Multiple events lead to dendritic spine loss in triple transgenic Alzheimer's disease mice. *PLoS ONE* 5:e15477. doi: 10.1371/journal.pone.0015477

Boillee, S., and Cleveland, D. W. (2004). Gene therapy for ALS delivers. *Trends Neurosci.* 27, 235–238. doi: 10.1016/j.tins.2004.03.002

Broadwell, R. D. (1975). Olfactory relationships of the telencephalon and diencephalon in the rabbit. II. An autoradiographic and horseradish peroxidase study of the efferent connections of the anterior olfactory nucleus. *J. Comp. Neurol.* 164, 389–409. doi: 10.1002/cne.901640402

Brosamle, C., and Schwab, M. E. (1997). Cells of origin, course, and termination patterns of the ventral, uncrossed component of the mature rat corticospinal tract. *J. Comp. Neurol.* 386, 293–303. doi: 10.1002/(SICI)1096-9861(19970922)386:2%3C293::AID-CNE9%3E3.0.CO;2-X

Brown, R. H. Jr., and Robberecht, W. (2001). Amyotrophic lateral sclerosis: pathogenesis. *Semin. Neurol.* 21, 131–139. doi: 10.1055/s-2001-15260

Bunt, A. H., Hendrickson, A. E., Lund, J. S., Lund, R. D., and Fuchs, A. F. (1975). Monkey retinal ganglion cells: morphometric analysis and tracing of axonal projections, with a consideration of the peroxidase technique. *J. Comp. Neurol.* 164, 265–285. doi: 10.1002/cne.901640302

Bunt, A. H., Lund, R. D., and Lund, J. S. (1974). Retrograde axonal transport of horseradish peroxidase by ganglion cells of the albino rat retina. *Brain Res.* 73, 215–228. doi: 10.1016/0006-8993(74)91045-2

Burger, C., Nash, K., and Mandel, R. J. (2005). Recombinant adeno-associated viral vectors in the nervous system. *Hum. Gene Ther.* 16, 781–791. doi: 10.1089/hum.2005.16.781

Cai, D., Cohen, K. B., Luo, T., Lichtman, J. W., and Sanes, J. R. (2013). Improved tools for the Brainbow toolbox. *Nat. Methods* 10, 540–547. doi: 10.1038/nmeth.2450

Canty, A. J., and Murphy, M. (2008). Molecular mechanisms of axon guidance in the developing corticospinal tract. *Prog. Neurobiol.* 85, 214–235. doi: 10.1016/j.pneurobio.2008.02.001

Casale, E. J., Light, A. R., and Rustioni, A. (1988). Direct projection of the corticospinal tract to the superficial laminae of the spinal cord in the rat. *J. Comp. Neurol.* 278, 275–286. doi: 10.1002/cne.902780210

Catapano, L. A., Arnold, M. W., Perez, F. A., and Macklis, J. D. (2001). Specific neurotrophic factors support the survival of cortical projection neurons at distinct stages of development. *J. Neurosci.* 21, 8863–8872.

Catapano, L. A., Magavi, S. S., and Macklis, J. D. (2002). Neuroanatomical tracing of neuronal projections with Fluoro-Gold. *Methods Mol. Biol.* 198, 299–304. doi: 10.1385/1-59259-186-8:299

Caviness, V. S. Jr., and Yorke, C. H. Jr. (1976). Interhemispheric neocortical connections of the corpus callosum in the reeler mutant mouse: a study based on anterograde and retrograde methods. *J. Comp. Neurol.* 170, 449–459. doi: 10.1002/cne.901700405

Chalfie, M., Tu, Y., Euskirchen, G., Ward, W. W., and Prasher, D. C. (1994). Green fluorescent protein as a marker for gene expression. *Science* 263, 802–805. doi: 10.1126/science.8303295

Chang, Q., and Martin, L. J. (2011). Glycine receptor channels in spinal motoneurons are abnormal in a transgenic mouse model of amyotrophic lateral sclerosis. *J. Neurosci.* 31, 2815–2827. doi: 10.1523/JNEUROSCI.2475-10.2011

Chattopadhyaya, B., Di Cristo, G., Higashiyama, H., Knott, G. W., Kuhlman, S. J., Welker, E., et al. (2004). Experience and activity-dependent maturation of perisomatic GABAergic innervation in primary visual cortex during a postnatal critical period. *J. Neurosci.* 24, 9598–9611. doi: 10.1523/JNEUROSCI.1851-04.2004

Clasca, F., Rubio-Garrido, P., and Jabaudon, D. (2012). Unveiling the diversity of thalamocortical neuron subtypes. *Eur. J. Neurosci.* 35, 1524–1532. doi: 10.1111/j.1460-9568.2012.08033.x

Courtine, G., Bunge, M. B., Fawcett, J. W., Grossman, R. G., Kaas, J. H., Lemon, R., et al. (2007). Can experiments in nonhuman primates expedite the translation of treatments for spinal cord injury in humans? *Nat. Med.* 13, 561–566. doi: 10.1038/nm1595

Cull, R. E. (1975). Role of axonal transport in maintaining central synaptic connections. *Exp. Brain Res.* 24, 97–101. doi: 10.1007/BF00236020

Davies, S. E., Hallett, P. J., Moens, T., Smith, G., Mangano, E., Kim, H. T., et al. (2013). Enhanced ubiquitin-dependent degradation by Nedd4 protects against alpha-synuclein accumulation and toxicity in animal models of Parkinson's disease. *Neurobiol. Dis.* 64C, 79–87. doi: 10.1016/j.nbd.2013.12.011

Day, R. N., and Davidson, M. W. (2012). Fluorescent proteins for FRET microscopy: monitoring protein interactions in living cells. *Bioessays* 34, 341–350. doi: 10.1002/bies.201100098

Decressac, M., Mattsson, B., Lundblad, M., Weikop, P., and Bjorklund, A. (2012). Progressive neurodegenerative and behavioural changes induced by AAV-mediated overexpression of alpha-synuclein in midbrain dopamine neurons. *Neurobiol. Dis.* 45, 939–953. doi: 10.1016/j.nbd.2011.12.013

De Olmos, J., and Heimer, L. (1980). Double and triple labeling of neurons with fluorescent substances; the study of collateral pathways in the ascending raphe system. *Neurosci. Lett.* 19, 7–12. doi: 10.1016/0304-3940(80)90247-5

Depry, C., Mehta, S., and Zhang, J. (2013). Multiplexed visualization of dynamic signaling networks using genetically encoded fluorescent protein-based biosensors. *Pflugers Arch.* 465, 373–381. doi: 10.1007/s00424-012-1175-y

D'Errico, P., Boido, M., Piras, A., Valsecchi, V., De Amicis, E., Locatelli, D., et al. (2013). Selective vulnerability of spinal and cortical motor neuron subpopulations in delta7 SMA mice. *PLoS ONE* 8:e82654. doi: 10.1371/journal.pone.0082654

Di Giorgio, F. P., Carrasco, M. A., Siao, M. C., Maniatis, T., and Eggan, K. (2007). Non-cell autonomous effect of glia on motor neurons in an embryonic stem cell-based ALS model. *Nat. Neurosci.* 10, 608–614. doi: 10.1038/nn1885

Dodge, J. C., Haidet, A. M., Yang, W., Passini, M. A., Hester, M., Clarke, J., et al. (2008). Delivery of AAV-IGF-1 to the CNS extends survival in ALS mice through modification of aberrant glial cell activity. *Mol. Ther.* 16, 1056–1064. doi: 10.1038/mt.2008.60

Dombeck, D. A., Khabbaz, A. N., Collman, F., Adelman, T. L., and Tank, D. W. (2007). Imaging large-scale neural activity with cellular resolution in awake, mobile mice. *Neuron* 56, 43–57. doi: 10.1016/j.neuron.2007.08.003

Doyle, J. P., Dougherty, J. D., Heiman, M., Schmidt, E. F., Stevens, T. R., Ma, G., et al. (2008). Application of a translational profiling approach for the comparative analysis of CNS cell types. *Cell* 135, 749–762. doi: 10.1016/j.cell.2008.10.029

Dudanova, I., Gatto, G., and Klein, R. (2010). GDNF acts as a chemoattractant to support ephrinA-induced repulsion of limb motor axons. *Curr. Biol.* 20, 2150–2156. doi: 10.1016/j.cub.2010.11.021

Dugas, J. C., Mandemakers, W., Rogers, M., Ibrahim, A., Daneman, R., and Barres, B. A. (2008). A novel purification method for CNS projection neurons leads to the identification of brain vascular cells as a source of trophic support for corticospinal motor neurons. *J. Neurosci.* 28, 8294–8305. doi: 10.1523/JNEUROSCI.2010-08.2008

During, M. J., and Leone, P. (1995). Adeno-associated virus vectors for gene therapy of neurodegenerative disorders. *Clin. Neurosci.* 3, 292–300.

Eisen, A., and Weber, M. (2001). The motor cortex and amyotrophic lateral sclerosis. *Muscle Nerve* 24, 564–573. doi: 10.1002/mus.1042

Feng, G., Mellor, R. H., Bernstein, M., Keller-Peck, C., Nguyen, Q. T., Wallace, M., et al. (2000). Imaging neuronal subsets in transgenic mice expressing multiple spectral variants of GFP. *Neuron* 28, 41–51. doi: 10.1016/S0896-6273(00)00084-2

Fink, J. K. (2001). Progressive spastic paraparesis: hereditary spastic paraplegia and its relation to primary and amyotrophic lateral sclerosis. *Semin. Neurol.* 21, 199–207. doi: 10.1055/s-2001-15265

Franz, C. K., Rutishauser, U., and Rafuse, V. F. (2005). Polysialylated neural cell adhesion molecule is necessary for selective targeting of regenerating motor neurons. *J. Neurosci.* 25, 2081–2091. doi: 10.1523/JNEUROSCI.4880-04.2005

Genç, B., and Ozdinler, P. H. (2013). Moving forward in clinical trials for ALS: motor neurons lead the way please. *Drug Discov. Today*. doi: 10.1016/j.drudis.2013.10.014. [Epub ahead of print].

Gerfen, C. R., Paletzki, R., and Heintz, N. (2013). GENSAT BAC cre-recombinase driver lines to study the functional organization of cerebral cortical and basal ganglia circuits. *Neuron* 80, 1368–1383. doi: 10.1016/j.neuron.2013.10.016

Gong, S., Doughty, M., Harbaugh, C. R., Cummins, A., Hatten, M. E., Heintz, N., et al. (2007). Targeting Cre recombinase to specific neuron populations with bacterial artificial chromosome constructs. *J. Neurosci.* 27, 9817–9823. doi: 10.1523/JNEUROSCI.2707-07.2007

Gong, S., Zheng, C., Doughty, M. L., Losos, K., Didkovsky, N., Schambra, U. B., et al. (2003). A gene expression atlas of the central nervous system based on bacterial artificial chromosomes. *Nature* 425, 917–925. doi: 10.1038/nature02033

Grutzendler, J., Kasthuri, N., and Gan, W. B. (2002). Long-term dendritic spine stability in the adult cortex. *Nature* 420, 812–816. doi: 10.1038/nature01276

Gurney, M. E., Pu, H., Chiu, A. Y., Dal Canto, M. C., Polchow, C. Y., Alexander, D. D., et al. (1994). Motor neuron degeneration in mice that express a human Cu,Zn superoxide dismutase mutation. *Science* 264, 1772–1775. doi: 10.1126/science.8209258

Han, Y., Chang, Q. A., Virag, T., West, N. C., George, D., Castro, M. G., et al. (2010). Lack of humoral immune response to the tetracycline (Tet) activator in rats injected intracranially with Tet-off rAAV vectors. *Gene Ther.* 17, 616–625. doi: 10.1038/gt.2010.6

Hendry, I. A., and Hill, C. E. (1980). Retrograde axonal transport of target tissue-derived macromolecules. *Nature* 287, 647–649. doi: 10.1038/287647a0

Henriques, A., Pitzer, C., Dittgen, T., Klugmann, M., Dupuis, L., and Schneider, A. (2011). CNS-targeted viral delivery of G-CSF in an animal model for ALS: improved efficacy and preservation of the neuromuscular unit. *Mol. Ther.* 19, 284–292. doi: 10.1038/mt.2010.271

Hester, M. E., Foust, K. D., Kaspar, R. W., and Kaspar, B. K. (2009). AAV as a gene transfer vector for the treatment of neurological disorders: novel treatment thoughts for ALS. *Curr. Gene Ther.* 9, 428–433. doi: 10.2174/156652309789753383

Huang, Z. J., and Zeng, H. (2013). Genetic approaches to neural circuits in the mouse. *Annu. Rev. Neurosci.* 36, 183–215. doi: 10.1146/annurev-neuro-062012-170307

Huber, A. B., Kania, A., Tran, T. S., Gu, C., De Marco Garcia, N., Lieberam, I., et al. (2005). Distinct roles for secreted semaphorin signaling in spinal motor axon guidance. *Neuron* 48, 949–964. doi: 10.1016/j.neuron.2005.12.003

Huisman, A. M., Kuypers, H. G., and Verburgh, C. A. (1981). Quantitative differences in collateralization of the descending spinal pathways from red nucleus and other brain stem cell groups in rat as demonstrated with the multiple fluorescent retrograde tracer technique. *Brain Res.* 209, 271–286. doi: 10.1016/0006-8993(81)90153-0

Hutson, T. H., Verhaagen, J., Yanez-Munoz, R. J., and Moon, L. D. (2011). Corticospinal tract transduction: a comparison of seven adeno-associated viral vector serotypes and a non-integrating lentiviral vector. *Gene Ther.* 19, 49–60. doi: 10.1038/gt.2011.71

Ikrar, T., Olivas, N. D., Shi, Y., and Xu, X. (2011). Mapping inhibitory neuronal circuits by laser scanning photostimulation. *J. Vis. Exp.* pii:3109. doi: 10.3791/3109

Jara, J. H., Villa, S. R., Khan, N. A., Bohn, M. C., and Ozdinler, P. H. (2012). AAV2 mediated retrograde transduction of corticospinal motor neurons reveals initial and selective apical dendrite degeneration in ALS. *Neurobiol. Dis.* 47, 174–183. doi: 10.1016/j.nbd.2012.03.036

Jones, E. G., and Leavitt, R. Y. (1974). Retrograde axonal transport and the demonstration of non-specific projections to the cerebral cortex and striatum from thalamic intralaminar nuclei in the rat, cat and monkey. *J. Comp. Neurol.* 154, 349–377. doi: 10.1002/cne.901540402

Jones, E. G., Schreyer, D. J., and Wise, S. P. (1982). Growth and maturation of the rat corticospinal tract. *Prog. Brain Res.* 57, 361–379. doi: 10.1016/S0079-6123(08)64137-0

Karumbayaram, S., Kelly, T. K., Paucar, A. A., Roe, A. J., Umbach, J. A., Charles, A., et al. (2009). Human embryonic stem cell-derived motor neurons expressing SOD1 mutants exhibit typical signs of motor neuron degeneration linked to ALS. *Dis. Model. Mech.* 2, 189–195. doi: 10.1242/dmm.002113

Kaspar, B. K., Llado, J., Sherkat, N., Rothstein, J. D., and Gage, F. H. (2003). Retrograde viral delivery of IGF-1 prolongs survival in a mouse ALS model. *Science* 301, 839–842. doi: 10.1126/science.1086137

Keifer, O. P. Jr., O'Connor, D. M., and Boulis, N. M. (2014). Gene and protein therapies utilizing VEGF for ALS. *Pharmacol. Ther.* 141, 261–271. doi: 10.1016/j.pharmthera.2013.10.009

Kelsch, W., Stolfi, A., and Lois, C. (2012). Genetic labeling of neuronal subsets through enhancer trapping in mice. *PLoS ONE* 7**:**e38593. doi: 10.1371/journal.pone.0038593

Kiritani, T., Wickersham, I. R., Seung, H. S., and Shepherd, G. M. (2012). Hierarchical connectivity and connection-specific dynamics in the corticospinal-corticostriatal microcircuit in mouse motor cortex. *J. Neurosci.* 32, 4992–5001. doi: 10.1523/JNEUROSCI.4759-11.2012

Kristensson, K., and Olsson, Y. (1974). Retrograde transport of horseradish peroxidase in transected axons. 1. Time relationships between transport and induction of chromatolysis. *Brain Res.* 79, 101–109. doi: 10.1016/0006-8993(74)90569-1

Kunzle, H. (1977). Evidence for selective axon-terminal uptake and retrograde transport of label in cortico- and rubrospinal systems after injection of 3H-proline. *Exp. Brain Res.* 28, 125–132. doi: 10.1007/BF00237090

Kuypers, H. G., Bentivoglio, M., Catsman-Berrevoets, C. E., and Bharos, A. T. (1980). Double retrograde neuronal labeling through divergent axon collaterals, using two fluorescent tracers with the same excitation wavelength which label different features of the cell. *Exp. Brain Res.* 40, 383–392. doi: 10.1007/BF00236147

Lanciego, J. L., and Wouterlood, F. G. (2011). A half century of experimental neuroanatomical tracing. *J. Chem. Neuroanat.* 42, 157–183. doi: 10.1016/j.jchemneu.2011.07.001

Landmesser, L. (1978). The development of motor projection patterns in the chick hind limb. *J. Physiol.* 284, 391–414.

Langou, K., Moumen, A., Pellegrino, C., Aebischer, J., Medina, I., Aebischer, P., et al. (2010). AAV-mediated expression of wild-type and ALS-linked mutant VAPB selectively triggers death of motoneurons through a Ca2+-dependent

ER-associated pathway. *J. Neurochem.* 114, 795–809. doi: 10.1111/j.1471-4159.2010.06806.x

Laskowski, C. J., and Bradke, F. (2013). *In vivo* imaging: a dynamic imaging approach to study spinal cord regeneration. *Exp. Neurol.* 242, 11–17. doi: 10.1016/j.expneurol.2012.07.007

Lavail, J. H., and Lavail, M. M. (1972). Retrograde axonal transport in the central nervous system. *Science* 176, 1416–1417. doi: 10.1126/science.176.4042.1416

Lavail, J. H., and Lavail, M. M. (1974). The retrograde intraaxonal transport of horseradish peroxidase in the chick visual system: a light and electron microscopic study. *J. Comp. Neurol.* 157, 303–357. doi: 10.1002/cne.901570304

Lavail, J. H., Winston, K. R., and Tish, A. (1973). A method based on retrograde intraaxonal transport of protein for identification of cell bodies of origin of axons terminating within the CNS. *Brain Res.* 58, 470–477. doi: 10.1016/0006-8993(73)90016-4

Leighton, P. A., Mitchell, K. J., Goodrich, L. V., Lu, X., Pinson, K., Scherz, P., et al. (2001). Defining brain wiring patterns and mechanisms through gene trapping in mice. *Nature* 410, 174–179. doi: 10.1038/35065539

Lemon, R. N. (2008). Descending pathways in motor control. *Annu. Rev. Neurosci.* 31, 195–218. doi: 10.1146/annurev.neuro.31.060407.125547

Liang, H., Paxinos, G., and Watson, C. (2011). Projections from the brain to the spinal cord in the mouse. *Brain Struct. Funct.* 215, 159–186. doi: 10.1007/s00429-010-0281-x

Liedgren, S. R., Kristensson, K., Larsby, B., and Odkvist, L. M. (1976). Projection of thalamic neurons to cat primary vestibular cortical fields studied by means of retrograde axonal transport of horseradish peroxidase. *Exp. Brain Res.* 24, 237–243. doi: 10.1007/BF00235012

Liu, X., Ramirez, S., Pang, P. T., Puryear, C. B., Govindarajan, A., Deisseroth, K., et al. (2012). Optogenetic stimulation of a hippocampal engram activates fear memory recall. *Nature* 484, 381–385. doi: 10.1038/nature11028

Livet, J., Weissman, T. A., Kang, H., Draft, R. W., Lu, J., Bennis, R. A., et al. (2007). Transgenic strategies for combinatorial expression of fluorescent proteins in the nervous system. *Nature* 450, 56–62. doi: 10.1038/nature06293

Lopez-Bendito, G., Sturgess, K., Erdelyi, F., Szabo, G., Molnar, Z., and Paulsen, O. (2004). Preferential origin and layer destination of GAD65-GFP cortical interneurons. *Cereb. Cortex* 14, 1122–1133. doi: 10.1093/cercor/bhh072

Lu, Y. Y., Wang, L. J., Muramatsu, S., Ikeguchi, K., Fujimoto, K., Okada, T., et al. (2003). Intramuscular injection of AAV-GDNF results in sustained expression of transgenic GDNF, and its delivery to spinal motoneurons by retrograde transport. *Neurosci. Res.* 45, 33–40. doi: 10.1016/S0168-0102(02)00195-5

Luo, L. (2007). Fly MARCM and mouse MADM: genetic methods of labeling and manipulating single neurons. *Brain Res. Rev.* 55, 220–227. doi: 10.1016/j.brainresrev.2007.01.012

Mandel, R. J., Spratt, S. K., Snyder, R. O., and Leff, S. E. (1997). Midbrain injection of recombinant adeno-associated virus encoding rat glial cell line-derived neurotrophic factor protects nigral neurons in a progressive 6-hydroxydopamine-induced degeneration model of Parkinson's disease in rats. *Proc. Natl. Acad. Sci. U.S.A.* 94, 14083–14088. doi: 10.1073/pnas.94.25.14083

Markram, H., Toledo-Rodriguez, M., Wang, Y., Gupta, A., Silberberg, G., and Wu, C. (2004). Interneurons of the neocortical inhibitory system. *Nat. Rev. Neurosci.* 5, 793–807. doi: 10.1038/nrn1519

Martinov, V. N., Sefland, I., Walaas, S. I., Lomo, T., Nja, A., and Hoover, F. (2002). Targeting functional subtypes of spinal motoneurons and skeletal muscle fibers *in vivo* by intramuscular injection of adenoviral and adeno-associated viral vectors. *Anat Embryol. (Berl.)* 205, 215–221. doi: 10.1007/s00429-002-0233-1

McCown, T. J. (2005). Adeno-associated virus (AAV) vectors in the CNS. *Curr. Gene Ther.* 5, 333–338. doi: 10.2174/1566523054064995

McGovern, V. L., Gavrilina, T. O., Beattie, C. E., and Burghes, A. H. (2008). Embryonic motor axon development in the severe SMA mouse. *Hum. Mol. Genet.* 17, 2900–2909. doi: 10.1093/hmg/ddn189

McLeod, D. (1975). Clinical sign of obstructed axoplasmic transport. *Lancet* 2, 954–956. doi: 10.1016/S0140-6736(75)90364-5

Miles, G. B., Yohn, D. C., Wichterle, H., Jessell, T. M., Rafuse, V. F., and Brownstone, R. M. (2004). Functional properties of motoneurons derived from mouse embryonic stem cells. *J. Neurosci.* 24, 7848–7858. doi: 10.1523/JNEUROSCI.1972-04.2004

Molnar, Z., and Cheung, A. F. (2006). Towards the classification of subpopulations of layer V pyramidal projection neurons. *Neurosci. Res.* 55, 105–115. doi: 10.1016/j.neures.2006.02.008

Molyneaux, B. J., Arlotta, P., Menezes, J. R., and Macklis, J. D. (2007). Neuronal subtype specification in the cerebral cortex. *Nat. Rev. Neurosci.* 8, 427–437. doi: 10.1038/nrn2151

Morfini, G. A., Burns, M., Binder, L. I., Kanaan, N. M., Lapointe, N., Bosco, D. A., et al. (2009). Axonal transport defects in neurodegenerative diseases. *J. Neurosci.* 29, 12776–12786. doi: 10.1523/JNEUROSCI.3463-09.2009

Nagai, M., Re, D. B., Nagata, T., Chalazonitis, A., Jessell, T. M., Wichterle, H., et al. (2007). Astrocytes expressing ALS-linked mutated SOD1 release factors selectively toxic to motor neurons. *Nat. Neurosci.* 10, 615–622. doi: 10.1038/nn1876

Novarino, G., Fenstermaker, A. G., Zaki, M. S., Hofree, M., Silhavy, J. L., Heiberg, A. D., et al. (2014). Exome sequencing links corticospinal motor neuron disease to common neurodegenerative disorders. *Science* 343, 506–511. doi: 10.1126/science.1247363

O'Leary, D. D., and Koester, S. E. (1993). Development of projection neuron types, axon pathways, and patterned connections of the mammalian cortex. *Neuron* 10, 991–1006. doi: 10.1016/0896-6273(93)90049-W

Olsson, T., and Kristensson, K. (1979). Uptake and retrograde axonal transport of horseradish peroxidase in normal and axotomized motor neurons during postnatal development. *Neuropathol. Appl. Neurobiol.* 5, 377–387. doi: 10.1111/j.1365-2990.1979.tb00636.x

Oppenheim, R. W., and Heaton, M. B. (1975). The retrograde transport of horseradish peroxidase from the developing limb of the chick embryo. *Brain Res.* 98, 291–302. doi: 10.1016/0006-8993(75)90007-4

Oray, S., Majewska, A., and Sur, M. (2004). Dendritic spine dynamics are regulated by monocular deprivation and extracellular matrix degradation. *Neuron* 44, 1021–1030. doi: 10.1016/j.neuron.2004.12.001

Ozdinler, P. H., Benn, S., Yamamoto, T. H., Guzel, M., Brown, R. H. Jr., and Macklis, J. D. (2011). Corticospinal motor neurons and related subcerebral projection neurons undergo early and specific neurodegeneration in hSOD1G93A transgenic ALS mice. *J. Neurosci.* 31, 4166–4177. doi: 10.1523/JNEUROSCI.4184-10.2011

Ozdinler, P. H., and Macklis, J. D. (2006). IGF-I specifically enhances axon outgrowth of corticospinal motor neurons. *Nat. Neurosci.* 9, 1371–1381. doi: 10.1038/nn1789

Packer, A. M., Roska, B., and Hausser, M. (2013). Targeting neurons and photons for optogenetics. *Nat. Neurosci.* 16, 805–815. doi: 10.1038/nn.3427

Paravicini, U., Stoeckel, K., and Thoenen, H. (1975). Biological importance of retrograde axonal transport of nerve growth factor in adrenergic neurons. *Brain Res.* 84, 279–291. doi: 10.1016/0006-8993(75)90982-8

Penzes, P., Cahill, M. E., Jones, K. A., Vanleeuwen, J. E., and Woolfrey, K. M. (2011). Dendritic spine pathology in neuropsychiatric disorders. *Nat. Neurosci.* 14, 285–293. doi: 10.1038/nn.2741

Pittet, M. J., and Weissleder, R. (2011). Intravital imaging. *Cell* 147, 983–991. doi: 10.1016/j.cell.2011.11.004

Placantonakis, D. G., Tomishima, M. J., Lafaille, F., Desbordes, S. C., Jia, F., Socci, N. D., et al. (2009). BAC transgenesis in human embryonic stem cells as a novel tool to define the human neural lineage. *Stem Cells* 27, 521–532. doi: 10.1634/stemcells.2008-0884

Price, D. L., and Griffin, J. W. (1977). Tetanus toxin: retrograde axonal transport of systemically administered toxin. *Neurosci. Lett.* 4, 61–65. doi: 10.1016/0304-3940(77)90145-8

Ravits, J., Paul, P., and Jorg, C. (2007). Focality of upper and lower motor neuron degeneration at the clinical onset of ALS. *Neurology* 68, 1571–1575. doi: 10.1212/01.wnl.0000260965.20021.47

Reh, T., and Kalil, K. (1981). Development of the pyramidal tract in the hamster. I. A light microscopic study. *J. Comp. Neurol.* 200, 55–67. doi: 10.1002/cne.902000105

Richter, M. W., and Roskams, A. J. (2009). Corticospinal neurons respond differentially to neurotrophins and myelin-associated glycoprotein *in vitro*. *J. Neurosci. Res.* 87, 2222–2236. doi: 10.1002/jnr.22053

Rustioni, A., and Hayes, N. L. (1981). Corticospinal tract collaterals to the dorsal column nuclei of cats. An anatomical single and double retrograde tracer study. *Exp. Brain Res.* 43, 237–245. doi: 10.1007/BF00238364

Schaefer, A. M., Sanes, J. R., and Lichtman, J. W. (2005). A compensatory subpopulation of motor neurons in a mouse model of amyotrophic lateral sclerosis. *J. Comp. Neurol.* 490, 209–219. doi: 10.1002/cne.20620

Schmidt, E. F., Kus, L., Gong, S., and Heintz, N. (2013). BAC transgenic mice and the GENSAT database of engineered mouse strains. *Cold Spring Harb. Protoc.* 2013. doi: 10.1101/pdb.top073692

Schwab, M. E., Suda, K., and Thoenen, H. (1979). Selective retrograde transsynaptic transfer of a protein, tetanus toxin, subsequent to its retrograde axonal transport. *J. Cell Biol.* 82, 798–810. doi: 10.1083/jcb.82.3.798

Shaner, N. C., Steinbach, P. A., and Tsien, R. Y. (2005). A guide to choosing fluorescent proteins. *Nat. Methods* 2, 905–909. doi: 10.1038/nmeth819

Sheets, P. L., Suter, B. A., Kiritani, T., Chan, C. S., Surmeier, D. J., and Shepherd, G. M. (2011). Corticospinal-specific HCN expression in mouse motor cortex: I(h)-dependent synaptic integration as a candidate microcircuit mechanism involved in motor control. *J. Neurophysiol.* 106, 2216–2231. doi: 10.1152/jn.00232.2011

Shepherd, G. M. (2011). The microcircuit concept applied to cortical evolution: from three-layer to six-layer cortex. *Front. Neuroanat.* 5:30. doi: 10.3389/fnana.2011.00030

Shepherd, G. M. (2013). Corticostriatal connectivity and its role in disease. *Nat. Rev. Neurosci.* 14, 278–291. doi: 10.1038/nrn3469

Shinoda, Y., Yokota, J., and Futami, T. (1981). Divergent projection of individual corticospinal axons to motoneurons of multiple muscles in the monkey. *Neurosci. Lett.* 23, 7–12. doi: 10.1016/0304-3940(81)90182-8

Shneider, N. A., Brown, M. N., Smith, C. A., Pickel, J., and Alvarez, F. J. (2009). Gamma motor neurons express distinct genetic markers at birth and require muscle spindle-derived GDNF for postnatal survival. *Neural Dev.* 4, 42. doi: 10.1186/1749-8104-4-42.

Singh Roy, N., Nakano, T., Xuing, L., Kang, J., Nedergaard, M., and Goldman, S. A. (2005). Enhancer-specified GFP-based FACS purification of human spinal motor neurons from embryonic stem cells. *Exp. Neurol.* 196, 224–234. doi: 10.1016/j.expneurol.2005.06.021

Smedemark-Margulies, N., and Trapani, J. G. (2013). Tools, methods, and applications for optophysiology in neuroscience. *Front. Mol. Neurosci.* 6:18. doi: 10.3389/fnmol.2013.00018

Snyder, B. R., Gray, S. J., Quach, E. T., Huang, J. W., Leung, C. H., Samulski, R. J., et al. (2011). Comparison of adeno-associated viral vector serotypes for spinal cord and motor neuron gene delivery. *Hum. Gene Ther.* 22, 1129–1135. doi: 10.1089/hum.2011.008

Sohal, G. S., and Holt, R. K. (1978). Identification of the trochlear motoneurons by retrograde transport of horseradish peroxidase. *Exp. Neurol.* 59, 509–514. doi: 10.1016/0014-4886(78)90241-8

Somogyi, P., Hodgson, A. J., and Smith, A. D. (1979). An approach to tracing neuron networks in the cerebral cortex and basal ganglia. Combination of Golgi staining, retrograde transport of horseradish peroxidase and anterograde degeneration of synaptic boutons in the same material. *Neuroscience* 4, 1805–1852. doi: 10.1016/0306-4522(79)90059-9

Stanfield, B. B. (1992). The development of the corticospinal projection. *Prog. Neurobiol.* 38, 169–202. doi: 10.1016/0301-0082(92)90039-H

Steiger, H. J., and Buttner-Ennever, J. (1978). Relationship between motoneurons and internuclear neurons in the abducens nucleus: a double retrograde tracer study in the cat. *Brain Res.* 148, 181–188. doi: 10.1016/0006-8993(78)90387-6

Stepanenko, O. V., Stepanenko, O. V., Shcherbakova, D. M., Kuznetsova, I. M., Turoverov, K. K., and Verkhusha, V. V. (2011). Modern fluorescent proteins: from chromophore formation to novel intracellular applications. *Biotechniques* 51, 313–314, 316, 318 passim. doi: 10.2144/000113765

Stoeckel, K., and Thoenen, H. (1975). Retrograde axonal transport of nerve growth factor: specificity and biological importance. *Brain Res.* 85, 337–341. doi: 10.1016/0006-8993(75)90092-X

Suter, B. A., Migliore, M., and Shepherd, G. M. (2012). Intrinsic electrophysiology of mouse corticospinal neurons: a class-specific triad of spike-related properties. *Cereb. Cortex* 23, 1965–1977. doi: 10.1093/cercor/bhs184

Tanaka, Y. H., Tanaka, Y. R., Fujiyama, F., Furuta, T., Yanagawa, Y., and Kaneko, T. (2011). Local connections of layer 5 GABAergic interneurons to corticospinal neurons. *Front. Neural Circuits* 5:12. doi: 10.3389/fncir.2011.00012

Tang, J. C., Szikra, T., Kozorovitskiy, Y., Teixiera, M., Sabatini, B. L., Roska, B., et al. (2013). A nanobody-based system using fluorescent proteins as scaffolds for cell-specific gene manipulation. *Cell* 154, 928–939. doi: 10.1016/j.cell.2013.07.021

Taniguchi, H., He, M., Wu, P., Kim, S., Paik, R., Sugino, K., et al. (2011). A resource of Cre driver lines for genetic targeting of GABAergic neurons in cerebral cortex. *Neuron* 71, 995–1013. doi: 10.1016/j.neuron.2011.07.026

Tatom, J. B., Wang, D. B., Dayton, R. D., Skalli, O., Hutton, M. L., Dickson, D. W., et al. (2009). Mimicking aspects of frontotemporal lobar degeneration and Lou Gehrig's disease in rats via TDP-43 overexpression. *Mol. Ther.* 17, 607–613. doi: 10.1038/mt.2009.3

Terashima, T. (1995). Anatomy, development and lesion-induced plasticity of rodent corticospinal tract. *Neurosci. Res.* 22, 139–161. doi: 10.1016/0168-0102(95)00895-9

Thomson, A. M., and Lamy, C. (2007). Functional maps of neocortical local circuitry. *Front. Neurosci.* 1:2. doi: 10.3389/neuro.01.1.1.002.2007

Tolbert, D. L., Bantli, H., and Bloedel, J. R. (1978). Organizational features of the cat and monkey cerebellar nucleocortical projection. *J. Comp. Neurol.* 182, 39–56. doi: 10.1002/cne.901820104

Towne, C., Setola, V., Schneider, B. L., and Aebischer, P. (2011). Neuroprotection by gene therapy targeting mutant SOD1 in individual pools of motor neurons does not translate into therapeutic benefit in fALS mice. *Mol. Ther.* 19, 274–283. doi: 10.1038/mt.2010.260

Tsien, R. Y. (1998). The green fluorescent protein. *Annu. Rev. Biochem.* 67, 509–544. doi: 10.1146/annurev.biochem.67.1.509

Udaka, F., Kameyama, M., and Tomonaga, M. (1986). Degeneration of Betz cells in motor neuron disease. *A Golgi study. Acta Neuropathol* 70, 289–295. doi: 10.1007/BF00686086

Ullan, J., and Artieda, J. (1981). Somatotopy of the corticospinal neurons in the rat. *Neurosci. Lett.* 21, 13–18. doi: 10.1016/0304-3940(81)90049-5

van den Pol, A. N., and Ghosh, P. K. (1998). Selective neuronal expression of green fluorescent protein with cytomegalovirus promoter reveals entire neuronal arbor in transgenic mice. *J. Neurosci.* 18, 10640–10651.

van der Kooy, D., and Kuypers, H. G. (1979). Fluorescent retrograde double labeling: axonal branching in the ascending raphe and nigral projections. *Science* 204, 873–875. doi: 10.1126/science.441742

Walberg, F., Brodal, A., and Hoddevik, G. H. (1976). A note on the method of retrograde transport of horseradish peroxidase as a tool in studies of afferent cerebellar connections, particularly those from the inferior olive; with comments on the orthograde transport in Purkinje cell axons. *Exp. Brain Res.* 24, 383–401. doi: 10.1007/BF00235005

Wang, L., Muramatsu, S., Lu, Y., Ikeguchi, K., Fujimoto, K., Okada, T., et al. (2002a). Delayed delivery of AAV-GDNF prevents nigral neurodegeneration and promotes functional recovery in a rat model of Parkinson's disease. *Gene Ther.* 9, 381–389. doi: 10.1038/sj.gt.3301682

Wang, L. J., Lu, Y. Y., Muramatsu, S., Ikeguchi, K., Fujimoto, K., Okada, T., et al. (2002b). Neuroprotective effects of glial cell line-derived neurotrophic factor mediated by an adeno-associated virus vector in a transgenic animal model of amyotrophic lateral sclerosis. *J. Neurosci.* 22, 6920–6928.

Weigert, R., Porat-Shliom, N., and Amornphimoltham, P. (2013). Imaging cell biology in live animals: ready for prime time. *J. Cell Biol.* 201, 969–979. doi: 10.1083/jcb.201212130

Weinberg, M. S., Samulski, R. J., and McCown, T. J. (2013). Adeno-associated virus (AAV) gene therapy for neurological disease. *Neuropharmacology* 69, 82–88. doi: 10.1016/j.neuropharm.2012.03.004

Weiss, P. S. (2008). 2008 Nobel Prize in Chemistry: green fluorescent protein, its variants and implications. *ACS Nano* 2, 1977. doi: 10.1021/nn800671h

Wichterle, H., Lieberam, I., Porter, J. A., and Jessell, T. M. (2002). Directed differentiation of embryonic stem cells into motor neurons. *Cell* 110, 385–397. doi: 10.1016/S0092-8674(02)00835-8

Wise, S. P., and Jones, E. G. (1976). The organization and postnatal development of the commissural projection of the rat somatic sensory cortex. *J. Comp. Neurol.* 168, 313–343. doi: 10.1002/cne.901680302

Wong, F., Fan, L., Wells, S., Hartley, R., Mackenzie, F. E., Oyebode, O., et al. (2009). Axonal and neuromuscular synaptic phenotypes in Wld(S), SOD1(G93A) and ostes mutant mice identified by fiber-optic confocal microendoscopy. *Mol. Cell. Neurosci.* 42, 296–307. doi: 10.1016/j.mcn.2009.08.002

Wu, C. Y., Whye, D., Mason, R. W., and Wang, W. (2012). Efficient differentiation of mouse embryonic stem cells into motor neurons. *J. Vis. Exp.* e3813. doi: 10.3791/3813

Yamashita, T., Chai, H. L., Teramoto, S., Tsuji, S., Shimazaki, K., Muramatsu, S., et al. (2013). Rescue of amyotrophic lateral sclerosis phenotype in a mouse model by intravenous AAV9-ADAR2 delivery to motor neurons. *EMBO Mol. Med.* 5, 1710–1719. doi: 10.1002/emmm.201302935

Yasvoina, M. V., Genç, B., Jara, J. H., Sheets, P. L., Quinlan, K. A., Milosevic, A., et al. (2013). eGFP expression under UCHL1 promoter genetically labels corticospinal motor neurons and a subpopulation of degeneration-resistant

spinal motor neurons in an ALS mouse model. *J. Neurosci.* 33, 7890–7904. doi: 10.1523/JNEUROSCI.2787-12.2013

Yorke, C. H. Jr., and Caviness, V. S. Jr. (1975). Interhemispheric neocortical connections of the corpus callosum in the normal mouse: a study based on anterograde and retrograde methods. *J. Comp. Neurol.* 164, 233–245. doi: 10.1002/cne.901640206

Yu, J., Anderson, C. T., Kiritani, T., Sheets, P. L., Wokosin, D. L., Wood, L., et al. (2008). Local-circuit phenotypes of layer 5 neurons in motor-frontal cortex of YFP-H mice. *Front. Neural Circuits* 2:6. doi: 10.3389/neuro.04.006.2008

Conflict of Interest Statement: The authors declare that the research was conducted in the absence of any commercial or financial relationships that could be construed as a potential conflict of interest.

Received: 30 November 2013; accepted: 10 March 2014; published online: 26 March 2014.

Citation: Jara JH, Genç B, Klessner JL and Özdinler PH (2014) Retrograde labeling, transduction, and genetic targeting allow cellular analysis of corticospinal motor neurons: implications in health and disease. Front. Neuroanat. ***8****:16. doi: 10.3389/fnana.2014.00016*

This article was submitted to the journal Frontiers in Neuroanatomy.

frontiers in
NEUROANATOMY

OPINION ARTICLE
published: 28 August 2013
doi: 10.3389/fnana.2013.00027

Evolutionary development of the amygdaloid complex

Mohan Pabba *

Neurosciences Unit, Department of Cellular and Molecular Medicine, Faculty of Medicine, University of Ottawa, Ottawa, ON, Canada
**Correspondence: mpabb044@uottawa.ca; mpabba@ohri.ca*

Edited by:
Makoto Fukuda, Baylor College of Medicine, USA

Reviewed by:
Joshua Corbin, Children's National Medical Center, USA

Keywords: amygdala, anatomy, tetrapods, mammals, evolution

In the early 19th century, Burdach discovered an almond-shaped mass of gray matter in the anterior portion of the mammalian temporal lobe, which he called "amygdala" (Burdach, 1819–1822). The first anatomical description of the amygdala was made in 1867 by Meynert (1867). Subsequently, a large number of other nuclei were added to the amygdala to constitute what is now known as the "amygdaloid complex" (AC) (Johnston, 1923). Until this day, AC remains a subject of intense investigation in terms of content and evolutionary development since it is a much more complicated structure than what was previously thought. It is therefore, important to know the evolutionary developmental origin of AC before we can completely understand its function.

The AC is a multinuclear complex comprised of 13 nuclei. These nuclei are divided into three major groups: the basolateral, cortical-like, and centromedial. Other accessory nuclei such as the intercalated cell masses (I) and the amygdalo-hippocampus area have also been described. The basolateral group is comprised of the lateral nucleus (LA), basal nucleus (B), and accessory basal nucleus (AB) (Johnston, 1923). The cortical-like group of nuclei includes the nucleus of the lateral olfactory tract (NLOT), bed nucleus of the accessory olfactory tract (BAOT), anterior and posterior cortical nuclei (CoA and CoP, respectively), and periamygdaloid cortex (PAC). The centromedial nucleus consists of the central nucleus (CeA), medial nucleus (M), and amygdaloid part of the bed nucleus of stria terminalis (BST). The major remaining groups of AC are the amygdalohippocampal area (AHA) and intercalated nuclei (I) (Aggleton, 2000; Sah et al., 2003). These different nuclei of AC are connected within and also with various brain regions, and thus, process various types of information (e.g., olfactory and **Figure 1A**).

Swanson and Petrovich (1998) definition of amygdala as neither a structural nor a functional unit provides an attractive point to explore the evolutionary developmental aspects of AC because a growing number of evidence suggests AC as an evolutionarily conserved structure. Earlier, research on structural organization of AC in different amniotic vertebrates revealed a common pattern of organization, along with shared functional roles. Conversely, research on anamniotes provided little comparative information regarding structural organization of AC. However, recent studies have shown a homology between amygdaloid components of amniotes and anamniotes. To better understand the evolutionary and developmental history of a particular brain region, one needs to follow a "sequential (step by step) approach," which takes into account the developmental, topological, hodological, genetical, and functional history. Interestingly, recent data on AC of mammals, reptiles, and anurans suggest that the evolution of AC occurred as common traits of telencephlon, for example, regions of cortical amygdala such as nLOT and accessory olfactory bulb (AOB) (Remedios et al., 2007; Huilgol et al., 2013); but not as the sum of unrelated structures with different origins. The present understanding of AC in developmental and adult vertebrates suggests two major divisions of telencephlon: the pallium and the subpallium (Puelles et al., 2000; Martinez-Garcia et al., 2002; Moreno and Gonzalez, 2007b; Remedios et al., 2007). This dual view or origin makes AC a histogenetic complex structure of the adult brain, with extremely intense morphogenetic and migratory processes during the development in all tetrapods (Puelles et al., 2000). In mammals, the pallial component is composed of "cortical amygdala" and "basolateral amygdala." In turn, the subpallial component consists of the striatal component, central amygdala, and medial amygdala. This basic plan is shared by reptiles, birds, and also by anuran amphibians (Martinez-Garcia et al., 2002; Medina et al., 2004). Interestingly, this basic description is possible only in few mammalian tetrapods, but not in the non-mammalian amniotes and the anurans where they have no clear anatomical subdivisions. The existence of shared embryological AC components in all tetrapods provides clues to the presence of precursors of the amygdaloid nuclei from anamniotes (Moreno and Gonzalez, 2007b). The following sections deal with the current view on accepted and shared components of AC in tetrapods.

The amygdala is a part of a phylogentically conserved olfactory system, particularly the olfactory bulb, in vertebrate evolution in terms of embryological origin, neurochemistry, connectivity, and function (Martinez-Garcia et al., 2002; Huilgol et al., 2013). Additionally, a major part of amygdala is also an integral component of the vomeronasal system of the tetrapod (except avian) brain (Swanson and Petrovich, 1998; Moreno and Gonzalez, 2005a).

In mammals, the vomeronasal information passes via the AOB to medial (MeA) and cortical postero-medial amygdala (CoApm) (Swanson and Petrovich, 1998). In addition, the amygdala also receives information from the main olfactory bulb (MOB) and hypothalamus to modulate reproductive and defensive behaviors (Canteras et al., 1995). In reptiles and anurans, the existence of a well-developed "vomeronasal amygdala"

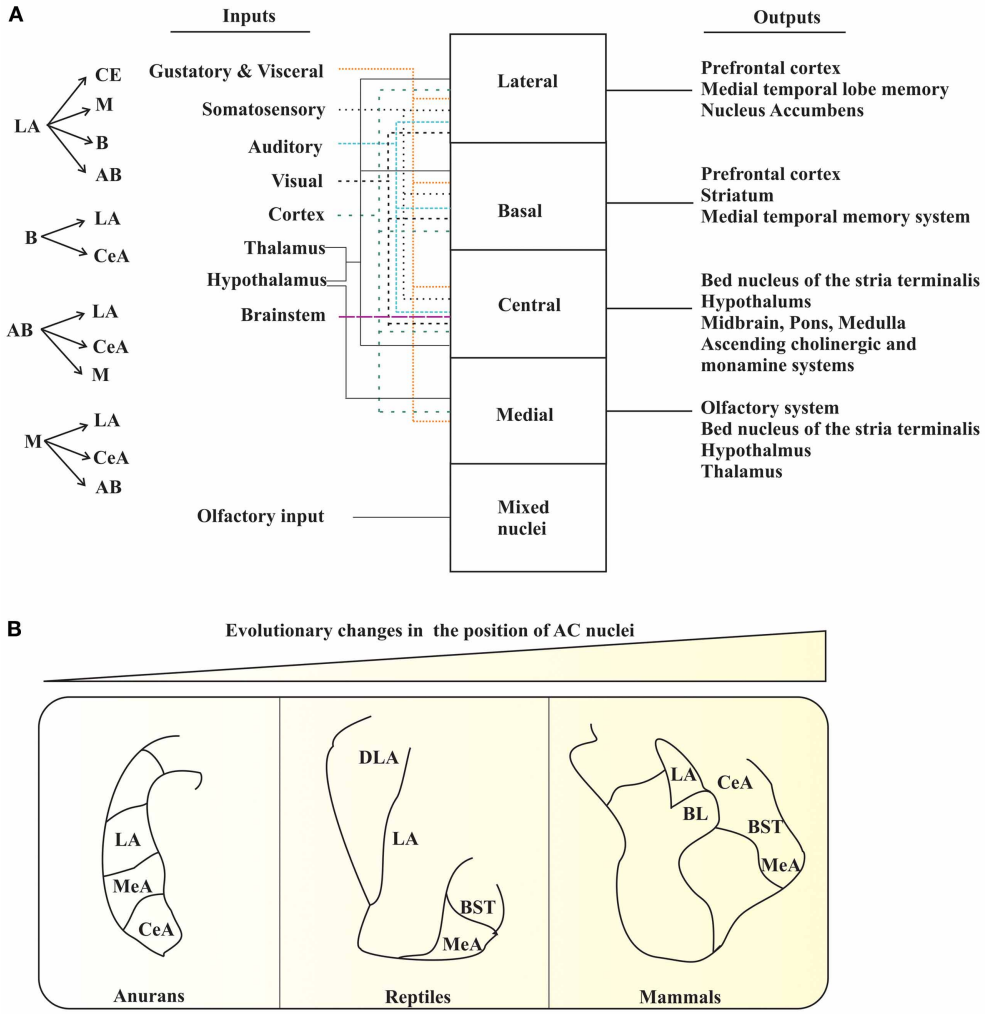

FIGURE 1 | AC of tetrapods. (A) The interconnections (*left panel*) and summary of the main inputs to AC and outputs from AC (*right panel*). The various types of inputs to AC are denoted with different types of colored arrows. **(B)** Pictorial diagram depicting the changes in the position of certain AC nuclei during the course of evolution. LA, lateral nucleus; MeA, medial nucleus; CeA, central nucleus; DLA, dorsal division of lateral nucleus; BST, bed nucleus of stria terminalis; BL, basolateral amygdala. The figure panels **(A)** and **(B)** are adapted and modified from Sah et al. (2003); Moreno and Gonzalez (2007b).

has also been reported (Moreno and Gonzalez, 2003), although no vomeronasal amygdaloid nuclei has been described in birds so far (Martinez-Garcia et al., 2006). Thus, in all tetrapods, the main secondary vomeronasal brain areas belong to AC.

In mammals, the olfactory amygdaloid system consists of the distinct cortical (CoA, CoP nuclei, etc.) and basolateral amygdala (BL, M, LA nuclei). LA receives major sensory input, and is important for emotional behavior (Ledoux et al., 1990). Studies on birds indicate the presence of nuclei that are comparable to CoP of the mammalian amygdala. These studies also revealed the possession of counterparts similar to BM and LA of the mammalian amygdala (Martinez-Garcia et al., 2006). In reptiles, studies on the olfactory system showed comparable functional circuitry with the mammalian BA complex. The anuran counterpart of the mammalian olfactory amygdala is LA (Moreno and Gonzalez, 2004). This part of the amygdala in anurans receives directly or indirectly olfactory, visual, auditory, somatosensory, vomeronasal, and gustatory information. The observed integration that occurs in AC of tetrapods is responsible for the acquisition of "emotional memory," which pertains to the survival of individuals during their defence against danger, their interaction with sexual partners, or their fight with an enemy (Ledoux, 2000). Therefore, the amygdala receives large sensory input information from olfactory and vomeronasal projections, and are conserved in tetrapods.

Studies on tetrapods showed CeA as the main receiver of a wide range of sensory information from other amygdaloid regions in addition to the thalamus and brain stem. Moreover, CeA is known to link and integrate the emotional and motor components of behavior (Han et al., 1997), behavioral responses to nociceptive and visceral pain (Han and Neugebauer, 2004), and

behavioral responses to stressful stimuli (Saha et al., 2000). CeA also mediates many of the autonomic, somatic, endocrine, and behavioral responses in different tetrapods. The autonomic amygdala provides a link between environmental stimuli and animal behavioral responses, and thus, provides an important significance in terms of evolutionary conservation.

Another conserved shared system of tetrapods is the strong amygdalo-hypothalamic connections (Martinez-Marcos et al., 1999; Moreno and Gonzalez, 2005a). In mammals, nuclei that project to hypothalamus through the stria terminalis arise from the medial and basolateral amygdala (Swanson and Petrovich, 1998). As in mammals, the amygdalo-hypothalamic projections of anurans (Moreno and Gonzalez, 2005b) also project through the stria terminalis. In anurans, the amygdalo-hypothalamic connections control functions mediated by the hypothalamus in response to pheromones and odors (Reiner and Karten, 1985; Swanson and Petrovich, 1998).

As in mammals, the amygdalo-hypothalamic projections of anurans, project through the stria terminalis. The main similarity with amniotes is the projection to the hypothalamus from comparable amygdaloid territories carrying vomeronasal, olfactory, and multimodal information (Reiner and Karten, 1985; Swanson and Petrovich, 1998). The situation of amygdalo-hypothalamic projections in birds is more complicated because of the lack of a well-developed olfactory/vomeronasal system.

On the other hand, studies that compare the distribution of neuronal markers (either proteins or genes/transcription factors) across the development of analogous AC nuclei from different species as well as within the same species have also provided valuable information on the evolution of AC. For instance, similarities in the molecular profiles of the pallium and subpallium of mice and chickens were obtained by comparing the nested expression domains of genes such as Dlx-2, Tbr-1, Pax-6, NKx-2.1, and Emx-1 (Puelles et al., 2000). Moreno and Gonzalez, using the distribution of somatostatin, nitric oxide synthase, etc. in anuran CeA and MeA in a series of studies, has predicted that these parts of AC could be related to AC of amniotes (Moreno and Gonzalez, 2005a, 2007a). Medina et al. demonstrated a possible existence of evolutionary relationship in various AC nuclei of mammals, reptiles and birds by testing the expression patterns of genes/transcription factors such as Lhx2, Lhx9, Pax6, Islet 1, NKx2, Lhx6, and Lhx5 in forebrain regions of these animals (Medina et al., 2011). Using the similarities and differences in the expression of Lhx1 and Lhx5, Abellan et al. suggested a common pattern of evolutionary conservation in telencephalon between mice and chickens during various stages of development (Abellan et al., 2010). By examining the distribution of Lhx2, Trb1, reelin, and CdK5, Remedios et al. estimated a possible developmental and evolutionary link between nLOT of AC and neocortex (Remedios et al., 2007; Subramanian et al., 2009). Another study from Tole's group, using migratory genetic markers (e.g., NP2 and AP2α), showed that the distinct halves of AOB [posterior and anterior (pAOB and aAOB)] has different developmental origins, and that pAOB could be a component of AC as it was positioned closely to MeA in anamniotes (*Xenopus*) (Huilgol et al., 2013). Finally, Barger et al. using a different approach, i.e., by comparing the percentage of neurons in individual nuclei of AC between humans and apes, suggested that during the course of human evolution, LA of AC has further progressed in humans (Barger et al., 2012).

CONCLUDING REMARKS

The classical hypothesis proposed by Edinger regarding the evolution of the brain attracted much attention (Edinger, 1908). He proposed that the telencephlon evolved in progressive stages of complexity and size, culminating to the human brain. He also stated that there is an "old brain" (the subpallium at the telencephalic base) followed by the addition of a "new brain" (the pallium at the top of the telencephlon). Nevertheless, this classical hypothesis provides evidence on the existence of a basic plan in the origin, regionalization, and organization of the forebrain of vertebrates. Based on the data pertaining to the organization of AC, there seems to have several important features that are common to all tetrapods: (1) it is formed by pallial and subpallial derivatives; (2) it is topographically situated in the ventrolateral caudal telencephalic hemispheres; (3) it has shared features in relation with different functional systems like the vomeronasal, olfactory, autonomic, and multimodal systems along with an intricate intra-amygdaloid network; (4) it is the origin of important hypothalamic projections; (5) it has a common embryological origin for several prominent features of AC; (6) it has the presence of a main output for autonomic system; finally, (7) it has abundant local circuit neurons that are shared by most amniotes. Thus, in the light of recent findings on AC (Remedios et al., 2007; Butler et al., 2011; Huilgol et al., 2013) also strongly support the idea that tetrapods share the same basic plan.

The increase in size of the pallium, especially in mammals, has an evolutionary importance. The current spatial arrangements of the mammalian AC are still found in living anurans. Therefore, it is now obvious that these "new evolutionary nuclei" would have pushed the "most conserved nuclei" (Moreno and Gonzalez, 2007b). It explains why mammals have the central, medial, and basolateral nuclei occupying the most medial positions, whereas the cortical amygdaloid nuclei occupy the most lateral positions (**Figure 1B**) (Moreno and Gonzalez, 2007b). Consequently, the brain of ancestral tetrapods developed an elaborate AC in response to new requirements imposed on them as a part of the transition from water-to-land. Therefore, the basic organization of the brain system, at least in the case of the AC, is still recognizable in all existing tetrapods, and can be compared with that of mammals.

ACKNOWLEDGMENTS

I am thankful to Dr. Richard Bergeron, Dr. Marzia Martina, and Wissam B. Nassrallah for their helpful feedback on the manuscript.

REFERENCES

Abellan, A., Vernier, B., Retaux, S., and Medina, L. (2010). Similarities and differences in the forebrain expression of Lhx1 and Lhx5 between chicken and mouse: insights for understanding telencephalic development and evolution. *J. Comp. Neurol.* 518, 3512–3528. doi: 10.1002/cne.22410

Aggleton, J. (2000). *The Amygdala: A Functional Analysis*. Oxford: Academic Press.

Barger, N., Stefanacci, L., Schumann, C. M., Sherwood, C. C., Annese, J., Allman, J. M.,

et al. (2012). Neuronal populations in the basolateral nuclei of the amygdala are differentially increased in humans compared with apes: a stereological study. *J. Comp. Neurol.* 520, 3035–3054. doi: 10.1002/cne.23118

Burdach, K. F. (1819–1822). *Vom Baue und Leben des Gehims. 2 vols.* Leipzig: Dyk'sche Buchhdl.

Butler, A. B., Reiner, A., and Karten, H. J. (2011). Evolution of the amniote pallium and the origins of mammalian neocortex. *Ann. N.Y. Acad. Sci.* 1225, 14–27. doi: 10.1111/j.1749-6632.2011.06006.x

Canteras, N. S., Simerly, R. B., and Swanson, L. W. (1995). Organization of projections from the medial nucleus of the amygdala: a PHAL study in the rat. *J. Comp. Neurol.* 360, 213–245. doi: 10.1002/cne.903600203

Edinger, L. (1908). The relations of comparative anatomy to comparative psychology. *J. Comp. Neurol. Pscychol.* 18, 437–457. doi: 10.1002/cne.920180502

Han, J. S., McMahan, R. W., Holland, P., and Gallagher, M. (1997). The role of an amygdalonigrostriatal pathway in associative learning. *J. Neurosci.* 17, 3913–3919.

Han, J. S., and Neugebauer, V. (2004). Synaptic plasticity in the amygdala in a visceral pain model in rats. *Neurosci. Lett.* 361, 254–257. doi: 10.1016/j.neulet.2003.12.027

Huilgol, D., Udin, S., Shimogori, T., Saha, B., Roy, A., Aizawa, S., et al. (2013). Dual origins of the mammalian accessory olfactory bulb revealed by an evolutionarily conserved migratory stream. *Nat. Neurosci.* 16, 157–165. doi: 10.1038/nn.3297

Johnston, J. B. (1923). Further contributions to the study of the evolution of the fore-brain. *J. Comp. Neurol.* 35, 371–482. doi: 10.1002/cne.900350502

Ledoux, J. E. (2000). Emotion circuits in the brain. *Annu. Rev. Neurosci.* 23, 155–184. doi: 10.1146/annurev.neuro.23.1.155

Ledoux, J. E., Cicchetti, P., Xagoraris, A., and Romanski, L. M. (1990). The lateral amygdaloid nucleus: sensory interface of the amygdala in fear conditioning. *J. Neurosci.* 10, 1062–1069.

Martinez-Garcia, F., Martinez-Marcos, A., and Lanuza, E. (2002). The pallial amygdala of amniote vertebrates: evolution of the concept, evolution of the structure. *Brain Res. Bull.* 57, 463–469. doi: 10.1016/S0361-9230(01)00665-7

Martinez-Garcia, F., Novejarque, A., and Lanuza, E. (2006). "*Evolution of the* amygdala in vertebrates," in *Evolution of Nervous Systems*. Vol. 2, ed J. H. Kaas (Elsevier Inc.), 255–334.

Martinez-Marcos, A., Lanuza, E., and Halpern, M. (1999). Organization of the ophidian amygdala: chemosensory pathways to the hypothalamus. *J. Comp. Neurol.* 412, 51–68.

Medina, L., Bupesh, M., and Abellan, A. (2011). Contribution of genoarchitecture to understanding forebrain evolution and development, with particular emphasis on the amygdala. *Brain Behav. Evol.* 78, 216–236. doi: 10.1159/000330056

Medina, L., Legaz, I., Gonzalez, G., De Castro, F., Rubenstein, J. L., and Puelles, L. (2004). Expression of Dbx1, Neurogenin 2, Semaphorin 5A, Cadherin 8, and Emx1 distinguish ventral and lateral pallial histogenetic divisions in the developing mouse claustroamygdaloid complex. *J. Comp. Neurol.* 474, 504–523. doi: 10.1002/cne.20141

Meynert, T. (1867). Der Bau der Grosshirnrinde und seine ortlichen verschiedenheiten, nebst einem pathologisch-anatomischen Corollarium. *Vjschr. Psychiat.* 1, 77–93, 126–170, 198–217.

Moreno, N., and Gonzalez, A. (2003). Hodological characterization of the medial amygdala in anuran amphibians. *J. Comp. Neurol.* 466, 389–408. doi: 10.1002/cne.10887

Moreno, N., and Gonzalez, A. (2004). Localization and connectivity of the lateral amygdala in anuran amphibians. *J. Comp. Neurol.* 479, 130–148. doi: 10.1002/cne.20298

Moreno, N., and Gonzalez, A. (2005a). Central amygdala in anuran amphibians: neurochemical organization and connectivity. *J. Comp. Neurol.* 489, 69–91. doi: 10.1002/cne.20611

Moreno, N., and Gonzalez, A. (2005b). Forebrain projections to the hypothalamus are topographically organized in anurans: conservative traits as compared with amniotes. *Eur. J. Neurosci.* 21, 1895–1910. doi: 10.1111/j.1460-9568.2005.04025.x

Moreno, N., and Gonzalez, A. (2007a). Development of the vomeronasal amygdala in anuran amphibians: hodological, neurochemical, and gene expression characterization. *J. Comp. Neurol.* 503, 815–831. doi: 10.1002/cne.21422

Moreno, N., and Gonzalez, A. (2007b). Evolution of the amygdaloid complex in vertebrates, with special reference to the anamnio-amniotic transition. *J. Anat.* 211, 151–163. doi: 10.1111/j.1469-7580.2007.00780.x

Puelles, L., Kuwana, E., Puelles, E., Bulfone, A., Shimamura, K., Keleher, J., et al. (2000). Pallial and subpallial derivatives in the embryonic chick and mouse telencephalon, traced by the expression of the genes Dlx-2, Emx-1, Nkx-2.1, Pax-6, and Tbr-1. *J. Comp. Neurol.* 424, 409–438.

Reiner, A., and Karten, H. J. (1985). Comparison of olfactory bulb projections in pigeons and turtles. *Brain Behav. Evol.* 27, 11–27. doi: 10.1159/000118717

Remedios, R., Huilgol, D., Saha, B., Hari, P., Bhatnagar, L., Kowalczyk, T., et al. (2007). A stream of cells migrating from the caudal telencephalon reveals a link between the amygdala and neocortex. *Nat. Neurosci.* 10, 1141–1150. doi: 10.1038/nn1955

Saha, S., Batten, T. F., and Henderson, Z. (2000). A GABAergic projection from the central nucleus of the amygdala to the nucleus of the solitary tract: a combined anterograde tracing and electron microscopic immunohistochemical study. *Neuroscience* 99, 613–626. doi: 10.1016/S0306-4522(00)00240-2

Sah, P., Faber, E. S., Lopez De Armentia, M., and Power, J. (2003). The amygdaloid complex: anatomy and physiology. *Physiol. Rev.* 83, 803–834.

Subramanian, L., Remedios, R., Shetty, A., and Tole, S. (2009). Signals from the edges: the cortical hem and antihem in telencephalic development. *Semin. Cell Dev. Biol.* 20, 712–718. doi: 10.1016/j.semcdb.2009.04.001

Swanson, L. W., and Petrovich, G. D. (1998). What is the amygdala. *Trends Neurosci.* 21, 323–331. doi: 10.1016/S0166-2236(98)01265-X

Received: 09 July 2013; accepted: 06 August 2013; published online: 28 August 2013.

Citation: Pabba M (2013) Evolutionary development of the amygdaloid complex. Front. Neuroanat. 7:27. doi: 10.3389/fnana.2013.00027

This article was submitted to the journal Frontiers in Neuroanatomy.

frontiers in
NEUROANATOMY

ORIGINAL RESEARCH ARTICLE
published: 06 May 2014
doi: 10.3389/fnana.2014.00026

Investigation of spinal cerebrospinal fluid-contacting neurons expressing PKD2L1: evidence for a conserved system from fish to primates

Lydia Djenoune[1,2,3,4,5,6], Hanen Khabou[1,2,3,4‡], Fanny Joubert[4,7‡], Feng B. Quan[5,6], Sophie Nunes Figueiredo[1,2,3,4], Laurence Bodineau[4,7], Filippo Del Bene[8,9,10], Céline Burcklé[1,2,3,4†], Hervé Tostivint[5,6] and Claire Wyart[1,2,3,4]*

[1] *Institut du Cerveau et de la Moelle Épinière, Hôpital de la Pitié-Salpêtrière, Paris, France*
[2] *Institut National de la Santé et de la Recherche Médicale UMR 1127, Paris, France*
[3] *Centre National de la Recherche Scientifique UMR 7225, Paris, France*
[4] *UPMC Univ. Paris 06, Paris, France*
[5] *Muséum National d'Histoire Naturelle, Paris, France*
[6] *Centre National de la Recherche Scientifique UMR 7221, Paris, France*
[7] *Institut National de la Santé et de la Recherche Médicale UMR S 1158, Paris, France*
[8] *Institut Curie, Paris, France*
[9] *Centre National de la Recherche Scientifique UMR 3215, Paris, France*
[10] *Institut National de la Santé et de la Recherche Médicale U 934, Paris, France*

Edited by:
Laurent Gautron, The University of Texas Southwestern Medical Center, USA

Reviewed by:
Marina Bentivoglio, Université di Verona, Italy
Ramon Anadon, Universidad de Santiago de Compostela, Spain

***Correspondence:**
Claire Wyart, Institut du Cerveau et de la Moelle épinière, Hôpital de la Pitié-Salpêtrière, 83, bld de l'hôpital, 75013 Paris, France
e-mail: claire.wyart@inserm.fr

†Present address:
Céline Burcklé, Institut de Biologie du Développement de Marseille, Marseille, France

‡*These authors have contributed equally to this work.*

Over 90 years ago, Kolmer and Agduhr identified spinal cerebrospinal fluid-contacting neurons (CSF-cNs) based on their morphology and location within the spinal cord. In more than 200 vertebrate species, they observed ciliated neurons around the central canal that extended a brush of microvilli into the cerebrospinal fluid (CSF). Although their morphology is suggestive of a primitive sensory cell, their function within the vertebrate spinal cord remains unknown. The identification of specific molecular markers for these neurons in vertebrates would benefit the investigation of their physiological roles. PKD2L1, a transient receptor potential channel that could play a role as a sensory receptor, has been found in cells contacting the central canal in mouse. In this study, we demonstrate that PKD2L1 is a specific marker for CSF-cNs in the spinal cord of mouse (*Mus musculus*), macaque (*Macaca fascicularis*) and zebrafish (*Danio rerio*). In these species, the somata of spinal PKD2L1$^+$ CSF-cNs were located below or within the ependymal layer and extended an apical bulbous extension into the central canal. We found GABAergic PKD2L1-expressing CSF-cNs in all three species. We took advantage of the zebrafish embryo for its transparency and rapid development to identify the progenitor domains from which *pkd2l1*$^+$ CSF-cNs originate. *pkd2l1*$^+$ CSF-cNs were all GABAergic and organized in two rows—one ventral and one dorsal to the central canal. Their location and marker expression is consistent with previously described Kolmer–Agduhr cells. Accordingly, *pkd2l1*$^+$ CSF-cNs were derived from the progenitor domains p3 and pMN defined by the expression of *nkx2.2a* and *olig2* transcription factors, respectively. Altogether our results suggest that a system of CSF-cNs expressing the PKD2L1 channel is conserved in the spinal cord across bony vertebrate species.

Keywords: cerebrospinal fluid-contacting neurons (CSF-cNs), PKD2L1, mouse, macaque, zebrafish, GABAergic neurons, spinal cord

INTRODUCTION

Spinal cerebrospinal fluid-contacting neurons (CSF-cNs) were identified and described by Kolmer (1921, 1931) and Agduhr (1922) in over 200 species based on cellular morphology, location, and Nissl staining. They independently noted that these cells exhibit an apical bulbous extension in the central canal and send basal axonal projections to other cells. Their observations suggested that CSF-cNs could constitute a sensory organ (referred to as the sagittal organ by Kolmer) interfacing the cerebrospinal

Abbreviations: cc, Central canal; CSF, Cerebrospinal fluid; CSF-cNs, Cerebrospinal fluid-contacting neurons; dpf, days post fertilization; FISH, Fluorescent *in situ* hybridization; GAD, Glutamic Acid Decarboxylase; GABA, γ-aminobutyric acid; GFP, Green Fluorescent Protein; GFP$^+$, GFP positive; hpf, hours post fertilization; IHC, Immunohistochemistry; KAs, Kolmer–Agduhr cells; MAP2, microtubule-associated protein 2; PB, Phosphate Buffer; PBS, Phosphate Buffered Saline; PFA, paraformaldehyde; *pkd2l1*, mRNA form of polycystic kidney disease 2-like 1 in zebrafish; *pkd2l1*$^+$, *pkd2l1* positive; PKD2L1, polycystic kidney disease 2-like 1 protein in mouse and macaque; PKD2L1$^+$, PKD2L1 positive; TRP, Transient Receptor Potential; VGAT, vesicular GABA transporter.

fluid (CSF) with the nervous system at the level of the spinal cord.

Since the discovery of CSF-cNs, electron microscopy studies have shown that these cells exhibit a sensory tuft, previously referred to as a "brush border" (Dale et al., 1987b), a "central body" (Vigh and Vigh-Teichmann, 1973) or a "bud" (Stoeckel et al., 2003). The apical bulbous extension projects from the perikarya of CSF-cNs toward the central canal and ends with a terminal bud in contact with its lumen. This apical extension is characterized by the dendritic marker microtubule-associated protein 2 (MAP2) (Orts-Del'Immagine et al., 2014).

Immunohistochemistry (IHC) studies showed evidence for GABAergic CSF-cNs in many species such as rat (Barber et al., 1982; Stoeckel et al., 2003), turtle (Reali et al., 2011), African clawed frog (Dale et al., 1987a; Binor and Heathcote, 2001), zebrafish (Bernhardt et al., 1992; Martin et al., 1998; Higashijima et al., 2004a,b; Wyart et al., 2009; Yang et al., 2010), eel and trout (Roberts et al., 1995), dogfish (Sueiro et al., 2004), and lampreys (Brodin et al., 1990; Christenson et al., 1991a,b; Melendez-Ferro et al., 2003; Robertson et al., 2007; Rodicio et al., 2008; Villar-Cervino et al., 2008). In African clawed frog and zebrafish, these GABAergic CSF-cNs were named Kolmer–Agduhr cells (KAs) to distinguish them from ciliated ependymal cells (Dale et al., 1987a; Bernhardt et al., 1992). In these species CSF-cNs project an ascending axon ventrally in the spinal cord (Dale et al., 1987a; Bernhardt et al., 1992; Higashijima et al., 2004a; Wyart et al., 2009).

Despite the anatomical studies of CSF-cNs and their implication in modulating locomotion (Wyart et al., 2009), their physiological role in vertebrates remains unknown. One obstacle to answering this question is the lack of a specific genetic marker to identify these cells. Recently the calcium-permeable polycystic kidney disease 2-like 1 (PKD2L1) channel (Huang et al., 2006; Ishimaru et al., 2006), first identified in kidney, retina, and heart (Basora et al., 2002) was found to be expressed in cells contacting the CSF at the level of the brainstem and spinal cord in mouse (Huang et al., 2006; Orts-Del'Immagine et al., 2012). This channel belongs to the family of Transient Receptor Potential (TRP) channels. These are known to be chemo-, thermo- or mechanosensitive (Delmas, 2004; Delmas et al., 2004). Expression of this channel and location of these cells at the interface with the CSF are consistent with the hypothesis that CSF-cNs have a proprioceptive sensory function.

In this study, we investigated whether PKD2L1 was a specific marker for CSF-cNs across vertebrates, by examining mouse, macaque and zebrafish. In mouse and macaque PKD2L1 was enriched in the sensory tuft of CSF-cNs in cervical, thoracic and lumbar spinal cord. The soma of PDK2L1$^+$ cells was located in the ependymal layer or just underneath. In both species, a significant proportion of PKD2L1$^+$ CSF-cNs was distinctly identified as GABAergic. We took advantage of the zebrafish model organism to thoroughly characterize the properties and lineage of *pkd2l1*$^+$ cells in the spinal cord. In this model, all *pkd2l1*$^+$ cells contacting the central canal were confirmed as GABAergic neurons. Reciprocally, all KAs, defined by their location and their GABAergic phenotype expressed *pkd2l1*. Using specific transgenic lines, we confirmed that these cells derive from two progenitor domains. The dorsal *pkd2l1*$^+$ KAs originated from pMN and were labeled by the Enhanced Green Fluorescent Protein (EGFP) in the *Tg(olig2:EGFP)* while the ventral *pkd2l1*$^+$ KAs originated from p3 and were labeled by *Tg(nkx2.2a:mEGFP)*. Altogether our data show that PKD2L1 is a specific marker of CSF-cNs shared between multiple vertebrate species. We found evidence for PKD2L1-expressing GABAergic CSF-cNs in all examined species. Our results on the developmental origin of CSF-cNs in zebrafish open new paths of investigation in mammals.

MATERIALS AND METHODS

MOUSE

Experimental animals

Wild type (WT) mice (*Mus musculus*, OF1 strain) were kept on a 12 h light/dark cycle with free access to food and water. Experiments were performed at embryonic (E), postnatal (P) and adult stages: four WT adult mice, one WT newborn, and three WT embryos were used in the present study. One adult male and two E16.5 GAD67-GFP knock-in embryos (Tamamaki et al., 2003), resulting of the insertion of the cDNA encoding EGFP into the locus encoding GAD67, have been used. After mating, the day of detection of the vaginal plug was considered as embryonic day E0.5. Pregnant females were sacrificed by decapitation at E14.5, E16.5, or E18.5. Uterine horns were removed from the mother and embryos were excised from their individual bag, soaked in cold 0.1 M Phosphate Buffer (PB) for 10 min and fixed by immersion in cold 2% paraformaldehyde (PFA) solution in 0.1 M PB for 3 h at 4°C. Newborn mice (P1) were deeply anesthetized by an exposure to low temperature and the spinal cord was immediately removed and fixed with 2% PFA for 4 h. Adult mice were deeply anesthetized with intraperitoneal injection of Nembutal® (150 mg·kg^{-1}) and transcardially perfused sequentially with NaCl 0.9% (20 ml) and PFA (2%, 30 ml for WT adults and 4%, 30 ml for the GAD67-GFP mouse). After fixation, spinal cords were dissected out and post-fixed for 24 h in the fixative solution (2% PFA for WT mice and 4% for the GAD67-GFP mouse) at 4°C. Following fixation (and post-fixation if appropriate), tissues were cryo-protected for 24–48 h in 30% sucrose in 0.1 M PB at 4°C and then stored at -20°C for later use. Experiments were performed in accordance with the European Communities Council (EEC) Directive of 22 September 2010 (2010/63/EU) and French law (87/848).

Immunohistochemistry

Standard immunofluorescence procedures were used to localize antigens of interest (Voituron et al., 2011). At the cervical level, 10 µm-thick coronal sections of the spinal cord were obtained using a cryostat (Leica CM 3050S), mounted on silanized slides and stored at −20°C for later IHC using a rabbit anti-Polycystin-L (anti-human PKD2L1, 1:500 dilution; Millipore, Billerica, MA, USA). This PKD2L1 antibody was raised against the synthetic peptide from the N-terminal of human Polycystin-L. For PKD2L1 IHC at E14.5 and E16.5, we used an Antigen Unmasking Solution (Vector Laboratories). Briefly, the sections were incubated in 1% Bovine serum albumin (BSA) and 0.1% Triton X-100 for 20 min at room temperature (RT). After rinsing with 0.1 M phosphate

buffered saline (PBS), the sections were incubated for 30 min at RT with DAPI (1.25 μg/ml; Life Technologies) and with Alexa-conjugated anti-rabbit secondary antibodies (1:500 dilution; Life Technologies). For GFP and PKD2L1 double IHC, 30 μm-thick coronal floating sections obtained using a cryostat (Leica CM 1850S) were immunostained by co-incubating two primary antibodies, a chicken anti-GFP (1:1000 dilution; Abcam, Cambridge, UK) with the rabbit anti-PKD2L1 (1:500 dilution) overnight at 4°C, and then the specific secondary antibodies Alexa Fluor 488 donkey anti-chicken IgG (1:500 dilution, Life Technologies) and Alexa 555-conjugated goat anti rabbit for 2 h at RT. In all IHC experiments, control sections were processed in parallel by omitting primary antibodies. Finally, sections were washed with PBS before being mounted onto glass slides with fluorescent mounting medium (AquaPolyMount, Biovalley, Marne La Vallée, France). Sections were observed under an Olympus FV1000 confocal microscope.

Quantification of cells

On 10 μm-thick sections, we performed Z-stacks with a step size of 1–1.5 μm in a region of interest (ROI) centered on the central canal (approximately 150 × 220 μm width, $n = 13$ sections for E16.5 GAD67-GFP and 115 × 140 μm width, $n = 7$ sections for adult GAD67-GFP sections). For each analyzed section, cells were identified by the DAPI staining in order to avoid counting multiple times the same cell. Within the ROI, all PKD2L1$^+$ cells were counted manually and probed for GFP in the GAD67-GFP line.

MACAQUE

Experimental animals

Tissue from two adult macaques (*Macaca fascicularis*, a 25-year old female and an 8-year old male) was used for this study. These animals were sacrificed for other purposes and spinal cord tissue samples were subsequently collected and devoted to the present study. Spinal cord collection was performed after the sacrifice of animals, in strict accordance with the recommendations of the Weatherall Report regarding good animal practice. All surgical procedures and experimental protocols were carried out in strict accordance with the National Institutes of Health guidelines (2013) and the recommendations of the EEC (2010/63/EU).

Tissue extraction and preparation

Macaques were deeply anesthetized with intramuscular injection of ketamine and xylazine at 50 and 5 mg/kg, respectively. Following the anesthesia, each animal was exsanguinated and perfused with 0.9% NaCl before their tissues were fixed by an intracardial perfusion containing 4% PFA in 0.1 M PBS. Spinal cord was extracted and meninges were removed using fine forceps. Tissue was embedded in 5% agarose and sectioned at 50 μm using a vibratome (Leica VT1000S). Additionally, frozen tissue blocks were obtained by passing tissue through a series of cryoprotection solutions (20, 30% sucrose in PBS) and freezing in isopentane; frozen sections were cut at 20 μm (HM 650V Microtome, Thermo Scientific). All sections were stored in 0.4% Sodium Azide in 0.1 M PBS at 4°C until IHC.

Immunohistochemistry

Free-floating sections from cervical, thoracic, and lumbar spinal cord tissue were used for IHC. Sections were first incubated in a blocking solution composed of 1% BSA, 0.5% Triton X-100 and 2% normal goat serum in PBS to reduce non-specific labeling. Sections were then incubated in primary antibodies overnight at 4°C. After multiple washes, sections were incubated in secondary antibodies for 4 h at 4°C. Primary antibodies used were rabbit anti-Polycystin-L (anti-human PKD2L1, 1:1,000 dilution; Millipore, Billerica, MA, USA), guinea pig anti-vesicular GABA Transporter (anti-VGAT, 1:500; Synaptic Systems, Germany) and rabbit anti-GAD65/67 (1:500; Abcam, MA, USA). Secondary antibodies were Alexa Fluor 488- or Alexa Fluor 568-conjugated anti-rabbit (1:500; Life Technologies) and Alexa Fluor 488-anti-guinea pig (1:500; Life Technologies). The same blocking solution as previously was used to dilute the antibodies. PBS was used for washing sections between each step. Sections were mounted on glass slides, cover slipped with Prolong® Gold Antifade Reagent (Life Technologies) mounting medium and then imaged on a Leica SP2 AOBS AOTF inverted confocal laser scanning microscope. Single optical slice images of individual labeled cells were taken using a 63× oil objective.

ZEBRAFISH

Experimental animals

All zebrafish (*Danio rerio*) lines were maintained and raised on a 14/10 h light cycle and water was regulated at 28.5°C, conductivity at 500 μS and pH at 7.4 (Westerfield, 2000). WT AB and Tüpfel long fin (TL) embryos were used for whole mount *in situ* hybridization (ISH). *Tg(nkx2.2a:mEGFP)* (Ng et al., 2005; Kirby et al., 2006) and *Tg(olig2:EGFP)* (Shin et al., 2003) transgenic lines were kindly provided by Prof. Bruce Appel, University of Colorado, Denver, USA. Embryos were dechorionated and staged according to number of somites as described (Kimmel et al., 1995): the 30-somite stage corresponds to Prim-5 or 24 h post fertilization when raised at 28.5°C. Adult fish were anesthetized in 0.02% MS 222 (Sandoz, Levallois-Perret, France) and killed by decapitation. All procedures were approved by the Institutional Ethics Committee at the Institut du Cerveau et de la Moelle épinière (ICM), Paris, France, the Ethical Committee Charles Darwin and received subsequent approval from the EEC (2010/63/EU).

Generation of the pkd2l1 probe

To generate the *pkd2l1* ISH probe, the coding fragment for *pkd2l1* was amplified from zebrafish embryo total cDNA using the following primers (5′ to 3′): pkd2l1_For: TAGTGGTGATACTGCTTGCTGTGGTGG (from the end of the exon 6 of the *pkd2l1* gene and the beginning of exon 7) and pkd2l1_Rev: TGGTTCCACACTGTTCTCGAGGTCACG (from the end of exon 13). The PCR fragment was cloned into the pCRII-TOPO vector (Life Technologies, Carlsbad, CA, USA). The resulting plasmid was linearized with NotI. The *gad67* plasmid, kindly provided by Dr. Uwe Strähle, Karlsruhe Institute of Technology, Germany, was linearized with NcoI. Digoxigenin (DIG)- and fluorescein (Fluo)-labeled probes were synthesized using SP6 RNA polymerase with the RNA Labeling

Kit (Roche Applied Science, Basel, Switzerland) to generate both *pkd2l1* and *gad67* antisense probes. To generate *pkd2l1* sense probes, the plasmid was linearized with KpnI and transcription was carried out using T7 RNA polymerase. All probes were purified using the mini Quick Spin RNA Column (Roche, Basel, Switzerland).

In situ hybridization

Whole-mount ISH were performed as previously described (Parmentier et al., 2011; Alunni et al., 2013) on embryos or dissected adult spinal cords fixed in 4% PFA in PBS overnight at 4°C. To reveal *pkd2l1* expression, probes were detected with anti-DIG or anti-Fluo antibodies conjugated to alkaline phosphatase followed by a chromogenic reaction using a solution of NBT/BCIP as substrate (Roche Diagnostics, France). To quantify cell density or ascertain transcript colocalization, probes were detected by the antibodies conjugated to horseradish peroxidase and were revealed by Tyramide Signal Amplification using Tyramide-FITC or Tyramide-TAMRA as substrates. The specificity of the *pkd2l1* probe was verified using a *pkd2l1* sense probe as negative control (data *not shown*). Double fluorescent *in situ* hybridization (FISH) for *pkd2l1* and *gad67* were performed on adult zebrafish spinal cords and coupled with respectively DIG and Fluo.

Immunohistochemistry and sectioning

The following primary antibodies were used for IHC: rabbit anti-GABA (1:2000, Sigma-Aldrich, St. Louis, MO, USA), rabbit anti-GAD65/67 and chicken anti-GFP (both used at 1:500 dilution, Abcam, Cambridge, UK). Immunostaining specificity was established by omitting the primary specific antibodies, no immunoreactive signal was observed. Agarose sections were collected as described above. In the zebrafish embryo, we performed either 50 μm-thick sagittal (for anti-GAD65/67 IHC) or transverse (for anti-GFP IHC) sections. In the adult, we performed 50 μm-thick sagittal and frontal sections of previously FISH stained adult spinal cords.

Combination of pkd2l1 FISH with immunohistochemistry

pkd2l1 FISH was performed before IHC against GFP or GAD65/67: embryos were washed and immunostained with the chicken anti-GFP antibody or the rabbit anti-GAD65/67 antibody overnight at 4°C, and then incubated with the corresponding Alexa conjugated secondary antibodies IgG (1:500, Life Technologies) combined with DAPI (2.5 μg/ml, Life Technologies).

Microscopy

Whole-mount embryos stained by NBT/BCIP were mounted in 80% glycerol. Sections of adult spinal cord were mounted in a solution of Mowiol. Embryos were imaged using a Nikon AZ100M macroscope and a Leica DM5000 B Upright microscope. Adult spinal cord sections were imaged using a Nikon AZ100M macroscope. To quantify *pkd2l1*$^+$ and GABA$^+$ cells, stained embryos were imaged using the Fixed Stage microscope AxioExaminer Z1 equipped with a 20× water immersion objective and a Yokogawa CSU-X1 spinning disk unit ($n = 13$ embryos for *pkd2l1* and $n = 10$ for GABA). To quantify the overlap of GFP with *pkd2l1* FISH in the *Tg(nkx2.2a:mEGFP)* and the *Tg(olig2:EGFP)* transgenic embryos, 50 μm-thick sections were analyzed on an Olympus FV1000 confocal microscope equipped with a 40× water immersion objective using 405, 473, and 543 nm laser lines. Images were processed using Fiji (Schindelin et al., 2012) and Adobe Illustrator (Adobe Systems, Mountain View, CA, USA) software.

Quantification of cells

To quantify the total number of *pkd2l1*$^+$ cells revealed by FISH per embryo, Z-stacks of the entire embryos from somite 1 to 30 were acquired. Total numbers of cells were counted per somite labeled on both sides of the midline. The boundaries for each somite were established with transmitted light. The three subtypes of *pkd2l1* expressing cells were defined according to their position relative to the central canal. We distinguished: (i) the row of cells that was ventral and in proximity to the central canal, (ii) the row that was dorsal and in proximity to the central canal and (iii) the sparse cells that were dorsal and distant from the central canal. The proportion of *pkd2l1*$^+$ cells double-labeled for GAD65/67 in 30-somite (Prim-5) embryos was quantified based on 50 μm-thick sagittal sections performed after the FISH and before GAD65/67 IHC. The proportion of *pkd2l1*$^+$ cells double-labeled for GFP in *Tg(nkx2.2a:mEGFP)* and *Tg(olig2:EGFP)* in 30-somite embryos was quantified based on 50 μm-thick transverse sections performed after the FISH and IHC. The total number of cells is given as the mean ± Standard Error of the Mean (SEM). The same method was applied for counting of GABA$^+$ KAs. There are four GABAergic interneuron types in the zebrafish embryo (Bernhardt et al., 1992; Higashijima et al., 2004a); KAs were identified as the only GABAergic ascending neurons with a soma located just below (KA") or above (KA') the central canal.

RESULTS

PKD2L1 IS EXPRESSED IN CSF-cNs FROM EMBRYONIC STAGES TO ADULTHOOD IN THE MOUSE SPINAL CORD

PKD2L1 was originally identified in CSF-cNs at postnatal stages P1–P4 in the mouse spinal cord (Huang et al., 2006). We investigated PKD2L1 expression in the spinal cord at the embryonic, postnatal and adult stages. PKD2L1 expression could not be detected before E14.5 in the spinal cord at the cervical, thoracic and lumbar levels. At E14.5, few PKD2L1$^+$ cells could be identified in the cervical spinal cord (**Figure 1A**). Starting at E16.5, PKD2L1$^+$ cells localized around the central canal exhibited the typical morphology of spinal CSF-cNs (**Figures 1B–E**, arrows). At E18.5, the soma of PKD2L1$^+$ cells was usually located under the layer of ependymal cells (91 out of 102, while 11 out of 102 were located within the ependyma, **Table 1**). PKD2L1$^+$ cells sent an apical bulbous extension toward the central canal ending in the lumen with a bud enriched in PKD2L1 (**Figures 1B–E**, arrows). In the adult, the soma of PKD2L1$^+$ CSF-cNs was located in lamina X and always under the ependyma (95 out of 95 PKD2L1$^+$ cells) (**Figure 1E**, **Table 1**). We also observed PKD2L1$^+$ cells with similar morphology localized away from the central canal, though these cells lacked a visible apical extension to the central canal (**Figures 1A–C**, arrowheads). Our data identify PKD2L1 as a general marker of CSF-cNs.

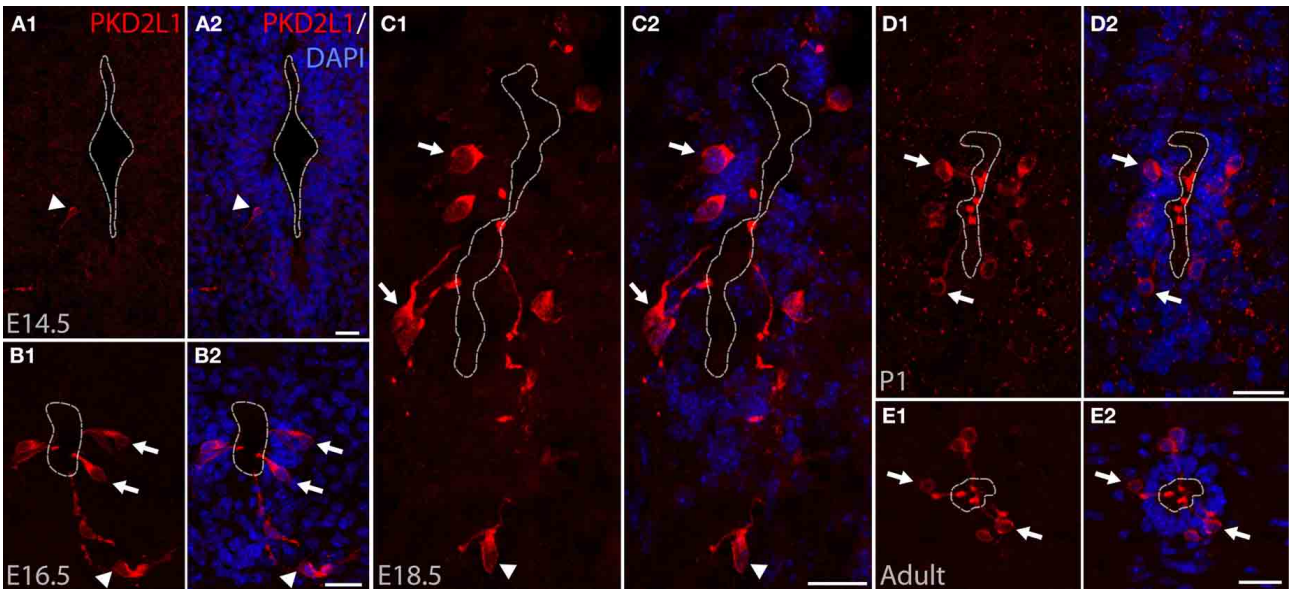

FIGURE 1 | PKD2L1 expression in CSF-cNs is present from embryonic stage E14.5 to adulthood in mouse. (A–E) Immunostaining for PKD2L1 at E14.5 **(A)**, E16.5 **(B)**, E18.5 **(C)**, P1 **(D)**, and in the adult **(E)** performed on coronal sections of the mouse cervical spinal cord. At E14.5, few PKD2L1$^+$ cells are detected (arrowhead). From E16.5 **(B)** to adult **(E)**, multiple PKD2L1$^+$ CSF-cNs (arrows) surround the central canal where they project an apical bulbous dendritic extension contacting its lumen. Note that PKD2L1$^+$ cells exhibiting a similar morphology but not distinctly contacting the central canal (arrowheads) can also be observed **(A–C)**. Dorsal is up. White dashed line delineates the central canal. DAPI staining appears in blue. Scale bars = 20 μm.

Table 1 | Distribution of PKD2L1$^+$ cells based on the location of their soma relative to the ependyma in the mouse spinal cord.

Stage	Total number of PKD2L1$^+$ cells	Number of PKD2L1$^+$ cells located in the ependymal layer	Number of PKD2L1$^+$ cells located in the subependymal layer
E16.5	84	8	76
E18.5	102	11	91
P1	184	6	178
Adult	95	0	95

PKD2L1$^+$ cells located within the ependyma represent only a small number (<11%) of the total population of PKD2L1$^+$ cells counted at embryonic and newborn stages. In the adult mouse spinal cord, the somata of all PKD2L1$^+$ cells are located subependymally.

PKD2L1 IS PRESENT IN GABAergic CSF-cNs IN THE MOUSE SPINAL CORD

As mentioned before, cells contacting the CSF had been described as GABAergic in many species, but the neurotransmitter phenotype has not been thoroughly established yet in mouse. We tested whether CSF-cNs were GABAergic in the embryonic and adult mouse spinal cord (**Figure 2**). We took advantage of the well-characterized GAD67-GFP knock-in mouse where the enhanced GFP was targeted to the locus encoding GAD67 using homologous recombination (Tamamaki et al., 2003). In these animals, we performed IHC for GFP to amplify the endogenous GFP signals (**Figure 2**). In GAD67-GFP knock-in embryos, double IHC for GFP and PKD2L1 on coronal sections of E16.5 mice spinal cords (**Figure 2A**) revealed that most of PKD2L1$^+$ cells were GFP$^+$ (arrows) indicating their GABAergic nature ($n = 2$ embryos, 107 out of 162 PKD2L1+ cells). In one adult, we observed the same findings and found 47 out of 73 cells labeled for both PKD2L1 and GFP (**Figure 2B**, arrows). Note that both in the embryos and in the adult, we observed PKD2L1$^+$cells that were not distinctly GFP$^+$ (**Figures 2A,B**, double arrowhead). Notably, we never observed GFP$^+$ CSF-cNs that were not PKD2L1$^+$. Altogether we show evidence for PKD2L1$^+$ CSF-cNs that are GABAergic in the mouse spinal cord.

PKD2L1$^+$ GABAergic CSF-cNs SURROUND THE CENTRAL CANAL IN THE ADULT MACAQUE SPINAL CORD

We next asked whether PKD2L1 labels CSF-cNs in the spinal cord of primates (**Figure 3**). In transverse sections from cervical, thoracic and lumbar spinal cord, we observed the distribution of PKD2L1 immunofluorescence around the central canal in lamina X (**Figures 3A–C**). PKD2L1$^+$ cells were localized around the central canal and exhibited the typical morphology of spinal CSF-cNs with an apical extension toward the central canal ending with a bud in the lumen. PKD2L1 was enriched in the terminal bud of cerebrospinal fluid-contacting cells (**Figures 3A–C**) and faintly expressed (**Figures 3B,C**) or absent (**Figure 3G**) in the cell soma and in the rest of the apical extensions. PKD2L1$^+$CSF-cNs closely surrounded the central canal; they had a round nucleus and were located under (**Figures 3B–E**) or within the ependyma (**Figures 3F,G**). In order to test whether PKD2L1$^+$ CSF-cNs were GABAergic, we used IHC for the enzymes GAD65/67 and the VGAT transporter. Positive immunostaining for GAD65/67 and VGAT was found in cells surrounding the central canal at the level of their apical bulbous extension, soma and putative axon

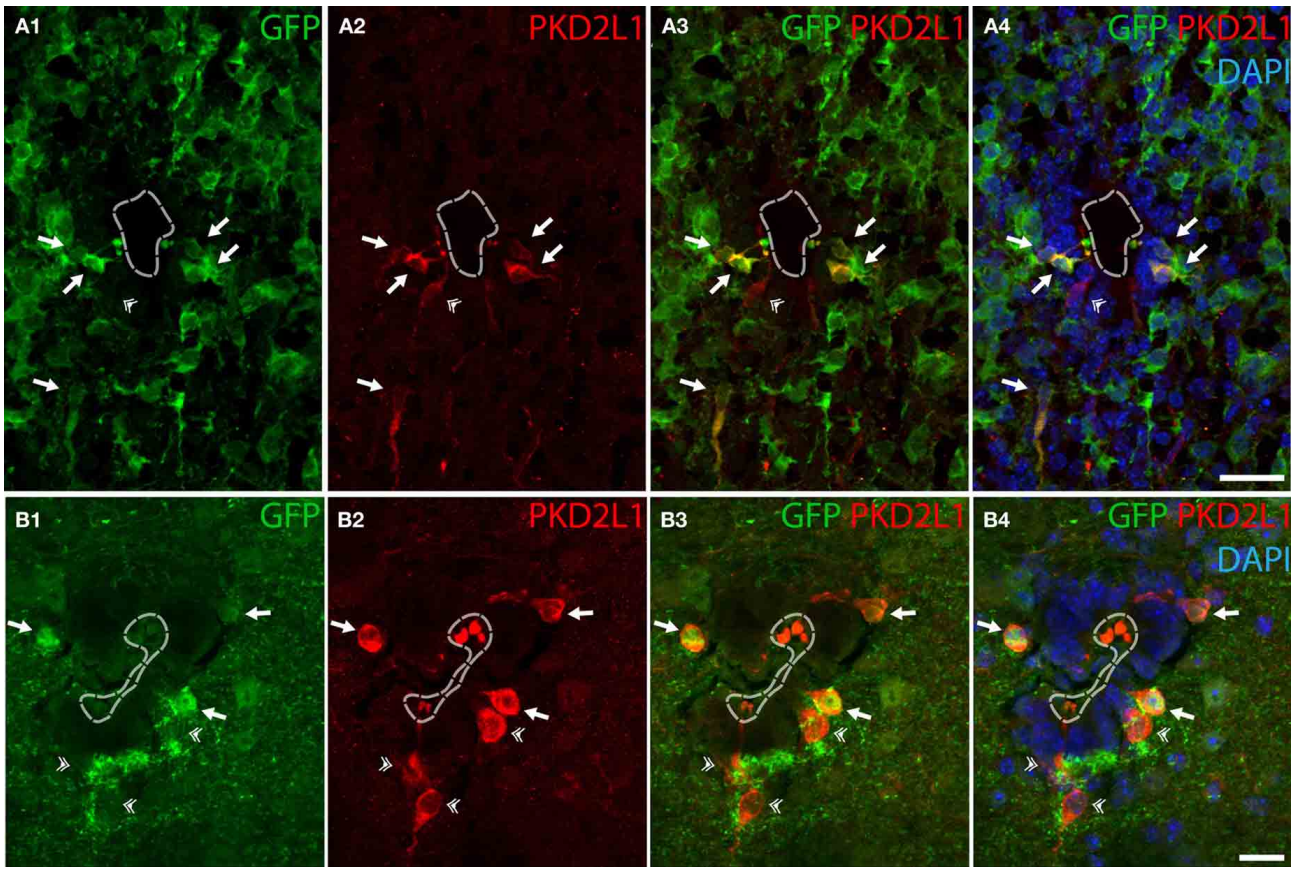

FIGURE 2 | Some PKD2L1$^+$ cells surrounding the central canal of cervical spinal cord of adult mouse are immunoreactive for GFP in the knock-in GAD67-GFP mouse. (A) 10 μm-thick coronal sections of GAD67-GFP E16.5 mouse spinal cord immunostained for GFP **(A1,A3,A4)** and PKD2L1 **(A2–A4)**. Most PKD2L1$^+$ cells are GFP$^+$ (arrows) but not all (double arrowheads). **(B)** 30 μm-thick coronal sections of a GAD67-GFP adult mouse spinal cord immunostained for GFP **(B1,B3,B4)** and PKD2L1 **(B2–B4)**. While many PKD2L1$^+$cells are distinctly GFP$^+$ (arrows), some cells are not (double arrowheads). Dorsal is up. White dashed line delineates the central canal. DAPI staining appears in blue. Scale bars = 25 μm **(A)**, 15 μm **(B)**.

(**Figures 3D–F**, arrowheads, arrows, and asterisks, respectively) but buds were labeled by GABAergic markers less frequently than they were by PKD2L1. Double immunofluorescence for PKD2L1 and VGAT showed evidence for CSF-cNs double-labeled at the level of the soma and the intraluminal bud (**Figure 3G**). Nonetheless VGAT could not be detected in all PKD2L1$^+$ buds (**Figure 3H**, double arrowheads). Cells double-labeled for PKD2L1 and VGAT were observed at the cervical, thoracic and lumbar level in the spinal cord. Taken together, our data show for the first time the presence of immunoreactive CSF-cNs containing PKD2L1 and GABAergic markers (GAD65/67 or VGAT) in the macaque lamina X. These findings demonstrate that a population of GABAergic CSF-cNs expressing PKD2L1 is present as well in the spinal cord of adult primates. Our results also support the idea that PKD2L1 is a specific marker of CSF-cNs in primates and labels more of these cells than GABAergic markers do in our experimental conditions.

THE EXPRESSION OF *pkd2l1* mRNA IN ZEBRAFISH EMBRYO ENABLES AN EXTENSIVE QUANTIFICATION AND LINEAGE ANALYSIS OF CSF-cNs

The developmental origin of CSF-cNs has not been established yet in mammals. To tackle the question of the developmental origin of *pkd2l1*$^+$ cells, we took advantage of the zebrafish embryo for its transparency and the rapidity of development of the spinal cord.

pkd2l1 is expressed in CSF-cNs in zebrafish

To assess whether *pkd2l1* was expressed in CSF-cNs in zebrafish, we performed ISH using the antisense probe for *pkd2l1* (**Figure 4**). We observed the expression of *pkd2l1* in CSF-cNs along the central canal in sagittal sections of the adult spinal cord (**Figure 4A**). *pkd2l1*$^+$ cells contacting the CSF were located ventrally and dorsally to the central canal (**Figures 4A1,A2**). In the zebrafish embryo, we investigated the 10-, 14-, 18-, 20-, and 30-somite stages ($n > 6$ embryos per condition). A weak signal in the rostral spinal cord (black arrow) could be detected at the 18-somite stage (**Figure 4B**). Gradually, the staining appeared rostro-caudally within the spinal cord (**Figures 4C,D**). Cells with dense labeling were located in two parallel rows along the ventral margin of the spinal cord (**Figures 4E,F**). Dorsal views of the spinal cord showed that these cells were located on either side of the midline (**Figure 4G**). At the larval stages, we observed that *pkd2l1*$^+$ CSF-cNs covered the entire length of the spinal cord and the organization in two parallel rows was not distinct anymore (data *not shown*). In zebrafish, CSF-cNs (named KAs) have

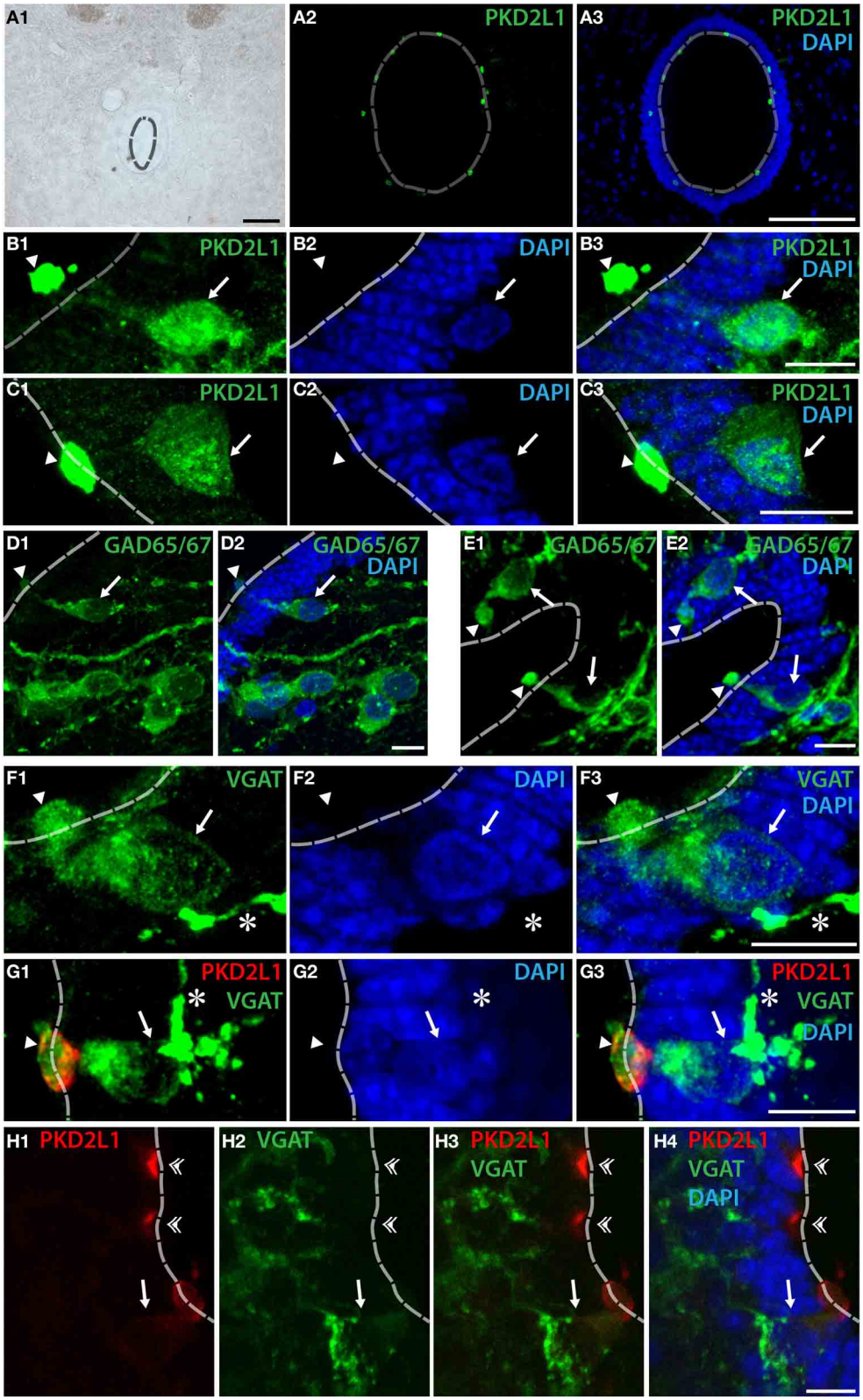

FIGURE 3 | PKD2L1^{+} CSF-cNs can be found as GABAergic neurons surrounding the central canal in the spinal cord of the adult macaque. **(A–C)** PKD2L1 immunostaining labels intraluminal buds **(A–C)** and rarely subependymal or ependymal cell bodies **(B,C). (D,E)** GAD65/67 immunoreactive cells are numerous in the vicinity of the central canal: proximal cells show a clear apical extension contacting the lumen while cells located away do not. **(F)** CSF-cNs surrounding the central canal are

(Continued)

FIGURE 3 | Continued
immunoreactive for the vesicular GABA transporter VGAT. **(G,H)** Double immunostaining for VGAT and PKD2L1 shows that some but not all PKD2L1$^+$ CSF-cNs are clearly GABAergic. The intraluminal buds can be found double-labeled for PKD2L1 and VGAT (arrowheads) but not systematically (double arrowheads), while apical extensions, cell body and putative axon are usually only labeled by VGAT. All panels are coronal sections of the macaque adult spinal cord taken at the lumbar level for **(A,G)**, at the cervical level for **(B–F)** and at the thoracic level for **(H)**. In all panels, arrows point to the somata, asterisks to the putative axons and arrowheads to the intraluminal buds of CSF-cNs. White dashed line delineates the central canal. DAPI staining appears in blue. Scale bars = 100 μm **(A)** and 10 μm **(B–H)**.

FIGURE 4 | *pkd2l1* is expressed from the embryonic 18-somite stage to adulthood in the zebrafish spinal cord. (A) Adult; **(B–G)** embryonic stages: 18-somite **(B)**, 20-somite **(C)** and 30-somite stages **(D–G)**. **(A)** In sagittal sections from the adult spinal cord, *pkd2l1*$^+$ CSF-contacting cells are located ventral and dorsal to the central canal. White dash line: central canal, dark gray line: ventral limit of the spinal cord. *pkd2l1* expression appears in the rostral spinal cord (**B,C**, arrows) and is distributed in two rows of cells along the rostro-caudal axis **(E,F)** and on each side of the midline **(G)**. **(E)** is a close-up of the black box from **(D)**. Rostral is to the left for all panels. Lateral views with dorsal up for **(A–F)** and dorsal view for **(G)**. DAPI staining appears in blue. Scale bars = 40 μm **(A)**, 100 μm for **(B–D)**, 50 μm for **(E–G)**.

been shown to derive from two progenitor domains, p3 and pMN (Park et al., 2004; Schafer et al., 2007; Shin et al., 2007; Yeo and Chitnis, 2007; Yang et al., 2010; England et al., 2011; Huang et al., 2012). KAs were therefore divided into two subpopulations on this basis, dorsal KA' and ventral KA" (Park et al., 2004). To identify the nature of *pkd2l1* expressing cells, we performed FISH in 30-somite stage zebrafish embryos (i.e., Prim-5 stage or 24 h post fertilization, **Figure 5**). This staining confirmed that expression of *pkd2l1* mRNA was localized in the ventral spinal cord and mainly distributed in two rows of cells along the rostro-caudal axis (**Figures 5A–C**). At higher magnification, we observed that these cells were lining the central canal either ventrally (arrowhead) or dorsally (arrow) (**Figures 5B–D**). Transverse sections confirmed that the somata of these cells directly surround the central canal (**Figure 5D**). While most *pkd2l1*$^+$ cells lined the central canal, we observed faint *pkd2l1* expressing cells away from the central canal in the dorsal spinal cord (**Figures 5C,D**, double arrowhead). We quantified the number of cells for each subpopulation based on lateral views originating from 13 embryos at the 30-somite stage (**Figure 5E**). *pkd2l1*$^+$ cells localized mainly in the rostral two thirds of the spinal cord in 30-somite stage zebrafish embryos with 3–4 cells per somite for both ventral KA" and dorsal KA' between somites 5 and 15. At this stage, cell density decreased from somite 16 to 21 after which expression ceased (**Figure 5E**). We quantified the total number of *pkd2l1*$^+$ cells for each subpopulation per embryo (**Figure 5F**). We found that *pkd2l1*$^+$ cells from the ventral row reached 45.4 ± 2.4 cells ($n = 13$ embryos), similar to counts performed previously on KA" at the same stage (Huang et al., 2012). These observations on cell body location and number suggest that the ventral *pkd2l1*$^+$ cells are KA" and dorsal ones are KA'.

All pkd2l1$^+$ *CSF-cNs are GABAergic in the zebrafish spinal cord*

To demonstrate that zebrafish *pkd2l1*$^+$ CSF-cNs are GABAergic, we investigated the expression of GABA and of GAD65/67 (**Figure 6**). An immunostaining for GABA at the 30-somite stage revealed multiple GABAergic cell types (Bernhardt et al., 1992; Higashijima et al., 2004a) including ventral and dorsal cells surrounding the central canal (**Figure 6A**, arrowhead and arrow, respectively). A short ascending axon originating from the soma of these cells can be observed (**Figure 6A**, asterisks). Based on morphology and location (see Materials and Methods), we estimated the number of GABAergic ventral (34.6 ± 2.3) and dorsal (49.9 ± 1.8) CSF-cNs per embryo ($n = 10$ embryos). We performed *pkd2l1* FISH followed by IHC for GAD65/67 to determine whether *pkd2l1*$^+$ CSF-cNs are also GABAergic. All *pkd2l1*$^+$ cells ($n = 160$) along the central canal were GAD65/67 immunoreactive (**Figure 6B**) (92 ventral *pkd2l1*$^+$ cells, 68 dorsal *pkd2l1*$^+$ cells). Based on their location, density and GABAergic phenotype, these *pkd2l1*$^+$ CSF-cNs correspond to KA" and KA'.

To test whether zebrafish CSF-cNs persist as GABAergic neurons until adulthood, we performed *pkd2l1* and *gad67* double FISH on whole adult spinal cord indicating that *pkd2l1*$^+$ CSF-cNs express *gad67* throughout development (**Figure 6C**). Contrary to what we observed in mouse and macaque, these results demonstrate that in zebrafish all *pkd2l1*$^+$ CSF-cNs are clearly GABAergic.

pkd2l1$^+$ *CSF-cNs originate from the p3 and pMN progenitor domains in zebrafish*

To confirm the developmental origins of *pkd2l1*$^+$ cells, we took advantage of the zebrafish model in which *pkd2l1* is expressed in the 30-somite stage embryo when progenitor domains are well-defined. Previous studies have shown that dorsal KA' cells are derived from the pMN domain and express the transcription factor *olig2* (Park et al., 2004). Ventral KA" cells originate from the p3 progenitor domain (Schafer et al., 2007) and express the transcription factor *nkx2.2a* (Yang et al., 2010; Huang et al., 2012). We therefore performed *pkd2l1* FISH combined with an anti-GFP immunostaining in the *Tg(nkx2.2a:mEGFP)* and the *Tg(olig2:EGFP)* transgenic lines (Shin et al., 2003; Ng et al., 2005) (**Figures 7**, **8**). In the *Tg(nkx2.2a:mEGFP)* transgenic embryos, the p3 domain was labeled by GFP staining as expected (**Figure 7A**). Ventral *pkd2l1*$^+$cells contacting the central canal were labeled for GFP while dorsal cells were not (**Figure 7B**). In the *Tg(olig2:EGFP)* transgenic embryos (**Figure 8**), the progenitor domain pMN was labeled by GFP (**Figure 8A**). In these animals, only dorsal *pkd2l1*$^+$ cells contacting the central canal were GFP$^+$ (**Figure 8B**). Transverse sections allowed to estimate the number of *pkd2l1*$^+$ cells contacting the central canal that were positive for GFP in the *Tg(nkx2.2a:mEGFP)* and in the *Tg(olig2:EGFP)* transgenic embryos (**Table 2**). While only ventral *pkd2l1*$^+$cells expressed GFP in the *Tg(nkx2.2a:mEGFP)* line (38 out of 38 cells), dorsal cells solely expressed GFP in the *Tg(olig2:EGFP)* line (93 out of 93 cells) (**Table 2**). Our data indicate that *pkd2l1*$^+$cells lining the central canal in zebrafish are KAs originating from p3 (for KA") and from pMN (for KA') depending on their dorso-ventral location relative to the central canal.

DISCUSSION

PKD2L1 APPEARS AS A SPECIFIC MARKER OF SPINAL CSF-cNs IN BONY VERTEBRATE SPECIES

PKD2L1$^+$ neurons projecting their apical bulbous dendritic extension into the central canal of the spinal cord had been described only in mouse at the P1–P4 stages (Huang et al., 2006) and in the adult (Orts-Del'Immagine et al., 2012, 2014). We hypothesized that the channel PKD2L1 could be a specific marker of spinal CSF-cNs shared among vertebrates. We demonstrate here that the TRP channel PKD2L1 is a marker of CSF-cNs in three vertebrate species: *Mus musculus*, *Macaca fascicularis*, and *Danio rerio*. For the first time, we show the expression of this channel in primate and zebrafish CSF-cNs. In the adult macaque spinal cord, CSF-cNs express PKD2L1 at the cervical, thoracic and lumbar levels. In the zebrafish embryo, *pkd2l1*$^+$ CSF-cNs originally differentiate in two rows along rostro-caudal gradient.

Taken together, our results demonstrate the shared expression of PKD2L1 in spinal CSF-cNs across bony vertebrate species. GABA has been previously reported to label some CSF-cNs (Barber et al., 1982; Dale et al., 1987a,b; Brodin et al., 1990; Christenson et al., 1991a,b; Bernhardt et al., 1992; Martin et al., 1998; Binor and Heathcote, 2001; Stoeckel et al., 2003; Robertson et al., 2007; Rodicio et al., 2008; Villar-Cervino et al., 2008; Reali et al., 2011). In mouse and macaque, PKD2L1 appeared always highly enriched in the intraluminal buds of CSF-cNs. On the contrary, GABAergic markers (GAD65/67, VGAT) rarely labeled in these species the soma or the apical bulbous extension of CSF-cNs. Notably we never observed CSF-cNs labeled by GABAergic markers and not by PKD2L1. In mammals, PKD2L1 seems therefore to label more CSF-contacting cells than GABAergic markers do. Nonetheless, with the approach we developed here, we cannot assess the existence of CSF-cNs that would not express PKD2L1.

EXPRESSION OF PKD2L1 IN CSF-cNs OF THE EMBRYONIC SPINAL CORD

In mouse and zebrafish, we detected the expression of the channel at early embryonic stages of development (E14.5 stage for the mouse and 18-somite stage for the zebrafish). In mouse, PKD2L1 expression could be found in few spinal cells contacting the central canal at E14.5 but became more evenly expressed from E16.5 to adulthood. This observation is consistent with a recent report showing that CSF-cNs emerged at E14 in the rat spinal cord (Kutna et al., 2013). It suggests that PKD2L1 expression may start soon after the cell differentiates into a CSF-cN.

We demonstrate here that within the spinal cord of the zebrafish embryo *pkd2l1* mRNA is enriched in CSF-cNs that are mainly arranged in two rows, one ventral and one dorsal to the central canal. Previous studies have shown that KA cells can be subdivided into two populations of CSF-cNs: the ventral KA" and the dorsal KA' (Park et al., 2004; Schafer et al., 2007; Shin et al., 2007; Yeo and Chitnis, 2007; Yang et al., 2010; England et al., 2011; Huang et al., 2012). We showed that *pkd2l1* can be detected in both KA" and KA'.

In the three species studied here, we observed PKD2L1$^+$ perikarya away from the central canal and for which we could not observe an apical bulbous extension reaching the lumen. In the zebrafish embryonic spinal cord, *pkd2l1* expression was weak in cells that were localized dorsally and away from the central canal. These cells were less than 8% (7.6% $\pm$ 2.3) of the *pkd2l1*$^+$ cells in our FISH experiments (**Figure 5**). Some of them expressed GFP in the *Tg(olig2:EGFP)* line (**Table 2**) suggesting that they could be either CSF-cNs originating from pMN, motoneurons or ventral longitudinal descending neurons (VeLDs) (Bernhardt et al., 1990; Park et al., 2004; Warp et al., 2012). A more extensive characterization would be necessary to identify the nature of these marginal dorsal cells. In cross sections of mouse, macaque and zebrafish spinal cords, those distant cells did not distinctly contact the central canal. However, as shown in rats (Lu et al., 2008), they could extend a long apical bulbous extension reaching the central canal that would be difficult to capture in thin sections.

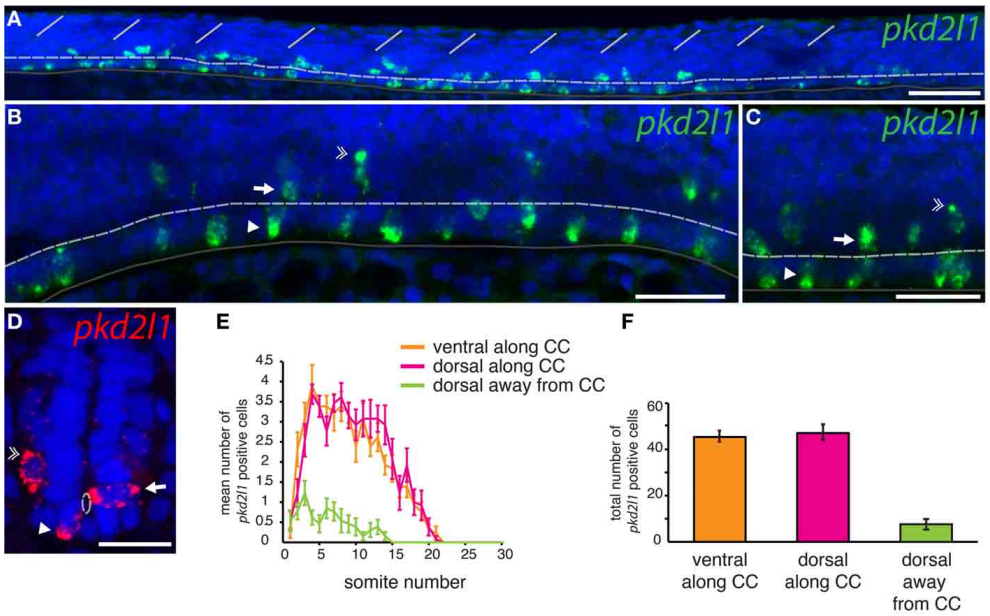

FIGURE 5 | *pkd2l1* is expressed in cells contacting the CSF and surrounding the central canal in the spinal cord of the zebrafish embryo. (A–D) FISH of *pkd2l1* mRNA at the 30-somite stage. Lateral views for **(A–C)** and transverse section for **(D)**. Two subpopulations of *pkd2l1* bright expressing cells surround the central canal ventrally (arrowhead) and dorsally (arrow). Note the existence of dorsal *pkd2l1* weak expressing cells away from the central canal (double arrowhead). The white dashed line, dark gray solid line and the solid white lines indicate respectively the central canal, the ventral limit of the spinal cord, and the somite boundaries. DAPI staining appears in blue. Scale bars = 50 μm for **(A)**, 30 μm for **(B,C)**, and 20 μm for **(D)**. **(E)** Mean number of *pkd2l1*$^+$ cells per somite along the rostro-caudal axis at the 30-somite stage. **(F)** Total cell counts per embryo ($n = 13$ embryos). We counted 45.4 ± 2.4 ventral *pkd2l1*$^+$ cells, 47.1 ± 3.4 dorsal *pkd2l1*$^+$ cells and 7.6 ± 2.3 dorsal away from the central canal *pkd2l1*$^+$ cells per embryo. **(E,F)** Mean values are given ± s.e.m.

ON THE DEVELOPMENTAL ORIGINS OF *pkd2l1* EXPRESSING CSF-cNs

At the embryonic stage, the neural tube is subdivided into molecularly defined neural progenitor domains generating distinct neuronal subtypes in vertebrates (Ericson et al., 1997; Briscoe et al., 1999; Jessell, 2000; Novitch et al., 2001; Goulding, 2009). In zebrafish, CSF-cNs referred to as KA cells derive from the two most ventral domains of the spinal cord; the ventral to the central canal p3 domain labeled by *nkx2.2a* and the more dorsal pMN marked by *olig2* (Park et al., 2004; Schafer et al., 2007; Shin et al., 2007; Yeo and Chitnis, 2007; Yang et al., 2010; England et al., 2011; Huang et al., 2012). By analyzing transverse sections of stable transgenic lines where GFP reports the expression of these transcription factors, we found that *pkd2l1*$^+$ CSF-cNs were derived from the *nkx2.2a* and from the *olig2* expression domains. This observation confirms the double developmental origin of CSF-cNs in zebrafish.

In the embryonic mouse spinal cord, the progenitor domains p3 and pMN form well-defined bands labeled by NKX2.2 and OLIG2, respectively, between E9.5 and E12.5 (Briscoe et al., 1999; Jessell, 2000; Novitch et al., 2001). At these stages, PKD2L1 is not yet expressed (*data not shown*). Therefore, by IHC for these transcription factors and PKD2L1, we could not test whether PKD2L1$^+$CSF-cNs originate as well from p3 and pMN (*data not shown*). To reveal the developmental origin of these cells in mouse, lineage tracing based on the use of inducible transgenic lines for p3 and pMN markers will be necessary. Previous results relying on a tamoxifen-inducible Cre-recombinase inserted into the Olig2 locus indicate that a subpopulation of cells originating from pMN between E9.5 and E14.5 are located at the ependymal border circling the central canal (Srinivas et al., 2001; Masahira et al., 2006). This observation suggests that some CSF-cNs could originate from pMN in mouse, although a thorough investigation would be necessary to address this question in this model organism.

GABAergic CSF-cNs EXPRESS PKD2L1 IN THE SPINAL CORD

GABAergic CSF-cNs have been described in the spinal cord of various vertebrate species (Barber et al., 1982; Dale et al., 1987a,b; Brodin et al., 1990; Christenson et al., 1991a,b; Bernhardt et al., 1992; Martin et al., 1998; Binor and Heathcote, 2001; Stoeckel et al., 2003; Robertson et al., 2007; Rodicio et al., 2008; Villar-Cervino et al., 2008; Reali et al., 2011). Here we used different GABAergic markers, GABA itself, the synthesis enzyme GAD or the GABA transporter VGAT, to test whether PKD2L1$^+$ CSF-cNs were GABAergic. In zebrafish, we demonstrate that all *pkd2l1*$^+$ cells are GABAergic in spinal CSF-cNs. In mouse and macaque, we could not demonstrate a complete co-localization of PKD2L1 with GABAergic markers (GAD67-GFP or VGAT) in CSF-cNs. In macaque, a minority of PKD2L1$^+$ intraluminal buds was clearly double-labeled with VGAT. In mouse, the observation of GABAergic PKD2L1$^+$ CSF-cNs was confirmed in the GAD67-GFP transgenic line by the co-expression of PKD2L1 and GFP in only some cells. The lack of systematic colocalization between PKD2L1 and GABAergic markers in CSF-cNs could be due to

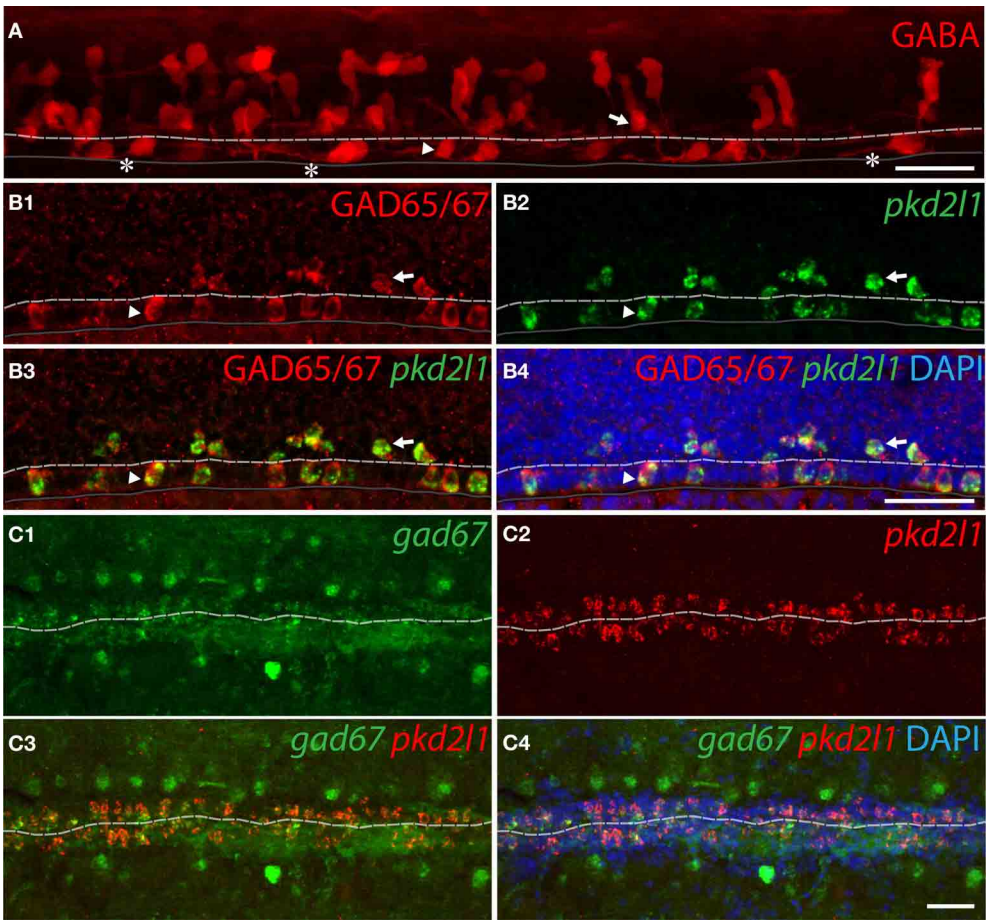

FIGURE 6 | *pkd2l1*$^+$ CSF-cNs are GABAergic neurons expressing GABA and GAD in zebrafish. (A) GABA IHC on WT 30-somite embryos shows ventral (arrowhead) and dorsal (arrow) KAs and their ascending axon (asterisks). **(B1–B4)** Ventral and dorsal *pkd2l1*$^+$KAs are GAD65/67 immunoreactive in 30-somite embryos as shown by FISH for *pkd2l1* (green) coupled to a GAD65/67 IHC (red). **(C1–C4)** In the adult, *pkd2l1*$^+$ KAs are *gad67*$^+$ as shown by FISH for *gad67* **(C1,C3,C4)** and *pkd2l1* **(C2–C4)** on sections of WT spinal cord. The white dash line indicates the central canal, the dark line the ventral limit of the spinal cord. **(A)** is a projection from the lateral view of a whole-mount embryo immunostained for GABA while **(B1–B4)** correspond to sagittal sections and **(C1–C4)** to frontal sections. DAPI staining appears in blue. Scale bars = 30 μm.

the expression of other isoforms of GAD (such as GAD65) or to other neurotransmitters expressed in PKD2L1$^+$ CSF-cNs. Although we could not demonstrate that GABA is expressed in all CSF-cNs in mammals, our results show evidence for GABAergic PKD2L1$^+$ CSF-cNs in the spinal cord of the three species studied here.

Previous studies characterized a diversity of markers potentially expressed in CSF-cNs in multiple species. Peptides such as the vasoactive intestinal polypeptide (VIP), somatostatin or urotensin II-related peptide (URP2) have been found in CSF-cNs (Buchanan et al., 1987; Yulis and Lederis, 1988a,b; Christenson et al., 1991a; Lamotte and Shapiro, 1991; Lopez et al., 2007; Wyart et al., 2009; Parmentier et al., 2011; Jalalvand et al., 2014). Ventral CSF-cNs were found dopaminergic in tetrapods such as birds (Acerbo et al., 2003) and amphibians (Gonzalez and Smeets, 1991, 1993; Gonzalez et al., 1993), as well as in some teleosts such as the eel and the trout (Roberts et al., 1995), in dogfish (Sueiro et al., 2004) and lampreys (Schotland et al., 1996; Rodicio et al., 2008). It would be interesting to determine in these species whether the dopaminergic and non-dopaminergic CSF-cNs derive as well from two different progenitor domains. However, the dopaminergic phenotype does not seem to be conserved in all vertebrate species as shown in some teleosts and in mammals (Nagatsu et al., 1988; McLean and Fetcho, 2004).

Other markers such as the subunit $P2X_2$ of the purinergic receptor have been found in adult CSF-cNs together with early neuronal markers such as the polysialylated neural cell adhesion molecule (PSA-NCAM) in rats (Stoeckel et al., 2003) and HuC in turtles (Reali et al., 2011) and dogfish (Sueiro et al., 2004).

All markers listed above are not highly specific for CSF-cNs. However, in the three species studies here, PKD2L1 appears as a specific marker of CSF-cNs that is highly expressed and broadly targets CSF-cNs within the spinal cord. Despite existing variations in expression of peptides, neuromodulators and receptors, our results in zebrafish, mouse and macaque suggest the existence of a conserved system of spinal CSF-cNs defined by their morphology, their location—ependymally or subependymally—and their enriched expression of PKD2L1.

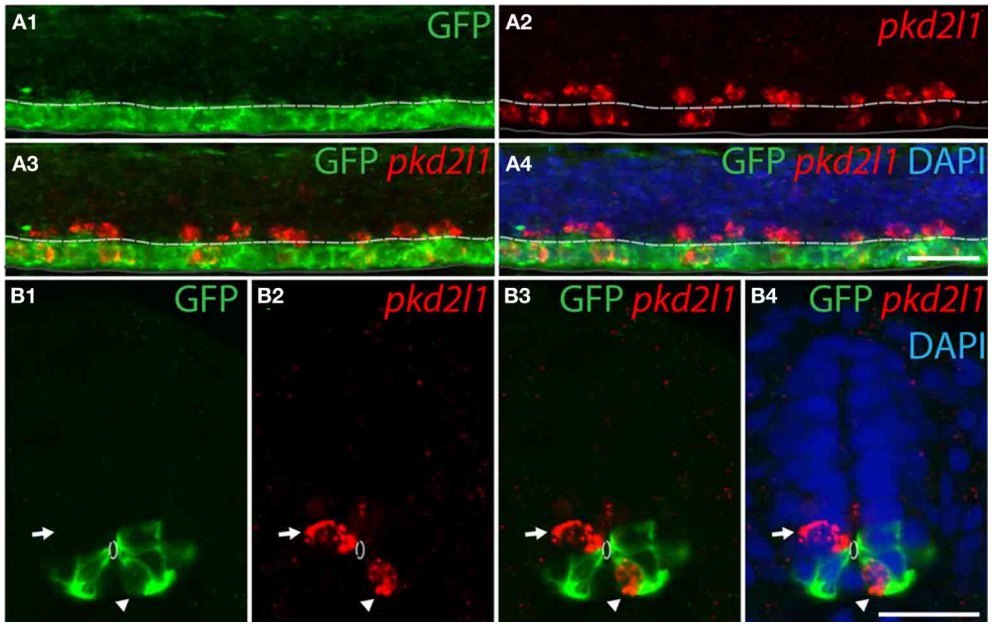

FIGURE 7 | Ventral *pkd2l1*$^+$ cells express *nkx2.2a* and derive from the p3 progenitor domain in the zebrafish embryo. (A,B) *pkd2l1* FISH in *Tg(nkx2.2a: mEGFP)* embryos immunostained for GFP at the 30-somite stage. IHC for GFP reveals the p3 domain. **(A)** Lateral view showing that the most ventral *pkd2l1*$^+$ cells are GFP$^+$. **(B)** A typical transverse section shows a ventral *pkd2l1*$^+$ cell contacting the central canal and expressing GFP (arrowhead) while a dorsal *pkd2l1*$^+$ cell contacting the central canal does not express GFP (arrow) in the *Tg(nkx2.2a: mEGFP)* transgenic embryo. White dashed line delineates the central canal, dark line the ventral limit of the spinal cord. DAPI staining appears in blue. Scale bars = 20 μm.

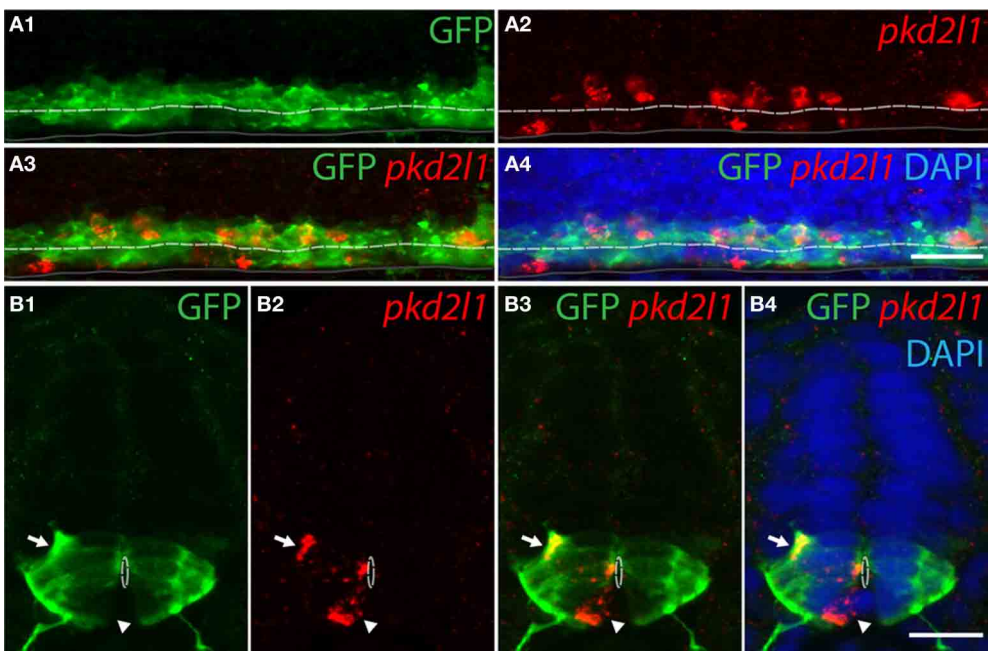

FIGURE 8 | Dorsal *pkd2l1*$^+$ CSF-cNs express *olig2* and derive from the pMN progenitor domain in the embryonic spinal cord of zebrafish. (A,B) *pkd2l1* FISH in *Tg(olig2:EGFP)* embryos immunostained for GFP at the 30-somite stage. IHC for GFP reveals the pMN domain. **(A)** Lateral view showing dorsal *pkd2l1*$^+$ cells express GFP. **(B)** Transverse sections showing dorsal *pkd2l1*$^+$ cells contacting the central canal express GFP (arrow) while a ventral *pkd2l1*$^+$ cell contacting the central canal (arrowhead) does not express GFP in the *Tg(olig2:EGFP)* transgenic line. White dashed line delineates the central canal, dark line the ventral limit of the spinal cord. DAPI staining appears in blue. Scale bars = 20 μm.

Table 2 | Distribution of ventral and dorsal *pkd2l1*$^+$ cells expressing GFP in *Tg(nkx2.2a:mEGFP)* and *Tg(olig2:EGFP)* zebrafish transgenic lines at the 30-somite stage.

	Number of cells	%
COLOCALIZATION OF GFP AND *pkd2l1* IN *Tg(nkx2.2a:mEGFP)*		
Total number of *pkd2l1*$^+$ counted cells	76	
Ventral to CC *pkd2l1*$^+$ GFP$^+$/ventral to the CC *pkd2l1*$^+$	38/38	100
Dorsal to CC *pkd2l1*$^+$ GFP$^+$/dorsal to the CC *pkd2l1*$^+$	0/32	0
Dorsal and away from the CC *pkd2l1*$^+$ GFP$^+$/ dorsal and away from the CC *pkd2l1*$^+$	0/6	0
COLOCALIZATION OF GFP AND *pkd2l1* IN *Tg(olig2:EGFP)*		
Total number of *pkd2l1*$^+$ counted cells	149	
Ventral to CC *pkd2l1*$^+$ GFP$^+$/ ventral to the CC *pkd2l1*$^+$	0/52	0
Dorsal to CC *pkd2l1*$^+$ GFP$^+$/ dorsal to the CC *pkd2l1*$^+$	93/93	100
Dorsal and away from the CC *pkd2l1*$^+$ GFP$^+$/ dorsal and away from the CC *pkd2l1*$^+$	2/4	50

All ventral pkd2l1$^+$ *cells are GFP*$^+$ *in Tg(nkx2.2a:mEGFP) but none of the dorsal ones. Reciprocally all the dorsal pkd2l1*$^+$ *cells are GFP*$^+$ *in the Tg(olig2:EGFP) but none of the ventral ones.*

PKD2L1 has been involved in multiple functions from sour taste (Huang et al., 2006; Ishimaru et al., 2006; Inada et al., 2008; Ishii et al., 2009; Shimizu et al., 2009; Chang et al., 2010; Shimizu et al., 2011; Horio et al., 2011) to primary cilium signaling (Decaen et al., 2013; Delling et al., 2013). The peculiar location of CSF-cNs in contact with the CSF strongly suggests a role for PKD2L1 as a sensor of CSF composition, pH and/or osmolarity (Huang et al., 2006; Orts-Del'Immagine et al., 2012) since the channel is activated upon acidification (Ishimaru et al., 2006; Inada et al., 2008; Orts-Del'Immagine et al., 2012), alkalinization (Shimizu et al., 2011; Orts-Del'Immagine et al., 2012) or hypo-osmotic variations (Shimizu et al., 2009; Orts-Del'Immagine et al., 2012).

The role(s) of CSF-cNs in the vertebrate spinal cord is (are) poorly understood. They could be proprioceptors sensitive to the CSF composition (Huang et al., 2006; Orts-Del'Immagine et al., 2012) and modulating locomotion (Wyart et al., 2009), or enabling the differentiation of progenitors in the ependymal neurogenic niche via GABA release (Reali et al., 2011). The investigation of PKD2L1 functions in CSF-cNs across multiple species should reveal whether its physiological role in the spinal cord is conserved in vertebrates.

AUTHOR CONTRIBUTIONS

Lydia Djenoune and Claire Wyart conceived, designed, and supervised all experiments. Lydia Djenoune performed the experiments on zebrafish embryos helped by Céline Burcklé at the early stages of the project. Hanen Khabou performed all experiments on the macaque spinal cord. Fanny Joubert and Laurence Bodineau performed experiments on the mouse spinal cord. Feng B. Quan performed FISH experiments on the zebrafish adult spinal cord. Sophie Nunes Figueiredo performed GABA immunohistochemistry on zebrafish embryos. Filippo Del Bene designed the *pkd2l1 in situ* probe. Lydia Djenoune analyzed the data under supervision of Claire Wyart and Hervé Tostivint. Lydia Djenoune and Claire Wyart wrote the manuscript. All authors discussed the results and implications and commented on the manuscript.

ACKNOWLEDGMENTS

We thank Prof. Bruce Appel, University of Colorado in Denver, USA for sharing the *Tg(nkx2.2a:mEGFP)* and *Tg(olig2:EGFP)* fish transgenic lines and Prof. Yuchio Yanagawa, Gunma University Graduate School of Medicine in Maebashi, Japan for sharing the GAD67-GFP knock-in mice used in this study. We thank Dr. Uwe Strähle, Karlsruhe Institute of Technology, Germany for sharing the *gad67* plasmid. We thank Jean Simonnet, Dr. Desdemona Fricker, and Dr. Richard Miles for help with the GAD67-GFP knock-in mouse. We thank Dr. Vanessa Ribes for helpful advices regarding experiments on the embryonic mouse spinal cord. We thank Dr. Carlos Parras, Sowmya Sekizar, Dr. Mariana Graciarena, Melissa Fauveau, and Dr. Brahim Nait-Oumesmar who gave valuable insights for IHC in the mouse embryonic spinal cord. We thank Dr. Pierre Pouget and Prof. Marie Vidailhet for providing access to the tissue of adult macaque spinal cord and Virgile Brochard and Dominique Tandé for precious advices. We thank Prof. Herwig Baier, Max Planck Institute of Neurobiology in Martinsried, Germany, the team of the "Plateforme d'Imagerie Cellulaire Pitié Salpêtrière" and Prof. Thomas Similowski for their support. We thank Urs Lucas Böhm, Kevin Fidelin, Jenna Sternberg, Dr. Pierre-Luc Bardet, Dr. Andrew E. Prendergast, Dr. Jean Paul Rio, and Dr. Kristen Severi for critical reading of the manuscript. This work received financial support from the Institut du Cerveau et de la Moelle épinière (ICM with the French program "Investissements d'avenir" ANR-10-IAIHU-06), the network Ecole des Neurosciences de Paris (ENP), the Fondation Bettencourt Schueller (FBS), Mr Pierre Belle, the City of Paris Emergence program, the Atip/Avenir junior program from Institut National de la Santé et de la Recherche Médicale and Centre National de la Recherche Scientifique, the Fyssen foundation, the International Reintegration Grant from Marie Curie Actions Framework Program 6, and the European Research Council (ERC) starter grant "OptoLoco."

REFERENCES

Acerbo, M. J., Hellmann, B., and Gunturkun, O. (2003). Catecholaminergic and dopamine-containing neurons in the spinal cord of pigeons: an immunohistochemical study. *J. Chem. Neuroanat.* 25, 19–27. doi: 10.1016/S0891-0618(02)00072-8

Agduhr, E. (1922). Über ein Zentrales Sinnesorgan (?) bei den Vertebraten. *Z. Anat. Entwicklungs.* 66, 223–360. doi: 10.1007/BF02593586

Alunni, A., Krecsmarik, M., Bosco, A., Galant, S., Pan, L., Moens, C. B., et al. (2013). Notch3 signaling gates cell cycle entry and limits neural stem cell amplification in the adult pallium. *Development* 140, 3335–3347. doi: 10.1242/dev.095018

Barber, R. P., Vaughn, J. E., and Roberts, E. (1982). The cytoarchitecture of GABAergic neurons in rat spinal cord. *Brain Res.* 238, 305–328. doi: 10.1016/0006-8993(82)90107-X

Basora, N., Nomura, H., Berger, U. V., Stayner, C., Guo, L., Shen, X., et al. (2002). Tissue and cellular localization of a novel polycystic kidney disease-like gene product, polycystin-L. *J. Am. Soc. Nephrol.* 13, 293–301.

Bernhardt, R. R., Chitnis, A. B., Lindamer, L., and Kuwada, J. Y. (1990). Identification of spinal neurons in the embryonic and larval zebrafish. *J. Comp. Neurol.* 302, 603–616. doi: 10.1002/cne.903020315

Bernhardt, R. R., Patel, C. K., Wilson, S. W., and Kuwada, J. Y. (1992). Axonal trajectories and distribution of GABAergic spinal neurons in wildtype and mutant zebrafish lacking floor plate cells. *J. Comp. Neurol.* 326, 263–272. doi: 10.1002/cne.903260208

Binor, E., and Heathcote, R. D. (2001). Development of GABA-immunoreactive neuron patterning in the spinal cord. *J. Comp. Neurol.* 438, 1–11. doi: 10.1002/cne.1298

Briscoe, J., Sussel, L., Serup, P., Hartigan-O'Connor, D., Jessell, T. M., Rubenstein, J. L., et al. (1999). Homeobox gene Nkx2.2 and specification of neuronal identity by graded Sonic hedgehog signalling. *Nature* 398, 622–627. doi: 10.1038/19315

Brodin, L., Dale, N., Christenson, J., Storm-Mathisen, J., Hokfelt, T., and Grillner, S. (1990). Three types of GABA-immunoreactive cells in the lamprey spinal cord. *Brain Res.* 508, 172–175. doi: 10.1016/0006-8993(90)91134-3

Buchanan, J. T., Brodin, L., Hokfelt, T., Van Dongen, P. A., and Grillner, S. (1987). Survey of neuropeptide-like immunoreactivity in the lamprey spinal cord. *Brain Res.* 408, 299–302. doi: 10.1016/0006-8993(87)90392-1

Chang, R. B., Waters, H., and Liman, E. R. (2010). A proton current drives action potentials in genetically identified sour taste cells. *Proc. Natl. Acad. Sci. U.S.A.* 107, 22320–22325. doi: 10.1073/pnas.1013664107

Christenson, J., Alford, S., Grillner, S., and Hokfelt, T. (1991a). Co-localized GABA and somatostatin use different ionic mechanisms to hyperpolarize target neurons in the lamprey spinal cord. *Neurosci. Lett.* 134, 93–97. doi: 10.1016/0304-3940(91)90516-V

Christenson, J., Bongianni, F., Grillner, S., and Hokfelt, T. (1991b). Putative GABAergic input to axons of spinal interneurons and primary sensory neurons in the lamprey spinal cord as shown by intracellular Lucifer yellow and GABA immunohistochemistry. *Brain Res.* 538, 313–318. doi: 10.1016/0006-8993(91)90446-3

Dale, N., Roberts, A., Ottersen, O. P., and Storm-Mathisen, J. (1987a). The development of a population of spinal cord neurons and their axonal projections revealed by GABA immunocytochemistry in frog embryos. *Proc. R. Soc. Lond. B Biol. Sci.* 232, 205–215. doi: 10.1098/rspb.1987.0069

Dale, N., Roberts, A., Ottersen, O. P., and Storm-Mathisen, J. (1987b). The morphology and distribution of 'Kolmer-Agduhr cells,' a class of cerebrospinal-fluid-contacting neurons revealed in the frog embryo spinal cord by GABA immunocytochemistry. *Proc. R. Soc. Lond. B Biol. Sci.* 232, 193–203. doi: 10.1098/rspb.1987.0068

Decaen, P. G., Delling, M., Vien, T. N., and Clapham, D. E. (2013). Direct recording and molecular identification of the calcium channel of primary cilia. *Nature* 504, 315–318. doi: 10.1038/nature12832

Delling, M., Decaen, P. G., Doerner, J. F., Febvay, S., and Clapham, D. E. (2013). Primary cilia are specialized calcium signalling organelles. *Nature* 504, 311–314. doi: 10.1038/nature12833

Delmas, P. (2004). Polycystins: from mechanosensation to gene regulation. *Cell* 118, 145–148. doi: 10.1016/j.cell.2004.07.007

Delmas, P., Padilla, F., Osorio, N., Coste, B., Raoux, M., and Crest, M. (2004). Polycystins, calcium signaling, and human diseases. *Biochem. Biophys. Res. Commun.* 322, 1374–1383. doi: 10.1016/j.bbrc.2004.08.044

England, S., Batista, M. F., Mich, J. K., Chen, J. K., and Lewis, K. E. (2011). Roles of Hedgehog pathway components and retinoic acid signalling in specifying zebrafish ventral spinal cord neurons. *Development* 138, 5121–5134. doi: 10.1242/dev.066159

Ericson, J., Rashbass, P., Schedl, A., Brenner-Morton, S., Kawakami, A., Van Heyningen, V., et al. (1997). Pax6 controls progenitor cell identity and neuronal fate in response to graded Shh signaling. *Cell* 90, 169–180. doi: 10.1016/S0092-8674(00)80323-2

Gonzalez, A., and Smeets, W. J. (1991). Comparative analysis of dopamine and tyrosine hydroxylase immunoreactivities in the brain of two amphibians, the anuran *Rana ridibunda* and the urodele *Pleurodeles waltlii*. *J. Comp. Neurol.* 303, 457–477. doi: 10.1002/cne.903030311

Gonzalez, A., and Smeets, W. J. (1993). Noradrenaline in the brain of the South African clawed frog *Xenopus laevis*: a study with antibodies against noradrenaline and dopamine-beta-hydroxylase. *J. Comp. Neurol.* 331, 363–374. doi: 10.1002/cne.903310306

Gonzalez, A., Tuinhof, R., and Smeets, W. J. (1993). Distribution of tyrosine hydroxylase and dopamine immunoreactivities in the brain of the South African clawed frog *Xenopus laevis*. *Anat. Embryol.* 187, 193–201. doi: 10.1007/BF00171750

Goulding, M. (2009). Circuits controlling vertebrate locomotion: moving in a new direction. *Nat. Rev. Neurosci.* 10, 507–518. doi: 10.1038/nrn2608

Higashijima, S., Mandel, G., and Fetcho, J. R. (2004a). Distribution of prospective glutamatergic, glycinergic, and GABAergic neurons in embryonic and larval zebrafish. *J. Comp. Neurol.* 480, 1–18. doi: 10.1002/cne.20278

Higashijima, S., Schaefer, M., and Fetcho, J. R. (2004b). Neurotransmitter properties of spinal interneurons in embryonic and larval zebrafish. *J. Comp. Neurol.* 480, 19–37. doi: 10.1002/cne.20279

Horio, N., Yoshida, R., Yasumatsu, K., Yanagawa, Y., Ishimaru, Y., Matsunami, H., et al. (2011). Sour taste responses in mice lacking PKD channels. *PLoS ONE* 6:e20007. doi: 10.1371/journal.pone.0020007

Huang, A. L., Chen, X., Hoon, M. A., Chandrashekar, J., Guo, W., Trankner, D., et al. (2006). The cells and logic for mammalian sour taste detection. *Nature* 442, 934–938. doi: 10.1038/nature05084

Huang, P., Xiong, F., Megason, S. G., and Schier, A. F. (2012). Attenuation of Notch and Hedgehog signaling is required for fate specification in the spinal cord. *PLoS Genet.* 8:e1002762. doi: 10.1371/journal.pgen.1002762

Inada, H., Kawabata, F., Ishimaru, Y., Fushiki, T., Matsunami, H., and Tominaga, M. (2008). Off-response property of an acid-activated cation channel complex PKD1L3-PKD2L1. *EMBO Rep.* 9, 690–697. doi: 10.1038/embor.2008.89

Ishii, S., Misaka, T., Kishi, M., Kaga, T., Ishimaru, Y., and Abe, K. (2009). Acetic acid activates PKD1L3-PKD2L1 channel–a candidate sour taste receptor. *Biochem. Biophys. Res. Commun.* 385, 346–350. doi: 10.1016/j.bbrc.2009.05.069

Ishimaru, Y., Inada, H., Kubota, M., Zhuang, H., Tominaga, M., and Matsunami, H. (2006). Transient receptor potential family members PKD1L3 and PKD2L1 form a candidate sour taste receptor. *Proc. Natl. Acad. Sci. U.S.A.* 103, 12569–12574. doi: 10.1073/pnas.0602702103

Jalalvand, E., Robertson, B., Wallen, P., Hill, R. H., and Grillner, S. (2014). Laterally projecting cerebrospinal fluid-contacting cells in the lamprey spinal cord are of two distinct types. *J. Comp. Neurol.* 522, 1753–1768. doi: 10.1002/cne.23542

Jessell, T. M. (2000). Neuronal specification in the spinal cord: inductive signals and transcriptional codes. *Nat. Rev. Genet.* 1, 20–29. doi: 10.1038/35049541

Kimmel, C. B., Ballard, W. W., Kimmel, S. R., Ullmann, B., and Schilling, T. F. (1995). Stages of embryonic development of the zebrafish. *Dev. Dyn.* 203, 253–310. doi: 10.1002/aja.1002030302

Kirby, B. B., Takada, N., Latimer, A. J., Shin, J., Carney, T. J., Kelsh, R. N., et al. (2006). *In vivo* time-lapse imaging shows dynamic oligodendrocyte progenitor behavior during zebrafish development. *Nat. Neurosci.* 9, 1506–1511. doi: 10.1038/nn1803

Kolmer, W. (1921). Das "Sagittalorgan" der Wirbeltiere. *Z. Anat. Entwicklungs.* 60, 652–717. doi: 10.1007/BF02593657

Kolmer, W. (1931). Über das Sagittalorgan, ein Zentrales Sinnesorgan der Wirbeltiere, Insbesondere Beim Affen. *Z. Zellforsch. Mik. Ana.* 13, 236–248. doi: 10.1007/BF00406356

Kutna, V., Sevc, J., Gombalova, Z., Matiasova, A., and Daxnerova, Z. (2013). Enigmatic cerebrospinal fluid-contacting neurons arise even after the termination of neurogenesis in the rat spinal cord during embryonic development and retain their immature-like characteristics until adulthood. *Acta Histochem.* 116, 278–285. doi: 10.1016/j.acthis.2013.08.004

Lamotte, C. C., and Shapiro, C. M. (1991). Ultrastructural localization of substance P, met-enkephalin, and somatostatin immunoreactivity in lamina X of the primate spinal cord. *J. Comp. Neurol.* 306, 290–306. doi: 10.1002/cne.903060206

Lopez, J. M., Moreno, N., Morona, R., Munoz, M., Dominguez, L., and Gonzalez, A. (2007). Distribution of somatostatin-like immunoreactivity in the brain of the caecilian *Dermophis mexicanus* (Amphibia: Gymnophiona): comparative aspects in amphibians. *J. Comp. Neurol.* 501, 413–430. doi: 10.1002/cne.21244

Lu, X., Geng, X., Zhang, L., and Zeng, Y. (2008). The methodology for labeling the distal cerebrospinal fluid-contacting neurons in rats. *J. Neurosci. Methods* 168, 98–103. doi: 10.1016/j.jneumeth.2007.09.033

Martin, S. C., Heinrich, G., and Sandell, J. H. (1998). Sequence and expression of glutamic acid decarboxylase isoforms in the developing zebrafish. *J. Comp. Neurol.* 396, 253–266. doi: 10.1002/(SICI)1096-9861(19980629)396:2<253::AID-CNE9>3.0.CO;2-#

Masahira, N., Takebayashi, H., Ono, K., Watanabe, K., Ding, L., Furusho, M., et al. (2006). Olig2-positive progenitors in the embryonic spinal cord give rise not only to motoneurons and oligodendrocytes, but also to a subset of astrocytes and ependymal cells. *Dev. Biol.* 293, 358–369. doi: 10.1016/j.ydbio.2006.02.029

McLean, D. L., and Fetcho, J. R. (2004). Ontogeny and innervation patterns of dopaminergic, noradrenergic, and serotonergic neurons in larval zebrafish. *J. Comp. Neurol.* 480, 38–56. doi: 10.1002/cne.20280

Melendez-Ferro, M., Perez-Costas, E., Villar-Cheda, B., Rodriguez-Munoz, R., Anadon, R., and Rodicio, M. C. (2003). Ontogeny of gamma-aminobutyric acid-immunoreactive neurons in the rhombencephalon and spinal cord of the sea lamprey. *J. Comp. Neurol.* 464, 17–35. doi: 10.1002/cne.10773

Nagatsu, I., Sakai, M., Yoshida, M., and Nagatsu, T. (1988). Aromatic L-amino acid decarboxylase-immunoreactive neurons in and around the cerebrospinal fluid-contacting neurons of the central canal do not contain dopamine or serotonin in the mouse and rat spinal cord. *Brain Res.* 475, 91–102. doi: 10.1016/0006-8993(88)90202-8

Ng, A. N., De Jong-Curtain, T. A., Mawdsley, D. J., White, S. J., Shin, J., Appel, B., et al. (2005). Formation of the digestive system in zebrafish: III. Intestinal epithelium morphogenesis. *Dev. Biol.* 286, 114–135. doi: 10.1016/j.ydbio.2005.07.013

Novitch, B. G., Chen, A. I., and Jessell, T. M. (2001). Coordinate regulation of motor neuron subtype identity and pan-neuronal properties by the bHLH repressor Olig2. *Neuron* 31, 773–789. doi: 10.1016/S0896-6273(01)00407-X

Orts-Del'Immagine, A., Kastner, A., Tillement, V., Tardivel, C., Trouslard, J., and Wanaverbecq, N. (2014). Morphology, distribution and phenotype of polycystin kidney disease 2-like 1-positive cerebrospinal fluid contacting neurons in the brainstem of adult mice. *PLoS ONE* 9:e87748. doi: 10.1371/journal.pone.0087748

Orts-Del'Immagine, A., Wanaverbecq, N., Tardivel, C., Tillement, V., Dallaporta, M., and Trouslard, J. (2012). Properties of subependymal cerebrospinal fluid contacting neurones in the dorsal vagal complex of the mouse brainstem. *J. Physiol.* 590, 3719–3741. doi: 10.1113/jphysiol.2012.227959

Park, H. C., Shin, J., and Appel, B. (2004). Spatial and temporal regulation of ventral spinal cord precursor specification by Hedgehog signaling. *Development* 131, 5959–5969. doi: 10.1242/dev.01456

Parmentier, C., Hameury, E., Dubessy, C., Quan, F. B., Habert, D., Calas, A., et al. (2011). Occurrence of two distinct urotensin II-related peptides in zebrafish provides new insight into the evolutionary history of the urotensin II gene family. *Endocrinology* 152, 2330–2341. doi: 10.1210/en.2010-1500

Reali, C., Fernandez, A., Radmilovich, M., Trujillo-Cenoz, O., and Russo, R. E. (2011). GABAergic signalling in a neurogenic niche of the turtle spinal cord. *J. Physiol.* 589, 5633–5647. doi: 10.1113/jphysiol.2011.214312

Roberts, B. L., Maslam, S., Scholten, G., and Smit, W. (1995). Dopaminergic and GABAergic cerebrospinal fluid-contacting neurons along the central canal of the spinal cord of the eel and trout. *J. Comp. Neurol.* 354, 423–437. doi: 10.1002/cne.903540310

Robertson, B., Auclair, F., Menard, A., Grillner, S., and Dubuc, R. (2007). GABA distribution in lamprey is phylogenetically conserved. *J. Comp. Neurol.* 503, 47–63. doi: 10.1002/cne.21348

Rodicio, M. C., Villar-Cervino, V., Barreiro-Iglesias, A., and Anadon, R. (2008). Colocalization of dopamine and GABA in spinal cord neurones in the sea lamprey. *Brain Res. Bull.* 76, 45–49. doi: 10.1016/j.brainresbull.2007.10.062

Schafer, M., Kinzel, D., and Winkler, C. (2007). Discontinuous organization and specification of the lateral floor plate in zebrafish. *Dev. Biol.* 301, 117–129. doi: 10.1016/j.ydbio.2006.09.018

Schindelin, J., Arganda-Carreras, I., Frise, E., Kaynig, V., Longair, M., Pietzsch, T., et al. (2012). Fiji: an open-source platform for biological-image analysis. *Nat. Methods* 9, 676–682. doi: 10.1038/nmeth.2019

Schotland, J. L., Shupliakov, O., Grillner, S., and Brodin, L. (1996). Synaptic and nonsynaptic monoaminergic neuron systems in the lamprey spinal cord. *J. Comp. Neurol.* 372, 229–244. doi: 10.1002/(SICI)1096-9861(19960819)372:2<229::AID-CNE6>3.0.CO;2-5

Shimizu, T., Higuchi, T., Fujii, T., Nilius, B., and Sakai, H. (2011). Bimodal effect of alkalization on the polycystin transient receptor potential channel, PKD2L1. *Pflugers Arch.* 461, 507–513. doi: 10.1007/s00424-011-0934-5

Shimizu, T., Janssens, A., Voets, T., and Nilius, B. (2009). Regulation of the murine TRPP3 channel by voltage, pH, and changes in cell volume. *Pflugers Arch.* 457, 795–807. doi: 10.1007/s00424-008-0558-6

Shin, J., Park, H. C., Topczewska, J. M., Mawdsley, D. J., and Appel, B. (2003). Neural cell fate analysis in zebrafish using olig2 BAC transgenics. *Methods Cell Sci.* 25, 7–14. doi: 10.1023/B:MICS.0000006847.09037.3a

Shin, J., Poling, J., Park, H. C., and Appel, B. (2007). Notch signaling regulates neural precursor allocation and binary neuronal fate decisions in zebrafish. *Development* 134, 191–120. doi: 10.1242/dev.001602

Srinivas, S., Watanabe, T., Lin, C. S., William, C. M., Tanabe, Y., Jessell, T. M., et al. (2001). Cre reporter strains produced by targeted insertion of EYFP and ECFP into the ROSA26 locus. *BMC Dev. Biol.* 1:4. doi: 10.1186/1471-213X-1-4

Stoeckel, M. E., Uhl-Bronner, S., Hugel, S., Veinante, P., Klein, M. J., Mutterer, J., et al. (2003). Cerebrospinal fluid-contacting neurons in the rat spinal cord, a gamma-aminobutyric acidergic system expressing the P2X2 subunit of purinergic receptors, PSA-NCAM, and GAP-43 immunoreactivities: light and electron microscopic study. *J. Comp. Neurol.* 457, 159–174. doi: 10.1002/cne.10565

Sueiro, C., Carrera, I., Molist, P., Rodriguez-Moldes, I., and Anadon, R. (2004). Distribution and development of glutamic acid decarboxylase immunoreactivity in the spinal cord of the dogfish *Scyliorhinus canicula* (elasmobranchs). *J. Comp. Neurol.* 478, 189–206. doi: 10.1002/cne.20285

Tamamaki, N., Yanagawa, Y., Tomioka, R., Miyazaki, J., Obata, K., and Kaneko, T. (2003). Green fluorescent protein expression and colocalization with calretinin, parvalbumin, and somatostatin in the GAD67-GFP knock-in mouse. *J. Comp. Neurol.* 467, 60–79. doi: 10.1002/cne.10905

Vigh, B., and Vigh-Teichmann, I. (1973). Comparative ultrastructure of the cerebrospinal fluid-contacting neurons. *Int. Rev. Cytol.* 35, 189–251. doi: 10.1016/S0074-7696(08)60355-1

Villar-Cervino, V., Holstein, G. R., Martinelli, G. P., Anadon, R., and Rodicio, M. C. (2008). Glycine-immunoreactive neurons in the developing spinal cord of the sea lamprey: comparison with the gamma-aminobutyric acidergic system. *J. Comp. Neurol.* 508, 112–130. doi: 10.1002/cne.21661

Voituron, N., Frugiere, A., Mc Kay, L. C., Romero-Granados, R., Dominguez-Del-Toro, E., Saadani-Makki, F., et al. (2011). The kreisler mutation leads to the loss of intrinsically hypoxia-activated spots in the region of the retrotrapezoid nucleus/parafacial respiratory group. *Neuroscience* 194, 95–111. doi: 10.1016/j.neuroscience.2011.07.062

Warp, E., Agarwal, G., Wyart, C., Friedmann, D., Oldfield, C. S., Conner, A., et al. (2012). Emergence of patterned activity in the developing zebrafish spinal cord. *Curr. Biol.* 22, 93–102. doi: 10.1016/j.cub.2011.12.002

Westerfield, M. (2000). *The Zebrafish Book. A Guide for the Laboratory Use of Zebrafish (Danio rerio)*. Eugene, OR: University of Oregon Press.

Wyart, C., Del Bene, F., Warp, E., Scott, E. K., Trauner, D., Baier, H., et al. (2009). Optogenetic dissection of a behavioural module in the vertebrate spinal cord. *Nature* 461, 407–410. doi: 10.1038/nature08323

Yang, L., Rastegar, S., and Strahle, U. (2010). Regulatory interactions specifying Kolmer-Agduhr interneurons. *Development* 137, 2713–2722. doi: 10.1242/dev.048470

Yeo, S. Y., and Chitnis, A. B. (2007). Jagged-mediated Notch signaling maintains proliferating neural progenitors and regulates cell diversity in the ventral spinal cord. *Proc. Natl. Acad. Sci. U.S.A.* 104, 5913–5918. doi: 10.1073/pnas.0607062104

Yulis, C. R., and Lederis, K. (1988a). Occurrence of an anterior spinal, cerebrospinal fluid-contacting, urotensin II neuronal system in various fish species. *Gen. Comp. Endocrinol.* 70, 301–311. doi: 10.1016/0016-6480(88)90150-5

Yulis, C. R., and Lederis, K. (1988b). Relationship between urotensin II- and somatostatin-immunoreactive spinal cord neurons of *Catostomus commersoni* and *Oncorhynchus kisutch* (Teleostei). *Cell Tissue Res.* 254, 539–542. doi: 10.1007/BF00226503

Conflict of Interest Statement: The authors declare that the research was conducted in the absence of any commercial or financial relationships that could be construed as a potential conflict of interest.

Received: 05 January 2014; accepted: 10 April 2014; published online: 06 May 2014.
*Citation: Djenoune L, Khabou H, Joubert F, Quan FB, Nunes Figueiredo S, Bodineau L, Del Bene F, Burcklé C, Tostivint H and Wyart C (2014) Investigation of spinal cerebrospinal fluid-contacting neurons expressing PKD2L1: evidence for a conserved system from fish to primates. Front. Neuroanat. **8**:26. doi: 10.3389/fnana.2014.00026*
This article was submitted to the journal Frontiers in Neuroanatomy.

frontiers in
NEUROANATOMY

METHODS ARTICLE
published: 11 October 2013
doi: 10.3389/fnana.2013.00033

Intravital imaging of hair-cell development and regeneration in the zebrafish

Filipe Pinto-Teixeira[1,2†], Mariana Muzzopappa[1], Jim Swoger[1,2], Alessandro Mineo[1,2], James Sharpe[1,2,3] and Hernán López-Schier[1,4]*

[1] *Centre for Genomic Regulation (CRG), Barcelona, Spain*
[2] *Universitat Pompeu Fabra (UPF), Barcelona, Spain*
[3] *Institució Catalana de Recerca i Estudis Avançats (ICREA), Barcelona, Spain*
[4] *Unit Sensory Biology and Organogenesis, Helmholtz Zentrum München, Munich, Germany*

Edited by:
Laurent Gautron, UT Southwestern Medical Center, USA

Reviewed by:
Kazuhide Asakawa, National Institute of Genetics, Japan
Mireille Montcouquiol, INSERM, France

***Correspondence:**
Hernán López-Schier, Unit Sensory Biology and Organogenesis, Helmholtz Zentrum München, Ingolstaedter Landstrasse 1, 85764 Munich, Germany
e-mail: hernan.lopez-schier@helmholtz-muenchen.de

† Present address:
Filipe Pinto-Teixeira, Department of Biology, New York University, New York, USA

Direct videomicroscopic visualization of organ formation and regeneration *in toto* is a powerful strategy to study cellular processes that often cannot be replicated *in vitro*. Intravital imaging aims at quantifying changes in tissue architecture or subcellular organization over time during organ development, regeneration or degeneration. A general feature of this approach is its reliance on the optical isolation of defined cell types in the whole animals by transgenic expression of fluorescent markers. Here we describe a simple and robust method to analyze sensory hair-cell development and regeneration in the zebrafish lateral line by high-resolution intravital imaging using laser-scanning confocal microscopy (LSCM) and selective plane illumination microscopy (SPIM). The main advantage of studying hair-cell regeneration in the lateral line is that it occurs throughout the life of the animal, which allows its study in the most natural context. We detail protocols to achieve continuous videomicroscopy for up to 68 hours, enabling direct observation of cellular behavior, which can provide a sensitive assay for the quantitative classification of cellular phenotypes and cell-lineage reconstruction. Modifications to this protocol should facilitate pharmacogenetic assays to identify or validate otoprotective or reparative drugs for future clinical strategies aimed at preserving aural function in humans.

Keywords: hair cells, auditory, zebrafish, intravital fluorescence microscopy, regeneration, lateral line system, development

INTRODUCTION

Direct *in toto* visualization of organ formation and repair is a powerful strategy to study cellular processes that often cannot be replicated *in vitro* (Megason and Fraser, 2007; Pittet and Weissleder, 2011; Rompolas et al., 2012). A general feature of high-resolution intravital imaging is its reliance on the optical isolation of cells or sub-cellular structures in the whole animal by the transgenic expression of fluorescent markers (Faucherre et al., 2010; Dempsey et al., 2012). The formation of specialized organs during embryonic development involves the activation of genetic programs that determine cell fate, cell proliferation, and the assembly of tissues into functional organs. Animals spend the overwhelming majority of their lives as adults, when many organs are under acute or chronic physical or toxicological stress and can sustain damage. Most organisms have evolved two general strategies to maintain organ function throughout life. The most prevalent is protection by isolating organs into body cavities. Although effective, isolation is not optimal for sensory systems because their external components need to be exposed to the environment to fulfill their function. Therefore, organisms have evolved a second strategy to maintain sensory abilities over long periods: regeneration and repair. Paradoxically, however, mammals have lost the capacity to repair the sensory elements of the inner ear (Corwin and Oberholtzer, 1997; Kelley, 2003; Kros, 2007; Edge and Chen, 2008; Brigande and Heller, 2009; Rubel et al., 2013). If damaged by infection, drugs or stress, the ear's mechanosensory hair cells cannot be replaced, leading to irreversible loss of hearing and balance (Collado et al., 2008). The resulting sensory dysfunction develops into a major handicap that dramatically decreases the quality of life of the affected individuals. Deafness often causes acute communication difficulties, which represents a significant socioeconomic problem considering that it afflicts more than 10% of the population in industrialized countries (Magilvy, 1985). According to the British charity "Deafness Research UK," 1 in 7 people in the United Kingdom suffer from hearing impairment. Notwithstanding the biological and clinical interest of deafness and balance disorders, the mechanisms that underlie hair-cell homeostasis remain poorly understood because of the inherent difficulty to study the inner ear in animals after birth. By contrast, aquatic vertebrates such as the zebrafish have a superficial and anatomically simple "hearing" system called lateral line (**Figures 1A–C**) (Raible and Kruse, 2000; Ghysen and Dambly-Chaudiere, 2007; Behra et al., 2009). This mechanosensory system detects hydromechanical variations around the animal body and serves to command behaviors such as schooling, rheotaxia, prey capture, and obstacle and predator avoidance (Dijkgraaf, 1963; Ghysen and Dambly-Chaudiere, 2007; Bleckmann and Zelick, 2009). Fishes of lotic and lentic freshwater ecosystems have a well-developed superficial lateral-line system, whose functional units

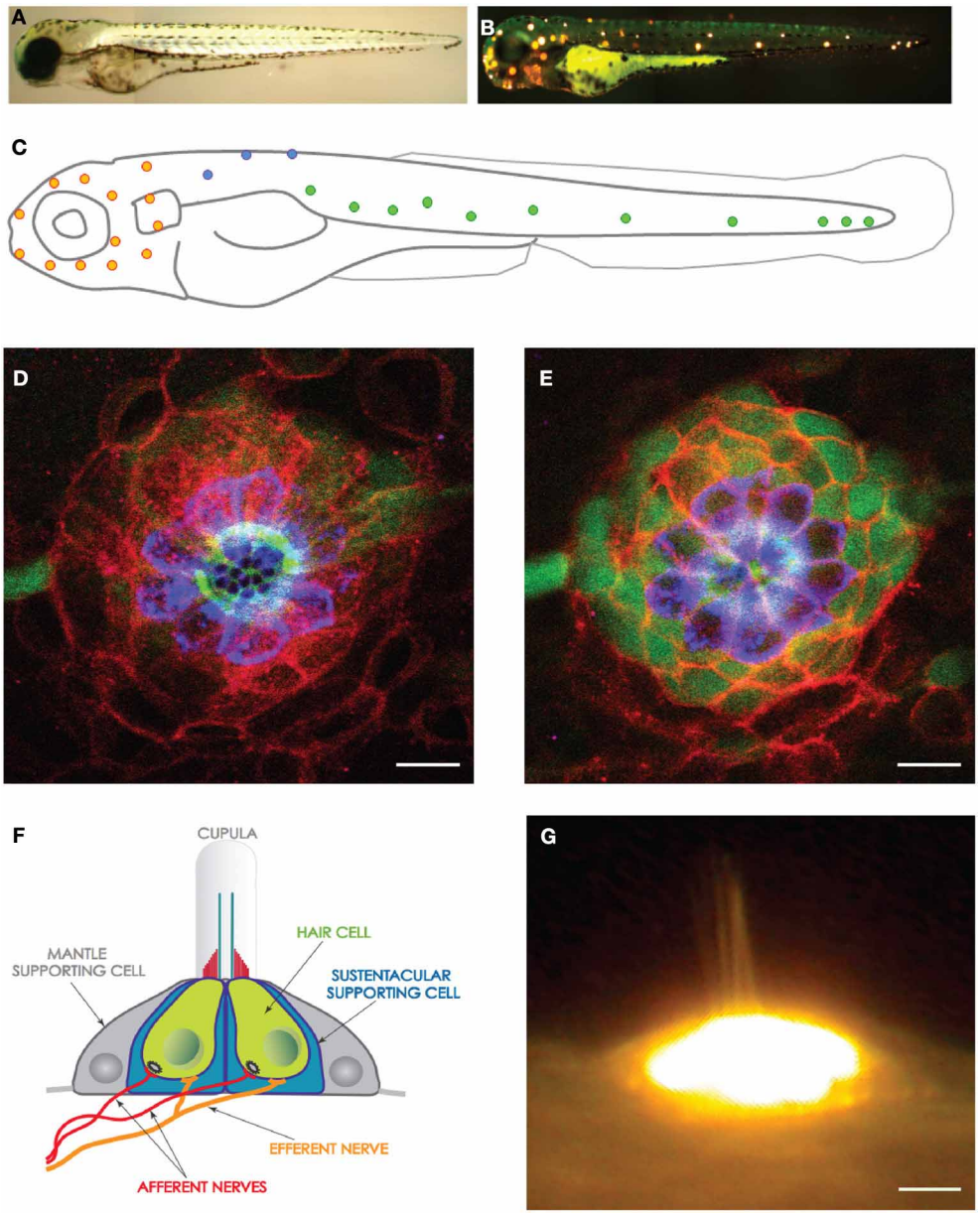

FIGURE 1 | The lateral line and neuromasts in the zebrafish larva. (A) Low magnification view of a zebrafish larva under transmitted light. **(B)** Hair cells in the lateral line were labeled with the fluorescent vital dye DiAsp (bright orange). It shows the superficial distribution of neuromasts along the anterior (head) and posterior (trunk and tail) lateral-line systems. **(C)** Schematic representation of the distribution of the neuromasts in the lateral line of a zebrafish larva. Orange highlights the anterior neuromasts, green the posterior neuromasts, and blue the dorsal neuromasts. **(D,E)** High magnification confocal image of a frontal view of a posterior neuromast revealing the hair cells (blue), supporting cells (red and green). **(F)** Schematic representation of a neuromast viewed from the side, depicting every known cell, including the neurons. **(G)** High magnification side-view image of a mature neuromast labeled with the vital dye DiAsp. Scale bars are 10μm.

are called neuromasts (**Figures 1D–G**). The superficial lateral line is very accessible to experimentation and imaging. The neuromast is a volcano-shaped epithelium that projects from the animal's body surface, into the water (**Figure 1F**). A mature neuromast is 20 μm in height and has a diameter of 50 μm. It is formed by around 60 cells, of which one third are hair cells and the remainder divided between peripheral mantle cells and central sustentacular (supporting) cells (**Figures 1D,E**). Importantly, identically to their mammalian counterparts, hair cells in the zebrafish are susceptible to ototoxicity or mechanical damage (Harris et al., 2003; Chiu et al., 2008; Behra et al., 2009; Brignull et al., 2009). However, unlike mammals, fishes can regenerate hair cells rapidly and orderly after damage (Williams and Holder, 2000; Harris et al., 2003; López-Schier and Hudspeth, 2006; Behra et al., 2009). Our group was the first to unambiguously identify resident hair-cell progenitors, and to study how their dynamic relationship with

supporting cells maintains a constant, functional organ throughout the animal's life (López-Schier and Hudspeth, 2006). Our results have revealed that hair cells in neuromast are always born sequentially and in pairs along a single axis (**Figure 2**) (López-Schier and Hudspeth, 2006). These observations allowed us to predict the compartmentalization of the neuromast epithelium. We subsequently confirmed this prediction using the SqET4 transgenic zebrafish line that identified resident hair-cell progenitors, and the SqET20 line that revealed a cellular territory where hair-cell progenitors generate at high frequencies (Wibowo et al., 2011). Thus, the detailed intravital *in vivo* analyses have unveiled two previously unknown cell types in neuromasts. Here we detail a simple, fast and inexpensive protocol to characterize hair-cell development and regeneration by *in toto* high-resolution live imaging. This protocol has been optimized during over 10 years of experience using the zebrafish and high-resolution imaging (López-Schier and St. Johnston, 2001; López-Schier et al., 2004; López-Schier and Hudspeth, 2006; López-Schier, 2010; Swoger et al., 2011; Wibowo et al., 2011). It relies on the stable expression of engineered transgenes coding for fluorescent proteins in specific cellular populations of the lateral line. The procedure only requires a small zebrafish colony and access to a Laser-Scanning Confocal Microscope (LSCM) for image acquisition (Wibowo et al., 2011). We also describe the handling and mounting of samples to enable imaging by Selective Plane Illumination Microscopy (SPIM) (Huisken et al., 2004; Greger et al., 2007; Huisken and Stainier, 2009; Swoger et al., 2011; Kaufmann et al., 2012). Finally, this approach requires a desktop computer equipped with free or inexpensive commercial software for qualitative or quantitative image analysis and rendering.

RATIONALE

Hair-cell development is likely regulated by mechanisms that are cell-type specific, and controlled by a complex activation of signaling pathways in both hair-cell progenitors and supporting cells (López-Schier, 2004). Notwithstanding its major scientific and clinical significance, the mechanisms that underlie the normal production of hair cells remain poorly understood. Studies aimed at characterizing the behavior of endogenous hair-cell progenitors should be carried out in animal model systems with accessible neuroepithelia and capable of regenerating hair cells efficiently. Pharmacological treatments that produce deafness in mammals are also lethal to hair cells in the zebrafish. Hair cells in the zebrafish lateral line begin to regenerate less than 12 h after loss, to eventually produce a complete anatomical and functional recovery of the organ in less than 72 h. Many important questions remain unanswered: What is the source of newly formed hair cells? How is the process of hair-cell regeneration controlled? How the three-dimensional architecture of the epithelium recovers? Results from experiments in several species suggest that hair cells regenerate from supporting cells by trans-differentiation. Other results indicate that supporting cells re-enter mitosis before producing new hair cells. Although supporting cell trans-differentiation may be a simple mechanism to replace damaged hair cells, supporting-cell amplification is also required because animals need to maintain the number and proportion of the different cell types over many years. Thus, cell proliferation is eventually essential for neuroepithelial homeostasis. An attractive possibility is that the neuroepithelium harbors a population of pluripotent progenitor cells dedicated to regenerate hair cells (Harris et al., 2003; Huisken et al., 2004; Rivolta et al., 2006; Oshima et al., 2009, 2010). This hypothesis has taken some impulse from a series of results suggesting the existence of stem cells in the utricle. These cells could be characterized further for potential clinical applications. Stem-cell-based therapies represent one promising avenue to repair damaged inner ears (Brigande and Heller, 2009; Chen et al., 2012; Rivolta, 2013). However, they require invasive surgical procedures and post-operative follow-up. The shortcomings of cell replacement therapy suggest that mobilizing resident progenitor cells to replace damaged tissues is a viable alternative with therapeutic potential (Mizutari et al., 2013). This protocol provides a simple and robust method to obtain information about the molecular profile, localization, and behavior of progenitor cells within a mature organ.

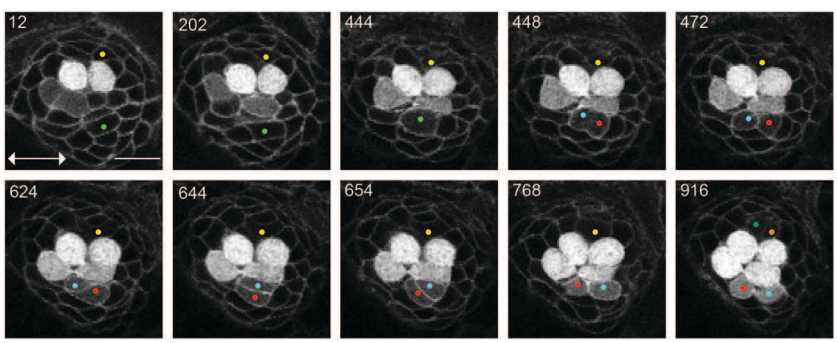

FIGURE 2 | UHCPs division and planar cell inversion. Frames from Supplementary Movie 1 at the time-points indicated A 916′ min series of confocal images of a double-transgenic Tg[Cldnb:mGFP;SqET4] regenerating neuromast. Two prospective UHCPs were identified retrospectively by playing the time series backwards and labeled with a yellow and green dot. Each UHCP eventually divides into a pair of sister hair cells, labeled in Cyan/Red and Green/Orange, respectively. On minute 624′ the sibling hair cells in the lower part of the neuromast begin to rotate around their contact point, eventually breaking the line of mirror symmetry. This complete inversion of the sister hair cells restores the line of mirror symmetry realigning the cells along the neuromast axis of planar polarity (double-headed arrow in the first panel). All images correspond to a single focal plane with the cells of interest in focus. Scale bar is 10 μm.

THE ZEBRAFISH AS AN EXPERIMENTAL MODEL SYSTEM

The zebrafish (*Danio rerio*) is a small tropical fish whose biology has been extensively characterized. Interesting developmental and behavioral aspects of the zebrafish have made it a favorite research organism in genetics, biomedicine, and drug discovery for the past three decades. It compares favorably with other experimental animal model systems, offering the following advantages:

- It has a rapid life cycle. Adult pairs produce thousands of progeny economically and several generations per year. This permits quantitative/statistical analyses, and facilitates the recovery of offspring carrying multiple mutations and transgenes.
- The embryo develops rapidly, externally, and is optically transparent, which enables easy visualization of organs for detailed cellular and physiological analyses (Kemp et al., 2009).
- The large-scale generation of transgenic zebrafish is technically simple, and the maintenance of large colonies for experimentation and high-throughput drug screening is feasible even in single-laboratory settings (Murphey and Zon, 2006; Detrich et al., 2011).
- Alternatively, engineered genes can be expressed transiently in the zebrafish by DNA or RNA injections or electroporation, facilitating, and speeding functional studies by gain- or loss-of-gene function. A trained person can inject up to 500 eggs, or generate up to three transgenic lines per day (Xu et al., 2008).
- Unlike *Drosophila, C.elegans* or the mouse, many organs in the zebrafish regenerate after damage.
- Because all vertebrates share many of the cellular and physiological mechanisms that underlie how organs develop and perform, the zebrafish provides a highly relevant model to human biology and disease, as has been demonstrated by numerous studies (Santoriello and Zon, 2012).
- The lateral line organ combines the three-dimensional organization of a sensory receptor with the possibility of systematic experimental intervention, offering a simple model whose dynamics can be visualized *in vivo* over long periods and under controlled physiological conditions.
- The extensive collection of reagents for experimentation has significantly improved the capabilities of this system (Moens et al., 2008; Faucherre and López-Schier, 2011; Kettleborough et al., 2011), and reinforced the general belief that the lateral line is an ideal model to study the basic mechanisms that control sensory-organ development and regeneration.

METHODS

HANDLING OF THE ZEBRAFISH

The success of these procedures crucially depends on the proper handling and mounting of the zebrafish embryo or larva. Sample handling needs to be practiced to ensure animal survival. We routinely monitor the animal's vital signs after imaging (heart beating and blood flow). If samples will be further processed for immunohistochemistry staining after live imaging, they should be fixed as soon as possible after imaging ceases.

OBTAINING ZEBRAFISH LARVAE FOR EXPERIMENTS

Zebrafish are maintained in E3 Embryo medium. To make an E3 medium stock solution (60×) dissolve 172 g NaCl, 7.6 g KCl, 29 g $CaCl_2.2H_2O$ and 49 g $MgSO_47H_2O$ in 10 L of distilled H_2O (dH_2O). To avoid water spoilage add methylene blue (Sigma-Aldrich; cat. No.M4159). Make a methylene blue stock solution of 4 $mgml^{-1}$ in water. For a final working solution, add 70 µl of stock solution to 1 L of E3 Embryo medium. Fish used were maintained under standardized conditions and experiments were performed in accordance with protocols approved by the PRBB Ethical Committee of Animal Experimentation.

NECESSARY EQUIPMENT FOR RAISING FISH AND COLLECTING EGGS

Divisible acrylic tanks for zebrafish breeding and plastic strainers for egg or larva collection. Incubator set at 28.5°C to maintain embryos and larvae at constant temperature. An epifluorescence-equipped stereomicroscope for initial screening of experimental animals. In addition, disposable 6 or 12 well culture plastic plates, Pasteur plastic pipettes will be needed.

HAIR-CELL ABLATION IN ZEBRAFISH LARVAE

A stock solution of Neomycin 500 mM (neomycin trisulphate salt hydrate, SIGMA-Aldrich N6386) should be maintained at 4°C, and diluted in E3 medium without methylene blue to a working concentration of 250 µM. The stock solution should be kept in a 1.5 ml Eppendorf tube sealed with Parafilm and saved in an Eppendorf box to minimize the risk of contamination. It is important to be cautious with the use of neomycin. Mechanosensitive hair cells, including those of humans, are extremely sensitive to aminoglycosides. Neomycin is quickly absorbed by the body surface, therefore, gloves and protective goggles should be used during all the steps that involve the use of neomycin.

COMPONENTS FOR MOUNTING ZEBRAFISH LARVAE

To anesthesize zebrafish, prepare a stock solution of tricaine (MS222 or MESAB: 3-amino benzoic acidethylester) at 25×. Dissolve 0.4 g Tricaine, in 97.9 mL of dH_2O. Adjust the pH to ∼7 by adding 9.1 mL of 1 M Tris (pH 9). Store at 4°C. Make one percent low–melting point agarose in E3 to mount embryos for observation. In an Erlenmeyer flask make 50 ml of 1% LMP agarose 436 (Bio Rad, Cat. 161-3112) by adding 500 mg of agarose to 50 ml 437 of E3 medium without methylene blue. Heat the solution for 2 min in a microwave at maximum power to dissolve the agarose. If small aggregates are still found agitate the solution and heat up to obtain a clear solution. The solution will be very hot. Use a temperature protective gear to handle the Erlenmeyer flask at this stage. Transfer the solution to a 50 ml Falcon tube and store in a water bath at 42°C. Let the agarose cool down to 42°C before using it. This agarose can be used for one week. For confocal microscopy, hair loops are appropriate to manipulate the zebrafish larvae on cover-glass-bottomed culture dishes. For SPIM imaging, 100/200 µL glass capillaries (cat. no. 701910) and piston rods (cat. no. 701936) from Brand GmbH.

OBSERVATION AND ANALYSIS OF HAIR-CELL DEVELOPMENT AND REGENERATION

A fluorescence stereomicroscope equipped with an external light source for fluorescence excitation and appropriate filter set for GFP and RFP detection can be used for screening the samples to be imaged.

For confocal imaging, a microscope equipped with lasers for GFP (488 nm), RFP (543 nm) excitation and preferentially with a motorized stage to allow multi-position imaging.

For SPIM imaging, the microscope can be equipped with lasers operating at 488 nm (for excitation of GFP) and 543 nm (RFP), and the appropriate emission filters. Excitation power and wavelength are computer-controlled via an Acousto-Optic Tunable Filter (AOTF); the filter wheel for changing emission filters is also computer controlled. Typically water-dipping objective lenses are used for detection, ranging from 20 × /0.5 to 63 × /0.9, depending on the desired resolution and field of view. Illumination is with air objectives, e.g., a 10 ×/0.3. Detection is performed with a CCD or sCMOS camera (in this work we assume a Hamamatsu Orca-ER CCD camera). The sample is mounted on a computer-controlled mechanical stage with 3 spatial and one rotational degrees of freedom (the rotation axis is perpendicular to the illumination and detection axes). See Greger et al. (2007) for a technical description of a SPIM microscope similar to the one used in the present work (Greger et al., 2007). We routinely use the public domain ImageJ/Fiji software for image processing.

IDENTIFICATION OF TRANSGENIC EXPRESSION OF FLUORESCENT PROTEINS IN THE ZEBRAFISH LATERAL LINE

Collect the zebrafish larvae to be screened in a Petri dish with 50 ml of methylene-blue-free E3 medium with tricaine (250 μM). Screen and select embryos with a stereomicroscope using the appropriate light filter and select those larvae expressing fluorescence in the lateral line neuromasts. If the larvae to be analysed are younger than 3 dpf they have to be dechorionated. We do not recommend dechorionation with pronase as this decreases the survival rate. We favour manual dechorionation. This can easily be achieved with the help of a pair of microsurgical forceps. Hold the chorion with one forceps and with the other forceps grip the chorion and tear it. It is important to minimize the exposure of the larvae to tricaine. If the larvae are not to be treated with neomycin for the next hours transfer them to fresh methylene-blue-free E3 medium without tricaine.

NEOMYCIN INDUCED HAIR CELL ABLATION

This step takes about 3 h. In a 100 ml Erlenmeyer flask prepare 50 ml of E3 medium without methylene blue with neomycin (250 μM) by adding 250 μl of the neomycin stock to 50 ml of E3 medium. Carefully agitate the Erlenmeyer to mix and transfer the neomycin solution from the Erlenmeyer to a 50 ml Petri dish. Additionally prepare one Petri dish with 50 ml of E3 medium without methylene blue. Collect the larvae in a 50 ml Petri dish with E3 medium without methylene blue with tricaine (250 μM). A critical step is to keep the larvae in E3 medium with methylene blue until the desired developmental stage and transfer them to methylene-blue-free E3 medium at least 2 h before the neomycin treatment, as methylene blue affects the survival of the larvae upon treatment. With the help of a plastic Pasteur pipette transfer the larvae with the minimum amount of medium to the Petri dish with the neomycin solution. Carefully disperse the larvae in the plate by gently squeeze the Pasteur pipette. To collect the larvae hold the Petri dish on the bench and move it horizontally in very small circles until the larvae gather centripetally in the center of the petri dish. Another possibility is to use the Pasteur pipette to promote flow of the medium. This can be done by placing the tip of the pipette parallel and next to the inside border of the petri dish and gently squeeze. With the help of a clean plastic Pasteur pipette transfer the larvae with the minimal amount of medium to the previously prepared petri dish with 50 ml of E3 medium without methylene blue and let the larvae recover for at least 2 h. Some larvae will eventually die due to the neomycin treatment. These larvae should be removed from the medium.

Mechanosensitive hair cells, including those from humans, are extremely sensitive to neomycin. Use gloves throughout these steps.

MOUNTING OF LARVAE FOR LIVE CONFOCAL IMAGING

In a 1.5 ml Eppendorf tube prepare 1 ml of 1% LMP agarose with tricaine by adding 60 μl of the tricaine stock solution to 940 μl of the agarose solution. Keep the Eppendorf at 37°C in a bench thermomixer. Transfer the zebrafish larvae directly to a coverglass-bottomed culture dish. With a plastic Pasteur pipette release a drop of the agarose solution to cover the larvae. Carefully rotate

HOW TO IDENTIFY TRANSGENIC LARVAE USED IN THIS STUDY

Tg[SqEt4] fish	The SeqEt4 line strongly expresses the green-fluorescent protein (GFP) in the cytoplasm of neuromast hair cell, and weakly in the unipotent hair-cell progenitors (UHCPs) (Parinov et al., 2004; Choo et al., 2006; Wibowo et al., 2011). GFP is also weakly expressed in the skin (periderm), which makes the identification of SqEt4 larvae straightforward by fluorescent light under low-magnification stereomicroscopy.
Tg[Cldnb:mEGFP; SqET4] fish	In the *Tg[Cldnb:mEGFP*] a membrane-localized green-fluorescent protein (EGFP) is expressed in all the cells of the migrating primordium, and in all the cells of the neuromasts and interneuromast cells. In this line mEGFP is also strongly expressed in the olfactory placode (Haas and Gilmour, 2006). The identification of *Tg[Cldnb:mEGFP; SqET4]* larva should be done by the strong expression of GFP in the olfactory placode and the weak expression of GFP in the fish skin.
Tg[Cldnb:mGFP; atho1a:tdTomato] Histone2B.GFP cRNA injected fish	The *Tg[atho1a:tdTomato*] line expresses a red-fluorescent protein in the cells of the neuromast that activate atho1a expression, including UHCPs and young hair cells (Wibowo et al., 2011). *Histone2B.GFP* marks every nucleus in the embryo and larva.

the larvae with a hair loop so that the desired side to image faces the bottom side of the holder. The larvae should be mounted all in the same orientation and in the center of the dish (**Figure 3**). This step is essential if the imaging needs to be done at the early stages of neuromast development. No more than 3 larvae should be mounted per culture dish to maximize survival rate. Wait for a few minutes to let the agarose solidify (∼35 min at room temperature). When solidified, the agarose becomes a translucent and hard gel, which can be tested by touching it with the hair loop. At this stage carefully fill the dish with 2.5 ml of E3 medium without methylene blue and tricaine (250 μM). Cover the dish with its lid.

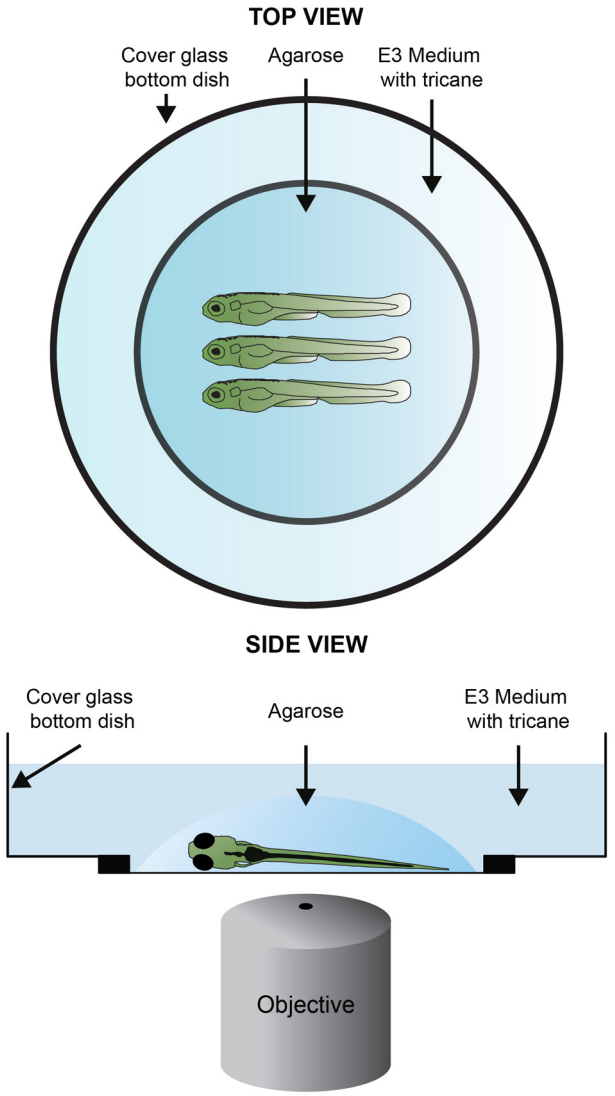

FIGURE 3 | Sample mounting for confocal imagin. One to four larvae are, laterally and equally oriented, placed in the center of a cover glass bottom dish. One drop or two of 1% LMP (low–melting point) agarose in E3 are added covering the larvae. If needed readjust the position of the larvae using an embryo loop. Once the agarose solidifies, the embryos are covered with methylene-blue-free E3 medium containing tricaine and the lid is placed on top of the dish.

MOUNTING OF LARVAE FOR LIVE SPIM IMAGING

In a 1.5 ml Eppendorf tube prepare 1 ml of 1% LMP agarose with tricaine by adding 60 μl of the tricaine stock solution to 940 μl of the agarose solution. Keep the Eppendorf at 37°C in a bench thermomixer. Prepare a p20 pipette with a yellow tip by cutting 0.5 cm from the end, so that the hole is big enough for the larvae to enter. Place the capillary on the surface of the liquid agarose and pull the plunger back until the capillary is filled with 1 cm of agarose. (**Figure 4**). Immediately take the anesthetized larvae in E3 medium with the p20 pipette and carefully inject it in the capillary with the minimal amount of liquid that is possible. Lay the capillary horizontal for a few minutes to let the agarose solidify (10 min at room temperature). Mount the capillary in the SPIM device and fill the sample chamber with methylene-blue-free E3 medium with tricane.

IMAGING SETUP FOR CONFOCAL MICROSCOPY

This step takes about 1 h. To minimize photobleaching, evaporation of the medium and "burning" the larvae, the lasers should be set to the lowest settings that allow a sharp visualization of the neuromasts. As a guideline, in a Leica SP5 system laser configuration window set the Argon laser power to 30%. In the laser power adjustment window located in the beam path screen set the laser power intensity between 13% and 19%. Place the dish covered with its lid in the appropriate support. Place the dish so that the larvae are horizontally aligned in the computer acquisition screen. Locate the neuromast with a low magnification objective (20×). Use the microscope oculars to screen the larvae and identify potential neuromasts of interest. Save their location in the software location panel. From this moment, it is crucial not to touch the dish. A typical experiment allows the imaging of 4 neuromasts with a 2-min acquisition time. We recommend to save the location of 8–10 neuromasts at this pre-screening stage.

NEUROMAST IDENTIFICATION

The identification of a neuromast in the *Tg[SeqEt4]* upon the neomycin treatment, can typically be done by the presence 1–4 hair cells (**Figure 5**). These correspond to hair cells that were not mature during the treatment, and were therefore insensible to neomycin. During lateral line development, when a neuromast is deposited a UHCP is typically dividing giving rise to two hair cells. In both cases the presence of these hair cells makes the identification of the neuromasts easier, even with a 20× objective. However, if the researcher wishes to image neuromasts where no hair cells are present, the screening has to be done using a 40× objective. In this case favor the use of *Tg[Cldnb:mGFP; SqET4]* larvae where neuromast identification can be easily done by the expression of *Tg[Cldnb:mGFP]*. The identification of neuromasts without hair cells during regeneration in the *Tg[SeqEt4]* is significantly more difficult. In this case the neuromast has to be identified using bright field light. As a guideline, neuromasts are typically located at the somite boundaries, in the middle of the myoseptum where the chevron shifts orientation (**Figure 5**). If the researcher wants to image the first pair of hair cells being produced it is necessary to start the time series when a neuromast is being deposited. The researcher

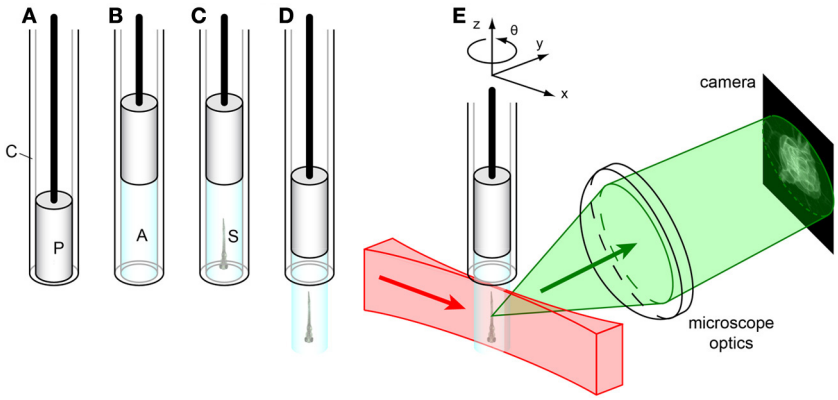

FIGURE 4 | Sample mounting for SPIM imaging. (A) Glass capillary (C) with plunger (P). **(B)** The plunger is pulled back, drawing liquid agarose (A, cyan) into the capillary. **(C)** Before the agarose solidifies, the sample (S) is carefully injected into the liquid agarose in the capillary by using a p20-pipette and a yellow tip cut in the end. **(D)** After the agarose solidifies, the plunger is pushed down, extruding the agarose plug containing the sample from the capillary. **(E)** The sample is mounted on a *xyz*θ positioning stage in the SPIM. The laser light sheet (red) illuminates the sample along the *x*-axis, and the detected light (green) is collected orthogonally (along the *y*-axis) by the microscope optics to form an image on the camera.

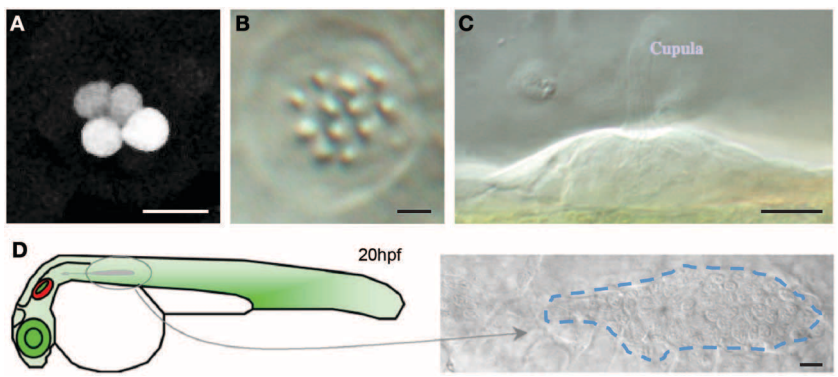

FIGURE 5 | Neuromast identification (A) ***Tg[SeqEt4]*** **upon neomycin treatment, typically 1–4 hair cells can be found in the neuromasts. (B,C)** Top **(B)** and lateral **(C)** brightfield view of a neuromast. **(D)** Scheme depicting primordium migration in a 20 hpf larvae and top brightfield view of a migrating primordium, identifiable as a group of ∼100 cells just under the epidermis. Scale bars are 10 μm.

should then identify the migrating primordium, which is easily identifiable as a group of ∼100 cells just under the epidermis (**Figure 5**).

Change to a higher magnification lens (40×). For long imaging sessions an Oil Immersion objective must be used to avoid evaporation. Adjust the pixel configuration to 512 × 1024. If imaging has to be done at the early stages of neuromast development it is essential that larvae are positioned with the lateral line aligned along the long axis of the field of view, because the neuromasts are still being deposited and can move significantly during the first hours of the time lapse. Proper orientation of the lateral line avoids having the neuromasts moving out of the field of view as they are deposited. Using the previously saved locations screen the samples and identify the neuromasts you want to image. Delete undesired locations. A typical experiment allows the simultaneous imaging of 4 neuromasts.

Adjust the Z-stack for the first location. Use existing hair cells or *Tg[Cldnb:mGFP]* expression to identify the Z-stack limits. Set up the Z-stack so that it contains the entire extent of the neuromast. The Z-stack should start on the tip of the hair cells and end in the bottom part of the neuromast. As default use a step size of 2 μm. If using the *Tg[Cldnb:mGFP]* with the purpose of cell tracking do not use a step size bigger than 2 μm. Because hair cells develop/regenerate the neuromast assumes its typical volcano shape and its volume changes as it grows in size. This, and the continuous development of the larvae, might originate movement of the region of interest out of the Z-stack boundaries during data acquisition. To avoid this add an extra 2 μm to the boundary that sets the beginning of the stack and 5 μm to the boundary that sets the end of the stack on the bottom of the neuromast/hair-cells. If the system does not allow specific Z-stacks for individual positions use as general stack boundaries the tip of the hair cells/neuromast that is closest to the objective and

the bottom of the neuromast/hair-cell that is furthest away from the objective. If imaging a *Tg[SeqEt4]* larvae where no hair cells are present use the skin of the animal as a reference to set the beginning boundary and from there set a ∼20 μm stack. Adjust the position of the neuromast to the center of the field of view and resave the position with the new settings. Repeat this procedure for each position to be imaged.

Adjust the Gain settings. To visualize UHCP's that weakly express GFP, set up the gain so that the peak GFP signal from existing hair cells is just above the saturation threshold. If imaging neuromasts without hair cells use hair cells of another neuromast in the sample as a reference. Activate the Bidirectional Scanning option to double the scanning speed, run a trial scan and judge the quality of the images. Adjust the acquisition time and length according to the needs. If the acquisition time is less than the total time between the start of consecutive time-points, it might be ideal to apply an increased number of averaging passes to improve image quality. For live imaging it is always recommended to use an average between lines to avoid any image disturbance due to movement of the tissue. Save the LIF file and then save each time-lapse as individual TIFF series with the name "STACKNAME_STACK TIFFS." Create a logbook with the following details of each time lapse: Transgenic line used, duration of time lapse, Z-stack step size, Z-stack number of steps.

IMAGING SETUP FOR SPIM

The primary advantage for live-sample imaging that SPIM has over confocal microscopy is the reduced photo-damage of the sample. In confocal microscopy, for each plane that is imaged in the sample the entire volume is illuminated, and sectioning is achieved by rejecting out-of-focus fluorescent emission with a confocal pinhole. In contrast, in SPIM only the in-focus plane of the sample is illuminated, so no out-of-focus light is generated and all of the emitted fluorescence can be used. This means that SPIM provides more information per unit of exposure of the sample. One can therefore achieve higher signal-to-noise ratios in SPIM than would be possible in confocal imaging without excessive photo-bleaching or damage. Similarly, because of the lower photo-toxicity, with SPIM one can image more often and over longer periods of time.

The following steps assume a custom-built SPIM instrument similar to that described in Greger et al. (2007). Although SPIM induces substantially less photo-damage than confocal imaging, it is still advisable to minimize over-exposure of the sample. One typically begins with the camera gain set to maximum and the laser power ∼10% of maximum. If the resulting signal-to-noise ratio is insufficient, the gain can be reduced and/or the laser power increased. Before imaging, align the SPIM so that the light sheet coincides with the focal plane of the detection arm, and adjust the light sheet so that it is as narrow as possible, but of uniform thickness over the camera's field of view. In our custom-built SPIM, this is done by adjusting a gimble mirror and adjustable slit that were built into the illumination path for this purpose. However, the procedure will vary between different implementations of SPIMs. Insert the sample with the region of interest to be imaged facing approximately toward the detection objective lens. See Swoger et al. (2011) for a discussion of how to optimally orient the sample. Using transmission contrast, try to center the approximate region of interest in the field of view of the camera. Depending on the developmental stage of the neuromasts, this may not be possible in transmission, but at a minimum it should be possible to find the myoseptum. This will save time and exposure of the sample when working in fluorescence. Switching to fluorescence contrast, use the sample translation stage to locate and center a neuromast in the field of view. Determine the limits of the axial scanning as described for confocal imaging. Typical slice spacing is 1–2 μm. Save the positioning parameters to define the scan for that neuromast. Translate the embryo to locate another neuromast and repeat these procedures until about 4 scans have been defined. The exact number that can be done will depend on the number of slices in each stack and the maximum time between repeated stack acquisitions. Set parameters for each desired channel: emission filter, laser wavelength and intensity, and camera gain and exposure. Multiple channels can be acquired in plane-interlaced mode. The parameters for each channel should be selected to optimize image quality while imaging a typical neuromast "live." Set the timing parameters: temporal spacing of the sequential acquisitions, Δt, (typically 2–5 min) and total time of the experiment (anywhere from minutes to days, as desired). Δt will be limited by the time it takes to scan each neuromast and the number of neuromasts scanned. Before beginning the full time-lapse, it can be helpful to do a single scan of all of the neuromasts, in order to determine the minimum value of Δt. If this turns out to be longer than the desired Δt it will be necessary to reduce the required time by, e.g., reducing the number of neuromasts imaged. See also the "The acquisition time is too long" section under Troubleshooting, below. Choose a filename prefix and destination folder, and start the time-lapse acquisition.

During the initial 2 or 3 h of the scanning, occasionally check that the neuromasts are each still centered in their fields of view. Because the agarose is not a completely rigid gel it can relax slightly when the sample is first put into the microscope, resulting in a shift of the region(s) of interest. This is especially important when imaging freshly deposited neuromasts, because these can still move relative to the surrounding tissue even if the agarose is stable. Any drifts can be corrected "on-the-fly" by updating the position parameters in the software user interface.

DATA PROCESSING

Open the TIFF series in ImageJ/Fiji. Convert stack to Image5D using the Image5D Plugin. When requested use "Z" for 3rd dimension and "Time" for 4th dimension. Fill in the details of the time lapse according to your log book. Project the Z-stack to a single plane using the project Z-stack option from the Image5D plugin. To add a time counter, use the Time stamper plugin. Fill in the details of the time lapse according to your log book. Save the file as a TIFF file. To make a movie save the file as AVI and choose an appropriate frame rate for your needs. As a reference a 12 h long time lapse with an acquisition time of 2 min takes 36 s to play with a speed of 10 frames per second. The timing of data processing ranges from ∼15 min to 6 h per dataset.

IF PROCESSING A DATA SET OBTAINED USING *Tg[Cldnb:mGFP; SqET4]* WITH THE PURPOSE OF CELL TRACKING

Open the TIFF series in ImageJ/Fiji and reverse the stack using the reverse tool in Image/Stacks/Tools. Save the LIF file as Image Sequence in a designated folder with the name "STACKNAME_Reversed STACK TIFFS." It is crucial to tick the option use slice labels as file names. You have just inverted the stack so that the last time point of the acquired data is now the first to be displayed and the first time point is the last to be displayed. CRUCIAL! Remove the scale of the stack in Analyze/Set Scale. Convert stack to Image5D using the Image5D Plugin. When requested, use "Z" for 3rd dimension and "Time" for 4th dimension. Fill in the details of the time lapse according to your log book. Open the MtrackJ plugin. In the displaying menu tick the option "Display only track points at current time" and reduce the "track width" to 0. Identify the cell(s) to be tracked. Press ADD in the MtrackJ panel and with the mouse cursor over the cell of interest press the mouse button. The program will save the details (XYZT coordinates) of the selection and move to the next time index after adding the point. If the selection is no longer visible on the current Z-axis use the Z-axis scroll bar in the Image5D window to relocate the region of interest. Repeat these steps until the end of the time lapse. Save the tracking using the saving function In the MtrackJ control panel. In the MtrackJ control panel press the Measure Button. Observe that the measurement window shows for each time point the details of the selection (XYZT coordinates). Save the measurement results as an excel file. If more cells will be tracked, restart MtrackJ to clear the memory, go to the first image of the stack and identify the cell to be tracked. Repeat the described procedure for each desired tracking.

Open the folder "STACKNAME_Reversed STACK TIFFS" where the stacks were saved as an Image sequence. Observe that each file name contains a reference to the time point and a Z coordinate. Using the details of the selection (XYZT coordinates) in the excel file select for each time point the file corresponding to the Z coordinate of the selection. If tracking more than one cell use only the Z coordinates of one of the cells for the selection. The selected files should be copied to a new folder named "STACKNAME_Z_SELECTION." You have just created a time lapse of the dataset that follows the cell(s) of interest. Open the files in "STACKNAME_Z_SELECTION" as image sequence in ImageJ. Open MtrackJ. Load the previous saved tracking results. To show the tracks along all time points, in the MtrackJ control panel Displaying options select a Track width size of 3 pixels. If do not want the number of each MtrackJ point to be shown in the MtrackJ control panel under the section Displaying/Font size choose 0 pixels. Crop the time lapse to the region of interest. For this use the rectangular selection tool to define the region of interest and then use the function crop in Image/Crop. Reverse the reversed time lapse using the reverse tool in Image/Stacks/Tools. You have just inverted the time lapse so that the first time point of the acquired data is now the first to be displayed and the last time point is the last to be displayed. To add a time counter, use the Time stamper plugin. Fill in the details of the time lapse according to your log book. This is the final TIFF file. Save it with the appropriate name. To make a movie from the file save it as an AVI and choose an appropriate frame rate for your needs. As a reference a 12 h long time lapse with an acquisition time of 2 min takes 36 s to play with a speed of 10 frames per second (**Figures 3**, **6**).

TROUBLESHOOTING

THE ACQUISITION TIME IS TOO LONG

The acquisition time can be reduced by:

(1) Reducing the amount of neuromasts imaged.
(2) Increasing the Zstack step size.
(3) Reducing the amount of line averaging passes.
(4) Acquiring more than one neuromast in the same microscopy field.

THE FISH DIE DURING IMAGE ACQUISITION

(1) Check the concentration of the anesthetic and eventually reduce it to a minimum of 0.7X
(2) Laser power is too high and you are "frying" the fish. Reduce the intensity of the lasers.
(3) Too many larvae in the dish. Reduce the number of larvae to be imaged.

THE DATA SET DOES NOT OPEN IN IMAGE J

If using a 32 bits operating system, the maximum amount of memory that can be allocated in ImageJ is 1.7 GB. By default, ImageJ sets the memory limit to 2/3 of physical memory (640 MB maximum) the first time it is run. Use the *Edit* > *Options* > *Memory* command to make more than the default amount of memory available to ImageJ. Note that setting the "Maximum Memory" value to more than about 75% of real RAM may result in poor performance due to virtual memory "thrashing." Make sure the to tick the option "Use virtual stack," which only reads one image plane into memory at a time, which is essential to open datasets that are too large. If after following the ImageJ Wiki instructions you still cannot open the data set:

(1) Before saving the original tiff files use the cropping tool in the Leica Software to reduce the size of the image to the region of interest.
(2) If the data set is still too big to open in ImageJ divide the TIFF series in batches of a maximum size of 1.7 GB. Save each batch in an individual folder with the name "STACKNAME_STACK TIFFS_BATCH_XX," where XX is the number of the batch. Do not separate the data of one time point between batches.
(3) Perform the data processing of each batch as described previously. Save each new file as "STACKNAME_BATCH_XX," where XX is the number of the batch in a folder named "STACKNAME_BATCHES."
(4) Open the files in "STACKNAME_BATCHES" as an image sequence in ImageJ. This is the final TIFF file. Save it with the appropriate name.

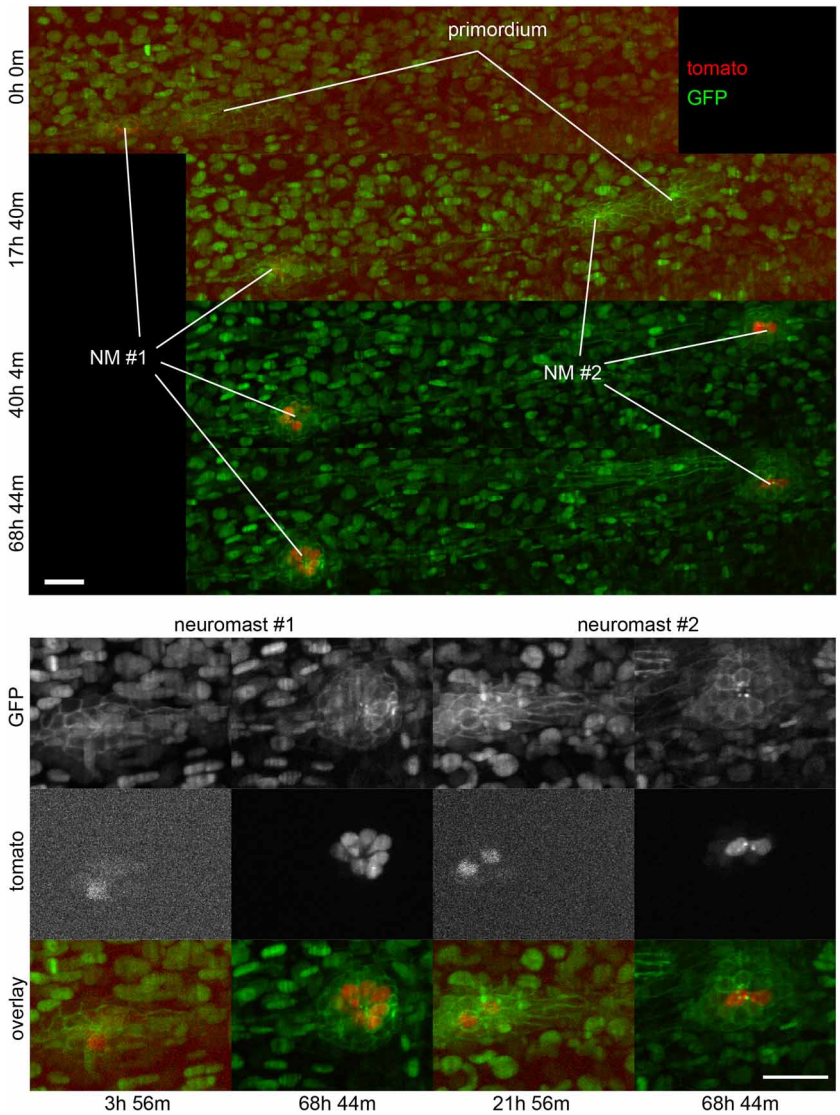

FIGURE 6 | Three-dimensional imaging by SPIM. Frames from Supplementary Movie 2 at the time-points indicated. **Top**, full field of view. **Bottom**, selected regions of interest containing neuromasts 1 and 2. A 2-channel 68 h time-lapse recorded using SPIM, showing the deposition of 2 neuromasts and their subsequent development. Ath1 (showed in red) is expressed in hair-cells and can be detected in hair-cell progenitors a few hours before the neuromasts are deposited. ath1:RFP is observed later in dividing, young and mature hair-cells. All the cell nuclei are stained in green (H2B:GFP RNA) and the lateral line system is highlighted in green with the Cldnb:mEGFP reporter. All images are maximum-value projections along the detection axis. The brightness of each image has been normalized independently, so that the tdTomato fluorescence at early time-points is visible. Scale bars are 25 μm.

ANTICIPATED RESULTS AND CONCLUDING REMARKS

ADVANTAGES AND LIMITATIONS OF INTRAVITAL IMAGING IN THE ZEBRAFISH LATERAL LINE

Key advantages:

- The main advantage of using live imaging in whole living zebrafish to study hair-cell regeneration in the lateral line is the possibility of following every cell over very long periods at very high resolution in the normal cellular environment.
- Alterations of gene function by targeted mutagenesis or transgene expression in the zebrafish enables the easy study of gene function.
- Hair-cell ablation with aminoglycoside drugs is simple, effective, and does not cause unnecessary stress to the animals during treatments because there is no need for injections or anesthesia. Hundreds of animals can be treated simultaneously.

Main limitations:

- Confocal and SPIM imaging remains relatively expensive.
- The study of a large number of zebrafish by long-term live imaging for statistical analyses is a long and tedious procedure.
- These protocols are not likely to be affective in fish older than 4 weeks. However, if older fish are necessary, imaging can be performed on neuromasts located in the animal's caudal fin.

INTRAVITAL IMAGING IN THE ZEBRAFISH LARVA

The powerful techniques available in the zebrafish render it an excellent model system to study normal physiology or disease onset and progression at the level of genes, cells, and whole organ systems. Genetically encoded fluorescent sensors are a powerful tool to visualize cellular structures dynamically *in vivo/in toto* in wild type and genetically- or pharmacologically-modified specimens. One of the most important reasons for developing an *in vivo/in toto* analysis is that it will provide a remarkably accurate and rapid assay for screening factors that control of hair-cell development and regeneration in the natural context.

OTHER APPLICATIONS OF THE PROTOCOL AND FUTURE USES

Mechanosensory hair cells serve to detect sound and to sense head movements and acceleration. Hearing and balance are complex processes that allow organisms to react appropriately to relevant environment stimuli. Because hair cells are exclusive to vertebrates, their development, function, and regeneration cannot be studied in other classical experimental model systems such as the fruit fly or the roundworm. Currently, hundreds of cell type-specific Gal4 driver lines are available for the zebrafish, making it possible to unambiguously define cell types, cell status, and to perform genetic mis-expression studies. In addition, marking cells with genetically encoded fluorescent proteins will enable the sorting of such cells after dissociation, for transcriptomic or proteomic analyses.

AUTHOR CONTRIBUTIONS

Hernán López-Schier designed the study. Filipe Pinto-Teixeira, Mariana Muzzopappa, Alessandro Mineo, and Jim Swoger performed the experiments. James Sharpe and Jim Swoger designed the SPIM system. Hernán López-Schier, Filipe Pinto-Teixeira, Mariana Muzzopappa analyzed the data. Jim Swoger, James Sharpe, Hernán López-Schier, Filipe Pinto-Teixeira, Mariana Muzzopappa participated in designing and discussing the project. Hernán López-Schier wrote the paper with assistance from Filipe Pinto-Teixeira, Jim Swoger, and Mariana Muzzopappa.

ACKNOWLEDGMENTS

We thank the generosity of S-i Higashijima, V. Korzh and D. Gilmour for supplying zebrafish lines, and A. Durán for technical help. The original research that encouraged the development of this protocol was supported by a grant from the European Research Council (ERC-2007-StG SENSORINEURAL) and by the Ministerio de Ciencia e Innovación of Spain to Hernán López-Schier. Filipe Pinto-Teixeira was supported by a fellowship from Fundação para a Ciência e Tecnologia, Portugal through the GABBA PhD program. Mariana Muzzopappa was supported by a Marie Curie fellowship.

SUPPLEMENTARY MATERIAL

The Supplementary Material for this article can be found online at: http://www.frontiersin.org/journal/10.3389/fnana.2013.00033/abstract

Supplementary Movie 1 | UHCPs division and planar cell inversion. A 916′ minute series of confocal images of a double-transgenic Tg[Cldnb:mGFP;SqET4] regenerating neuromast. Two identified, and labeled with a yellow and green dot, UHCP eventually divide into a pair of sister hair cells.

Supplementary Movie 2 | Three-dimensional imaging by SPIM. A 2-channel 68 h maximum-value projection time-lapse recorded using SPIM, showing the deposition of 2 neuromasts and their subsequent development. Ath1 (showed in red) is expressed in hair-cells and can be detected in hair-cell progenitors a few hours before the neuromasts are deposited. atho1a:tdTomato is observed later in dividing, young and mature hair-cells. All the cell nuclei are stained in green (H2B:GFP RNA) and the lateral line system is highlighted in green with the Clndnb:mGFP reporter. The brightness of each image has been normalized independently, so that the tdTomato fluorescence at early time-points is visible.

REFERENCES

Behra, M., Bradsher, J., Sougrat, R., Gallardo, V., Allende, M. L., and Burgess, S. M. (2009). Phoenix is required for mechanosensory hair cell regeneration in the zebrafish lateral line. *PLoS Genet.* 5:e1000455. doi: 10.1371/journal.pgen.1000455

Bleckmann, H., and Zelick, R. (2009). Lateral line system of fish. *Integr. Zool.* 4, 13–25. doi: 10.1111/j.1749-4877.2008.00131.x

Brigande, J. V., and Heller, S. (2009). Quo vadis, hair cell regeneration? *Nat. Neurosci.* 12, 679–685. doi: 10.1038/nn.2311

Brignull, H. R., Raible, D. W., and Stone, J. S. (2009). Feathers and fins: non-mammalian models for hair cell regeneration. *Brain Res.* 1277, 12–23. doi: 10.1016/j.brainres.2009.02.028

Chen, W., Jongkamonwiwat, N., Abbas, L., Eshtan, S. J., Johnson, S. L., Kuhn, S., et al. (2012). Restoration of auditory evoked responses by human ES-cell-derived otic progenitors. *Nature* 490, 278–282. doi: 10.1038/nature11415

Chiu, L. L., Cunningham, L. L., Raible, D. W., Rubel, E. W., and Ou, H. C. (2008). Using the zebrafish lateral line to screen for ototoxicity. *J. Assoc. Res. Otolaryngol.* 9, 178–190. doi: 10.1007/s10162-008-0118-y

Choo, B. G., Kondrichin, I., Parinov, S., Emelyanov, A., Go, W., Toh, W-C., et al. (2006). Zebrafish transgenic enhancer TRAP line database (ZETRAP). *BMC Dev. Biol.* 6:5. doi: 10.1186/1471-213X-6-5

Collado, M. S., Burns, J. C., Hu, Z., and Corwin, J. T. (2008). Recent advances in hair cell regeneration research. *Curr. Opin. Otolaryngol. Head Neck Surg.* 16, 465–471. doi: 10.1097/MOO.0b013e32830f4ab5

Corwin, J. T., and Oberholtzer, J. C. (1997). Fish n' chicks: model recipes for hair-cell regeneration? *Neuron* 19, 951–954. doi: 10.1016/S0896-6273(00)80386-4

Dempsey, W. P., Fraser, S. E., and Pantazis, P. (2012). PhOTO zebrafish: a transgenic resource for *in vivo* lineage tracing during development and regeneration. *PLoS ONE* 7:e32888. doi: 10.1371/journal.pone.0032888

Detrich, H. W. 3rd., Westerfield, M., and Zon, L. I. (2011). The zebrafish. Preface. *Methods Cell Biol.* 105, xxi–xxii. doi: 10.1016/B978-0-12-381320-6.00027-8

Dijkgraaf, S. (1963). The functioning and significance of the lateral-line organs. *Biol. Rev. Camb. Phil. Soc.* 38, 51–105. doi: 10.1111/j.1469-185X.1963.tb00654.x

Edge, A. S., and Chen, Z. Y. (2008). Hair cell regeneration. *Curr. Opin. Neurobiol.* 18, 377–382. doi: 10.1016/j.conb.2008.10.001

Faucherre, A., Baudoin, J. P., Pujol-Martí, J., and López-Schier, H. (2010). Multispectral four-dimensional imaging reveals that evoked activity modulates peripheral arborization and the selection of plane-polarized targets by sensory neurons. *Development* 137, 1635–1643. doi: 10.1242/dev.047316

Faucherre, A., and López-Schier, H. (2011). Delaying Gal4-driven gene expression in the zebrafish with morpholinos and Gal80. *PLoS ONE* 6:e16587. doi: 10.1371/journal.pone.0016587

Ghysen, A., and Dambly-Chaudiere, C. (2007). The lateral line microcosmos. *Genes Dev.* 21, 2118–2130. doi: 10.1101/gad.1568407

Greger, K., Swoger, J., and Stelzer, E. H. (2007). Basic building units and

properties of a fluorescence single plane illumination microscope. *Rev. Sci. Instrum.* 78, 023705. doi: 10.1063/1.2428277

Haas, P., and Gilmour, D. (2006). Chemokine signaling mediates self-organizing tissue migration in the zebrafish lateral line. *Dev. Cell* 10, 673–680. doi: 10.1016/j.devcel.2006.02.019

Harris, J. A., Cheng, A. G., Cunningham, L. L., MacDonald, G., Raible, D. W., and Rubel, E. W. (2003). Neomycin-induced hair cell death and rapid regeneration in the lateral line of zebrafish (*Danio rerio*). *J. Assoc. Res. Otolaryngol.* 4, 219–234. doi: 10.1007/s10162-002-3022-x

Huisken, J., and Stainier, D. Y. (2009). Selective plane illumination microscopy techniques in developmental biology. *Development* 136, 1963–1975. doi: 10.1242/dev.022426

Huisken, J., Swoger, J., Del Bene, F., Wittbrodt, J., and Stelzer, E. H. (2004). Optical sectioning deep inside live embryos by selective plane illumination microscopy. *Science* 305, 1007–1009. doi: 10.1126/science.1100035

Kaufmann, A., Mickoleit, M., Weber, M., and Huisken, J. (2012). Multilayer mounting enables long-term imaging of zebrafish development in a light sheet microscope. *Development* 139, 3242–3247. doi: 10.1242/dev.082586

Kelley, M. W. (2003). Exposing the roots of hair cell regeneration in the ear. *Nat. Med.* 9, 1257–1259. doi: 10.1038/nm1003-1257

Kemp, H. A., Carmany-Rampey, A., and Moens, C. (2009). Generating chimeric zebrafish embryos by transplantation. *J. Vis. Exp.* pii:1394. doi: 10.3791/1394

Kettleborough, R. N., Bruijn, E., Eeden, F., Cuppen, E., and Stemple, D. L. (2011). High-throughput target-selected gene inactivation in zebrafish. *Methods Cell Biol.* 104, 121–127. doi: 10.1016/B978-0-12-374814-0.00006-9

Kros, C. J. (2007). How to build an inner hair cell: challenges for regeneration. *Hear. Res.* 227, 3–10. doi: 10.1016/j.heares.2006.12.005

López-Schier, H. (2004). Regeneration: did you hear the news? *Curr. Biol.* 14, R127–R128. doi: 10.1016/S0960-9822(04)00037-5

López-Schier, H. (2010). Fly fishing for collective cell migration. *Curr. Opin. Genet. Dev.* 20, 428–432. doi: 10.1016/j.gde.2010.04.006

López-Schier, H., and Hudspeth, A. J. (2006). A two-step mechanism underlies the planar polarization of regenerating sensory hair cells. *Proc. Natl. Acad. Sci. U.S.A.* 103, 18615–18620. doi: 10.1073/pnas.0608536103

López-Schier, H., and St. Johnston, D. (2001). Delta signaling from the germ line controls the proliferation and differentiation of the somatic follicle cells during Drosophila oogenesis. *Genes Dev.* 15, 1393–1405. doi: 10.1101/gad.200901

López-Schier, H., Starr, C., Kappler, J., Kollmar, R., and Hudspeth, A. J. (2004). Directional cell migration establishes the axes of planar polarity in the posterior lateral-line organ of the zebrafish. *Dev. Cell* 7, 401–412. doi: 10.1016/j.devcel.2004.07.018

Magilvy, J. K. (1985). Quality of life of hearing-impaired older women. *Nurs. Res.* 34, 140–144. doi: 10.1097/00006199-198505000-00003

Megason, S. G., and Fraser, S. E. (2007). Imaging in systems biology. *Cell* 130, 784–795. doi: 10.1016/j.cell.2007.08.031

Mizutari, K., Fujioka, M., Hosoya, M., Bramhall, N., Okano, H. J., Okano, H., et al. (2013). Notch inhibition induces cochlear hair cell regeneration and recovery of hearing after acoustic trauma. *Neuron* 77, 58–69. doi: 10.1016/j.neuron.2012.10.032

Moens, C. B., Donn, T. M., Wolf-Saxon, E. R., and Ma, T. P. (2008). Reverse genetics in zebrafish by TILLING. *Brief. Funct. Genomics Proteomics* 7, 454–459. doi: 10.1093/bfgp/eln046

Murphey, R. D., and Zon, L. I. (2006). Small molecule screening in the zebrafish. *Methods* 39, 255–261. doi: 10.1016/j.ymeth.2005.09.019

Oshima, K., Shin, K., Diensthuber, M., Peng, A. W., Ricci, A. J., and Heller, S. (2010). Mechanosensitive hair cell-like cells from embryonic and induced pluripotent stem cells. *Cell* 141, 704–716. doi: 10.1016/j.cell.2010.03.035

Oshima, K., Senn, P., and Heller, S. (2009). Isolation of sphere-forming stem cells from the mouse inner ear. *Methods Mol. Biol.* 493, 141–162. doi: 10.1007/978-1-59745-523-7_9

Parinov, S., Kondrichin, I., Korzh, V., and Emelyanov, A. (2004). Tol2 transposon-mediated enhancer trap to identify developmentally regulated zebrafish genes *in vivo*. *Dev. Dyn.* 231, 449–459. doi: 10.1002/dvdy.20157

Pittet, M. J., and Weissleder, R. (2011). Intravital imaging. *Cell* 147, 983–991. doi: 10.1016/j.cell.2011.11.004

Raible, D. W., and Kruse, G. J. (2000). Organization of the lateral line system in embryonic zebrafish. *J. Comp. Neurol.* 421, 189–198. doi: 10.1002/(SICI)1096-9861(20000529)421:2<189::AID-CNE5>3.3.CO;2-B

Rivolta, M. N. (2013). New strategies for the restoration of hearing loss: challenges and opportunities. *Br. Med. Bull.* 105, 69–84. doi: 10.1093/bmb/lds035

Rivolta, M. N., Li, H., and Heller, S. (2006). Generation of inner ear cell types from embryonic stem cells. *Methods Mol. Biol.* 330, 71–92. doi: 10.1385/1-59745-036-7:71

Rompolas, P., Deschene, E. R., Zito, G., Gonzalez, D. G., Saotome, I., Haberman, A. M., et al. (2012). Live imaging of stem cell and progeny behaviour in physiological hair-follicle regeneration. *Nature* 487, 496–499. doi: 10.1038/nature11218

Rubel, E. W., Furrer, S. A., and Stone, J. S. (2013). A brief history of hair cell regeneration research and speculations on the future. *Hear. Res.* 297, 42–51. doi: 10.1016/j.heares.2012.12.014

Santoriello, C., and Zon, L. I. (2012). Hooked! Modeling human disease in zebrafish. *J. Clin. Invest.* 122, 2337–2343. doi: 10.1172/JCI60434

Swoger, J., Muzzopappa, M., López-Schier, H., and Sharpe, J. (2011). 4D retrospective lineage tracing using SPIM for zebrafish organogenesis studies. *J. Biophotonics* 4, 122–134. doi: 10.1002/jbio.201000087

Wibowo, I., Pinto-Teixeira, F., Satou, C., Higashijima, S., and López-Schier, H. (2011). Compartmentalized Notch signaling sustains epithelial mirror symmetry. *Development* 138, 1143–1152. doi: 10.1242/dev.060566

Williams, J. A., and Holder, N. (2000). Cell turnover in neuromasts of zebrafish larvae. *Hear. Res.* 143, 171–181. doi: 10.1016/S0378-5955(00)00039-3

Xu, Q., Stemple, D., and Joubin, K. (2008). Microinjection and cell transplantation in zebrafish embryos. *Methods Mol. Biol.* 461, 513–520. doi: 10.1007/978-1-60327-483-8_35

Conflict of Interest Statement: The authors declare that the research was conducted in the absence of any commercial or financial relationships that could be construed as a potential conflict of interest.

Received: 27 July 2013; paper pending published: 08 August 2013; accepted: 17 September 2013; published online: 11 October 2013.

Citation: Pinto-Teixeira F, Muzzopappa M, Swoger J, Mineo A, Sharpe J and López-Schier H (2013) Intravital imaging of hair-cell development and regeneration in the zebrafish. Front. Neuroanat. 7:33. doi: 10.3389/fnana.2013.00033

This article was submitted to the journal Frontiers in Neuroanatomy.